CENTRO DE ASTROBIOLOGÍA
(CSIC-INTA)
Departamento de Astrofísica

UNIVERSIDAD AUTÓNOMA DE MADRID
Facultad de Ciencias
Departamento de Física Teórica

Optical and high-energy monitoring of variable sources observed with INTEGRAL/OMC

PhD dissertation submitted by

Julia Alfonso Garzón

for the degree of Doctor in Physics

Supervised by
Dr. J. Miguel Mas Hesse

Academic advisor
Dr. Carlos Eiroa de San Francisco

Madrid, April 2015

A mi abuela Luisa

Agradecimientos

En primer lugar, quiero agradecer enormemente a Miguel Mas el haberme animado para que continuara con la investigación y me diera la oportunidad de realizar esta tesis. Quiero darle las gracias por todo lo que me ha enseñado y el apoyo que me ha mostrado en todo momento. Y aparte de su labor como director de tesis, quiero expresarle mi gratitud por su cercanía y el trato que me ha brindado, que ha sido siempre inmejorable.

También quiero mostrar mi más sincero agradecimiento a Benjamín Montesinos, por toda su ayuda con el estudio de DY Aqr, por estar siempre dispuesto a ayudarme en lo que pudiera y por tener siempre una sonrisa y palabras de ánimo.

Quiero dar también las gracias a Carmen Morales, que fue la persona que me introdujo en el LAEFF y que, con mucha paciencia y amabilidad, me guió en mis primeros pasos en la investigación, enseñándome IDL y muchas cosas más.

Muchas gracias a Isabel Caballero por todos sus consejos y comentarios para la tesis, por su optimismo y por todos los ánimos y el apoyo que me ha dado. Parece que fue ayer cuando íbamos juntas a estudiar a la biblioteca...

A Celia Sánchez por su gran ayuda con *INTEGRAL* y con las binarias de rayos X y por todo el tiempo que ha dedicado a ayudarme con esta tesis.

A Andy Moya por introducirme en el mundo de las estrellas pulsantes, enseñándome casi todo lo que sé de las delta Scuti y haciendo que resultara hasta divertido.

A Albert Domingo por su ayuda con OMC, shell, etc., siempre que la he necesitado.

A Carlos Eiroa, por su labor como tutor en la universidad.

A Peter Kretschmar por sus comentarios sober la tesis y su ayuda con las Bes.

A Victoria Grinberg por las discusiones respecto a Cyg X–1.

Gracias también a Guillaume Belanger y a Tony Bird por proporcionarme las curvas de luz de IBIS.

Me gustaría agradecer también a todos mis compañeros y excompañeros del LAEFF (aunque hace tiempo que ya es el CAB), que durante todos estos años me hayan hecho sentir como en casa. No digo nada nuevo al decir que el LAEFF es el mejor sitio de trabajo en el que he estado y eso es sobre todo por la calidad de las personas.

Quiero dar las gracias especialmente a mis amigos, probablemente los que, sin saberlo, más me han ayudado a no rendirme con esta tesis. Muchas gracias por todos los momentos buenos, por estar siempre ahí y por todos vuestros ánimos.

Y por último quiero dar las gracias a mi familia por su cariño y preocupación, y por apoyarme siempre en todas mis decisiones. Y como diría mi abuela, sigo con "los astros"...

Abstract

Since the discovery of the first variable stars in the 16th century, their study has been one of the principal areas of astronomical research. During the 20th century and the beginning of the 21st, many optical photometric surveys have been carried out with the aim of understanding the physical mechanisms producing the observed variations of brightness. With the discovery of the first X-ray sources in the sky in the 60's and the development of X-ray astronomy, several X-ray observatories have been launched into space in order to study the properties of these X-ray sources at higher energies. Multiwavelength analyses are required for a better knowledge of these systems. For this reason, an optical monitoring camera was included on the X- and gamma-ray space observatory *INTEGRAL* of the European Space Agency (ESA).

In this thesis, the main results of the analysis of the optical photometric data obtained with the optical monitoring camera (OMC) on board *INTEGRAL* are presented. The major goal of this work was to classify the thousands of light curves obtained and to identify and study relevant scientific cases extracted from the large sample of data.

In its 12 years of operations, OMC has observed a very large amount of classical variable sources, including pulsating stars, eclipsing binaries, rotating stars, AGN, etc. The compilation of the first catalog of optically variable sources observed by OMC, including information on their brightness, variability, periodicity, and object type classification, is presented.

Within the sources in this catalog, a search for eclipsing binaries with one pulsating component has been carried out. One of the identified systems, DY Aqr, has been studied in detail.

On the other hand, apart from these serendipitous observations, OMC was designed to provide optical monitoring of the sources observed by the main X- and gamma-ray instruments IBIS and JEM-X on board *INTEGRAL*. For the first time, simultaneous observations of the optical and X- and gamma-ray sky over more than 12 years are presented. In this thesis, two different works including multiwavelength information provided by INTEGRAL have been performed.

In the first one the global properties of the emission of high-energy sources in different energy bands (hard X-rays, optical, IR, and MIR) have been studied. The emission from the different types of objects has been compared, looking for similarities and differences that could reveal information about the nature of their powerful sources.

The second one consists of a multiwavelength long-term variability analysis, using light curves of the *INTEGRAL* instruments IBIS, JEM-X, and OMC, as well as from other high-energy missions and optical surveys, with a temporal coverage of more than 12 years.

Resumen

Desde el descubrimiento de las primeras estrellas variables en el siglo XVI, su estudio ha sido una de las principales áreas de investigación en astronomía. Durante el siglo XX y a principios de siglo XXI, se han realizado numerosos cartografiados ópticos del cielo, con el objetivo de entender los mecanismos físicos que producen las variaciones de brillo observadas. Más recientemente, con la detección de las primeras fuentes de rayos X en los años 60 y el desarrollo de las astronomía de altas energías, fueron diseñadas varias misiones para realizar observaciones en este rango. Para entender los mecanismos que prevalecen en los objetos emisores en altas energías, es fundamental realizar estudios multifrecuencia. Por esta razón, se decidió incluir un monitor óptico a bordo del observatorio espacial de rayos X y gamma *INTEGRAL*, de la Agencia Espacial Europea.

En esta tesis se presentan los principales resultados del análisis de parte de los datos obtenidos durante más de 12 años por la cámara óptica OMC del observatorio *INTEGRAL*. El principal objetivo de la tesis era analizar y clasificar las miles de curvas de luz obtenidas, e identificar los casos científicos potencialmente interesantes que se podían extraer de la gran cantidad de datos que se han generado con OMC a lo largo de estos años.

En los últimos 12 años OMC ha observado una gran cantidad de fuentes variables, incluyendo estrellas pulsantes, sistemas binarios eclipsantes, estrellas rotantes, etc. En esta tesis se incluye la compilación del primer catálogo de fuentes variables en el óptico observadas con OMC, proporcionando información de su brillo, variabilidad, periodicidad y clasificación por tipo de objeto.

Entre las fuentes de este catálogo se ha realizado una búsqueda de sistemas binarios eclipsantes que contuvieran una componente pulsante. Uno de los sistemas identificados, DY Aqr, ha sido estudiado en detalle.

Por otro lado, OMC fue diseñada para monitorizar las fuentes que se observaran con los principales instrumentos de rayos X y rayos gamma. En este momento y por primera vez, se presentan observaciones simultáneas en el óptico y en rayos X/gamma de fuentes emisoras en altas energías durante más de 12 años. En esta tesis se presentan dos trabajos distintos basados en información multifrecuencia incluyendo datos de INTEGRAL.

En el primero se estudian las propiedades globales de la emisión de los objetos que emiten en rayos X, en los distintos rangos de energía (rayos X duros/gamma blandos, óptico, IR cercano e IR medio). Se han estudiado los flujos, luminosidades, cocientes de flujo y colores, comparándolos para cada tipo de objeto, buscando similitudes y diferencias que ayudaran a desvelar la naturaleza de sus fuentes de energía.

El segundo consiste en un estudio de variabilidad a largo plazo en distintos rangos de energía, en el que se comparan curvas de luz de los instrumentos de *INTEGRAL*: IBIS, JEM-X y OMC y de otras misiones, con una cobertura temporal de más de 12 años.

Contents

List of Figures

List of Tables

List of Abbreviations

AAVSO American Association of Variable Stars Observers

AGN active galactic nucleus

BH black hole

BLRG broad-line radio galaxy

CAB Centro de Astrobiología

CCD Charge-coupled device

CD color-color diagram

DPE Data Processing Electronics

ESA European Space Agency

FCFOV fully coded field of view

FOV field of view

FSRQ Flat-Spectrum Radio Quasar

GCVS *General Catalogue of Variable Stars*

HBL high-frequency peaked BL Lac

HPQ highly polarized quasar

HST Hubble Space Telescope

IDV intraday variability

INTEGRAL *INTErnational Gamma-Ray Astrophysics Laboratory*

ISDC *INTEGRAL* Science Data Centre

ISOC *INTEGRAL* Science Operations Centre

LBL low-frequency peaked BL Lac

LINER low-ionization nuclear emission-line region

NASA National Aeronautics and Space Administration

NLRG narrow-line radio galaxy

NS neutron star

OG Observation Group

OMC Optical Monitoring Camera

OSA Off-line Scientific Analysis

OVV optically violent variable

quasar quasi-stellar radio source

ScW Science Window

SED Spectral Energy Distribution

SFXT super fast X-ray transient

SMBH supermassive black hole

SXT soft X-ray transient

ULIRG Ultraluminous infrared galaxy

VSX Variable Star Index

WD white dwarf

Chapter 1

Introduction

With the advent of large-scale surveys and space astronomy, and the development of modern astrostatistical tools, a re-emergence of time-domain astrophysics is taking place. The main goal of this thesis is the study of stellar and extragalactic variability through the analysis of the long-term optical light curves provided by OMC, the optical monitoring camera on board the gamma ray space observatory *INTEGRAL*. This work has been divided in the following parts:

- Compilation of a catalog of optically variable sources observed by OMC, including the study of periodicity of the selected sources.
- Analysis of the most interesting cases of optical variability: Search for eclipsing binaries with a pulsating component and characterization of one of these systems, DY Aqr. In order to determine the physical parameters of this source, echelle high-resolution spectroscopy data were acquired and analyzed.
- Global analysis of the multiwavelength emission from the sources observed with *INTEGRAL*, comparing the optical information provided in the OMC catalog with the information of the hard X-ray emission given in the IBIS catalog. These data were complemented with IR and MIR data from 2MASS and WISE respectively.
- Analysis of long-term variability of high-energy sources in the optical and X-ray bands, using *INTEGRAL* observations from IBIS (the gamma-ray imager), JEM-X (the X-ray monitor) and OMC.

Since this thesis is mainly based on *INTEGRAL* data, and is especially focused on the optical observations acquired by OMC, the *INTEGRAL* mission and the OMC instrument are described here. Furthermore, an overview of astrophysical variability is provided in Chapter 2.

1.1 The *INTEGRAL* mission

The *INTErnational Gamma-Ray Astrophysics Laboratory* (*INTEGRAL*; (Winkler et al., 2003)) is an European Space Agency (ESA) mission in cooperation with the Russian Federal Space Agency (FKA) and the National Aeronautics and Space Administration (NASA). The spacecraft was launched by a Proton rocket, Russia's largest operational launch vehicle, on 17 October 2002 and is still operational. *INTEGRAL* surrounds the Earth in a highly elliptical orbit once every three days. The orbit was calculated so the satellite spends most of the time above 60 000 km (far enough from the Earth's radiation belts) to avoid the background radiation effects which would interfere with the measurement of gamma rays.

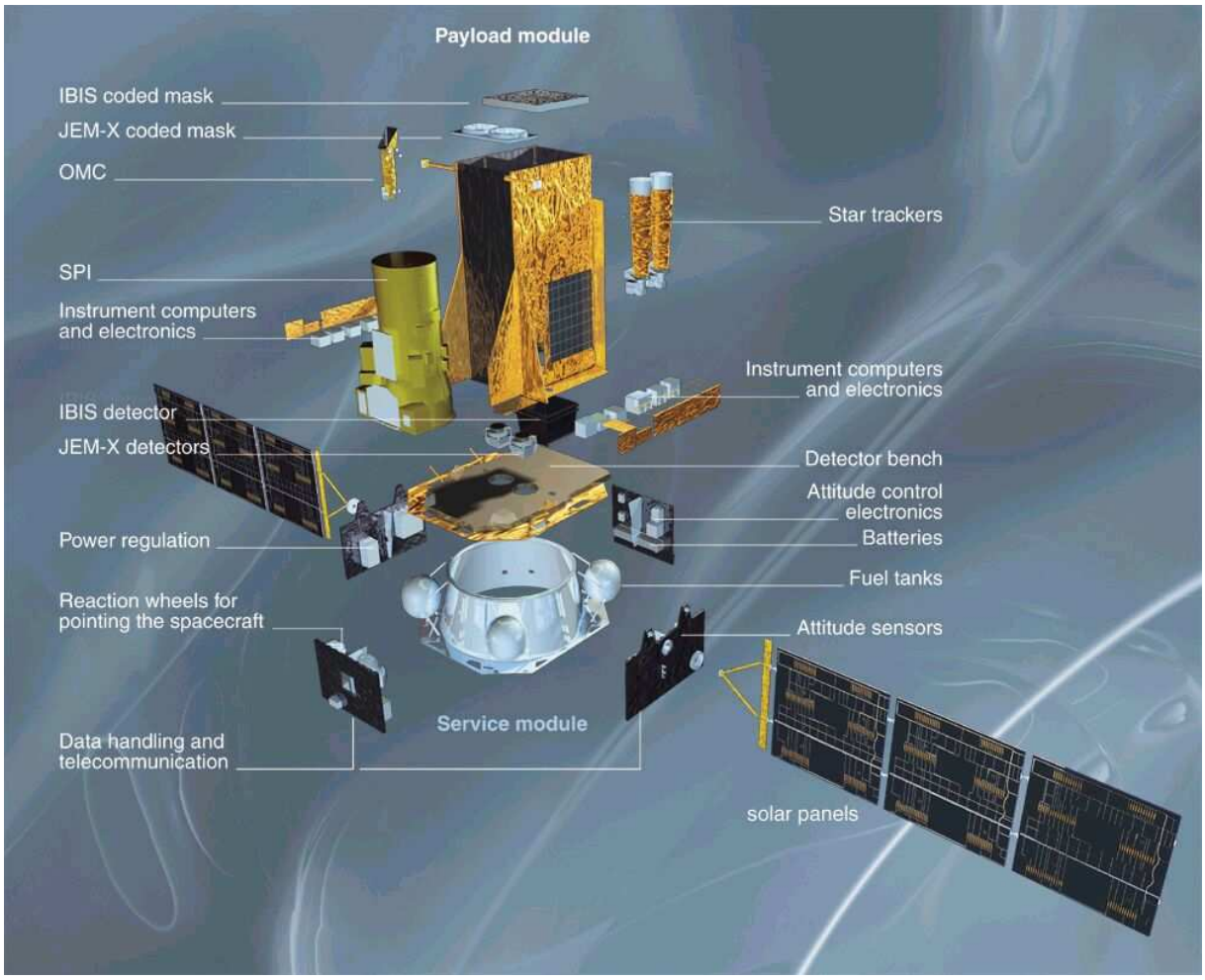

Figure 1.1: Detailed view of the *INTEGRAL* spacecraft showing the service module and the payload module. Credits: ESA

Gamma rays are produced by very energetic events in the Universe such as supernovae, solar flares, matter falling into black holes or neutron stars and celestial objects collisions. By observing gamma rays, astronomers are able to detect and study these violent events. *INTEGRAL* was designed to capture not only gamma rays but also X-rays and visible light. This complementary information is crucial to identify the sources releasing the gamma rays and learn more about the nature of these phenomena.

1.1.1 Instruments on board *INTEGRAL*

Four scientific instruments are integrated on the spacecraft (see Fig. 1.1). The two main gamma-ray instruments, the imager IBIS optimized for high-angular resolution imaging and the spectrometer SPI optimized for the high-resolution gamma-ray line spectroscopy works in gamma rays. Two monitors support these instruments: JEM-X in the soft X-ray band, and OMC in the optical Johnson V–band. All instruments on board *INTEGRAL*, except the OMC have coded masks. A summary of the complementary features of the instruments on *INTEGRAL* is given in Table 1.1.

All four instruments are co-aligned and observe the same region of the sky simultaneously (see Fig. 1.2). The main features of each instrument are:

- SPI (*Spectrometer on* INTEGRAL): The high-resolution gamma-ray line spectrometer SPI (Vedrenne et al., 2003) performs fine spectroscopy ($E/\Delta E \simeq 500$) of gamma-ray point

Table 1.1: Complementary features of the *INTEGRAL* instruments

Instrument	Energy range	Main purpose
Spectrometer SPI	18 keV–8 MeV	Fine spectroscopy of narrow lines Study diffuse emission on $> 1^{o}$ scale
Imager IBIS	15 keV–10 MeV	Accurate point source imaging Broad line spectroscopy and continuum
X-ray Monitor JEM-X	3 – 35 keV	Source identification X-ray monitoring of high-energy sources
Optical Monitor OMC	500–600 nm (V–band)	Optical monitoring of high-energy sources

sources and extended regions over an energy range between 18 keV and 8 MeV. It provides an unprecedented energy resolution of 2.2 keV (FWHM) at 1.33 MeV. The total detection area is 500 square centimeters. The fully coded field of view (FCFOV) is of $16^{o}\times16^{o}$ and has an angular resolution of 2^{o}.

- IBIS (*Imager on Board the* INTEGRAL *Satellite*): The high-angular resolution imager IBIS (Ubertini et al., 2003) provides diagnostic capabilities of fine imaging ($12'$ FWHM), source identification and spectral sensitivity to both continuum and emission lines over a broad energy range (15 keV–10 MeV). There are two detector operating simultaneously and located one on top of the other: the *INTEGRAL Soft Gamma-Ray Imager* (ISGRI, 18 keV–1 Mev), a semiconductor array optimized for lower energies; and the PIxelated CsI Telescope (PICsIT; 175 keV–1 MeV), a crystal scintillator for higher energies. ISGRI is composed of 16 384 cadmium telluride (CdTe) pixels, covering 2600 square centimeters. PICsIT consists of 4096 caesium iodide (CsI) pixels, covering 3100 square centimeters. The FCFOV is $8.3^{o} \times 8.0^{o}$.

- JEM-X (*Joint European X-Ray Monitor*): The JEM-X instrument (Lund et al., 2003) plays a crucial role in the detection and identification of the X-ray counterparts of the gamma ray sources. It observes simultaneously with the main gamma ray instruments and provides images in the 3–35 keV energy band with an angular resolution of $3'$. This helps with the identification of sources in crowded fields. The FCFOV has a diameter of 4.8^{o}.

- OMC (*Optical Monitoring Camera*): The optical monitor OMC (Mas-Hesse et al., 2003) provides simultaneous observations of the optical emission (in the V-Johnson band) coming from gamma-ray and X-ray sources. It has a field of view (FOV) of $5^{\circ}\times5^{\circ}$ and an angular resolution of $\sim 23''$. More details on OMC are given in Sect. 1.2.

The key parameters of the four instruments were obtained from Kuulkers (2014), and are summarized in Table 1.2.

In order to reconstruct the image on the detectors for all sky pixels, an appropriate dithering strategy has to be adopted for every observation. Two different dither patterns, rectangular and hexagonal, and a staring mode (no dithering) are used as operational baseline (see Fig. 1.2). The usual separation between pointings is $2\overset{\prime}{.}17$ and the duration of each pointing varies between 30 minutes and one hour.

1.1.2 The *INTEGRAL* Off-line Scientific Analysis

To reduce and analyze the data collected by the *INTEGRAL* instruments, the *INTEGRAL* Off-line Scientific Analysis (OSA) package has to be used. This software is developed and

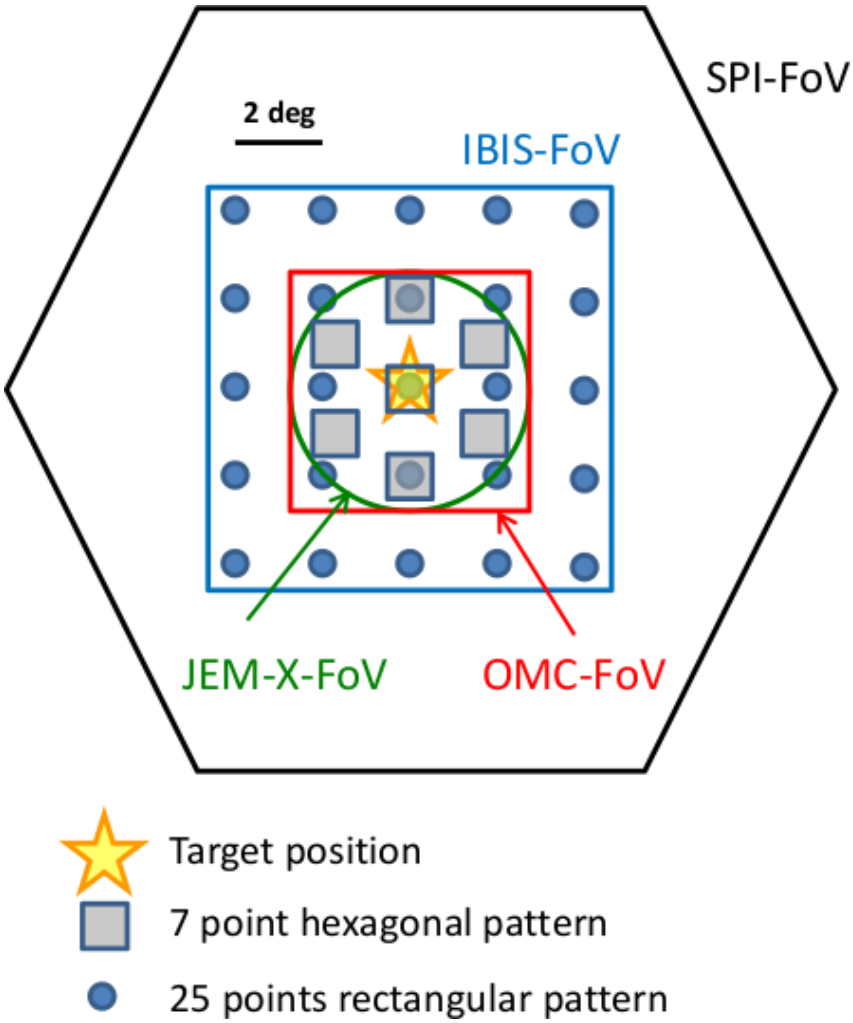

Figure 1.2: Fields of view of the four *INTEGRAL* instruments and dither patterns for *INTEGRAL* observations. Figure adapted from Jensen et al. (2003).

Table 1.2: Key parameters of the *INTEGRAL* instruments

Parameter	SPI	IBIS	JEM-X	OMC
Energy range	18 keV - 8 MeV	15 keV–10 MeV	3 keV–35 keV	5500Å
Detectors	19 Ge	CdTe and CsI	Xe/CH4-gas	CCD
Spectral resolution (FWHM)	3 keV @ 1.7 MeV	8 keV @ 100 keV	3.6 keV @ 22 keV	
FCFOV	$16^o \times 16^o$	$8.3^o \times 8.0^o$	$4.8^o \times 4.8^o$	$5° \times 5°$
Angular resolution (FWHM)	2.5^o (point source)	$12'$	$3'$	$23''$
Source location (radius)	$< 1.3^o$	$3'$ @100 keV (5σ)	$1'$ (10σ)	$2\,''(10\sigma)$
Absolute timing accuracy (3σ)	$\sim 130\mu s$	$\sim 90\mu$ s	$\sim$ 1ms	>3 s
Mass (kg)	1309	746	65	17
Power [max/average] (W)	385/110	240/208	50/37	26/17

maintained by the *INTEGRAL* Science Data Centre (ISDC) and can be downloaded using the ISDC archive browser[1] (Courvoisier et al., 2003).

[1] http://www.isdc.unige.ch/integral/analysis

The first task before starting the analysis of *INTEGRAL* data is to identify and download the relevant pointings, referred as Science Windows (ScWs).

Once the list of ScWs is known, an Observation Group (OG) can be created using the routine OG_CREATE. An OG relates all data from all SWGs together, and it is conveniently used for data access. In most cases, the only thing the ISDC software needs to know about input data is the name of the OG.

The ISDC software includes four pipelines (*jemx_science_analysis, ibis_science_analysis, spi_science_analysis, omc_science_analysis*) which allow to carry out sky image reconstruction, and spectrum and light curve extraction, from the OG. Each of these pipelines is documented by a "cookbook" guiding the user through practical simple examples with some explanatory information. The OMC pipeline was developed by the OMC team (see Domingo 2011 for details).

1.2 The Optical Monitoring Camera (OMC)

The Optical Monitoring Camera (OMC) is based on a refractive optics with an aperture of 50 mm (see Fig. 1.3) focused onto a large format Charge-coupled device (CCD) of 1024 × 2048 pixels working in frame transfer mode (1024 × 1024 pixels imaging area). As mentioned in Sect. 1.1, OMC was designed to observe the optical emission from the prime targets of the gamma-ray instruments on board *INTEGRAL*, has the same FOV as the FCFOV of the *INTEGRAL* X-ray monitor (JEM-X). It is co-aligned with the central part of the prime gamma-ray instruments, the IBIS imager and the SPI spectrometer, which have larger FOVs (see Fig. 1.2). The need to have a FOV as large as possible (the OMC FOV is $5^o \times 5^o$) led to a rather large pixel angular size ($17''.5 \times 17''.5$), with a Gaussian Point Spread Function (PSF) with FWHM ~ 1.4 pixels. The scientific performances and additional parameters of OMC are summarized in Table 1.3.

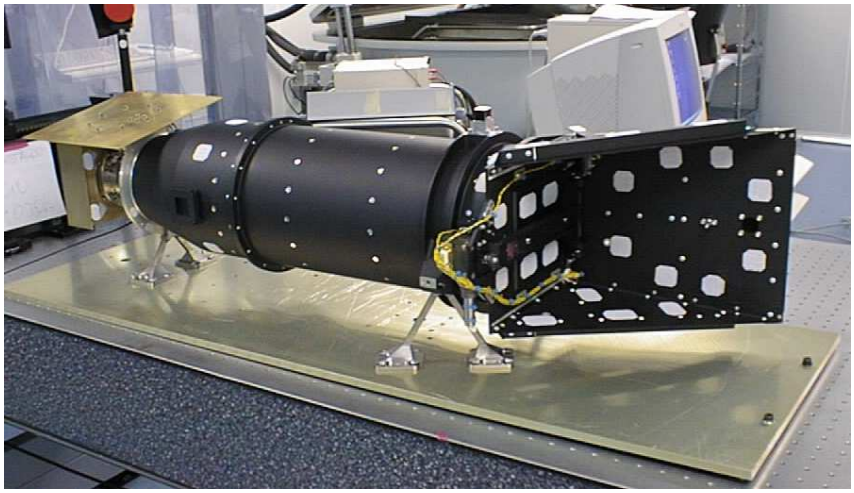

Figure 1.3: Picture of OMC before *INTEGRAL* was assembled.

1.2.1 Photometry with OMC

The OMC monitors the sources in its FOV performing integrations of variable duration. The Data Processing Electronics (DPE) process the image of each source by first running a fast centering algorithm, based on the location of around 10 bright stars with accurately known coordinates in the field. Then, windows of typically 11×11 pixels around each object of interest are extracted and transferred to the spacecraft central computer for transmission to ground.

Table 1.3: OMC Scientific performances.

Parameter	Value
field of view (FOV)	$4^{\circ}.979 \times 4^{\circ}.979$
Aperture	50 mm diameter
Focal length	153.7 mm (f/3.1)
Optical throughput	>70% at 550 nm
Straylight reduction factor (within the unobstructed FOV)	$<10^{-5}$ (for diffuse background)
Point spread function	Gaussian with FWHM ∼1.4 pix (corresponding to $\sim 24''.5$)
Point source location accuracy	$\sim 6''$
CCD pixels	2061 × 1056 (1024 × 1024 image area) (13×13 μm^2 per pixel)
Image area	13.3×13.3 mm^2
Angular pixel size	$17''.504 \times 17''.504$
CCD Quantum efficiency	88% at 550 nm
Full well capacity	120.000 electrons per pixel
Analogue to digital converter levels	12 bits: ∼30 cts/digital level (low gain) ∼5 cts/digital level (high gain)
Frame transfer time	∼2 ms
Time resolution	≥3s
Typical integration times	10 – 100 s
Wavelength range	V filter (centered at 550 nm)
Limit magnitude (10×100 s, 3σ)	17.6 (V)
(50×100 s, 3σ)	18.2 (V)
Sensitivity to variations (10×100 s, 3σ)	$\delta m_V < 0.1$ mag for V < 16
Average number of stars per pixel ($m_V < 19.5$)	0.6 (full sky) 2.0 (b = 0°); < 0.1 (b > 40°)

Absolute photometric calibration is achieved by comparison with a number of reference standard stars within the FOV of the instrument.

OMC provides photometry in the Johnson V-band (centered at 5500 Å) for sources from $V \sim 7$ mag (for brighter sources saturation effects appear) to $V \sim 16$–17 mag (limit magnitude for 3σ source detection and 200 s integration time). Typical observations are performed as a sequence of different integration times to increase the dynamical range (currently the sequences are 10 - 50 - 200 s while in the beginning of the mission the sequences were 10 - 60 - 100 s). This allows for photometric uncertainties below 0.1 mag for objects with V ≤ 16, although for the brightest sources the accuracy is always limited to 0.01 mag by the flat field correction matrix.

I have performed the flat-field and photometric calibrations of OMC every 12 *INTEGRAL* revolutions (∼ 36 days) since I started working with OMC. An explanation of this procedure is given in Appendix A.

1.2.2 The OMC Input Catalogue

In addition to monitoring the *INTEGRAL* primary high-energy targets, OMC has the capability to observe serendipitously ∼100 sources within its FOV. These targets have to be pre-selected on ground, since the limited telemetry available to OMC (only ∼ 2.2 kbps) does not allow to

download the entire OMC images to ground. These additional targets are automatically selected from the *OMC Input Catalogue* (OMC–IC hereafter) by a specific OMC Pointing Software (OMCPS) running at the *INTEGRAL* Science Operations Centre (ISOC). Only windows of 11×11 pix of the CCD containing those objects are transmitted to ground. The OMC–IC was compiled before the start of the mission, and is described in detail in Domingo et al. (2003). It has been updated several times to include new targets of interest or to improve the accuracy in target coordinates, especially of the high-energy objects.

The current version of the OMC–IC contains over 500 000 entries, namely:

- astrometric and photometric reference stars,
- known optical counterparts of gamma-ray sources,
- known optical counterparts of X-ray sources,
- point-like X-ray sources detected and cataloged by ROSAT,
- quasars observable by OMC,
- known additional AGN and
- a big fraction of the known variable stars (including eruptive variable stars, novae and cataclysmic stars).

The OMC–IC includes both known variable stars and suspected variable stars. Special care was devoted to the compilation of extragalactic objects (AGN, QSO, starburst galaxies, narrow emission line galaxies, etc.) as they are potential high-energy emitters, and in many cases show significant optical flux variations. Indeed, Beckmann et al. (2009) compiled *the second INTEGRAL AGN catalogue* including optical information from OMC for 57 AGN (see Chapter 5).

In the compilation of optical sources, mostly available before the INTEGRAL launch, the SIMBAD database and the following catalogs were used:

1. *Combined General Catalogue of Variable Stars, 4.1* (GCVS; Kholopov et al. 1998).
   It includes a catalog of all known Galactic variable stars prior to 1997, a catalog of extragalactic variable stars, a catalog of supernovae and a catalog of suspected variable stars not designated as variables prior to 1980 (published in *The New Catalogue of Suspected Variable Stars*, Kukarkin & Kholopov 1982).

2. *New Catalogue of Suspected Variable Stars. Supplement* (Kazarovets et al., 1998).
   It contains 11 206 stars suspected of variability which were not designated as variables prior to 1997.

3. *The 74th Special Name-list of Variable Stars* (Kazarovets et al., 1999).
   It contains 3157 variable stars whose variability was discovered by the Hipparcos mission. All the stars satisfy the GCVS variability criteria.

4. *The Hipparcos Catalogue* (Perryman et al., 1997).
   The 11 597 variable stars in the Hipparcos catalog were included.

5. *Variable stars in the Tycho photometric observations.*
   To search for variability among faint stars of the Tycho catalog (Hoeg et al., 1997), Piquard et al. (2001) made a treatment that took into account truncated detections and censored measurements. The list contains 1091 stars suspected to be variable stars.

6. *Quasars and Active Galactic Nuclei, 8th Ed.* (Veron-Cetty & Veron, 1996).

7. *The Active Galactic Nuclei Catalogue* (Padovani priv. comm.).
This catalog includes 12 021 quasars and active galaxies and is heavily based on the catalog of *Quasars and Active Galactic Nuclei, 7th Ed.* (Veron-Cetty & Veron, 1996). It also includes the *BL Lac Catalogue* (Padovani & Giommi, 1995) updated with BL Lac′s discovered in 1996, and the radio galaxies in the 1 Jy, S4, and S5 radio catalogs. The AGN catalog reports V magnitudes almost for all of their objects. Nevertheless, in some cases V magnitudes were derived from B magnitudes by assuming a $(B-V)$ color index.

8. *Narrow Emission Line Galaxies* (Kunth, priv. comm.).
Compilation of 441 objects dominated by intense starburst activity. These objects show strong optical emission lines and/or very blue stellar continuum, both being tracers of young, massive stellar populations and therefore candidates for host supernovae.

9. *Catalogue of Cataclysmic Variables* (Downes et al., 2001). This catalog contains 1134 sources that were included in the OMC–IC.

10. *Candidates for classical T-Tauri stars*
Classical T Tauri stars are good targets for OMC because they emit in the optical band in a periodic or non periodic way, but always have some type of variability related to their physical conditions. The amplitudes of the light curves are in the range 0.01–3 mag. Periods are often ∼1 day, so the monitorization from a space platform should overcome the lack of observing them from the ground. 732 candidates for classical T-Tauri stars were selected (Caballero-García, 2003) based on the segregation shown by these stars in a 2MASS $(J-H)$ vs. $(H-Ks)$ color-color diagram (Lee & Chen, 2002).

11. *Candidates for cool dwarfs of G-K-M spectral type.*
It is broadly known that cool dwarfs of G-K-M spectral type can be variable at a certain degree (mainly in the range 0.05–0.1 mag. and not greater than 0.2 mag.), showing very interesting properties of the behavior of this kind of stars. A selection of 35 101 candidates was made by Caballero-García (2003) based on proper motions and the 2MASS $(J-H)$ and $(H-Ks)$ colors.

1.2.3 OMC pipeline processing software

Due to restrictions in the telemetry, usually around 100 CCD windows, each of 11×11 pixels, are downloaded to Earth every 10 to 200 seconds, without any on board processing. When this occurs, the data are received at the *INTEGRAL* Science Data Centre (ISDC) (Courvoisier et al., 2003), where they are completely processed in an automatic way, providing to the user the next products:

- CCD raw image windows, without any correction.
- Processed and corrected CCD windows (in photoelectrons per pixel).
- The photometric light curve with different sampling times.
- Corresponding flat-field and photometric calibration matrices.

The pipeline processing can be performed off-line in an interactive way with OSA (see Section 1.1.2), which allows the observer to modify some parameters, like the extraction box size (3×3 or 5×5 pixels) or the sampling time, or to select different calibration files. For a detailed reference on the OMC pipeline see Domingo (2011).

1.2.4 The OMC Archive

After the proprietary period of one year, all the *INTEGRAL* data are open to the scientific community and are ingested in the OMC Archive[2] (Gutiérrez et al., 2004).

At the moment of writing this thesis, *INTEGRAL* has been in orbit for more than twelve years and the OMC Archive now contains observations for about 150 000 objects, of which more than 80 000 have light curves with at least 50 photometric data points. In this moment, the OMC Data Server includes all observations from revolutions 11-1385 (publicly available on 13 March 2015) and public observations up to revolution 1505.

The query to access the archive is made by means of an HTML fill-in form which allows to perform queries by object name, coordinates, object type, V-magnitude range, date of observation, time binning (one photometric point per shot, per 630 seconds or per ScW), centroid method (source coordinates or brightest pixel) and/or number of points of the light curve. A capture of the OMC Archive search form is printed in Fig. 1.4.

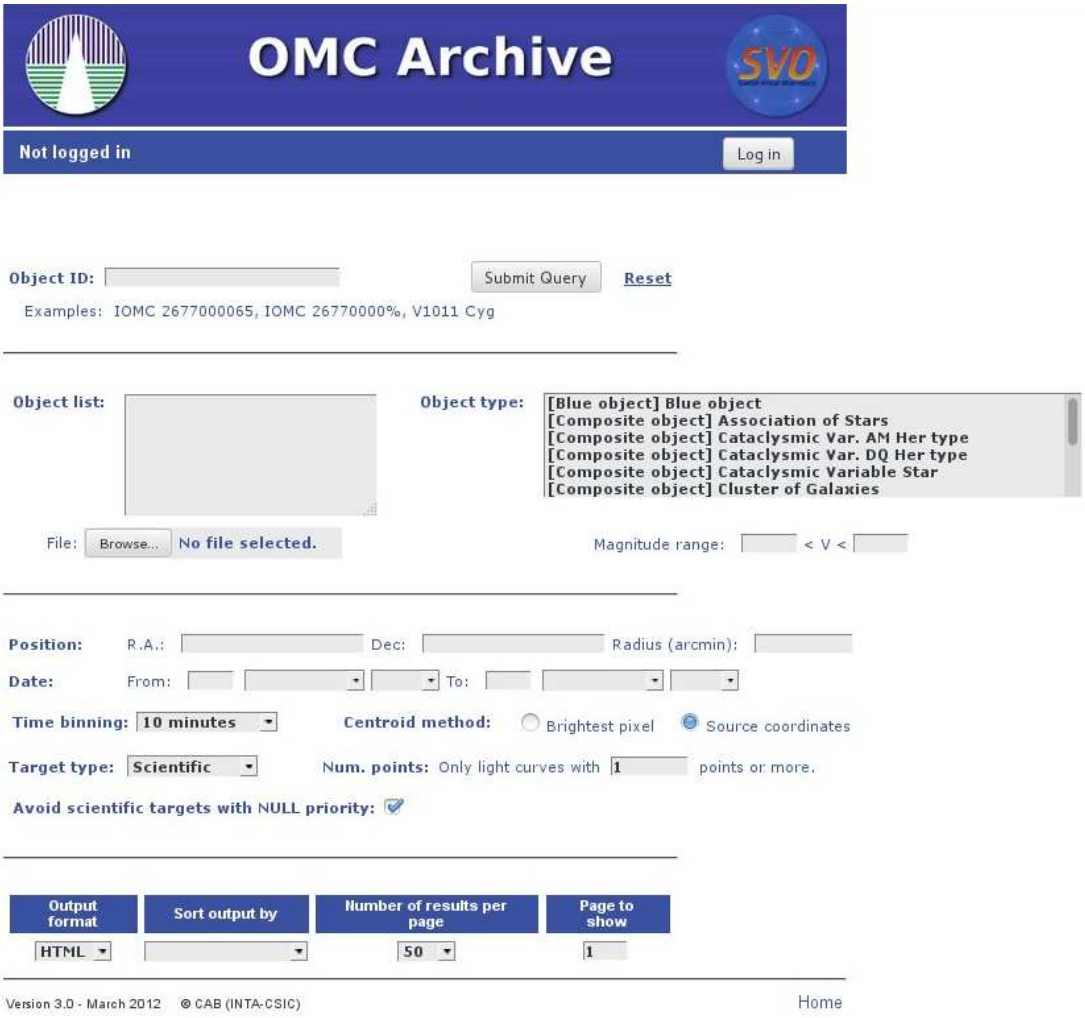

Figure 1.4: OMC Archive search form.

[2]The OMC Archive was developed in the framework of the Spanish Virtual Observatory project and is maintained by the Data Archive Unit at CAB. The system is based on data pre-processed by the ISDC, further processed by the OMC Team at CAB. It can be accessed at https://sdc.cab.inta-csic.es/omc/

1.3 Thesis outline

The main goal of this thesis has been to exploit the large amount of scientific data provided by the OMC instrument, on board the *INTEGRAL* satellite. Tthe *INTEGRAL* mission and the OMC instrument have been introduced in this chapter. The main aspects of astrophysical variability are described in Chapter 2. The scientific work of this thesis can be divided into three main parts. The compilation of the catalog of variable sources observed by OMC (Alfonso-Garzón et al., 2012) is presented in Chapter 3. The search for eclipsing binaries with an oscillating component inside the compiled catalog is described in Chapter 4 and in Alfonso-Garzon et al. (2014). Finally, a multiwavelength study of the high-energy sources observed by OMC has been carried out. This analysis have been divided in two parts. The first one, presented in Chapter 5, consists on a global characterization of the multiwavelength emission of these sources, and includes hard X-ray, optical, NIR and MIR data. The second part, focused on the long-term evolution of these objects in the optical and at high-energies, is discussed in Chapter 6. The final conclusions and future work are summarized in Chapter 7. The appendices include a brief description of the OMC calibration procedure (Appendix A), and the INTEGRAL light curves of all the high-energy sources monitored by OMC (Appendix B).

Chapter 2

Astrophysical Variability

The main aspects of astrophysical variability are presented in this chapter. The traditional classification of variable stars, mainly based on optical observations, is summarized in Section 2.1. The different types of variable stars are briefly described to provide a general vision of the field. The different types of high-energy sources, with an introduction on X-ray binaries (XBs) and active galactic nuclei (AGN), are summarized in Section 2.2. The mechanisms and observational properties related to the variability of high-energy sources are described in Section 2.3.

2.1 Classification of Variable Stars

It is difficult to establish a consistent taxonomy of classes and types of variable stars. The most used classification of variable stars is the one given in the *General Catalogue of Variable Stars* (GCVS; Samus et al. 2012), which is the main reference source on all known variable stars. Another complete reference on variable stars is given in the book *Understanding Variable Stars* Percy (2007). The first classification criteria can be whether a star is an intrinsic or an extrinsic variable. Intrinsic variable stars are those in which the change in brightness is due to some physical change within the star itself, while extrinsic variable stars are those in which the brightness variations are due to geometrical effects either due to the position of the object relative to the observer or due to rotation. Figure 2.1, provides an schematic organization of variable objects. An overview of the different types of variable stars is provided below. The abbreviations used in the GCVS, which will be used along this thesis work, are shown in parentheses.

2.1.1 Intrinsic variables

In these stars, the variability is due to physical changes in the star itself. These systems provide a wealth of information about the internal structure of stars and models of stellar evolution, but perhaps their greatest value is the role that some types such as Cepheids and supernovae play in distance determinations (Colgate, 1979; Freedman et al., 1994). Intrinsic variables are further classified as to whether they exhibit periodic pulsations, if they experiment flares occurring in their chromospheres and coronae and if they are more explosive as cataclysmic variables.

Pulsating stars

Pulsating stars show periodic expansion and contraction of their surface layers of the stars. The pulsations may be radial or nonradial. A radially pulsating star remains spherical in shape, while in the case of nonradial pulsations the star's shape periodically deviates from a sphere, and even neighboring zones of its surface may have opposite pulsation phases.

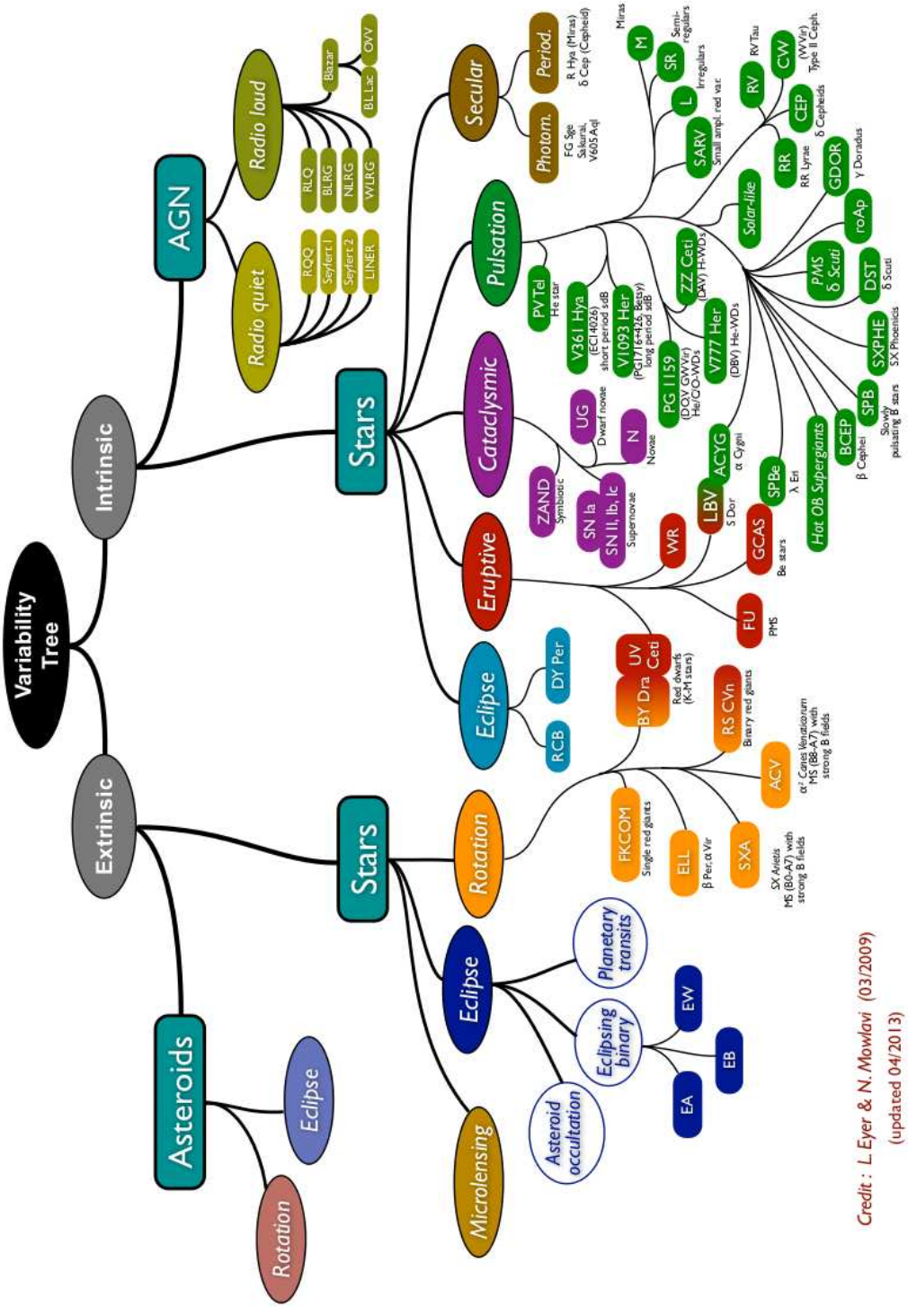

Figure 2.1: Variability tree. Variable objects are organized in different types. The figure has been provided by Dr Laurent Eyer and it is an update version of the one from Eyer & Mowlavi (2008).

The different types of pulsating variable stars are distinguished by their periods of pulsation and the shapes of their light curves. These in turn are a function of the mass and evolutionary stage of a given star. The location of the different types of pulsating stars in a theoretical HR diagram are shown in Fig. 2.2.

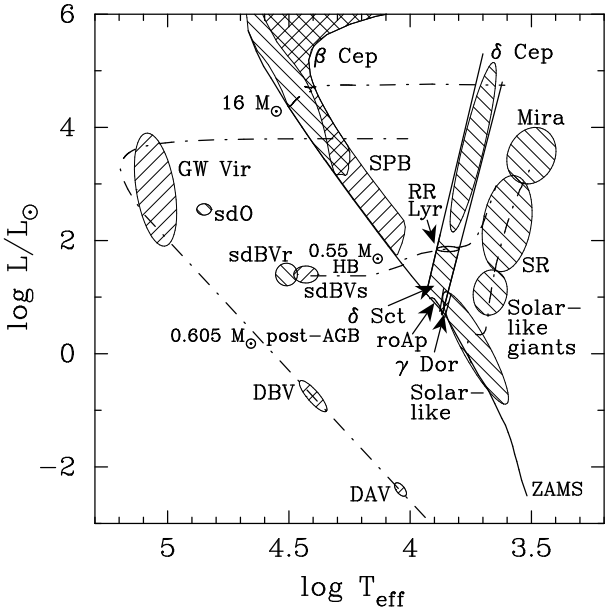

Figure 2.2: Theoretical HR diagram schematically showing the locations of different confirmed types of pulsating stars. Parts of model evolutionary tracks for main sequence, horizontal branch and post-AGB stars are shown as dashed-dotted lines for orientation. Figure taken from Handler (2009).

The main types of pulsating stars are briefly described below. An excellent reference on pulsating stars is provided by Aerts et al. (2010).

- Cepheids (DCEP): Cepheids are very luminous, massive variables with periods of 1–70 days. Cepheid light curves are characteristic and show a rapid rise in brightness followed by a more gradual decline, shaped like a shark fin. Their amplitude range is typically 0.5 to 2 magnitudes. The spectral class of a Cepheid actually changes as it pulsates, being about an F at maximum luminosity and down to a G or K at minimum. There are two types of Cepheids, the original Type I or Classical Cepheids (CEP) and the slightly dimmer Type II or W Virginis Cepheids (CW). The strong direct relationship between their luminosity and pulsation period makes Cepheids important distance indicators for establishing the galactic and extragalactic distance scales (Feast & Walker, 1987; Majaess et al., 2009; Freedman & Madore, 2010).

- RR Lyrae (RR): They are radial pulsators with relatively low metallicities. These old population II giant stars are mostly found in globular clusters. They are characterized by their short periods, usually about 1.5 hours to a day and have a brightness range of 0.3 to 2 magnitudes. Spectral classes range from A7 to F5. Their light curves are different depending on the overtone number of the primary pulsation mode. In this way, the RRab subclass shows light curves which are strongly asymmetric, with a steep rise and a slow decay, while the RRc subclass has more sinusoidal light curves and smaller amplitudes. RR Lyrae stars are often used as standard candles to measure galactic distances (Layden et al., 1996; Marconi, 2009).

- RV Tau variables (RV): They are yellow supergiants, mostly G and K-class stars. Their

distinctive light curves show alternating deep and shallow minima. Typical values are 20 - 100 days.

- β Cephei type (BCEP): They are O8–B6 I–V stars with photometric periods and radial-velocity variations in the range of 0.1–0.6 days and light amplitudes from 0.01 to 0.3 mag in the V-band.
- Slowly pulsating B stars (SPB): They are main sequence B2–B9 stars that pulsate in their pulsations are non-radial, that is, they vary in shape rather than volume. There may be multiple periods ranging from 0.4 to 5 days, with amplitudes smaller than 0.1 mag. A good review of β Cephei and Slowly Pulsating B stars is presented in De Cat (2002).
- δ Scuti variables (DSCT): They have spectral types A0–F5 III–V and their light curves display amplitudes from 0.003 to 0.9 mag in the V-band with periods from 0.01 to 0.2 days. The shapes of the light curves, periods, and amplitudes usually vary greatly. Radial and nonradial pulsations are observed. A review on this type of pulsators is given in Lampens & Boffin (2000).
- γ Dor variables (GDOR): These are late A or early F type main sequence stars displaying variations due to non-radial pulsations with multiple periods from several 0.3 to 3 days. Amplitudes usually do not exceed 0.1 mag.
- Long-Period Variables (LPV): They are cool red giants or supergiants and have periods of months to years. Long-period variables are further classified according to whether they exhibit regular periodicity, such as the Miras (M) or semirregular variables (SR).

Additional pulsating stars types such as α Cygni variables, β Cygni variables, ZZ Ceti variables are identified in the GCVS.

Eruptive stars

Eruptive variables are stars displaying brightness variations caused by violent processes and flares occurring in their chromospheres and coronae. The brightness variations are usually accompanied by shell events or mass outflow in the form of stellar winds of variable intensity and/or by interaction with the surrounding interstellar medium. There are different types of eruptive stars which have different light curves such as:

- Cataclysmic (explosive and nova-like) variables (CV): These are variable stars showing outbursts caused by thermonuclear runaways in their surface layers (novae) or deep in their interiors (supernovae). Cataclysmic variables include any type of cataclysmic binary systems, some types of symbiotic stars (Z Andromedae type (ZAND)), and all supernovae. The majority of the CVs are binaries. They are explained in detail in the 2.2.1. A review on CVs is given by Giovannelli (2008).
- Flare stars or UV Ceti Type (UV): Dwarf K and M stars which randomly increase in brightness within seconds to minutes, by up to several magnitudes and minutes later return to pre-flare levels. In the GCVS they are classified as UV, UVN if they are associated with pre-main sequence stars or RS if they happen in an RS Canum Venaticorum system.
- R Coronae Borealis variables (RCB): They are high-luminosity stars, which are simultaneously pulsating and eruptive variables. They show slow non-periodic fading by 1 to 9 magnitudes which last from about a month to several hundred days. A possible explanation is that the carbon particles at the outer layers of the star are built up and they blown away darkening the radiation of the star. These eruptive changes are superposed on cyclic pulsations, with periods in the range of 30–100 days.

- Orion variables of the FU Orionis type (FU): These are pre-main sequence stars which display an extreme change in magnitude (~ 6 mag) and spectral type in several months, followed by either almost complete constancy at maximum that is sustained for long periods of time or slow decline by 1–2 mag. The current model associates the FU Orionis flares with an abrupt mass transfer from an accretion disk onto a young, low mass, T Tauri star.

Other types of pre-main sequence stars (Orion variables), luminous blue variables (S Doradus type stars), γ Cas type and Wolf-Rayet (WR) stars are eruptive stars in the GCVS.

2.1.2 Extrinsic variables

The brightness variability in extrinsic variables is either due to geometrical effects, external to the star itself, such as eclipses, or due to the rotation of the star.

Eclipsing variables

According to the shape of the light curve, eclipsing binaries have been traditionally classified as:

- Algol (Beta Persei)-type eclipsing systems (EA in the GCVS; Giuricin et al. 1983): These systems present spherical or slightly ellipsoidal components. The most common class of Algols are semidetached interacting binaries composed of a cool F-K giant or subgiant secondary filling its Roche lobe (it is the region of space in which material is bound to the star by gravity; Eggleton 1983), sometimes transferring mass onto a hot B-A main sequence star. Less common are the detached Algol systems with cooler primaries. Algol systems typically present a deep primary minimum, occurring when the hotter component is eclipsed by the cooler companion. The secondary minima may be absent. Outside the eclipses, the brightness is nearly constant. An extremely wide range of periods is observed, from 0.2 to $\geq$ 10000 days. Light curve amplitudes are also quite different and may reach several magnitudes.

- β Lyrae-type eclipsing systems (EB in the GCVS; Kuiper 1941): These systems can contain stars with very different evolutionary states, ranging from main-sequence stars in tight orbits, to semi-detached systems with mass-transfer or very eccentric system with one component much more evolved than the other one. These systems have ellipsoidal components due to tidal distortions. In their light curves, it is impossible to specify the exact times of onset and end of eclipses because of a continuous change of the system's apparent combined brightness between eclipses. The secondary minimum is always observed and its depth is usually considerably smaller than that of the primary minimum. Periods are usually longer than 0.5 days.

- W Ursae Majoris-type eclipsing variables (EW in the GCVS; Binnendijk 1970): These are close contact binary systems with main-sequence components from early A to early K, both filling their Roche lobe. They usually have short periods, between 0.25 and 1.2 days. W Uma light curves are characterized by nearly equal depths of the minima produced by the nearly uniform surface temperature of the common envelope. Light amplitudes are usually $<$2 mag in V.

Representative optical light curves of these three types of eclipsing binaries are shown in Fig. 2.3. The figure is from Huemmerich & Bernhard (2012) and is based on OGLE-II data (Szymanski, 2005).

Although this classification is still widely used today and useful for a preliminary classification of eclipsing binaries, it has become less important in modern astrophysics and nowadays, the concept of Lagrangian surfaces and Roche lobes is more accurate (Percy, 2007). In this way,

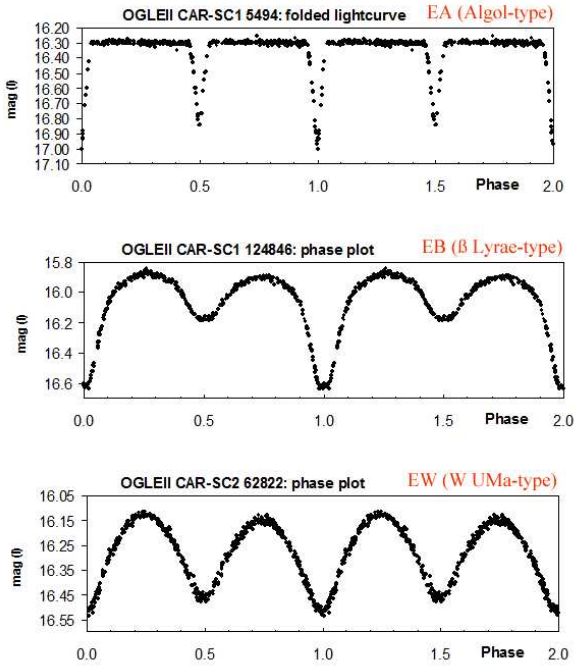

Figure 2.3: Representative light curves of the different types of eclipsing binaries (EA, EB and EW). Figure taken from Huemmerich & Bernhard (2012).

eclipsing binaries can also be classified based on the degree of filling of inner Roche lobes as detached, semidetached or contact systems. Very often, the classification makes also reference to the physical characteristics of their components (if they are main sequence stars, giants, subgiants, white dwarfs, etc.).

Rotating stars

When a star with nonuniform surface brightness and/or ellipsoidal shape rotates, its brightness varies with a period equal to the period of rotation. Stars exhibiting such behavior are called rotating variables:

- Ap and or Ap stars: Main sequence B8 to F2 stars whose apparent abundance of certain elements is thousands of times larger than in the sun.
- BY Draconis variables: Cool stars (K and M type) whose variability is due to cool spots and rotation. They can be single or binary and many of them can also show flares (being also UV Ceti stars).
- FK Comae variables: They are Sun-like stars, displaying high level of activity, including X-ray emission. RS Canum Venaticorum stars fall in this group. These stars rotate so fast that are believed to be the product of a merged W Ursae Majoris binary system.
- Pulsars: They are rapidly rotating highly magnetized neutron stars which emit radio pulses with periods from milliseconds to several seconds. The radio emission is actually continuous, but beamed, so the observer sees a pulse of radiation each time the beam sweeps across his/her line of sight.
- Ellipsoidal variables: The shape of the star is distorted by the tidal gravitational effect of the companion star, as the star orbits the center of mass of the system.

2.2 High-energy sources

The first hint of the existence of X-rays of cosmic origin dates from 1949, when X-ray detectors aboard rockets were briefly carried above the atmosphere where they detected X-rays produced by the Sun. It took more than a decade before a greatly improved detector discovered X-rays coming from sources beyond the solar system, with Sco X–1 being the first extrasolar source discovered by Giacconi et al. (1962). Since the late 60's, there have been many scientific satellites dedicated to the detection and study of X-ray emission from celestial objects. Some of the major X-ray astronomy missions include *Uhuru* (Giacconi et al., 1971), *Ariel V* (Smith & Courtier, 1976), *SAS-3* (Mayer, 1975), *HEAO-1* (Peterson, 1975), *Einstein* (Giacconi et al., 1979), *ROSAT* (Trümper, 1984), *ASCA*, *RXTE* (Bradt et al., 1993), *BeppoSAX* (Boella et al., 1997), *XMM-Newton* (Jansen et al., 2001), *Chandra* (Weisskopf et al., 2002), *INTEGRAL* (Winkler et al., 2003), *Suzaku* (Mitsuda et al., 2004) , *Swift* (Gehrels et al., 2004), and *MAXI* (Matsuoka et al., 2009).

There are several types of astrophysical X-ray emitters, from galaxy clusters, through supermassive black holes (SMBHs) in active galactic nuclei (AGN) to Galactic objects. Most of the Galactic X-ray sources are X-ray binaries (XBs) or Cataclysmic binaries (CVs), but there are other types. A few of them are isolated young pulsars. There are also supernova remnants (the debris left after a supernova explosion when a neutron star or black hole was formed). Other sources of X-rays in our Galaxy include some stars and solar-system bodies. A brief description of the main X-ray sources is given below.

2.2.1 X-ray binaries

X-ray binaries consist of a compact object and a companion star orbiting around the center of mass of the system. The main characteristic of these systems is that the compact star accretes gas from the atmosphere of the companion star and the gravitational potential energy of the accreted material is released as electromagnetic energy. This accretion can be wind-driven or produced by Roche-lobe overflow (see reviews by van Paradijs & McClintock 1995, Remillard & McClintock 2006, Done et al. 2007 and Lewin & van der Klis 2006). If the compact object is a white dwarf (WD), they are called cataclysmic binaries (CVs). Although CVs also emit in X-rays, the term "X-ray binaries" is often used to refer to binary systems in which the compact object can be either a neutron star (NS) or a black hole (BH) (Liu et al., 2006, 2007). Moreover, some of these systems, known as microquasars, produce relativistic jets. On the other hand, the companion star can be a normal star or a WD. According to the physical properties of the donor star, X-ray binaries can be classified as High-mass X-ray binaries (HMXBs) and Low-mass X-ray binaries (LMXBs).

Cataclysmic binaries

Cataclysmic binaries are the most populous subtype of Cataclysmic Variables, as explained above. These binary systems consist of a white dwarf (WD) and an orange or red (K- or M-type) main-sequence or giant secondary, in which matter flows from the secondary toward the primary. The infalling matter usually forms an accretion disk around the WD. Strong UV and X-ray emission is produced in the accretion disk, although in some cases the magnetic field of the WD is strong enough to disrupt the inner accretion disk or even prevent its formation. The X-ray properties of CVs are described in detail in Kuulkers et al. (2006) and in Balman (2012). CVs can be classified in:

- The "non-magnetic" group (corresponding to a magnetic field strength $B \leq 10^4$G), including:

- Classical Novae: They are caused by thermonuclear fusion and detonation of accreted hydrogen on the surface of the WD and present very large outbursts of 6 to 19 magnitudes in the optical within a few days. The eruptive event is followed by a steady decline back to the pre-nova magnitude over a few months.
- Recurrent Novae: These are similar to novae with outbursts of about 4 to 9 magnitudes, repeating every 10 to 80 years.
- Dwarf novae (also U Geminorum stars, UG): They brighten repeatedly, though they are smaller in amplitude (increase of 2 to 5 magnitudes) and higher in frequency (with intervals of weeks or months) than classical novae and differ from them in the mechanisms that produce the outbursts. Dwarf novae result from instability in the accretion disk, when the gas reaches a critical temperature that causes a change in viscosity, resulting in a collapse onto the WD that releases large amounts of gravitational potential energy. They are classified in three subtypes: SS Cygni stars (UGSS) which have outbursts of two distinct durations, SU Ursae Majoris stars (UGSU) having "superoutbursts" which are brighter than the average and Z Camelopardalis stars (UGZ) which temporarily "halt" at a particular brightness below their peak.

Figure 2.4: Artists view of a polar CV (left) and of an intermediate polar CV (right). Credits: Max-Planck-Institut für extraterrestrische Physik, Die Physik Galaktischer Kompakter Objekte.

- The much rarer, "magnetic"group includes:
  - Polars (or AM Herculis systems): They have strong magnetic fields (10^7G $\leq$ B $\leq$ 10^8G) which prevent the formation of an accretion disk. In these systems the matter couples directly onto the magnetic field at the point where the ram pressure equates the magnetic field pressure and they exhibit only accretion streams (see Fig. 2.4, left).
  - Intermediate polars (also DQ Herculis stars): In these sources, the magnetic field is between that of non-magnetic CVs and strongly magnetic systems (10^6G $\leq$ B $\leq$ 10^7G). The matter passes through an accretion disc and then is threaded onto the magnetic field lines (see Fig. 2.4, right).

Type Ia supernovae occur in this kind of systems when instead of igniting a thin surface layer, as in the novae, the accretion produces the WD to become unstable and the entire star is consumed in a gigantic thermonuclear explosion.

Neutron star X-ray binaries

Different phenomena related to the neutron star characteristics, which determine the accretion geometry (polar or via accretion disk) are detected in NS systems. They can be mainly divided

in X-ray pulsars and X-ray bursters, being the age of the system the principal difference between both types of systems.

- X-ray pulsars: An X-ray pulsar consists of a magnetized neutron star in orbit with a normal stellar companion. In these systems polar accretion onto the neutron star takes place and pulsations are observed. See Caballero & Wilms (2012) for a review. Since a strong magnetic field ($\sim 10^{12}$ G) is needed to channel the material onto the poles of the neutron star, X-ray pulsations are only expected in young neutron stars (those with massive stellar companions). Indeed, not all the accreting compact objects show evidence for periodic pulsations. For NSs, the absence of pulsations is related to a rather weak magnetic field ($\leq 10^8$ G), while for BHs the accretion is randomly distributed.

- X-ray bursters: The bursters are associated with LMXBs and are likely to be very old. The age is critical in determining the strength of the magnetic field, which gradually decays with time. There are two types of X-ray bursts.Type I X-ray bursts light curves display a fast rise ($\sim$ few seconds) followed by a slower exponential decline ($\sim$ tens of seconds). They are caused by thermonuclear explosions of H and/or He on the surface of a weakly magnetized neutron star. Type II bursts display more symmetrical light curves and are produced by instabilities of the accretion flow onto the neutron star. While there are ~ 100 sources displaying type I X-ray bursts (Galloway et al., 2008), only two objects have been found to show Type II X-ray bursts, the *Rapid Burster*, which shows both types of bursts, and GRO 1744–28, the *Bursting Pulsar* (Finger et al., 1996).

These two scenarios have been thought to be mutually exclusive, but this changed with the discovery of GRO 1744–28, the *Bursting Pulsar*. It was the first source found presenting pulsations and bursts (type II bursts). This system seems to have a magnetic field of intermediate strength which suppresses thermonuclear burst activity (type I bursts) (see Degenaar et al. 2014 and references therein).

Black hole X-ray binaries

Black hole systems can be identified for the lack of pulses and X-ray bursts and for their X-ray spectra. BHs present state transitions with high-soft states, which are ultrasoft and low-hard states, with a high-energy power law tail above 20 keV (see Fig. 2.5). On the other hand, for a given period, quiescent BH binaries are fainter than quiescent NS binaries.

Cygnus X-1, was the first black hole candidate with mass established via dynamical observations (Webster & Murdin, 1972; Bolton, 1972). Its black hole nature has been controversial, due to the lack of direct observation but has generally been accepted from indirect evidence of its influence on the surrounding material, and many studies support it (Orosz et al., 2011; Gou et al., 2014). Another black hole candidate that has been very studied is SS 433. This system probably consists of a black hole accreting matter from a high-mass star filling its Roche lobe (see Fabrika 2004 for a review). In the last years, better black holes candidates have been found within transient LMXBs also called soft X-ray transients (SXTs; they will be explained below). In these systems the lower mass of the companion star allows for more accurate estimations of the black hole mass.

Microquasars

Microquasars are X-ray binary stars which exhibit jets of relativistic matter ejected perpendicularly to both sides of an accretion disk surrounding a compact object which is either a black hole or a neutron star (Mirabel, 1994). The jets contain relativistic electrons that produce synchrotron radiation detected at radio wavelengths.

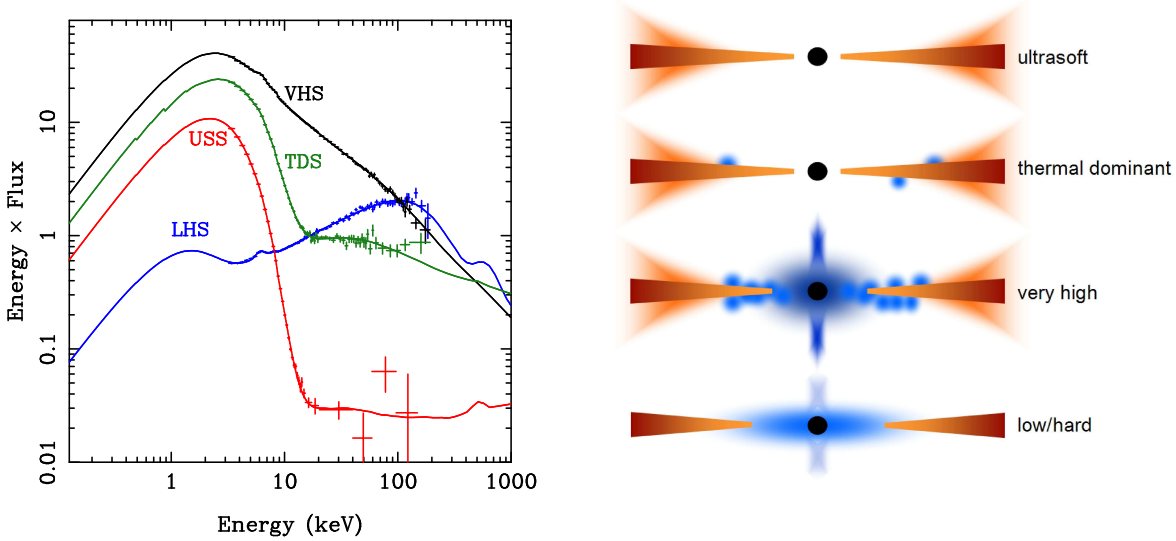

Figure 2.5: Illustration of the BH spectral states. The left panel shows a selection of states taken from the 2005 outburst of GRO J1655–40. The right panel shows the accretion flow changes explaining these different spectra, with differing contributions from the disk, hot inner flow and its associated jet, active regions above the disk and a wind. Figure taken from Done et al. (2007).

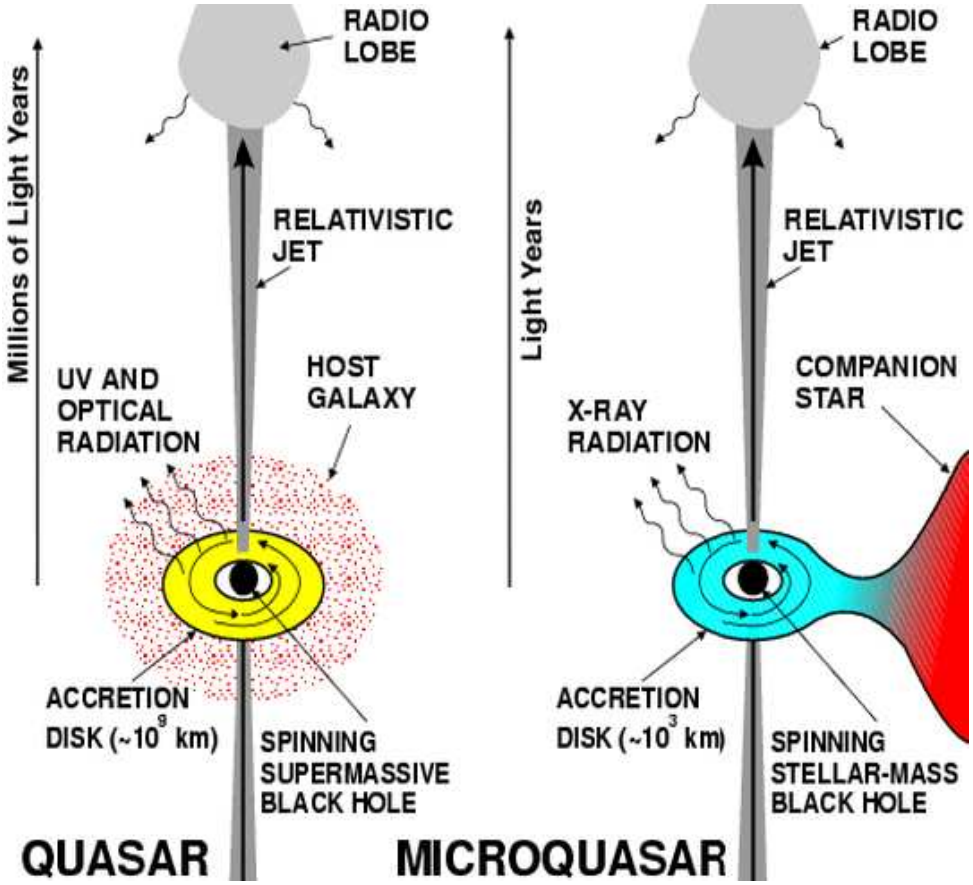

Figure 2.6: Microquasars behave like extragalactic quasars but at a reduced scale, hence their name. Figure taken from Mirabel & Rodríguez (1998).

Microquasars are found in several X-ray binaries in our Galaxy and are scaled down versions of quasi-stellar radio sources (quasars) (for a description of quasars see Section 2.2.2), as pointed out by Felix Mirabel, who also coined the name "microquasar" (see Fig. 2.6). It is known that black holes display different spectral states in X-ray emission, with transitions between a low/hard state, where a compact radio jet is seen, to a high/soft state, where the radio emission is reduced by large factors or not detectable at all. The small size of these objects compared to those of quasars, makes them especially easy to monitor in time. Considering that the characteristic time of matter accretion onto the compact object is proportional to its mass, the variations observed in a microquasar in time scales of minutes correspond to similar phenomena that would take thousands of years in a quasar with a SMBH.

Low-mass X-ray binaries

In Low-mass X-ray binaries (LMXBs) the mass of the companion star is below ~ 2 $M_\odot$ and the spectral type is A or later. The optical emission of LMXBs is dominated by the reprocessing of part of the X-rays into optical photons in the accretion disk (see Fig. 2.7).

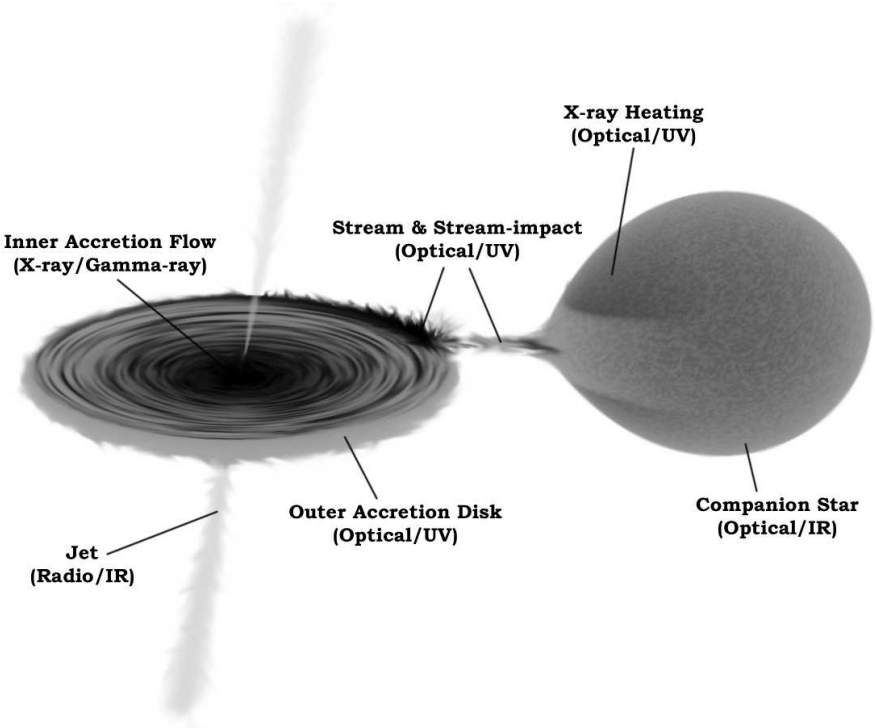

Figure 2.7: Geometry of a Roche lobe overflow low-mass X-ray binary. The color scale is inverted with the brightest areas appearing darkest. Figure taken from Hynes (2010).

The LMXBs comprise the globular cluster X-ray sources, X-ray bursters, soft X-ray transients and the bright galactic bulge X-ray sources (van Paradijs & van der Klis, 2002).

According to the X-ray activity, non-pulsating compact objects appear both as persistent and as transient.

- Persistent: Their distinguishing characteristic is the fact that they have always been at detectable flux levels in the history of X-ray astronomy. Their X-ray fluxes can be variable by up to several factors of 2 over timescales ranging from milliseconds to months.

- Transient: These systems are characterized by long periods of inactivity lasting months to decades. Eventually they turn on for typically several months in which their X-ray and

optical fluxes increase by several orders of magnitude, and then drop back to the quiescent state (Bradt et al., 2000). These systems are called soft X-ray transients (SXTs). The majority ($\sim 75\%$) of SXTs contain a black hole and a low-mass main sequence companion star. There are only about 14 confirmed SXTs with a neutron star as the compact object (Liu et al., 2007), all of which also show Type I X-ray bursts. A well-studied SXT is Aql X-1 (Maitra & Bailyn, 2008).

X-ray bursts can occur in both, persistent and transient LMXBs, if the system consists of a low-mass main sequence star and a weakly magnetized NS.

Most of the LMXBs, accrete matter by Roche lobe overflow, but a small group of them with low-mass red giant donors do accrete from the donor wind. These kind of LMXBs are called symbiotic X-ray binaries (Corbet et al., 2008), by analogy with symbiotic stars (where a WD accretes from the wind of a M-type giant companion). The prototype of symbiotic X-ray binary is GX 1+4 (González-Galán et al., 2012).

According to the correlation of their X-ray timing and spectral properties, NS LMXBs can be further classified as Z-type sources (like GX 340+0, GX 17+2) and atoll sources (like 4U 1636-536, 4U 1735-44). X-ray fluxes of the Z sources are higher than those of the atoll sources, so the mass accretion rate must be substantially higher in the Z sources. The spectra of Atoll sources are harder than those of Z sources. It has recently been discovered one NS LMXBs, IGR J17480–2446, evolves between both types (Chakraborty et al., 2011).

High-mass X-ray binaries

High-mass X-ray binaries (HMXBs) are X-ray binaries in which the mass of the companion star, with spectral type O or B, is above ~ 8 $M_\odot$. Depending on the evolutionary status of the donor star, they can be divided into:

- Supergiant X-ray binaries (SGXBs): the optical component is a supergiant or a bright giant star (luminosity class I-II).
  - Classical SGXBs: divided in high luminosity or disk-fed (Cen X–3, SMC X–1, LMC X–4) and low luminosity or persistent wind-fed (GX 301–2, 4U 1538–52).
  - Super fast X-ray transients (SFXTs):. Discovered by *INTEGRAL*, the prototype is IGR J17544–2619 (Sunyaev et al., 2003). They have O/B supergiant companions and their outbursts last only some hours. See Negueruela et al. 2006; Blay et al. 2012; Sidoli 2013 for reference.

- Be/X-ray binaries (BeXRBs): the donor star is a OBe star with luminosity class V, IV or III. They present spectral lines in emission and an IR excess with respect to a normal star of the same spectral type. These characteristics are attributed to an equatorial disk around the rapidly rotating Be star. The X-ray emission is only seen in separate outbursts, occurring during the periastron passages (see Fig.2.8). Almost all the observed BeXRBs have a NS as compact object. The only Be containing a BH was recently discovered by Casares et al. (2014). A detailed review on the basic properties of BeXRBs can be found in Negueruela (1998), Coe (2000) and Reig (2011).
  - Transient: Most of the BeXRBs are transient sources and can display three different luminosity states (classification according to Stella et al. 1986):
    * Type I or normal outbursts: moderate intensity outbursts ($L_X \approx 10^{36}$–10^{37} erg s^{-1}), occurring close to the periastron passage of the neutron star.

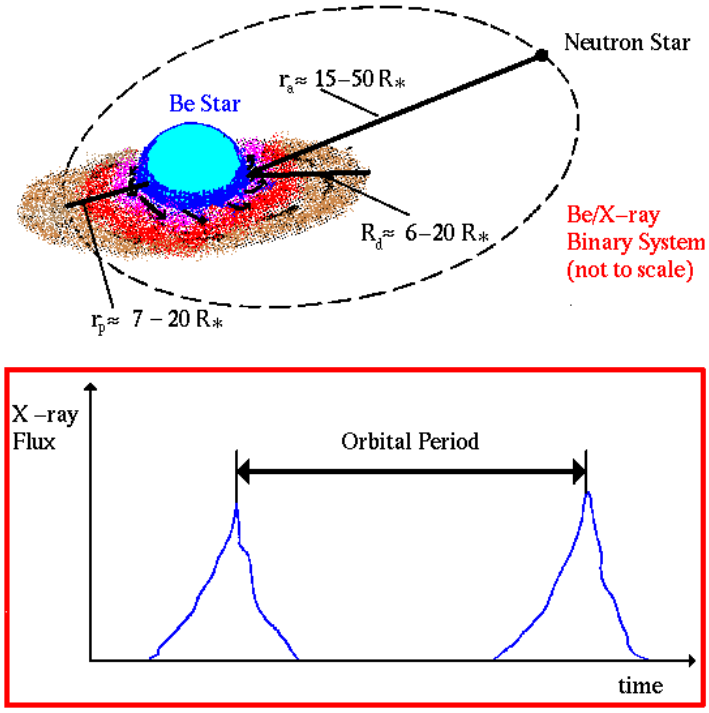

Figure 2.8: Conventional model for a Be/X-ray binary transient: The neutron star evolves around the Be star in a very wide orbit. At apastron (maximum distance to the companion) the NS is very far away from the Be star to capture a significant amount of matter and there is no X-ray emission. However, at periastron (minimum distance), the NS comes inside the circumstellar envelope of the Be star and accretes matter, being detected as a transient source. Figure taken from the Ignacio Negeruela's BeXRB's page[1].

    - Type II or giant outbursts: ($L_X > 10^{37}\,\mathrm{erg\,s^{-1}}$). The parameters of these outbursts have not to be related to the orbital period, although in some cases, like for 1A 0535+262, they appear close to the periastron passages.
    - Quiescent states: when they are not in outburst, some present low X-ray luminosity ($L_X < 10^{36}\,\mathrm{erg\,s^{-1}}$), and others are not visible at all in X-rays.
  - Persistent: some BeXRBs do not present outbursts or they have not been observed. These sources present less X-ray variability, lower luminosity, slower neutron stars and longer orbital periods.

- Obscured HMXBs exhibiting a huge intrinsic and local extinction, this subtype of HMXBs was discovered by *INTEGRAL* (IGR J16318–1818; Walter et al. 2003).

2.2.2 Active Galactic Nuclei

An active galactic nucleus (AGN) is a compact region at the center of a galaxy that has a very high luminosity. Such excess emission has been observed in all wavelengths and this radiation is believed to be a result of accretion of mass by a supermassive black hole (SMBH) at the center of its host galaxy (see Fig. 2.9). For a complete and updated general reference in AGN, see Beckmann & Shrader (2012).

Radio-loudness of AGN

The definition of radio-loudness arises from the comparison of the radio flux to the optical flux (Peterson, 1997). Then, based on their radio activity, AGN can be divided in:

[1] http://dfists.ua.es/~ignacio/bex.html

Figure 2.9: Artist's impression of an Active Galactic Nucleus (AGN) within the currently leading scenario, the so-called unified model. Credits: ESA/NASA, the AVO project and Paolo Padovani.

- Radio-quiet AGN: If none or a small amount of radio emission is detected. Within the radio-quiet AGN, these subtypes can be found:
  - Seyfert galaxies: In the optical range they show nuclear continuum emission, narrow and occasionally broad emission lines, occasionally strong nuclear X-ray emission and sometimes a weak small-scale radio jet. Originally they were divided into two types known as Seyfert 1 and 2: Seyfert 1s show strong broad emission lines while Seyfert 2s do not, and Seyfert 1s are more likely to show strong soft X-ray emission. See Weedman (1977) and Sulentic et al. (2000) for reviews on Seyfert galaxies.
  - Radio-quiet quasars: They are the most energetic and distant of the AGN (Willott et al., 2010; Véron-Cetty & Véron, 2010). Their optical spectra show emission lines and depending on their characteristics, quasars are divided in Type 1 (if they display both broad and narrow lines) and Type 2 (if they only present narrow lines).
  - Low-ionization nuclear emission-line regions (LINERs): they show weak nuclear emission-line regions. Most of the optically classified LINERs nuclei host an AGN, although an AGN alone cannot explain all the optical emission observed in these systems (Singh et al., 2013; Gonzalez-Martin et al., 2015).
  - Ultraluminous infrared galaxies (ULIRGs): About 70% of the ULIRGs display a Seyfert or LINER core (Veilleux et al., 1997; Lutz et al., 1998; Veilleux et al., 1999). Star formation and AGN activity are close in these galaxies, and the AGN core dominates the emission of the most luminous ULIRGs.
- Radio-loud AGN: the radio emission is a signature of the presence of a relativistic jet, which produces synchrotron radiation. This group includes:
  - Radio galaxies: When the central region is hidden but the object produces bright radio jets, and large radio luminosities, the presence of an AGN is assumed. Radio galaxies can be divided in two subgroups:

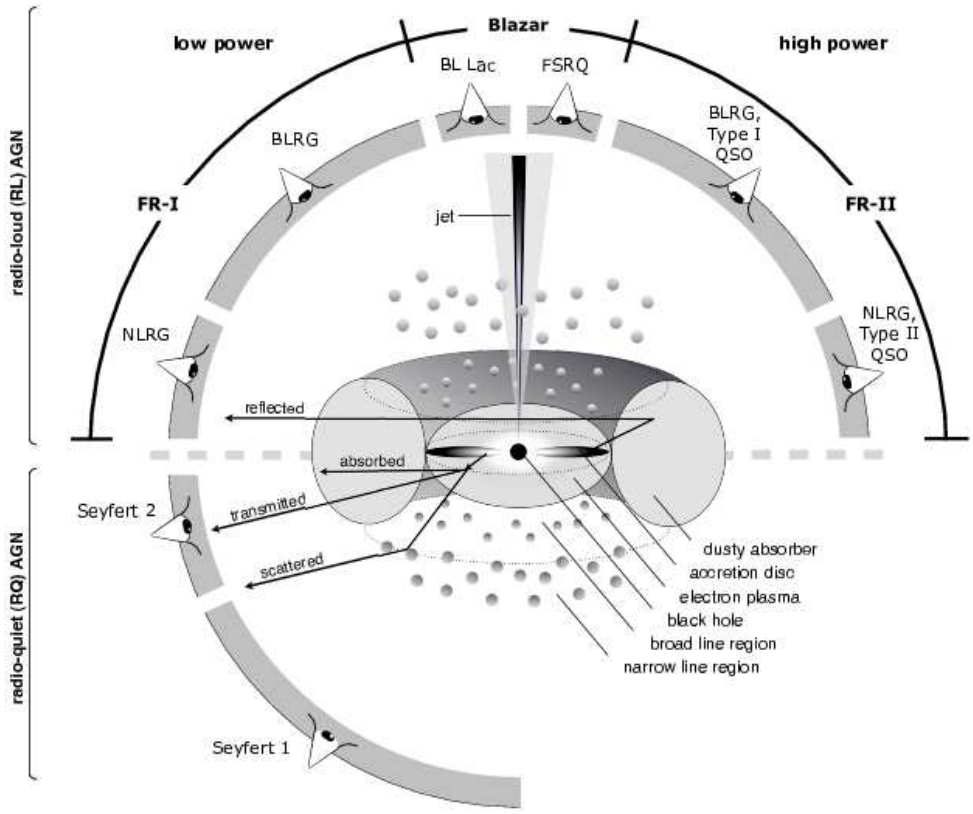

Figure 2.10: Schematic representation of the AGN phenomenon in the unified scheme. The type of object we see depends on the viewing angle, whether or not the AGN produces a significant jet emission, and how powerful the central engine is. Note that radio-loud objects are generally thought to display symmetric jet emission. Figure taken from Beckmann & Shrader (2012).

    - The low-luminosity Fanaroff-Riley class I (FR-I) galaxies: they show a compact radio emission arising from close to the core. Broad-line radio galaxies (BLRGs) and narrow-line radio galaxies (NLRGs) are found in this subgroup.
    - The high-luminosity Fanaroff-Riley class II (FR-II) galaxies: the structure is dominated by the radio lobes and the emission seems to come from the far end of the extended emission.
- Radio-loud quasars: Similar to radio-quiet quasars but presenting emission from a jet.
- Blazars: Their main characteristic is a rapidly variable, polarized optical, radio and X-ray emission, believed to come from a relativistic jet oriented close to the line of sight. They are usually divided in :
    - Weak-lined blazars, or BL Lac objects. They are subdivided in low-frequency peaked BL Lacs (LBLs) and high-frequency peaked BL Lacs (HBLs) depending on whether $\alpha_{\rm rx} = \log\,(F_{\rm 5GHz}\,/\,F_{\rm 1keV})\,/\,7.68$ is greater than or less than 0.75, respectively (Padovani & Giommi, 1995). The observed differences in continuum spectral shape, are that the synchrotron power of LBL peaks at submm to IR wavelengths while that of HBLs peaks at UV to X-ray wavelengths, and the Compton components peak at GeV energies for LBLs and at much higher (TeV) energies for HBLs. Some examples of BL Lac objects are 3C 454.3, BL Lacertae, PKS 2155-304, Mrk 421, and Mrk 501.
    - Strong-emission-line blazars, or Flat-Spectrum Radio Quasars (FSRQs), which are again divided into optically violent variables (OVVs), and highly polarized

quasars (HPQs). These are highly variable and (at least part of the time) highly polarized, as well as superluminal. The continuum shapes of FSRQs are very similar to those of LBLs, but they show stronger broad emission lines. An example of these strong-lined blazars is 3C 279.

Optical spectra of AGN

On the other hand, according to the characteristics of their optical and ultraviolet spectra, three classes of AGN can be distinguished (Tadhunter, 2008):

- Type 1: they have bright continua and broad and narrow emission lines. The broad lines trace high-velocity gas, presumably located deep in the gravitational well of the central black hole. In the radio-quiet group, they include the Seyfert 1 galaxies at low power, and the radio-quiet quasars at high-luminosity. In the radio-loud group, Type 1 AGN include the BLRGs at low luminosities and radio-loud quasars at high luminosities.

- Type 2: they display weak continua and only narrow emission lines, meaning either that they have no high-velocity gas, or the line of sight to such gas is obscured by a thick wall of absorbing material. Radio-quiet Type 2 AGN include Seyfert 2 galaxies at low luminosities. In the radio-loud group, Type 2 AGN include the NLRGs at low power and the Type 2 quasars at high power.

- Type 0: with weak or unusual line emission. These include the BL Lac objects and OVV.

Obscuration of AGN

Finally, from their appearance at the soft X-ray band (up to few keV), the AGN can be classified according to the degree of obscuration by material (dust and gas) located in the inner part of the central engine (see Bianchi et al. 2012 for a review). In this way, those AGN with N_H between 4×10^{21} and 10^{24} cm^2 are considered absorbed and those with N_H $<4\times10^{21}$cm^{-2} are unabsorbed. AGN with N_H $>10^{24}$cm^{-2} are called "Compton thick".

The Unified Model

These types of AGN can be in principle understood as a similar phenomenon, but seen from different angles. The theory that explain this is known as the "unified model" (Antonucci, 1993; Urry & Padovani, 1995). This model postulates the presence of a central engine consisting in a SMBH surrounded by an accretion disk, a clumpy torus consisting mainly of dust, the broad-line region (close to the center and clumpy) and the narrow-line region (further away, but still near the nucleus), presenting jets in the radio loud AGN (see Fig. 2.10). Unified models of AGN postulate that all the observed differences between Type 1 and Type 2 objects are due to orientation effects with respect to the viewing angle. The key ingredient of these models is the obscuring medium, historically related to a toroidal structure on a parsec scale. However, many results obtained in the last few years are clearly showing the need for a more complex geometrical distribution of the absorbing media (see Bianchi et al. 2012; Malizia et al. 2012 and references therein).

2.3 Variability of high-energy sources

The high-energy sources described in the previous section display variability across all the electromagnetic spectrum. These variations are due to very different processes and appear in timescales

from milliseconds to years. The main mechanisms driving the optical and X-ray brightness variations detected in XBs and AGN and the typical effects observed in their light curves are described below.

2.3.1 Variability in X-ray binaries

The light curves of X-ray binaries usually present orbital modulations, associated to the periastron passage or to geometrical effects, but many times, superimposed to these variations, long-term variations appear. X-ray binaries present very different variations depending on the properties of the donor star, the compact object, the accretion disk or the elements of the orbit.

Orbital modulations in X-ray binaries

The orbital modulations in X-ray binaries can be due to different phenomena depending on the nature of the companion star. The emission from the donor star in HMXB systems is often dominant in the optical band and the optical emission is not much affected by the presence of the compact object, while the companion stars in LMXBs are faint and most of the optical emission originates from the accretion process and comes from viscous thermal emission of the accretion disk. Also X-ray reprocessing in the accretion disk and in the secondary star may take place. The observed properties of LMXBs depend on the viewing angle, as will be explained below. A good review on the multiwavelength properties of LMXBs can be found in Hynes (2010). The main orbital phenomena observed in X-ray binaries are:

- Ellipsoidal modulations: The optical light curves of many HMXBs and some LMXBs in quiescence show a double-waved shape, with two maxima and two minima per orbital cycle. They are called ellipsoidal variations and are caused by the different aspects that the tidally distorted donor star offers to the observer along its orbit (see Fig. 2.11 a). The optical emission of Cyg X–1 is dominated by this effect.

- X-ray heating: Often, the observed optical light curves cannot be just described by ellipsoidal variations. X-ray heating of the accretion disk around the compact object and of the donor star, contributes to the optical emission as well. When transient XBs move from quiescence into luminous or outburst states, the X-ray luminosity increases. The inner face of the companion star is heated by the X-rays and this offsets the gravity darkening effect, reversing the depths of the minima (see Fig. 2.11 b.). If the heating is strong enough, the ellipsoidal variations are not distinguished and the light curve will have only one minimum at 0.0 phase and one maximum at 0.5 phase (see Fig. 2.11 c.). The orbital period of Sco X–1 was discovered applying this model.

- Related to the disk of the Be star: Be/X-ray binaries (BeXRBs) display periodic outbursts due to the interaction of the neutron star with the Be equatorial disk during the periastron passage (Okazaki & Negueruela, 2001). Apart from the normal outbursts, giant outbursts can occur, not necessarily associated to the periastron passages. Theoretically, a giant outburst is explained by an interaction between the neutron star orbit and the warped Be-disk (Okazaki et al., 2013). A representative case of a system displaying this kind of variations is 1A 0535+262.

- Eclipses: In LMXBs with high enough inclination ($>75^{o}$), eclipses of the accretion disk by the companion star can occur and they affect to the optical light curves, producing a sharp minimum at phase 0.0, while eclipses of the heated face of the companion star by the disk may introduce a secondary eclipse at phase 0.5 (see Fig. 2.11 d.). In HMXBs, the eclipses are detected only in X-rays because, as explained above, the optical emission is dominated by the emission from the donor star.

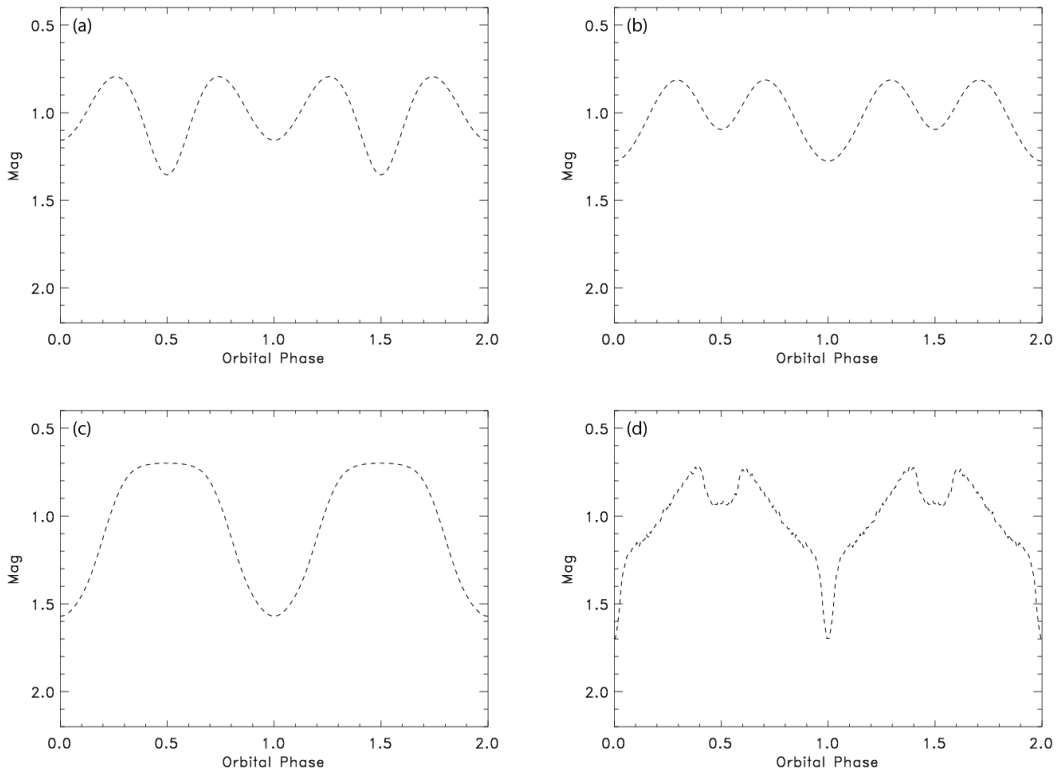

Figure 2.11: Optical orbital light curves of LMXBs. a) Pure ellipsoidal variations. b) Ellipsoidal variations plus weak irradiation of the donor. c) Strong irradiation of the donor. d) Irradiation of disk and donor with mutual eclipses. These figures have been taken from Hynes (2010).

- Dipping sources: Some LMXBs with intermediate inclination (between 60 and 80^{o}) show periodic dips in their X-ray light curves. They are explained as obscuration of the accretion disk caused by the gas stream from the companion star (Mason et al., 1986; Díaz Trigo et al., 2006). Examples of dipping sources are XB 1916–053 and XB 1323–619. In HMXBs, eclipses of the compact object (observed in X-rays) are more common than dips because of the size of the companion star. However, when observed, dips are usually related to clumps from the companion star wind intercepting X-rays from the compact object on our line of sight. This seems to be the cause of the secondary X-ray variations found in Cyg X–1 (Balucinska-Church et al., 2000), although they could also be due to the interaction of this wind with the edge of the accretion disk (Poutanen et al., 2008).

Long-term modulations in X-ray binaries

Long-term ('superorbital') periods or modulations have been detected in a wide variety of both low and high-mass X-ray binaries at X-ray and optical wavelengths (Kotze & Charles, 2012). Some systems are remarkably stable, but others show a range of variability properties, from longer variability time-scales to a quite chaotic behavior. The main emission processes that could describe these long-term modulations are:

- Disk precession: This effect can appear when $q = M_2/M_X < 0.25$–0.33, where M_2 is the mass of the donor star and M_X is the mass of the compact object, due to resonances excited in the disks resulting from tidal interactions with the donor (Whitehurst & King, 1991).

- Radiation-induced warping/tilting: Accretion disks can develop radiation-induced warps that are functions of their binary separation and system mass ratio. Ogilvie & Dubus (2001) show that radiation-driven warping is probably not a common phenomenon in LMXBs. They also find that stable, steadily precessing disks exist for a narrow range of parameters close to the stability limit. This could be an explanation of why there are so few systems with clear, repeatable 'superorbital' variations (Her X–1, SS 433 and LMC X–4). Ogilvie & Dubus (2001) found that all of these systems are close to the stability limit for a reasonable choice of parameters. On the other hand, those systems far from the stability limit, including Cyg X–2, Cen X–3 and SMC X–1, will probably present quasi-periodic or chaotic variability.

- Magnetic warping: The inner region of the accretion disk around a magnetized star (T Tauri star, white dwarf, or neutron star) is subjected to magnetic torques that induce warping and precession of the disk. These torques arise from the interaction between the stellar field and the induced electric currents in the disk. Pfeiffer & Lai (2004) carry out numerical simulations of the nonlinear evolution of warped, viscous accretion disks driven by the magnetic torques. They show that an accretion disk surrounding a magnetic star can develop warps in the inner disk that steadily precess. The retrograde precession observed in Her X–1 is well reproduced by these simulations (Staubert et al., 2009a).

- Wind-driven tilting: Other mechanisms involving coronal wind torques have been suggested for driving the warps (Schandl & Meyer, 1994; Corbet & Krimm, 2013).

- X-ray state changes: Long-term modulation of the mass-transfer rate through the disks has been associated with X-ray state changes in many sources such as Cyg X–1 and GX 339–4.

- Precessing relativistic jets: The behavior of the microquasar SS 433 is well established as coming from precessing relativistic jets and this process seems to provide stability to the 162-d superorbital period.

- Be-X-ray binaries: Apart from the orbital periodic outburst, many Be/X-ray binaries show long-term quasi-periodic modulations (from hundreds of days to years). These superorbital variations seem to be related to the formation and depletion of the circumstellar disk around the Be star (Clark et al., 1999; McGowan & Charles, 2003; Rajoelimanana et al., 2011; Yan et al., 2012; Camero-Arranz et al., 2012). Since the circumstellar disk is the accretion mechanism in these systems, the X-ray and optical variabilities are expected to be correlated.

These long timescale variations have been analyzed by different authors in the last years. Rajoelimanana et al. (2011) searched for correlations with the orbital periods. A study of long-term variability of high-mass X-ray binaries has been published by Reig & Zezas (2014). These authors compare the behavior of the Be/X-ray binaries with the supergiant systems, finding that the first ones present larger amplitude of variability and that this amplitude depends more on the wavelength for these Be/X-ray systems. This is due to the fact that in Be/X-ray binaries, the main source of both optical and X-ray variability is the circumstellar disk of the Be star.

2.3.2 AGN Variability

Variable emission over the whole electromagnetic spectrum is usually observed in all types of AGN. The study of variability on simultaneous data at different wavelengths is crucial to understand the physical processes at work in these objects.

As explained in Section 2.2.2, AGN can be first divided in type 1 and type 2, based on the emission lines visible in the optical domain, and in radio-quiet and radio-loud sources, according to their radio emission.

In radio-quiet AGN, the optical-UV variability seems to be originated in the accretion disk as a combination of thermal emission and reprocessing of X-ray radiation (Koratkar & Blaes, 1999; Uttley & Mchardy, 2004; Uttley, 2006; Gaskell, 2008). The first mechanism produces long-term optical variations (months-years) while the second one should lead to a short-term correlation (days) between the X-ray and optical light curves. According to standard disk theory, the disk temperature is expected to be a function of black hole mass and accretion rate, scaling as $T \propto (\dot{m}/M_{BH})^{(1/4)}$, where $\dot{m}$ is the accretion rate and M_{BH} is the mass of the supermassive black hole (SMBH). Possible optical/X-ray interactions in the 'standard' AGN disk-corona picture and how they depend on mass and accretion rate are represented in Fig. 2.12. In hot disks, the accretion rate is high and the mass is low, the main connection between X-ray and optical variations is likely to be reprocessing, by optical emitting disk at large radii, and the amplitudes of the optical variations are smaller than the X-ray ones. Moreover, an inverse correlation with longer lags due to variations of the accretion flow propagating from the outer (optically emitting) parts of the accretion disk into its inner (X-ray emitting) region is expected too (Shemmer et al., 2003). In cooler disks, for which the mass is high and the accretion rate is low, the optical and X-ray emitting regions are much closer and may be co-spatial. In this case, the optical emission could drive X-ray variations through Comptonisation, leading to larger amplitude of optical variability compared to X-rays. Sometimes, the correlations are not so obvious or no correlations are found between X-ray and optical variability. On the other hand, in Seyfert galaxies, especially in type 2, the optical variability produced in the accretion disk can be masked by the stellar continuum from the host galaxies, leading to smaller observed amplitudes of variations.

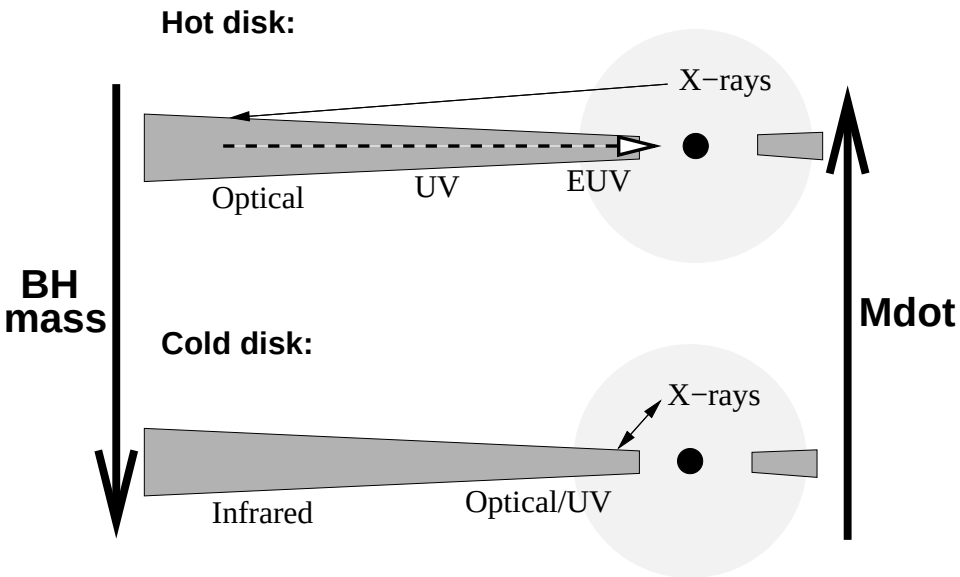

Figure 2.12: Summary of some possible optical/X-ray interactions in the 'standard' AGN disk-corona picture, and how they depend on mass and accretion rate. Solid arrows represent interactions due to photons, i.e. reprocessing and Comptonisation, while the dashed arrow denotes the indirect connection due to propagating accretion variations. Figure from Uttley (2006).

In radio-loud AGN, the variability is mainly dominated by the emission from a relativistic jet (see Ulrich et al. 1997, Boettcher 2012 and references therein). The continuum radiation observed from radio to optical, and some times in X-rays, is originated by synchrotron radiation

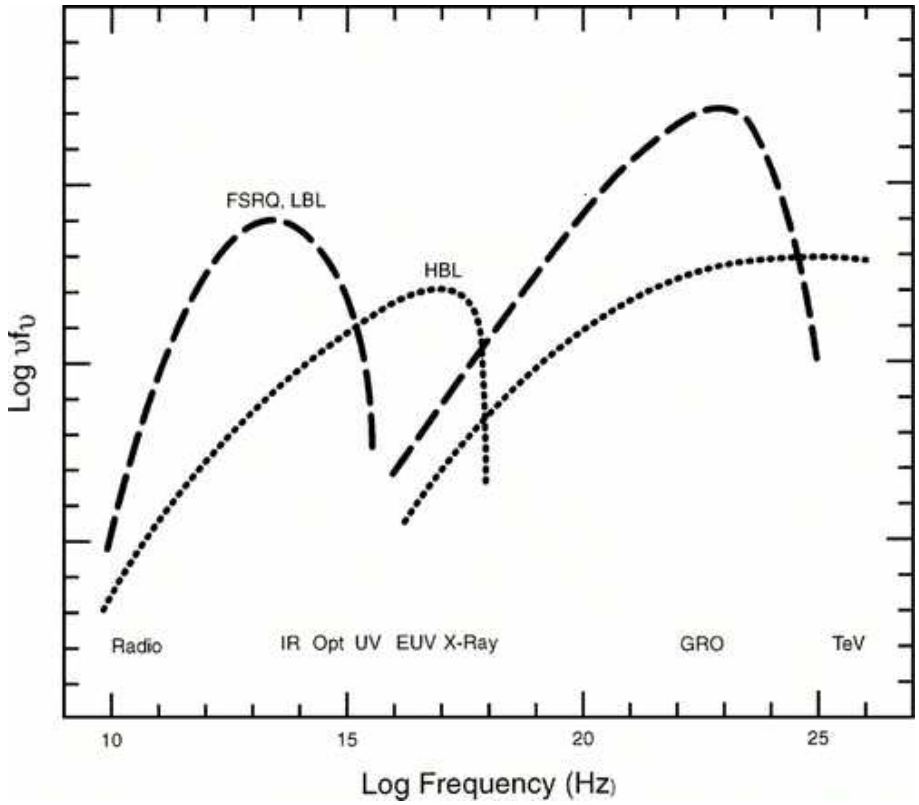

Figure 2.13: Schematic broadband spectra of blazars from radio through TeV gamma rays. The low-energy component is due to synchrotron radiation and the high-energy component to Compton scattering of lower-energy seed photons, possibly the synchrotron photons or ambient UV/X-ray disk or line photons. Figure from Ulrich et al. (1997).

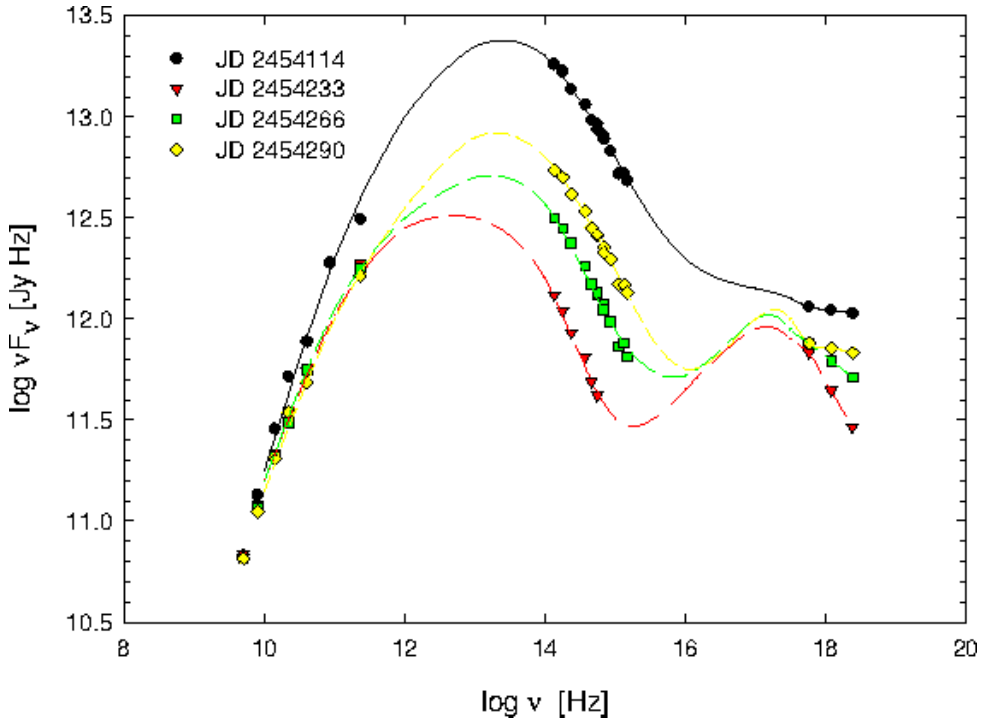

Figure 2.14: Radio-to-X-ray spectral energy distributions of 3C 279 at various epochs in 2007. Figure from Larionov et al. (2008).

from accelerated charged particles in the jet that interact with the magnetic field of the AGN (see Fig. 2.13). The amplitude of the variability in radio-loud AGN is larger at frequencies higher than the peak of the synchrotron spectrum (see Fig. 2.14, where the Spectral Energy Distributions (SEDs) of 3C 279 in different epochs are plotted). The SED shows a two-bump structure. The low-energy bump ranges from radio to UV or soft X-ray frequencies and is believed to come from synchrotron emission of non-thermal electrons in a relativistic jet (Padovani & Giommi, 1996). However, for the high-energy bump, from X-ray to gamma-ray, leptonic and hadronic models were both involved (Böttcher & Dermer, 2006; Boettcher, 2012). According to the peak frequency of its synchrotron bump, blazars are divided into low-, intermediate- and high-synchrotron peaked sources, defined by synchrotron emission peaks below 10^{14} Hz, between 10^{14} Hz and 10^{15} Hz, and above 10^{15} Hz, respectively (Padovani & Giommi, 1995; Abdo et al., 2010). For low-frequency peaked BL Lacs (LBLs), the optical emission lies above the peak frequency while for high-frequency peaked BL Lacs (HBLs) it lies below it. This explains why LBLs are highly variable in the optical while HBLs are not. On the other hand, at X-rays, HBLs are among the most rapidly variable AGN known. The emission at higher energies is likely the result from inverse Compton scattering. It peaks at GeV energies for Flat-Spectrum Radio Quasars (FSRQs) and LBLs and at much higher (TeV) energies for HBLs.

Blazars are known to show variability across the entire electromagnetic spectrum on different time-scales ranging from minutes to years. The variations that occur within one day (minutes to several hours) are known as intraday variability or microvariability (hereafter IDV; Wagner & Witzel 1995). Variability, time delay, correlations and color variation have been used to probe the emission location and physical processes of the radiation mechanisms (Chatterjee et al., 2008, 2012; Chen, 2014).

Apart from the expected long-term variations, rapid variability (called microvariability) has been detected in some AGN in optical and gamma rays. There are several models to explain the microvariability and short-term variability of blazars. When blazars are in an outburst state, they are strongly dominated by jet-based models (Ulrich et al., 1997). On the other hand, when they are in the low state, the microvariability and short-term variability can be explained by models based on instabilities in the accretion disk (Chakrabarti & Wiita, 1993).

Chapter 3

The first *INTEGRAL*–OMC catalogue of optically variable sources

This chapter describes the compilation of the *first INTEGRAL–OMC catalogue of optically variable sources* (OMC–VAR). The objectives of this work were to characterize the potential variability of the objects monitored by OMC, to identify periodic sources and to compute their periods, taking advantage of the stability and long-term monitoring of the OMC.

An overview of the history of variable star astronomy is given in Section 3.1. The analysis of the data is explained in Section 3.2. In this Section, the methods employed to detect potential variability, to study the periodicity, and to estimate the contamination, are described. The contents of the catalog are presented in Section 3.3. The main results of this work are summarized in Section 3.4.

The results of this chapter have already been published in Alfonso-Garzón et al. (2012).

3.1 Introduction

Nowadays, the study of variable stars is one of the principal areas of astronomical research. The beginning of their study dates back to the 16th century when the first variable star, a supernova, was identified, and shortly thereafter telescopes started to be used for astronomy. Since then, an increasing number of variable stars were discovered and observed but it was with the upcoming of photography and photoelectric photometry first, and of the digital imaging technology and multiwavelength astronomy later, that the number of known variable stars increased very rapidly. In 1948, the first edition of the *General Catalogue of Variable Stars* (GCVS) was published containing 10 820 stars. The GCVS has been updated regularly until its last release (Samus et al., 2012). The number of known variable stars has increased up to around 200 000 objects compiled in the *Variable Star Index* (VSX; Watson 2006; Watson et al. 2012). The VSX is maintained by the American Association of Variable Stars Observers (AAVSO), and contains all objects from the GCVS and the catalogs of the *Northern Sky Variability Survey* (NSVS; Woźniak et al. 2004), as well as data resulting from other automated surveys, like the *All Sky Automated Survey* (ASAS; Pojmanski 1997), or the catalogs compiled from the *Optical Gravitational Lensing Experiment* (OGLE; Udalski et al. 1992) observations: the Miras and eclipsing binaries from OGLE-II data or the catalog of variable stars from OGLE-III.

The advent of space astronomy has provided additional high-quality data for thousands of objects. The most significant impact has been produced by the missions specifically dedicated to obtain photometric data of high accuracy, in some cases during very long periods of time. While

optimized for astrometric studies, the *Hipparcos/Tycho* mission also produced high-accuracy photometric time series (Perryman et al., 1997; Hoeg et al., 1997). Even higher photometric accuracy is provided by dedicated missions, aimed to study asteroseismology or to search for exoplanetary transits, like the Canada's *Microvariability and Oscillations of STars* (*MOST*; Walker et al. 2003), *the COnvection, ROtation and planetary Transits* (*CoRoT*) mission (Auvergne et al., 2009) or *Kepler* (Borucki et al., 2010; Koch et al., 2010), which is yielding the highest accuracy light curves available up to now.

Furthermore, spacecraft systems or secondary instruments on the satellites can provide very useful photometric information as well. Zwintz et al. (2000) performed a detailed analysis of more than 4500 data sets from the Hubble Space Telescope (HST) guide star data. In a similar way, the observations performed by the spacecraft tracking cameras of Chandra have allowed to produce the *Chandra Variable Guide Star Catalogue* (VGUIDE; Nichols et al. 2010). A catalog of ultraviolet (UV) sources detected serendipitously by the Optical Monitor (XMM-OM) on board the *XMM-Newton* observatory, the *XMM-Newton Serendipitous Ultraviolet Source Survey* (XMM-SUSS) has been published by Page et al. (2012). And from the UV/optical instrument on *Swift*, the first *Swift Ultraviolet/Optical Telescope Serendipitous Source Catalogue* (UVOTSSC) has been published by Page et al. (2015).

The *INTErnational Gamma-Ray Astrophysics Laboratory* (*INTEGRAL*) mission, launched on 17 October 2002, (Winkler et al., 2003) includes a small optical telescope, the Optical Monitoring Camera (OMC), to provide photometry in the Johnson V–band simultaneously to the high-energy observations (Mas-Hesse et al., 2003). In addition to monitoring the primary high-energy targets, OMC has been observing serendipitously tens of thousands of potentially variable objects within its FOV, preselected from existing catalogs of variable stars.

3.2 Data analysis

After the proprietary period of one year, all *INTEGRAL* data are open to the scientific community. At the moment of the compilation of the first OMC catalog, *INTEGRAL* had been in orbit for more than nine years and the Optical Monitoring Camera (OMC) archive[1] (Gutiérrez et al., 2004) contained observations for more than 130 000 objects, of which more than 70 000 had light curves with at least 50 photometric data points. The data included in this catalog contain observations from the beginning of the mission to February 2010.

3.2.1 Selection of the sources and cleaning of the light curves

For this work, sources with more than 300 photometric points were selected from the OMC database, in order to deal with light curves with enough points to study their variability and when possible, their periodicity. With the aim of improving the quality of the data some selection criteria were applied to the individual photometric points.

First of all, it was checked if the coordinates in the *OMC Input catalogue* (OMC–IC, see Section 1.2.2) agreed with the coordinates given in SIMBAD. The OMC database allows the user to select between two different centroid methods to extract the photometry, which corresponds to different options in the standard OMC Off-line Scientific Analysis (OSA) software (see Section 1.1.2). If *Source coordinates* (default) is selected as the centroid method, the pipeline looks for the centroid allowing a maximum offset of 10 arcsec with respect to the given coordinates. If the centroid algorithm fails for any reason, the extraction mask is nevertheless re-centered right on the source coordinates as given in the OMC–IC. However, if *brightest pixel* is selected as the centroid method, the position of the extraction mask is re-centered on the brightest pixel within

[1] http://sdc.cab.inta-csic.es/omc/

the central 5×5 pixel section. For the sources with a difference between the coordinates of the input catalog and the coordinates given by SIMBAD greater than 10 arcseconds, the brightest pixel method was used. Moreover, in all the cases, those photometric points with a distance to the coordinates of SIMBAD greater than 10 arcseconds have been rejected.

Secondly, the existence of duplicated entries in the catalog has been checked. There are sources in the input catalog with different OMC identifiers, but with the same SIMBAD name or very close coordinates. These two situations have been taken into account and the duplicated sources were removed from the list.

Typical OMC integration times are 10 s, 50 s and 200 s, although at the beginning of the mission, shots of 10 s, 30 s and 100 s were obtained. Therefore, photometric points with different integration times can be found in the database. The longest integration times led to saturation of the brightest objects. For this reason, for each light curve, the photometric points that could be saturated were rejected. In general, all the photometric points within light curves where the median brightness is less than 7.1 were rejected. When the median brightness was less than 8.3, those photometric points with exposure times greater than 20 s were eliminated. If the median brightness was between 8.3 and 8.8, only the photometric points with exposure times of 10 or 30 s were selected. For light curves with median brightness between 8.8 and 9.6 the exposures of 100 and 200 s were rejected. When the median brightness was between 9.6 and 10.3, the photometric points with exposure times of 200 s were removed. And finally, for those sources with median brightness greater than 10.3, it was considered that no problems of saturation should appear, and no photometric points were rejected.

In a similar way, some detection limits were defined to avoid photometric points with too low signal-to-noise ratio (S/N). For each light curve, those photometric points with exposure times $t_{exp} = 10$ s and a median brightness $V > 12$, exposure times $t_{exp} = 30$ s and a median brightness $V > 13$, and exposure times $t_{exp} = 50$ s and a median brightness $V > 14$ were removed.

Furthermore, measurements with low S/N were excluded. A minimum S/N of 10 was required for the shortest integrations (10, 30 and 50 s) while for the longest ones (100 s and 200 s), a criteria of S/R > 3 was imposed.

The observations were filtered from the effects of cosmic rays hits and some occasional detector artifacts. Each photometric point was compared with the 20 closest ones within 3 days (to avoid the temporal gaps). For these 20 points, the standard deviation was computed and a 5-sigma rejection criteria was applied. Finally, the photometric points that contained any hot pixel within their extracting mask of 3×3 pixels were removed.

In this first version of the OMC catalog, only those objects with a given SIMBAD object type in the OMC–IC were included. Applying these filters, 6071 sources with high-quality light curves to be studied were obtained. In the next version of the OMC catalog, all objects in the OMC database complying with the previous requirements, independently of their assigned type, will be included and they are estimated to be around 25 000.

3.2.2 Detection of variability

To detect which light curves showed variability, the χ^2 goodness-of-fit test was used. This test compares a null hypothesis to an alternative hypothesis. If the value obtained for the test statistic is greater than a value corresponding to the chosen significance level of the χ^2 distribution with k = n-1 degrees of freedom, being n the number of data points, then the null hypothesis is rejected. For each source, the null hypothesis of being non-variable and having a constant magnitude equal to the mean was supposed. The alternative hypothesis was that the star is variable. Then, the χ^2 and the significance α were calculated. This significance gives the probability of being wrong when rejecting the null hypothesis (the source is constant). As a criterion of variability of $\alpha < 0.05$ was considered (which is equivalent to a lower limit

probability of being variable of 95%). Following this criterion, 5263 sources showing variability in their OMC light curves, were identified. Although all 6071 sources were expected to be variable, no variability was detected for 808 of them, according to the applied criteria. In some cases this can be due to the time span of the OMC observations, and in other cases the amplitude is likely below the OMC variability detection threshold used for this first version of the catalog.

3.2.3 Study of the periodicity

To determine which sources are periodic and to derive their periods, an algorithm based on the Phase Dispersion Minimization (PDM) technique (Stellingwerf, 1978) was developed. Given the variety of variability patterns present in our data the Lomb-Scargle (L-S) periodogram technique by Scargle (1982) was discarded. This method evaluates the discrete Fourier transform for nonevenly sampled data. Since this is equivalent to assuming a prior sinusoidal light curve, it is not adequate for most eclipsing and non-sinusoidal light curves.

A wide range of frequencies was explored, corresponding to periods from 0.8 h (a lower limit of the periods that can be detected by OMC, considering the typical exposure times), up to half of the time range of the observations (the maximum period to have at least two cycles in the folded light curve). A frequency increment of $\frac{1}{3B}$ was first used, being B the total time baseline of the observations, and in a second iteration around the first trial period, a period increment of $2P^2/(nB)$ (see Giménez & García, 1983) was chosen, where P is the trial period and n is the number of points in the light curve. For each period, the time-folded light curve is divided into a series of bins and the variance of the amplitude within each bin with respect to a mean curve is computed. In our algorithm the number of bins is variable and it depends on the quality of each light curve. For each bin, the mean value is calculated and linear interpolations are done between the means in order to obtain one average curve for each folded light curve. The ratio between the sum of the bin variances and the overall variance of the data set is called Θ, and the period that minimizes this parameter has been considered to be the best estimate.

With the values of the trial periods and their corresponding values of Θ, the periodograms were computed. The uncertainty in the period was calculated by fitting a gaussian to the peak corresponding to the minimum value of Θ in the periodogram. The 1-sigma error in the determination of the centroid of the gaussian was provided for each source as the standard uncertainty of the period and corresponds to a confidence interval of 68.3% (see Fig. 3.1). For most of the sources the process above works fine, but in some cases aliasing becomes a problem. Aliasing occurs when a curve is observed with an insufficient sampling. For some sources in the catalog there are temporal gaps in the observations much greater than the value of the period, and the time intervals of the different observations are not long enough to determine the period accurately. For a given estimated period P_i, if the temporal gap, $t_{\rm gap}$ (the time when the source has not been observed), is such as $t_{\rm gap} = N \times P_i$ (with N big enough), there will be many significant peaks in the periodogram, close to the deepest one, corresponding to that values of the period that make $t_{\rm gap} = (N+1) \times P_{i-1}$ or $t_{\rm gap} = (N-1) \times P_{i+1}$ (see Fig. 3.1, right panel). In these cases, the periodogram were smoothed with a window size wider than the distance between these false peaks. This smoothed curve was used to determine the limit of significance of the peak and the half width of this peak was used as initial value of sigma in the gaussian fit. Finally, a visual inspection of each folded light curve was performed to identify and correct potential problems due to ambiguities in the results, such as deriving the half or double period in some eclipsing binaries or pulsating stars with symmetrical light curves.

The method used in this work yields only the primary periods. To obtain second or multiple periods, if present, a manual analysis of each source is required and this was out of the scope of this work.

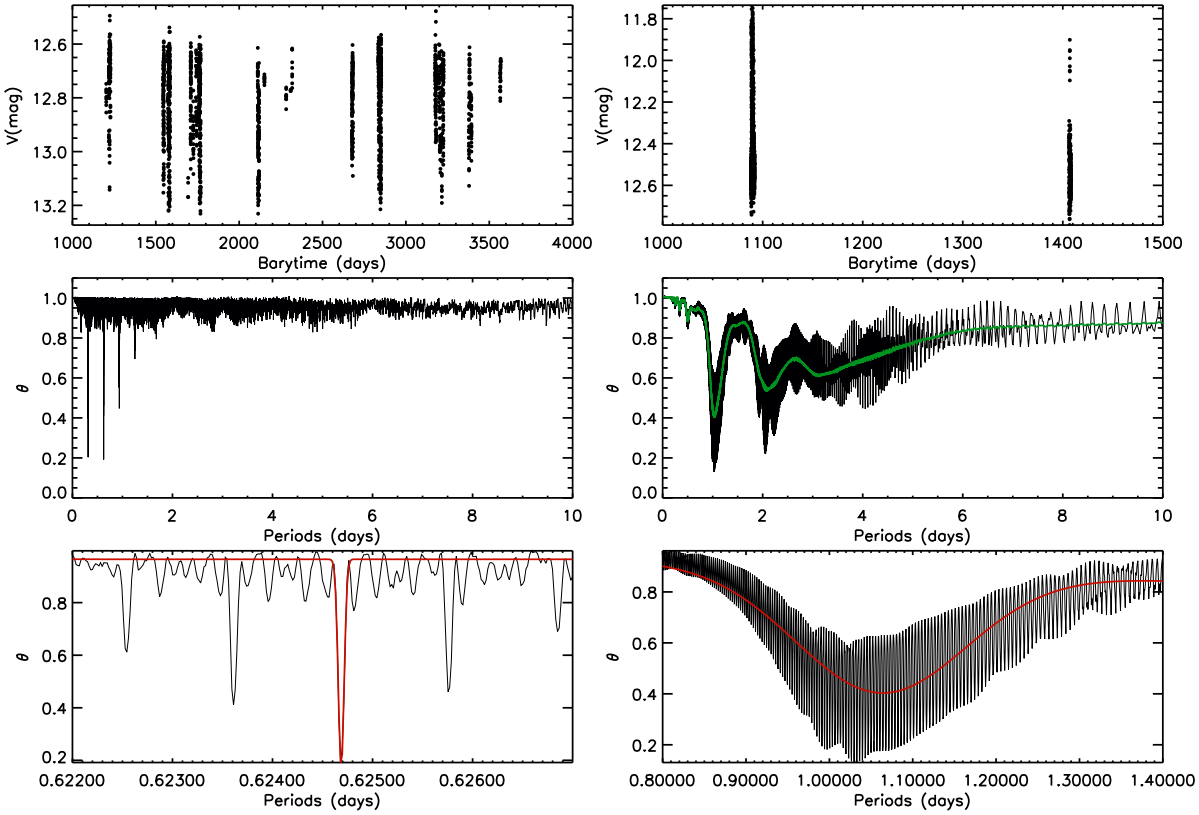

Figure 3.1: Visual description of the process of period determination for two different cases: a standard situation (analysis of IOMC 0460000022) on the left and an example of aliasing (IOMC 5228000021) on the right. In both cases, the plots are: **Top:** The light curve without folding. For the light curve affected by aliasing the large temporal gap can be appreciated. **Middle:** Periodogram from 0 to 10 days. The peaks are much narrower in the standard case. In the aliasing example, the smoothed periodogram taking into account the aliasing effect (see text) is overplotted in green. **Bottom:** Detail of the method used to determine the uncertainty of the period. In red, the continuum plus gaussian fit to the peak is plotted.

3.2.4 Photometric contamination by nearby stars

For the data analyzed in this study, fluxes and magnitudes were derived from a photometric aperture of 3×3 pixels (1 pixel = 17″.504), slightly circularized, i.e., removing $\frac{1}{4}$ of a pixel from each corner (standard output from OSA). Therefore the computed values include the contributions by any other source inside the photometric aperture. Those sources that might be affected by this kind of photometric contamination were flagged in a column of the catalog. Due to the variable nature of the sources in the catalog and the difficulty to accurately estimate the contamination by the nearby and background stars, three different methods were developed. The first one was to take into account the photometric information of the sources close to the extraction aperture present in the UCAC3 (Zacharias et al., 2010) and NOMAD1 (Zacharias et al., 2004) catalogs. The second one was to compare the V magnitude provided by SIMBAD (for variable sources it is usually the magnitude at maximum brightness) with the lowest magnitude measured with OMC data. The third one was to compare the median magnitude in Variable Star Index (VSX) with the median magnitude measured in the OMC data. A source has been considered significantly contaminated when the measured flux was a factor of 2 higher than expected. This is equivalent to a difference between expected and observed magnitude of more than 0.75 mag. While this criterion is not very restrictive in terms of photometric accuracy, it allows to study variability and search for periodicity for objects with a significant degree of contamination. Nevertheless, it should be stressed that this procedure has the caveat that in some cases the variability/periodicity found might be originated by the contaminating

object(s), and not by the target source. One of the objects mostly affected by blending is HH Nor, shown in Fig. 3.13, whose variability pattern is completely dominated by the variability of the brighter, nearby object VSX J154329.4–515037, which is indeed a variable RR Lyr star with a much shorter period. Being located at just 12″, a fraction of an OMC pixel, the intrinsic variability of this contaminating star completely hides the variability of the target source, HH Nor.

The results of these three methods are coded in the column of contamination with three numbers (a reference to each method) where 1 means that the source is not contaminated (under the conditions defined above), 2 means that it is contaminated and 3 means no photometric information has been found for that source. Because of the inherent difficulties of estimating the contamination of variable sources, this flag is for guidance only and to study individual sources a more exhaustive analysis of the sky field around each source is recommended.

3.3 Contents of the OMC–VAR catalog

In this first release on the OMC–VAR catalog, information about the variability of 5263 objects distributed all over the sky is provided (see Fig. 3.2). The majority of the objects are located in the Galactic plane and Galactic bulge, as well as on specific areas of the sky. This distribution reflects the integration time density maps of *INTEGRAL*, driven by the location of the most interesting high-energy sources.

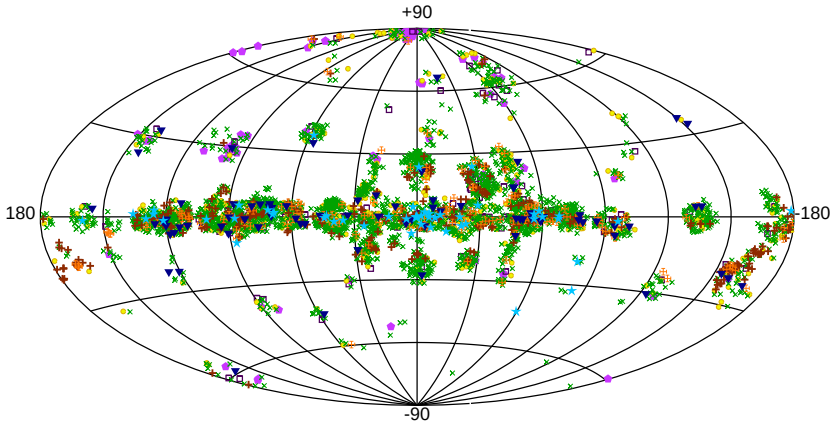

Figure 3.2: Distribution in galactic coordinates of all the sources in the catalog. The green crosses represent pulsating stars, the red filled points correspond to eclipsing binaries, the brown plusses are eruptive stars, the orange complex plusses represent rotating stars, the inverted dark blue filled triangles represent cataclysmic variables, the light blue filled stars are X-ray binaries, the yellow filled points correspond to objects simply classified as variable stars, the purple filled pentagons represent extragalactic objects and the empty purple squares are other types of objects.

Table 3.1 describes the contents of the OMC–VAR catalog, which is fully accessible online. For each source, the median value of the V magnitude, the mean of the photometric errors of the points and the magnitudes at maximum and minimum brightness, estimated as the 2nd and 98th percentiles, respectively, of the points in the light curve, has been included. For those sources classified as periodic or probably periodic, the best estimated period and its calculated uncertainty are also provided. The time base for each light curve is also provided.

The values of the median magnitudes go from 7.10 mag to 16.27 mag. In Fig. 3.3 left, the histogram of the median magnitudes is shown, showing a peak at around 12.3 mag. A similar plot for the amplitudes (calculated as the difference between the magnitude at minimum and the magnitude at maximum of the light curve) is shown in Fig. 3.3 right. The amplitudes go from 0.06 mag to 7.41 mag with a mean value of 0.84 mag.

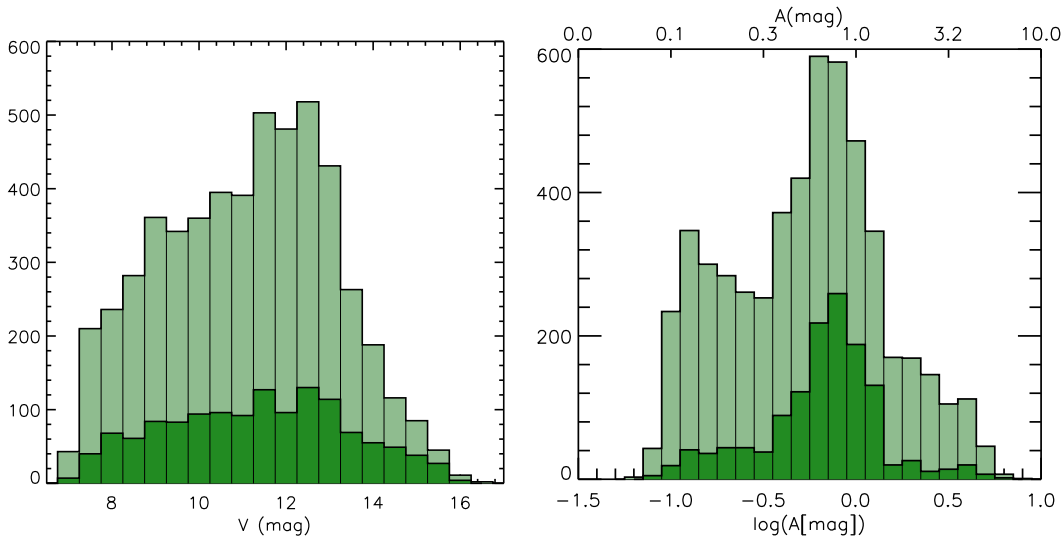

Figure 3.3: Left: Histogram of magnitudes, covering the range from 7.10 to 16.27, with a peak of the distribution at around 12.3 mag. In this and subsequent histograms the fraction of sources for which a period was determined in this work are represented with dark green. **Right:** Histogram of amplitudes (calculated as the difference between the magnitude at minimum and the magnitude at maximum of the light curve) with a peak of the distribution at around 0.84 mag. In dark green are represented the sources for which a period was determined in this work.

Table 3.1: Contents of the OMC–VAR catalogue, accessible at the OMC–VAR web[2]and at CDS services.

Field	Source	Description
IOMC	OMC	OMC Identifier
SIMBAD name	SIMBAD	SIMBAD Basic Identifier
RA	SIMBAD	Right Ascension in sexagesimal units (J2000)
DE	SIMBAD	Declination in sexagesimal units (J2000)
RAdeg	SIMBAD	Right Ascension in degrees (J2000)
DEdeg	SIMBAD	Declination (J2000) in degrees (J2000)
otype	SIMBAD	SIMBAD object type
sptype	SIMBAD	SIMBAD spectral type
vartype	VSX	VSX variability type
vargroup	VSX, SIMBAD, others	General Variability Group
V mag	OMC	Median V magnitude
magerr	OMC	Mean of the magnitude error
magMax	OMC	Magnitude at maximum brightness
magMin	OMC	Magnitude at minimum brightness
per	OMC	Period of variability in days
errper	OMC	Uncertainty of the period in days
timebase	OMC	Time base of the observations in days
tagcont	UCAC3, NOMAD1, SIMBAD, VSX	Tag of contamination

[2] http://sdc.cab.inta-csic.es/omc/var/

3.3.1 New period determinations and improvement of previously ones

Out of the 5263 variable objects compiled in the catalog, periods for 1337 sources have been measured. The distribution of periods is shown in Fig. 3.4. Typical values vary between a few hours and 10 days, with a peak of frequency at around 15 h. Some sources present periods of up to some hundreds of days, but there are not many of them given the time span and distribution of the observations.

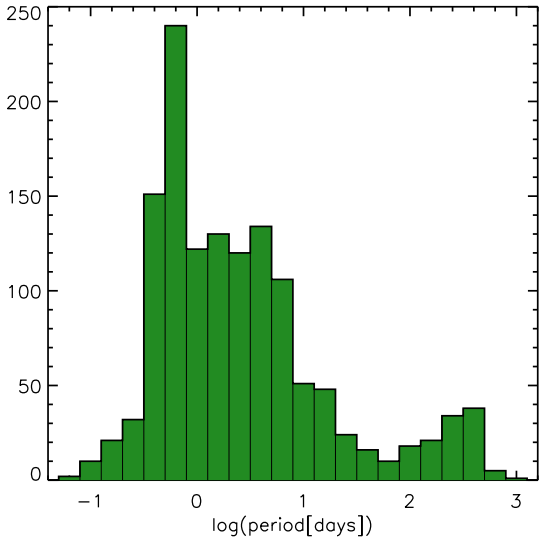

Figure 3.4: Histogram of the periods derived. Typical values vary between a few hours and 10 days, with a peak of frequency at around 15 h.

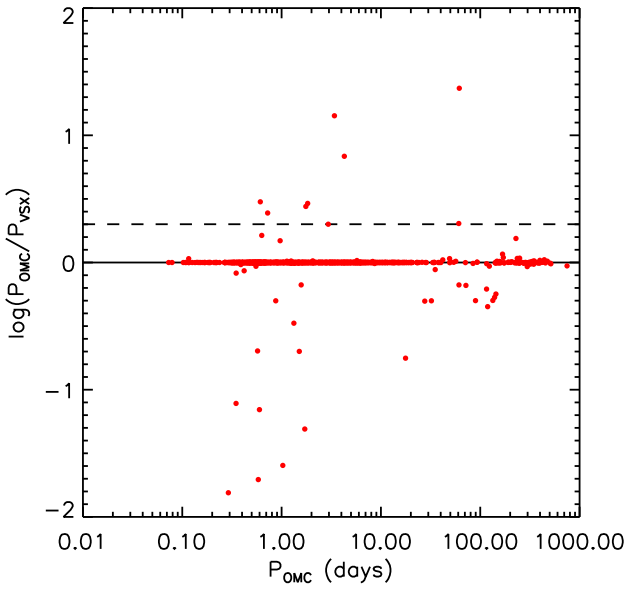

Figure 3.5: Comparison of periods derived from OMC data (this work) with the values compiled by the VSX. The solid line represents $P_{OMC} = P_{VSX}$ while the dashed line marks the condition $P_{OMC} = 2P_{VSX}$.

The VSX database also provides information about the periodicity of the sources and this information has been compared with our results. In Fig. 3.5, the periods derived from OMC data in this work with the values compiled in the VSX, are compared. For the large majority of objects the values are consistent, though it should be stressed that in many cases, even a

very small improvement on the determination of the period is enough to yield a satisfactory folding of the light curve (some examples can be found in Section 3.3.3). A dashed line marks the points for which $P_{\rm OMC} = 2 \times P_{\rm VSX}$, to identify those cases of binaries with eclipses of similar shape that could have been misidentified in the VSX. In the rest of the cases we have verified that the period given in the VSX was not consistent with the OMC light curves. This happened sometimes for systems with multiple periods due to different variability mechanisms like rotation, orbital, X-rays, etc. One example is Her X–1 for which, as mentioned in Section 3.2.3, the period given by VSX does not correspond to the orbital one to which OMC is more sensitive (see Fig. 3.13).

However, in many cases the previously published periods were incorrect or less accurate than ours. For 194 sources, improvements on the previously reported periods were obtained. Table 3.2 lists the OMC identifier, the main SIMBAD identifier, the period derived in this work and the period appearing in the VSX before this work.

Table 3.2: Improvements on previously detected periods

IOMC	Name	$P_{this\ work}$ (days)	P_{VSX} (days)
0112000025	RX J0518.0+0712	0.87881734	0.872
0114000046	[ATW96] RX J0532.4+0131a	2.0598717	2.0
0118000032	GSC 00118-00605	3.2970518	0.0
0118000034	RX J0533.1+0224	1.4713773	1.49
0244000019	V* Y Sex	0.41982248	0.487736
0282000031	V* EI Vir	0.59607247	0.596109
0282000037	V* BI Vir	0.33566221	0.3356548
0288000027	V* FK Vir	35.190626	40.0
0289000023	V* BO Vir	0.52003773	0.52005117
0289000033	V* BR Vir	0.6009989	0.6019
0297000023	V* CT Vir	17.693136	100.0
0398000018	V* V370 Oph	0.56945662	0.5694273
0415000034	FASTT 933	0.57475301	0.574744
0449000056	FASTT 1195	1.529962	1.53002
0455000047	V* BT Ser	0.72381695	0.29548
0458000047	V* V634 Oph	160.14869	158.0
0475000025	V* V526 Aql	4.2103145	4.2112
0490000063	V* V1458 Aql	147.37622	144.0
0700000014	RX J0524.1+0730	1.2127804	0.0
0742000032	AG+13 539	0.38843636	0.4033
0869000050	V* AH Vir	0.40753293	0.407521
0874000025	V* DS Vir	0.53220749	0.53216
0901000032	V* AA Boo	60.782935	30.0
1043000024	V* V800 Aql	20.034788	20.065
1049000021	V* V1316 Aql	318.36753	328.0
1052000027	V* FI Aql	235.72692	219.0
1060000048	V* SS Aql	228.68537	148.0
1063000029	SV* SON 8099	0.39610831	0.39611
1067000043	V* KS Aql	167.62788	144.0
1167000015	V* IX Peg	0.60301239	0.60099
1303000022	AAVSO 0539+18	2.1023179	2.10248
1306000019	V* HY Tau	3.016927	3.01682
1698000022	V* BG Peg	1.95247	1.95272
1822000010	V* V1022 Tau	0.34717194	0.3471783
1825000012	V* AN Tau	1.6143973	1.61464
1862000029	V* CR Tau	0.68270259	0.681346
1864000028	V* EO Tau	1.3291304	3.9874
1868000024	V* DT Gem	0.61127473	0.6112879
1871000034	V* CT Tau	0.66682619	0.6668303
1873000033	V* V356 Aur	0.18926777	0.18916
1878000036	V* LT Gem	4.2810042	0.6258
1991000096	V* S Com	0.58658722	0.5866195
1992000091	V* DV Com	0.5408332	0.5408441
1993000053	V* BD Com	0.54161856	0.54165
1993000088	V* RY Com	0.46893953	0.468943
2137000073	V* V874 Cyg	0.34873045	0.4226339
2141000060	V* HS Vul	0.33208158	0.3320669
2531000080	V* EM Com	0.54239712	0.542555

Continued on next page

IOMC	Name	$P_{this\ work}$ (days)	P_{VSX} (days)
2585000067	V* GZ Her	0.48306458	0.4830495
2597000037	V* HL Her	0.54263251	0.543169
2664000025	V* V802 Cyg	0.59557132	0.595482
2668000036	V* V781 Cyg	0.43663846	0.43665186
2674000055	V* V1033 Cyg	4.9501028	4.937512
2680000045	GSC 02680-01262	6.718268	6.72379
2683000039	V* V2107 Cyg	4.2846028	4.2851
2685000063	V* V388 Cyg	0.85902614	0.8590372
2689000062	V* V505 Cyg	0.66765874	0.667672
2691000059	V* V373 Cyg	297.1717	320.0
3063000133	V* GY Her	0.52353425	0.5243814
3137000043	V* OO Cyg	0.13445268	0.2689
3137000054	V* CV Cyg	0.98340666	0.9834308
3141000044	V* NS Cyg	0.55032107	0.5503
3153000088	V* FF Cyg	328.9996	323.82
3155000053	NSV 12891	133.24773	0.0
3156000064	V* V455 Cyg	8.7526118	8.76573
3159000070	V* V1187 Cyg	1.5070018	7.535
3162000048	V* V395 Cyg	1.0285077	40.5
3167000083	V* V2197 Cyg	0.46574847	0.46566
3171000062	V* V2138 Cyg	1.2467537	1.21327
3171000073	V* V830 Cyg	0.40148094	0.40147246
3173000066	SV* BV 400	1.2727276	1.27268
3179000095	V* V348 Cyg	0.28424312	0.28423
3181000066	V* V1554 Cyg	337.02831	330.0
3186000071	V* V533 Cyg	1.0147888	1.0147
3190000044	V* V2152 Cyg	6.2770663	6.272
3190000053	V* V604 Cyg	139.35207	262.0
3576000046	V* V497 Cyg	249.08094	230.2
3583000051	V* V750 Cyg	441.6417	432.8
3595000052	V* V628 Cyg	0.96658748	0.651652
3599000036	V* V707 Cyg	71.72994	108.6
3619000046	V* CZ Lac	0.43216049	0.432205
3665000051	LD 80	5.2100273	0.0
3681000055	V* V765 Cas	1.7158357	1.71628
3682000064	V* BS Cas	0.44046971	0.4404832
3683000044	AAVSO 0136+59	3.8430015	3.845
3956000047	V* DQ Cep	0.07886919	0.07886444
3993000054	V* V427 Cas	1.3059617	1.30399
4014000075	V* V363 Cas	0.5465739	0.546556
4015000058	V* V379 Cas	4.3068823	4.30575
4018000055	GSC 04018-02473	11.070972	11.038
4023000051	V* AS Cas	3.0244376	3.02125
4030000087	V* AX Cas	0.60036756	0.600376
4034000083	CSV 139	6.0405968	6.035
4038000058	V* BR Cas	0.60827569	0.608317
4040000057	V* V423 Cas	1.8303136	0.627858
4273000048	V* RZ Cep	0.30864291	0.3086853
4279000041	V* QV Cep	0.55520225	0.554
4285000085	V* V375 Cas	1.4734273	1.4733843
4288000051	V* DY Cep	1.5745292	2.3620175
4421000058	V* AU Dra	0.51526649	0.51514
4944000020	V* VX Vir	0.54299732	0.5430115
4949000035	FASTT 539	0.36099807	0.361027
5119000027	V* V802 Aql	0.26760771	0.26769479
5130000027	V* YZ Aql	4.6730267	4.6723
5282000041	GSC 05282-02210	8.2721053	8.115
5538000022	V* AS Vir	0.55340399	0.5534156
5615000009	V* DY Lib	0.58308398	0.58347
5615000010	V* FQ Lib	0.62180174	0.6221
5615000013	V* V774 Sco	0.5705921	0.57078
5619000013	V* FT Lib	0.89096095	0.8916
5619000017	V* V772 Sco	0.44765896	0.44762
5621000013	V* V801 Sco	0.51105162	0.51231
5621000017	V* V810 Sco	0.64927478	0.64922
5622000026	V* FF Lib	0.62655513	0.62649
5623000024	V* V768 Sco	0.47496117	0.475
5624000014	V* V784 Sco	1.5263212	1.526
5624000016	V* V786 Sco	0.59257504	0.59282
5624000017	V* V790 Sco	0.56438605	0.56427

Continued on next page

IOMC	Name	$P_{this\ work}$ (days)	P_{VSX} (days)
5624000021	V* V795 Sco	0.51224485	0.51227
5624000022	V* V796 Sco	0.69441602	0.6939512
5624000023	V* V799 Sco	0.5153241	0.51569
5625000018	V* V812 Sco	0.65144637	0.65168
5634000011	V* V757 Sco	0.72413341	0.724183
5635000016	V* V1005 Oph	0.63125599	0.38655
5638000009	V* V990 Oph	0.5957232	0.595744
5639000008	V* V998 Oph	0.45677023	0.456795
5688000015	V* CQ Ser	0.76005957	0.760076
5695000007	V* VW Sct	236.42037	234.0
5721000039	V* EN Sgr	143.8286	254.5
5763000014	SV* R 85	0.40100706	0.40101
5763000016	V* WZ Aqr	0.4942641	0.4942677
6230000016	V* SY Oph	123.45931	132.0
6840000031	V* V734 Sgr	1.2382919	1.238322
6853000030	V* V779 Sgr	0.44502982	0.4450342
6855000032	HD 166612	61.519773	2.62462
7276000038	SV* HV 12279	0.33912182	0.339629
7277000036	SV* HV 12290	0.58538241	0.58534
7292000023	V* V674 Cen	0.49399108	0.493919
7324000027	V* HP Lup	1.1545742	1.1546
7359000044	V* V380 Sco	115.7334	187.17
7384000015	V* V487 Sco	0.32912655	0.329141
7386000068	V* CR Sco	133.81953	266.0
7399000060	V* V1008 Sgr	11.59803	11.615001
7404000126	V* V2509 Sgr	1.0870205	1.0869739
7438000011	V* V2158 Sgr	0.60353974	0.6035
7663000045	SV* BV 1575	0.44639111	0.446394
7673000043	V* AY Vel	1.6177107	1.617677
7683000053	V* BU Vel	0.51628865	0.5162856
7690000058	V* GG Vel	2.9504426	1.475216
7690000059	V* EU Vel	0.37438197	0.3743755
7788000025	SV* HV 12285	0.7094765	0.70943
7791000028	SV* HV 12272	0.27421782	0.274223
7810000036	V* V534 Cen	0.62912426	0.62915
7820000014	V* V564 Cen	0.48953172	0.48955
7820000015	V* V678 Cen	1.3017834	1.301858
7827000033	V* V559 Cen	0.57025423	0.57056
7864000021	V* IT Nor	1.7541407	0.63579
7884000022	V* V1084 Sco	0.30330923	0.303315
7885000013	V* FX Sco	118.74087	264.0
7891000024	V* V633 Sco	0.49331086	0.493333
7917000017	ASAS J190537-3904.6	0.33832896	0.338325
7918000018	V* DN CrA	0.48238516	0.4823327
7933000027	V* V2194 Sgr	0.61044394	0.203479
8155000093	AAVSO 0840-47	23.399553	23.441
8163000033	V* FT Vel	1.1305924	1.1306
8166000055	V* DL Vel	0.56354796	0.56355802
8212000041	V* ST Cen	1.2233984	1.2234184
8252000028	V* V594 Cen	0.31709888	0.31709593
8319000033	V* V Nor	170.74398	155.9
8321000028	V* SX Nor	3.7406888	3.74008
8341000030	V* AL Ara	89.613428	178.7
8587000041	V* TX Vel	56.717472	55.5
8606000043	HD 86441	5.711199	5.73
8619000042	V* XY Vel	2.5102982	2.5101982
8619000043	V* AX Cen	0.51367526	0.5137541
8622000025	AAVSO 1040-57	18.88355	18.936
8626000087	NSV 5002	41.956132	40.0
8668000038	V* V615 Cen	0.40666262	0.4066346
8668000047	V* IM Cen	49.97457	49.2
8674000056	V* OP Cen	0.46232395	0.462313
8676000030	V* OZ Cen	0.35577371	0.35577
8698000037	CPD-54 6382	8.2198583	8.23862
8708000028	V* SU Nor	1.6864524	1.68639
8710000037	V* HT Nor	5.4154464	5.416
8714000031	V* TX Nor	3.0318523	3.03049
8956000031	AAVSO 1017-60	14.068296	14.0464
8960000033	V* CO Car	8.3088	8.3121
8973000057	V* SV Cen	1.6575202	1.657589

Continued on next page

IOMC	Name	$P_{this\ work}$ (days)	P_{VSX} (days)
8992000060	V* VY Cru	0.69562989	0.695599
8992000065	ASAS J123748-6219.4	0.21746698	0.217457
8993000060	ASAS J125953-6159.5	1.4808174	1.480892
9015000036	V* AQ Cir	1.1457017	1.14568
9266000064	V* YY Aps	0.85555068	0.855468
9272000047	V* AN Aps	1.045536	1.0452
9458000059	V* BH Oct	0.56503189	0.5652

Moreover, periods for 175 objects whose periodicity was unknown, have been determined. In Table 3.3, a compilation of these new period determinations is provided.

Table 3.3: New determinations of periods

IOMC	Name	Period (days)
0122000035	V* V651 Ori	0.3782734
0126000033	V* BN Ori	0.65296789
0289000017	FASTT 531	0.16954098
0296000017	SV* SON 10679	0.7644219
0314000023	V* UX Vir	0.51275451
0399000012	NSV 8235	0.48680197
0448000044	FASTT 1190	22.444244
0462000036	FASTT 1181	0.32637677
0464000036	V* FQ Aql	320.52303
0476000023	NSV 11937	290.00868
1046000025	V* V1352 Aql	775.7543
1048000032	V* V1442 Aql	21.555976
1050000041	V* QR Aql	388.15927
1055000027	V* V819 Aql	388.47519
1059000033	V* V612 Aql	237.04046
1059000039	SV* SON 8111	443.09108
1063000037	V* V976 Aql	125.60279
1610000062	V* CO Vul	451.63013
1856000013	SV* SON 10485	0.1497397
1995000218	V* IP Com	0.64062732
2128000055	V* V335 Vul	353.64569
2585000065	V* V854 Her	0.78064629
2588000053	V* V853 Her	0.45687712
2602000036	V* V868 Her	0.50553184
2683000031	V* V1821 Cyg	0.11339384
2695000072	V* V1851 Cyg	311.64584
2696000061	V* V1871 Cyg	682.75255
2699000074	V* V1850 Cyg	290.33701
2699000085	V* V1861 Cyg	266.69667
3072000038	V* V867 Her	0.52852562
3153000087	RAFGL 2617	433.1248
3154000064	V* V424 Cyg	90.474635
3166000078	V* V1788 Cyg	14.090671
3167000086	V* V1792 Cyg	3.3034183
3168000077	V* V2145 Cyg	22.073213
3170000077	V* V2131 Cyg	35.791156
3173000060	SV* ZI 1990	28.93088
3320000049	Cl Melotte 20 699	0.49242081
3576000044	V* V1970 Cyg	457.5818
3603000037	V* V1734 Cyg	424.69477
3617000039	V* V2172 Cyg	0.76111048
3970000044	NSV 13732	3.8113687
3976000034	NSV 13895	0.84930198
3981000033	V* V394 Cep	5.6871395
3982000042	ALS 12262	2.1782339
4004000047	V* V403 Cas	6.337129
4010000047	V* V570 Cas	30.89788
4020000064	V* V446 Cas	37.28074
4024000038	V* V660 Cas	344.33077
4207000030	V* GS Dra	18.751485
4246000041	V* V778 Cyg	0.11650688
4278000050	V* QQ Cep	0.91486243
4766000070	V* V1130 Ori	2.7016613

Continued on next page...

Table 3.3 – Continued

IOMC	Name	Period (days)
4771000086	V* V615 Ori	3.152588
4948000021	FASTT 536	0.26187571
5067000021	NSV 8593	0.54285566
5081000013	V* V976 Oph	93.388168
5082000020	FASTT 1091	0.35434326
5082000050	FASTT 1140	0.59229457
5083000021	FASTT 1088	0.29933686
5096000086	FASTT 1076	0.66091853
5097000026	FASTT 1128	88.453788
5111000014	V* V431 Sct	2.1510141
5732000016	V* FF Sgr	0.55862768
5760000018	V* UY Aqr	0.66755506
5979000051	AN 122.1943	10.978506
6208000020	NTTS 160233-1931	2.6443046
6209000016	NTTS 160735-1857	6.675739
6209000022	V* AN Sco	0.61605374
6211000003	V* TZ Oph	323.03622
6214000022	V* AS Sco	1.4548234
6217000010	GSC 06217-00126	3.5076635
6247000023	V* V2374 Oph	87.175704
6250000015	V* UX Ser	29.552176
6281000023	SV* ZI 1525	0.10285146
6318000014	V* V4091 Sgr	16.918084
6839000169	AX J1740.5-2937	1.0538365
6839000180	HD 315992	33.937796
6853000044	V* V785 Sgr	967.12366
7169000034	NSV 4706	0.139707
7270000024	SV* HV 12305	0.4999713
7272000032	SV* HV 12280	0.52877805
7274000038	SV* HV 12304	0.64986977
7274000040	SV* HV 12307	0.30362663
7276000036	SV* HV 12277	0.59217985
7276000037	SV* HV 12278	0.54722181
7288000026	V* V991 Cen	0.17597082
7301000022	V* V741 Cen	0.45754427
7364000017	V* HX Sco	142.2096
7365000030	V* V462 Sco	0.46415499
7384000029	V* V490 Sco	3.0036919
7386000052	V* V959 Sco	1.94602
7386000054	CD-34 12215	0.22159676
7438000012	V* V2159 Sgr	0.4667797
7687000059	V* LT Vel	4.2905222
7699000056	HD 80834	5.2514073
7787000024	SV* HV 12271	0.99558931
7788000028	SV* HV 12295	0.47992019
7789000019	SV* HV 12302	0.58673633
7792000026	SV* HV 12291	0.60502105
7839000034	V* LZ Lup	0.63252933
7866000028	V* V954 Sco	1.2685884
7867000011	V* V1065 Sco	3.2652093
7869000032	V* V974 Sco	2.6842259
7877000030	SV* HV 10843	21.076073
7888000020	CD-40 11648	3.3803875
7933000020	V* V2180 Sgr	0.55292031
7937000019	V* V2170 Sgr	0.5273687
8144000041	V* KW Vel	1.1825118
8152000056	V* OT Vel	25.814097
8262000034	V* V618 Cen	341.37831
8275000036	V* V892 Cen	3.2560211
8282000056	NSV 6683	0.21996843
8295000034	[KWS97] TTS 44	3.0926661
8297000032	V* AD Lup	3.50679135
8300000039	V* GL Lup	449.97659
8315000024	V* V366 Nor	86.58525
8604000030	HD 89249	25.306195
8629000045	ASAS J113210-5948.9	0.45348099
8667000033	CD-55 5223	0.37952541
8672000033	V* HQ Cen	9.9542272
8697000052	2E 1552.8-5316	5.1471375

Continued on next page...

Table 3.3 – Continued

IOMC	Name	Period (days)
8698000036	V* RR Nor	1.5137809
8704000030	V* V359 Nor	20.254742
8715000035	V* V371 Nor	2.3484453
8771000021	SV* SON 7128	0.57990834
8962000023	V* V408 Car	308.7174
8990000085	SV* HV 110	90.127676
9006000053	AX J1434.2-6024	5.9867797
9013000066	NSV 6525	0.73574718
9023000052	V* AR Nor	0.7387132
9059000034	V* AP Pav	0.77828229
9068000029	SV* SON 7113	0.47640495
9073000048	SV* SON 7122	0.44956767
9142000330	X SMC X-1	3.8945857
9268000073	V* FM Aps	208.389

3.3.2 Classification

A big variety of variable objects have been observed by OMC and are presented in this version of the catalog. The distribution in galactic coordinates of the different kind of objects is displayed in Fig. 3.2. In order to perform a statistical study of the type of objects in the catalog, the information available in the literature was used. When available, the object classification was extracted from the VSX. Otherwise, the type of variability was taken from the SIMBAD database. According to the above classifications different variability groups were defined and each source was assigned to one of them. In the case of pulsating stars, 10 additional subgroups were defined, and in the case of eclipsing binaries, 4 additional subgroups based only on the shape of the light curve, were included. In this way, the different variable objects found in the catalog are:

- 2631 pulsating stars (Pu), including
  - 297 Cepheids (Ce),
  - 261 RR Lyrae (RR) pulsators,
  - 37 δ Scuti pulsators (δ Sct),
  - 32 RV Tau stars (RV),
  - 28 β Cephei stars (β Cep),
  - 26 SPB pulsators (SPB),
  - 680 Mira type stars (M),
  - 591 semi-regular stars (SR),
  - 630 slow pulsators (L),
  - 49 simply classified as pulsators (other).
- 1132 eclipsing binaries (EB), including
  - 728 Algol (β Persei)-type eclipsing systems (EA),
  - 191 β Lyrae-type eclipsing systems (EB),
  - 117 W Ursae Majoris-type eclipsing variables (EW),
  - 96 simply classified as eclipsing (E)

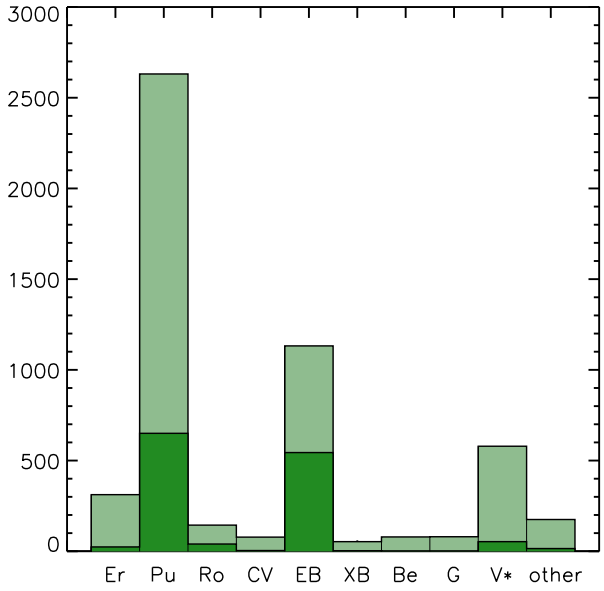

Figure 3.6: Histogram of the different groups of variability types present in the catalog. There are a big number of objects which are unclassified, or just classified as variable objects.

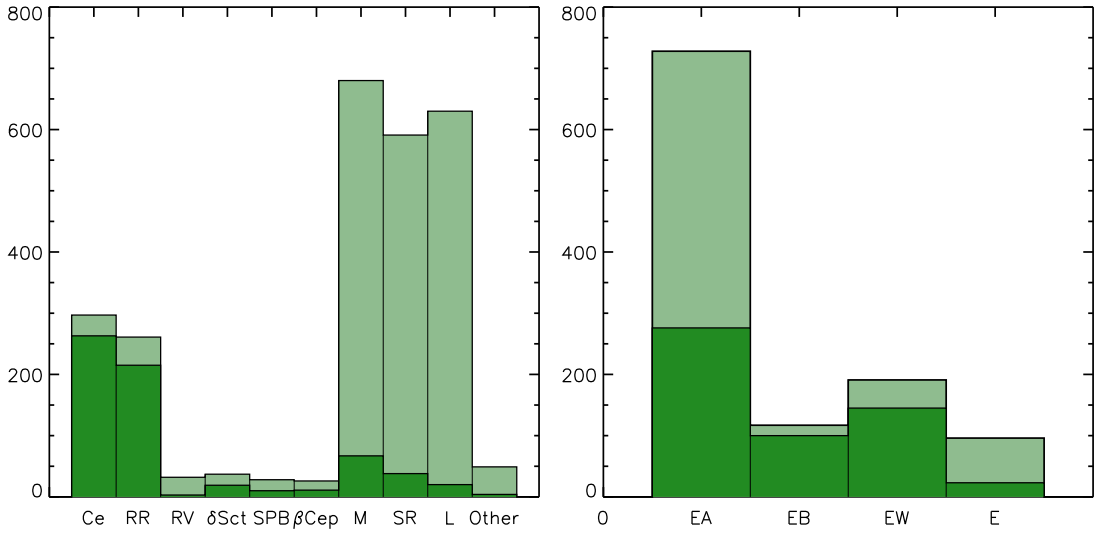

Figure 3.7: Histogram of the subgroups of variability types present in the catalog. **Left:** Histogram of the different kinds of pulsating stars. **Right:** Histogram of the subtypes of eclipsing binary stars.

- 53 X-ray binaries (XB),
- 78 cataclysmic variables (CV),
- 312 eruptive stars (Er),
- 144 rotating stars (Ro),
- 79 Be stars (Be),
- 579 stars just classified as variable (V*),
- 80 extragalactic sources (G), and
- 162 objects of other types.

In Fig. 3.6, the histogram corresponding to the different groups is displayed. It is clearly dominated by the groups of pulsating stars and eclipsing binaries. In Fig. 3.7, more detailed histograms for the subgroups of pulsating stars and eclipsing binary systems, the latter dominated by Algol-type systems, are shown.

New classifications

Several new variable objects were found in this study, most of them with new period determinations. In Table 3.4 a list of the new classifications is given. The classification was carried out by visual examination of the light curves. Most of the previously unknown variable sources have been classified as pulsators or eclipsing binaries. In summary, 23 RRABs, 9 EWs, 8 EAs, 6 EBs, 4 SRAs, 3 SRs, 1 RRs, 1 DCEP, 1 CWB, 1 M, 1 ACV and 1 ELL have been classified.

Table 3.4: New classifications of previously unknown variable sources

IOMC	Name	Otype	Vartype	New class	$P_{this\ work}$ (days)	P_{VSX} (days)
0122000035	V* V651 Ori	V*	RR:	EW	0.3782734	
0296000017	SV* SON 10679	EB*		RRAB	0.7644219	
0314000023	V* UX Vir	V*		RRAB	0.51275451	
0399000012	NSV 8235	V*	S	RRAB	0.48680197	
0455000047	V* BT Ser	RR*	RR	RRAB	0.72381695	0.29548
0462000036	FASTT 1181	V*	MISC	EW	0.32637677	
1059000033	V* V612 Aql	Pu*	LB	SRA	237.04046	
1059000039	SV* SON 8111	Pu*	L	SR	443.09108	
1610000062	V* CO Vul	Pu*	LB	SRA	451.63013	
2585000065	V* V854 Her	V*	EB:	EA	0.78064629	
3154000064	V* V424 Cyg	Pu*	LB	SRA	90.474635	
3155000053	NSV 12891	V*		SRA	133.24773	
3162000048	V* V395 Cyg	V*	SRD:	DCEP:	1.0285077	40.5
3167000086	V* V1792 Cyg	El*	ELL	EB	3.3034183	
3170000077	V* V2131 Cyg	Pu*	LB	SR	35.791156	
3171000062	V* V2138 Cyg	V*	ACV:	ACV	1.2467537	1.21327
3595000052	V* V628 Cyg	WU*	EW	EB	0.96658748	0.651652
3665000051	LD 80	V*		EA	5.2100273	
3970000044	NSV 13732	V*		EA	3.8113687	
3976000034	NSV 13895	V*		EA	0.84930198	
3982000042	ALS 12262	SB*	ELL?	ELL:	2.1782339	
4024000038	V* V660 Cas	sr*	SR:	M	344.33077	
4040000057	V* V423 Cas	WU*	EW	EB	1.8303136	0.627858
4278000050	V* QQ Cep	V*	EB:	EB	0.91486243	
4421000058	V* AU Dra	Al*	EA/SD:	EB	0.51526649	0.51514
4948000021	FASTT 536	V*	MISC	EW	0.26187571	
5067000021	NSV 8593	V*		RRAB	0.54285566	
5082000020	FASTT 1091	V*	MISC	EW	0.35434326	
5082000050	FASTT 1140	V*	MISC	EW	0.59229457	
5096000086	FASTT 1076	V*	MISC	EW:	0.66091853	
5113000025	GSC 05113-01089	V*	EW/KW	EA	0.43580028	0.4358
5624000014	V* V784 Sco	EB*	E	EA	1.5263212	1.526
5732000016	V* FF Sgr	V*		RRAB	0.55862768	
5760000018	V* UY Aqr	V*		RRAB	0.66755506	
6209000022	V* AN Sco	V*	INS:	RRAB	0.61605374	
6214000022	V* AS Sco	V*		CWB:	1.4548234	
6839000180	HD 315992	*		EA	33.937796	
6853000044	V* V785 Sgr	Pu*	LB	SR	967.12366	
7270000024	SV* HV 12305	V*		RRAB	0.4999713	
7272000032	SV* HV 12280	V*		RRAB	0.52877805	
7274000038	SV* HV 12304	V*		RRAB	0.64986977	
7274000040	SV* HV 12307	V*		EW	0.30362663	
7276000036	SV* HV 12277	V*		RRAB	0.59217985	
7276000037	SV* HV 12278	V*		RRAB	0.54722181	
7438000012	V* V2159 Sgr	RR*	RR	RRAB	0.4667797	
7787000024	SV* HV 12271	V*		RRAB	0.99558931	
7788000028	SV* HV 12295	V*		RRAB	0.47992019	
7789000019	SV* HV 12302	V*		RRAB	0.58673633	
7792000026	SV* HV 12291	V*		RRAB	0.60502105	
7933000020	V* V2180 Sgr	RR*	RR	RRAB	0.55292031	

Continued on next page

IOMC	Name	Otype	Vartype	New class	$P_{this\ work}$ (days)	P_{VSX} (days)
7937000019	V* V2170 Sgr	RR*	RR	RRAB	0.5273687	
7937000025	V* V1643 Sgr	WU*	RR	RRC	0.33956215	0.33956
8166000055	V* DL Vel	Al*	EA	EB	0.56354796	0.56355802
8297000032	V* AD Lup	V*		EA	3.50679135	
8771000021	SV* SON 7128	V*		RRAB	0.57990834	
9023000052	V* AR Nor	Ir*	S:	EW	0.7387132	
9059000034	V* AP Pav	EB*	E	EW	0.77828229	
9068000029	SV* SON 7113	V*	S	RRAB	0.47640495	
9073000048	SV* SON 7122	V*		RRAB	0.44956767	

3.3.3 Charts provided for each object in the catalog

For each source in the catalog, a chart including the DSS image around the target, its OMC light curves, unfolded and folded with the periods derived in this work and/or with the cataloged ones, was prepared. The time in the light curves is the Barycentric *INTEGRAL* Julian Date expressed in Barycentric Dynamical Time (TDB). To convert this time to Barycentric Julian Date expressed in TDB, you have to add 2,451,544.5 d. These charts and the complete light curves in machine readable format for all the sources contained in the OMC–VAR catalog can be retrieved from the catalog web[3] and at CDS services[4]. Some illustrative examples of the charts are provided below.

3.4 Conclusions

The optical photometric light curves provided by OMC, including data from the beginning of the mission to February 2010, were analyzed with the aim of characterizing their expected variability and potential periodicity. To detect potential variability, a chi-squared test was performed. In this first version of the *INTEGRAL–OMC catalogue of optically variable sources*, variability was detected for 5263 objects, with median brightness in the range from 7.1 to 16.27 in V.

The potential periodicity of these sources was analyzed, using a method based on the phase dispersion minimization (PDM) technique, optimized to handle light curves with very different shapes. For 1337 of them we have been able to derive a period with enough significance. The periods found vary from a few hours to some hundreds of days, with a peak in the histogram of typical periods around 15 h. The light curves were visually inspected to check the validity of the estimated periods, rejecting those false positives yielded by the PDM algorithm.

For each source in the catalog, the median value of the V magnitude, the mean of the photometric errors of the points and the minimum and maximum value of V, estimated as the 98th and 2nd percentiles, respectively, of the points in the light curve were given. For those sources classified as periodic or probably periodic, the best estimate of the period and its calculated uncertainty were provided. A set of tags to identify those sources whose photometry can be significantly affected by nearby stars, as well as some ancillary data, are also included.

This catalog contains data useful for the study of several classes of variable stars: eclipsing binaries, pulsating stars, active stars, cataclysmic variables, X-ray binaries, etc. The most frequent objects in the present compilation are pulsating stars and eclipsing binary systems, according to the classification provided by the VSX catalog and SIMBAD.

The next version of the *INTEGRAL–OMC catalogue of optically variable sources* will include all other objects in the OMC database complying with the same photometric requirements, estimated to be around 25 000.

[3] http://sdc.cab.inta-csic.es/omc/var/

[4] The catalog can be accessed through VizieR, the catalog database of the Centre de Donnes astronomiques de Strasbourg (CDS) at http://vizier.u-strasbg.fr/viz-bin/VizieR. The identifier of the OMC–VAR catalog is J/A+A/548/A79.

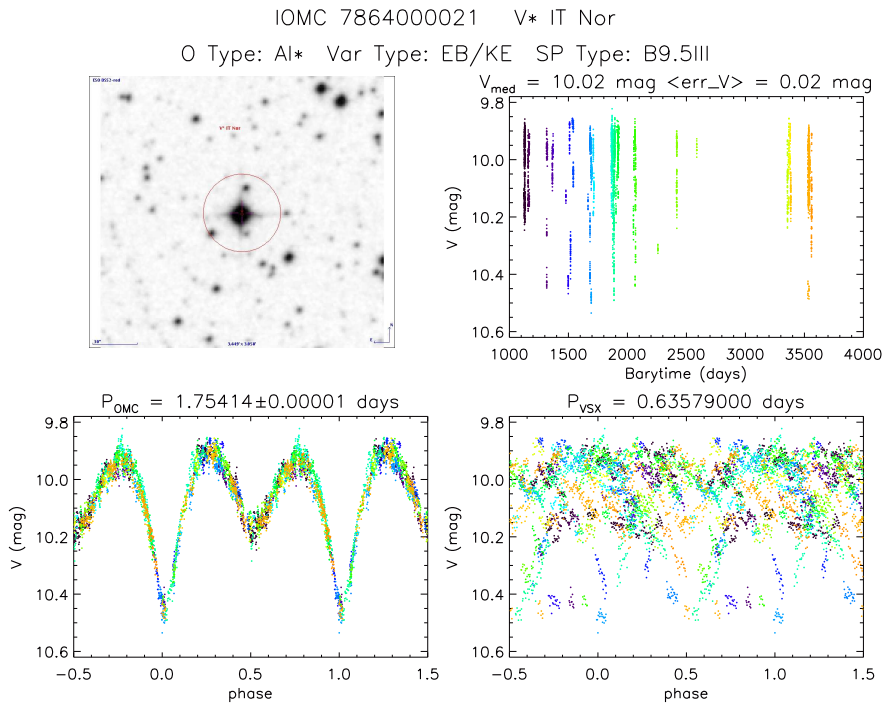

Figure 3.8: IT Nor, an Algol-type eclipsing binary. **Top left:** the DSS red image of the OMC FOV (the red circle represent the OMC photometric aperture). **Top right:** the OMC V-band light curve without folding. **Bottom right:** The OMC light curve folded with the period estimated in this work. **Bottom left:** the OMC light curve folded with the period given in the VSX. In this case, the period derived in this work improves significantly the value provided by the VSX and yields a satisfactory folding.

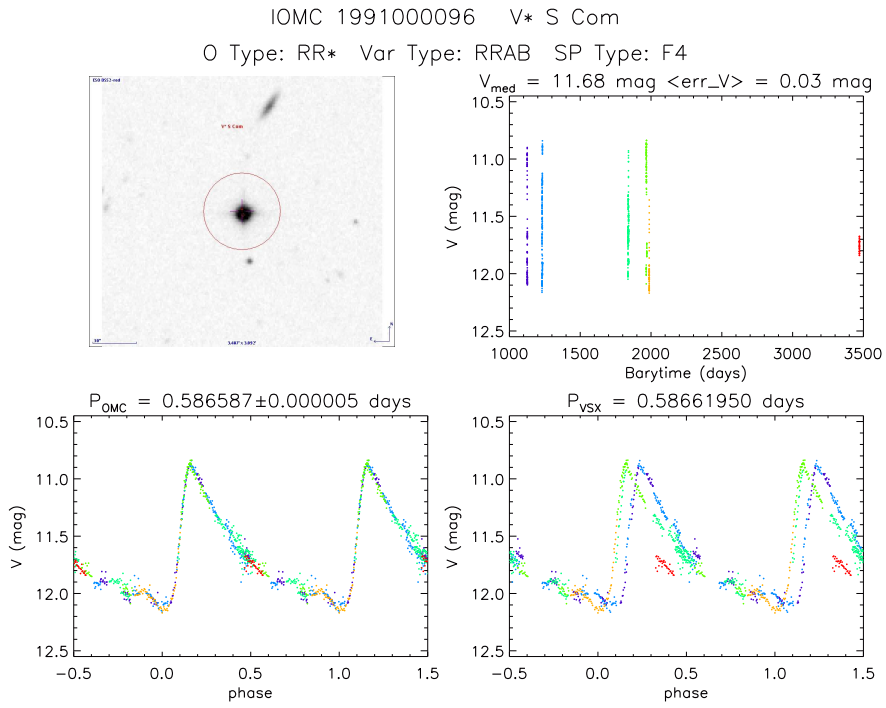

Figure 3.9: For some objects, like the RR Lyrae star S Com, a very small increase in the accuracy of the period is enough to get a perfect folding of the light curve.

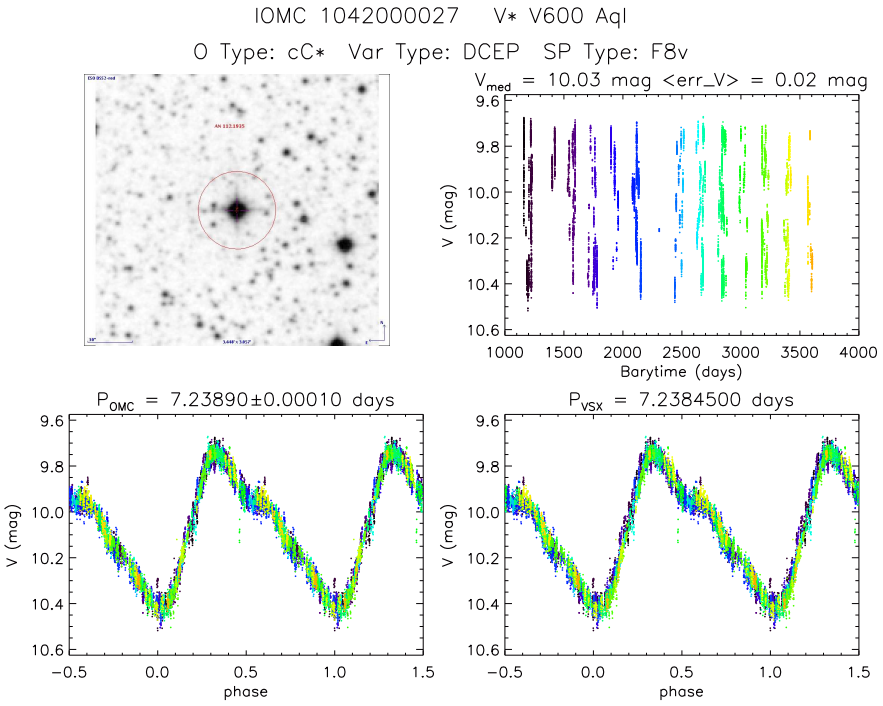

Figure 3.10: Chart of V* V600 Aql, a classic Cepheid.

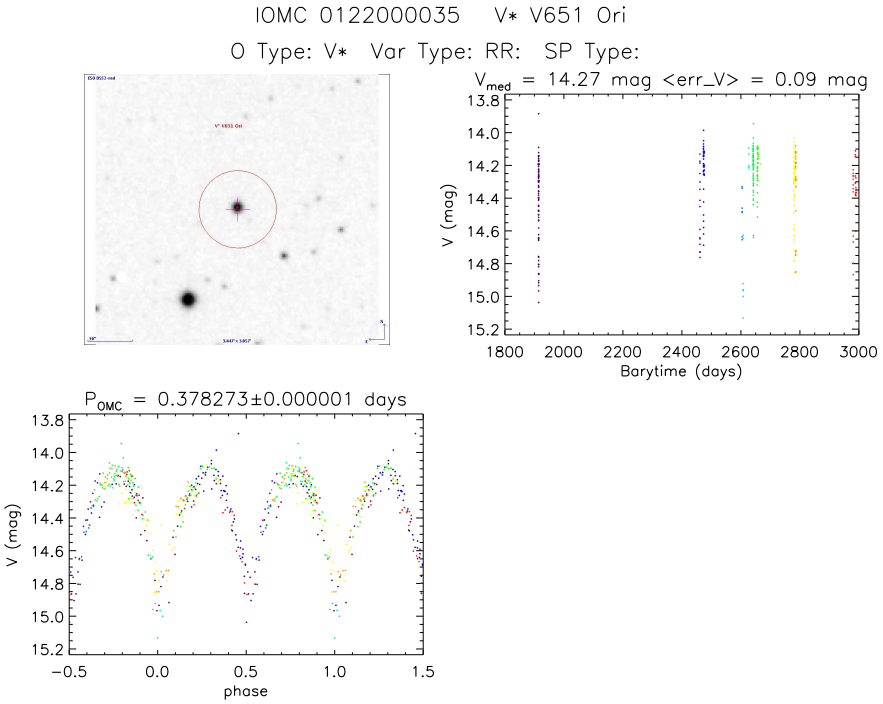

Figure 3.11: New period determination from this work for V651 Ori. Moreover, the variability classification in VSX should be corrected from RR Lyrae to eclipsing binary, according to our light curve.

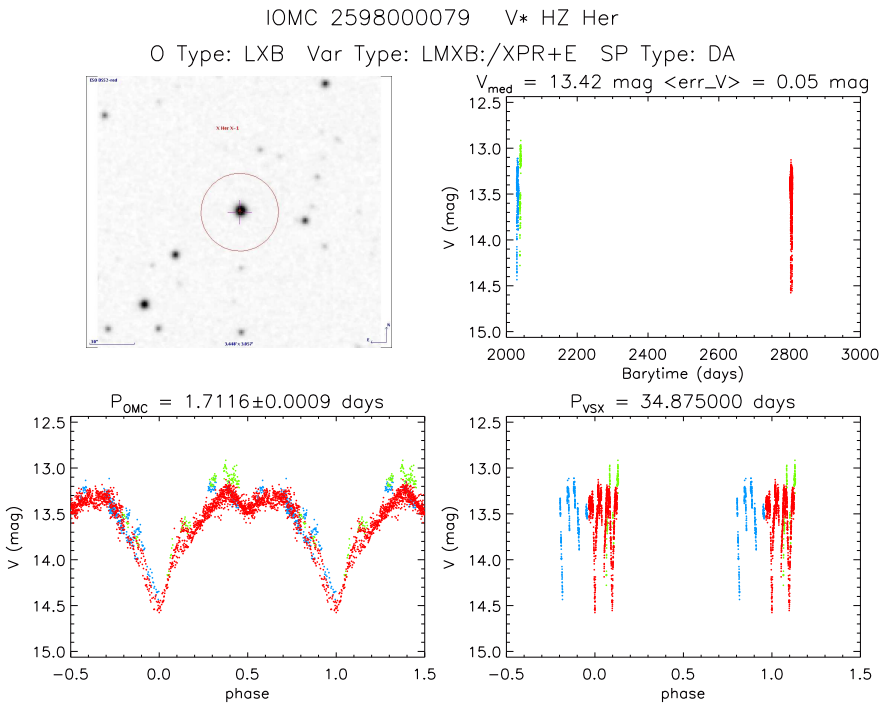

Figure 3.12: In the case of Her X–1, the VSX period corresponds to the 35 day cycle in the X-ray intensity, while the OMC optical light curve is dominated by the orbital eclipses.

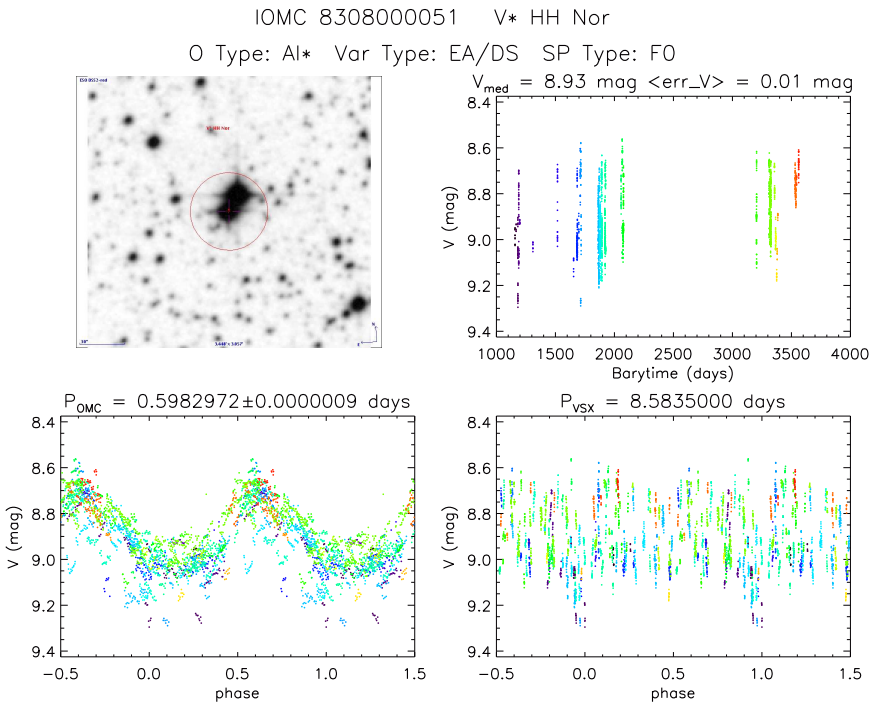

Figure 3.13: The photometry of the intended target, HH Nor, is heavily dominated by the brighter, nearby object VSX J154329.4–515037, which is indeed a variable RR Lyr star (RRAB) with a period of 0.59 days. In fact, HH Nor is an eclipsing binary with mean V magnitude of 10.9 and a period of 8.58 days.

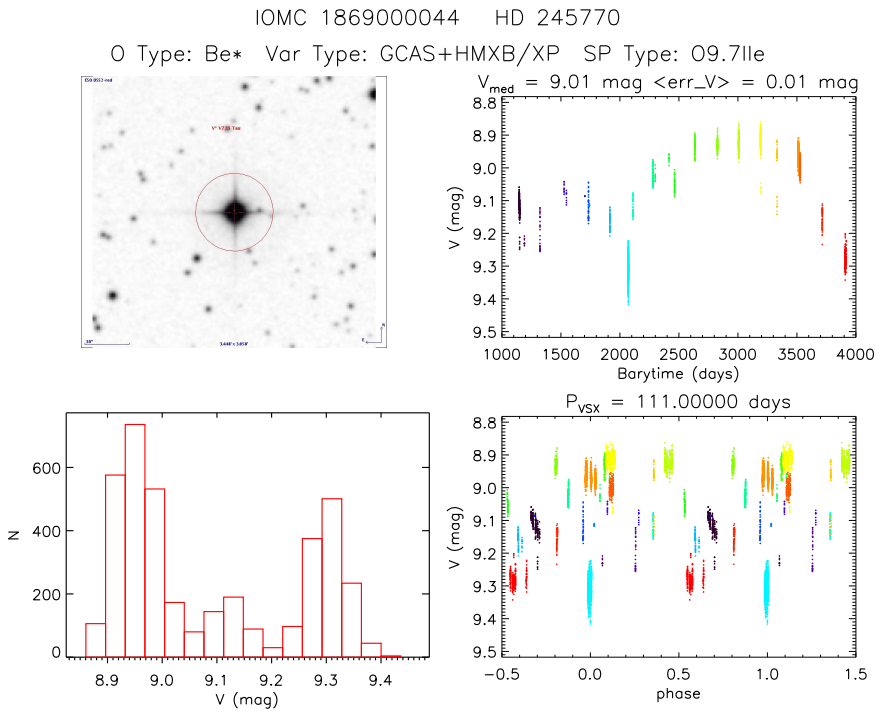

Figure 3.14: In the light curve of the high-mass X-Ray binary 1A 0535+262, a long term variation during the nearly 3000 days of monitoring dominates over the orbital period given by VSX. When there is no determination of the period from this work, the chart of the corresponding object includes a histogram of the observed magnitudes. The shape of these histograms helps to understand the variability pattern of the different objects.

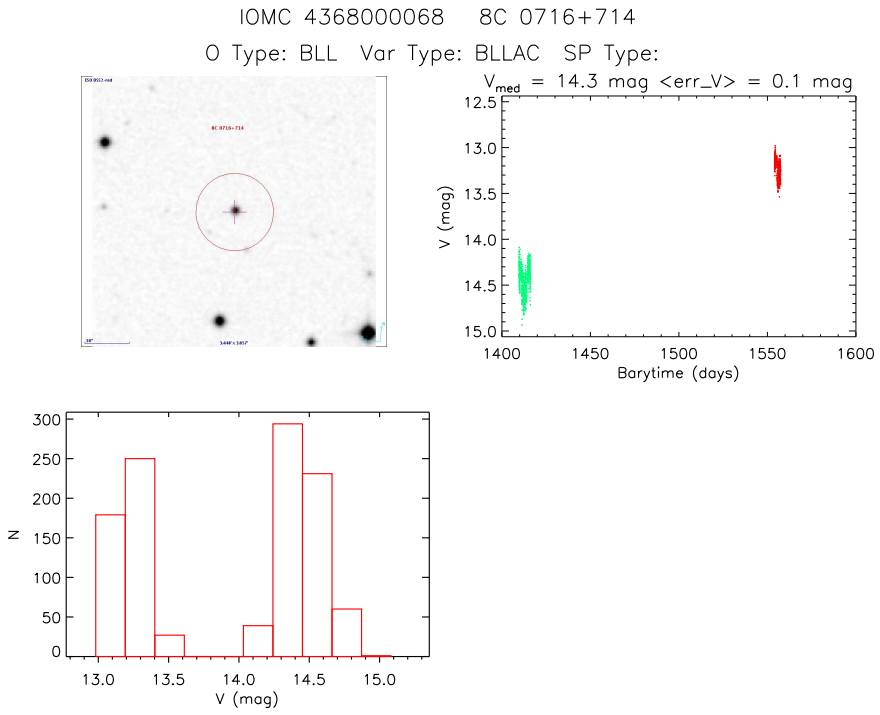

Figure 3.15: The OMC light curve of the blazar S5 0716+714 shows two different states, separated by around 150 days. They can be clearly observed in the magnitude histogram.

Chapter 4

OMC/INTEGRAL photometric observations of pulsating components in eclipsing binaries and characterization of DY Aqr

This chapter provides an interesting scientific case of optical variability observed with OMC data. Because of the importance of this kind of studies in astrophysics, a search for pulsating components in the eclipsing binaries in OMC–VAR was performed. An introduction on the field of these systems is provided in Section 4.1. The search for eclipsing binaries inside the OMC–VAR catalog is described in Section 4.2. As a result, five objects presenting these characteristics were found and a detailed analysis of one of them, DY Aqr, has been carried out. A short introduction to DY Aqr is included in Section 4.3. The observations obtained to characterize DY Aqr are presented in Section 4.4. The results of the spectral classification are discussed in Section 4.5. The O-C evolution is analyzed in Section 4.6. The modeling of the binary features from the photometric and radial velocity curves is explained in Section 4.7. Section 4.8 contains the results of the pulsational frequency analysis performed after subtracting the orbital fit. The evolutionary state of the system, considering DY Aqr is a close binary system, is analyzed in Section 4.9. Finally, the possible relation between the orbital and pulsational period of DY Aqr is examined in 4.10.

The main results of this chapter can be found in Alfonso-Garzon et al. (2014).

4.1 Introduction

Asteroseismology aims to understand the structure and evolution of stars by examining their oscillation modes (Brown & Gilliland, 1994; Aerts et al., 2010; Chaplin & Miglio, 2013). Among the classical pulsators, δ Scuti stars, which are located at the intersection of the Cepheid instability strip and the main sequence, where the stellar structure transits from a highly developed outer convective zone to its absence (Rodríguez & Breger, 2001), are rather common. They pulsate with amplitudes from milimagnitudes up to tenths of a magnitude (Breger, 2000), but only a fraction of the theoretically predicted modes are observed, which results in many free parameters in the pulsation models. It is therefore important to infer some of the fundamental stellar properties of these pulsators from other methods, like for example by studying the pulsating components in binary (multiple) systems. In this kind of systems it is possible to characterize precisely their components, supplying additional constraints for a more reliable modeling. About 70% of all stars in the Solar neighborhood are members of binary or multiple

systems ($\sim$ 60–70% for late-type stars (Mayor et al., 2001; Chini et al., 2013), $\sim$ 70–80% for early-type stars (Mason et al., 2009; Sana & Evans, 2011; Chini et al., 2012)). This fact is usually ignored in the study of stellar pulsations although there is strong evidence that binarity might affect the pulsation properties in specific cases (e.g. the eccentric binaries HD 177863 (De Cat, 2002), HD 209295 (Handler et al., 2002) and KIC 4544587 (Hambleton et al., 2013)). It is thus essential to understand the possible link(s) between binarity and pulsation (Lampens, 2006). Recent studies point to the fact that single and binary-member δ Scuti stars can show different behavior because of their different evolutionary status (Mkrtichian et al., 2003; Soydugan et al., 2006; Liakos et al., 2012). Mkrtichian et al. (2004) introduced the *oscillating eclipsing Algols* (oEAs) as main sequence pulsators in semi-detached Algol-type eclipsing binary systems. For several of these systems, they found variable pulsational characteristics which could be related to mass transfer episodes or tidal distortions.

Several surveys have been carried out in the last years to increase the number of known objects of this type. Soydugan et al. (2006) compiled a catalog of close eclipsing binary systems (detached and semi-detached ones) with one δ Scuti component. Zhou (2010) made a compilation of 190 oscillating eclipsing binaries (60 of them containing a δ Scuti component) and more than 370 pulsating binary or multiple stellar systems. Liakos et al. (2012) published a catalog with 74 eclipsing binaries with a δ Scuti component, and this number is increasing at a very rapid rate thanks to the results of *MOST* (Walker et al., 2003), *CoRot* (Baglin et al., 2009) and *Kepler* (Borucki et al., 2010; Gilliland et al., 2010). However, just a few members of this group have been investigated in depth (some recent examples are Lehmann et al. (2013); Maceroni et al. (2014); da Silva et al. (2014)).

This work presents the search for eclipsing binaries with a pulsating component in *the first INTEGRAL–OMC catalogue of optically variable sources* (OMC–VAR; Alfonso-Garzón et al. 2012). A detailed follow-up study of the physical properties of DY Aqr, an Algol-type binary with its primary component showing δ Scuti oscillations, has been performed, by combining optical photometry obtained with OMC and the 90-cm telescope at the Observatorio de Sierra Nevada (OSN, Granada, Spain), with high-resolution spectra taken with the HERMES instrument on the MERCATOR telescope at the Observatorio del Roque de los Muchachos (ORM, La Palma, Spain)).

4.2 The search for eclipsing binaries with pulsating components in OMC–VAR

The first edition of the catalog of variable objects observed by OMC, OMC–VAR, contains photometric and variability information for more than 5000 objects, resulting from the analysis of an initial sample of more than 6000 light curves observed by OMC during its first 8 years of operations (see Chapter 3). As discussed in Alfonso-Garzón et al. (2012) and in Chapter 3, there are many objects in the OMC–VAR catalog classified as eclipsing binaries according to the *Variable Star Index* (VSX; Watson (2006); Watson et al. (2012)). Out of the 1132 classified eclipsing binaries, a period in the literature or in the OMC–VAR, was found for 1072 systems. Whenever available, the periods determined in OMC–VAR were used (see Table 4.1). The three types of eclipsing binaries in Table 4.1: Algol (EA), β Lyrae (EB) and W Ursae Majoris (EW), correspond to the classification in the *General Catalogue of Variable Stars* (GCVS; Samus et al. (2012)), adopted in the VSX, and is based purely on the shape of the light curves (see 2.1.2).

In order to detect pulsations in the components of these systems, all eclipsing binaries in OMC–VAR were analyzed, by modeling their folded OMC light curves with *polyfit* (Prša et al., 2008), aiming to fit just their overall shape. Then, the fitted curves were subtracted from the original data. The residuals obtained, avoiding the intervals when eclipses occur, were analyzed

Table 4.1: Eclipsing binaries in OMC–VAR and period information available.The three types (EA, EB, EW) correspond to the classification in the GCVS (see text).

Eclipsing type	All	with $P_{\rm OMC}$	with $P_{\rm VSX}$
Algol (EA)	728	272	703
Beta Lyrae (EB)	191	145	184
W Ursae Majoris (EW)	117	100	108
Other	96	23	61

for periodic signals by calculating the Fourier periodogram. With this method four previously known eclipsing systems with a pulsating component were confirmed and a new candidate, AW Vel, was proposed. Pulsational periods similar to the values previously reported in the literature were found for Y Cam, MX Pav and BG Peg. For DY Aqr, the pulsational period measured in previous works was also detected, but it was not the main one. These results are summarized in Table 4.2 and the folded light curves and periodograms are plotted in Fig. 4.1.

Table 4.2: Results from the search of pulsating components in eclipsing binaries.

Name	SpT (A+B)	$P_{\rm orb}$ (days)	$P_{\rm puls}$ (*lit.*) (days)	Reference	$P_{\rm puls}$ (*this work*) (days)	Semi-amplitude (mag)
Y Cam	A9IV+K1IV	3.3057	0.0665	1, 2, 3, 4, 5	0.0685(1)	0.018(2)
AW Vel	A4 + [G2IV]	1.9925			0.0664700(1)	0.026(1)
MX Pav	A5 + K3IV	5.7308	0.0756	6, 7	0.0756005(2)	0.081(2)
DY Aqr	A0 + [F3]	2.1597	0.0427	8, 9	0.051113(1)	0.0141(7)
BG Peg	A2 + [G2IV]	1.9527	0.0391	8, 10	0.03912730(4)	0.014(1)

(1) Broglia & Marin (1974); (2) Broglia & Conconi (1984); (3) Kim et al. (2002); (4) Rodríguez et al. (2007); (5) Rodriguez et al. (2010); (6) Michalska & Pigulski (2007); (7) Pigulski & Michalska (2007); (8) Soydugan et al. (2009); (9) Soydugan et al. (2010); (10) Soydugan et al. (2011)

4.3 Introduction to DY Aqr

DY Aqr was identified as an Algol-type binary showing δ Scuti oscillations by Soydugan et al. (2009, 2010). The only information known before this study about the spectral type of the components was given by Svechnikov & Kuznetsova (1990) and Malkov et al. (2006), who proposed it to be A0+[F3]. Zasche (2011) modeled the binary system using only the OMC photometric light curve, assuming the primary component to be an A0 V star. As far as we know, there was no spectroscopic information available for this source before this work. The lack of precise multiband photometric and spectroscopic data led us to perform a more detailed follow-up study of this binary system, which has allowed us to refine the properties of its components.

4.4 Observations

DY Aqr was observed by OMC for 5 days in two different epochs in 2002 and 2003. With the aim of characterizing the system, ground-based multicolor photometry and high-resolution spectroscopy were carried out and analyzed. Time for 6 nights of photometric and 6 nights of spectroscopic observations was obtained.

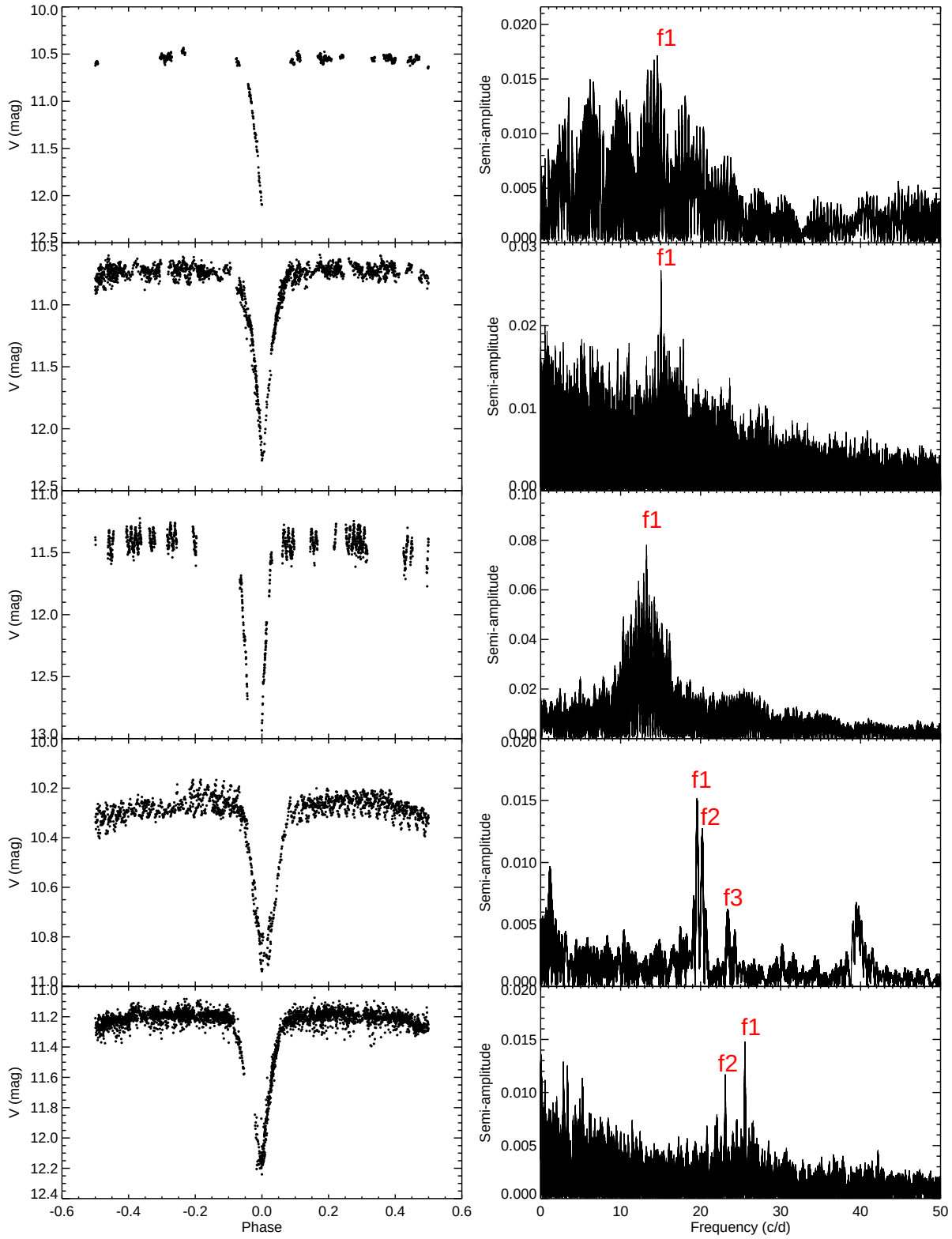

Figure 4.1: Folded OMC photometric light curves and Fourier periodograms from PERIOD04 of the five eclipsing binary systems with a δ Scuti component found in the OMC–VAR catalog. From top to bottom the plots correspond to Y Cam, AW Vel, MX Pav, DY Aqr and BG Peg. The frequencies detected for each source are marked in red in the periodograms.

4.4.1 Photometric observations

OMC photometric data for DY Aqr in the Johnson V filter were extracted from the OMC database (Gutiérrez et al., 2004). DY Aqr was observed on 24–26 December 2002 and 7–8 November 2003. The OMC light curve has 1699 photometric measurements.

Additional multicolor photometric observations were collected at the Observatorio de Sierra Nevada (OSN, Granada, Spain) on 7–8 and 10–13 September 2012. Strömgren *uvby* photometry was carried out using the six channel $uvby\beta$ photometer attached to the 90-cm telescope at OSN (OSN/T90) to determine the physical characteristics of the components of the system and to perform a detailed study of the pulsational frequency peaks through different filters. These light curves have 369 photometric measurements each one.

The OSN light curves provide differential magnitudes from a comparison star, HD 211250 (V = 8.51 mag). Since additional $UBVJHK$ photometry for HD 211250 is available in SIMBAD, the apparent fluxes in the Strömgren filters modeling the Spectral Energy Distribution (SED) of the star and doing synthetic photometry on the model, were derived. Once the Strömgren magnitudes for the comparison star are obtained, the photometry for our target can be directly derived. The best fit for the SED of HD 211250 was obtained for $T_{\rm eff}$ = 6900 K, $\log g$ = 3.5 and solar metallicity. Another comparison star, HD 211517, was used to check the stability of the photometry.

4.4.2 Spectroscopic observations

Time series of high-resolution spectra for 6 nights from 27 August to 2 September 2012 were obtained. In order to reject cosmic rays and to get better signal-to-noise ratio (S/N), for each observation, 3 or 4 exposures of 1200 s were taken and combined. In this way, 22 combined spectra were obtained in this campaign, covering reasonably well the different phases in the folded light curve. All spectra were taken with HERMES, a fiber-fed prism-cross-dispersed echelle spectrograph on the MERCATOR telescope, in the high-resolution mode (HRF, R$\sim$ 85000), covering a wavelength range between 3800 and 8750 Å. The MERCATOR Telescope is a 1.2 m semi-robotic telescope located at the Observatorio del Roque de los Muchachos (ORM) on La Palma (Canary Islands, Spain).

The calibration of the spectra was performed with the automated reduction pipeline (Raskin et al., 2011). It performs the corrections for the bias level, the inter-order background level, the fringing on the detector, and the modulation of the intensity in each spectral order and applies a pre-normalization eliminating the global wavelength-dependency of the flatfield calibration system. Finally, it applies a (non-absolute) flux calibration to each order and merges them into a single spectrum.

4.5 Spectral classification

The spectral type and physical parameters of the primary component of DY Aqr were determined using the spectra obtained with HERMES/MERCATOR.

With the aim of separating each component spectra, the spectral disentangling technique was applied, using KOREL, a FORTRAN code for disentangling spectra of binary and multiple systems which uses Fourier transform in the wavelength domain (Hadrava, 1995, 1997). KOREL assumes that an observed double-lined spectrum is a simple linear combination of two single-lined spectra whose velocities reflect the orbital properties of the system. When applied to a set of spectra covering the orbital phases, KOREL extracts the contribution of each component and provides the corresponding velocities relative to the system barycenter. For the 22 spectra, different regions along the spectral range were studied, covering the most significant spectral lines (Ca II-K 3933.73 Å, Fe I 4957.60 Å, Na I D 5889.95 Å, 5895.92 Å, Hα 6562.80 Å, O I 8446.36 Å and

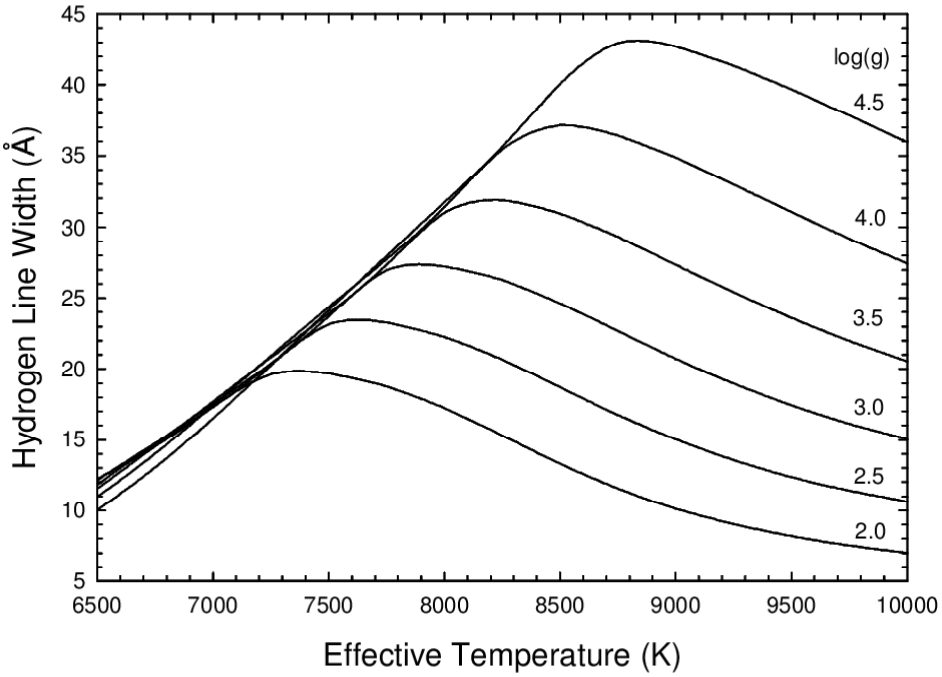

Figure 4.2: Dependence of hydrogen-line width on effective temperature and gravity ($\log g$). Figure reprinted from Gray & Corbally (2009).

Ca II 8662.14 Å) and it was found that in all the cases the secondary contribution was below the detection level. In Fig. 4.3, the 22 spectra vertically arranged according to the orbital phase in the regions of Fe I 4957.60 Å, Hα 6562.80 Å and O I 8446.36 Å, are plotted. The solid lines represent the rest wavelengths. No hints of the secondary component can be appreciated. On the other hand, examining the profiles of the lines close to the primary minimum, the Rossiter-McLaughlin effect (hereafter RME; Rossiter (1924); McLaughlin (1924)) can be observed.

Based on the KOREL results and as will be discussed in Section 4.7, the contribution of the secondary component to the combined spectra were considered to be not significant enough for our purpose of making a spectral classification, since the spectral lines expected to come from it are not detected. Although the contribution to the continuum is about 3–4% in the V-band (see Table 4.4), the effect in the spectral lines should be less noticeable. Moreover, the spectral lines are diluted because of the rotational velocity and are probably below the noise level. All the available spectra, except those affected by the RME, were combined taking into account the Doppler shifts for each phase point. In this way, a normalized spectrum with higher signal-to-noise ratio to work with, was obtained.

First of all, the blue region of the spectrum was examined. In this region, the hydrogen lines are enhanced by Stark broadening (Mihalas, 1978), but these lines become narrower toward later types. For DY Aqr a width of 33 Å for Hγ, which is compatible with an effective temperature around 7500-8000 K and $\log g$ between 3.5 and 4.5, was measured (see Fig. 4.2). Moreover, in this part of the spectrum, there are other features that can be used in the classification of A-type stars, like the comparison of the hydrogen Balmer lines, which are broadest for A2, with the Ca II K-line, which grows in strength as the temperature decreases. Finally, looking at the near-infrared region of the spectrum, the most interesting trend is the appearance of the hydrogen Paschen lines. In the early A-type stars, these lines are much stronger than the near-infrared Ca II triplet, but in the late A-type stars and in F-type stars, the Ca II triplet becomes stronger. As the effective temperature decreases, the P13, P15 and P16 lines become stronger relative to the other unblended Paschen lines. On the other hand, the O I λ8446 and some N I lines in this region are sensitive to gravity. Examining these lines, it can be concluded that the spectrum of

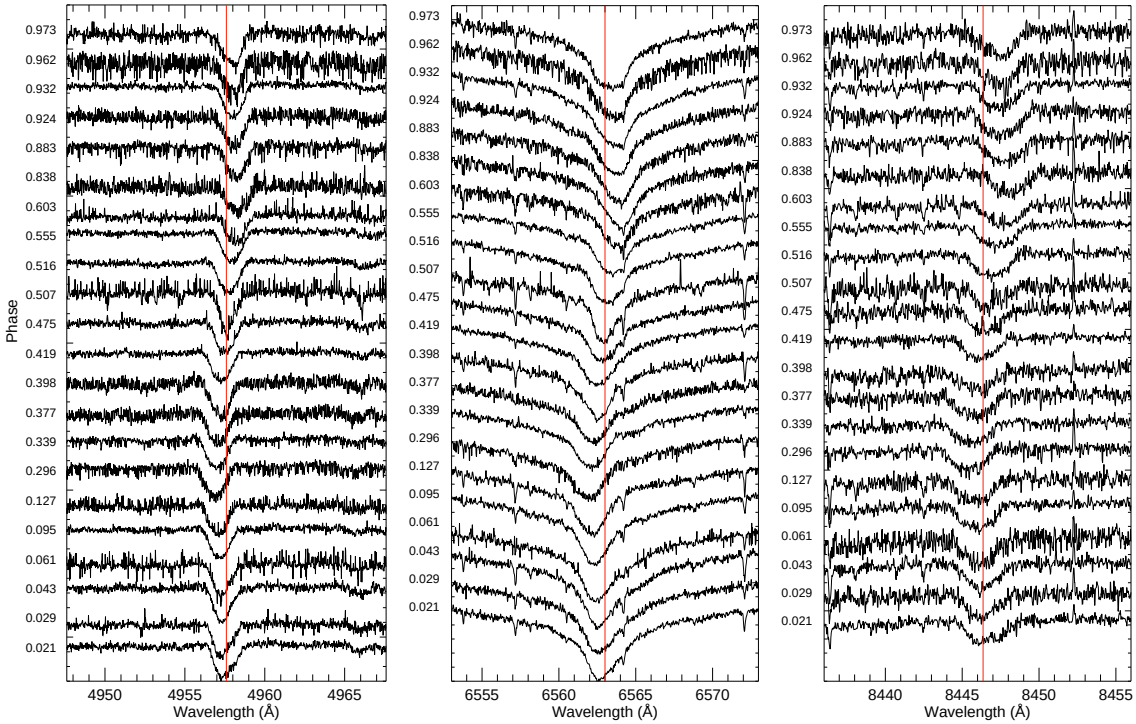

Figure 4.3: The 22 OSN spectra vertically ordered by orbital phase in the regions of Fe I 4957.60 (left), Hα 6562.80 (middle) and O I 8446.36 (right). Arbitrary units have been used in the y-axis corresponding. The normalized fluxes and the orbital phase is labeled for each spectrum. The solid lines represent the rest wavelengths.

DY Aqr corresponds to a main sequence star.

According to these criteria, the primary component has to be a main sequence star with an effective temperature around 7500-8000 K. To quantify its properties, a set of high-resolution spectra, using the suite of programmes SYNTHE (Kurucz, 1993), were synthesized. SYNTHE takes as input the list of the atomic and molecular transitions and the spectral range to be synthesized, together with the corresponding model atmosphere (Castelli & Kurucz, 2003) for a given temperature, gravity and metallicity, including the atomic fractions of the different elements. SYNTHE computes the excitation and ionization populations of neutrals and ions and then produces the final spectrum within the defined spectral range. A special module of SYNTHE computes intensities at several inclinations in the atmosphere and uses these, along with the value of $v \sin i$, to reproduce the spectrum of the star.

The parameter space with $T_{\rm eff}$ between 7000 and 8500 K and $\log g$ between 3.5 and 4.5, with steps of 125 K and 0.25 dex respectively, was explored. The synthetic spectra were broadened with rotational velocities, $v \sin i$, between 0 and 100 km s^{-1}, with a step of 10 km s^{-1}. Typical uncertainties in $T_{\rm eff}$ and $\log g$ are $\pm$125 K and $\pm$0.25 dex, correspondingly. It was concluded that the model with $T_{\rm eff} = 7625 \pm 125$ K, $\log g = 4.25 \pm 0.25$, solar metallicity and $v \sin i = 50 \pm 10$ km s^{-1} provides the best fit to the data (see Fig. 4.4). These parameters correspond to a spectral type A7.5 V (Schmidt-Kaler, 1982), plus or minus one spectral subtype, which indicates that DY Aqr is much cooler than assumed in the past.

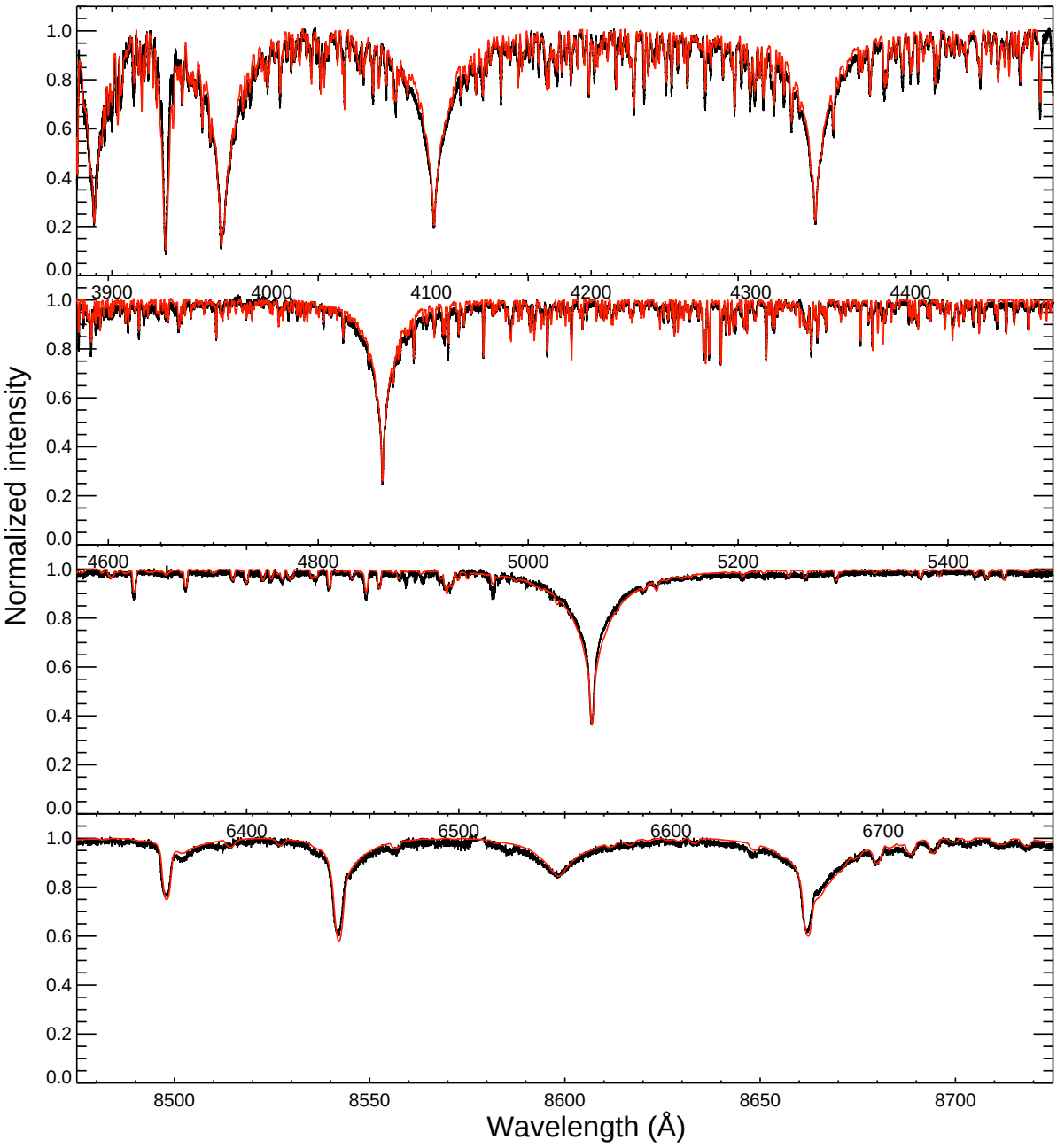

Figure 4.4: Combined spectrum of DY Aqr and the best-fitting synthetic spectrum computed for $T_{\rm eff}$ = 7625 K, $\log g_* = 4.25$ and solar metallicity (red solid line) broadened with $v \sin i = 50$ km s^{-1}.

4.6 O-C evolution

In order to construct the O-C diagram, the linear ephemeris T_0 = HJD 2 426 929.485 +E × 2.159695 were used (Kreiner, 2004; Paschke & Brat, 2006). Two primary minima at different times were determined from our photometric data, using the method described in Kwee & van Woerden (1956). From the OMC data, a primary minimum at T_0 = HJD 2 452 634.1946 ± 0.0020 was measured and from OSN data, another minimum was observed at T_0 = HJD 2 456 182.5476 ±0.0008. As can be seen in Fig. 4.5, no significant long-term changes in the period are appreciated.

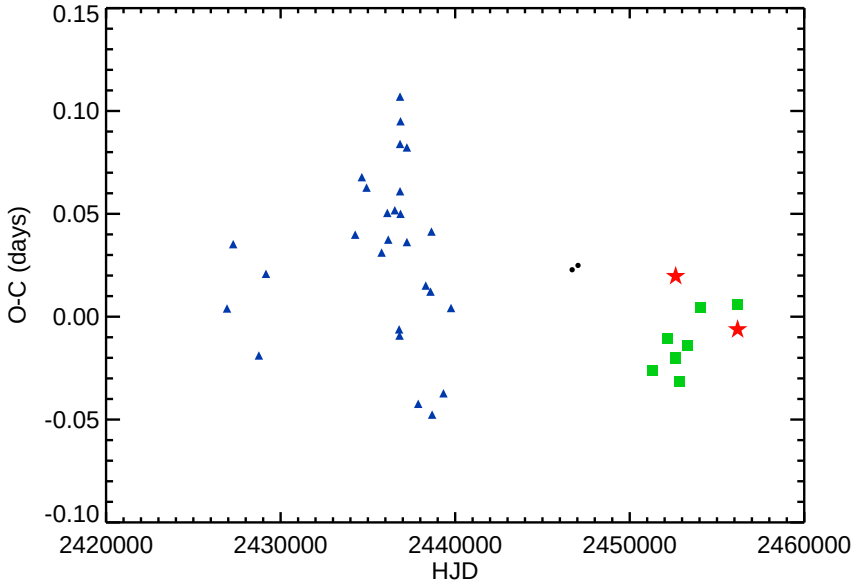

Figure 4.5: The O-C diagram of DY Aqr. All the points correspond to primary minima. The small black dots are from visual observations, the medium blue triangles are from photographic observations and the bigger green squares are from CCD observations. The red stars represent the results from this work.

4.7 Binary modeling

It is only after removing the effects from binarity that the pulsational characteristics of the primary component of the system can be analyzed on the residual data. The properties of the binary system were derived from the photometric light curves in five colors (Johnson V from OMC and Strömgren *uvby* from OSN) and from the radial velocity (RV) curve of the primary component extracted from the high-resolution HERMES/MERCATOR spectra.

The binary modeling was made using PHOEBE (Prša & Zwitter, 2005), a package based on the Wilson-Devinney code (hereafter WD; (Wilson & Devinney, 1971; Wilson, 1979)). Two different configurations were tried, detached and semi-detached with the secondary star filling its Roche lobe, founding that the first one converges to the second one, a modeling of our data with the configuration of a semi-detached system with the secondary component filling its Roche lobe was performed. First, the radial velocity curve and the multicolor photometric light curves were analyzed separately and then, all the available data were combined to get the final solution.

Using the HERMES/MERCATOR spectra we derived the radial velocity curve for the primary component (see Fig. 4.6) but not for the secondary, because it was too weak compared to the primary to distinguish any of its spectral features. To measure the radial velocities the IRAF package *fxcor*, with the spectrum closest to the secondary eclipse (to minimize the secondary

component contribution) as template, was used. According to the spectral type of the star, the best wavelength region of the spectra to carry out the correlation is 3900-5100 Å.

When the spectral disentangling technique was applied (see Section 4.5), the radial velocity curves provided by KOREL for the primary component disentangled spectrum for each region were found to be in good agreement with the results found with *fxcor*.

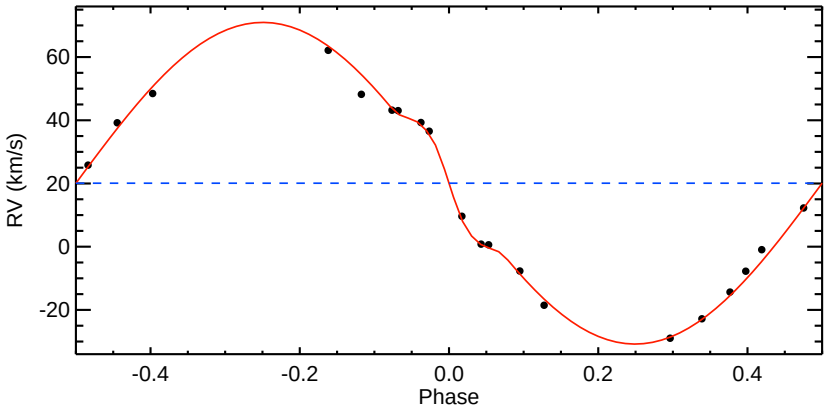

Figure 4.6: Radial velocity curve of the primary component of DY Aqr. Filled circles are the *fxcor* measurements. Typical errors are below 1 km s^{-1}. The red solid line is the PHOEBE fit and the blue dashed line represents the fitted center-of-mass velocity as provided by PHOEBE. Note the clear evidence of the RME around zero phase.

In the RV curve, the effects of the RME can be appreciated. The RME occurs in eclipsing systems when the companion crosses in front of the star; it is due to stellar rotation and creates a distortion in the radial velocity curve of the star. It strongly depends on the radii and separation of the stars, on the orbital inclination or impact parameter and on the position angle of the rotation axis. Its modeling allows to determine these values with a higher precision. In this case, the anomaly is symmetric with a similar redshift during the first half of the eclipse as the blueshift during the second half, so that it can be concluded that the rotational spin and the orbital axis are aligned. PHOEBE considers the RME and proximity effects in the modeling. In Fig. 4.6, the RV measurements of the primary (black dots) and the PHOEBE fit of the radial velocity curve (red solid line), as well as the modeled systemic velocity (blue dashed line) are plotted. The RV semi-amplitude of the primary component is $k_1 = 49.0 \pm 0.1$ km s^{-1}.

To solve the photometric light curves some basic assumptions were made (see Table 4.3). According to the results from the grid of synthetic spectra, the effective temperature of the primary was fixed to 7625 K. The orbital period, that was obtained from OMC data and the Phase Dispersion Minimization (PDM) method (Stellingwerf, 1978), as explained in Alfonso-Garzón et al. (2012), was also fixed. As the secondary eclipse is centered at phase 0.5 and the light curve appears symmetrical, it has been considered that the orbit is circular so the eccentricity e was fixed to 0.

The mass-function has been calculated from the values of the orbital period and the semi-amplitude of the radial velocity curve of the primary component, considering that the orbit is circular. This leads to a value of 0.028 ± 0.001 $M_\odot$. The effective temperature and gravity of the primary component, determined from the spectroscopic analysis ($T_{\rm eff} = 7625 \pm 125$ K and $\log g = 4.25 \pm 0.25$), can be placed on a HR diagram along with the evolutionary tracks from Girardi et al. (2002). This allows to estimate a mass of 1.8 $M_\odot$. The uncertainties in the effective temperature and gravity lead to an uncertainty of ± 0.2 $M_\odot$. As will be shown in Section 4.9, a classical mass-luminosity relation (MLR) will provide us with an approximate value of the mass, although the luminosity of a star that is a member of a close binary system is usually larger than expected. From the mass-function and considering the uncertainties in the mass of the primary

Table 4.3: Fixed parameters for the binary modelling with PHOEBE.

Parameter	Values
Time of primary minimum (BJD)	2452632.03258
Orbital period (d)	2.15967989(1)
Orbital eccentricity, e	0.0
Primary $T_{\rm eff}$ (K)	7625(125)
Primary Bolometric albedo	1.0
Secondary Bolometric albedo	0.60
Primary gravity brightening	1.0
Secondary gravity brightening	0.32
Primary rotation	1.00
Secondary rotation	1.00
Third light	0.0

component, the mass of the secondary component has been estimated to be between 0.51 $M_\odot$ and 0.59 $M_\odot$. The mass-ratio is therefore constrained to the range 0.29 and 0.32, leading to a value of $q = 0.31 \pm 0.02$. Combining this information with the expected radius of the Roche-lobe filling component for a mass-ratio (Eggleton, 1983) and the relative sum of the radii obtained from the width of the eclipses, we could put some constraints in the fit. Theoretical values of the bolometric albedos (A1 = 1.0 and A2 = 0.6) and gravity-darkening exponents (g1 = 1.0 and g2 = 0.32) were adopted for the primary and secondary stars, corresponding to radiative and convective envelopes, respectively, in agreement with their final surface temperatures (Rucinski, 1969). The limb darkening coefficients were taken from the PHOEBE limb darkening tables (Prša et al., 2011). The combined depths and widths of the eclipses were then adjusted by altering the inclination and stellar potentials, respectively.

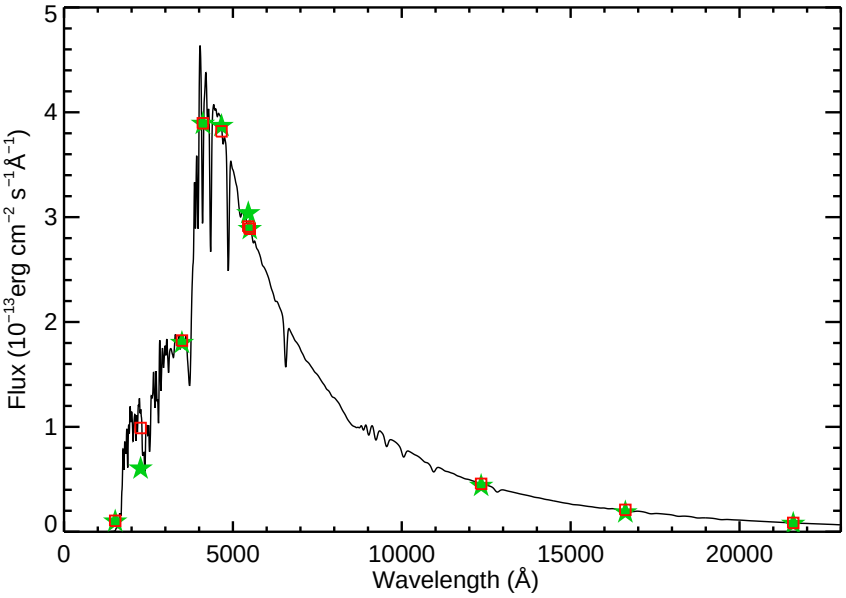

Figure 4.7: Spectral energy distribution of DY Aqr. The green filled stars represent the observed photometric points taken from GALEX and 2MASS catalogs and our observations. The black line represents the synthetic composite spectrum, calculated with the parameters resulting from the binary modeling. The red crosses are the synthetic photometric points extracted from this spectrum. The synthetic spectrum and photometric points were reddened with $E(B-V) = 0.07$ to fit the observations.

With the system parameters resulting from the first iteration of the modeling, we proceeded to estimate the reddening. The SED of DY Aqr was built using data from our observations and from the 2MASS (Cutri et al., 2003) and GALEX catalogs (Bianchi et al., 2011). With the parameters of the first fit, the combined synthetic spectrum was extracted and the photometrical points at various bands were obtained. By comparing these photometrical points with the observed ones, the $E(B-V)$ value corresponding to the derived reddening was estimated. The best fit of the models to our SED was provided assuming a value of $E(B-V) = 0.07$ (see Fig. 4.7). A standard Galactic extinction law (Cardelli et al., 1989) was used.

Then, the photometric light curves were dereddened using the derived value of $E(B-V) = 0.07$. As the reddening is wavelength dependent, the contribution of the reddening for each filter and for each point of the light curve, was calculated. In the case of binary systems, the composite spectrum in each phase point is slightly different due to geometrical effects and this fact has to be taken into account. The best way for the treatment of reddening of the light curves is the following: Using the model spectra of the primary and of the secondary, and the values of the radial velocities of the primary and the estimated mass-ratio, we can doppler-shift the model spectra and add them together to get the composite spectrum for each phase point. Then we have to multiply the composite spectrum by the reddening function. After that, we integrate the resulting reddened spectrum. If we compare this flux with the one resulting from the same process but without convolving it with the reddening function, the ratio between the flux obtained from both cases is the reddening correction for each data point. Doing this for each phase point and for each filter, the corresponding dereddening corrections were derived. This process was performed for the five photometric light curves.

Table 4.4: Parameters and coefficients from the PHOEBE best fit model.

Parameter	Values
System parameters	
Semi-major axis ($R_\odot$), a	9.4(5)
Mass ratio, q	0.31(2)
Center-of-mass velocity (km s^{-1}), γ	20.10(5)
Orbital inclination (degrees), i	75.4(5)
Argument of periastron (rad), ω	1.57(1)
Stellar parameters	
Secondary effective temperature (K), $T_{\rm eff2}$	3800(200)
Primary mass ($M_\odot$), M_1	1.8(2)
Secondary mass ($M_\odot$), M_2	0.55(4)
Primary radius ($R_\odot$), R_1	2.1(1)
Secondary radius ($R_\odot$), R_2	2.7(1)
Primary potential, Ω_1	4.8(1)
Primary $\log g$ (cgs), $\log g_1$	4.1(1)
Secondary $\log g$ (cgs), $\log g_2$	3.3(1)
Luminosity ratio in u band, L_2^u/L_1^u	0.003(2)
Luminosity ratio in v band, L_2^v/L_1^v	0.008(5)
Luminosity ratio in b band, L_2^b/L_1^b	0.02(1)
Luminosity ratio in y band, L_2^y/L_1^y	0.04(2)
Luminosity ratio in V band, L_2^V/L_1^V	0.037(1)

Note: The values in parentheses give the 1σ uncertainty in the previous digit.

Once the light curves were corrected for extinction, a second iteration of the orbital fit with

similar considerations as for the first one was carried out. The final results of the binary model are summarized in Table 4.4. Synthetic and observed light curves are presented in Fig. 4.8. The errors assigned to the masses and to the mass-ratio come from the errors of the effective temperature and gravity, as we explained above and the errors of the other parameters were estimated measuring the variations of each value considering the range of different plausible solutions. These error bars are larger than those obtained from the covariation matrix, but are more realistic because many of the parameters involved in the modeling of binary stars are intercorrelated.

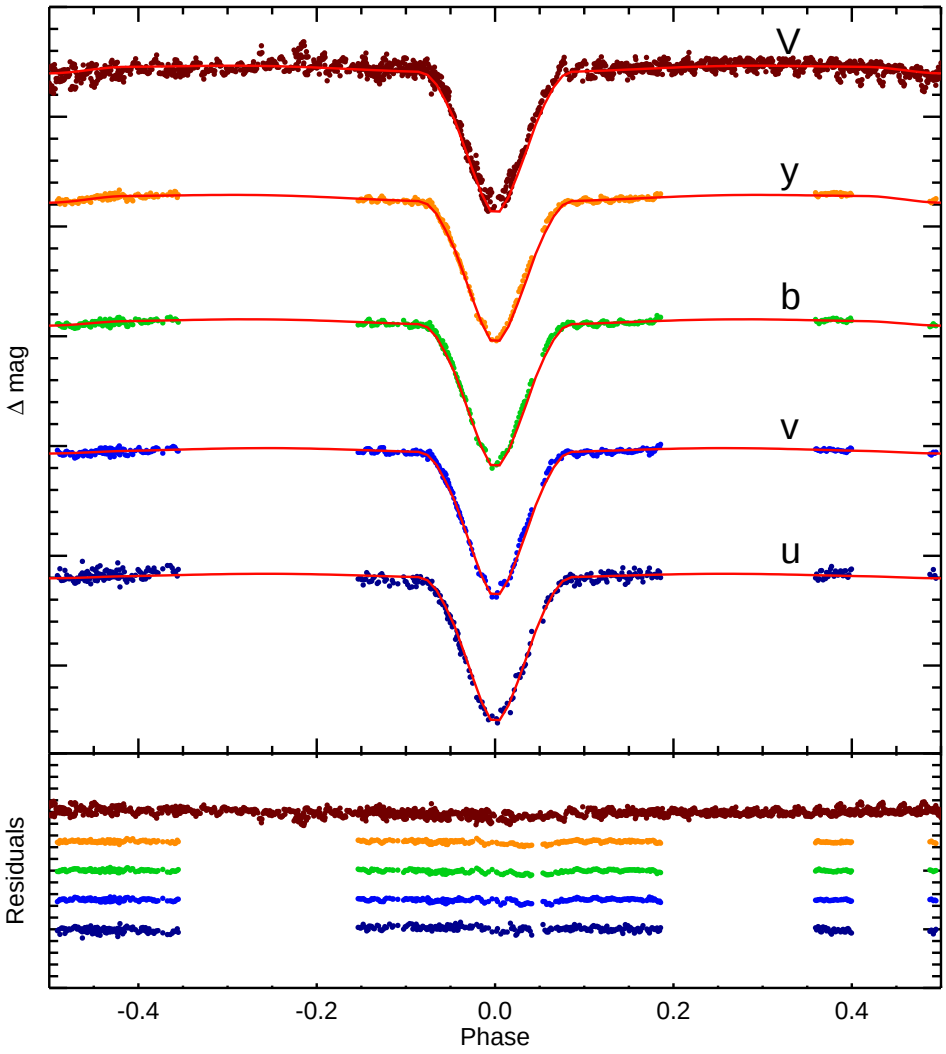

Figure 4.8: Top: Observed and fitted photometric light curves. Solid red lines represent the synthetic light curves provided by PHOEBE and colored points represent the observed photometric light curves for DY Aqr. **Bottom:** Residuals of the fits. In both cases, brown, orange, green, light blue and dark blue points correspond to V from OMC, Strömgren *y, b, v* and *u* filters respectively. The light curves have been arbitrarily offset for clarity.

From the derived parameters of the binary modeling and assuming synchronous rotation, the projected rotational velocities of each component were calculated, obtaining $v_1 \sin i = 52 \pm 2$ km s^{-1} for the primary and $v_2 \sin i = 62 \pm 2$ km s^{-1} for the secondary. The projected rotational velocity of the primary is in good agreement with the measurement from the grid of synthetic spectra. On the other hand, the $v \sin i$ of the secondary is quite high and the implied dilution

could explain why we have not detected the spectral lines of the secondary star in our spectra.

4.8 Pulsation frequencies

In order to study the pulsations from the primary component of DY Aqr, the frequency spectrum of the residual data, calculated by removing the binary model from the data, and avoiding the eclipses areas, was derived using PERIOD04 (Lenz & Breger, 2004). As mentioned above, DY Aqr was identified as an eclipsing binary system containing a δ-Scuti by Soydugan et al. (2009). In that work a frequency of 23.39 c/d and an semi-amplitude of 0.006 mag were measured.

With OMC data the pulsational frequency of 23.39 c/d found by Soydugan et al. (2009) was confirmed with a semi-amplitude of 0.005 mag, in agreement with the value they measured. However, with OMC data, two more frequencies at 19.56 c/d and semi-amplitude 0.014 mag and at 20.19 c/d and semi-amplitude 0.013 mag were found, being more significant than the previously reported one. This could be an indication of mode amplitude variations with time. In order to check if this was a real change in the pulsation characteristics of DY Aqr, we analyzed separately the Strömgren multicolor photometry. The frequencies found for each filter are summarized in Table 4.5.

Table 4.5: Results from frequency analysis of the OSN data.

Filter	Frequency (c/d)	Semi-amplitude (mag)	Phase	S/N
u	23.36(2)	0.0062	0.89	4.7
v	23.37(2)	0.0058	0.52	7.6
b	23.37(2)	0.0059	0.11	5.4
y	23.36(2)	0.0047	0.56	6.2

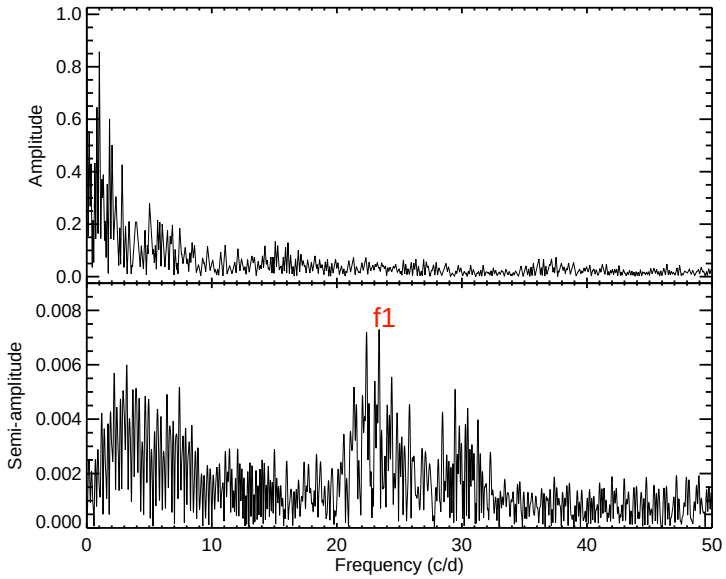

Figure 4.9: Spectral window (top) and power spectrum (bottom) of DY Aqr, obtained from the Strömgren multicolor photometry acquired at OSN.

We considered a peak to be significant if its S/N ratio is larger than 4.0. The error of these frequencies is the corresponding Rayleigh frequency resolution $\Delta f = \frac{1}{\Delta t} = 0.16$ c/d. The

spectral window and power spectrum for the first frequency are shown in Fig. 4.9, respectively. To confirm these results, we also performed the frequency analysis with SigSpec (Reegen, 2007) and the agreement between the two methods was good. We did not find any evidence from the analysis of the OSN data of the two additional frequencies detected in the OMC light curve.

Comparing our results with the values reported by Soydugan et al. (2009), no obvious amplitude variation was detected for the frequency of 23.39 c/d. We analyzed any potential instrumental effects that could explain the other frequencies detected in the OMC data, but none of them was able to justify these frequencies. Moreover, they appear in two different epochs, separated by one year.

4.9 Evolution

It is known that stars in close binary systems evolve in a different way than isolated stars do. Several mass-luminosity relations (MLRs) for eclipsing binaries have been obtained in the last years (Gorda & Svechnikov, 1998; Malkov, 2003). One of the main conclusions of these studies is that the systems with spectral type A and F have higher luminosities (radii) and temperatures than single stars with the same spectral type (Malkov, 2003). This fact is in good agreement with the results we obtained in our binary modeling. The primary component of DY Aqr has a larger radius than it would be expected for a single star with its temperature (Girardi et al., 2002). Ibanoğlu et al. (2006) compiled a sample of Algol-type systems with well-determined absolute parameters and found a MLR for the primary and secondary components of detached and semi-detached Algol-type stars. Figure 4.10 shows the luminosities of both components of detached and semi-detached systems against their masses, as in Ibanoğlu et al. (2006). The corresponding values for the primary and secondary components of DY Aqr obtained in this work have been overplotted. According to these plots, especially because of the behavior of the secondary component, DY Aqr seems to present luminosities in agreement with being a semi-detached system.

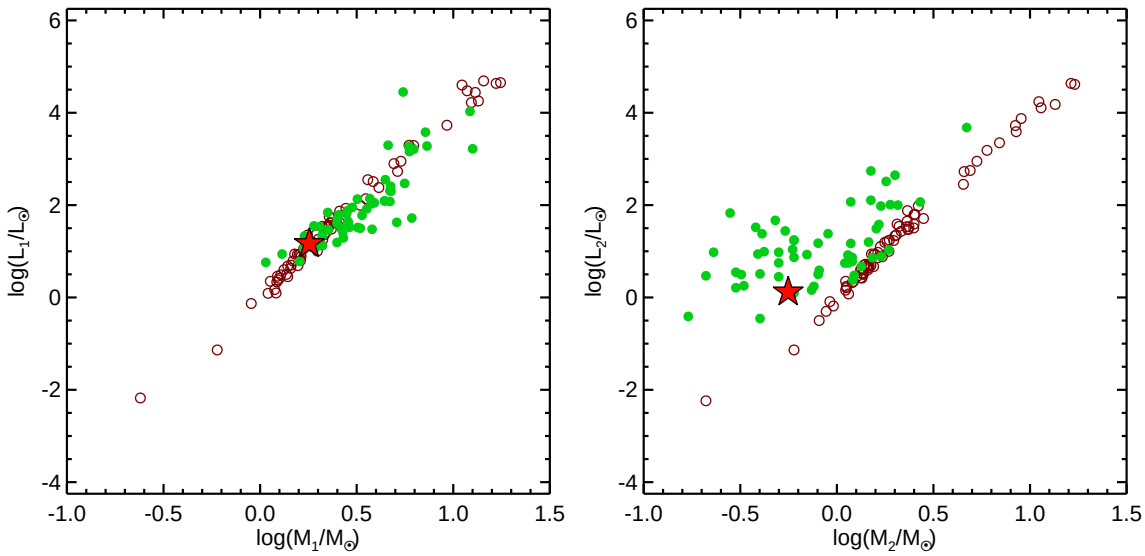

Figure 4.10: Plots adapted from Ibanoğlu et al. (2006). Luminosities of the primary components (left) and secondary components (right) of the sample of Algol-type systems compiled by Ibanoğlu et al. (2006). Brown open circles represent the detached systems and green circles correspond to semi-detached systems. The red star corresponds to the values for the primary and secondary components of DY Aqr obtained in this work.

4.10 Correlation between orbital and pulsational period

Soydugan et al. (2006) and Liakos et al. (2012) discovered a connection between the orbital and pulsation periods of the oEAs. Liakos et al. (2012) found an empirical relation between the pulsational frequency of the δ Scuti and the evolutionary state of the system, differing from the evolutionary behavior of single δ Scuti stars.

In Fig. 4.11 the parameters of DY Aqr are represented in similar plots as those shown by Liakos et al. (2012). It can be seen in the figure that DY Aqr behaves indeed as other semi-detached systems, which is consistent with our results, although the difference between detached and semi-detached behavior is not very evident in these plots. Furthermore, the bottom panel of this figure shows that DY Aqr is not very evolved yet, being located close to the ZAMS in the diagram.

On the other hand, Zhang et al. (2013) derived the following theoretical relation between the pulsation and orbital periods of pulsating stars in close binaries, based on their Roche lobe filling:

$$\log P_{\rm pul} = \log P_{\rm orb} + \log \alpha \tag{4.1}$$

where

$$\alpha = \frac{Q}{0.116} f_1^{3/2} r_{\rm cr1}^{3/2} (1+q)^{1/2} \tag{4.2}$$

being the pulsation constant $Q = P_{\rm pul}(\rho_1/\rho_\odot)^{1/2}$, $f_1 = r_1/r_{\rm cr1}$ the filling factor, $r_{\rm cr1}$ the equivalent radius of the Roche lobe calculated from Eggleton (1983), and q the mass ratio.

Fitting this equation to all the data they collected, they obtained the numerical relation:

$$\log P_{\rm pul} = \log P_{\rm orb} - 1.70(\pm 0.16) \tag{4.3}$$

which is very similar to the fit derived by Liakos et al. (2012) for semi-detached systems, as shown in the top panel of Fig. 4.11.

Applying the results obtained in this work, we derived for DY Aqr that $r_{\rm cr1} = 0.48$, $f_1 = 0.47$, and Q = 0.019 d. This value of the pulsation constant indicates that DY Aqr pulsates in p-modes, which is expected for a δ Scuti. If we use the orbital and pulsational periods of DY Aqr, we get $\log \alpha = 1.703$, which is in perfect agreement with equation 4.3.

4.11 Conclusions

A search for δ Scuti stars in eclipsing binaries in the OMC–VAR catalog of variable objects has been performed, confirming four previously detected eclipsing systems with a δ Scuti component and proposing a new candidate, AW Vel. A detailed analysis of one of the systems, DY Aqr, poorly studied in the past, and for which we had identified with OMC a possible change in the fundamental pulsational frequencies, has been carried out. Episodic mass-transfer events in these objects can indeed affect their pulsational characteristics.

High-resolution spectroscopy with HERMES/MERCATOR classifies the primary component of DY Aqr as an A7.5 V star, much cooler than previously reported.

The O-C diagram does not show any evidence of orbital period changes.

Binary modeling with PHOEBE combining the multicolor photometric light curves (OMC and OSN) and the radial velocity curve of the primary component (HERMES/MERCATOR) constraints the primary component to an effective temperature of 7625 ± 125 K and $\log g = 4.1 \pm 0.1$ and the secondary component to an effective temperature of 3800 ± 200 K and $\log g = 3.3 \pm 0.1$. The detection of the spectrum of the secondary component would provide a better

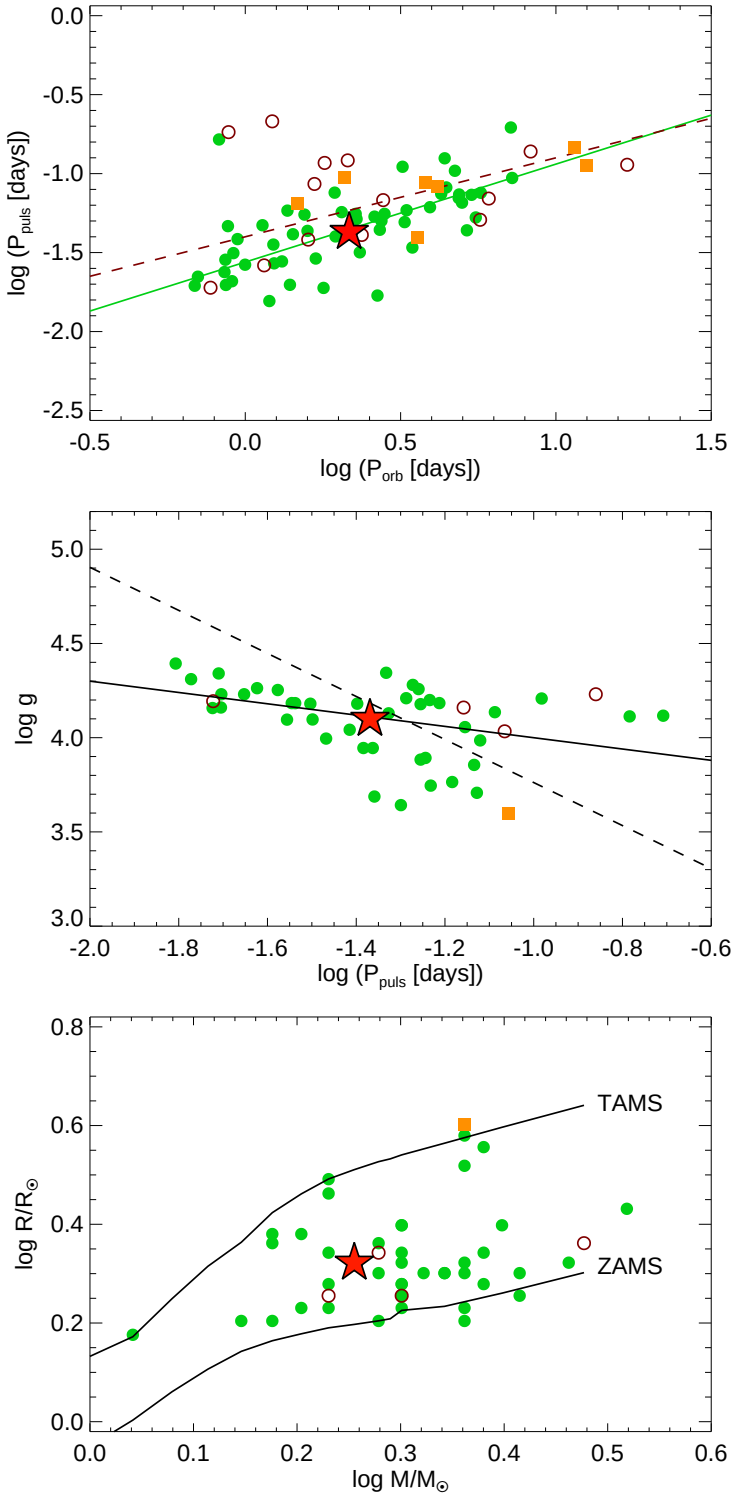

Figure 4.11: In all panels, brown empty circles correspond to detached systems, green filled circles are semi-detached systems, orange filled squares are undefined binary systems and the red star corresponds to the pulsating component in the binary system DY Aqr. **Top:** Correlation between pulsational and orbital periods for δ Scuti stars in binary systems (Liakos et al., 2012). Orange dashed line and green solid line represent the best fit for detached and semi-detached binaries respectively. **Middle:** Gravity acceleration versus the dominant pulsation frequency. The dashed line represents the best linear fit for single δ Scuti stars derived by Fernie (1995) and the solid line represents the linear fit for δ Scuti stars members of binary systems found by Liakos et al. (2012). **Bottom:** M-R diagram for the δ Scuti stars in binary systems for the objects in the same survey.

determination of the physical parameters of each component, but the secondary contribution was below the limit of detection in our data.

After removing the binarity effect from the light curves, the pulsational frequencies were studied through Fourier analysis. We did not confirm with the OSN data the first and second frequencies detected by OMC at 19.56 and 20.19 c/d. On the other hand, the same fundamental frequency found by Soydugan et al. (2009) at 23.39 c/d, also detected by OMC, was present in this ground-based photometry. The detection of these 2 additional frequencies by OMC can not be attributed to known instrumental effects, and point to a drastic, short-lived change in the pulsational characteristics. A further monitoring would be required to confirm short lived pulsational instabilities in this star.

The physical parameters obtained for each component of DY Aqr in the binary modeling are in agreement with the expected evolution of the components of a semi-detached Algol-system as given by Ibanoğlu et al. (2006).

Finally, our conclusion of DY Aqr being an oEA is compatible with the results by Liakos et al. (2012) and Zhang et al. (2013) on how the mass-transfer in these systems affects their pulsational behavior, but the detection of the secondary spectrum will be necessary to accurately determine the physical parameters of the system.

Chapter 5

Global multiwavelength emission from the sources observed with *INTEGRAL*

As explained in Chapter 1, OMC takes photometry of the optical emission coming from the prime targets of the gamma-ray instruments on board the *INTEGRAL* mission (Winkler et al., 2003). OMC has the same field of view (FOV) as the fully coded field of view (FCFOV) of JEM-X (Lund et al., 2003), and it is co-aligned with the central part of the larger FOVs of the imager IBIS (Ubertini et al., 2003) and the spectrometer SPI (Vedrenne et al., 2003). High-energy observations give information about the compact object or about the processes that lead to the X-ray emission, but in order to study the nature of these objects, it is important to perform multiwavelength observations, from optical-to-MIR wavelengths, because this is the only way to characterize the companion star or to detect the presence of jets or dust around these systems.

This chapter provides a global study of the multiwavelength characteristics of the *INTEGRAL* sources. The relation between the optical and hard X-ray emission of the objects in the *second INTEGRAL AGN catalogue* is discussed in Section 5.1. A multiwavelength analysis of the sources in the *fourth IBIS/ISGRI soft gamma-ray survey catalogue* observed by OMC, including stellar and extragalactic objects, is presented in Section 5.2. Conclusions of this chapter are summarized in Section 5.3.

5.1 The second *INTEGRAL* AGN catalogue

The *second INTEGRAL AGN catalogue* (Beckmann et al., 2009) includes an analysis of *INTEGRAL* IBIS/ISGRI, JEM-X, and OMC data for 199 AGN detected by *INTEGRAL* above 20 keV. Our contribution to this work, including the relationship between the optical and high-energy emission, is summarized here. Some of the optical quantities have been updated.

5.1.1 Introduction

Optical spectroscopy distinguishes between two main types of low-luminosity AGN, the broad-line Seyfert 1 and the narrow-line Seyfert 2 objects. A similar distinction can be made between unabsorbed sources with on-average softer X-ray spectra and the flatter spectra of absorbed sources. Thus a longstanding discussion has been whether these two groups indeed represent physically different types of objects, or whether they can be unified under the assumption that they are intrinsically the same kind of objects but seen from a different viewing angle with respect to the absorbing material in the vicinity of the central engine (Antonucci, 1993), and

that the difference in X-ray spectral slope can be explained solely by the absorption and reflection components. This unified model naturally explains the different Seyfert types in a way that the broad-line region is either visible (Seyfert 1) or hidden (Seyfert 2) possibly by the same material in the line of sight as is responsible for the absorption detectable at soft X-rays (Lawrence & Elvis, 1982). On the other hand, the model has some problems explaining other aspects of AGN, for example, that some Seyfert galaxies change their type from 1 to 2 and back, but also the observation that Seyfert 2 objects exhibit flatter hard X-ray spectra than Seyfert 1 even in the energy range >20 keV, where absorption should not play a major role unless $N_{\rm H} \gg 10^{24}$ cm^{-2}. Also, the existence of Seyfert 2 galaxies that show no absorption in the soft X-rays, like NGC 3147 and NGC 4698 (Pappa et al., 2001) cannot be explained by the unified model. Moreover, there seems to be a lack of absorbed sources at high X-ray luminosities (Malizia et al., 2012).

In the last years, two hard X-ray missions have provided surveys at >20 keV with enough sky coverage to be suitable for population studies of AGN. One is the NASA-led *Swift* mission (Gehrels et al., 2004) launched in 2004, the other one the ESA-led *INTEGRAL* satellite. Due to its observation strategy of following-up gamma-ray bursts, *Swift*/BAT (Barthelmy et al., 2005) provides a more homogeneous sky coverage in the 15–195 keV energy range, while the hard X-ray imager IBIS/ISGRI on board *INTEGRAL* is more sensitive and extends up to several hundred keV with better spectral resolution. Moreover, as explained in Chapter 1 *INTEGRAL* provides broad-band coverage through the additional X-ray monitor JEM-X in the 3–30 keV range and provides photometry with the optical camera OMC in the V-band.

5.1.2 Data analysis

The list of AGN presented here is based on all *INTEGRAL* detections of AGN reported in the literature, therefore entered into the *INTEGRAL general reference catalogue* (Ebisawa et al., 2003; Bodaghee et al., 2007). For each extragalactic source, the IBIS/ISGRI, JEM-X, and OMC data from the early mission (revolution 26 starting on 30 December 2002) up to spacecraft revolution 530 (ending on 17 February 2007) were analyzed, covering more than 4 years of data. To include only high-quality data, the selection considered ISGRI data taken at an off-axis angle smaller than 10° and included only those observations that lasted for at least 500 s. The final sample contains 187 objects with a detection significance above 3σ in the IBIS/ISGRI 18–60 keV energy band. Out of these 187 AGN, OMC data were available for 57.

5.1.3 X-ray spectral fitting

Spectral analysis was performed for the 187 AGN, using an absorbed power law with $N_{\rm H}$ fixed to the value reported in the literature and adopting XSPEC version 11.3.2 (Arnaud, 1996). When the significance was below 5σ, the photon index was fixed to $\Gamma = 2$. The $N_{\rm H}$ value used for the fitting is the intrinsic absorption plus the Galactic hydrogen column density. In cases where no absorption information was found, *Swift*/XRT and XMM-Newton data were analyzed to determine the level of absorption. For those objects detected only at a low significance level (i.e. between 3 and 5σ), the photon index was fixed to $\Gamma = 2.0$ in order to extract a flux value. More details on this part can be found in Beckmann et al. (2009).

5.1.4 Optical data

When available, OMC data were extracted from the OMC Archive, getting one photometric point per shot. The photometric apertures were centered on the source position, as listed in version 5 of the OMC Input Catalogue (Domingo et al., 2003). The fluxes and magnitudes were derived from a photometric aperture of 3 × 3 pixels (1 pixel = 17.504 arcsec), slightly circularized, i.e. removing $\frac{1}{4}$ pixel from each corner (standard output from OSA). Therefore the

computed values include the contributions by any other source inside the photometric aperture. We flagged those sources that might be affected by a nearby star (at less than $1'$), with a potential contamination below 0.2 mag in any case. Other 8 AGN containing a brighter contaminating source within the extraction aperture were not included in this compilation. In addition, for some extended AGN, this 3×3 aperture does not cover the full galaxy size, but just their central region.

As discussed in Chapter 3, to only include high-quality data, some selection criteria were applied to the individual photometric points. Shots were checked against saturation, rejecting those with long exposures for the brightest sources, if necessary. For faint sources, a minimum signal-to-noise ratio of 3 was required for the longest integration shots. The shortest shots were only used if the signal-to-noise ratio was greater than 10. Because these sources can show extended structure in the OMC images, "anomalous PSF", as well as "problems in the centroid determination", were allowed. Finally, to avoid contamination by cosmic rays, we excluded those points whose fluxes deviated more than 5 times the standard deviation from the median value of their surrounding points, applying three iterations of this filter. High-quality data were available for 57 out of the 187 AGN included in the IBIS sample.

In order to quantify the relationship between the optical and X-ray emission, the $\alpha_{\rm OX}$ was calculated for each object. This value is measured as the slope of a power law between the two energy ranges, optical and X-rays:

$$\alpha_{\rm OX} = -\frac{\log(f_{\rm O}/f_{\rm X})}{\log(\nu_{\rm O}/\nu_{\rm X})}.$$

Here, $f_{\rm O}$ and $f_{\rm X}$ are the monochromatic fluxes at the frequencies ν_O (at 5500 Å) and $\nu_{\rm X}$ (at 20 keV). The fluxes at 20 keV ($f_{\rm X}$) were calculated from the spectral index (Γ) and the integrated flux in the 20–100 keV band.

The fluxes at 5500 Å ($f_{\rm O}$) were calculated from the mean optical magnitudes using the calibration by Bessell (1990). The integrated flux in the V Johnson band is:

$$\log(F_{\rm OMC}) = -V/2.5 - 5.49$$

given in erg cm^{-2} s^{-1}, and the monochromatic flux at 5500 Å is obtained dividing the integrated flux $F_{\rm OMC}$ by the effective width of the filter (890 Å).

Table 5.1 lists the median V magnitude of each AGN, the average of error estimates (1σ level) of each photometric point given by OSA 7, $\langle\sigma_V\rangle$, a variability estimator which is the standard deviation of the V magnitude divided by the estimated error $\langle\sigma_V\rangle$, the optical luminosity in the Johnson V filter (centered on 5500 Å, effective width 890 Å), the $\alpha_{\rm OX}$ value, the number of photometric points used in the analysis and a flag indicating the potential contamination of the photometric value by a nearby star ('Y' indicates potential contamination by a nearby star up to 0.2 mag). No K correction has been applied to the V luminosities, since the redshifts are relatively low and the optical slope of these objects is not well known. Moreover, depending on the redshift, the V band might be contaminated to different degrees by the OIII and Hβ emission lines. We did not correct for this effect, either.

Table 5.1: Name and type in the second INTEGRAL AGN catalogue, median V magnitude, the average of error estimates $\langle\sigma_V\rangle$, a variability estimator which is the standard deviation of the V magnitude divided by the estimated error $\langle\sigma_V\rangle$, the optical luminosity in the Johnson V filter, $\alpha_{\rm OX}$, the number of photometric points used in this analysis, and contamination flag.

Name	Type	V	$\langle\sigma_V\rangle$	RMS$_V/\sigma_V$	log L_V	$\alpha_{\rm OX}$	N	Cont. flag
	[mag]	[mag]		[erg s^{-1}]				
1ES0 033+59.5	BL Lac	11.62	0.04	2.76	45.18	1.35	3887	

Continued on next page...

Table 5.1 – Continued

Name	Type	V	$\langle\sigma_V\rangle$	RMS_V/σ_V	$\log L_V$	α_{OX}	N	Cont. flag
	[mag]	[mag]	[erg s^{-1}]					
Mrk 348	Sy 2	13.76	0.05	1.01	42.71	1.01	81	Y
NGC 788	Sy 2	12.60	0.04	0.97	43.09	1.19	1342	
NGC 985	Sy 1	13.73	0.05	1.07	43.66	1.17	644	
NGC 1052	Sy 2	11.38	0.03	0.89	42.70	1.41	1004	
NGC 1068	Sy 2	9.99	0.02	1.37	44.80	1.51	693	
NGC 1275	Sy 2	12.51	0.04	1.03	43.27	1.27	856	
NGC 1365	Sy 1.5	11.51	0.05	0.82	42.72	1.36	35	
3C 120	Sy 1	14.00	0.05	1.21	43.31	1.03	225	
UGC 3142	Sy 1	15.12	0.22	0.59	43.49	0.91	259	
ESO 33-2	Sy 2	13.99	0.09	0.95	42.78	1.11	40	
Ark 120	Sy 1	12.91	0.04	3.08	43.74	1.13	2198	
Mrk 3	Sy 2	12.88	0.04	0.93	42.95	1.11	428	Y
Mrk 6	Sy 1.5	13.68	0.06	0.88	42.94	1.10	657	
QSO B0716+714	BL Lac	14.27	0.09	7.29	45.26	1.26	1116	
ESO 209-12	Sy 1.5	14.60	0.21	0.70	43.24	1.10	387	
PG 0804+761	Sy 1	14.07	0.08	0.91	44.28	1.12	299	
4U 0937-12	Sy 1	12.66	0.03	1.01	42.56	1.16	443	
MCG-05-23-016	Sy 2	13.12	0.05	0.84	42.47	1.04	1514	
NGC 3227	Sy 1.5	12.06	0.04	0.37	42.21	1.15	12	
NGC 3281	Sy 2	12.67	0.04	1.20	42.85	1.21	316	
Mrk 421	BL Lac	13.05	0.06	0.79	43.58	0.88	3112	
NGC 4051	Sy 1.5	12.26	0.06	0.45	41.67	1.27	91	
NGC 4138	Sy 1.5	11.87	0.04	1.14	42.06	1.34	910	
NGC 4151	Sy 1.5	11.50	0.04	4.56	42.29	1.04	9786	
Mrk 50	Sy 1	14.48	0.09	1.54	42.85	1.15	985	Y
NGC 4388	Sy 2	12.26	0.06	0.83	42.80	1.07	509	
NGC 4395	Sy 1.5	14.09	0.11	0.47	40.23	1.07	7	
3C 273	QSO	12.58	0.04	1.56	45.31	1.06	2576	Y
IGRJ 12391-1612	Sy 2	14.15	0.06	0.89	43.34	1.06	104	
NGC 4593	Sy 1	12.24	0.04	1.31	42.83	1.19	1295	
ESO 323-32	Sy 1	13.11	0.07	0.87	43.03	1.27	158	Y
3C 279	BL Lac	15.52	0.11	1.79	45.29	1.01	294	
Mrk 783	Sy 1.5	15.39	0.16	1.05	43.39	1.01	37	
NGC 4945	Sy 2	12.44	0.17	0.38	41.43	1.06	327	
ESO 323-77	Sy 1	12.46	0.04	2.52	43.23	1.31	380	
IGR J13091+1137	Sy 2	13.70	0.05	0.36	43.18	1.10	15	
NGC 5033	Sy 1.5	11.57	0.03	0.86	42.16	1.44	55	
Cen A	Sy 2	12.18	0.23	0.63	41.49	0.96	202	
ESO 383-18	Sy 2	14.32	0.08	0.69	42.32	1.12	706	Y
MCG-06-30-015	Sy 1	13.23	0.11	0.69	42.36	1.12	1330	Y
Mrk 268	Sy 2	14.30	0.06	0.69	43.37	1.11	7	
IC 4329A	Sy 1	13.19	0.04	0.99	43.00	0.97	524	
NGC 5506	Sy 2	12.93	0.05	0.72	42.38	1.05	701	
NGC 5548	Sy 1.5	13.14	0.05	0.70	43.08	1.22	256	
H 1426+428	BL Lac	16.11	0.25	0.61	43.72	0.98	619	
NGC 5995	Sy 2	13.47	0.07	1.10	43.29	1.07	118	Y
ESO 138-1	Sy 2	13.59	0.11	0.44	42.34	1.27	12	Y
NGC 6221	Sy 2	11.91	0.07	0.35	42.49	1.43	16	
NGC 6240	Sy 2	13.05	0.05	1.65	43.42	1.17	551	
Mrk 501	BL Lac	13.21	0.04	1.26	43.65	1.09	567	
IGR J16558-5203	Sy 1	13.95	0.27	0.49	43.77	1.13	164	
NGC 6300	Sy 2	11.52	0.05	0.83	42.38	1.26	31	
3C 390.3	Sy 1	14.61	0.13	2.15	43.54	0.99	482	Y
1H 1934-063	Sy 1	13.35	0.05	1.42	42.59	1.14	12	
NGC 6814	Sy 1.5	12.43	0.05	0.98	42.31	1.18	401	
QSO B1957+405	Sy 2	13.43	0.11	1.28	44.01	1.05	1292	
ESO 399-20	Sy 1	13.96	0.08	0.51	43.07	1.24	84	
Mrk 509	Sy 1.2	13.38	0.05	0.76	43.60	1.04	400	
NGC 7172	Sy 2	12.66	0.04	0.87	42.66	1.13	508	
Mrk 915	Sy 1	14.10	0.09	0.85	42.75	1.12	40	
3C 454.3	BL Lac	13.45	0.05	5.25	46.58	1.06	1402	
QSO 2251-179	Sy 1	14.20	0.09	0.85	43.83	0.98	1570	Y
NGC 7469	Sy 1	12.70	0.04	0.78	44.21	1.20	22	
MCG-02-58-022	Sy 1.5	14.13	0.06	0.76	43.59	1.08	93	

Among the 57 AGN for which OMC data are available, four show strong variability in the

photometric V-band data, with an amplitude larger than 0.5 mag: S5 0716+714, NGC 4151, 3C 279 and 3C 273. They are studied in more detail in Chapter 6. Other AGN monitored by OMC also showed some hints of variability, such as 3C 390.3, but at smaller amplitudes (just a few percent over the period considered).

5.1.5 Optical/X-ray correlations

In Fig. 5.1 the dispersion diagram of $L_{\rm X}$ vs. $L_{\rm V}$ is displayed, with different symbols for the different classes of objects considered. While the apparent correlation between both luminosities is certainly driven by the distance effect, it is remarkable that the different classes of objects, from Seyfert 2 to blazars, are approximately located on the same correlation line, over more than 5 dex in luminosity. Subtracting the common dependence on redshift through a partial correlation analysis, the correlation between the luminosities is still statistically significant, with a correlation coefficient of 0.74 and the probability of a chance occurrence is $\ll$0.01%. To test this correlation further, we made simulations using a bootstrap method (Simpson & Mayer-Hasselwander, 1986): to each couple of X-ray flux and redshift we randomly assigned an optical flux, drawn from the real values found for our sample and without excluding multiple choices of the same value (see also Bianchi et al. (2009), for a similar procedure). We then computed the X-ray and optical luminosities and calculated the Spearman and the partial correlation coefficients for the $L_{\rm X}$ - $L_{\rm V}$ relation and the Spearman coefficient for the $f_{\rm X} - f_{\rm V}$ relation. Repeating this procedure 100 000 times, we were able to build histograms of the correlation coefficients of the simulated samples and found that only 0.001% of the simulated samples have a (Spearman or partial) correlation coefficient greater than measured in the real sample for the $L_{\rm X}$ - $L_{\rm V}$ relation. For the $f_{\rm X} - f_{\rm V}$ correlation, the probability of chance occurrence is higher but still not significant, $\sim$2%. This indicates that the X-ray and optical emissions are indeed correlated, beyond the bias introduced by the common dependence on distance.

To further investigate this relation, we computed the histograms of the $\alpha_{\rm OX}$ values for the different subtypes (see Fig. 5.2). The mean values for the different kinds of objects are for Seyfert 2: 1.19, Seyfert 1.5: 1.18, Seyfert 1-1.2: 1.11, and BL Lac: 1.04. Seyfert 2 and 1.5 nevertheless show an extended wing towards higher $\alpha_{\rm OX}$ ratios. NGC 1068, the prototypical Seyfert 2 galaxy, shows the highest $\alpha_{\rm OX}$ value, 1.51. Since it is a Compton-thick object, the X-rays are heavily absorbed, so that this high $\alpha_{\rm OX}$ value can be understood clearly. Other Compton-thick Seyfert galaxies, such as ESO 138–1, also show $\alpha_{\rm OX}$ values above 1.25. But the explanation is not so obvious. For example, other objects with high $\alpha_{\rm OX}$ values, such as NGC 1052 and NGC 5033, have apparently low hydrogen column densities. In contrast, several objects with high neutral columns, like NGC 4945, and ESO 383–18, show relatively low $\alpha_{\rm OX}$ values. However, the general trend is that $\alpha_{\rm OX}$ decreases from Seyfert 2 galaxies to Blazars, due to the lowering relative contribution of the stellar disk with respect to the AGN to the optical light, and the decrease of the obscuration of the X-rays from the former to the latter.

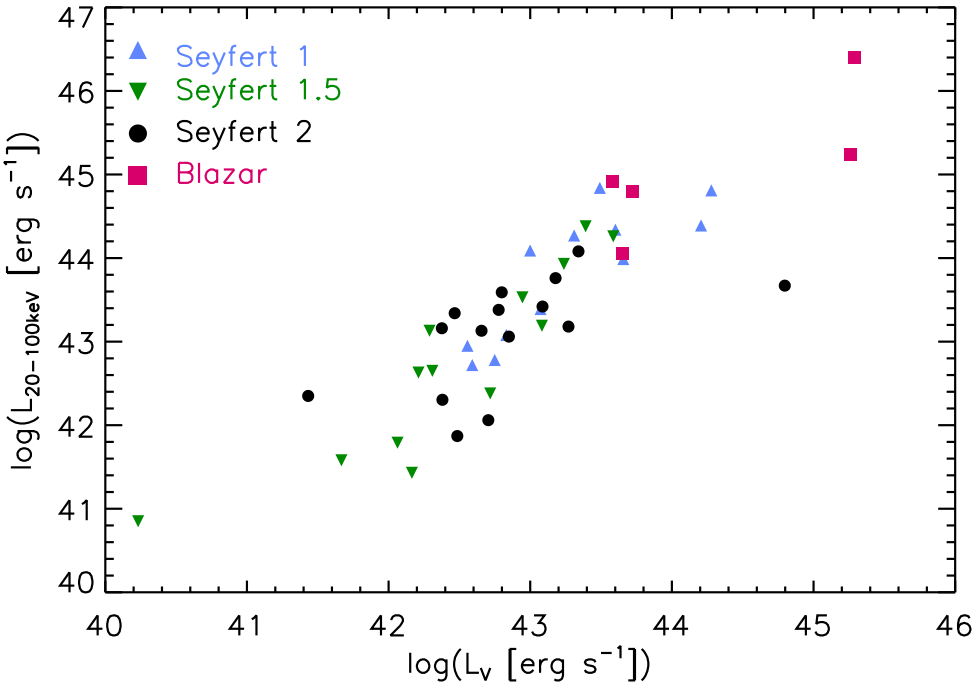

Figure 5.1: X-ray luminosity $L_{\rm X}$ versus V-band luminosity $L_{\rm V}$. AGN of different types are located along the same dispersion line, over more than 5 decades in luminosity.

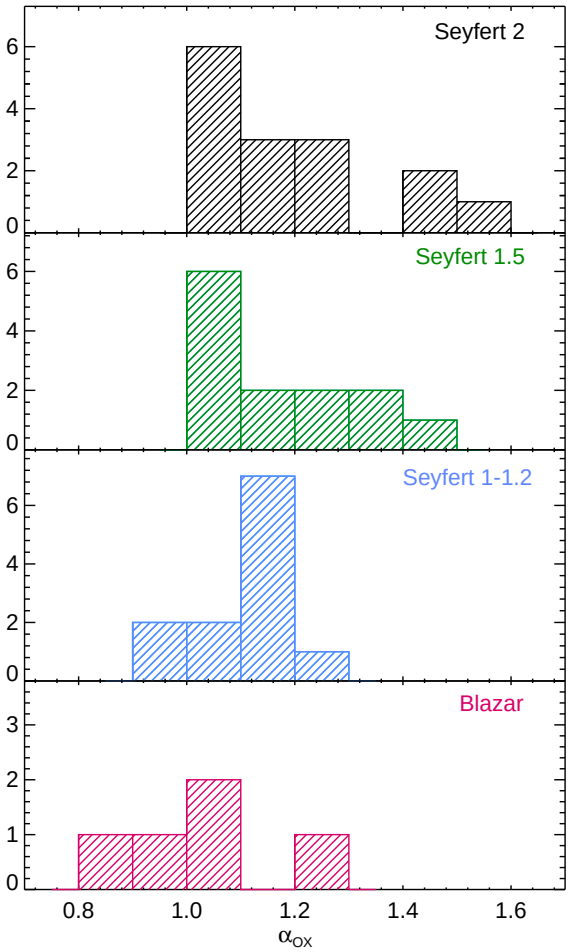

Figure 5.2: Histograms of $\alpha_{\rm OX}$ for the different subtypes of AGN.

5.1.6 A fundamental plane of AGN activity

In the view of unification of different AGN types, it has been pointed out that AGN, spanning black hole masses in the range $10^5\ M_\odot \leq M_{\rm BH} \leq 10^9\ M_\odot$, and even accreting black holes in X-ray binaries with $M_{\rm BH} \sim 10\ M_\odot$, show similarities in radiative efficiency and jet power versus accretion rate (Fender et al., 2007). This connection gave rise to the "fundamental plane" of black hole activity. It has been found that indeed there is a close connection between the radio and X-ray luminosity of Galactic and super massive black holes of the form $L_{\rm radio} \propto L_{\rm X}^{0.7}$ (Corbel et al., 2000, 2003), linking the jet activity to the total output of the central engine. Later on, a connection of these two parameters with the black hole mass itself was found, establishing the fundamental plane of AGN and Galactic black hole activity in the form of $L_{\rm radio} \propto L_{\rm X}^{0.6} M_{\rm BH}^{0.8}$ (Merloni et al., 2003).

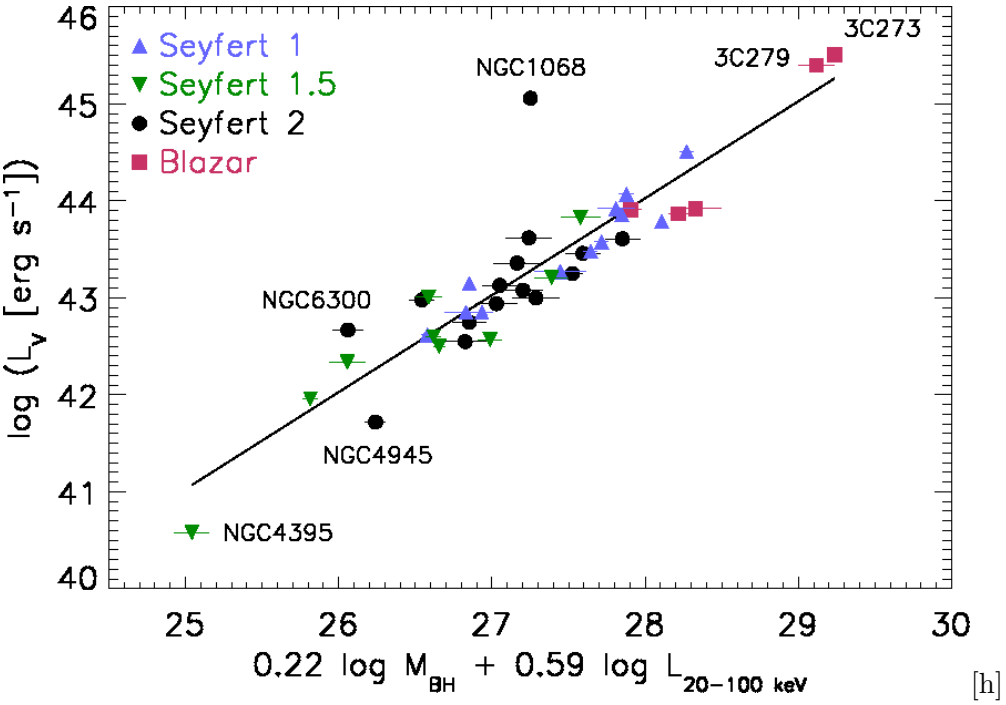

Figure 5.3: Fundamental plane of optical luminosity $L_{\rm V}$, X-ray luminosity $L_{\rm X}$, and mass of the central black hole $M_{\rm BH}$. Errors on luminosity are smaller than the symbols.

As discussed in detail in 5.1.5, there is also a significant correlation between optical and X-ray luminosity. Therefore, we found three significant correlations in our sample between the luminosities $L_{\rm X}$ and $L_{\rm V}$, and the mass of the central black hole $M_{\rm BH}$. This leads to the assumption that also these parameters, similar to $L_{\rm X}$, $L_{\rm R}$, and $M_{\rm BH}$, form a fundamental plane for AGN. By applying an analysis following Merloni et al. (2003), we fit the data with the function

$$\log L_V = \zeta_{V\rm X}\ \log L_{\rm X} + \zeta_{VM}\ \log M_{\rm BH} + b_V .$$

We obtain $\zeta_{V\rm X} = 0.59 \pm 0.07$, $\zeta_{VM} = 0.22 \pm 0.08$, and $\rm b_V = 16.0$, leading to

$$\log L_V = 0.59 \log L_{\rm X} + 0.22 \log M_{\rm BH} + 16.0;$$

i.e., $\rm L_V \propto L_X^{0.6} M_{BH}^{0.2}$. This relation is shown in Fig. 5.3. As already pointed out, we carefully investigated that the effects of distance and selection effect are not causing the correlation observed here.

While the fundamental plane including the radio and X-ray luminosity can be understood as a connection of the jet activity, as visible in the radio, and the accretion flow, as dominating the X-rays, the correlation found here shows a different connection. The optical luminosity is commonly thought to be dominated by the AGN accretion disk (Siemiginowska et al., 1995) and therefore by the accretion processes onto the supermassive black hole, but sometimes there is also a contribution by the jet (Soldi et al., 2008) and emission of the bulge, and therefore of the stars in the host galaxy contributing to it. The latter is especially important as the spatial resolution of OMC does not allow a deconvolution of the core and the bulge. Nevertheless it shows that there is a significant bulge-M_{BH} correlation and that accretion processes are closely linked to the mass of the central black hole. The finding that this fundamental plane holds for all Seyfert types indicates further that these AGN are indeed intrinsically very similar.

5.2 Emission from the sources in the *fourth IBIS/ISGRI soft gamma-ray survey catalogue*

With the aim of extending the analysis presented above to a sample containing stellar and extragalactic sources, a new selection of high-energy sources observed by IBIS and OMC has been carried out. The *fourth IBIS/ISGRI soft gamma-ray survey catalogue* (Bird et al., 2010) compiled 723 sources observed in a systematic analysis of the IBIS/ISGRI Core Program and public data spanning nearly five years of operations. In order to select those sources with simultaneous optical and high-energy observations, a cross-match of this catalog with the OMC Archive has been performed. These data have been complemented with near and mid-infrared photometry and colors. The results of the cross-match are presented in Section 5.2.1, the calculation of the hard X-ray and V-band luminosities and the correlation analysis of these quantities are shown in Section 5.2.2. Near and mid-infrared fluxes and colors of these sources are analyzed in Section 5.2.3.

5.2.1 Cross-match of the IBIS catalog with the OMC Archive

The fourth edition of the IBIS catalog contains 723 high-energy sources detected by IBIS/ISGRI until the end of April 2008, observed in the energy range $17 - 100$ keV. The scientific data set is based on more than 70 Ms of high-quality observations performed during the first five and a half years of the Core Programme and public observations. This is the last available version of the IBIS/ISGRI catalog. The next update is expected for 2016.

This catalog was cross-matched with the OMC Archive (*https://sdc.cab.inta-csic.es/ omc/*; Gutiérrez et al. 2004) by main SIMBAD identifiers and by coordinates, taking the position uncertainties into account. As a result 375 sources out of the 723 have been found in the OMC Archive, having at least one optical observation.

As explained in Chapter 3, the OMC optical fluxes can be contaminated by other sources falling inside the photometric aperture used to extract the fluxes. A more detailed analysis revealed that not only some sources are contaminated by others but in some cases the measured flux comes in its totality from other objects falling within the photometric aperture. In order to confirm the optical identifications of the high-energy sources and to discard the sources significantly affected by contamination, a visual inspection of the FOV with the IBIS and OMC positions and the error radius was performed for each source using the *Aladin sky atlas*[1] (Bonnarel et al., 2000). Most of the times, the optical counterparts of the IBIS sources

[1] Aladin is an interactive sky atlas allowing the user to visualize digitized astronomical images or full surveys, superimpose entries from astronomical catalogues or databases, and interactively access related data and information from the Simbad database, the VizieR service and other archives for all known astronomical objects in the field (http://aladin.u-strasbg.fr/).

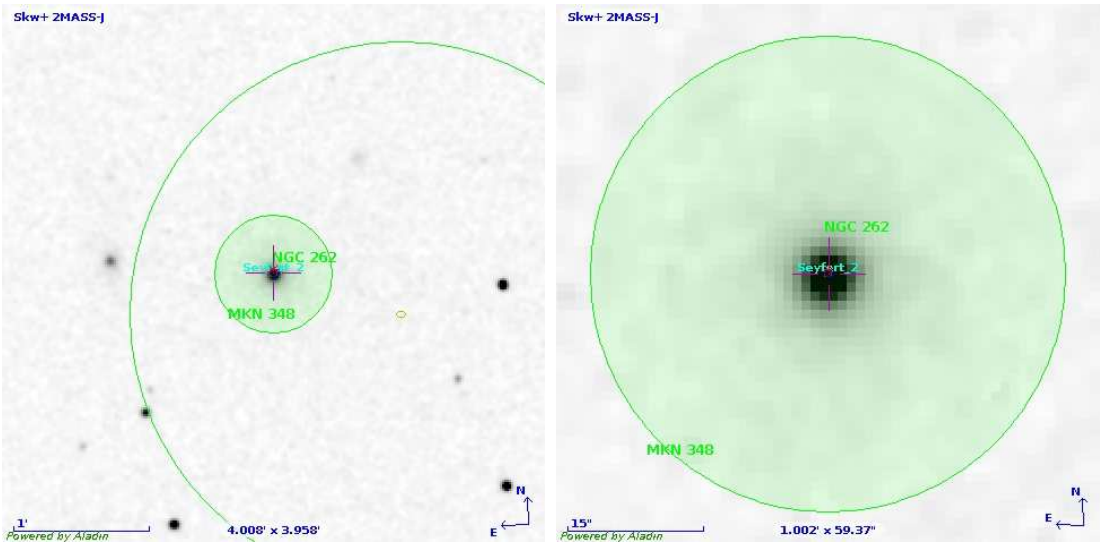

Figure 5.4: 2MASS-J images of the FOV of Mrk 348 (the OMC main identifier is NGC 262). On the left, the FOV is 10'×10'. The small filled circle is centered in the position provided by OMC and the radius corresponds to the region from where OMC extracts the photometry. The big open circle is centered in the IBIS position and the radius of the circle is the typical position error given by IBIS (5 arcmin). On the right, a zoom of 1'×1'of the OMC FOV is shown. In this case, the source is not contaminated.

are already known, so this procedure is mainly performed to evaluate the optical contamination, although the presence of another X-ray sources inside the IBIS field has also been checked. To illustrate the process, an example of the images used in this step is shown in Fig. 5.4. After this filter, the sample was reduced to 95 sources.

In order to include only high-quality data, some selection criteria similar to those used in Beckmann et al. (2009) and Alfonso-Garzón et al. (2012) were applied to the individual photometric points. In addition, those sources with less than 5 OMC photometric points and those reporting only upper limits in the fluxes in the IBIS catalog were rejected. After applying all these selection criteria the final sample contained 73 sources with well defined IBIS and OMC data.

5.2.2 Hard X-ray and V-band luminosities

Hard X-ray/soft gamma-ray luminosities in the 20–100 keV energy band were derived from the fluxes provided in the IBIS catalog. For most of the AGN, the source distances were extracted from the *second INTEGRAL AGN catalogue* (Beckmann et al. (2009), Section 5.1 of this thesis). For the rest of objects, the SIMBAD and NED databases were used. To derive the V-band luminosities, the median of all good optical fluxes was computed and transformed to magnitudes for each source.

In Fig. 5.5 the dispersion diagram of $L_{\rm X}$ vs. $L_{\rm V}$ is plotted. Different symbols have been used for the different classes of objects considered. The source-type classification follows that in the IBIS catalog, distinguishing between Blazars (Bla, 5), Seyfert 1 galaxies (Sy1, 19), Seyfert 2 galaxies (Sy2, 31), Cataclysmic Variables (CVs, 1), High-mass X-ray Binaries (HMXB, 13) and Low-mass X-ray Binaries (LMXBs, 3). While the apparent correlation between both luminosities is certainly driven by the distance effect, it is remarkable that the different classes of objects, from cataclysmic stars to AGN, are located on the same correlation line, over more than 15 dex in luminosity. The linear fit has been calculated with the IDL routine ROBUST_FIT, getting:

$$L_{20-100\,\rm keV} = (0.98 \pm 0.0.02) L_{\rm V} + (1.14 \pm 0.18)$$

To further investigate this relation, the histograms of the $\alpha_{\rm OX}$ values for the different types

of objects were computed, as explained in Section 5.1.4. This index has the advantage to be distance independent, removing the noise added by the errors in the distance determination.

Table 5.2 lists the X-ray flux in the 20–100 keV energy band, the median V magnitude, the average of error estimates (1σ level) given by OSA, the average of error estimates $\sigma_{\rm V}$, a variability index $\mathrm{RMS_V}/\sigma_{\rm V}$, the X-ray luminosity in the 20–100 keV energy band, the luminosity in the Johnson V band and the $\alpha_{\rm OX}$ of those sources used in this analysis.

Table 5.2: Optical and X-ray information of the objects with OMC data in the fourth IBIS/ISGRI soft gamma-ray survey catalogue. Name and type of object in the IBIS catalogue, X-ray flux in the 20-100 keV energy band, the median V magnitude, the average of error estimates $\sigma_{\rm V}$, a variability estimator which is the standard deviation of the V magnitude divided by the estimated error $\langle\sigma_V\rangle$, the X-ray luminosity in the 20-100 keV energy band, the luminosity in the Johnson V band and $\alpha_{\rm OX}$ values.

Name	Type	$F_{20-100\rm keV}$ [10^{-11} erg cm^{-2} s^{-1}]	V [mag]	$\sigma_{\rm V}$ [mag]	$\mathrm{RMS_V}/\sigma_{\rm V}$	$\log L_{20-100\rm keV}$ [erg s^{-1}]	$\log L_{\rm V}$ [erg s^{-1}]	$\alpha_{\rm OX}$
IGR J00370+6122	HMXB,XP,Sg?	0.9	9.65	0.02	2.28	34.01	35.68	1.68
Mrk 348	AGN,Sy2	10.6	13.75	0.09	0.75	43.67	42.65	1.00
1A 0114+650	HMXB,XP	13.0	11.04	0.03	1.57	35.88	35.86	1.25
RX J0146.9+6121	HMXB,XP,Be,T	1.5	11.42	0.04	1.19	34.04	34.82	1.45
NGC 788	AGN,Sy2	6.0	12.60	0.03	0.96	43.39	43.09	1.20
Mrk 1018	AGN,Sy1.5	1.7	13.84	0.08	0.86	43.84	43.58	1.19
NGC 985	AGN,Sy1	2.4	13.74	0.08	0.91	44.01	43.65	1.16
NGC 1052	AGN,Sy2	1.7	11.38	0.03	0.96	41.97	42.70	1.44
NGC 1068	AGN,Sy2	2.4	9.99	0.02	1.36	43.66	44.80	1.51
NGC 1275	AGN,Sy2	3.8	12.45	0.04	1.73	43.35	43.30	1.24
EXO 0331+530	HMXB,XP,Be,T	172.3	15.55	0.24	0.71	37.06	34.12	0.51
LEDA 15023	AGN,Sy2	1.9	15.79	0.26	0.60	43.94	42.87	0.98
UGC 3142	AGN,Sy1	4.9	15.12	0.24	0.58	44.71	43.49	0.94
SWIFT J0453.4+0404	AGN,Sy2	2.2	13.99	0.09	0.89	43.63	43.21	1.14
ESO 033-G02	AGN,Sy2	2.4	13.96	0.10	0.68	43.26	42.80	1.14
Ark 120	AGN,Sy1	6.5	12.96	0.04	3.51	44.21	43.72	1.12
SWIFT J0519.5-3140	AGN,Sy2	4.3	13.03	0.05	0.80	44.53	44.18	1.17
1A 0535+262	HMXB,XP,Be,T	8.7	9.14	0.01	9.86	34.62	35.53	1.48
NGC 2110	AGN,Sy2	17.9	12.73	0.04	0.89	43.37	42.54	1.08
Mrk 3	AGN,Sy2	9.5	12.88	0.05	0.83	43.57	42.95	1.12
Mrk 6	AGN,Sy1.5	4.3	13.68	0.06	0.89	43.54	42.94	1.09
ESO 209-12	AGN,Sy1.5	2.2	14.60	0.18	0.70	43.92	43.24	1.10
QSO B0836+710	AGN,Blazar	5.8	16.23	0.30	17.39	47.90	46.15	0.86
NGC 2992	AGN,Sy2	6.5	12.66	0.04	0.98	43.06	42.69	1.16
MCG-05-23-016	AGN,Sy2	14.5	13.12	0.06	0.88	43.36	42.47	1.03
NGC 3281	AGN,Sy2	5.1	12.67	0.04	1.22	43.12	42.85	1.19
Mrk 421	AGN,BL Lac	37.7	12.99	0.06	8.72	44.86	43.60	0.90
H 1145.5-619	HMXB,XP	3.4	9.35	0.02	8.30	34.59	35.83	1.57
SWIFT J1200.8+0650	AGN,Sy2	1.7	14.45	0.08	0.84	43.70	43.20	1.12
NGC 4051	AGN,Sy1.5	3.6	12.25	0.05	0.87	41.62	41.67	1.26
NGC 4074	AGN,Sy2	2.2	14.23	0.06	0.82	43.44	42.92	1.12
NGC 4138	AGN,Sy1.9	2.6	11.87	0.05	0.89	41.72	42.06	1.36
NGC 4151	AGN,Sy1.5	30.5	11.37	0.04	3.95	42.86	42.34	1.12
NGC 4395	AGN,Sy1.8	2.1	13.98	0.11	0.79	40.68	40.28	1.13
NGC 4388	AGN,Sy2	24.6	12.22	0.05	1.24	43.58	42.81	1.08
GX 301-2	HMXB,XP,T	134.5	10.86	0.03	1.35	36.43	35.47	1.01
3C 273	AGN,QSO	19.5	12.66	0.04	2.23	46.12	45.28	1.05
NGC 4593	AGN,Sy1	7.1	12.25	0.03	1.29	43.07	42.83	1.19
3C 279	AGN,QSO/Blazar	2.2	15.60	0.21	1.66	46.32	45.25	1.02
GX 304-1	HMXB,XP	0.9	14.19	0.11	4.44	33.80	33.67	1.22
NGC 4941	AGN,Sy2	1.1	12.40	0.04	0.90	41.75	42.26	1.38
IGR J13042-1020	AGN,Sy2	1.4	12.61	0.04	0.84	42.62	42.94	1.33
ESO 323-77	AGN,Sy1.2	2.6	12.44	0.03	3.26	43.13	43.24	1.33
MCG-06-30-015	AGN,Sy1.2	4.1	13.24	0.08	0.70	42.75	42.35	1.12
NGC 5252	AGN,Sy1.9	4.8	13.45	0.06	0.88	43.77	43.22	1.11
IC 4329A	AGN,Sy1.2	20.9	13.19	0.06	0.98	44.09	43.00	0.97
IGR J14080-3023	AGN,Sy1.5	1.9	15.29	0.27	0.62	43.38	42.50	1.03
NGC 5506	AGN,Sy1.9	14.9	12.93	0.04	0.84	43.21	42.38	1.03
NGC 5548	AGN,Sy1.5	3.0	12.97	0.04	2.74	43.31	43.15	1.21
H 1426+428	AGN,BL Lac	1.8	16.12	0.28	0.59	44.91	43.72	0.95
NGC 5643	AGN,Sy2	1.1	12.17	0.05	0.95	41.72	42.33	1.41
NGC 5728	AGN,Sy2	5.4	12.39	0.03	0.99	43.09	42.91	1.21

Continued on next page...

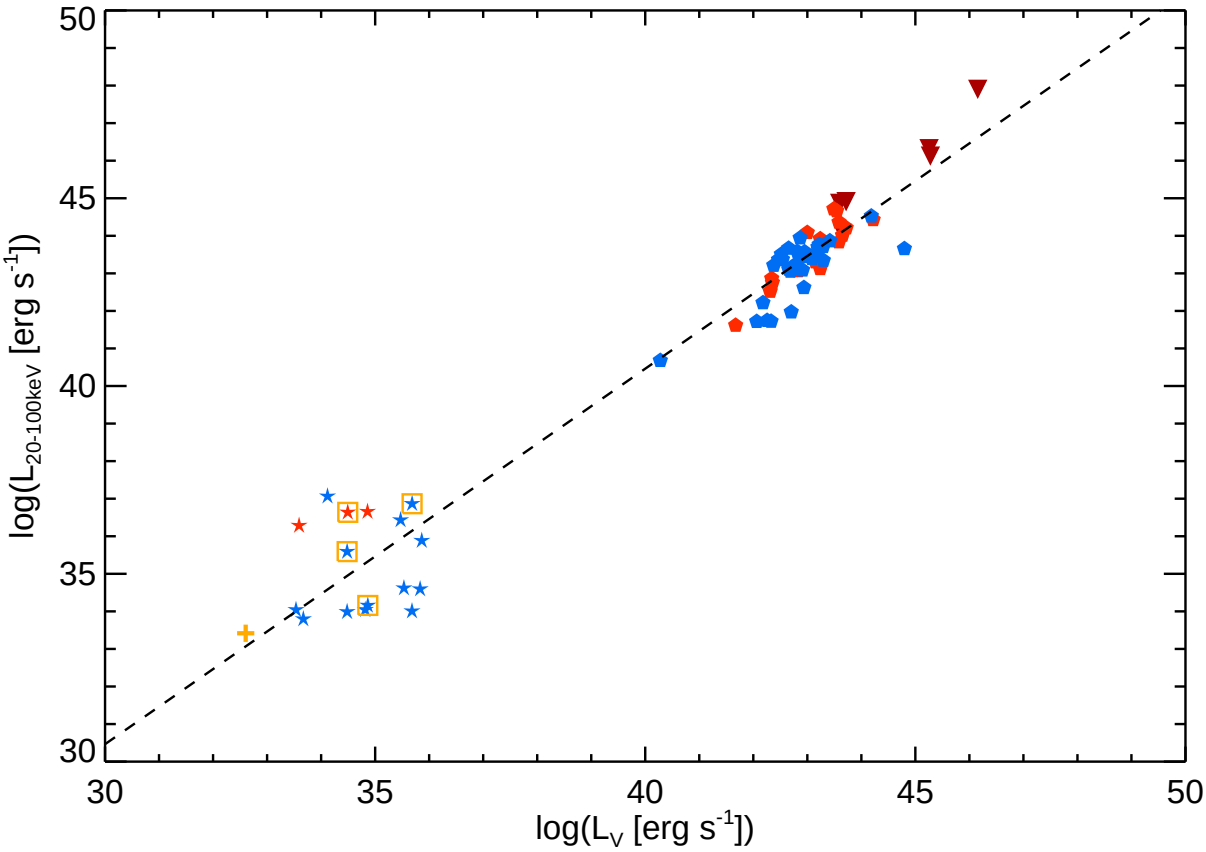

Figure 5.5: Hard X-ray luminosity $L_{\rm X}$ versus optical $L_{\rm V}$. Brown inverted triangles represent blazars, blue pentagons represent Seyfert 1–1.5 galaxies, blue pentagons represent Seyfert 1.8–2 galaxies, blue stars are HMXBs, red stars are LMXBs and orange crosses are CVs. Microquasars are represented with an additional orange square. The linear fit to the data $L_{20-100\,\rm keV} = (0.98 \pm 0.\ 0.02)\ L_{\rm V} + (1.14 \pm 0.18)$ is overplotted.

Table 5.2 – Continued

Name	Type	$F_{20-100\rm keV}$ [10^{-11} erg cm^{-2} s^{-1}]	V [mag]	$\sigma_{\rm V}$ [mag]	RMS (V) /$\sigma_{\rm V}$	log $L_{20-100\rm keV}$ [erg s^{-1}]	log $L_{\rm V}$ [erg s^{-1}]	$\alpha_{\rm OX}$
NGC 5995	AGN,Sy2	3.5	13.47	0.08	0.95	43.71	43.29	1.08
Sco X-1	LMXB,Z,M	462.3	12.47	0.04	9.28	36.64	34.49	0.71
NGC 6240	AGN,Sy2	5.4	13.06	0.06	1.71	43.87	43.42	1.17
Mrk 501	AGN,BL Lac	4.3	13.21	0.05	1.30	44.06	43.65	1.09
Her X-1	LMXB,XP	86.8	13.42	0.06	5.06	36.66	34.86	0.80
GX 1+4	LMXB,XP	79.5	15.76	0.29	4.00	36.28	33.59	0.57
XTE J1739-302	HMXB,SFXT	1.7	14.44	0.16	1.71	34.04	33.54	1.12
IGR J17544-2619	HMXB,SFXT	0.8	12.79	0.08	0.66	33.99	34.48	1.38
LS5039	HMXB,NS,M	1.9	11.30	0.05	0.76	34.16	34.86	1.43
ESO 103-35	AGN,Sy2	8.2	13.97	0.11	0.63	43.51	42.52	1.00
3C 390.3	AGN,Sy1	6.1	14.61	0.15	2.35	44.67	43.54	1.00
V1223 Sgr	CV,IP	8.1	13.54	0.13	1.67	33.42	32.60	1.05
SS 433	HMXB,M	10.8	13.97	0.10	2.59	35.59	34.48	0.97
NGC 6814	AGN,Sy1.5	5.7	12.42	0.04	0.98	42.52	42.31	1.22
Cyg X-1	HMXB,BH,M	1392.2	8.87	0.01	2.70	36.87	35.68	0.95
NGC 7172	AGN,Sy2	7.9	12.66	0.03	0.89	43.11	42.66	1.14
QSO 2251-178	AGN,Sy1	6.7	14.20	0.10	0.83	44.80	43.81	1.00
NGC 7465	AGN,Sy2	2.6	12.82	0.04	0.87	42.22	42.18	1.24
NGC 7469	AGN,Sy1	4.5	12.67	0.04	0.88	44.43	44.22	1.19
MCG-02-58-022	AGN,Sy1.5	4.3	14.13	0.07	1.02	44.36	43.59	0.99

Figure 5.6 shows the $\alpha_{\rm OX}$ histograms for the different types of objects. The mean value of $\alpha_{\rm OX} = 1.13$ is overplotted. The histogram corresponding to Blazars is tracing mostly the distribution associated to the active nucleus and the jet. These systems are less absorbed than Seyfert galaxies because of their viewing angle. As expected, they have values of $\alpha_{\rm OX}$ below

the average and the relative X-ray emission is in comparison, larger than for Seyfert galaxies. In Seyfert galaxies, the optical emission comes mainly from the AGN , but in many cases, the contribution of the host galaxy is significant as well. Seyfert 1 galaxies (in red) and Seyfert 2 galaxies (in blue) have been separated for comparison, showing lower values of α_{OX} for Sy1s. Moreover, in Seyfert 1 galaxies, the AGN is seen more directly and the obscuration by the torus is expected to be lower than in Seyfert 2 galaxies (Malizia et al., 2009). Then, Seyferts 2 are expected to be more absorbed and present lower X-ray fluxes, and then show higher α_{OX}, as can be seen in Fig. 5.6. In this way, NGC 1068, the prototypical obscured Sy2 galaxy, shows the highest value $\alpha_{OX} = 1.51$ within the AGN. These results are in agreement with what was found in Beckmann et al. (2009), as discussed in Section 5.1.5.

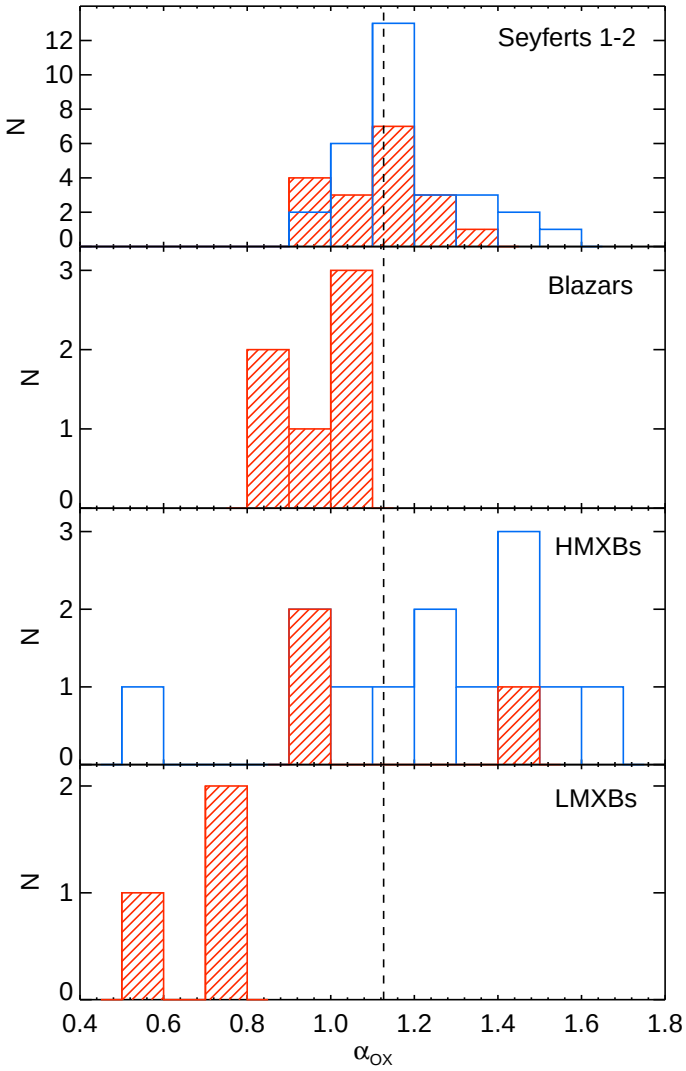

Figure 5.6: Histograms of α_{OX} for the different types of objects, from top to bottom: Seyfert galaxies (Sy 1–1.5 in red and Sy 1.8–2 in blue), Radio-galaxies and BL Lacertae objects, High-mass X-ray Binaries (Microquasars in red) and Low-mass X-ray Binaries. The vertical line shows the mean value of α_{OX}.

.

The behavior of α_{OX} for the LMXBs is dominated by their faint optical emission, which is mainly produced by the X-rays heating of the cool companion star and the accretion disk. However, the optical emission in HMXBs is dominated by the OB star and then the α_{OX} values are higher than for LMXBs. Moreover, in Be/X-ray binaries, the emission from the circumstellar

disk can be very significant and variable, leading to a more complex relation between the optical and X-ray emission in these systems. The lowest value of $\alpha_{\rm OX}$ within the HMXBs comes from EXO 0331+530 (also known as V 0332+53). This source is a Be/X-ray binary with E(B-V)=1.9 (Reig, 2011). If the optical flux was corrected for this extinction value, the $\alpha_{\rm OX}$ would be 1.18, more in agreement with the rest of HMXBs. However, E(B-V) in Be/X-ray binaries can be affected by circumstellar effects so this value could be over estimated. The disk emission of Bes can contributes to the optical (B-V) color making it redder by a few tenths of magnitudes (Dachs et al., 1988; Howells et al., 2001). Disentangling the circumstellar and interstellar reddening (Fabregat & Torrejon, 1998) to get reliable values of E(B-V), would be ideal for a more accurate analysis of the multiwavelength properties of Be/X-ray binaries. The data compiled in this work (including the near-infrared photometry from 2MASS and the mid-infrared photometry from WISE; see 5.2.3) can be used to reconstruct the SEDs in order to model and disentangle the contribution of the circumstellar discs, but this is out of the scope of this work. On the other hand, microquasars have been plotted in red, to explore if the effect of the jets could lead to lower values of $\alpha_{\rm OX}$. Two of the three microquasars within the HMXBs showed this expected effect.

Summarizing, the observed trend in this analysis is that the type 1 AGN, including Radio-galaxies, Blazars and some Seyferts 1, and the LMXBs have smaller $\alpha_{\rm OX}$ values and then higher relative X-ray fluxes compared to the optical ones than Seyfert 2 galaxies and HMXBs, which show a relatively higher optical emission.

5.2.3 Near and Mid-infrared Colors

The similar nature at different scales of the engines powering AGN and XBs seem to be affected by their different surroundings, producing in this way multiwavelength similarities and differences. Relativistic jets are among the most energetic phenomena in the Universe and are a basic component of accretion onto black holes on all scales: from stellar mass black holes (BH) in microquasars to the supermassive black holes (SMBH) in AGN. Despite the large range of scale, jets in stellar mass BH share physical properties that are analogous to those in SMBH and all systems producing jets appear to have accretion disks. The radio emission from jets in neutron star (NS) systems are an order of magnitude weaker than those of BH systems, but they are easily detected in the IR. Therefore, it is important to study the IR colors of X-ray sources since both jets and disks appear to be associated with every subtype of XBs and some AGN.

For this reason and to complement the analysis performed in 5.2.2 and to help to the understanding of the physical processes operating in these high-energy emitting sources, near and mid-infrared (NIR and MIR) photometry have been obtained from catalogs. Two surveys have performed photometric observations in these spectral regions in the last years and public catalogs with the acquired information are available.

The *Two Micron All Sky Survey* (2MASS: Skrutskie et al. (2006)) was a survey of the whole sky in the NIR. 2MASS used two highly-automated 1.3-m telescopes, one at Mt. Hopkins, Arizona, for the Northern Hemisphere data and one at Cerro Tololo Inter-American Observatory, Chile, for the Southern Hemisphere. Each telescope was equipped with a three-channel camera, each channel consisting of a 256×256 array of HgCdTe detectors, capable of observing the sky simultaneously at J (1.25 μm), H (1.65 μm), and $K_{\rm S}$ (2.17 μm).

The *Wide-field Infrared Survey Explorer* (WISE; Wright et al. (2010)) is a NASA satellite with a 40-cm aperture that images the whole sky in four MIR bands, centered at 3.4, 4.6, 12 and 22 μm. These bands are known as $W1$, $W2$, $W3$ and $W4$, respectively.

Cross-matches of the 73 sources in the sample with the 2MASS *All-Sky Point Source Catalog* (PSC; Cutri et al. (2003)) for the stellar sources and with the the 2MASS Extended Source Catalog (2MASX; Skrutskie et al. (2006)) for the AGN have been carried out. A cross-match

with the *AllWISE Data Release* (Cutri & et al., 2014) was also performed. These cross-matches were carried out using the Virtual Observatory (VO) tool TOPCAT[2] (Taylor, 2005).

The fluxes in the different bands have been calculated using the following relations. For the optical flux, as in Section 5.1.4, the relation given by Bessell (1990) has been applied:

$$log(F_{\rm OMC}) = -V/2.5 - 5.49$$

The fluxes in the 20-100 keV band has been taken from Bird et al. (2010).

To calculate the near-infrared flux , the in-band zero magnitude flux of the K_s band from Cohen et al. (2003) has been assumed, leading to the relation:

$$log(F_{\rm NIR}) = -K_{\rm s}/2.5 - 6.95$$

And for the mid-infrared fluxes, the relation provided by Jarrett et al. (2011) has been used:

$$log(F_{\rm MIR}) = -W3/2.5 - 8.45$$

In all cases fluxes are given in erg cm^{-2} s^{-1}.

Table 5.3 lists the X-ray fluxes in the 20–100 keV energy band, the fluxes in the V-Johnson band, the NIR fluxes and MIR fluxes of all the objects in the sample.

Table 5.3: Multiwavelength fluxes of the objects with OMC data in the IBIS/ISGRI catalog. Name and type of object in the IBIS catalogue, X-ray flux in the 20-100 keV energy band, flux in the V-Johnson band, NIR flux and MIR flux. The fluxes are in [erg cm^{-2} s^{-1}].

Name	Type	log $F_{20-100keV}$	log F_V	log F_{NIR}	log F_{MIR}
IGR J00370+6122	HMXB,XP,Sg?	-11.42	-9.35	-10.22	-11.64
Mrk 348	AGN,Sy2	-10.38	-10.99	-10.99	-10.48
1A 0114+650	HMXB,XP	-10.12	-9.91	-10.19	-11.51
RX J0146.9+6121	HMXB,XP,Be,T	-11.04	-10.06	-10.74	-11.90
NGC 788	AGN,Sy2	-10.62	-10.53	-10.58	-10.79
Mrk 1018	AGN,Sy1.5	-11.12	-11.02	-11.14	-11.23
NGC 985	AGN,Sy1	-11.17	-10.99	-11.17	-10.70
NGC 1052	AGN,Sy2	-11.08	-10.04	-9.93	-10.75
NGC 1068	AGN,Sy2	-10.94	-9.49	-9.27	-8.22
NGC 1275	AGN,Sy2	-10.67	-10.47	-10.20	-10.07
EXO 0331+530	HMXB,XP,Be,T	-8.84	-11.71	-11.25	-12.08
LEDA 15023	AGN,Sy2	-11.08	-11.81	-11.83	-11.08
UGC 3142	AGN,Sy1	-10.55	-11.54	-11.09	-11.14
SWIFT J0453.4+0404	AGN,Sy2	-10.97	-11.10	-11.14	-10.54
ESO 033-G02	AGN,Sy2	-10.89	-11.08	-10.96	-10.67
Ark 120	AGN,Sy1	-10.60	-10.67	-11.04	-10.59
SWIFT J0519.5-3140	AGN,Sy2	-10.72	-10.70	-10.96	-10.71
1A 0535+262	HMXB,XP,Be,T	-10.31	-9.16	-10.21	-10.91
NGC 2110	AGN,Sy2	-10.19	-10.58	-10.21	-10.38
Mrk 3	AGN,Sy2	-10.47	-10.64	-10.54	0.00
Mrk 6	AGN,Sy1.5	-10.80	-10.96	-10.77	-10.53
ESO 209-12	AGN,Sy1.5	-11.08	-11.33	-10.98	-10.70
QSO B0836+710	AGN,Blazar	-10.74	-11.99	-12.59	-12.12
NGC 2992	AGN,Sy2	-10.58	-10.55	-10.39	-10.45
MCG-05-23-016	AGN,Sy2	-10.20	-10.74	-10.69	-10.14
NGC 3281	AGN,Sy2	-10.74	-10.56	-10.27	-10.12
Mrk 421	AGN,BL Lac	-9.71	-10.69	-10.95	-11.25
2E 1145.5-6155	HMXB,XP	-10.74	-9.23	-10.31	-11.56
SWIFT J1200.8+0650	AGN,Sy2	-11.17	-11.27	-11.39	-11.27
NGC 4051	AGN,Sy1.5	-10.72	-10.39	-10.02	-10.28
NGC 4074	AGN,Sy2	-11.17	-11.18	-11.17	0.00
NGC 4138	AGN,Sy1.9	-10.92	-10.24	-10.23	-11.37
NGC 4151	AGN,Sy1.5	-9.93	-10.04	-9.90	-9.73
NGC 4388	AGN,Sy2	-10.02	-10.38	-10.15	-10.29

Continued on next page...

[2]The Tool for OPerations on Catalogues And Tables (TOPCAT) is an interactive graphical viewer and editor for tabular data, developed as part of several VO projects (http://www.star.bris.ac.uk/~mbt/topcat/).

Table 5.3 – Continued

Name	Type	log $F_{20-100keV}$	log F_V	log F_{NIR}	log F_{MIR}
NGC 4395	AGN,Sy1.8	-11.17	-11.09	-10.94	-11.89
GX 301-2	HMXB,XP,T	-8.93	-9.83	-9.22	-10.34
3C 273	AGN,QSO	-10.10	-10.55	-10.94	-10.50
NGC 4593	AGN,Sy1	-10.54	-10.39	-10.14	-10.51
3C 279	AGN,QSO/Blazar	-11.08	-11.73	-11.33	-11.32
GX 304-1	HMXB,XP	-11.28	-11.18	-10.57	-11.20
NGC 4941	AGN,Sy2	-11.28	-10.45	-10.24	-10.98
IGR J13042-1020	AGN,Sy2	-11.12	-10.53	-10.32	-11.19
ESO 323-77	AGN,Sy1.2	-10.94	-10.47	-10.47	-10.23
MCG-06-30-015	AGN,Sy1.2	-10.63	-10.78	-10.78	-10.42
NGC 5252	AGN,Sy1.9	-10.60	-10.87	-10.86	-10.99
IC 4329A	AGN,Sy1.2	-10.05	-10.77	-10.47	-9.95
IGR J14080-3023	AGN,Sy1.5	-11.12	-11.61	-11.91	-11.43
NGC 5506	AGN,Sy1.9	-10.07	-10.66	-10.23	-9.92
NGC 5548	AGN,Sy1.5	-10.92	-10.75	-10.70	-10.67
H 1426+428	AGN,BL Lac	-11.12	-11.94	-12.14	-12.57
NGC 5643	AGN,Sy2	-11.28	-10.36	-9.82	-10.35
NGC 5728	AGN,Sy2	-10.64	-10.45	-10.22	-10.59
NGC 5995	AGN,Sy2	-10.80	-10.88	-10.71	-10.36
Sco X-1	LMXB,Z,M	-8.35	-10.48	-11.41	-12.55
NGC 6221	AGN,Sy1/Sy2	-11.04	-10.25	-9.80	0.00
NGC 6240	AGN,Sy2	-10.67	-10.71	-10.59	-10.26
Mrk 501	AGN,BL Lac	-10.63	-10.77	-10.78	-11.39
Her X-1	LMXB,XP	-9.14	-10.85	-12.40	-13.40
GX 1+4	LMXB,XP	-9.40	-11.79	-10.14	-11.16
XTE J1739-302	HMXB,SFXT	-11.01	-11.27	-9.92	-11.34
IGR J17544-2619	HMXB,SFXT	-11.22	-10.61	-10.16	-11.45
LS5039	HMXB,NS,M	-11.22	-10.01	-10.39	-11.80
ESO 103-35	AGN,Sy2	-10.49	-11.08	-11.08	-10.19
3C 390.3	AGN,Sy1	-10.64	-11.34	-11.63	-10.84
V1223 Sgr	CV,IP	-10.29	-10.90	-12.01	-12.71
SS 433	HMXB,M	-10.17	-11.11	-10.22	-10.69
NGC 6814	AGN,Sy1.5	-10.64	-10.46	-10.01	-10.88
Cyg X-1	HMXB,BH,M	-8.25	-9.04	-9.55	-10.89
NGC 7172	AGN,Sy2	-10.47	-10.56	-10.28	-10.52
QSO B2251-178	AGN,Sy1	-10.55	-11.17	-11.40	-11.05
NGC 7465	AGN,Sy2	-11.08	-10.62	-10.77	-10.80
NGC 7469	AGN,Sy1	-10.62	-10.56	-10.49	-9.94
MCG-02-58-022	AGN,Sy1.5	-10.69	-11.14	-11.20	-10.86

Figure 5.7 shows the X-ray fluxes relative to the MIR and NIR fluxes, i.e. $F_{20-100\,\mathrm{keV}}/F_{\mathrm{MIR}}$ vs. $F_{20-100\mathrm{keV}}/F_{\mathrm{NIR}}$. In this plot, the AGN population and the XRBs are separated. The linear fit is overplotted for reference. It has been calculated with the IDL routine ROBUST_FIT, getting:

$$F_{20-100\,\mathrm{keV}}/F_{\mathrm{MIR}} = (0.88 \pm 0.09) F_{20-100\,\mathrm{keV}}/F_{\mathrm{NIR}} + (0.27 \pm 0.0.10)$$

All the stellar systems are above the line, while AGN are mostly along or below it. This is due to the emission in the MIR associated to the torus surrounding the core engine in AGN, which is dominating in the mid-infrared, especially for type 1 AGN, making these objects redder.

In Fig. 5.8, the (H-K_S) vs (J-H) color-color diagram (CD) is plotted. The intrinsic loci of stars are represented by the blue dashed line (Bessell & Brett, 1988). The Caltech (CIT) systems are transformed into the 2MASS photometric system by the method introduced by Carpenter et al. (2001) leading to the relation:

$$(J - H) = 1.70(H - K_{\mathrm{S}}) - 0.118$$

The stars can only shift in the diagram because of the reddening due to extinction, thus normal stars should not be found below this line. AGN type 1, with an important contribution of non-thermal emission from the AGN in the near-infrared, are usually found below this line (Kouzuma & Yamaoka, 2010), although if the redshift is 1<z<2, the AGN can present bluer colors and be located closer to the stellar loci (Kouzuma & Yamaoka, 2010). In Fig. 5.8, most of

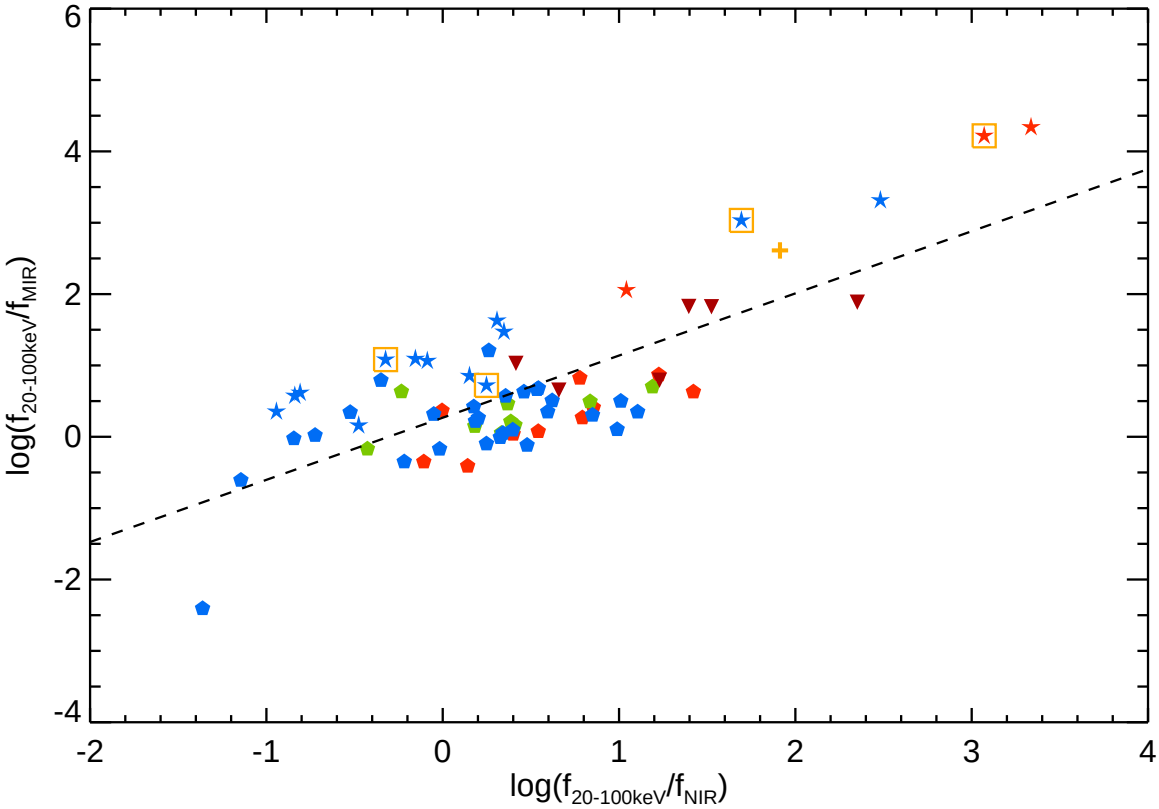

Figure 5.7: $F_{20-100\,\mathrm{keV}}/F_{\mathrm{MIR}}$ vs. $F_{20-100\,\mathrm{keV}}/F_{\mathrm{NIR}}$ for the IBIS counterparts in the OMC Archive. Blue pentagons represent Sy1, green pentagons represent Sy1.5, blue pentagons represent Sy2, brown inverted triangles represent blazars, blue stars are HMXBs, red stars are LMXBs and orange crosses are CVs. Microquasars are represented with an additional orange square. The linear fit to the data $F_{20-100\,\mathrm{keV}}/F_{\mathrm{MIR}}$ = (0.88 ±0.09) $F_{20-100\,\mathrm{keV}}/F_{\mathrm{NIR}}$ + (0.27 ±0. 0.10) is overplotted for reference to separate stellar systems (left) from AGN(right).

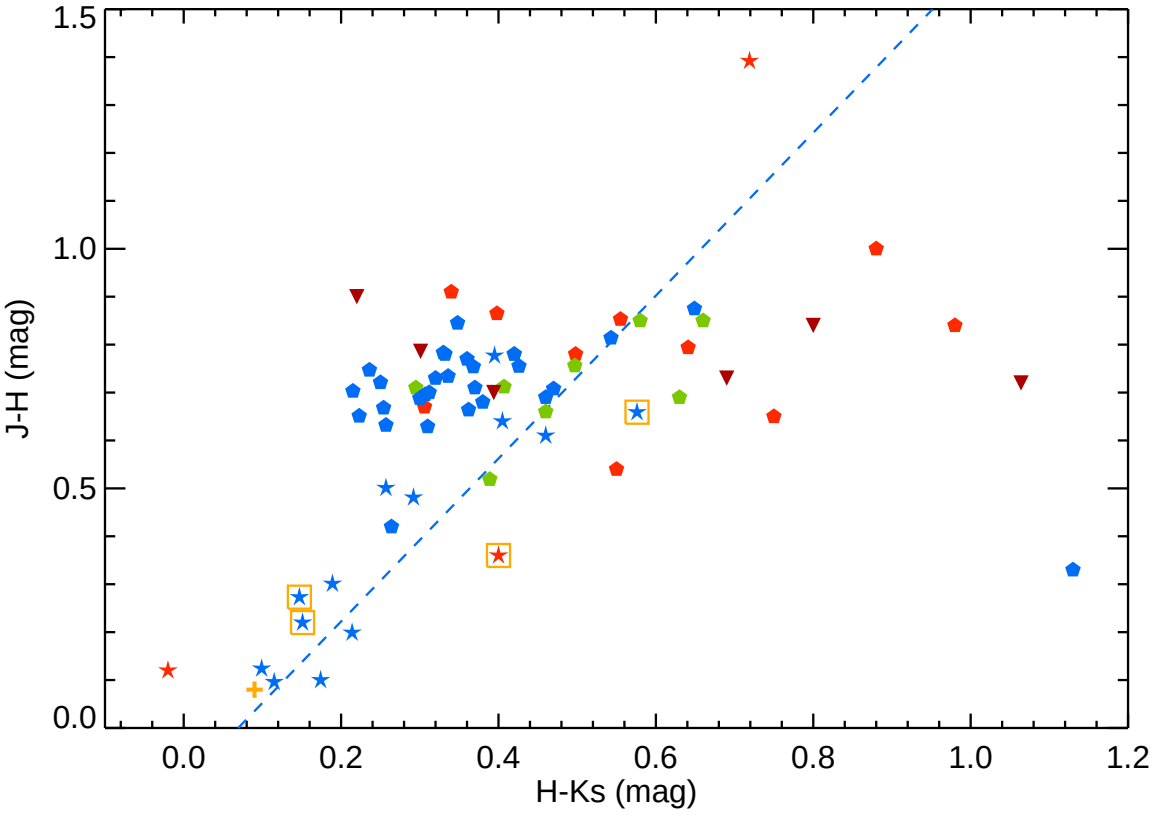

Figure 5.8: Near-infrared (H-K_S) vs (J-H) CD from 2MASS (J = 1.235 μm, H = 1.662 μm, K_S = 2.159 μm). Symbols as in Fig. 5.7. The blue dashed line corresponds to the intrinsic loci of stars as given by Bessell & Brett (1988).

the Seyfert 2 galaxies have stellar-like near-infrared colors. It is an indication that near-infrared emission is dominated by the contribution of the hosting galaxy for Sy2s. On the other hand, Sy1s and blazars present larger (H-K_S), in agreement with the results of Kouzuma & Yamaoka (2010). Seyferts 1.5 are located between Sy1s and Sy2s, as would be expected. There are stellar systems whose emission is not only thermal and this could lead to redder (H-K_S) colors, being these sources located in the AGN region. These systems are Microquasars and LMXBs or CVs, in which synchrotron emission from the jets and reprocessing of the strong UV-X ray are the main mechanisms emitting in the near-infrared, respectively. Near-infrared emission in HMXBs is expected to be dominated by the emission of the donor star. In Fig. 5.8, two microquasars (Sco X–1 and SS 433) are clearly located below the intrinsic loci of stars and this can be explained because of the synchrotron emission from the jets. This CD is useful to detect non-thermal emission, but not to discriminate between stars and AGN.

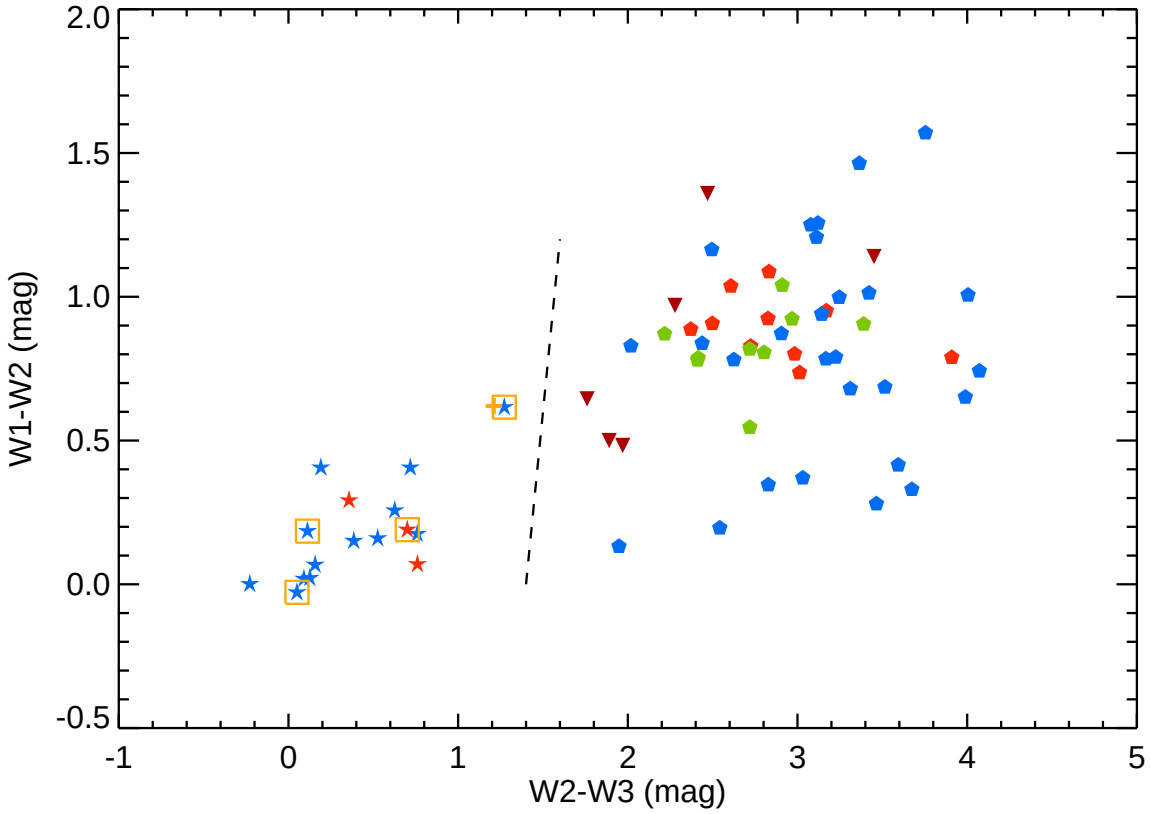

Figure 5.9: Mid-infrared $W1$-$W2$ vs $W2$-$W3$ CD from WISE ($W1$ = 3.4 μm, $W2$ = 4.6 μm, $W3$ = 12 μm). Symbols as in Fig. 5.7, The black dashed line has been plotted for reference.

As commented above, WISE is well suited to this purpose, as its bands are sensitive to the AGN characteristic warm dust emission beyond 10 μm and are hardly affected by the obscuration expected from either the dust in the torus or in the interstellar medium of the host galaxy. Several works on the power of WISE to identify AGN have been published (Jarrett et al., 2011; Edelson & Malkan, 2012; Stern et al., 2012; Mateos et al., 2012; Yan et al., 2013; Assef et al., 2013; Mateos et al., 2013, 2015). In Fig. 5.9, the $W1$-$W2$, $W2$-$W3$ CD is plotted. AGN can be clearly separated from stellar sources. The MIR emission coming from the accretion disk is probably hidden in AGN within the strong emission by the torus, produced by the reprocessing of the strong UV-X ray flux originated by the central engine, and which yields redder $W2$-$W3$ colors. This reprocessed luminosity seems to be also responsible for the systematic low values of $F_{20-100\mathrm{keV}}$ / F_{MIR} observed in Fig. 5.7. Since the effects of torus are present in all classes of AGN, this would explain why no differences are found between the different types of AGN in

this CD.

Table 5.4 provides NIR and MIR photometry and colors for the objects with OMC data in the IBIS catalog.

Table 5.4: Near and Mid infrared photometry and colours for the objects with OMC data in the IBIS catalog. Name and type of object in the IBIS catalogue; J, J-H, H-K from 2MASS; W1, W1-W2, W2-W3 from WISE.

Name	Type	J	J-H	H-K	W1	W1-W2	W2-W3
IGR J00370+6122	HMXB,XP,Sg?	8.39	0.12	0.10	8.10	0.02	0.09
Mrk 348	AGN,Sy2	11.24	0.69	0.46	9.40	1.21	3.11
1A 0114+650	HMXB,XP	8.60	0.30	0.19	7.90	0.07	0.16
RX J0146.9+6121	HMXB,XP,Be,T	9.90	0.20	0.21	9.31	0.16	0.53
NGC 788	AGN,Sy2	10.01	0.63	0.31	9.82	0.78	3.17
Mrk 1018	AGN,Sy1.5	11.59	0.66	0.46	10.16	0.78	2.41
NGC 985	AGN,Sy1	11.63	0.54	0.55	9.76	0.95	3.17
NGC 1052	AGN,Sy2	8.37	0.67	0.25	8.50	0.20	2.54
NGC 1068	AGN,Sy2	6.97	0.71	0.47	4.17	1.13	3.60
NGC 1275	AGN,Sy2	9.15	0.66	0.36	9.07	1.01	4.01
EXO 0331+530	HMXB,XP,Be,T	11.81	0.61	0.46	9.97	0.26	0.63
LEDA 15023	AGN,Sy2	13.67	0.33	1.13	10.91	1.25	3.08
UGC 3142	AGN,Sy1	11.60	0.91	0.34	10.51	0.80	2.98
SWIFT J0453.4+0404	AGN,Sy2	11.60	0.77	0.36	9.62	1.26	3.12
ESO 033-G02	AGN,Sy2	11.30	0.88	0.40	9.64	0.94	3.14
Ark 120	AGN,Sy1	12.04	0.84	0.98	8.63	0.89	2.37
SWIFT J0519.5-3140	AGN,Sy2	11.10	0.71	0.37	9.87	0.69	3.52
1A 0535+262	HMXB,XP,Be,T	8.37	0.10	0.12	7.11	0.17	0.76
NGC 2110	AGN,Sy2	9.26	0.78	0.33	8.24	0.78	2.63
Mrk 3	AGN,Sy2	10.02	0.73	0.32	9.25	0.87	8.38
Mrk 6	AGN,Sy1.5	11.07	0.85	0.66	8.41	0.79	2.42
ESO 209-12	AGN,Sy1.5	11.51	0.85	0.58	9.53	0.92	2.97
QSO B0836+710	AGN,Blazar	15.52	0.73	0.69	13.79	1.14	3.45
NGC 2992	AGN,Sy2	9.67	0.73	0.34	9.02	0.42	3.59
MCG-05-23-016	AGN,Sy2	10.53	0.76	0.43	8.49	1.00	3.25
NGC 3281	AGN,Sy2	9.31	0.70	0.31	9.02	1.46	3.36
Mrk 421	AGN,BL Lac	11.09	0.70	0.39	9.41	0.65	1.76
2E 1145.5-6155	HMXB,XP	8.68	0.10	0.17	8.32	0.15	0.38
SWIFT J1200.8+0650	AGN,Sy2	12.15	0.68	0.38	11.06	0.68	3.31
NGC 4051	AGN,Sy1.5	8.58	0.52	0.39	8.87	0.91	3.39
NGC 4074	AGN,Sy2	11.76	0.78	0.42	0.00	0.00	0.00
NGC 4138	AGN,Sy1.9	9.12	0.70	0.22	9.40	0.13	1.95
NGC 4151	AGN,Sy1.5	8.50	0.71	0.41	6.75	0.82	2.72
NGC 4388	AGN,Sy2	8.98	0.72	0.25	9.04	1.01	3.42
NGC 4395	AGN,Sy1.8	10.66	0.42	0.26	12.62	0.79	3.23
GX 301-2	HMXB,XP,T	6.72	0.64	0.41	5.34	0.41	0.19
3C 273	AGN,QSO	11.76	0.72	1.06	8.40	0.97	2.28
NGC 4593	AGN,Sy1	8.96	0.67	0.31	8.92	0.74	3.01
3C 279	AGN,QSO/Blazar	12.58	0.84	0.80	11.02	1.36	2.47
GX 304-1	HMXB,XP	9.80	0.50	0.26	8.02	0.41	0.72
NGC 4941	AGN,Sy2	9.09	0.65	0.22	9.74	0.37	3.03
IGR J13042-1020	AGN,Sy2	9.32	0.63	0.26	10.04	0.35	2.83
ESO 323-77	AGN,Sy1.2	10.21	0.85	0.56	8.01	0.83	2.72
MCG-06-30-015	AGN,Sy1.2	10.86	0.78	0.50	8.69	0.92	2.83
NGC 5252	AGN,Sy1.9	10.88	0.78	0.33	9.20	0.83	2.02
IC 4329A	AGN,Sy1.2	10.24	0.79	0.64	7.68	1.09	2.83
IGR J14080-3023	AGN,Sy1.5	13.73	0.69	0.63	11.40	1.04	2.91
NGC 5506	AGN,Sy1.9	9.71	0.88	0.65	7.36	1.16	2.50
NGC 5548	AGN,Sy1.5	10.64	0.76	0.50	9.17	0.81	2.80
H 1426+428	AGN,BL Lac	14.10	0.90	0.22	12.71	0.50	1.89
NGC 5643	AGN,Sy2	8.07	0.61	0.29	9.41	0.65	3.99
NGC 5728	AGN,Sy2	9.18	0.70	0.31	9.36	0.33	3.67
NGC 5995	AGN,Sy2	10.75	0.81	0.54	8.57	0.87	2.90
Sco X-1	LMXB,Z,M	11.90	0.36	0.40	11.16	0.19	0.70
NGC 6221	AGN,Sy1/Sy2	8.10	0.75	0.24	0.00	0.00	0.00
NGC 6240	AGN,Sy2	10.30	0.85	0.35	9.35	0.74	4.07
Mrk 501	AGN,BL Lac	10.66	0.79	0.30	9.82	0.48	1.97
Her X-1	LMXB,XP	13.72	0.12	-0.02	13.22	0.07	0.76
GX 1+4	LMXB,XP	10.09	1.39	0.72	7.43	0.29	0.36
XTE J1739-302	HMXB,SFXT	8.60	0.78	0.40	7.00	0.00	-0.23

Continued on next page...

Table 5.4 – Continued

Name	Type	J	J-H	H-K	W1	W1-W2	W2-W3
IGR J17544-2619	HMXB,SFXT	8.79	0.48	0.29	7.67	0.02	0.13
LS5039	HMXB,NS,M	9.02	0.27	0.15	8.40	-0.03	0.05
ESO 103-35	AGN,Sy2	11.37	0.74	0.31	9.69	1.57	3.75
3C 390.3	AGN,Sy1	13.59	1.00	0.88	9.64	1.04	2.61
V1223 Sgr	CV,IP	12.81	0.08	0.09	12.48	0.62	1.21
SS 433	HMXB,M	9.40	0.66	0.58	7.49	0.62	1.27
NGC 6814	AGN,Sy1.5	8.66	0.71	0.30	9.35	0.55	2.72
Cyg X-1	HMXB,BH,M	6.87	0.22	0.15	6.41	0.18	0.11
NGC 7172	AGN,Sy2	9.44	0.75	0.37	8.47	0.84	2.44
QSO B2251-178	AGN,Sy1	12.53	0.65	0.75	9.91	0.91	2.50
NGC 7465	AGN,Sy2	10.53	0.69	0.30	9.63	0.28	3.47
NGC 7469	AGN,Sy1	10.11	0.86	0.40	8.43	0.79	3.91
MCG-02-58-022	AGN,Sy1.5	11.83	0.78	0.42	9.12	0.87	2.22

5.3 Conclusions

The multiwavelength global properties of high-energy sources observed with *INTEGRAL* have been analyzed.

Section 5.1 presents our contribution to the compilation of the *second INTEGRAL AGN catalogue*. The hard X-ray and optical luminosities were calculated and compared. A partial correlation was performed to subtract the dependence on redshift. All the AGN were found to be approximately located on the same correlation line, over more than 5 dex in luminosity.

The $\alpha_{\rm OX}$ for each AGN was calculated and the histograms for the different types of AGN were compared, finding that $\alpha_{\rm OX}$ decreased from Seyfert 2 galaxies to blazars, indicating an increase of the relative X-ray to optical flux from type 2 towards type 1 objects.

Moreover, a fundamental plane of optical luminosity $L_{\rm V}$, X-ray luminosity $L_{\rm X}$, and mass of the central black hole $M_{\rm BH}$ is analyzed and presented.

A more extended analysis, including also stellar objects was performed and is provided in Section 5.2. A cross-match of the *fourth IBIS/ISGRI soft gamma-ray survey catalogue* with the OMC Archive was carried out and 73 sources with good-quality IBIS and OMC data were selected. The hard X-ray and optical luminosities were calculated and compared for the different types of objects. As a result, all the objects were located on the same correlation line, over more than 15 dex in luminosity.

For these 73 sources, the $\alpha_{\rm OX}$ was calculated. The histograms of this value were plotted for each type of object and HMXBs and Seyfert 2 galaxies were found to present lower values of $\alpha_{\rm OX}$ than Radio galaxies, blazars and LMXBs.

Infrared photometry was extracted from 2MASS and WISE catalogs. The 2MASS (H-K_S) vs (J-H) CD from 2MASS data turned out to be useful to identify non-thermal emission in the NIR, while the $W1$-$W2$ vs $W2$-$W3$ CD from WISE data was very useful to discriminate between AGN and stellar sources.

Chapter 6

Optical and X-ray monitoring of high-energy sources with *INTEGRAL*

In this chapter the X-ray and optical properties of the sources observed by *INTEGRAL*, over more than 12 years of operations are compared. The OMC, JEM-X, and IBIS/ISGRI light curves of the 73 objects found in the cross-match of the *fourth IBIS/ISGRI soft gamma-ray survey catalogue* with the OMC archive (see Section 5.2.1) have been extracted and analyzed. A brief introduction of the motivation of this study is given in Section 6.1. The data compilation is presented in Section 6.2. The analysis of the light curves for some selected sources is presented in Section 6.3. Finally, the conclusions of this chapter are summarized in Section 6.4.

6.1 Introduction

The mechanisms driving the optical and X-ray variability of high-energy sources were described in Section 2.3. As discussed in Section 2.3, simultaneous observations across the electromagnetic spectrum and long-term monitoring are crucial to understand the nature of the physical mechanisms leading to the extreme processes occurring in XBs and AGNs, but they are not always possible. Since *INTEGRAL* has been observing the high-energy sky for more than 12 years, simultaneous optical, soft X-ray, and hard X-ray observations of these sources over this long period of time are presented here for the first time.

6.2 Data compilation

For the 73 sources from the cross-match of the IBIS catalog with the OMC archive (see Chapter 5), the *INTEGRAL* light curves were obtained. Public data have been used and in some particular cases, private data with permissions of the PI have been added: for GX 304–1 and H 1145–619, *INTEGRAL* private data from Dr. Jian Li have been included with his permission. When private data were included and in some cases when the data had to be reprocessed, JEM-X and IBIS processing of the data was performed with the collaboration of Dr. Celia Sánchez-Fernández at the *INTEGRAL* Science Operations Centre (ISOC). Public *INTEGRAL* data were compiled from different sites, depending on the instrument:

- The OMC data were extracted from the OMC Archive (see 1.2.4, Gutiérrez et al. (2004)). The data used in this work include all observations from revolutions 11–1385 (publicly

available on 1 December 2014) and public observations up to revolution 1503 (2 February 2015).

- The *INTEGRAL*/JEM-X data were extracted through the High-Energy Astrophysics Virtually ENlightened Sky (HEAVENS)[1]. Light curves in the 3–10 keV and 10–25 keV bands and with a bin size of 15 minutes were extracted.

- The *INTEGRAL*/IBIS light curves were processed and provided by Dr. Guillaume Belanger, who extracted the IBIS light curves for each source in the 20–35, 35–65 and 65–100 keV energy bands. *INTEGRAL*/IBIS light curves including observations until the end of 2010 provided by Dr. Tony Bird were also used.

For the most interesting sources and when available, light curves from other high-energy instruments were obtained:

- The *Rossi* X-ray Timing Explorer (*RXTE*; Bradt et al. (1993)) was launched on 30 December 1995 and was decommissioned on 5 January 2012. The *RXTE* had three instruments: the Proportional Counter Array (PCA; Jahoda et al. 2006), the High-Energy X-ray Timing Experiment (HEXTE; Rothschild et al. 1998), and the All Sky Monitor (ASM; Levine et al. 1996). ASM and PCA data have been included in this work[2]. ASM provided light curves in the 1.3–12 keV band and PCA produced pointed observations with greater sensitivity in the 2–60 keV band, but the PCA data cover only a limited fraction of the sky. When available, PCA data were selected instead of the ASM ones.

- The Monitor of All-sky X-ray Imager (MAXI; Matsuoka et al. 2009), continuously monitors astronomical X-ray objects in the 2–20 keV band[3].

- The Burst Alert Telescope (BAT; Barthelmy et al. 2005; Krimm et al. 2013) on the *Swift Gamma-Ray Burst Mission* (Gehrels et al., 2004). *Swift*/BAT provides near real-time coverage of the X-ray sky in the energy range 15–50 keV[4].

- At very high energies, data from the Large Area Telescope (LAT), the main instrument on the *Fermi Gamma-ray Space Telescope* (Atwood et al., 2009) were also extracted[5]. *Fermi*/LAT detects gamma-rays over an energy range between 100 MeV and 300 GeV.

For H 1145–619, optical data from the All Sky Automated Survey (ASAS; Pojmanski (1997)) have been added to the OMC optical light curve.

For all the blazars presented in this Chapter, optical light curves in the Cousins R band (centered at 6470 Å) have been added. These data have been provided by the monitoring group for the MAGIC consortium[6]. These observations have been performed with the following telescopes: the 1.03-m telescope at Tuorla Observatory (Finland), the 35-cm telescope at the KVA observatory on La Palma, Canary islands (Spain), the 50-cm Searchlight Observatory Network telescope, San Pedro de Atacama (Chile), the 40-cm Searchlight Observatory Network telescope, New Mexico (USA), and the 60-cm telescope at Belogradchik (Bulgaria). Frequently, AGN are not so well monitored by *INTEGRAL* as stars. These light curves complement the

[1]The HEAVENS web interface (http://isdc.unige.ch/heavens/) provides on-the-fly remote analysis of *INTEGRAL* (and other high-energy instruments) data and allows to generate high-level products customized for specific scientific needs.

[2]The *RXTE* light curves were downloaded from the *RXTE* Archive at the *High Energy Astrophysics Science Archive Research Center* (HEASARChttp://heasarc.gsfc.nasa.gov/)

[3]The MAXI light curves are available at http://maxi.riken.jp

[4]The BAT light curves were collected from http://swift.gsfc.nasa.gov/results/transients/

[5]Fermi/LAT light curves are publicly available at http://fermi.gsfc.nasa.gov/ssc/data/access/lat/msl_lc/

[6]http://users.utu.fi/kani/1m/

OMC data very well, because although they are not so accurate and do not have good time resolution (they have usually one observation per night), their large temporal coverage is very useful to analyze the long-term optical behavior. On the other hand, as will be demonstrated below, OMC data are very helpful to analyze the short-term variability of AGN.

6.3 Particular cases

The *INTEGRAL* light curves from OMC, JEM-X, and IBIS were extracted and plotted for all the sources in the cross-match performed between the IBIS catalog and the OMC archive. The figures for all the sources are compiled in Appendix B. From the 73 sources analyzed, the most interesting ones with good-quality data and displaying optical and X-ray variability were selected for a more detailed analysis. For the analysis of the selected sources, complementary data from other missions were added as explained in Section 6.2. The high-energy and the optical light curves are compared, in order to understand the physical properties of these objects.

6.3.1 1A 0535+262

1A 0535+26 is one of the best studied Be/X-ray binaries. It was discovered by the Ariel V satellite (Smith & Courtier, 1976) during a giant outburst on 14 April 1975 (Coe et al., 1975; Rosenberg et al., 1975). The system consists of an X-ray pulsar of 103-s spin period (Caballero et al., 2007) orbiting around an O9.7IIIe star (HD 245770; Giangrande et al. 1980) in an eccentric orbit ($e = 0.47 \pm 0.02$; Finger et al. 1994). The ephemeris derived by Finger et al. (2006) are T_0=MJD 53613.0 and P_{orb}=111.1 d. Different ephemeris are obtained from optical observations. Giovannelli et al. (2013) derive T_0=MJD 44943.5 and P_{orb}=111.0 d. Since the first detected giant outburst in 1975, other seven giant X-ray outbursts have been observed in October 1980 (Nagase et al., 1982), June 1983 (Sembay et al., 1990), March 1989 (Makino et al., 1989), February 1994 (Finger et al., 1994), May/June 2005 (Tueller et al., 2005), December 2009 (Wilson-Hodge et al., 2009) and February 2011 (Camero-Arranz et al., 2011).

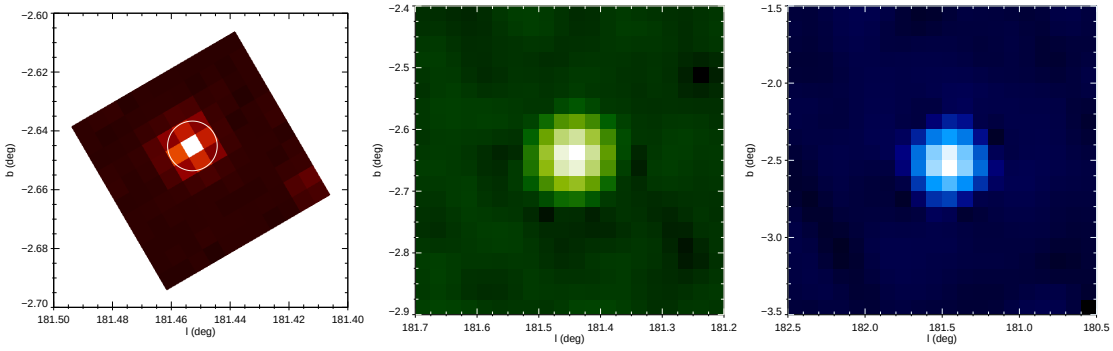

Figure 6.1: Left: OMC image of 1A 0535+262. The white circle represents approximately the area where the optical photometry is extracted. **Middle:** JEM-X image of 1A 0535+262 in the 3.0–25 keV energy band. **Right:** IBIS/ISGRI image of 1A 0535+262 in the 20–100 keV energy band. North is up and east is to the left. Note the different image scales for each instrument.

Long-term optical variability from this system has been reported by several authors (Moritani et al. (2010); Yan et al. (2012); Camero-Arranz et al. (2012) and references therein). The variability in the V-band magnitude and in the Hα equivalent width has been studied to unveil the nature of X-ray outbursts, since both are related to physical changes in the circumstellar disk around the Be star. Yan et al. (2012) used *INTEGRAL*/OMC data in their long-term optical variability analysis, with a coverage (including other optical observations) from 1987 to

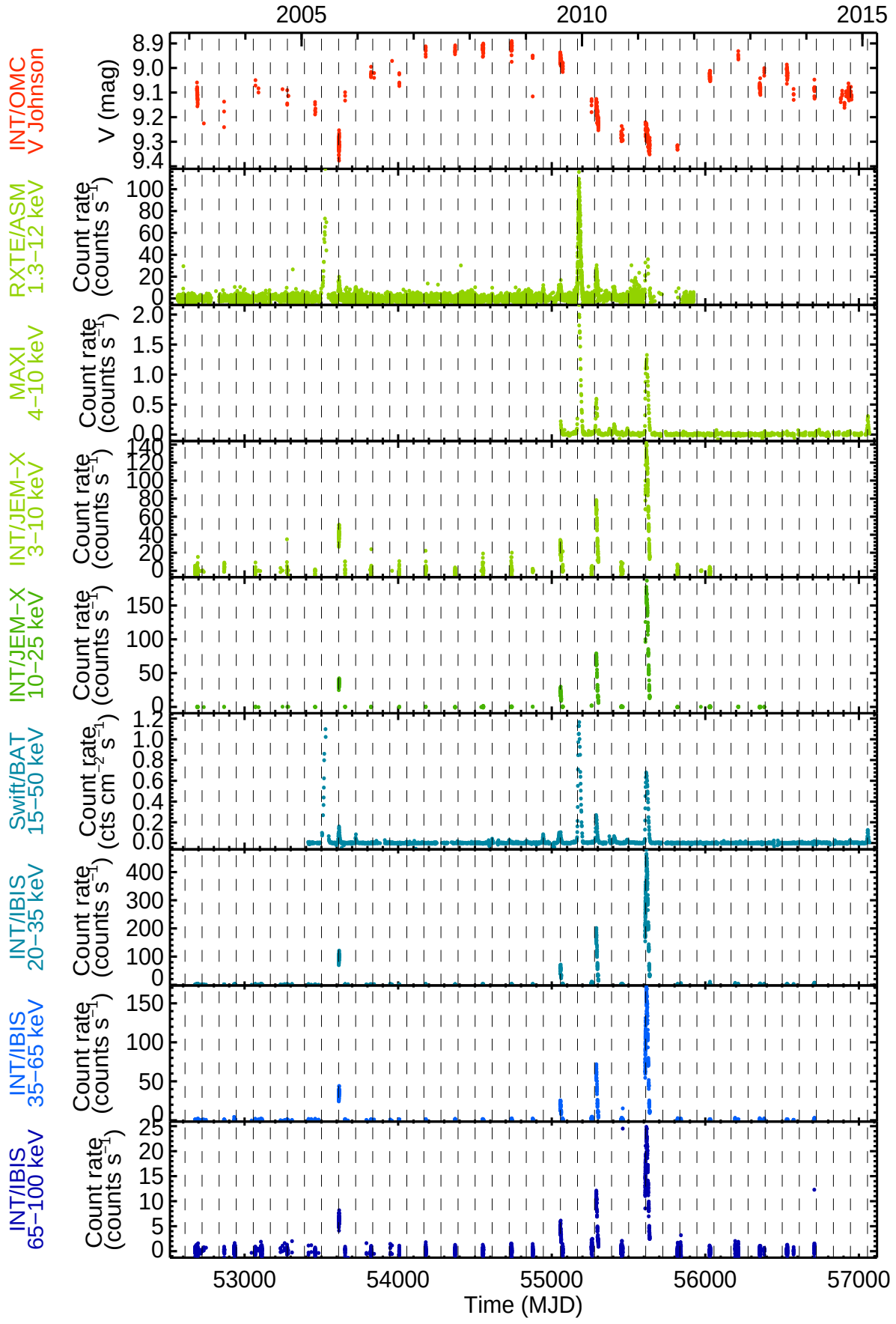

Figure 6.2: Light curves of the *INTEGRAL* and other X-ray instruments of 1A 0535+262 over the 12 years covered by *INTEGRAL*. The periastron passages were calculated using the ephemeris P_{orb} = 111.1 d; T_0 = MJD 52390.0 from Finger et al. (1994).

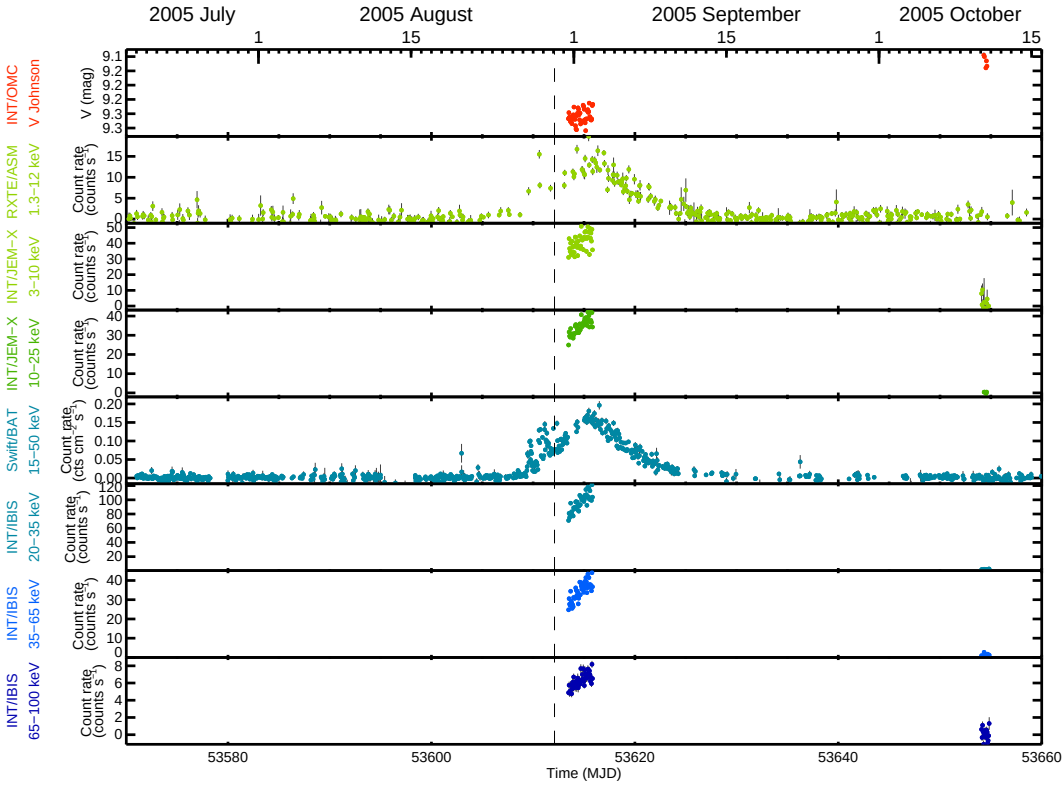

Figure 6.3: Zoom of the light curves of 1A 0535+262 showing the 2005 normal outburst. The periastron passage has been calculated using the ephemeris P_{orb} = 111.1 d; T_0 = MJD 52390.0 from Finger et al. (1994).

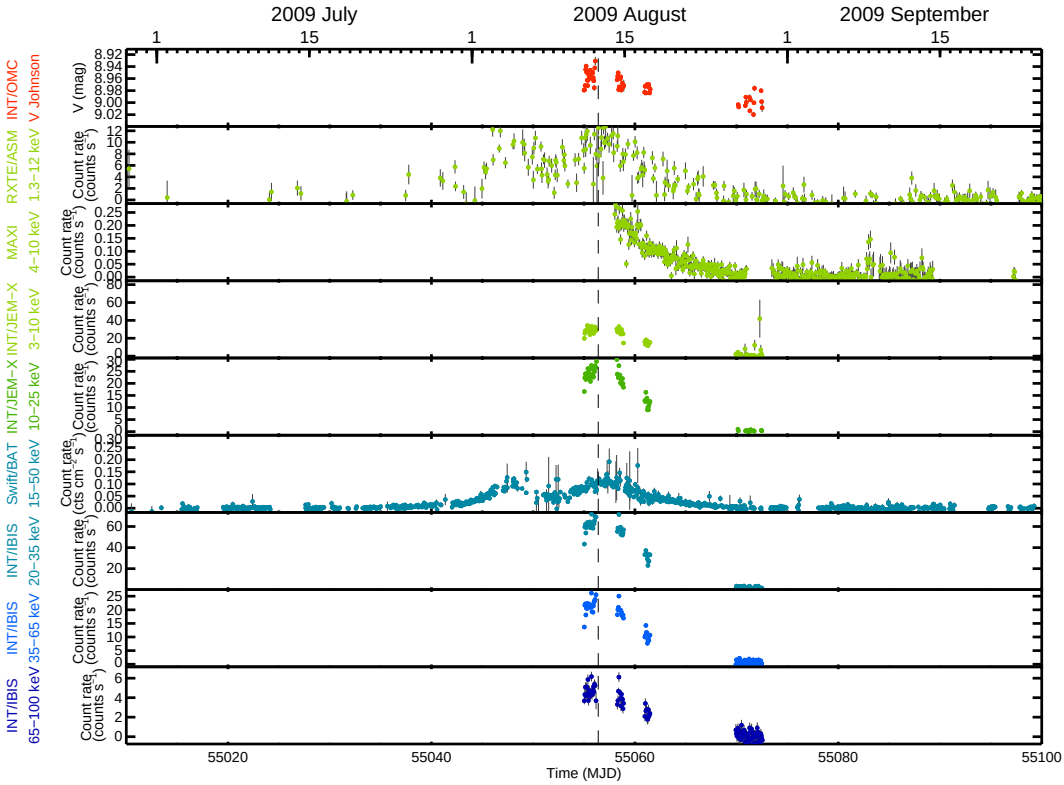

Figure 6.4: Zoom of the light curves of 1A 0535+262 showing the 2009 normal outburst. The periastron passage has been calculated using the ephemeris P_{orb} = 111.1 d; T_0 = MJD 52390.0 from Finger et al. (1994).

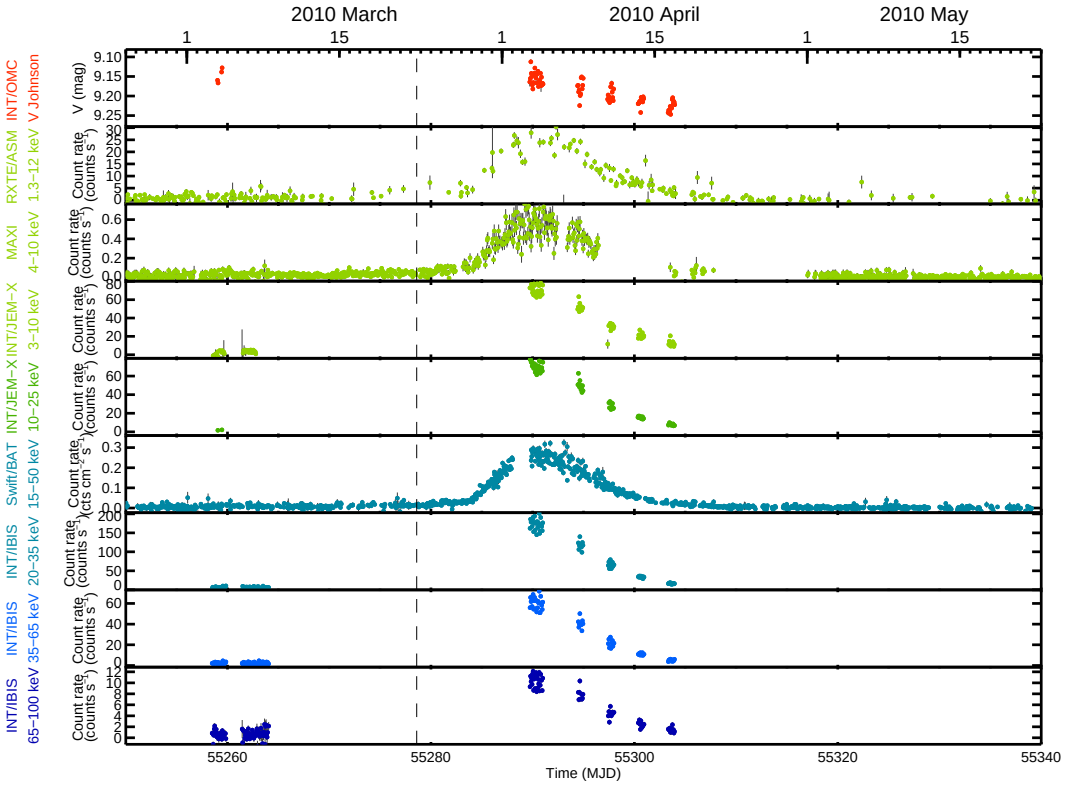

Figure 6.5: Zoom of the light curves of 1A 0535+262 showing the 2010 normal outburst. The periastron passage has been calculated using the ephemeris P_{orb} = 111.1 d; T_0 = MJD 52390.0 from Finger et al. (1994).

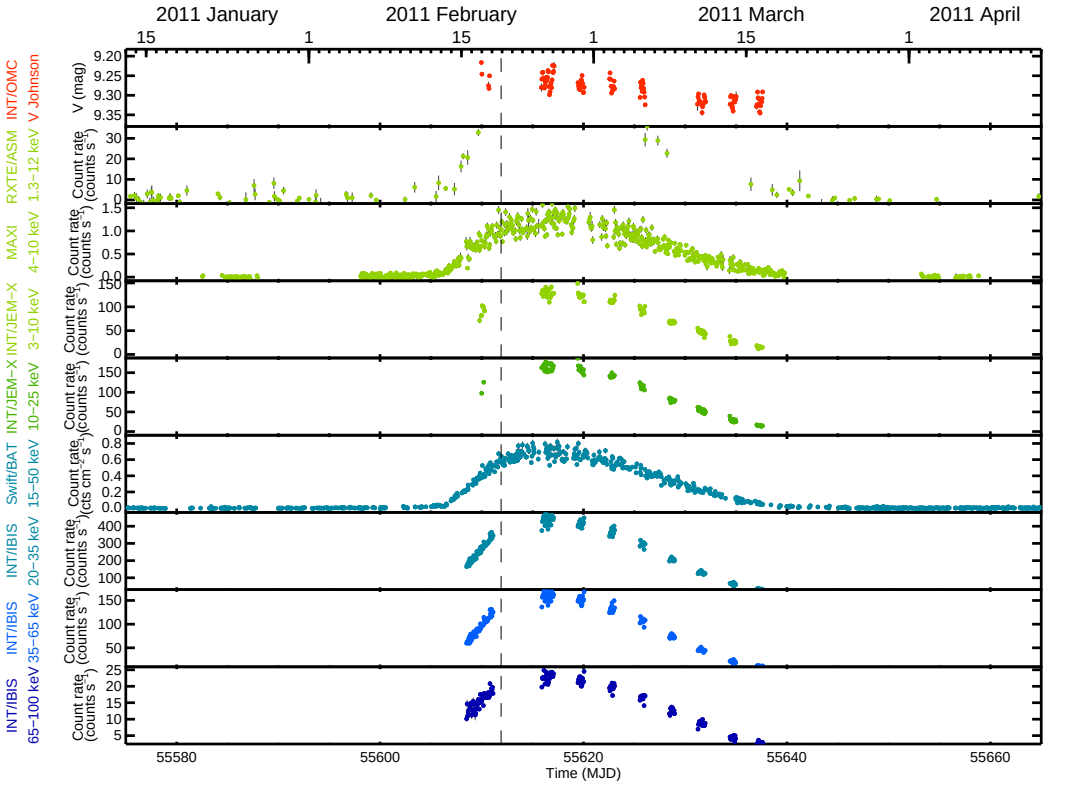

Figure 6.6: Zoom of the light curves of 1A 0535+262 showing the 2011 supergiant outburst. The periastron passage has been calculated using the ephemeris P_{orb} = 111.1 d; T_0 = MJD 52390.0 from Finger et al. (1994).

2010. In this work, OMC public data from 2003 to 2014 are included.

The *INTEGRAL*, *RXTE*/ASM, MAXI, and *Swift*/BAT light curves for the last 12 years are shown in Fig. 6.2. Four outbursts have been observed with *INTEGRAL*. A normal outburst was observed in August–September 2005 (Fig. 6.3), after the giant outburst in May 2005. It occurred when the optical flux was in a minimum value, and during the outburst, the optical brightness did not show any variations. Another normal outburst was observed in August 2009 (Fig. 6.4), just before the giant outburst in December 2009 (Caballero et al., 2009). In this case, OMC, JEM-X, and IBIS data show the same trends. This outburst had a double-peak structure and preceded a giant one (Caballero et al., 2013). Another normal outburst was observed in March–April 2010 (Fig. 6.5), the first one after the giant outburst in December 2009. In this outburst, the same descending trends were observed in OMC, JEM-X, and IBIS light curves. Finally, a giant outburst in February–March 2011 was observed by *INTEGRAL* (Fig. 6.6). It happened in a fading phase of the optical flux, almost reaching its local minimum. After this outburst, the source entered in quiescence and the optical flux increased again.

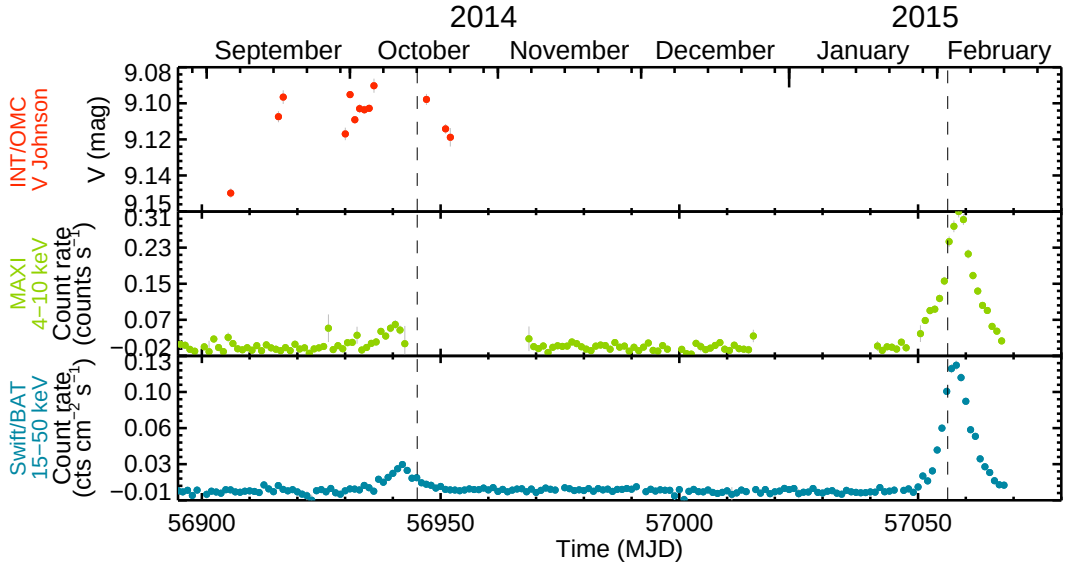

Figure 6.7: Recent activity of 1A 0535+262. Light curves from *INTEGRAL*/OMC, MAXI and *Swift*/BAT shows the most recent activity (at the time of writing) detected from this pulsar (see text). The periastron passages have been calculated using the ephemeris P_{orb} = 111.1 d; T_0 = MJD 52390.0 from Finger et al. (1994). The data have been binned into 1 day intervals.

The OMC light curve show a clear long-term variability, which seems to be quasi-periodic with time-scales of $\sim$ 2000 d. When the 2005 giant outburst occurred, OMC was in a fading phase, as observed in previous giant outbursts of this source (Yan et al., 2012). After this giant outburst, a normal one took place in August–September 2005 when the optical flux reached a minimum and then started to increase. After the mass ejection in the giant outburst, a cavity or low-density region may develop in the inner part of the circumstellar disk. The brightening of the optical flux seems to be related to the replenishment of this cavity region produced by the mass ejection of the subsequent outburst (Yan et al., 2012; Li et al., 2014). The next giant outburst took place in December 2009, but *INTEGRAL* could not observe it because of Sun observing constraints. It was coincident again with an optical flux fading phase. Three subsequent normal X-ray outbursts occurred after the giant one and then, a new giant outburst was detected in February 2011 (Camero-Arranz et al., 2011), when the optical flux was in a minimum (around MJD 55620). After that, a quiescent X-ray phase and an increasing phase of the optical emission took place. In early 2013, the optical flux entered in a fading phase. And as expected, after

that, recent activity has been detected with MAXI/GSC in October 2014 (Nakajima et al., 2014) and in January–February 2015 (Nakajima et al., 2015). Both normal outbursts were detected first in the optical, and the observed X-ray delay was predicted by Giovannelli et al. (2014) and Giovannelli et al. (2015). The OMC, MAXI, and *Swift*/BAT light curves of this last activity can be seen in Fig. 6.7. The second outburst is brighter than the first one and a giant outburst could occur on the next periastron passage (MJD 57167, 25 May 2015).

6.3.2 GX 304–1

The Be/X-ray binary pulsar GX 304–1 (4U 1258–61) was discovered by its high-energy X-ray emission in balloon observations carried out in 1970 (McClintock et al., 1971) and was found to have a spin period of $\sim$ 272 s (Huckle et al., 1977; McClintock et al., 1977). The optical counterpart of the X-ray source was identified by Mason et al. (1978) with a B2 Vne. The orbital period was measured by Priedhorsky & Terrell (1983), who found a 132.5 d periodicity of the outbursts, related to the orbital motion of the neutron star.

The *INTEGRAL*/OMC, JEM-X, and IBIS, the *RXTE*/ASM, the MAXI and the *Swift*/BAT light curves from 2003 to 2014 are shown in Fig. 6.9. After 30 years in quiescence, at the end of 2009 (Yamamoto et al., 2009), this pulsar became active again and it remained active showing regular outbursts until the beginning of 2013 (see Fig. 6.9). A clear evolution can be observed in the optical light curve: From 2004 to 2008, the optical flux remains almost constant. In this epoch, the source was in X-ray quiescence as well. Then, at the end of 2009 the source became active in X-rays and the optical flux started to increase. The optical magnitude varied from 14.7 to 13.8 in 1200 days. When the X-ray activity stopped, the optical flux kept increasing, reaching a maximum value in the OMC observations of 12.7 mag.

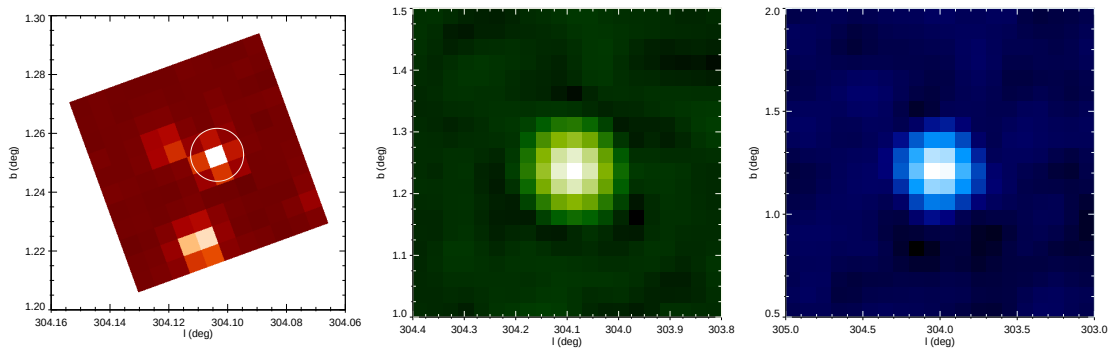

Figure 6.8: Left: OMC image of GX 304–1. The white circle represents approximately the area where the optical photometry is extracted. **Middle:** JEM-X image of GX 304–1 in the 3.0–25 keV energy band. **Right:** IBIS/ISGRI image of GX 304–1 in the 20–100 keV energy band. North is up and east is to the left. Note the different image scales for each instrument.

After several normal outbursts, on 21 September 2012, a double-peaked outburst was detected by MAXI (Nakajima et al., 2012). According to previous studies (Caballero et al., 2013), multi-peaked or double-peaked outbursts are often followed by a giant outburst. Indeed, a giant outburst took place in November 2012 (Jenke et al., 2012), and since then, GX 304–1 has not been very active in X-rays, but has varied significantly in the optical band (see Fig. 6.10).

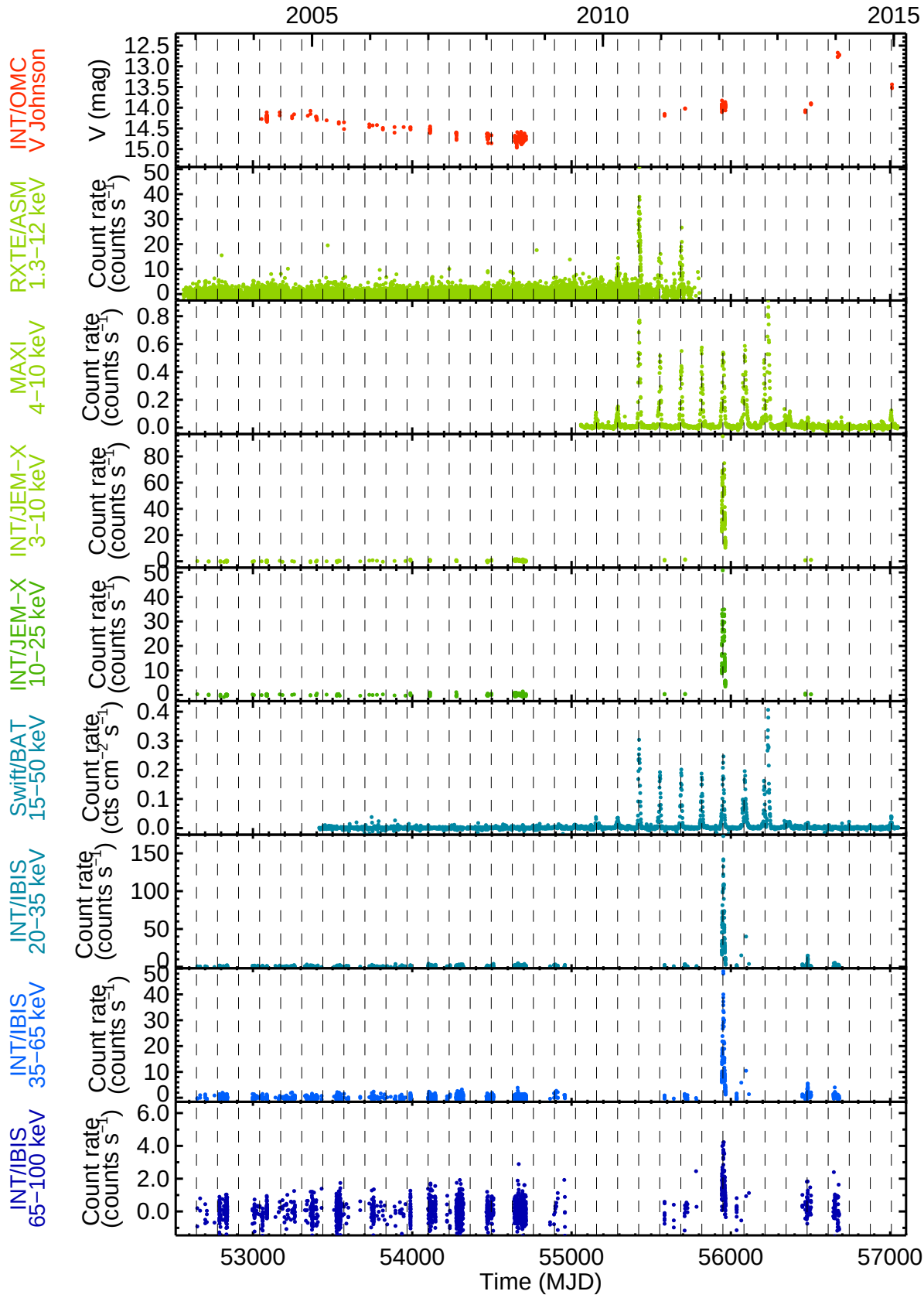

Figure 6.9: Light curves of the *INTEGRAL* and other X-ray instruments of GX 304–1 over the 12 years covered by *INTEGRAL*. GX 304–1 does not show significant variability in any of the X-ray light curves from 2003 to 2009. The periastron passages were calculated using the ephemeris P_{orb} = 132.190 d; T_0 = MJD 55421.4 from Sugizaki et al. (2014)). The light curves have been rebinned with a 72 min interval. All the data were publicly available, except the *INTEGRAL* data from July 2014 which have been included with the permission of Jian Li.

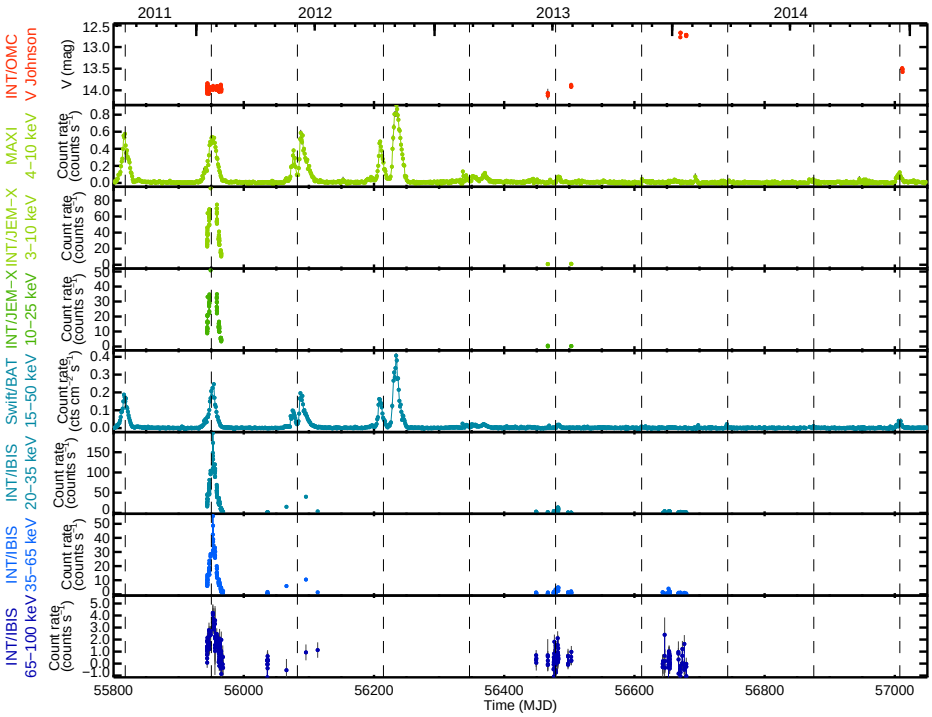

Figure 6.10: Light curves of GX 304–1 from MJD 55800 to 56800. The multi-peaked outburst and the giant outburst can be seen in the X-ray light curves. The strong optical brightening from June 2013 to June 2014 is shown. The light curves have been rebinned with a 72 min interval and the periastron passages were calculated using the ephemeris P_{orb} = 132.190 d; T_0 = MJD 55421.4 from Sugizaki et al. (2014). The *INTEGRAL* data from July 2014 were private and have been included with the permission of Jian Li.

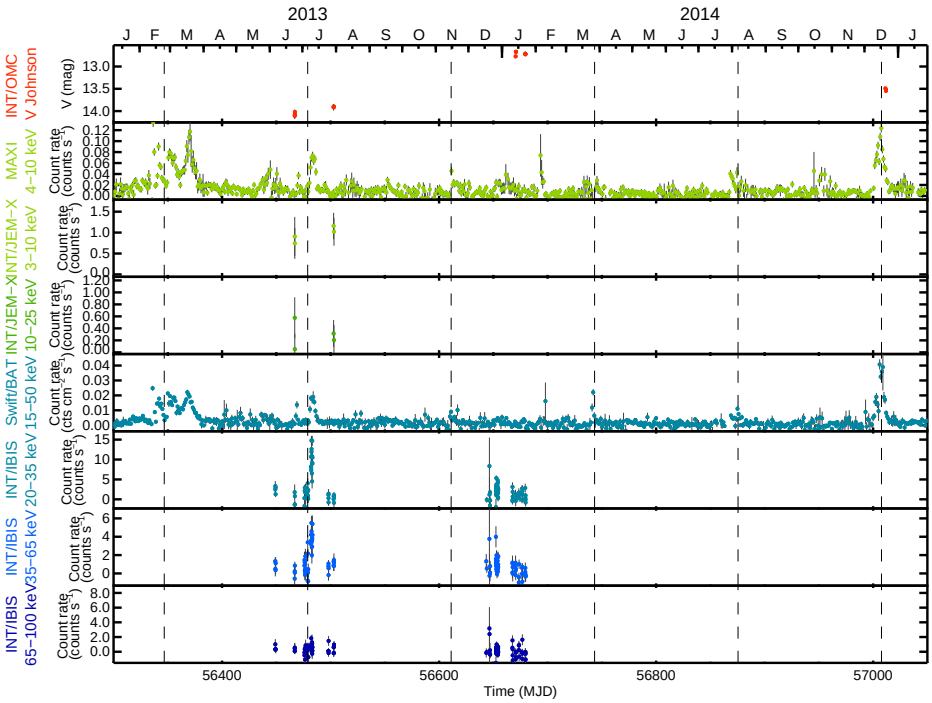

Figure 6.11: Last activity detected for GX 304–1. The light curves range from MJD 56300 to 57000. A multi-peaked weak outburst at the periastron passage on MJD 56349 is followed by some small outbursts. The optical emission increases significantly from June 2013 to January 2014 and is fainter in the last observations in December 2014. The light curves have been rebinned with a 72 min interval and the periastron passages were calculated using the ephemeris P_{orb} = 132.190 d; T_0 = MJD 55421.4 from Sugizaki et al. (2014). The *INTEGRAL* data from July 2014 were private and have been included with the permission of Jian Li.

The activity after the giant outburst in November 2012, is showed in Fig. 6.11. A multi-peaked weak outburst at the next periastron passage on February 2013 (MJD 56349) was detected by MAXI and BAT. After that, the source exhibited anomalous activity with a weak flux increase at 0.7 orbital phase on 29 May 2013. On July 2013 (MJD 56482), an X-ray flux increase from GX 304–1 was detected with MAXI (Nakajima et al., 2013), BAT and *INTEGRAL*/IBIS, corresponding to an orbital phase of 0.0 and then the X-ray activity stopped. From July 2013 to January 2014, the optical flux increased from 14.0 to 12.6 mag. This optical brightening could be explained by the replenishment of the Be disk after the X-ray activity. From January 2014 to December 2014, GX 304–1 was not observed by *INTEGRAL*. The last observations presented in this work were carried out in December 2014, during a normal X-ray outburst that can be seen in the MAXI and BAT light curves. In this epoch, the optical flux was fainter than in January by 0.8 mag. This decline of the optical flux seems to be related to changes in the emission coming from the inner disk.

6.3.3 H 1145–619

The X-ray pulsar H 1145–619 was discovered in 1980 with observations from OSO 8, HEAO 1 (Peterson, 1975) and the Einstein Observatory (Giacconi et al., 1979) by White et al. (1980). Pulsations from this pulsar, together with the pulsations from 1E 1145.1–6141 (17′ away), were detected in 1977 with Ariel V and two sources were distinguished by the Einstein observatory, identifying the 292 s pulsations coming from H 1145–619 (White et al., 1980; Lamb et al., 1980). A more precise value of the pulse period of 292.4 s was provided by Nagase (1989). The optical counterpart, Hen 715, was discovered in 1978 (Dower et al., 1978) and was classified as B1 Ve by Stevens et al. (1997).

Optical, infrared, and X-ray variability has been detected and analyzed from this source. Stevens et al. (1997) compiled a 13-yr optical and X-ray history. From 1991 to 1998 this source underwent 12 outbursts that were detected with *CGRO*/BATSE (Fishman et al., 1989). Wilson-Hodge (1999) analyzed these outbursts and derived the more recent ephemeris of the system, T_0 = MJD 48871.6±0.6 and P_{orb} = 186.68±0.05 d.

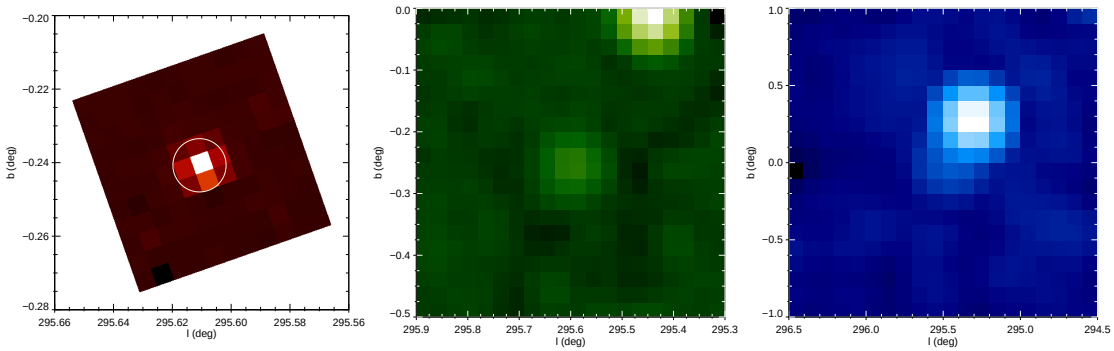

Figure 6.12: Left: OMC image of H 1145–619. The white circle represents approximately the area where the optical photometry is extracted. **Middle:** JEM-X image of H 1145–619 in the 3.0–25 keV energy band. **Right:** IBIS/ISGRI image of H 1145–619 in the 20–100 keV energy band. In this image, contamination by 1E 1145.1–6141 is evident (see text). North is up and east is to the left. Note the different image scales for each instrument.

This Be/X-ray binary is included in the *INTEGRAL*/IBIS 9-year Galactic Hard X-Ray Survey (Krivonos et al., 2012) and has been often observed during the *INTEGRAL* Galactic Plane Scanning (GPS). Private data kindly provided by Dr. Jian Li have been analyzed with the collaboration of Dr. Celia Sánchez, in the processing of JEM-X and IBIS data.

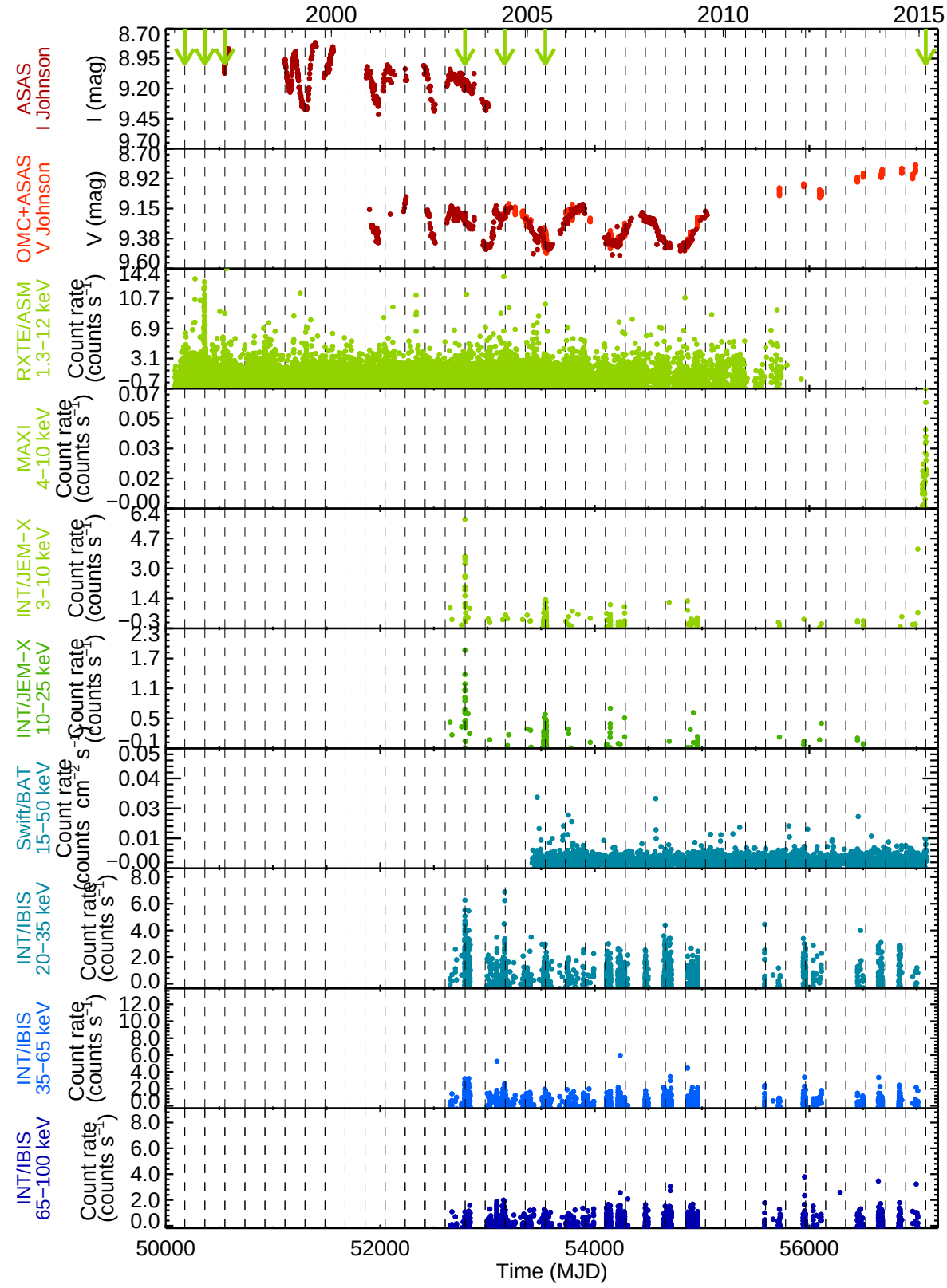

Figure 6.13: Light curves of H 1145–619 from 1996 to 2015. ASAS photometric points (in brown) have been added to the optical light curve. The periastron passages were calculated using the ephemeris P_{orb} = 186.68 d; T_0 = MJD 48871.6 (see text). The X-ray outbursts previously reported, the ones detected with *INTEGRAL* data, and the last outburst detected by MAXI and *Swift*/BAT are marked with green arrows. The light curves are rebinned with a 10 min interval. The *INTEGRAL* data from July 2014 were private and have been included with the permission of Jian Li.

The OMC, JEM-X, and IBIS images of the system are shown in Fig. 6.12. For this object, the OMC data have been corrected from contamination by other sources. Some faint stars are inside the area where the OMC photometry is extracted. Although the brightest one has magnitude f=14.552 in the UCAC4 catalog (Zacharias et al., 2012), while in this catalog, H 1145–619 has a magnitude of 9.615, a total contamination of $\sim$ 0.4 mag has been estimated. This value was calculated as the contribution to the total flux of the stars in the field, which was estimated using the UCAC4 catalog.

The *INTEGRAL* and ASAS light curves from 1996 to 2015 are shown in Fig. 6.13. The *RXTE*/ASM, MAXI and *Swift*/BAT light curves are plotted as well. ASAS data have been added to the OMC data to get a better coverage of the optical light curve.

The optical light curve presents a very intriguing behavior. From 1997 to 2000, the optical brightness was clearly modulated by the orbital period, as can be seen in the I-band ASAS light curve, although a larger period modulating the amplitude of the variations seemed to be present as well, because the brightness in the different minima and maxima are variable (see Fig. 6.14). From 2000 to 2002, the gaps in the optical observations make difficult to see if the same modulations are present, although it seems that they are still dominated by the orbital period.

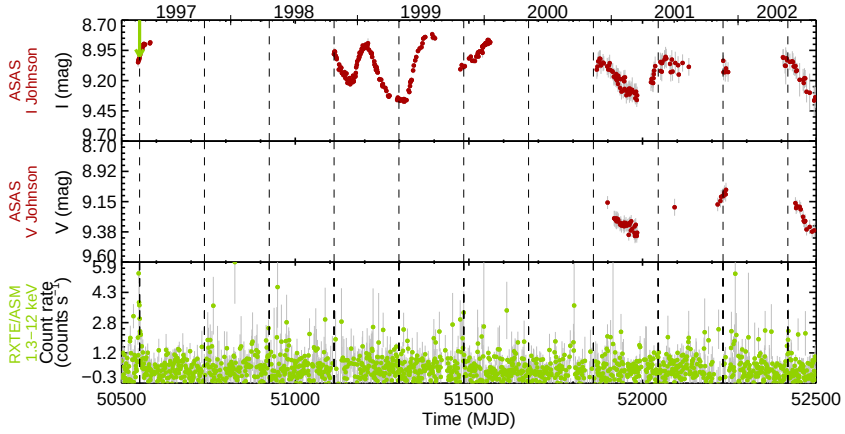

Figure 6.14: Light curves of H 1145–619 from 1997 to 2002. In the I-band ASAS light curve the orbital variation can be observed. The amplitude of the variations also varies. In this epoch, the source was in quiescence in X-rays, as can be observed in the *RXTE*/ASM light curve. The periastron passages were calculated using the ephemeris P_{orb} = 186.68 d; T_0 = MJD 48871.6 and the last outburst measured by *RXTE*/ASM in this epoch is marked with a green arrow. The light curves are rebinned with intervals of 1 d.

From 2002 to 2009, the optical brightness varied with a period of $\sim$ 600 d (superorbital variations), although there are still orbital modulations superimposed to this one (see Fig. 6.15). These superorbital variations in Be/X-ray binaries are usually explained by the development of low-density regions and the replenishment of these cavity regions in the circumstellar disk around the Be star. In the X-ray light curves, faint outbursts are detected in this epoch with *INTEGRAL* data, as will be seen below.

From 2010 to the beginning of 2015, the optical flux increased by 0.5 mag, probably due to an enhancement of the disk. In this period, there are not ASAS data available and the temporal coverage is poorer. From 2002 to 2010, the optical behavior of H 1145–619 is similar to the one of 1A 0535+262, while the last evolution is similar to the brightening of the optical flux measured for GX 304–1.

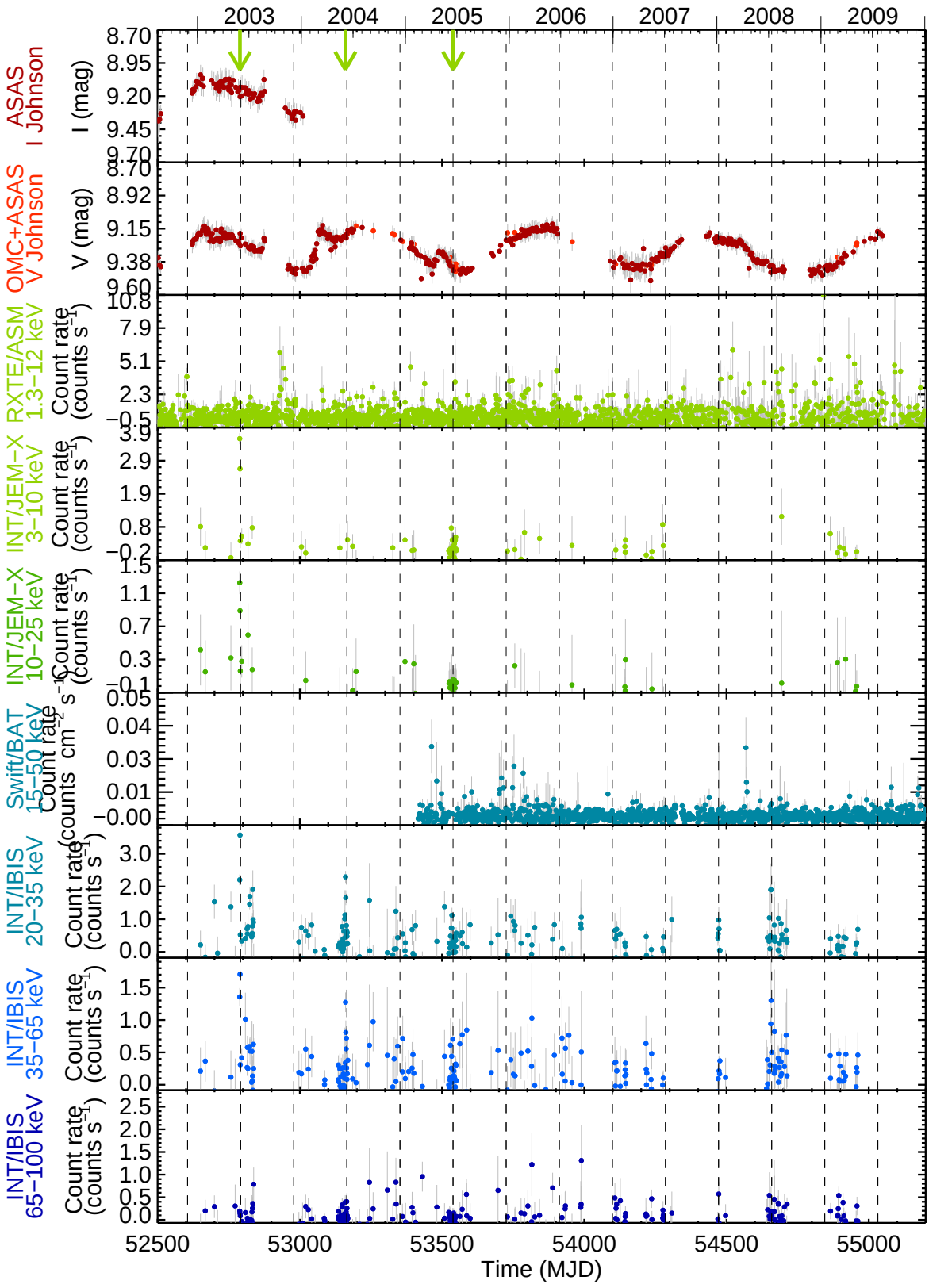

Figure 6.15: Light curves of H 1145–619 from 2002 to 2009. In the optical light curve the modulations with $\sim$ 400 d can be observed. Apart from these variations, orbital variability is also detected. In the X-ray light curves, fainter outbursts are detected in this epoch with *INTEGRAL* data. The periastron passages were calculated using the ephemeris P_{orb} = 186.68 d; T_0 = MJD 48871.6 and the times of the X-ray outbursts detected with *INTEGRAL* data in this period are marked with green arrows. The light curves are rebinned with intervals of 1 d.

Regarding the X-ray activity, the last outburst published from this source was detected between 29 September and 8 October 1996 by *RXTE*/ASM (Corbet & Remillard, 1996). In Fig. 6.16, three outbursts are evident in the *RXTE*/ASM light curve, consistent with the periastron passages in April 1995, September 1996, and April 1997. The three of them were studied by Wilson-Hodge (1999) using BATSE data. In the last one, simultaneous ASAS data in the I-band are available showing that when the outburst occurred the optical flux was increasing.

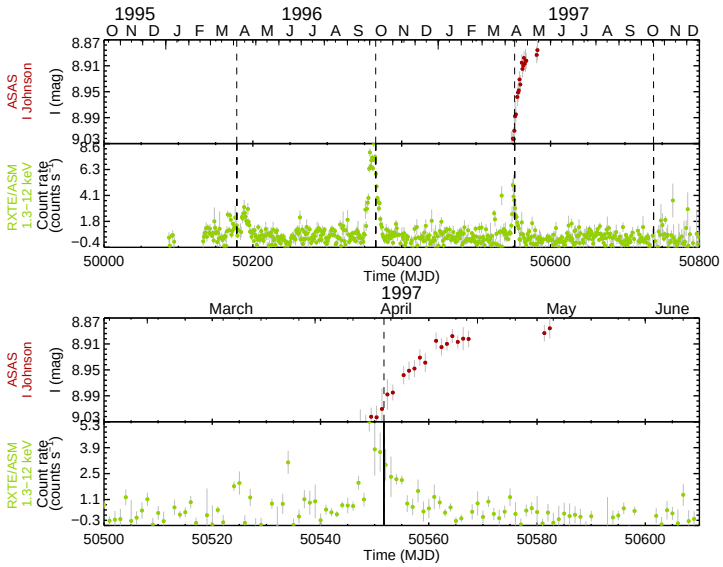

Figure 6.16: ASAS and *RXTE*/ASM light curve of H 1145–619 during its last recorded active phase. Top: ASAS and *RXTE*/ASM light curves of H 1145–619 in 1995–1997 epoch. Three outbursts, in April 1995, September 1996 and April 1997 are observed in the ASM light curve. Bottom: Zoom in the April 1997 outburst. The periastron passages were calculated using the ephemeris P_{orb} = 186.68 d; T_0 = MJD 48871.6 (see text). The light curves have been daily rebinned.

Three outbursts not reported by any other observatory have been detected by *INTEGRAL*/JEM-X and IBIS data in May 2003, June 2004 and June 2005 (see Figs. 6.18, 6.19 and 6.20). The three outbursts occurred a few days before the corresponding periastron passages, which is in agreement with the outbursts detected by Wilson-Hodge (1999) using BATSE data, within a narrow range of orbital phase (-0.1–0.1). The intensity of the outbursts decreases with time, while the duration increases from 2003 to 2005. Larger binnings were used to detect the faintest outbursts. The outburst in 2005 seems to be double-peaked in the IBIS data, but it is very faint.

Close to this source, there is another HMXB, 1E 1145.1–6141, at $\sim$ 17 arcmin from H 1145–619, and it should be noted that the IBIS angular resolution is 12 arcmin FWHM. The light curves of 1E 1145.1–6141 and the images of the source during the 2003 outburst and quiescence were extracted in order to rule out that it was actually occurring in this other source. In Fig. 6.17, images in quiescence (left) and outburst (right) during the epoch of the 2003 outburst are displayed. From top to bottom the energy bands are: 3–10 keV and 10–25 keV from JEM-X, and 20–35 keV and 35–65 keV from IBIS/ISGRI. Comparing the images in quiescence with the images in outburst, the brightening of the source in the last ones can be observed. In the JEM-X image both sources are resolved, and in the images corresponding to the outburst, two point sources are observed. However, in the IBIS images of the outburst epoch, the presence of a new source in the position of H 1145–619 is noticed, but it is blended with 1E 1145.1–6141 due to the poorer resolution.

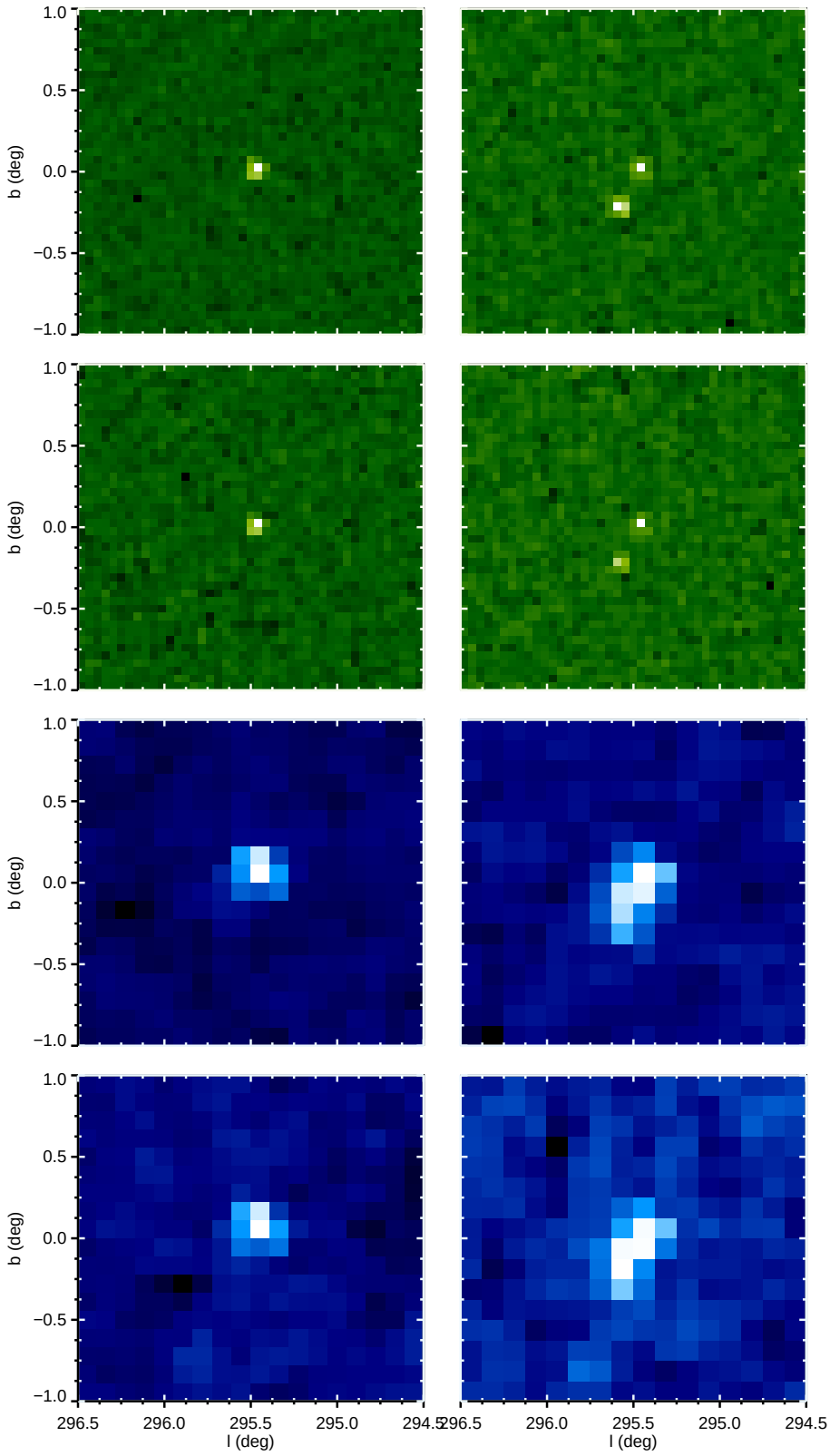

Figure 6.17: JEM-X (in green) and IBIS (in blue) images H 1145–619 in quiescence (left) and outburst (right) in the epoch of the outburst of 2003. H 1145–619 is the source locate more to the South and to the East appearing only in the images from the outburst, and the other one appearing in all the images is 1E 1145.1–6141. From top to bottom the energy bands are: 3–10 keV, 10–25 keV, 20–35 keV, and 35–65 keV. The same field has been represented for all the images.

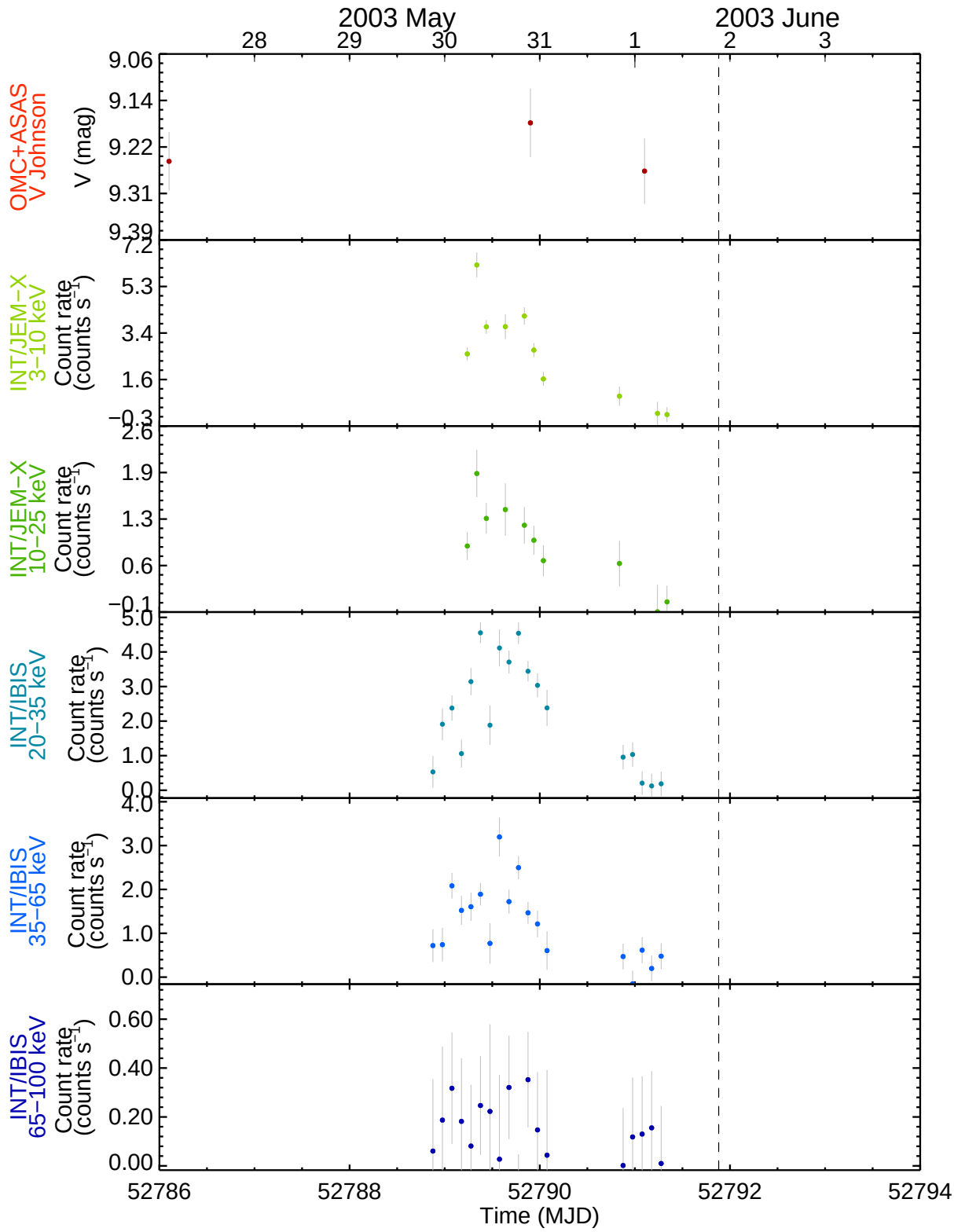

Figure 6.18: *INTEGRAL* light curves of the May 2003 outburst. ASAS photometric points (in brown) have been added to the optical light curve. The light curves have been rebinned with a 0.1 d time resolution. The periastron passage is marked with a black dashed line and was calculated using the ephemeris from Wilson-Hodge (1999) (P_{orb} = 186.68 d; T_0 = MJD 48871.6).

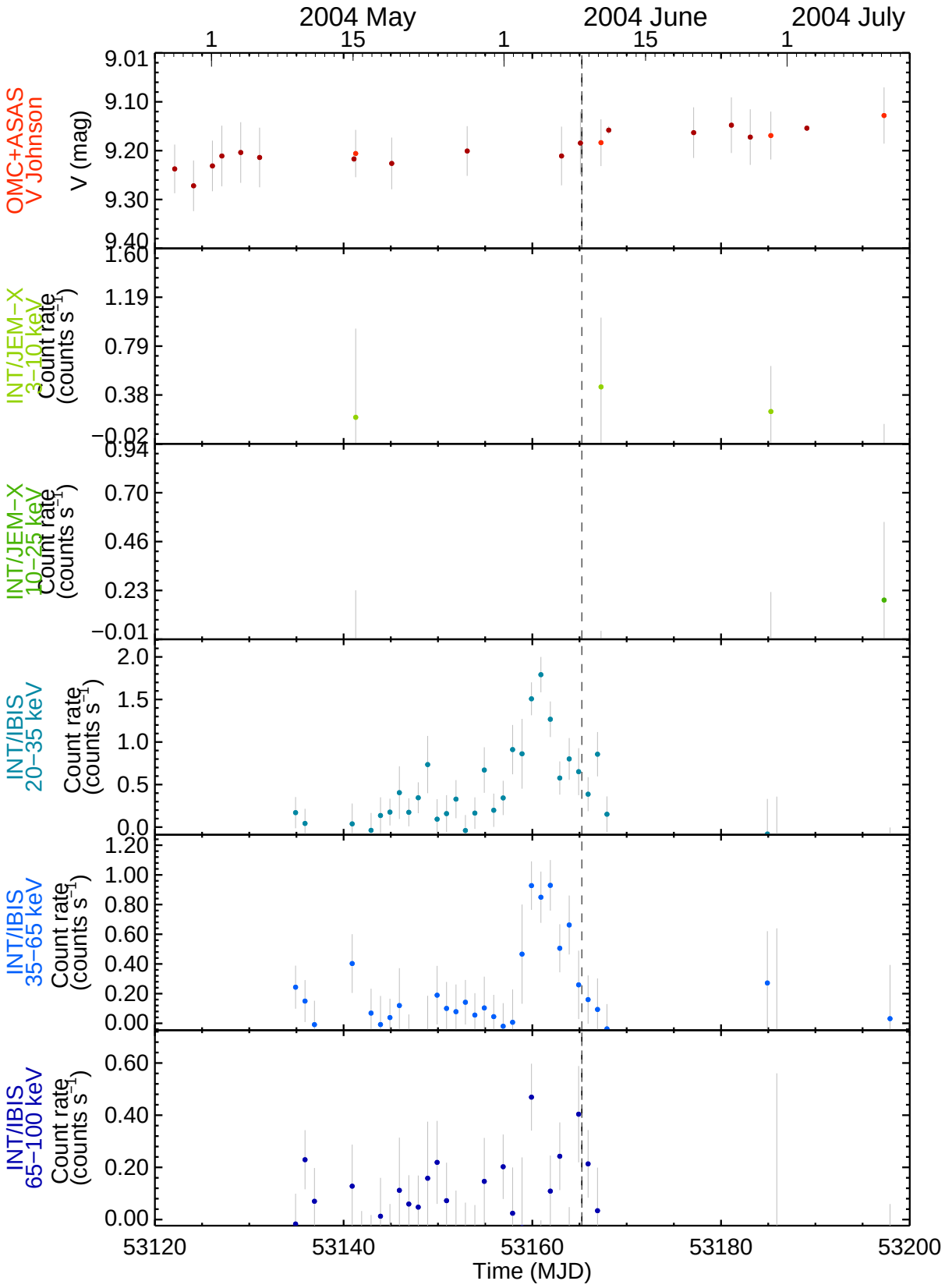

Figure 6.19: *INTEGRAL* light curves of the June 2004 outburst. ASAS photometric points (in brown) have been added to the optical light curve. The light curves have been rebinned with 1 d time resolution. The periastron passage is marked with a black dashed line and was calculated using the ephemeris from Wilson-Hodge (1999) (P_{orb} = 186.68 d; T_0 = MJD 48871.6).

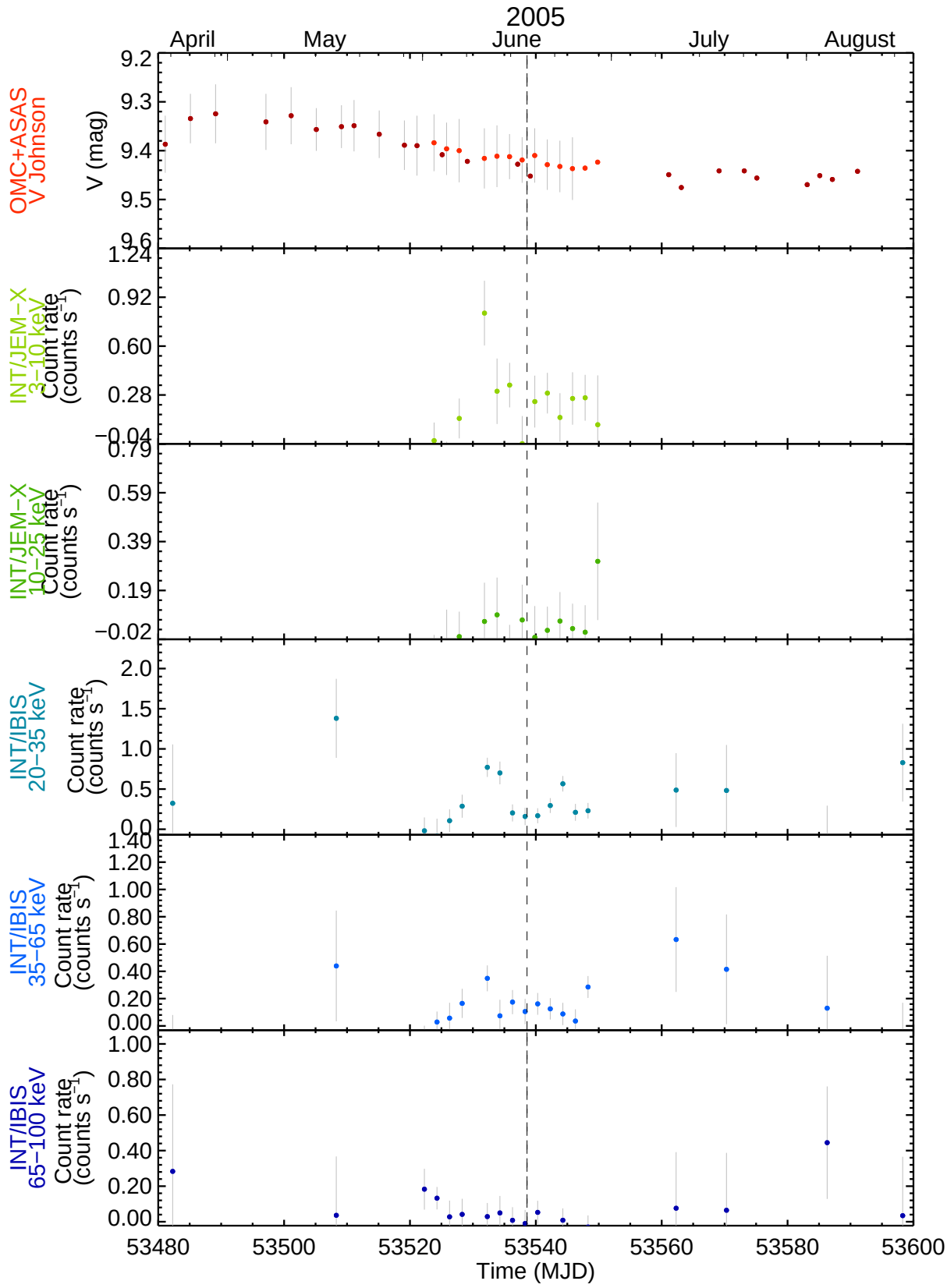

Figure 6.20: *INTEGRAL* light curves of the June 2005 outburst. ASAS photometric points (in brown) have been added to the optical light curve. The light curves have been rebinned into intervals of 2 d. The periastron passage is marked with a black dashed line and was calculated using the ephemeris from Wilson-Hodge (1999) (P_{orb} = 186.68 d; T_0 = MJD 48871.6).

The optical and high-energy light curves of this X-ray active period, from 2003 to 2005 are shown in Fig. 6.21. As commented above, in this period the optical variability is dominated by superorbital modulations. However, apart from them, three optical outbursts previous to the high-energy ones can be observed in the ASAS data. These brightenings are similar to those observed in the epoch from 1997 to 2000 (see Fig. 6.14) but with smaller amplitudes. The lags between the optical and X-ray outbursts decreases from 2003 to 2005, although these quantities are difficult to estimate with precision.

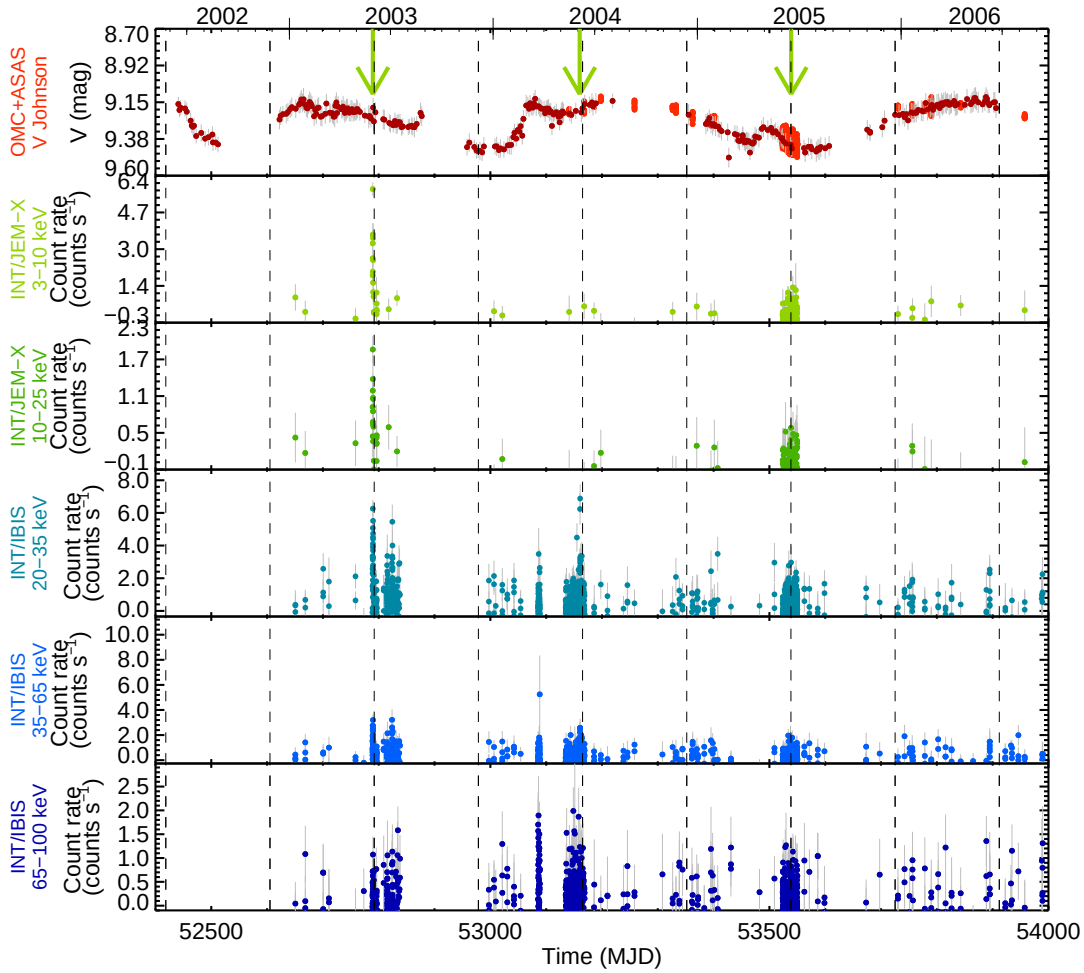

Figure 6.21: *INTEGRAL* and ASAS light curves of the overall active period of H 1145–619 reported on this work. Three optical outbursts previous to the X-ray ones can be observed in the optical light curve. The X-ray to optical lag decreases with time and with the intensity of the X-ray outbursts. The light curves have been rebinned with a 72 min time resolution. The periastron passages were calculated using the ephemeris P_{orb} = 186.68 d; T_0 = MJD 48871.6 and the X-ray outbursts detected with *INTEGRAL* data are marked with green arrows.

From 2009 to early 2015, there has been a substantial increase of the optical flux ($\sim$ 0.5 mag), probably caused by the replenishment of the disk (Okazaki & Negueruela, 2001; Haigh et al., 2004). In the last recorded active epoch of the source, Stevens et al. (1997) showed optical photometry simultaneous to the X-ray flares observed in that epoch, being these outbursts coincident with the optical fadings from magnitudes around 8.8 to 9.2. These values are close to the values H 1145–619 is reaching lately and an X-ray active period could take place in the near future. Indeed, in the last periastron passage observed (MJD 57081), an outburst has been measured by MAXI and *Swift*/BAT (see Fig 6.22, Mihara et al. 2015). The next periastron

passage will happen approximately on 7 September 2015 (Wilson-Hodge, 1999) and a new X-ray outburst would be expected. According to this work, an optical outburst should take place around three months before the X-ray outburst, and continuous optical monitoring of the source would be of interest. It is difficult to give an explanation for the very variable optical behavior of this source and its relation with the observed X-ray outbursts and a more detailed analysis is required. In order to do that, we plan to perform Hα monitoring of the source with SMARTS[7].

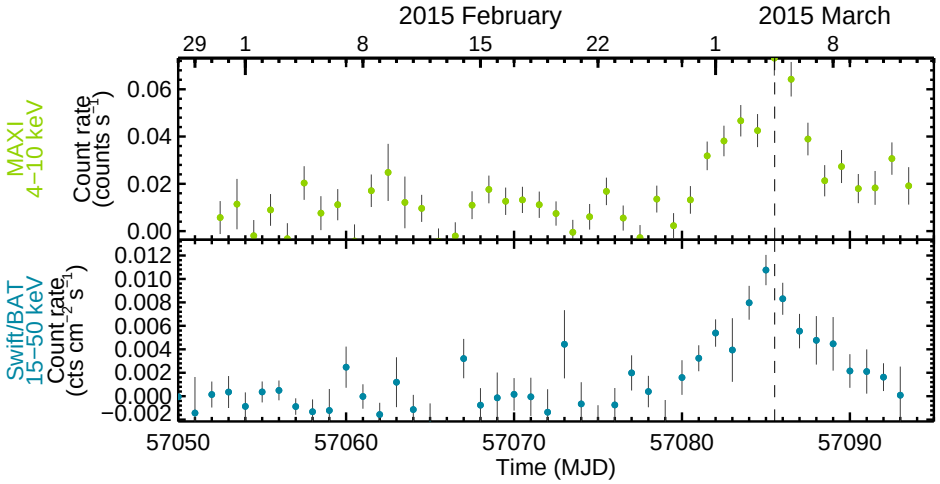

Figure 6.22: Last activity of H 1145–619 observed by MAXI and *Swift*/BAT. An outburst took place at the beginning of Mach 2015 coincident with the periastron passage. This was calculated using the ephemeris P_{orb} = 186.68 d; T_0 = MJD 48871.6 (see text). The light curves have been daily rebinned.

6.3.4 Cyg X–1

Cygnus X–1 is one of the most famous HMXBs and was the first identified stellar-mass black hole (Webster & Murdin, 1972; Bolton, 1972). The black hole pulls material from its massive companion, an O9.7 Iab star. The stellar wind of the donor star forms an accretion disk that rotates around the black hole before falling into it or being redirected away from the black hole in the form of powerful jets. Cyg X–1 is classified as a microquasar. As explained in Chapter 2, these objects are called microquasars because of their similarities with AGN, suggesting a common mechanism of energy generation involving a black hole, an accretion disk and jets.

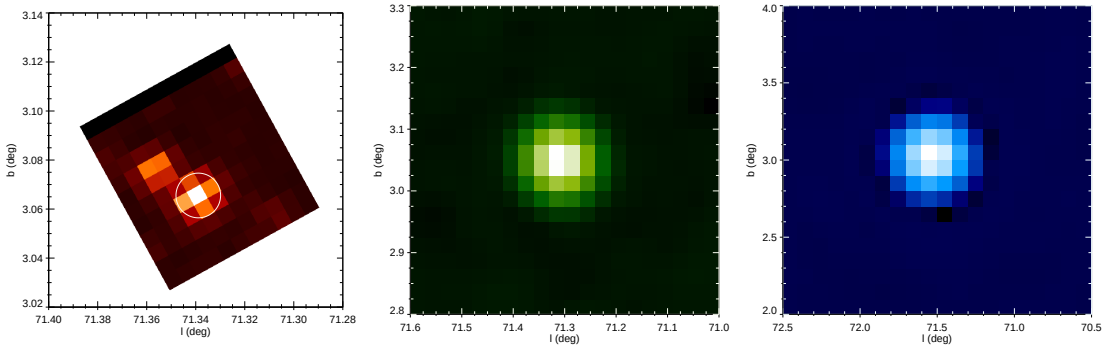

Figure 6.23: Left: OMC image of Cyg X–1. The white circle represents approximately the area where the optical photometry is extracted. **Middle:** JEM-X image of Cyg X–1 in the 3.0–25 keV energy band. **Right:** IBIS/ISGRI image of Cyg X–1 in the 20–100 keV energy band. North is up and east is to the left. Note the different image scales for each instrument.

[7] http://www.astro.yale.edu/smarts/

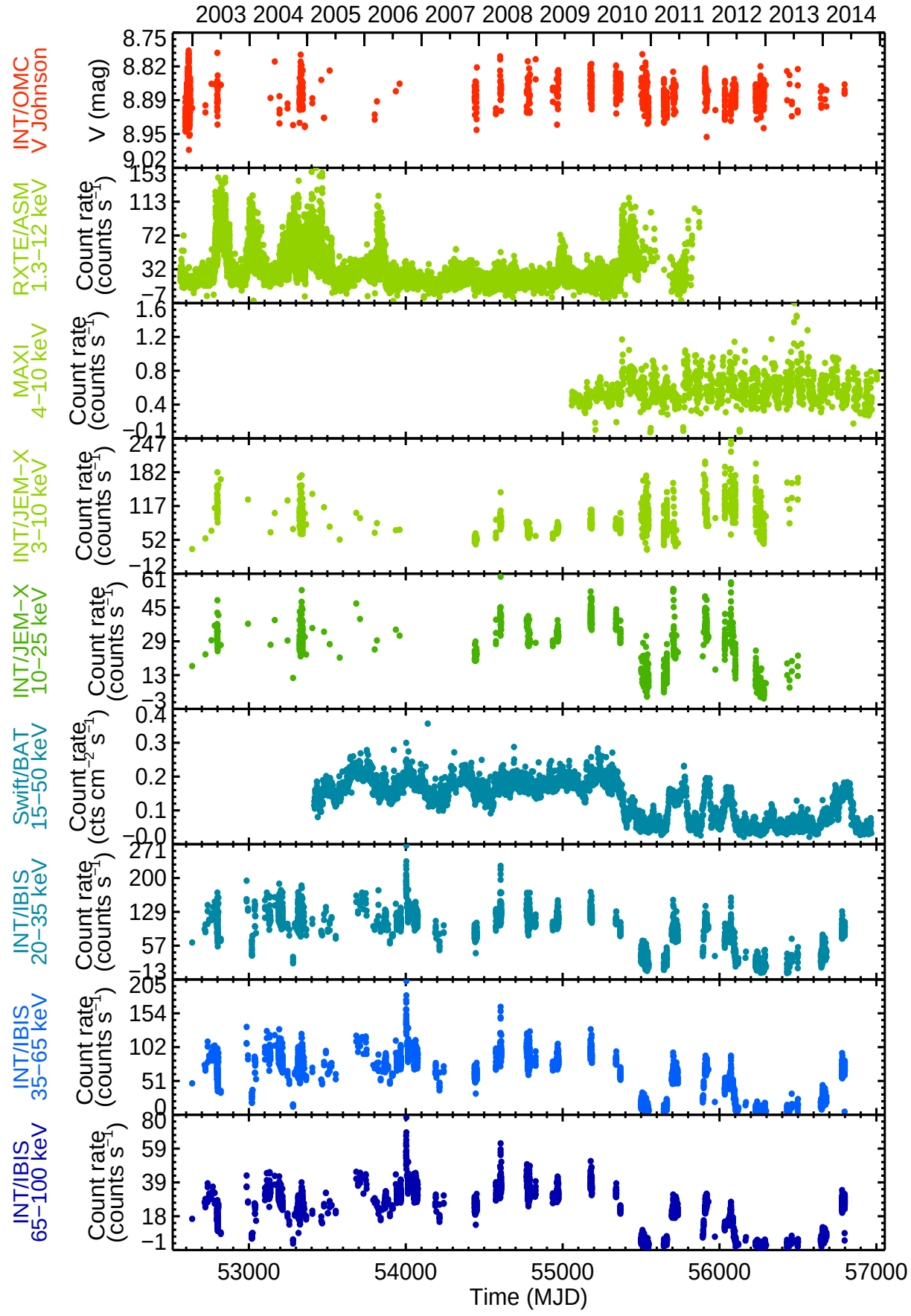

Figure 6.24: Light curves of Cyg X–1 along the 12 years in which this microquasar has been observed by *INTEGRAL*. The light curves have been rebinned with a 72 min resolution interval.

Cyg X–1 has been reported by many observers to undergo frequent short and long-term variations (Gleissner et al., 2004; Grinberg et al., 2013). The orbit of Cyg X–1 is slightly eccentric (e = 0.018; Orosz et al. 2011) and the system has an orbital period of $P_{orb} = 5.599829 \pm 0.000016$ d (Brocksopp et al., 1999). The low-amplitude (0.04–0.05 mag) quasi-sinusoidal (5.6 d) variations commonly seen in the optical light curves are due to ellipsoidal modulations arising from the tidal distortion of the donor star. These are superimposed on long-term variations with time scales of months to years (Karitskaya et al., 2000, 2001; Barron et al., 2002; Siah et al., 2007). The X-ray data also exhibit variations with the orbital period (Boroson & Vrtilek, 2010; Grinberg et al., 2015) and show transitions between two distinct X-ray spectral states (Zdziarski et al., 2002; Skipper et al., 2013; Grinberg et al., 2013). Some authors have searched for correlations between the spectral states and the variations found in the optical light curves (Barron et al., 2002; Siah et al., 2007).

The *INTEGRAL*, *RXTE*/ASM, MAXI, and *Swift*/BAT light curves are shown in Fig. 6.24. The X-ray light curves trace the different spectral states of the source. The *RXTE*/ASM, MAXI and *INTEGRAL*/JEM-X light curves are well correlated and anticorrelated with the *Swift*/BAT and *INTEGRAL*/IBIS ones. The optical variations in Cyg X–1 are mainly driven by ellipsoidal modulations. Apart from these, other mechanisms produce variability in different timescales. As explained in Section 2.3.1, variable X-ray heating due to changes in the spectral state of the system can introduce an extra optical variability.

Grinberg et al. (2013) determined the spectral states of Cyg X–1 from 1996 to 2012 using data from *RXTE*/ASM, MAXI, *Swift*/BAT, and *Fermi*/GBM. These authors provided criteria to define X-ray states (distinguishing between hard, intermediate, and soft states) and conclude that the hard state is the most stable of Cyg X–1, followed by the soft state. From MJD 51000 to 53900, the source alternates hard, intermediate, and soft states. From MJD 53900 to 55375 they observed that the source was in hard state almost all the time. However, from MJD 55375 to 56240, the source is most of the time in the soft state.

The relation between the optical variations and the spectral state of Cyg X–1 has been studied. Optical residuals, obtaining by subtracting the ellipsoidal variations modeled by Orosz et al. (2011) from the data have been calculated. These authors determined very accurately the orbital parameters of Cyg X–1 and provided an eclipsing light curve (ELC) model, which Dr. Orosz gently provided us for this analysis. The results are shown in Fig. 6.25 and the black line corresponds to the model by Orosz et al. (2011). This modeled light curve was subtracted from all the observed OMC data, and the absolute values of the residuals are shown in Fig. 6.25. To avoid phase dependence of the residuals, these have been rebinned with time-resolution equal to the orbital period. Blue points correspond to the periods in which Cyg X–1 is mainly in its low/hard state (from MJD 53900 to 55375, according to Grinberg et al. 2013), while red has correspond to the other states.

The residuals from the ellipsoidal variations and the fluxes, hardness and spectral state obtained from ASM and MAXI data, provided by Victoria Grinberg and calculated according to Grinberg et al. (2013), are plotted for comparison in Fig. 6.26. The boundaries defined in Grinberg et al. (2013) to delimit the different spectral states for Cyg X–1 are shown with dashed lines. The amplitude of the optical variations traced as the residuals from the ellipsoidal model, are smaller in the period from 2006 to 2010 (MJD 53900 to 55375). In this period, the source is mostly in the low/hard state. Larger optical residuals are found in other epochs, when the source is mainly in the soft state or changing of spectral states.

The extra optical variations can be explained by differential X-ray heating of the donor star producing a larger gradient between the two faces of the supergiant. The hardness of Cyg X–1 can change rather dramatically on very short timescales because of the changing absorption produced by clumpy winds, while the optical variations are expected to be slower, because of the time needed to change the temperature of the inner face of the star. For this reason, a

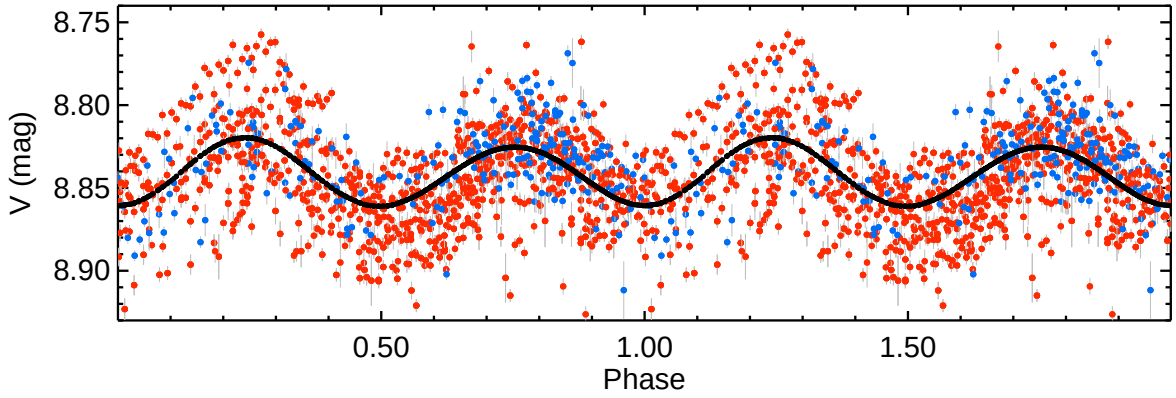

Figure 6.25: OMC folded light curve of Cyg X–1 folded with the orbital period given by Brocksopp et al. (1999). Black line represents the eclipsing light curve (ELC) model derived by Orosz et al. (2011) which has been subtracted from the OMC data.

direct correlation between the spectral state and the optical amplitude of the variations is not expected. However, the long-term trend of the spectral state can affect the optical behavior. When the spectral state is driven by the relative contribution of the powerlaw with respect to the contribution of the disk, the changes are expected to take longer times and then be more related to the optical changes. So the observed long-term optical behavior would only be explained by the general trends of the spectral state and not by fast changes of the spectral state.

According to this analysis, it seems that Cyg X–1 is more variable in its soft state. In order to study the averaged behavior, the folded light curves in the hard and in the soft state have been rebinned. These light curves have been fitted with a double sinusoidal wave using the expression:

$$V = V_{\rm mean} + A\cos(4\pi\phi) \tag{6.1}$$

with ϕ being the phase, and the zero phase corresponding to the inferior conjunction of the system. These results are shown in Fig. 6.27. The results of the fits are:

$$V_{\rm hard} = (8.8367 \pm 0.0003) + (0.0199 \pm 0.0004)\cos(4\pi\phi) \tag{6.2}$$

for the hard state and

$$V_{\rm soft} = (8.8424 \pm 0.0001) + (0.02143 \pm 0.0002)\cos(4\pi\phi) \tag{6.3}$$

for the soft state. This confirms the fact that in the soft state the amplitude of the variations is larger. On the other hand, according to these results, the source is slightly brighter in the hard state and it happens in all the orbital phases. It could be related to emission from the jet, but the available data do not allow to extract more conclusions.

Finally, a search for superorbital periodicities in the optical data has been performed. Several works have found a 150-d superorbital modulation in X-ray and radio emission, which seems to be connected with precession and/or radiative warping of the accretion disk (Brocksopp et al., 1999; Özdemir & Demircan, 2001; Ibragimov et al., 2007). The frequency spectrum of the residual OMC data have been derived using PERIOD04 (Lenz & Breger, 2004), and two periods of 12.731 d and 27.027 d have been found with amplitudes 0.014 and 0.010 respectively, but no hints of the $\sim$ 150 d period have been found.

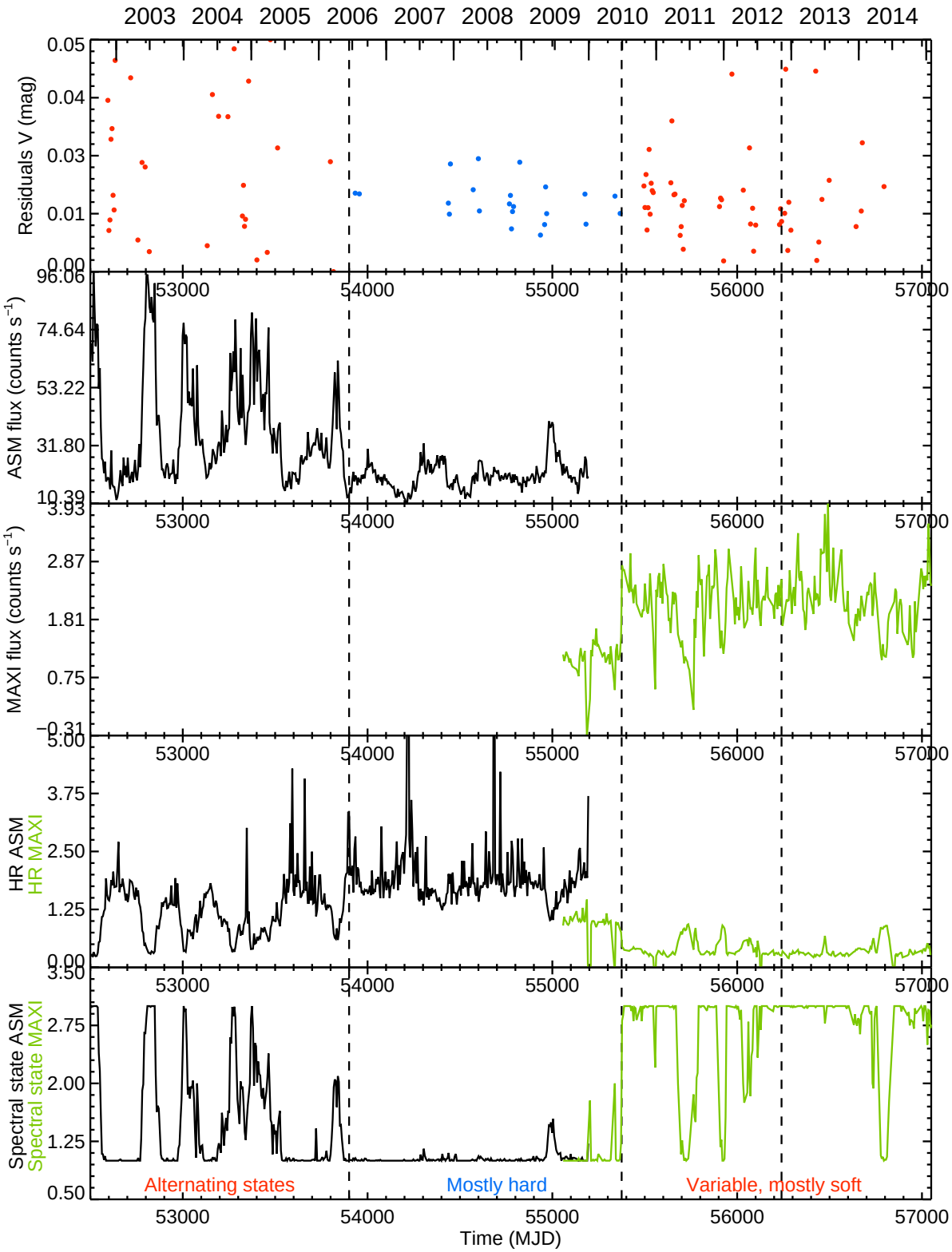

Figure 6.26: From top to bottom: Non-ellipsoidal optical variations of Cyg X–1 calculated as the residuals of the OMC light curve after subtracting the orbital model. In both plots, blue points have been used for the period mainly low/hard (from MJD 53900 to 55375) and red for the rest, according to Grinberg et al. (2013). Total ASM flux (1.3-12 keV), total MAXI flux (2–20 keV), ASM and MAXI hardness ratios and spectral states provided by Victoria Grinberg according to the criteria used in Grinberg et al. (2013). The black and green light curves represent the values obtained from ASN and MAXI data respectively.

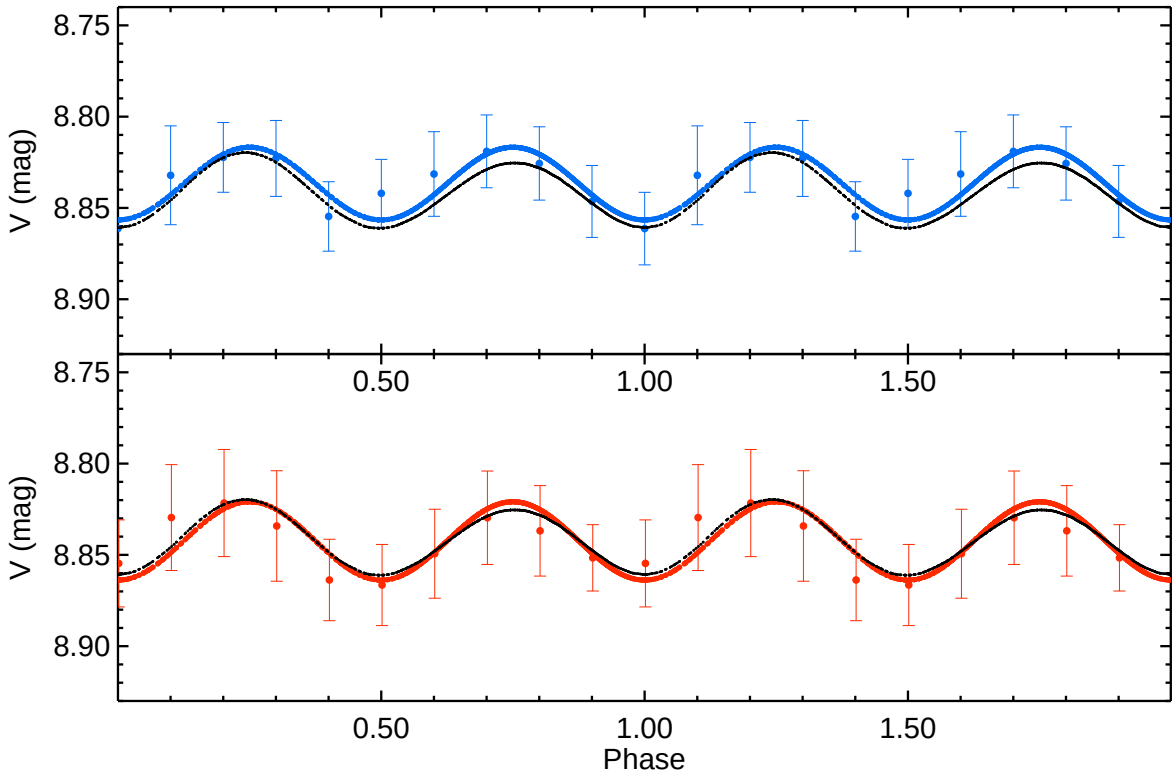

Figure 6.27: Averaged optical folded light curves of Cyg X–1 in the hard (top) and soft (bottom) states. OMC light curve of Cyg X–1 folded with the orbital period given by Brocksopp et al. (1999). The blue and red solid lines represent the fit for the hard and soft folded light curves respectively (see text). The black lines represent the eclipsing light curve (ELC) model derived by Orosz et al. (2011) and has been plotted for comparison.

6.3.5 Her X–1

Her X–1 was one of the first two X-ray pulsars discovered by the Uhuru satellite in 1972 (Tananbaum et al., 1972). It is a LMXB, formed by a neutron star accreting material from an A7V type star, HZ Her. Updated values of the orbital ephemeris of Her X–1 are given in Staubert et al. (2009b): $T_{\pi/2}$ = MJD 46 359.871940 and P_{orb} = 1.700167590 d . These authors measure a continuous change of the orbital period of dP_{orb}/dt = -(4.85 ± 0.13) × 10^{-11} s s^{-1}.

The accreting X-ray pulsar Her X–1 shows two types of long-term variations, observed in X-rays, both with a period of ∼ 35 days: a modulation of the flux with an 'on-off' cycle (with a 10 d main-on and a 5 d short-on states), separated by two 10 d off-states (Tananbaum et al., 1972) and a systematic variation of the shape of the 1.24 s pulse profile (Scott et al., 2000). They both change with an average period of 34.98 d (Staubert et al., 2013) and have traditionally been explained by the precession of the accretion disk and the neutron star. In this way, the precessing outer part of the accretion disk regularly would block the line of sight to the X-ray emitting polar caps of the neutron star, thereby producing the turn-off cycle, while the free precession of the neutron star would be the responsible for the orientation of the beamed X-ray emission, thereby producing the periodic modulation of the shape of the observed pulse profiles. Staubert et al. (2013) found that the clock behind the pulse profile variations shows exactly the same erratic behavior as the turn-on clock, even on short time scales (a few 35 d cycles), suggesting that there may in fact be only one 35 d clock in the system.

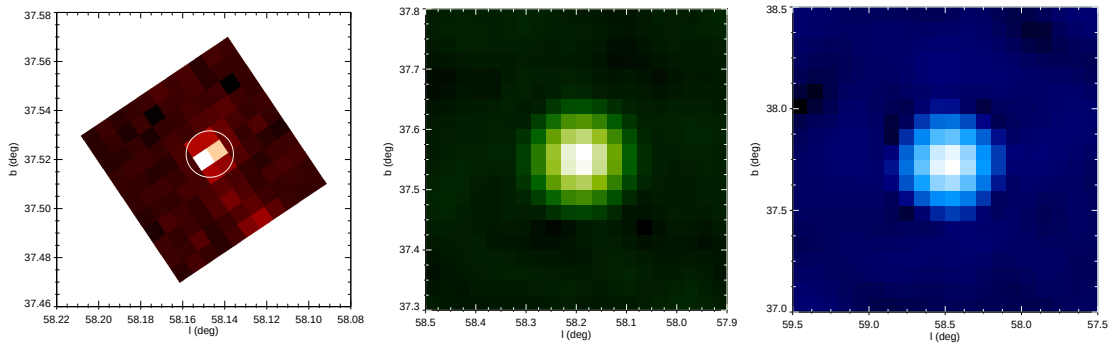

Figure 6.28: Left: OMC image of Her X–1. The white circle represents approximately the area where the optical photometry is extracted. **Middle:** JEM-X image of Her X–1 in the 3.0–25 keV energy band. **Right:** IBIS/ISGRI image of Her X–1 in the 20–100 keV energy band. North is up and east is to the left. Note the different image scales for each instrument.

The *INTEGRAL*, *RXTE*/ASM, and MAXI light curves of Her X–1 from 2003 to 2014 are shown in Fig. 6.29. The optical light curve is dominated by X-ray heating of the companion star and eclipses of the accretion disk and of the heated face of HZ Her produced by the tilted precessing accretion disk (Gerend & Boynton, 1976). It presents similar features to those in Fig. 2.11 d. The 35 d periodic variations can be seen in the *RXTE*/ASM, MAXI and *Swift*/BAT light curves in Fig. 6.30.

A zoom inside one 35 d cycle is shown in Fig. 6.31. Within the overall changes in the X-ray light curves, the orbital effects can be observed in all the energy bands. In the optical light curve, the modulations are dominated by the orbital effect.

The light curves corresponding to a main-on phase are shown in Fig. 6.32. The eclipses of the neutron star and the accretion disk associated with the optical view of the cooler face of HZ Her are shown in Fig. 6.31 and Fig. 6.32. In the optical light curve in the main-on state, secondary eclipses produced by the occultation of the heated face of HZ Her by the accretion disc are also seen. These secondary eclipses are not observed in the off states. Indeed, the shape of the folded optical light curve varies with the 35 d phase (as seen in Jurua et al. 2011) and it would be interesting to study if these variations are related to the features observed in the X-ray light curves.

Her X–1 also exhibits rapid and variable X-ray absorption features, called dips. Some dips properties depend on Her X–1's 35 d X-ray cycle and some others seem to be related to the orbital phase. These rapid variations can be observed in Fig. 6.32.

As can be seen in Fig. 6.33 the optical pattern varies with the 35 d cycle, showing different shapes depending on the variations of the X-ray heating. An interesting work on the variations of the optical flux and their relation with the X-ray flux was performed by Jurua et al. (2011).

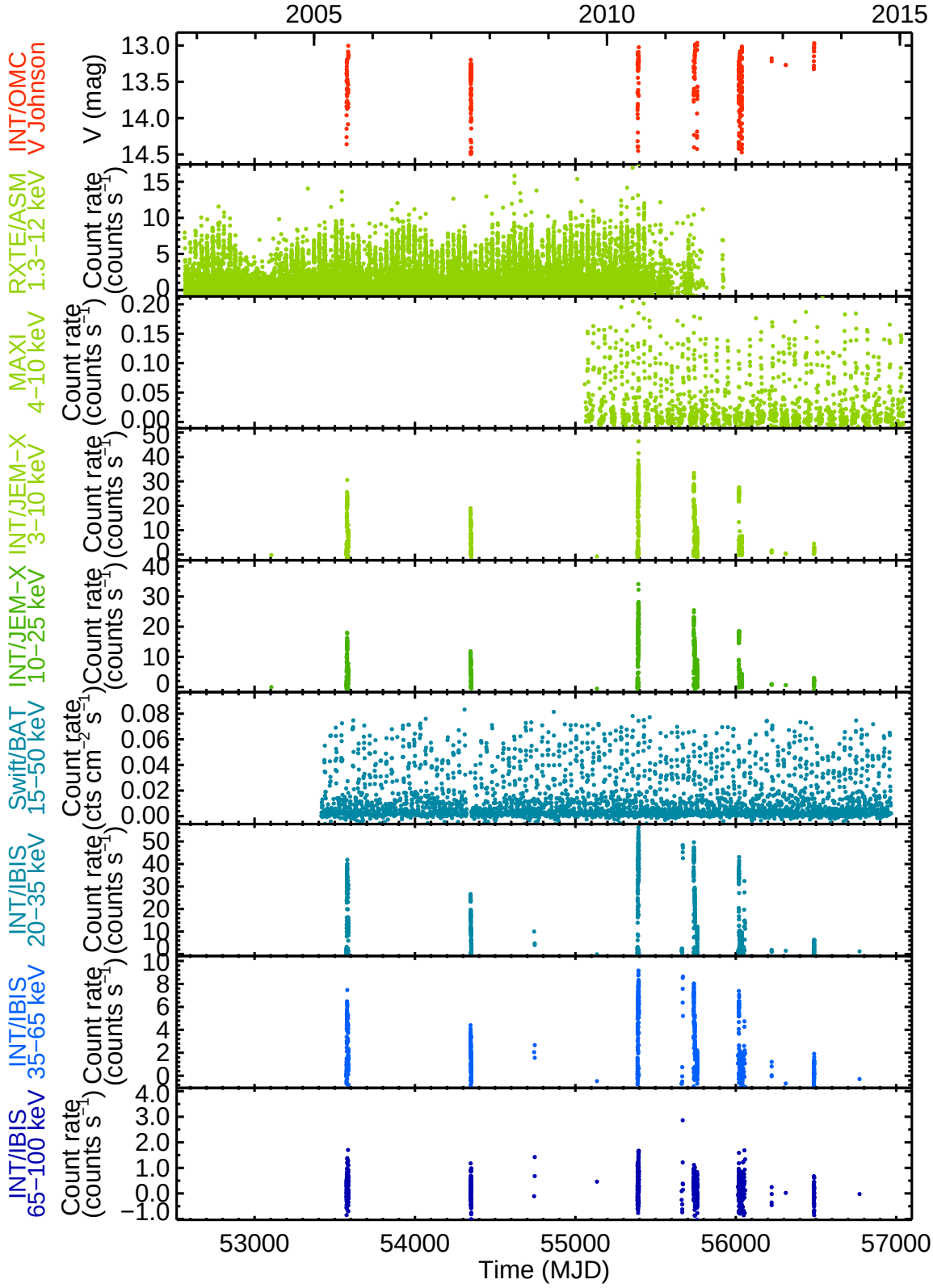

Figure 6.29: Light curves of Her X–1 along the 12 years in which Her X–1 has been observed by *INTEGRAL*.

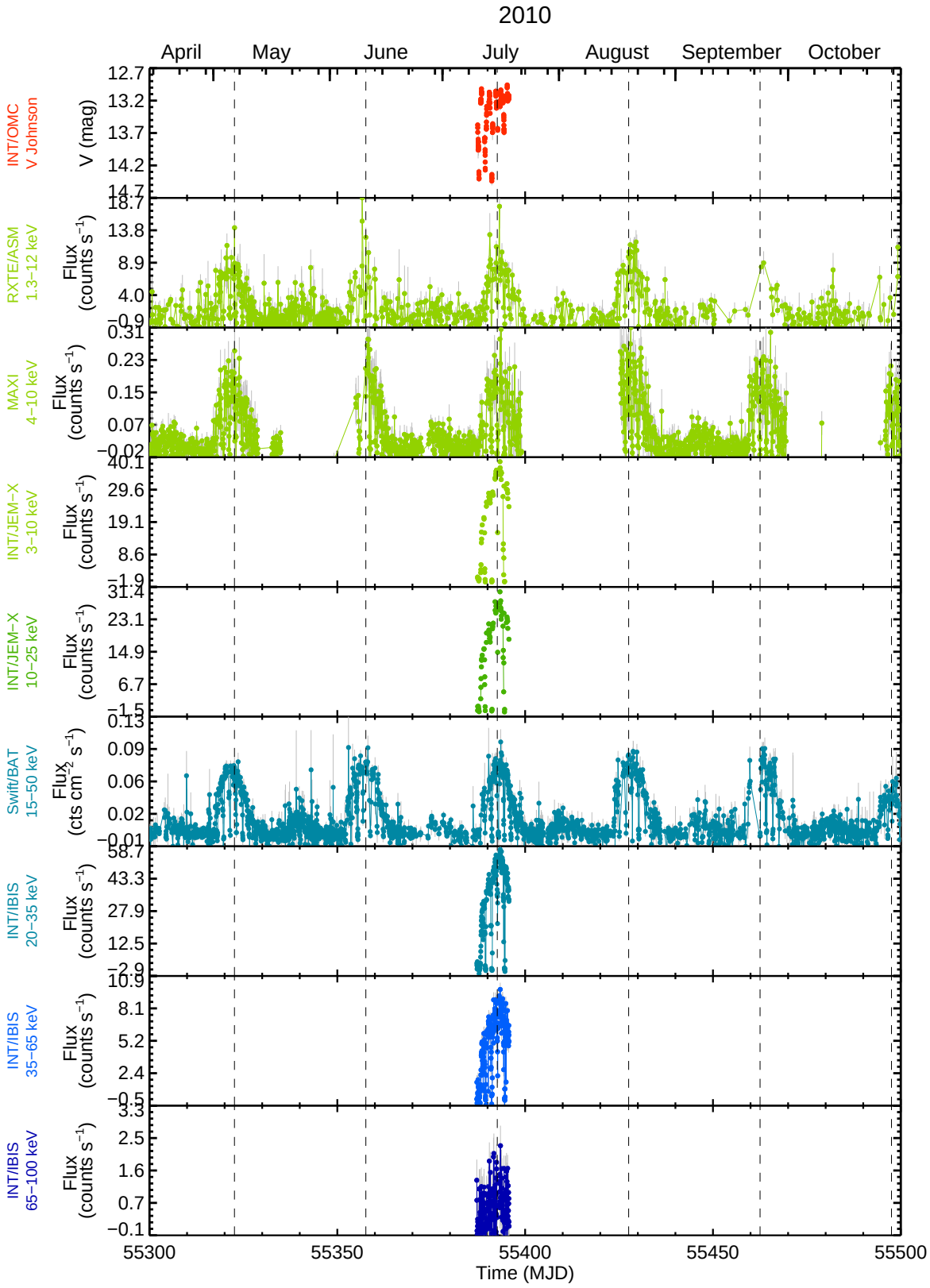

Figure 6.30: Light curves of Her X–1 in the MJD 55600 to 55900 interval. The 35 d variations and the cycle of the 10 d main-on and 5 d short-on states separated by two 10 d off states are shown in the *RXTE*/ASM, MAXI and *Swift*/BAT light curves. The turn-on times of the 35 d cycle from the ephemeris from Staubert et al. (2013) ($T_{0,35\,d}$=MJD 50285.5 and $P_{35\,d}$=34.98 d) are overplotted.

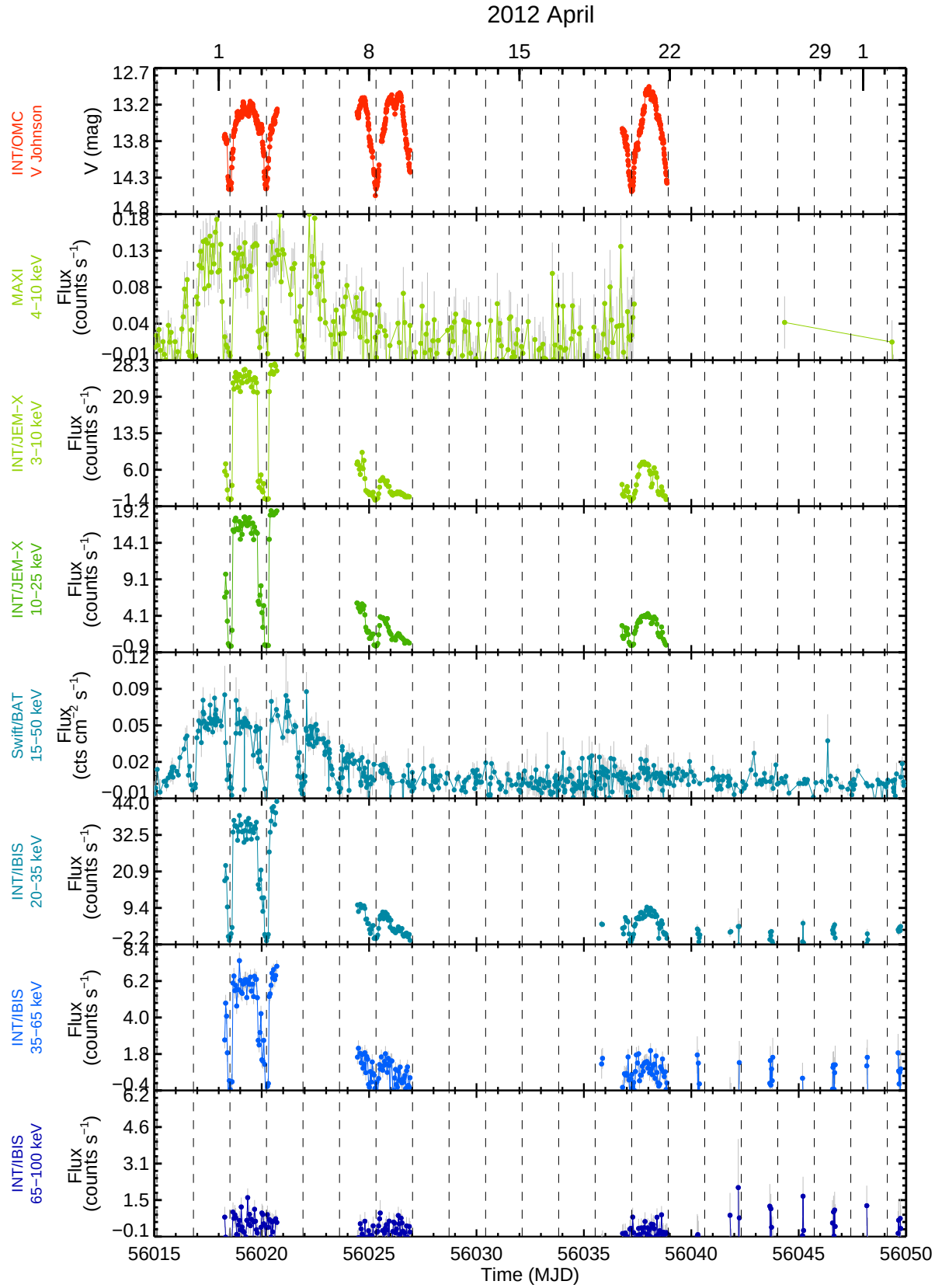

Figure 6.31: Light curves of Her X–1 inside a 35 d cycle, from MJD 56015 to 56050. The occultation times from the ephemeris given by Staubert et al. (2009b) are overplotted.

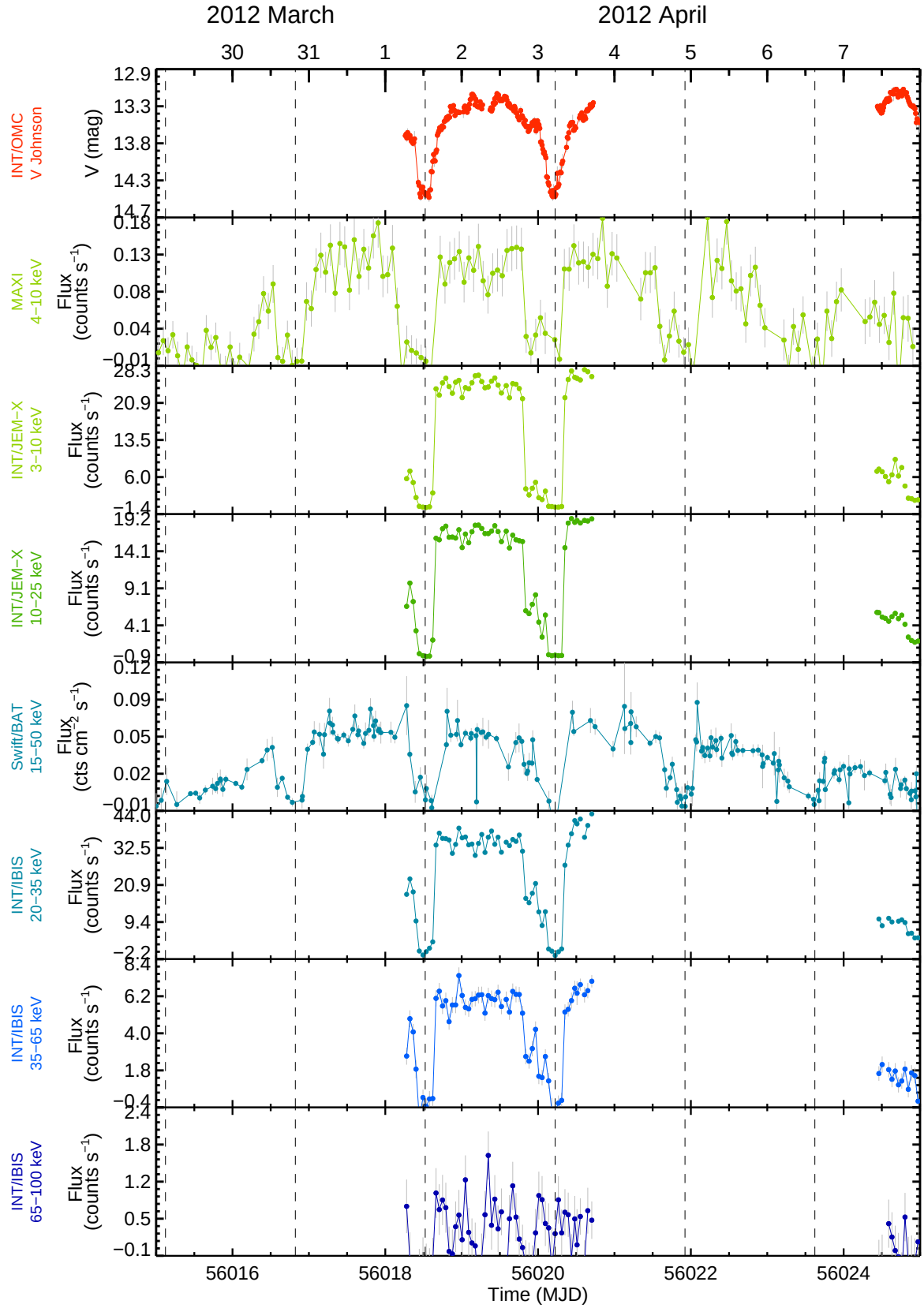

Figure 6.32: Light curves of Her X–1 in the MJD 56015 to 56025 interval. The occultation times from the ephemeris given by Staubert et al. (2009b) are overplotted.

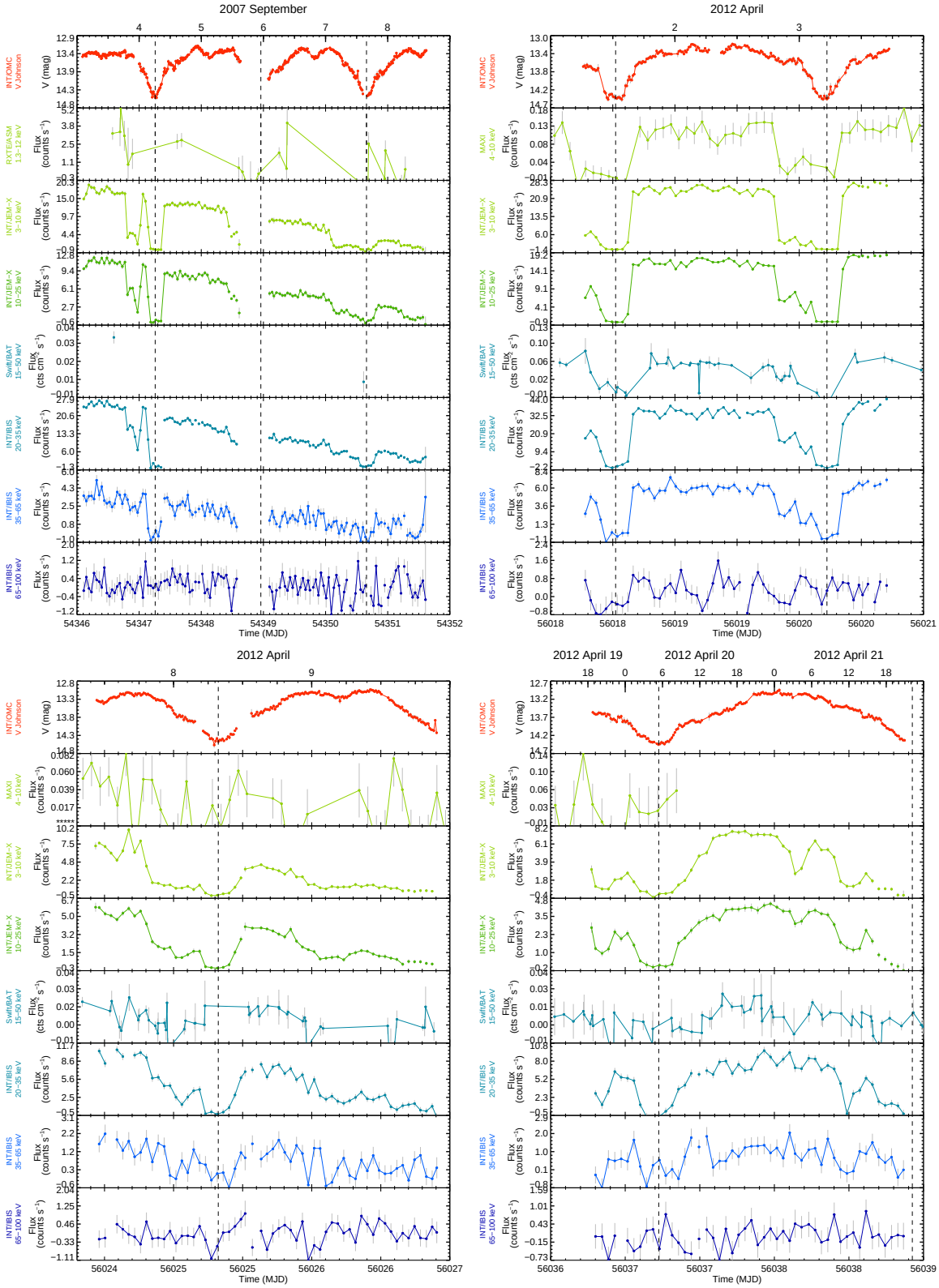

Figure 6.33: Light curves of Her X–1 in epochs corresponding to different phases of the 35 d period. As the X-ray flux varies, the optical pattern changes due to the variable X-ray heating on the accretion disc and the donor star.

6.3.6 Mrk 421

Mrk 421 is a very known bright BL Lac object (Ulrich 1973; Colla et al. 1975) of the high-frequency-peaked type and a strong source of gamma-rays (Ulrich, 1973; Colla et al., 1975). This is one of the closest (z=0.0308) and brightest blazars of the sky and was the first AGN detected at TeV energies (Punch et al., 1992).

The OMC, JEM-X, and IBIS images are shown in Fig. 6.34. This blazar is clearly detected by the three instruments. Although Mrk 421 is an extended source, the OMC photometry comes from the active nucleus and not from all the galaxy. Since the optical variability is expected to come from the AGN, this loss of flux from the hosting galaxy does not affect the variability analysis.

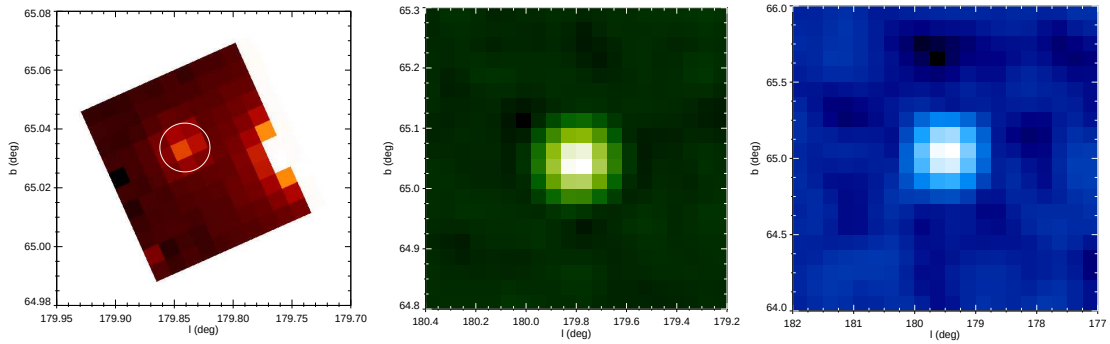

Figure 6.34: Left: OMC image of Mrk 421. The white circle represents approximately the area where the optical photometry is extracted. **Middle:** JEM-X image of Mrk 421 in the 3.0–25 keV energy band. **Right:** IBIS/ISGRI image of Mrk 421 in the 20–100 keV energy band. North is up and east is to the left. Note the different image scales for each instrument.

The *INTEGRAL* light curves for the last 12 years are shown in Fig. 6.35. The *R*-band light curve from the monitoring program of the MAGIC consortium, the *RXTE*/PCA, and the *Fermi*/LAT light curves have been included as well. As can be seen in the *R*-band light curve, Mrk 421 is very variable in the optical range, with timescales of hundreds of days and amplitudes of tenths of magnitude. This source also shows variability in soft X-rays, as can be seen in the *RXTE*/PCA light curve, and in gamma rays, as observed in the *Fermi*/LAT light curve. Indeed, the gamma ray peaks detected in 2011–2012 occurred in the highest optical state.

Mrk 421 has been observed by OMC in three epochs as a result of *INTEGRAL* ToOs of the programme for *INTEGRAL* follow-up of blazars in outburst. Different behaviors in the optical with respect to the high-energy emission were observed in each epoch.

The first *INTEGRAL* ToO observation of Mrk 421 was triggered by an active state starting in April 2006. *INTEGRAL* observations were performed in 14–25 June 2006 (MJD 53902–53911). Mrk 421 was detected by OMC, JEM-X, and IBIS with a significance up to 160σ between 20–50 keV Lichti et al. (2007, 2008). The *INTEGRAL* light curves corresponding to that epoch are shown in Fig. 6.36. Whereas the optical light curve measured by OMC scatters around a mean value of 13.05 mag, four strong flares are observed at hard X-rays by IBIS, the strongest one a factor of 4 more intense than the quiescent level of $\sim$ 3 counts s^{-1}. These flares were clearly detected by the JEM-X instrument as well.

The second ToO observation of Mrk 421 was triggered in response to an intense flaring detected at TeV energies by the VERITAS Cherenkov telescopes[8] on 2 May 2008 (MJD 54589). The *INTEGRAL* light curves corresponding to this epoch are shown in Fig. 6.37. The observations are divided in two parts, because they had to stop for one day due to observing constraints.

[8] http://veritas.sao.arizona.edu/

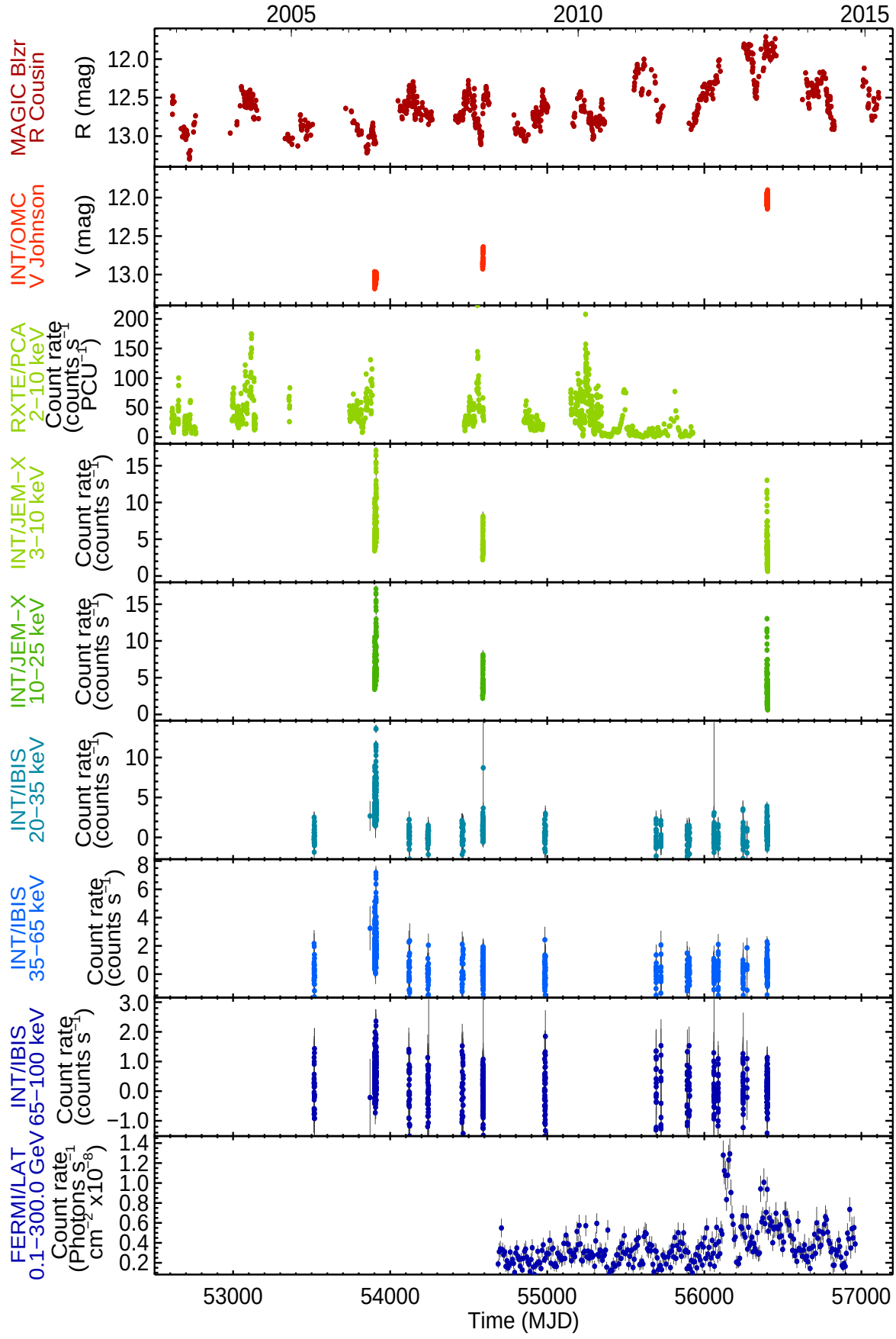

Figure 6.35: *INTEGRAL*, *RXTE*/ASM, *Swift*/BAT and *Fermi*/LAT light curves for Mrk 421. Fluxes have been daily rebinned, except *Fermi*/LAT curves that are weekly rebinned.

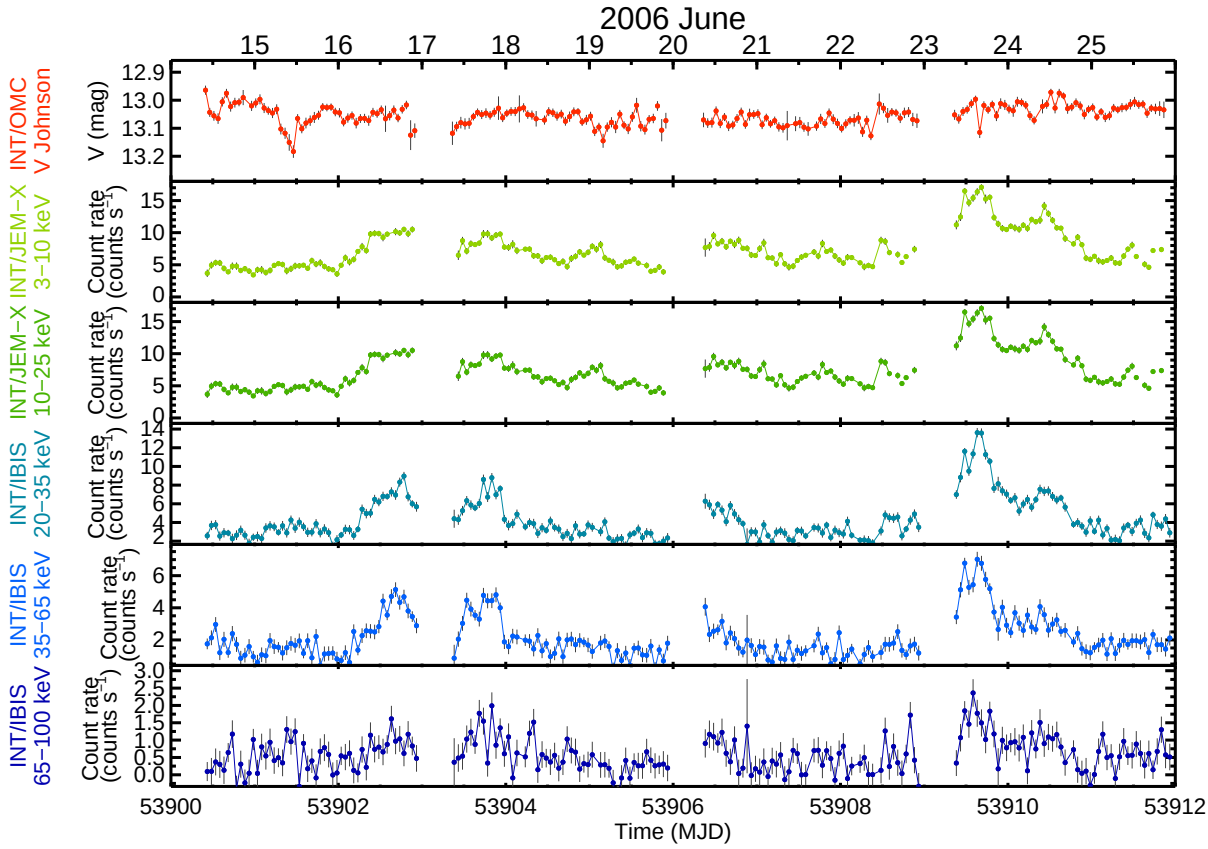

Figure 6.36: Light curves of Mrk 421 in June 2006. Fluxes have been binned with 72 min time-resolution.

The OMC light curve presents a steady increase in the first two days and then remains constant, showing a mean optical magnitude of 12.77 mag. The JEM-X light curves also show a brightening in the first two days, and after that, the JEM-X fluxes were fainter and constant. The IBIS light curves do not show any significant trend, except a slight increase in the flux in the 20–35 keV band coincident with the optical and soft X-ray ones.

In 2013, Mrk 421 underwent a prolonged state of high activity, with a peak around January 2013, and revived episodes in April 2013. This activated the third ToO and Mrk 421 was observed in 16–21 April (MJD 56398–56403) with the IBIS, JEM-X, and OMC instruments. The results of this campaign are presented in Pian et al. (2014). The *INTEGRAL* light curves are shown in Fig. 6.38. Two flares are detected by the three instruments, the first one on 17 April 2013 and the second one on 20 April 2013. The peak and early decay of the 17 April flare is found to be quasi-simultaneous in all X-ray bands, while in the OMC light curve a delay of $\sim$ 0.5 days is observed. The second flare suggests a similar trend in the two light curves of JEM-X, but the IBIS signal is not significant. Again, a lag of $\sim$ 0.5 days is observed in the optical emission. These lags point to the optical emission being due to reprocessing of the X-rays by material close to the AGN, but not immediately around it.

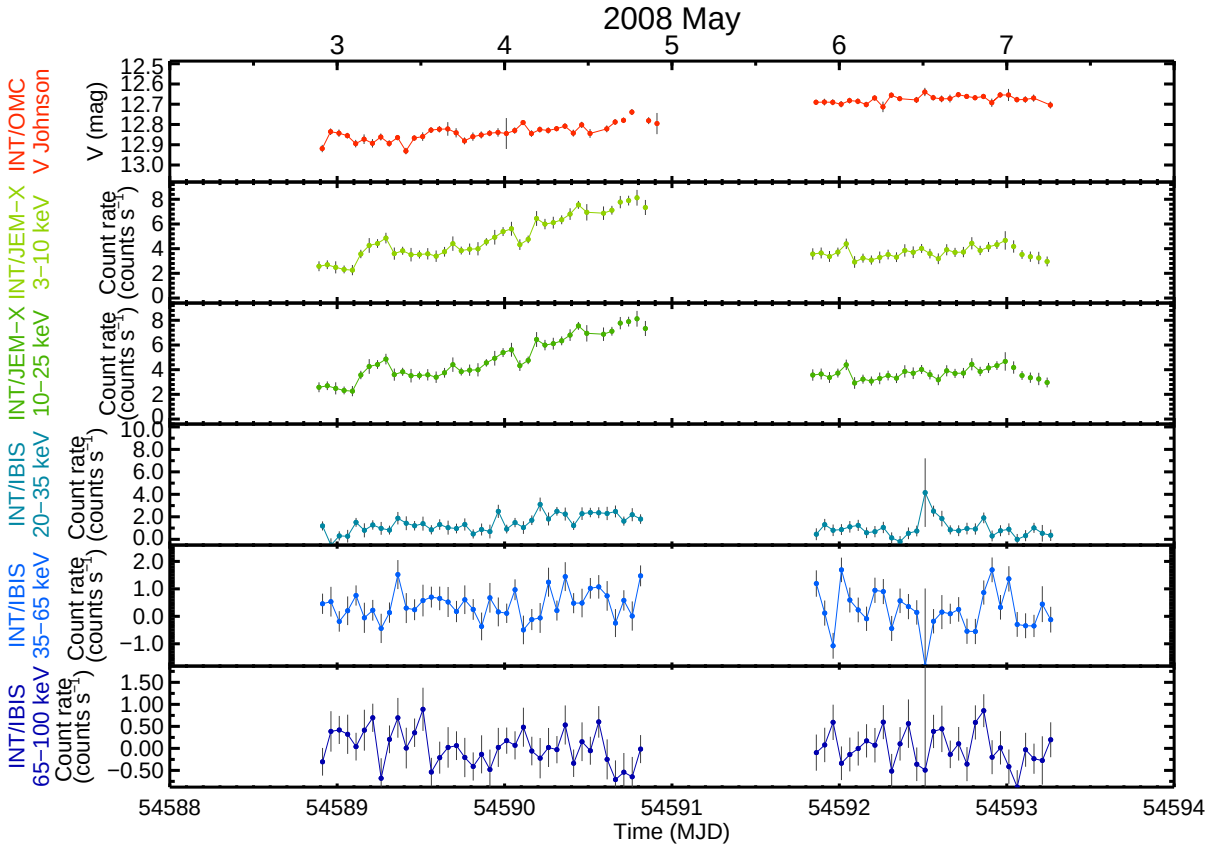

Figure 6.37: Light curves of Mrk 421 in May 2008. The light curves have been binned with 72 min time-resolution.

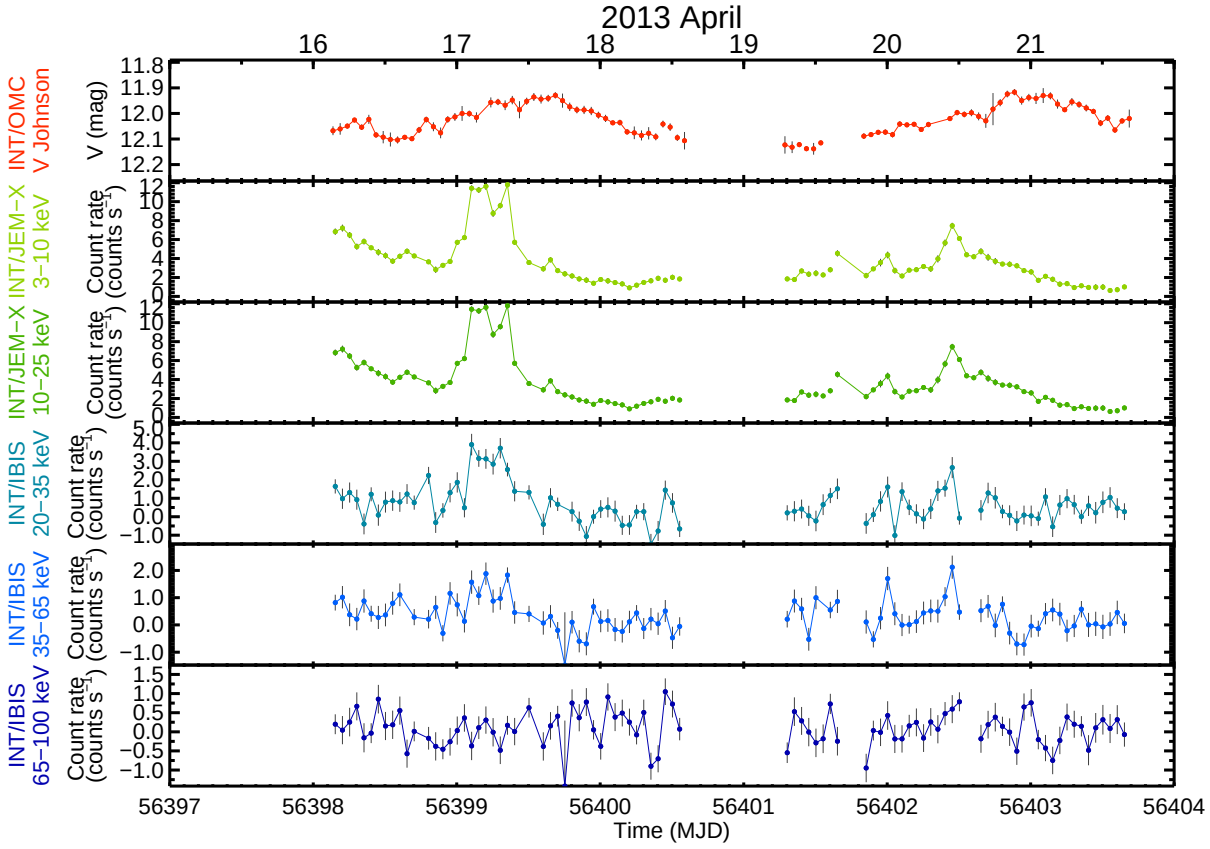

Figure 6.38: *INTEGRAL* light curves of Mrk 421 in April 2013. The light curves have been binned with 72 min time-resolution.

6.3.7 3C 279

The optically violent variable quasar (OVV) 3C 279 (z=0.538) was the first quasar in which apparent superluminal motion was detected (Whitney et al., 1971). It is known for its variations in the visible, radio, and X-ray bands, and is also one of the most bright and variable sources in the gamma-ray sky (Hartman et al., 1992).

The OMC, JEM-X, and IBIS images are shown in Fig. 6.39. This object is compact at optical wavelengths, so the OMC photometry includes all the light coming from the whole galaxy.

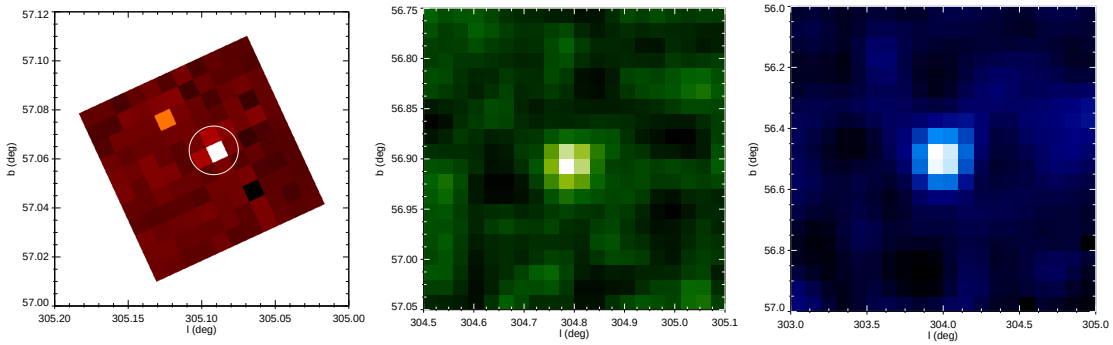

Figure 6.39: Left: OMC image of 3C 279. The white circle represents approximately the area where the optical photometry is extracted. **Middle:** JEM-X image of 3C 279 in the 3.0–25 keV energy band. **Right:** IBIS/ISGRI image of 3C 279 in the 20–100 keV energy band. North is up and east is to the left. Note the different image scales for each instrument.

The R-band light curve from the monitoring program of the MAGIC consortium, the *INTEGRAL*, *RXTE*/PCA, and *Fermi*/LAT light curves are displayed in Fig. 6.40.

The cataloged magnitude of 3C 279 in the low state is $V = 17.8$ mag (Eachus & Liller, 1975; Miller et al., 2011). However, as can be seen in the R-band light curve, 3C 279 varies dramatically in the optical band, in which it shows optical photometry in the range of R=12.8–18.0 mag. These kind of variations have been found on many different timescales, from 0.5 yr to several hours (Kartaltepe & Balonek, 2007). The source was barely detected in June 2003 with OMC, with a 2σ detection at $V = 17.0$. After May 2005 and in 2006 this blazar reached a brightness in the range $V = 14.8$–15.8 mag, which means that it brightened by up to a factor close to ~ 10.

In 2006–2007, 3C 279 was in a very active state, as can be observed in the R and in the *RXTE*/PCA light curves. There was a giant optical flare at the beginning of 2007 that might be related to the observed X-ray flares observed in this epoch (see Aleksić et al. 2011).

From 2008 to 2010, this blazar is almost in quiescence in X-rays and the optical flux decreases but with small flares during its fading. Some activity is also detected in gamma rays in the *Fermi* light curve.

INTEGRAL ToO observations of 3C 279 were carried out in August 2009 as a response to the high-energy activity detected by *Fermi* (Iafrate et al., 2009). The *INTEGRAL* observations confirmed the target as a hard X-ray source with a steep spectral slope of power-law index 1.3, the hardest one measured by *INTEGRAL* yet (Iafrate et al., 2009). An optical brightness of 15.8 mag was measured from our observations at this time.

From 2011 to 2015, small variations are observed in the R light curve with a mean brightness of $R \sim 15$ mag. In December 2013, an intense gamma-ray flare from this source was detected by *Fermi*/LAT (Buson, 2013) and in April 2014 the brightest gamma-ray outburst ever observed for 3C 279 was detected by the same instrument (Errando 2014, see Fig. 6.40). Unfortunately, OMC and JEM-X did not observe this blazar during the past few years and no remarkable activity was detected by IBIS during its observations in December 2013.

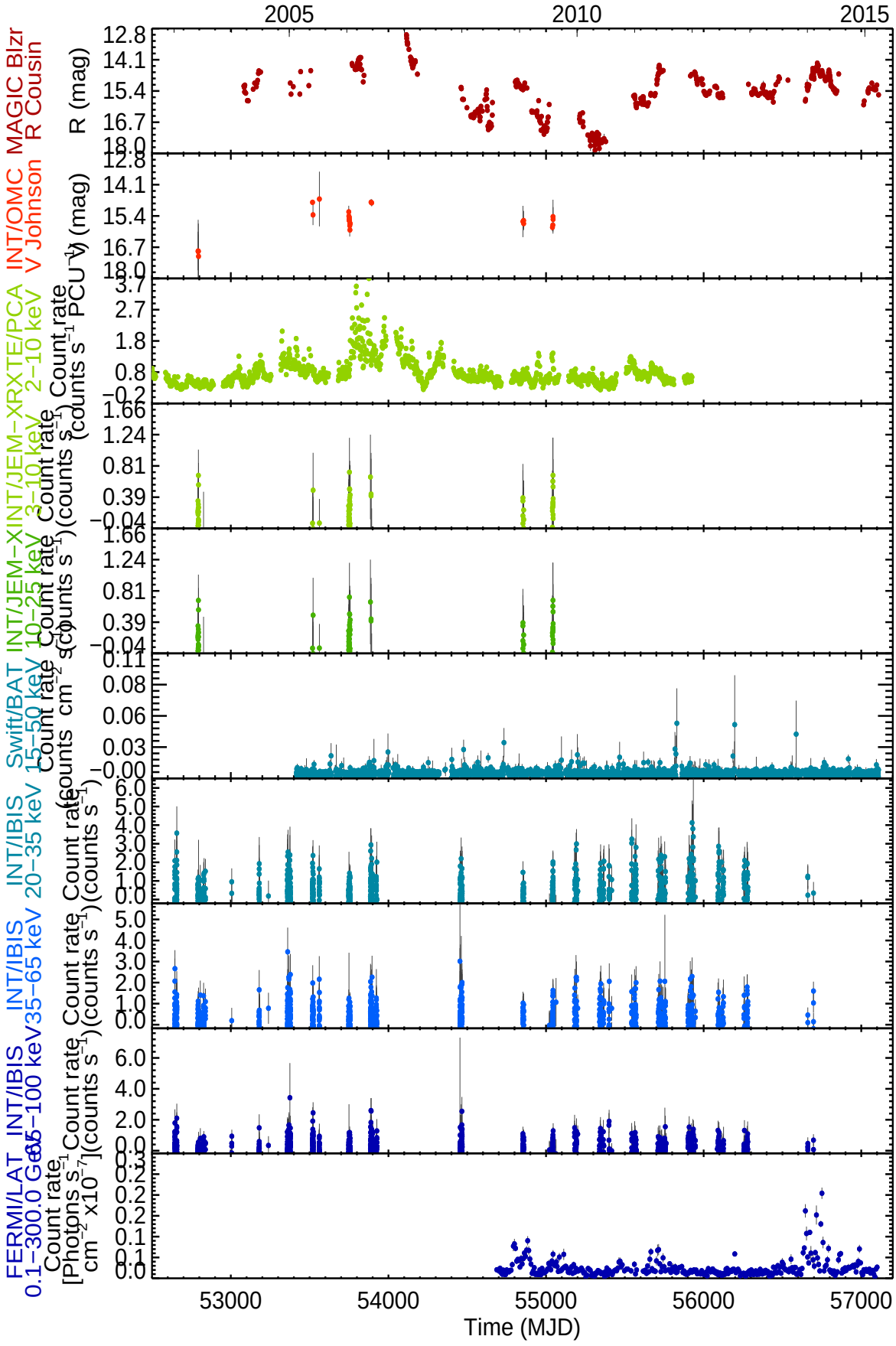

Figure 6.40: Light curves of 3C 279. *INTEGRAL* and *RXTE*/PCA fluxes have been binned with 1 day time-resolution and *Fermi*/LAT data have been weekly rebinned.

6.3.8 S5 0716+714

The BL Lac S5 0716+714 belongs to the bright flat-spectrum subsample of the S5 catalog (Kuehr et al., 1981). It presents rapid (from minutes to years) and large amplitude variation (Villata et al., 2004; Wu et al., 2007). S5 0716+714 is a distant BL Lac with a redshift of 0.31±0.08 (Nilsson et al., 2008). This source has been classified as an intermediate-peaked blazar (IBL) by Giommi et al. (1999), as the frequency of the first SED peak varies between 10^{14} and 10^{15} Hz, and thus does not fall into the wavebands specified by the usual definitions of low and high energy peaked blazars (i.e. LBLs and HBLs; see 2.3.2). S5 0716+714 is a VHE gamma-ray BL Lac and is also among the brightest blazars observed by *Fermi*/LAT.

It has been found that the broadband flaring activity of the source is not simultaneous at all the energy ranges, showing slow modes of variability at radio and hard X-ray bands and rapid variability in the optical, soft X-ray, and gamma-ray bands. The simultaneous optical-GeV variations point to a Synchrotron Self-Compton (SSC) mechanism (Chen et al., 2008), but the X-ray spectrum can be explained by Synchrotron and Inverse Compton (IC) emission (Foschini et al., 2006). An interesting radio to gamma-ray variability study of this blazar is performed by Rani et al. (2013).

The variations that occur within one night (minutes to several hours) are known as intraday variability (IDV) or microvariability (Wagner & Witzel, 1995; Bachev et al., 2012) and had been previously observed in this blazar (Gupta et al. (2009); Rani et al. (2010); Zhang et al. (2012); Hu et al. (2014) and references therein). Gupta et al. (2009) analyzed the intraday optical variability of the source and reported good evidence of nearly periodic oscillations ranging between 25 and 73 minutes on different nights. Zhang et al. (2012) found intraday variability in 162 nights of the 208 nights they analyzed, and they found the source varied with a 11.5-min timescale. Rani et al. (2010) detect the presence of 15-min periodic oscillations at optical frequencies. Hu et al. (2014) found a mild trend of having larger variability amplitude in the intranight variations in V and R bands, when the source was getting fainter. Long-term variability and possible variability mechanisms have been studied by Liao et al. (2014) using simultaneous multiband observations.

The OMC, JEM-X, and IBIS images of the source are shown in Fig. 6.41. S5 0716+714 is compact at optical wavelengths and the photometry extracted with OMC corresponds to the integrated optical blazar emission. This source is faint in soft and hard X-rays as can be seen in the JEM-X and IBIS images.

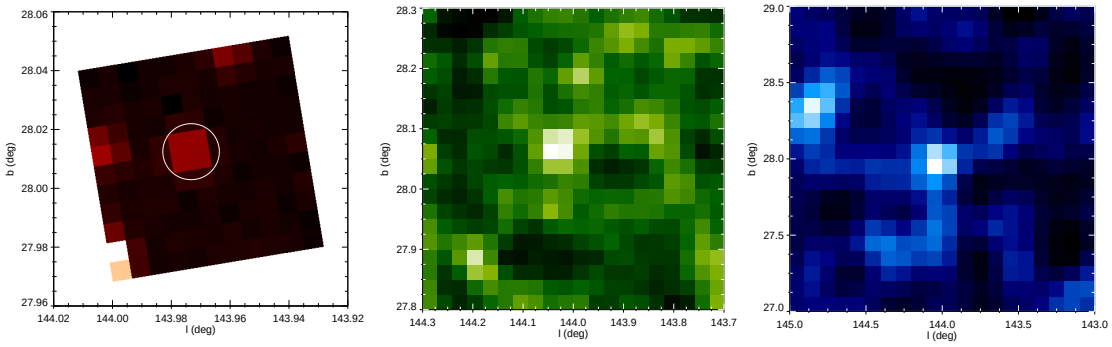

Figure 6.41: Left: OMC image of S5 0716+714. The white circle represents approximately the area where the optical photometry is extracted. **Middle:** JEM-X image of S5 0716+714 in the 3.0–10 keV energy band. **Right:** IBIS/ISGRI image of S5 0716+714 in the 20–100 keV energy band. North is up and east is to the left. Note the different image scales for each instrument. This source is very faint in X-rays.

The *INTEGRAL* light curves, the R-band light curve from the monitoring of MAGIC sources, and *Fermi*/LAT light curves for the last 12 years are shown in Fig. 6.42. In the R light curve, S5 0716+714 displays very violent optical activity, in timescales of days/months and amplitudes

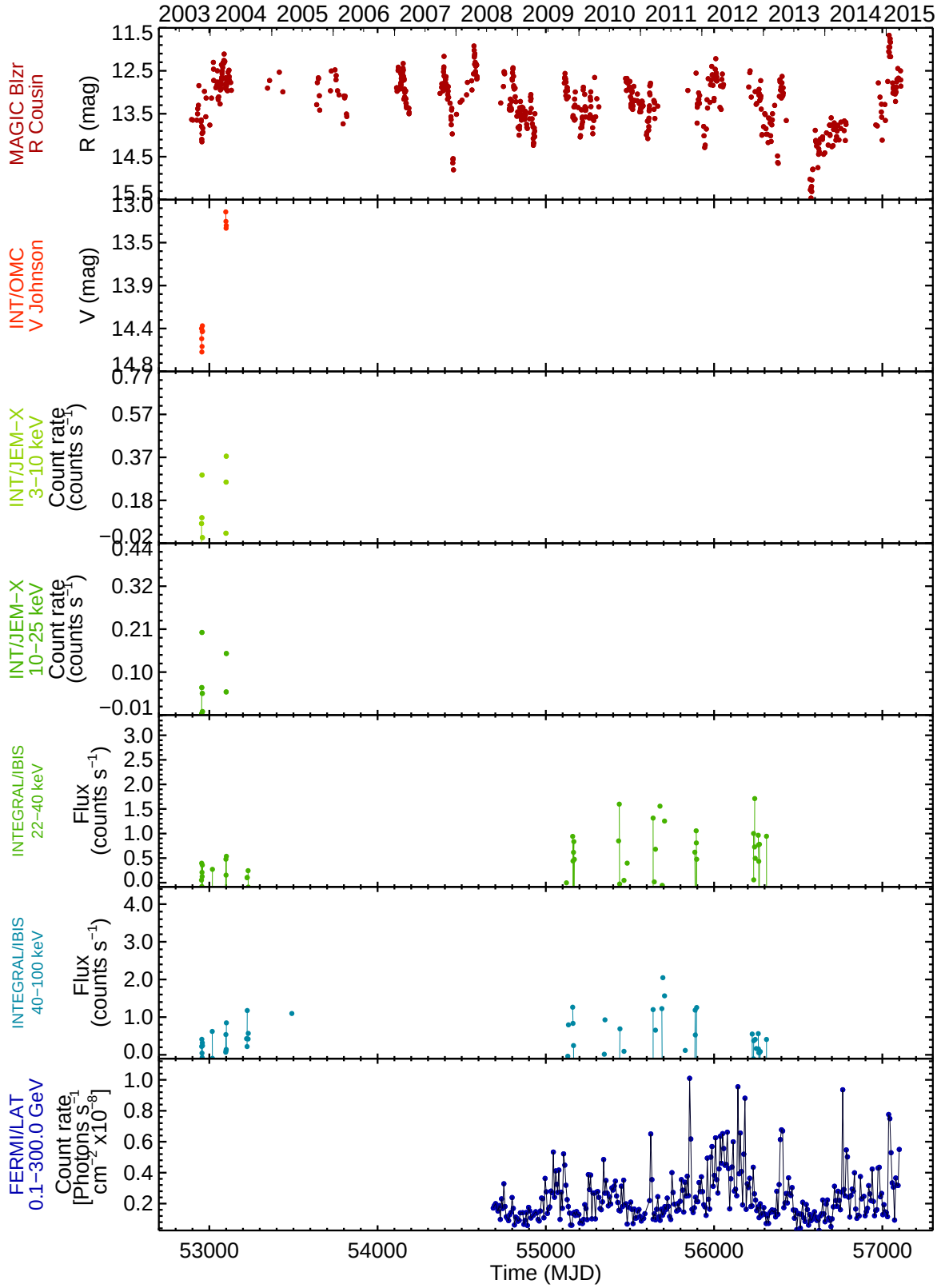

Figure 6.42: *INTEGRAL* and *Fermi*/LAT light curves of S5 0716+714 during the last 12 years. OMC observed this blazar in two active states, in November 2003 and in April 2004 (see text). *INTEGRAL* data are daily rebinned and *Fermi*/LAT data are weekly rebinned.

up 3 magnitudes. This blazar also appears very active in gamma rays in the *Fermi*/LAT light curve. However, it seems more quiet in soft and hard X-rays, as can be observed in the JEM-X and IBIS light curves.

This blazar has been observed by *INTEGRAL* several times, but OMC only observed it in two epochs. The first one was on 10–17 November 2003 during a very active radio state (Ostorero et al., 2006). OMC measured a mean magnitude of 14.45 during this period. The second time was while the blazar was undergoing a major optical outburst. In the first months of 2004, the source increased steadily in optical brightness and in January and March 2004, S5 0716+714 was in outburst and achieved its optical historical maximum until that moment. In late March 2004 it brightened by 2 magnitudes with respect to the November 2003 level, and by 1 magnitude in $\sim$ 2 weeks, reaching a magnitude of 12.1 in the optical R-band, which triggered an *INTEGRAL* ToO. *INTEGRAL* observed the target on 2–6 April 2004, where it was detected with IBIS/ISGRI up to 60 keV, with a flux of $\sim 3 \times 10^{-11}$ erg s^{-1} cm^{-2} in the 30–60 keV interval (Pian et al., 2005), a factor of $\sim$ 2 higher than observed by the *BeppoSAX* PDS in October 2000 (Tagliaferri et al., 2003). In that epoch the optical flux was slightly lower than during the observations in March 2004 at maximum brightness. OMC recorded a mean V magnitude of 13.24. OMC observations of this epoch were compared with the simultaneous XMM observations in Foschini et al. (2006).

In order to detect intraday variability (IDV) in the OMC light curves, zooms on the two region are plotted in Fig. 6.43. IDV is observed in both epochs and as in Hu et al. (2014), slightly larger relative amplitude of variability is found in the observations of November 2003, when the source was fainter.

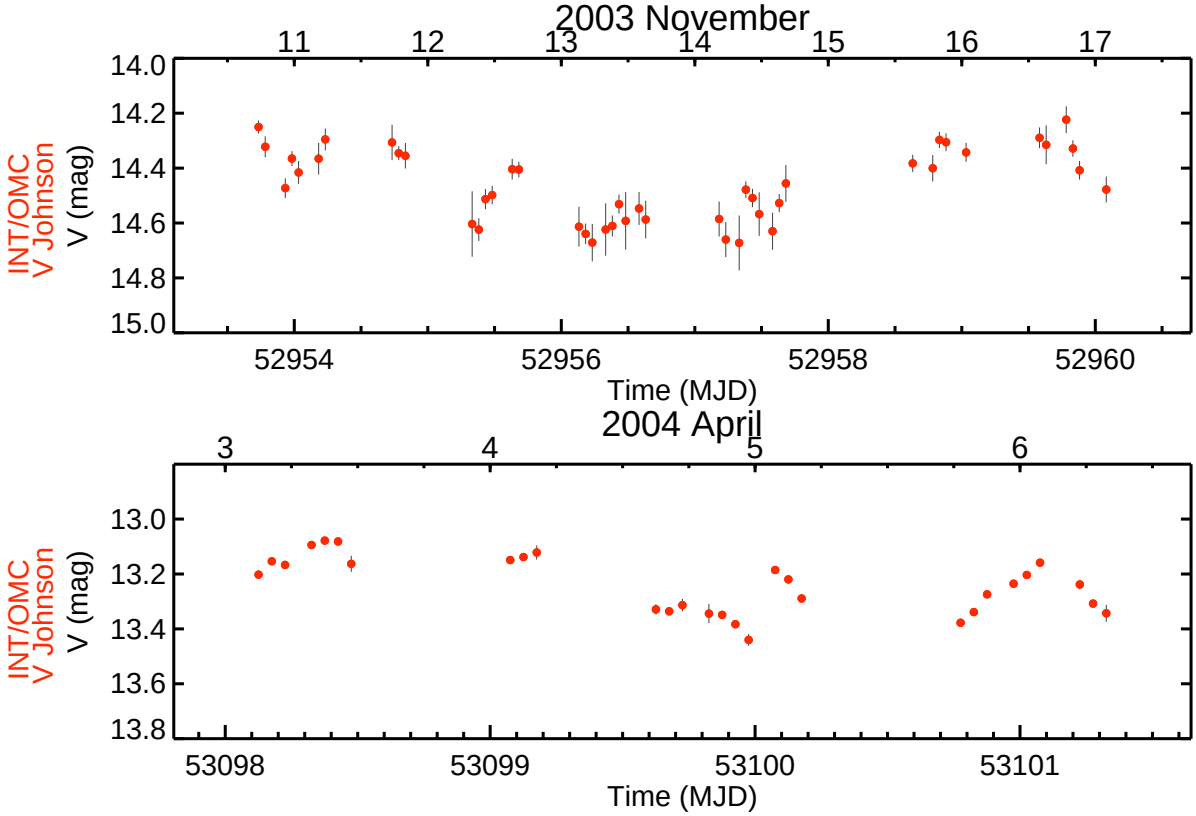

Figure 6.43: Zoom in the two epochs of OMC observations of S5 0716+714. Intra-day variability can be noted in both active states (November 2003 and in April 2004). Slightly larger relative amplitude of variability is found when the source is fainter. Data have been rebinned with 72 min time-resolution for clearness.

OMC has not observed this blazar since 2004, but *INTEGRAL*/IBIS and *Fermi*/LAT observed it during 2008–2013. While in the *Fermi*/LAT light curve intense variability is detected, the IBIS light curves do not show significant variations.

At the moment of writing this thesis, this blazar was in an active state and has displayed violent activity in the NIR and optical bands in January–February 2015, being brighter than ever during last ten years. S5 0716+714 became active at the beginning of January 2015, reaching the maximum light near 16 January (Arkharov et al., 2015; Bachev & Strigachev, 2015). It faded down to R =12.18 ± 0.03, and flared up to R = 11.77 ± 0.02 on 23 January (MJD = 57045.89) and then displayed flux variations above R = 11.9 (Spiridonova et al., 2015). This exceptionally high optical state triggered MAGIC observations of the source in very high energy gamma-rays (VHE, E>100 GeV), detecting VHE gamma-rays above 150 GeV from S5 0716+714 (Mirzoyan, 2015). S5 0716+714 was reported as VHE emitter in 2008 (Anderhub et al., 2009). However, this detection was the only significant detection of VHE gamma-ray emission from the system until the detection in 2015. Both active gamma-ray states have taken place during a high optical state. It would be interesting to perform simultaneous *INTEGRAL*/MAGIC observations of this blazar to compare the properties of the system at so different energy ranges.

6.3.9 3C 273

3C 273 is the brightest and one of the nearest quasars with a redshift of 0.158 (Strauss et al., 1992). It was discovered as the optical counterpart of a quasi-stellar radio source located in Virgo in 1963 (Schmidt, 1963; Oke, 1963). It was the first quasar to be observed in gamma-rays (in 1976, by the European COS-B satellite[9]), even though its jets are not quite perfectly aligned with the line of sight. The luminosity of 3C 273 is variable across the electromagnetic spectrum, from radio to gamma-rays on timescales of a few days to decades and even years. 3C 273 is considered a blazar because of its gamma-ray emission and its variability. However, it also displays some spectral line features including emission lines of hydrogen in the optical, and iron lines in X-rays. It is a radio-loud quasar, classified as a flat spectrum radio quasar (FSRQ), and its emission seems to be a combination of radiation from the accretion disk and from the large-scale visible jet (see Fig. 6.44, Türler et al. 2006; Soldi et al. 2008).

The OMC, JEM-X, and IBIS/ISGRI images of this quasar are shown in Fig. 6.45. In soft and hard X-rays, the source is bright enough to get long-term evolution in these bands.

The *INTEGRAL* light curves, the R-band light curve from the monitoring program of the MAGIC consortium, the *RXTE*/PCA and *Fermi*/LAT light curves of 3C 273 over the last 12 years are presented in Fig. 6.46.

Optical variability is clearly seen in the optical light curves. The OMC light curve shows a mean V magnitude of 12.66, varying from 12.52 to 12.81, with an observed RMS of 0.08. The *RXTE*/PCA light curves present large variability with their highest activity in the period from 2006 to 2008. In this epoch, the JEM-X and IBIS light curves show similar trends but the temporal coverage is poorer.

From 2003 to 2008, no significant variability is observed in the OMC data, but the temporal gaps are long. From 2005 to 2008, the source appears very active in the *RXTE*/PCA light curve, displaying several outbursts. Smoother variability is observed in the JEM-X and IBIS light curves, and only a long-term modulation can be observed. After this soft X-ray active period, an optical flare is detected in the R-band light curve at the beginning of 2008 (MJD 54525), and after that the optical flux decreased until the end of 2009 by $\sim$ 0.3 mag. Later on gamma-ray activity was detected by *Fermi*/LAT with two main peaks of activity around MJD 55100 and 55260 (September 2009 and March 2010). Between both peaks, another optical flare seems to be detected in the R light curve and after this happened the optical flux decreased reaching a

[9] http://sci.esa.int/cos-b/

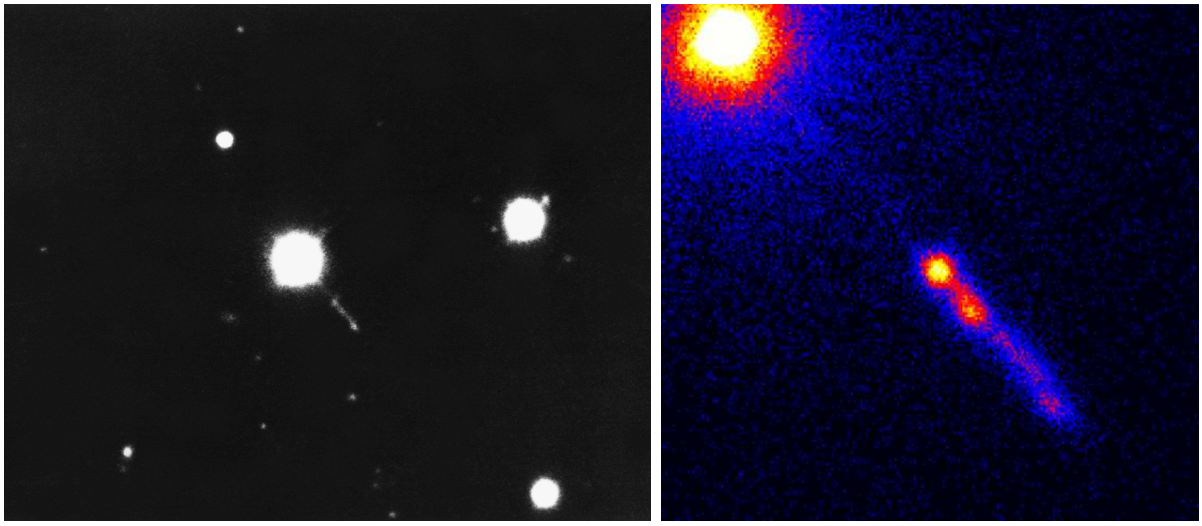

Figure 6.44: Structure of the optical and X-Ray emission from the jet of 3C 273. **Left:** Optical image obtained with the 4-meter Mayall telescope of Kitt Peak National Observatory (credit: AURA/NOAO/NSF) showing a very large jet coming from this object. **Right:** Chandra image shows important new details in the powerful jet shooting from the quasar 3C 273, providing an X-ray view into the area between 3C 273's core and the beginning of the jet (credit: NASA/CXC/SAO/Marshall et al. 2001).

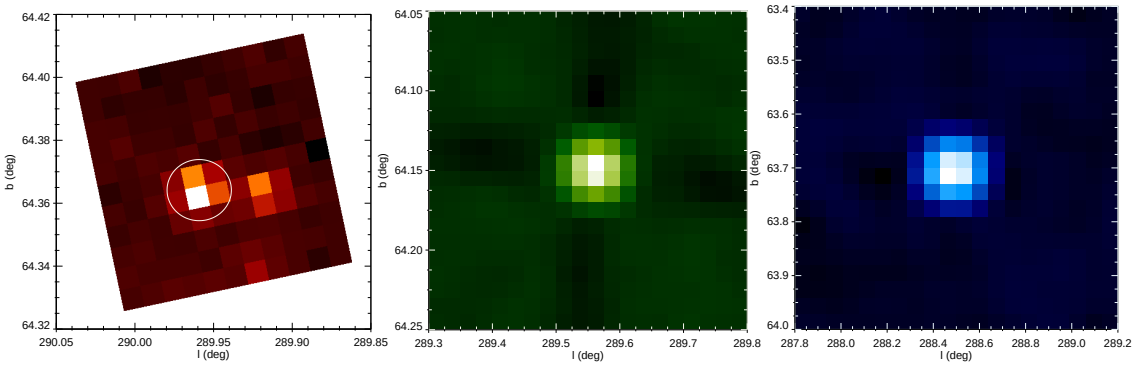

Figure 6.45: Left: OMC image of 3C 273. The white circle represents approximately the area where the optical photometry is extracted. **Middle:** JEM-X image of 3C 273 in the 3.0–25 keV energy band. **Right:** IBIS/ISGRI image of 3C 273 in the 20–100 keV energy band. North is up and east is to the left. Note the different image scales for each instrument.

minimum value of $R \sim 12.6$ mag just after the second gamma ray outburst at MJD 55260. Similar peaks, but delayed with respect to the *Fermi*/LAT ones, are observed by *RXTE*/PCA and INTEGRAL/JEM-X. These peaks lag the *Fermi*/LAT ones by more than 100 days. After the gamma and X-ray activity, the optical flux slowly brightened by ~ 0.3 mag in a year. This long-term variation points to the optical variability being produced in the intrinsic optical emitting region, probably due to accretion rate fluctuations, instead of being produced by reprocessing of X-rays. Since the gamma ray flare in 2010, 3C 273 has been quite in gamma rays. In the optical band, from 2010 to 2012, the optical flux increased by ~ 0.15 mag and from 2012 to the present, it has decreased by ~ 0.3 mag and it is now in an historical optical minimum with an optical magnitude of R=12.8 mag. Accretion rate fluctuations could be an explanation for the variability patterns found in this quasar, but the optical, X-ray and gamma ray behavior are too chaotic and are so weakly correlated that it is difficult to extract any firm conclusion only from these data.

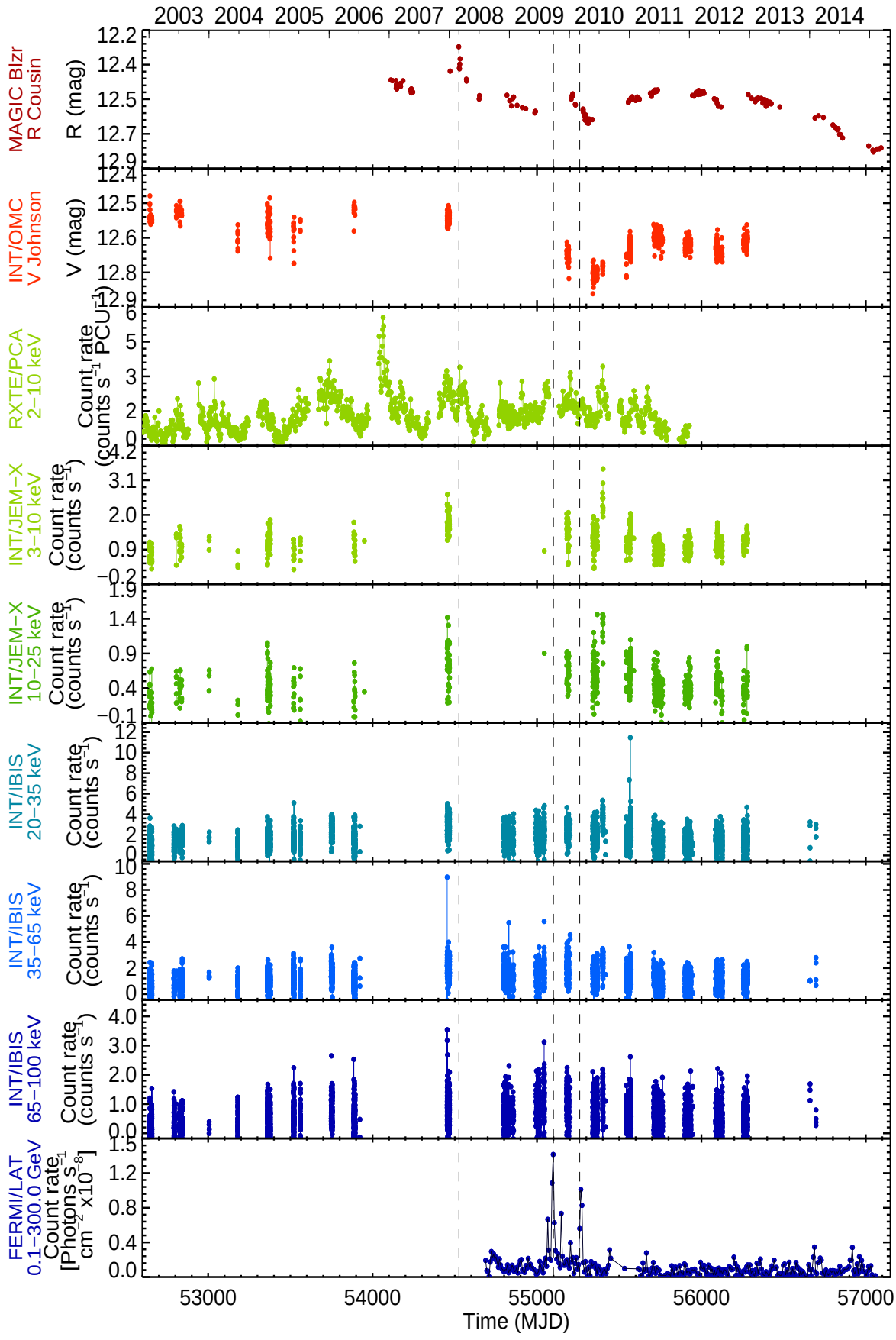

Figure 6.46: Light curves of 3C 273. *INTEGRAL*, *Swift*/BAT, and *RXTE*/PCA fluxes have been binned with 1 day time-resolution and *Fermi*/LAT data have been weekly rebinned. The times MJD 54525, 55100, and 55260 have been marked with dashed lines for reference (see text).

6.3.10 NGC 4151

The galaxy NGC 4151 was first mentioned by William Herschel on 17 March 1787 and it was one of the two Seyfert galaxies described in Seyfert (1943), in which the term "Seyfert" was coined. NGC 4151 is an extended source, classified as Seyfert 1.5 (Véron-Cetty & Véron, 2006) with z=0.003319 (de Vaucouleurs et al., 1991). It is one of the most studied Seyfert galaxies and has been the target of many multiwavelength long-term studies (Edelson et al. 1996; Czerny et al. 2003 and references therein).

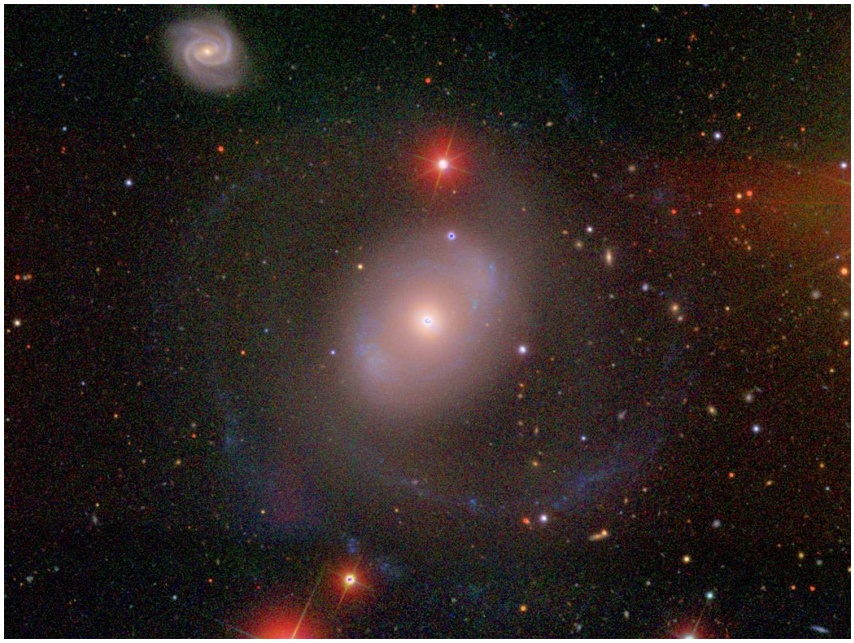

Figure 6.47: The galaxy NGC 4151 is located about 45 million light-years away toward the constellation Canes Venatici. Activity powered by its central black hole makes NGC 4151 one of the brightest active galaxies in X-rays. Credit: David W. Hogg, Michael R. Blanton, and the Sloan Digital Sky Survey Collaboration

The OMC, JEM-X, and IBIS images of NGC 4151 are shown in Fig. 6.48. This galaxy is more extended than the OMC aperture. Since the optical photometry is contaminated to some extent by bulge stellar light, the variation in the optical emission from the nucleus itself might appear significantly diluted. No contamination is found in the JEM-X and IBIS images.

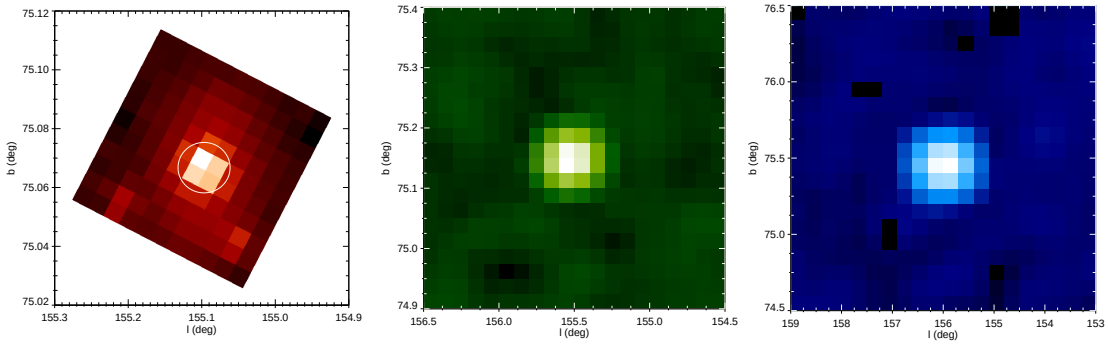

Figure 6.48: Left: OMC image of NGC 4151. The white circle represents approximately the area where the optical photometry is extracted. **Middle:** JEM-X image of NGC 4151 in the 3.0–25 keV energy band. **Right:** IBIS/ISGRI image of NGC 4151 in the 20–100 keV energy band. North is up and east is to the left. Note the different image scales for each instrument.

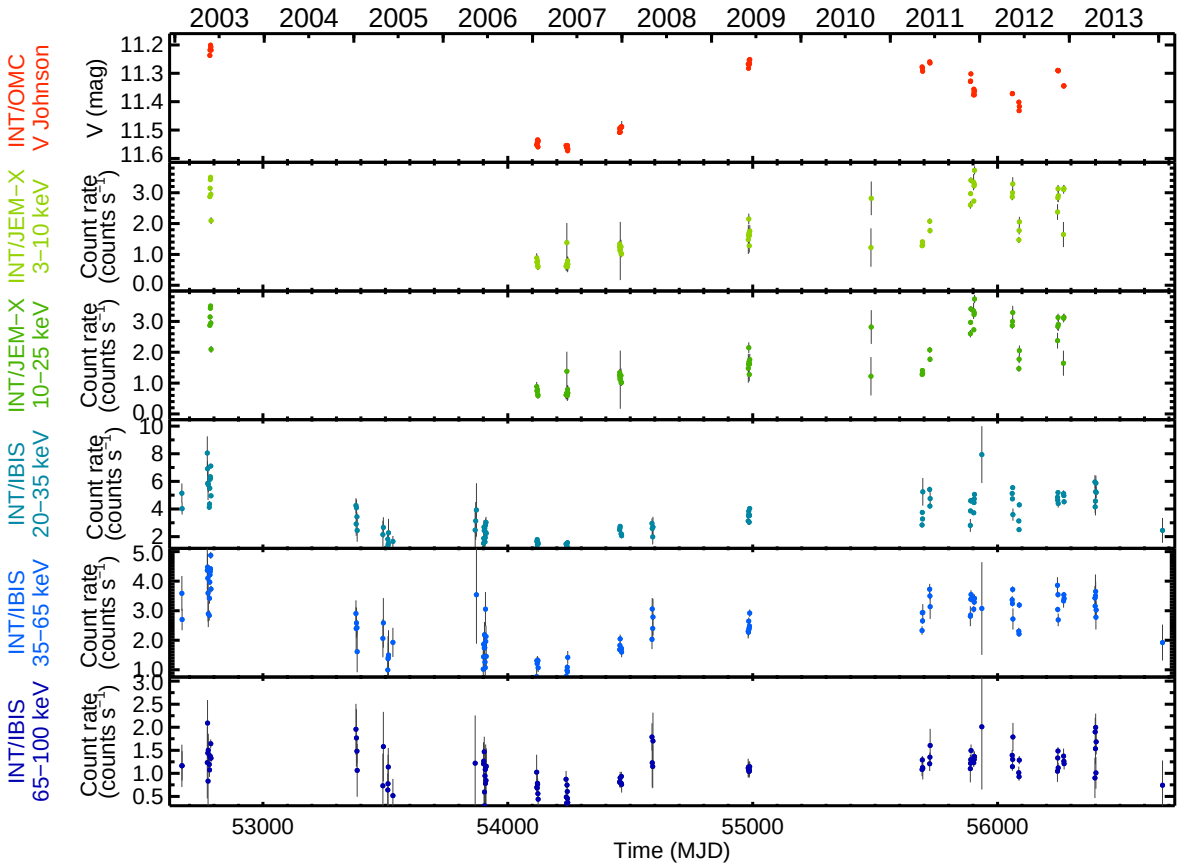

Figure 6.49: *INTEGRAL* light curves of NGC 4151 during the last 11 years. Data have been daily rebinned.

The *INTEGRAL* light curves of NGC 4151 from 2003 to 2013 are shown in Fig. 6.49. In the optical light curve, a clear weakening of its central region by around 0.5 mag (60% in flux) from 11.15 mag to 11.65 mag was measured between May 2003 and January 2007. Similar trends can be observed in the JEM-X and IBIS light curves in this epoch, probably because these variations have a common origin, although the amplitudes of their variability are smaller.

In May 2009 the source recovered its previous optical brightness, but no similar brightenings were found in the X-ray light curves. However, at the end of 2011, soft X-ray fluxes similar to those found in 2003 were measured. In 2011–2012, smooth variability was observed in the OMC and JEM-X light curves. During the 2011–2013 observations, no variability was observed in the IBIS light curves.

The observed long-term correlation between X-ray and optical variability points to a common underlying origin, different from reprocessing of X-rays, being the cause of the optical variability in NGC 4151 (see Gaskell 2006).

6.4 Conclusions

The optical, X-ray and gamma ray long-term light curves of a selected sample of high-energy sources observed by *INTEGRAL* have been compiled. The optical and X-ray variability of these sources has been analyzed.

OMC, JEM-X, and IBIS light curves were extracted for the 73 sources from the cross-match of the IBIS catalog with the OMC archive.

Five X-ray binaries and five AGN have been studied in more detail, confirming some previously published results and finding other new interesting ones.

For 1A 0535+262, three cycles of superorbital variations in the optical flux with a period of ~ 2000 d have been identified. It has been observed that the X-ray giant outbursts occur when the optical flux is fading. The fading and brightening optical states of this Be/X-ray binary can be explained by the formation of low-density regions in the inner part of its circumstellar disk and the replenishment of them after the X-ray outbursts.

The optical and X-ray light curves of GX 304–1 present a completely different behavior. This source was in quiescence from 2003 to 2010. After that, several X-ray outbursts took place and then, the optical flux brightened by ~ 1 mag. A decrease of the optical flux by ~ 0.8 mag and a new X-ray outburst were measured in December 2014.

Optical and X-ray observations of H 1145–619 from 1996 to 2015 have been compiled. An analysis of the optical variations has been performed and three epochs displaying different behaviors have been discovered. No X-ray activity on this source had been reported since 1997. An X-ray active period with three outburst detected by JEM-X and IBIS has been found. At the time of writing this thesis, a new outburst of H 1145–619 was detected by MAXI and *Swift*/BAT. As explained in this work, such activity was expected from the observed optical behavior.

The light curves of Cyg X–1 have been used to study the relation between the X-ray spectral state and soft X-ray flux and the non-ellipsoidal orbital variations (mainly produced by X-ray heating). It has been found that when Cyg X–1 is in its hard state, the amplitude of the optical variations is smaller than when it is in the soft (and usually high) state.

Finally, the light curves of Her X–1 display the expected multi-periodic variability that has been reported for it in many previous studies, but good time-coverage data for the last 12 years are provided. The changes in the optical pattern with the 35 d cycle of the X-ray emission, are also shown.

With respect to the AGN in the sample, Mrk 421 is the one showing the best-quality *INTEGRAL* data, presenting short-term correlations between the three *INTEGRAL* instruments.

Optical long-term and short-term (intraday) variability has been observed in the OMC optical light curve of S5 0716+714.

The light curves of 3C 279, 3C 273 and NGC 4151 showed variability in all the energy bands, confirming previous results, with different levels of correlations between them.

More *INTEGRAL* data will become available in the next years and it is our intention to perform a compilation of the *final catalogue of INTEGRAL/OMC variable sources*, including an extended long-term study of the optical and high-energy emission, that will be significantly improved by the longer temporal coverage provided by *INTEGRAL* at the end of the mission.

Chapter 7

Conclusions and future work

This last Chapter summarizes the main findings of this work and the planned future research activities.

7.1 Summary and conclusions

In this thesis, the optical photometric data provided by the optical monitoring camera (OMC) on board the *INTEGRAL* space observatory have been analyzed. Different studies have been performed.

First of all, the variability, periodicity and classification of the variable objects in the OMC archive have been studied. It led to the compilation of *the first INTEGRAL–OMC catalogue of optically variable sources*, which is presented here. A statistical analysis of the magnitudes, amplitudes of variations, periods, and types of objects has been performed. Regarding the periodicity, in several cases the periods previously provided in the literature have been improved. Moreover, new determinations of periods have been also included. In this first release of the catalog, information of the variability of 5263 objects and period determinations of 1337 objects are provided. During the compilation of the catalog, a few scientific cases were considered, and the more relevant ones have been included in this thesis.

A search for eclipsing binaries containing a pulsating component was carried out. Four previously known systems with these characteristics were found and confirmed, and one new candidate, AW Vel was found. Within these systems, DY Aqr was selected for a more detailed analysis. High-resolution spectroscopic and multicolor photometric data were acquired, and the physical parameters of the primary component, as well as the orbital components, were calculated. We classified the primary component of DY Aqr as an A7.5 V star, much cooler than previously reported. Finally, the evolution of the system was also considered, and our conclusion is that DY Aqr is compatible with being an *oscillating eclipsing Algol* (oEA).

OMC provides optical observations at the same time than the main X-ray and gamma-ray *INTEGRAL* instruments IBIS and JEM-X. For the first time, simultaneous observations of the optical and X-ray/gamma-ray sky over more than 12 years are presented. This unprecedented long term monitoring of the optical and gamma ray sky provides a unique opportunity to study the long-term evolution of high-energy sources and their properties at different wavelengths, which we have complemented with IR, MIR, and other X-ray and optical monitoring observations when possible. Two different scientific cases have been studied in detail:

The first one focused on the global properties of the high-energy sources. Optical and hard-X ray luminosities have been compared and IR and MIR data have been used to complement the analysis. Different behavior was found between the different classes of AGN and XBs. Within the AGN, it has been found that $\alpha_{\rm OX}$ decreased from Seyfert 2 galaxies to blazars, indicating

an increase in the relative X-ray to optical flux from type 2 towards type 1 objects. In the case of the X-ray binaries, HMXBs display lower values of $\alpha_{\rm OX}$ than LMXBs. On the other hand, redder MIR colors have been found for AGN than for XBs.

The objective of the second work was to analyze the variability of these sources along the 12 years of *INTEGRAL* observations. In this case, complementary data of other high-energy missions and optical surveys have been used. The most interesting cases are presented. Interesting long-term correlations between the optical and X-ray emission of three Be/X-ray binaries have been found. For one of them, H 1145–619, optical and X-ray activity from 2003 to 2005 has been detected for the first time using *INTEGRAL* data. The optical emission of Cyg X–1 in its different spectral states has been studied, and hints of a correlation between the non-ellipsoidal optical variations and the spectral state have been found. For the AGN included in this work, optical, X-ray and gamma-ray light curves are displayed, and the different trends for each one have been discussed. Most of the blazars included in this work present higher variability in the optical and in gamma rays than in X-rays, and for one of them, S5 0716+714, intraday variability has been detected and measured.

7.2 Future work

As the *INTEGRAL* observatory is still operational, a final version of the catalog of *INTEGRAL*/OMC optically variable sources is planned for the end of the mission, and it will contain variability information for more than 25 000 objects.

We also plan to publish a catalog of the multiwavelength monitoring of high-energy sources with INTEGRAL, including the light curves of OMC, JEM-X, and IBIS instruments, which are available in Appendix B.

We plan also to perform a deeper analysis of the most interesting high-energy sources, selected from the multiwavelength variability analysis presented in this thesis. For example, to complement our findings about H 1145–619, we are performing H_α observations along its orbital period. We also plan to analyze in more detail the preliminary results found for Cyg X–1.

The ESA's Science Programme Committee (SPC) has approved a new extension for the *INTEGRAL* mission until 31 December 2016, and it will probably remain operational for several more years. Thousands of light curves of variable objects monitored over more than 12 years, with consistent and well calibrated optical photometry from space, are now available, and more data will come in the next years. Apart from the results presented in this thesis, there are still many cases to study. With the compilation of these catalogs, the publication of this thesis, and the future planned activities, we want to make easier the access to the OMC data, and stress the scientific possibilities of their analysis.

Apart from the new contribution to the understanding of these variable objects, this kind of works are also important to develop statistical techniques for the treatment and analysis of large volumes of data covering long timescales. On the optical domain, the *Gaia* mission is scanning the sky to measure the positions and movements of stars in our Galaxy, and it will be expected to observe one billion stars. Other missions designed for the detection of planets, such as *PLATO*, will also require good statistical skills. Moreover, future X-ray missions, such as *Astro-H* and *Athena* will come in the next years, and will increase our knowledge on the emission properties of high-energy sources.

Capítulo 7

Conclusiones y trabajo futuro

En este capítulo se presentan las conclusiones de esta tesis y el trabajo futuro.

7.1 Conclusiones

El principal objetivo de esta tesis ha sido el análisis de los datos proporcionados por el monitor óptico (OMC) a bordo del observatorio espacial *INTEGRAL*.

En primer lugar se realizó la compilación del catálogo de fuentes variables en el óptico observadas por INTEGRAL/OMC. Este catálogo incluye el estudio de variabilidad, periodicidad y la clasificación por tipo de objeto de las distintas fuentes. Se ha realizado un estudio estadístico de las magnitudes, amplitudes de variabilidad, períodos y de tipos de objeto. En algunos casos, se han proporcionado nuevas clasificaciones o se han corregido las que figuraban en la literatura. Respecto a la periodicidad, en muchos casos se han mejorado los valores de los períodos que se encontraban previamente en la literatura, mientras que otros casos constituyen nuevas determinaciones. En esta primera versión del catálogo, se proporciona información sobre la variabilidad de 5263 fuentes y determinaciones de períodos para 1337 fuentes. Con la elaboración de este catálogo, se identificaron numerosos casos científicos potencialmente interesantes. Algunos de ellos se han incluido en este trabajo.

Uno de estos casos, fue la búsqueda en el catálogo de sistemas binarios eclipsantes con una componente pulsante. Se encontraron cuatro objetos que ya habían sido identificados previamente y se propuso un nuevo candidato, AW Vel. Uno de estos objetos, DY Aqr, se seleccionó para estudiarlo en más detalle. Para ello, se incluyeron datos de espectroscopia de alta resolución y fotometria multicolor, que permitieron la determinación de los parámetros físicos de la componente primaria y de los parámetros de la órbita. De acuerdo a nuestros resultados, esta estrella es una A7 V, mucho más fría de lo que se creía anteriormente. Se realizó también un estudio de la evolución del sitema, concluyendo que este sistema se comporta como un sistema eclipsante tipo Algol oscilante.

OMC proporciona observaciones ópticas a la vez que se observa con los instrumentos de rayos X y rayos gamma, IBIS y JEM-X. Por primera vez se presentan observaciones simultáneas en el óptico y en rayos X/gamma del cielo durante más de 12 años. Esta monitorización proporciona una oportunidad única para entender la evolución a largo plazo de las fuentes emisores en altas energías en los distintos rangos. El trabajo presentado en esta tesis, constituye el primer estudio sistemático que se ha realizado incluyendo datos proporcionados por los tres instrumentos de *INTEGRAL*: OMC, JEM-X e IBIS. Estos a su vez han sido complementados con datos en el IR, MIR y con observaciones ópticas y de otras misiones de rayos X/gamma.

El primero de ellos está enfocado en el estudio de las propiedades globales de estos objetos. Las luminosidades ópticas y en rayos X-duros y sus cocientes han sido analizadas. Para

complementar este estudio se han añadido datos en los rangos IR y MIR. Se ha realizado una comparación de las características presentadas por cada tipo de objeto.

El segundo estudio se centra en la variabilidad en las distintas longitudes de onda de estos objetos. Para ello se han analizado las curvas de luz de los tres instrumentos de *INTEGRAL*: OMC, JEM-X e IBIS. Asimismo, para los objetos más interesantes, se han incluido en el estudio curvas de luz de otras misiones de altas energías y de otros cartografiados ópticos. Para las estrellas binarias de rayos X tipo Be, se han hallado interesantes correlaciones entre la emisión óptica y en rayos X. Para una de ellas, H 1145–619, se ha encontrado un período de actividad en ambos rangos que no había sido detectado previamente. La emisión óptica de Cyg X–1 en los distintos estados espectrales ha sido analizada. Para los AGN, se han estudiado las tendencias en las distintas curvas de luz, encontrando que para los blázares, las variaciones en el óptico y en rayos gamma son mayores que en rayos X. Para uno de ellos, S5 0716+714, se ha medido micro-variabilidad con nuestros datos.

7.2 Trabajo futuro

La misión INTEGRAL sigue operativa y continuamente se reciben nuevos datos. Por este motivo está prevista la elaboración de la versión final del catálogo de fuentes variables en el óptico al final de la misión. Estimamos que esta contendrá información de más de 25000 objetos variables.

Por otro lado, también pretendemos publicar un catálogo con las curvas de luz de los tres instrumentos de *INTEGRAL*: OMC, JEM-X e IBIS, en el que se incluirán las curvas de luz que se adjuntan en el apéndice B.

Además se quiere llevar a cabo un análisis más detallado de los objetos más interesantes que se han identificado en el estudio de variabilidad multi-frecuencia. En particular, ya estamos realizando un seguimiento en H_α de la fuente H 1145–619 a lo largo de su órbita. También tenemos pensado realizar un análisis más profundo de los resultados preliminares que se han obtenido para de Cyg X–1.

El comité del programa científico de la ESA (SPC) ha aprobado la extensión de la misión *INTEGRAL* hasta el 31 de diciembre de 2016 y probablemente continúe operativa por varios años más. En este momento hay disponibles miles de curvas de luz con fotometria óptica desde el espacio y con una cobertura temporal de más de 12 años. Conforme avance la misión, se seguirán proporcionando nuevos datos. Con la compilación de estos catálogos, el trabajo de esta tesis y las actividades planeadas para el futuro, pretendemos hacer más accesibles los datos de OMC, así como potenciar la motivación de su análisis científico.

Además de la contribución que supone al conocimiento de los objetos variables, este tipo de trabajos son también importantes para el desarrollo de técnicas estadísticas para el tratamiento de grandes volúmenes de datos en escalas temporales muy grandes. En el dominio óptico, la misión *Gaia* está realizando un barrido del cielo para medir las posiciones y movimientos de las estrellas de nuestra Galaxia y a lo largo de la misión se prevé que observará mil millones de estrellas. Otras misiones diseñadas para la detección de planetas, como *PLATO*, también requerirán un tratamiento estadístico complejo. Por último, también se esperan nuevos datos de las futuras misiones de rayos X, como *Astro-H* y *Athena*, que ampliarán nuestro conocimiento sobre la emisión de las fuentes emisoras en altas energías.

Bibliography

Abdo, A. A., Ackermann, M., Ajello, M., et al. 2010, ApJ, 716, 835

Aerts, C., Christensen-Dalsgaard, J., & Kurtz, D. W. 2010, Asteroseismology (Springer Science+Business Media B.V)

Aleksić, J., Antonelli, L. A., Antoranz, P., et al. 2011, A&A, 530, A4

Alfonso-Garzón, J., Domingo, A., Mas-Hesse, J. M., & Giménez, A. 2012, A&A, 548, 79

Alfonso-Garzon, J., Montesinos, B., Moya, A., Mas-Hesse, J. M., & Martin-Ruiz, S. 2014, MNRAS, 443, 3022

Anderhub, H., Antonelli, L. A., Antoranz, P., et al. 2009, ApJ, 704, L129

Antonucci, R. 1993, ARA&A, 31, 473

Arkharov, A. A., Borman, G. A., Di Paola, A., Larionov, V. M., & Morozova, D. A. 2015, ATel, 6942, 1

Arnaud, K. A. 1996, in Astronomical Data Analysis Software and Systems V, Vol. 101, 17

Assef, R. J., Stern, D., Kochanek, C. S., et al. 2013, ApJ, 772, 26

Atwood, W. B., Abdo, A. A., Ackermann, M., et al. 2009, ApJ, 697, 1071

Auvergne, M., Bodin, P., Boisnard, L., et al. 2009, A&A, 506, 411

Bachev, R., Semkov, E., Strigachev, A., et al. 2012, MNRAS, 424, 2625

Bachev, R. & Strigachev, A. 2015, ATel, 6957, 1

Baglin, A., Auvergne, M., Barge, P., et al. 2009, in IAU Symposium, Vol. 253, IAU Symposium, 71–81

Balman, S. 2012, Memorie della Societa Astronomica Italiana, 83, 585

Balucinska-Church, M., Church, M. J., Charles, P. A., et al. 2000, MNRAS, 311, 861

Barron, E. G., Urban, J. A., Guinan, E. F., Sepinsky, J. F., & Ribas, I. 2002, in Bulletin of the American Astronomical Society, Vol. 201, American Astronomical Society Meeting Abstracts, 1122

Barthelmy, S. D., Barbier, L. M., Cummings, J. R., et al. 2005, Space Science Reviews, 120, 143

Beckmann, V. & Shrader, C. R. 2012, Active Galactic Nuclei (Wiley-VCH)

Beckmann, V., Soldi, S., Ricci, C., et al. 2009, A&A, 505, 417

Bessell, M. S. 1990, PASP, 102, 1181

Bessell, M. S. & Brett, J. M. 1988, PASP, 100, 1134

Bianchi, L., Herald, J., Efremova, B., et al. 2011, Ap&SS, 335, 161

Bianchi, S., Bonilla, N. F., Guainazzi, M., Matt, G., & Ponti, G. 2009, A&A, 501, 915

Bianchi, S., Maiolino, R., & Risaliti, G. 2012, Advances in Astronomy, 2012, 782030

Binnendijk, L. 1970, Vistas in Astronomy, 12, 217

Bird, A. J., Bazzano, A., Bassani, L., et al. 2010, ApJS, 186, 1

Blay, P., Negueruela, I., & Reglero, V. 2012, Memorie della Societa Astronomica Italiana, 83, 251

Bodaghee, A., Courvoisier, T. J., Rodriguez, J., et al. 2007, A&A, 467, 585

Boella, G., Butler, R. C., Perola, G. C., et al. 1997, A&AS, 122, 299

Boettcher, M. 2012, ArXiv e-prints, 1205, 539

Bolton, C. T. 1972, Nature, 235, 271

Bonnarel, F., Fernique, P., Bienaymé, O., et al. 2000, Astronomy and Astrophysics Supplement Series, 143, 33

Boroson, B. & Vrtilek, S. D. 2010, ApJ, 710, 197

Borucki, W. J., Koch, D., Basri, G., et al. 2010, Science, 327, 977

Böttcher, M. & Dermer, C. D. 2006, in High Energy Density Laboratory Astrophysics, ed. S. V. Lebedev (Springer Netherlands), 233–236

Bradt, H. V., Levine, A. M., Remillard, R. A., & Smith, D. A. 2000, 114

Bradt, H. V., Rothschild, R. E., & Swank, J. H. 1993, A&AS, 97, 355

Breger, M. 2000, in ASP Conf. Ser., Vol. 210, Delta Scuti and Related Stars, 3

Brocksopp, C., Fender, R. P., Larionov, V., et al. 1999, MNRAS, 309, 1063

Broglia, P. & Conconi, P. 1984, A&A, 138, 443

Broglia, P. & Marin, F. 1974, A&A, 34, 89

Brown, T. M. & Gilliland, R. L. 1994, ARA&A, 32, 37

Buson, S. 2013, ATel, 5680, 1

Caballero, I., Kretschmar, P., Pottschmidt, K., et al. 2009, ATel, 2337, 1

Caballero, I., Kretschmar, P., Santangelo, A., et al. 2007, A&A, 465, L21

Caballero, I., Pottschmidt, K., Marcu, D. M., et al. 2013, ApJ, 764, L23

Caballero, I. & Wilms, J. 2012, Memorie della Societa Astronomica Italiana, 83, 230

Caballero-García, M. D. 2003, PhD thesis, Universitat de Barcelona

Camero-Arranz, A., Finger, M. H., Wilson-Hodge, C., et al. 2011, ATel, 3166, 1

Camero-Arranz, A., Finger, M. H., Wilson-Hodge, C. A., et al. 2012, ApJ, 754, 20

Cardelli, J. A., Clayton, G. C., & Mathis, J. S. 1989, ApJ, 345, 245

Carpenter, J. M., Hillenbrand, L. A., & Skrutskie, M. F. 2001, AJ, 121, 3160

Casares, J., Negueruela, I., Ribó, M., et al. 2014, Nature, 505, 378

Castelli, F. & Kurucz, R. L. 2003, in IAU Symposium, Vol. 210, Modelling of Stellar Atmospheres

Chakrabarti, S. K. & Wiita, P. J. 1993, ApJ, 411, 602

Chakraborty, M., Bhattacharyya, S., & Mukherjee, A. 2011, MNRAS, 418, 490

Chaplin, W. J. & Miglio, A. 2013, ARA&A, 51, 353

Chatterjee, R., Bailyn, C. D., Bonning, E. W., et al. 2012, ApJ, 749, 191

Chatterjee, R., Jorstad, S. G., Marscher, A. P., et al. 2008, ApJ, 689, 79

Chen, A. W., D'Ammando, F., Villata, M., et al. 2008, A&A, 489, L37

Chen, L. 2014, ApJ, 788, 179

Chini, R., Hoffmeister, V. H., Nasseri, A., Stahl, O., & Zinnecker, H. 2012, MNRAS, 424, 1925

Chini, R., Nasseri, A., Dembsky, T., et al. 2013, in EAS Publications Series, Vol. 64, 155–162

Clark, J. S., Lyuty, V. M., Zaitseva, G. V., et al. 1999, MNRAS, 302, 167

Coe, M. J. 2000, in IAU Colloq. 175: The Be Phenomenon in Early-Type Stars, Vol. 214, eprint: arXiv:astro-ph/9911272, 656

Coe, M. J., Carpenter, G. F., Engel, A. R., & Quenby, J. J. 1975, Nature, 256, 630

Cohen, M., Wheaton, W. A., & Megeath, S. T. 2003, AJ, 126, 1090

Colgate, S. A. 1979, ApJ, 232, 404

Colla, G., Fanti, C., Fanti, R., et al. 1975, A&AS, 20, 1

Corbel, S., Fender, R. P., Tzioumis, A. K., et al. 2000, A&A, 359, 251

Corbel, S., Nowak, M. A., Fender, R. P., Tzioumis, A. K., & Markoff, S. 2003, A&A, 400, 1007

Corbet, R. & Remillard, R. 1996, International Astronomical Union Circular, 6486, 1

Corbet, R. H. D. & Krimm, H. A. 2013, ApJ, 778, 45

Corbet, R. H. D., Sokoloski, J. L., Mukai, K., Markwardt, C. B., & Tueller, J. 2008, ApJ, 675, 1424

Courvoisier, T. J. L., Walter, R., Beckmann, V., et al. 2003, A&A, 411, L53

Cutri, R. M. & et al. 2014, VizieR Online Data Catalog, 2328, 0

Cutri, R. M., Skrutskie, M. F., van Dyk, S., et al. 2003, VizieR Online Data Catalog, 2246, 0

Czerny, B., Doroshenko, V. T., Nikolajuk, M., et al. 2003, MNRAS, 342, 1222

da Silva, R., Maceroni, C., Gandolfi, D., Lehmann, H., & Hatzes, A. P. 2014, A&A, 565, 55

Dachs, J., Kiehling, R., & Engels, D. 1988, A&A, 194, 167

De Cat, P. 2002, in IAU Colloq. 185: Radial and Nonradial Pulsationsn as Probes of Stellar Physics, Vol. 259, 196

de Vaucouleurs, G., de Vaucouleurs, A., Corwin, H. G., J., et al. 1991, Third Reference Catalogue of Bright Galaxies. Volume I: Explanations and references. Volume II: Data for galaxies between 0h and 12h. Volume III: Data for galaxies between 12h and 24h. (Springer)

Degenaar, N., Miller, J. M., Harrison, F. A., et al. 2014, ApJ, 796, L9

Díaz Trigo, M., Parmar, A. N., Boirin, L., Méndez, M., & Kaastra, J. S. 2006, A&A, 445, 179

Domingo, A. 2011, PhD thesis, Universitat de Barcelona

Domingo, A., Caballero, M. D., Figueras, F., et al. 2003, A&A, 411, L281

Done, C., Gierliński, M., & Kubota, A. 2007, A&A Rev., 15, 1

Dower, R. G., Bradt, H. V., Doxsey, R. E., et al. 1978, Nature, 273, 364

Downes, R. A., Webbink, R. F., Shara, M. M., et al. 2001, PASP, 113, 764

Eachus, L. J. & Liller, W. 1975, ApJ, 200, L61

Ebisawa, K., Bourban, G., Bodaghee, A., Mowlavi, N., & Courvoisier, T. J. 2003, A&A, 411, L59

Edelson, R. & Malkan, M. 2012, ApJ, 751, 52

Edelson, R. A., Alexander, T., Crenshaw, D. M., et al. 1996, ApJ, 470, 364

Eggleton, P. P. 1983, AJ, 268, 368

Errando, M. 2014, in AAS/High Energy Astrophysics Division, Vol. 14, AAS/High Energy Astrophysics Division

Eyer, L. & Mowlavi, N. 2008, Journal of Physics Conference Series, 118, 012010

Fabregat, J. & Torrejon, J. M. 1998, A&A, 332, 643

Fabrika, S. 2004, Astrophysics and Space Physics Reviews, 12, 1

Feast, M. W. & Walker, A. R. 1987, ARA&A, 25, 345

Fender, R., Koerding, E., Belloni, T., et al. 2007, ArXiv e-prints, 0706, 3838

Fernie, J. D. 1995, AJ, 110, 2361

Finger, M. H., Camero-Arranz, A., Kretschmar, P., Wilson, C., & Patel, S. 2006, in Bulletin of the American Astronomical Society, Vol. 9, AAS/High Energy Astrophysics Division #9, 359

Finger, M. H., Koh, D. T., Nelson, R. W., et al. 1996, Nature, 381, 291

Finger, M. H., Wilson, R. B., & Hagedon, K. S. 1994, International Astronomical Union Circular, 5931, 1

Fishman, G. J., Meegan, C. A., Wilson, R. B., et al. 1989, in , 860

Foschini, L., Tagliaferri, G., Pian, E., et al. 2006, A&A, 455, 871

Freedman, W. L., Hughes, S. M., Madore, B. F., et al. 1994, ApJ, 427, 628

Freedman, W. L. & Madore, B. F. 2010, ARA&A, 48, 673

Galloway, D. K., Muno, M. P., Hartman, J. M., Psaltis, D., & Chakrabarty, D. 2008, ApJS, 179, 360

Gaskell, C. M. 2006, in , eprint: arXiv:astro-ph/0701008, 111

Gaskell, C. M. 2008, in , eprint: arXiv:0711.2113, 1–11

Gehrels, N., Chincarini, G., Giommi, P., et al. 2004, ApJ, 611, 1005

Gerend, D. & Boynton, P. E. 1976, ApJ, 209, 562

Giacconi, R., Branduardi, G., Briel, U., et al. 1979, ApJ, 230, 540

Giacconi, R., Gursky, H., Paolini, F. R., & Rossi, B. B. 1962, Physical Review Letters, 9, 439

Giacconi, R., Kellogg, E., Gorenstein, P., Gursky, H., & Tananbaum, H. 1971, ApJ, 165, L27

Giangrande, A., Giovannelli, F., Bartolini, C., Guarnieri, A., & Piccioni, A. 1980, A&AS, 40, 289

Gilliland, R. L., Brown, T. M., Christensen-Dalsgaard, J., et al. 2010, PASP, 122, 131

Giménez, A. & García, J. M. 1983, Revista de la Real Academia de Ciencias Exactas, 1, 297

Giommi, P., Massaro, E., Chiappetti, L., et al. 1999, Astronomy and Astrophysics, 351, 59

Giovannelli, F. 2008, Chinese Journal of Astronomy and Astrophysics Supplement, 8, 237

Giovannelli, F., Bisnovatyi-Kogan, G. S., Bruni, I., et al. 2014, ATel, 6528, 1

Giovannelli, F., Bisnovatyi-Kogan, G. S., & Klepnev, A. S. 2013, A&A, 560, 1

Giovannelli, F., Rossi, C., Bruni, I., Bisnovatyi-Kogan, G. S., & Procas, J. S. 2015, ATel, 6969, 1

Girardi, L., Bertelli, G., Bressan, A., et al. 2002, A&A, 391, 195

Giuricin, G., Mardirossian, F., & Mezzetti, M. 1983, ApJS, 52, 35

Gleissner, T., Wilms, J., Pottschmidt, K., et al. 2004, A&A, 414, 1091

González-Galán, A., Kuulkers, E., Kretschmar, P., et al. 2012, A&A, 537, A66

Gonzalez-Martin, O., Masegosa, J., Marquez, I., et al. 2015, ArXiv e-prints, 1501, 3826

Gorda, S. Y. & Svechnikov, M. A. 1998, Astronomy Reports, 42, 793

Gou, L., McClintock, J. E., Remillard, R. A., et al. 2014, ApJ, 790, 29

Gray, R. O. & Corbally, J., . C. 2009, Stellar Spectral Classification (Princeton University Press)

Grinberg, V., Hell, N., Pottschmidt, K., et al. 2013, A&A, 554, A88

Grinberg, V., Leutenegger, M. A., Hell, N., et al. 2015, ArXiv e-prints, 1502, 7343

Gupta, A. C., Srivastava, A. K., & Wiita, P. J. 2009, ApJ, 690, 216

Gutiérrez, R., Solano, E., Domingo, A., & García, J. 2004, in ASPC, Vol. 314, Astronomical Data Analysis Software and Systems (ADASS) XIII, 153

Hadrava, P. 1995, A&AS, 114, 393

Hadrava, P. 1997, A&AS, 122, 581

Haigh, N. J., Coe, M. J., & Fabregat, J. 2004, MNRAS, 350, 1457

Hambleton, K. M., Kurtz, D. W., Prša, A., et al. 2013, MNRAS, 434, 925

Handler, G. 2009, MNRAS, 398, 1339

Handler, G., Balona, L. A., Shobbrook, R. R., et al. 2002, MNRAS, 333, 262

Hartman, R. C., Bertsch, D. L., Fichtel, C. E., et al. 1992, ApJ, 385, L1

Hoeg, E., Bässgen, G., Bastian, U., et al. 1997, A&A, 323, L57

Howells, L., Steele, I. A., Porter, J. M., & Etherton, J. 2001, A&A, 369, 99

Hu, S. M., Chen, X., Guo, D. F., Jiang, Y. G., & Li, K. 2014, MNRAS, 443, 2940

Huckle, H. E., Mason, K. O., White, N. E., et al. 1977, MNRAS, 180, 21P

Huemmerich, S. & Bernhard, K. 2012, Peremennye Zvezdy Prilozhenie, 12, 11

Hynes, R. I. 2010, ArXiv e-prints, 1010, 5770

Iafrate, G., Longo, F., & Collmar, W. 2009, ATel, 2154, 1

Ibanoğlu, C., Soydugan, F., Soydugan, E., & Dervişoğlu, A. 2006, MNRAS, 373, 435

Ibragimov, A., Zdziarski, A. A., & Poutanen, J. 2007, MNRAS, 381, 723

Jahoda, K., Markwardt, C. B., Radeva, Y., et al. 2006, ApJS, 163, 401

Jansen, F., Lumb, D., Altieri, B., et al. 2001, A&A, 365, L1

Jarrett, T. H., Cohen, M., Masci, F., et al. 2011, ApJ, 735, 112

Jenke, P., Finger, M. H., Wilson-Hodge, C. A., & Connaughton, V. 2012, ATel, 4547, 1

Jensen, P. L., Clausen, K., Cassi, C., et al. 2003, A&A, 411,

Jurua, E., Charles, P. A., Still, M., & Meintjes, P. J. 2011, MNRAS, 418, 437

Karitskaya, E. A., Goranskiĭ, V. P., Grankin, K. N., & Mel'Nikov, S. Y. 2000, Astronomy Letters, 26, 22

Karitskaya, E. A., Voloshina, I. B., Goranskii, V. P., et al. 2001, Astronomy Reports, 45, 350

Kartaltepe, J. S. & Balonek, T. J. 2007, ApJ, 133, 2866

Kazarovets, A. V., Samus, N. ; . N., Durlevich, O. V., et al. 1999, Informational Bulletin on Variable Stars, 4659, 1

Kazarovets, V., Samus, N. ; . N., & Durlevich, O. V. 1998, Informational Bulletin on Variable Stars, 4655, 1

Kholopov, P. N., Samus, N. N., Frolov, M. S., et al. 1998, in Combined General Catalogue of Variable Stars, 4.1 Ed (II/214A). (1998), 0

Kim, S., Lee, J. W., Youn, J., Kwon, S., & Kim, C. 2002, A&A, 391, 213

Koch, D. G., Borucki, W. J., Basri, G., et al. 2010, ApJ, 713, L79

Koratkar, A. & Blaes, O. 1999, PASP, 111, 1

Kotze, M. M. & Charles, P. A. 2012, MNRAS, 420, 1575

Kouzuma, S. & Yamaoka, H. 2010, A&A, 509, A64

Kreiner, J. M. 2004, AcA, 54, 207

Krimm, H. A., Holland, S. T., Corbet, R. H. D., et al. 2013, ApJS, 209, 14

Krivonos, R., Tsygankov, S., Lutovinov, A., et al. 2012, A&A, 545, 27

Kuehr, H., Witzel, A., Pauliny-Toth, I. I. K., & Nauber, U. 1981, A&AS, 45, 367

Kuiper, G. P. 1941, ApJ, 93, 133

Kukarkin, B. V. & Kholopov, P. ; . N. 1982, New catalogue of suspected variable stars (Moscow: Publication Office 'Nauka')

Kurucz, R. L. 1993, SYNTHE spectrum synthesis programs and line data: Smithsonian Astrophysical Observatory, |c1993, December 4, 1993

Kuulkers, E. 2014, INTEGRAL Science Operations Centre. Announcement of Opportunity for Observing Proposals (AO-12)

Kuulkers, E., Norton, A., Schwope, A., & Warner, B. 2006, in Compact stellar X-ray sources, Lewin, W.˜H.˜G. and van der Klis, m. edn., 421–460

Kwee, K. K. & van Woerden, H. 1956, Bulletin of the Astronomical Institutes of the Netherlands, 12, 327

Lamb, R. C., Markert, T. H., Hartman, R. C., Thompson, D. J., & Bignami, G. F. 1980, ApJ, 239, 651

Lampens, P. 2006, in Astronomical Society of the Pacific Conference Series, Vol. 349, Astrophysics of Variable Stars, 153

Lampens, P. & Boffin, H. M. J. 2000, in Delta Scuti and Related Stars, Vol. 210, eprint: arXiv:astro-ph/0001351, 309

Larionov, V. M., Jorstad, S. G., Marscher, A. P., et al. 2008, A&A, 492, 389

Lawrence, A. & Elvis, M. 1982, ApJ, 256, 410

Layden, A. C., Hanson, R. B., Hawley, S. L., Klemola, A. R., & Hanley, C. J. 1996, AJ, 112, 2110

Lee, H. T. & Chen, W. P. 2002, in 8th Asian-Pacific Regional Meeting, Volume II, 161–162

Lehmann, H., Southworth, J., Tkachenko, A., & Pavlovski, K. 2013, A&A, 557, 79

Lenz, P. & Breger, M. 2004, in IAU Symposium, Vol. 224, The A-Star Puzzle, 786–790

Levine, A. M., Bradt, H., Cui, W., et al. 1996, ApJ, 469, L33

Lewin, W. & van der Klis, M., eds. 2006, Compact Stellar X-ray Sources (Cambridge: Cambridge University Press)

Li, H., Yan, J., Zhou, J., & Liu, Q. 2014, AJ, 148, 113

Liakos, A., Niarchos, P., Soydugan, E., & Zasche, P. 2012, MNRAS, 422, 1250

Liao, N. H., Bai, J. M., Liu, H. T., et al. 2014, ApJ, 783, 83

Lichti, G. G., Bottacini, E., Ajello, M., et al. 2008, A&A, 486, 721

Lichti, G. G., Bottacini, E., Charlot, P., et al. 2007, in American Institute of Physics Conference Series, Vol. 921, The First GLAST Symposium, eprint: arXiv:0704.2338, 371–372

Liu, Q. Z., van Paradijs, J., & van den Heuvel, E. P. J. 2006, A&A, 455, 1165

Liu, Q. Z., van Paradijs, J., & van den Heuvel, E. P. J. 2007, A&A, 469, 807

Lund, N., Budtz-J?rgensen, C., Westergaard, N. J., et al. 2003, A&A, 411, L231

Lutz, D., Kunze, D., Spoon, H. W. W., & Thornley, M. D. 1998, Astronomy and Astrophysics, 333, L75

Maceroni, C., Lehmann, H., da Silva, R., et al. 2014, A&A, 563, 59

Maitra, D. & Bailyn, C. D. 2008, ApJ, 688, 537

Majaess, D. J., Turner, D. G., & Lane, D. J. 2009, MNRAS, 398, 263

Makino, F., Cook, W., Grunsfeld, J., et al. 1989, International Astronomical Union Circular, 4769, 1

Malizia, A., Bassani, L., Bazzano, A., et al. 2012, MNRAS, 426, 1750

Malizia, A., Stephen, J. B., Bassani, L., et al. 2009, MNRAS, 399, 944

Malkov, O. Y. 2003, A&A, 402, 1055

Malkov, O. Y., Oblak, E., Snegireva, E. A., & Torra, J. 2006, A&A, 446, 785

Marconi, M. 2009, in American Institute of Physics Conference Series, Vol. 1170, eprint: arXiv:0909.0900, 223–234

Marshall, H. L., Harris, D. E., Grimes, J. P., et al. 2001, ApJ, 549, L167

Mas-Hesse, J. M., Giménez, A., Culhane, J. L., et al. 2003, A&A, 411, L261

Mason, B. D., Hartkopf, W. I., Gies, D. R., Henry, T. J., & Helsel, J. W. 2009, AJ, 137, 3358

Mason, K. O., Murdin, P. G., Parkes, G. E., & Visvanathan, N. 1978, MNRAS, 184, 45P

Mason, K. O., Watson, M. G., & White, N. E. 1986, in Lecture Notes in Physics, Berlin Springer Verlag, Vol. 266, The Physics of Accretion onto Compact Objects

Mateos, S., Alonso-Herrero, A., Carrera, F. J., et al. 2013, MNRAS, 434, 941

Mateos, S., Alonso-Herrero, A., Carrera, F. J., et al. 2012, MNRAS, 426, 3271

Mateos, S., Carrera, F. J., Alonso-Herrero, A., et al. 2015, ArXiv e-prints, 1501, 4335

Matsuoka, M., Kawasaki, K., Ueno, S., et al. 2009, Publications of the Astronomical Society of Japan, 61, 999

Mayer, W. F. 1975, Johns Hopkins APL Technical Digest, 14, 14

Mayor, M., Udry, S., Halbwachs, J., & Arenou, F. 2001, in IAU Symposium, Vol. 200, The Formation of Binary Stars, Postdam, Germany, 45

McClintock, J. E., Nugent, J. J., Li, F. K., & Rappaport, S. A. 1977, ApJ, 216, L15

McClintock, J. E., Ricker, G. R., & Lewin, W. H. G. 1971, ApJ, 166, L73

McGowan, K. E. & Charles, P. A. 2003, MNRAS, 339, 748

McLaughlin, D. B. 1924, ApJ, 60, 22

Merloni, A., Heinz, S., & di Matteo, T. 2003, MNRAS, 345, 1057

Michalska, G. & Pigulski, A. 2007, CoAst, 150, 71

Mihalas, D. 1978, Stellar Atmospheres (W. H. Freeman)

Mihara, T., Negoro, H., Krimm, H. A., et al. 2015, ATel, 7215, 1

Miller, H. R., Clemmons, H., Maune, J. D., et al. 2011, ArXiv e-prints, 1104, 3887

Mirabel, I. F. 1994, in The Nature of Compact Objects in Active Galactic Nuclei (Cambridge: Cambridge University Press), 385

Mirabel, I. F. & Rodríguez, L. F. 1998, Nature, 392, 673

Mirzoyan, R. 2015, ATel, 6999, 1

Mitsuda, K., Kunieda, H., Inoue, H., & Kelley, R. 2004, in , 177–186

Mkrtichian, D. E., Kusakin, A. V., Rodriguez, E., et al. 2004, A&A, 419, 1015

Mkrtichian, D. E., Nazarenko, V., Gamarova, A. Y., et al. 2003, in Interplay of Periodic, Cyclic and Stochastic Variability in Selected Areas of the H-R Diagram, Vol. 292, 113

Moritani, Y., Nogami, D., Okazaki, A. T., et al. 2010, MNRAS, 405, 467

Nagase, F. 1989, Publications of the Astronomical Society of Japan, 41, 1

Nagase, F., Hayakawa, S., Kunieda, H., et al. 1982, ApJ, 263, 814

Nakajima, M., Mihara, M., Sugizaki, M., et al. 2012, ATel, 4420, 1

Nakajima, M., Mihara, T., Ueno, S., et al. 2015, ATel, 7015, 1

Nakajima, M., Nakagawa, Y. E., Nakahira, S., et al. 2013, ATel, 5205, 1

Nakajima, M., Sakamoto, T., Mihara, T., et al. 2014, ATel, 6569, 1

Negueruela, I. 1998, A&A, 338, 505

Negueruela, I., Smith, D. M., Reig, P., Chaty, S., & Torrejón, J. M. 2006, in The X-ray Universe 2005, Vol. 604, eprint: arXiv:astro-ph/0511088, 165

Nichols, J. S., Henden, A. A., Huenemoerder, D. P., et al. 2010, VizieR Online Data Catalog, 218, 80473

Nilsson, K., Pursimo, T., Sillanpää, A., Takalo, L. O., & Lindfors, E. 2008, A&A, 487, L29

Ogilvie, G. I. & Dubus, G. 2001, MNRAS, 320, 485

Okazaki, A. T., Hayasaki, K., & Moritani, Y. 2013, PASJ, 65, 41

Okazaki, A. T. & Negueruela, I. 2001, A&A, 377, 161

Oke, J. B. 1963, Nature, 197, 1040

Orosz, J. A., McClintock, J. E., Aufdenberg, J. P., et al. 2011, ApJ, 742, 84

Ostorero, L., Wagner, S. J., Gracia, J., et al. 2006, A&A, 451, 797

Özdemir, S. & Demircan, O. 2001, Astrophysics and Space Science, 278, 319

Padovani, P. & Giommi, P. 1995, MNRAS, 277, 1477

Padovani, P. & Giommi, P. 1996, MNRAS, 279, 526

Page, M., Yershov, V., Breeveld, A., et al. 2015, ArXiv e-prints, 1503, 6597

Page, M. J., Brindle, C., Talavera, A., et al. 2012, MNRAS, 426, 903

Pappa, A., Georgantopoulos, I., Stewart, G. C., & Zezas, A. L. 2001, MNRAS, 326, 995

Paschke, A. & Brat, L. 2006, Open European Journal on Variable Stars, 23, 13

Percy, J. R. 2007, Understanding Variable Stars (Cambridge: Cambridge University Press)

Perryman, M. A. C., Lindegren, L., Kovalevsky, J., et al. 1997, A&A, 323, L49

Peterson, B. M. 1997, An Introduction to Active Galactic Nuclei (Cambridge University Press)

Peterson, L. E. 1975, ARA&A, 13, 423

Pfeiffer, H. P. & Lai, D. 2004, ApJ, 604, 766

Pian, E., Foschini, L., Beckmann, V., et al. 2005, Astronomy and Astrophysics, 429, 427

Pian, E., Türler, M., Fiocchi, M., et al. 2014, A&A, 570, A77

Pigulski, A. & Michalska, G. 2007, AcA, 57, 61

Piquard, S., Halbwachs, J. L., Fabricius, C., et al. 2001, A&A, 373, 576

Pojmanski, G. 1997, AcA, 47, 467

Poutanen, J., Zdziarski, A. A., & Ibragimov, A. 2008, MNRAS, 389, 1427

Priedhorsky, W. C. & Terrell, J. 1983, ApJ, 273, 709

Prša, A., Batalha, N., Slawson, R. W., et al. 2011, AJ, 141, 83

Prša, A., Guinan, E. F., Devinney, E. J., & Engle, S. G. 2008, A&A, 489, 1209

Prša, A. & Zwitter, T. 2005, ApJ, 628, 426

Punch, M., Akerlof, C. W., Cawley, M. F., et al. 1992, Nature, 358, 477

Rajoelimanana, A. F., Charles, P. A., & Udalski, A. 2011, MNRAS, 413, 1600

Rani, B., Gupta, A. C., Joshi, U. C., Ganesh, S., & Wiita, P. J. 2010, ApJ, 719, L153

Rani, B., Krichbaum, T. P., Fuhrmann, L., et al. 2013, A&A, 552, A11

Raskin, G., van Winckel, H., Hensberge, H., et al. 2011, A&A, 526,

Reegen, P. 2007, A&A, 467, 1353

Reig, P. 2011, Astrophysics and Space Science, 332, 1

Reig, P. & Zezas, A. 2014, A&A, 561, 137

Remillard, R. A. & McClintock, J. E. 2006, ARA&A, 44, 49

Rísquez, D. 2008, PhD thesis, Universidad Complutense de Madrid

Rodríguez, E. & Breger, M. 2001, A&A, 366, 178

Rodríguez, E., García, J. M., Costa, V., et al. 2007, CoAst, 150, 63

Rodriguez, J., Tomsick, J. A., & Bodaghee, A. 2010, A&A, 517, 14

Rosenberg, F. D., Eyles, C. J., Skinner, G. K., & Willmore, A. P. 1975, Nature, 256, 628

Rossiter, R. A. 1924, ApJ, 60, 15

Rothschild, R. E., Blanco, P. R., Gruber, D. E., et al. 1998, ApJ, 496, 538

Rucinski, S. M. 1969, AcA, 19, 245

Samus, N. N., Durlevich, O. V., & al, e. 2012, GCVS database, CDS B/gcvs

Sana, H. & Evans, C. J. 2011, in IAU Symposium, Vol. 272, IAU Symposium, eprint: arXiv:1009.4197, 474–485

Scargle, J. D. 1982, ApJ, 263, 835

Schandl, S. & Meyer, F. 1994, A&A, 289, 149

Schmidt, M. 1963, Nature, 197, 1040

Schmidt-Kaler, T. 1982, in Stars and Star Clusters, ed. K. Schaifers & H. H. Voigt, Landolt-Börnstein - Group VI Astronomy and Astrophysics No. 2b (Springer Berlin Heidelberg), 1–14

Scott, D. M., Leahy, D. A., & Wilson, R. B. 2000, ApJ, 539, 392

Sembay, S., Schwartz, R. A., Orwig, L. E., Dennis, B. R., & Davies, S. R. 1990, ApJ, 351, 675

Seyfert, C. K. 1943, ApJ, 97, 28

Shemmer, O., Uttley, P., Netzer, H., & McHardy, I. M. 2003, MNRAS, 343, 1341

Siah, J., Tammaro, E., Guinan, E., & McCook, G. 2007, in Bulletin of the American Astronomical Society, Vol. 209, American Astronomical Society Meeting Abstracts #209, 275

Sidoli, L. 2013, ArXiv e-prints, 1301, 7574

Siemiginowska, A., Kuhn, O., Elvis, M., et al. 1995, ApJ, 454, 77

Simpson, G. & Mayer-Hasselwander, H. 1986, A&A, 162, 340

Singh, R., van de Ven, G., Jahnke, K., et al. 2013, A&A, 558, A43

Skipper, C. J., McHardy, I. M., & Maccarone, T. J. 2013, MNRAS, 434, 574

Skrutskie, M. F., Cutri, R. M., Stiening, R., et al. 2006, AJ, 131, 1163

Smith, J. F. & Courtier, G. M. 1976, Royal Society of London Proceedings Series A, 350, 421

Soldi, S., Türler, M., Paltani, S., et al. 2008, A&A, 486, 411

Soydugan, E., Soydugan, F., Şenyüz, T., Püsküllü, c., & Demircan, O. 2011, New A, 16, 72

Soydugan, E., Soydugan, F., Şenyüz, T., et al. 2010, in ASPC, Vol. 435, Binaries - Key to Comprehension of the Universe, 331

Soydugan, E., Soydugan, F., Demircan, O., & İbanoğlu, C. 2006, MNRAS, 370, 2013

Soydugan, E., Soydugan, F., Senyuz, T., et al. 2009, IBVS, 5902, 1

Spiridonova, O. I., Vlasyuk, V. V., Moskvitin, A. S., & Bychkova, V. S. 2015, ATel, 6953, 1

Staubert, R., Klochkov, D., Postnov, K., et al. 2009a, A&A, 494, 1025

Staubert, R., Klochkov, D., Vasco, D., et al. 2013, A&A, 550, A110

Staubert, R., Klochkov, D., & Wilms, J. 2009b, A&A, 500, 883

Stella, L., White, N. E., & Rosner, R. 1986, in The Physics of Accretion onto Compact Objects, Vol. 266, 77

Stellingwerf, R. F. 1978, ApJ, 224, 953

Stern, D., Assef, R. J., Benford, D. J., et al. 2012, ApJ, 753, 30

Stevens, J. B., Reig, P., Coe, M. J., et al. 1997, MNRAS, 288, 988

Strauss, M. A., Huchra, J. P., Davis, M., et al. 1992, ApJS, 83, 29

Sugizaki, M., Yamamoto, T., Mihara, T., & Nakajima, M. 2014, 226

Sulentic, J. W., Marziani, P., & Dultzin-Hacyan, D. 2000, ARA&A, 38, 521

Sunyaev, R. A., Grebenev, S. A., Lutovinov, A. A., et al. 2003, ATel, 190, 1

Svechnikov, M. A. & Kuznetsova, E. F. 1990, Catalogue of approximate photometric and absolute elements of eclipsing variable stars, Vol. 1-2 (Sverdlovsk: Ural University)

Szymanski, M. K. 2005, AcA, 55, 43

Tadhunter, C. 2008, New Astronomy Reviews, 52, 227

Tagliaferri, G., Ravasio, M., Ghisellini, G., et al. 2003, A&A, 400, 477

Tananbaum, H., Gursky, H., Kellogg, E. M., et al. 1972, ApJ, 174, L143

Taylor, M. B. 2005, in Astronomical Data Analysis Software and Systems XIV, Vol. 347, 29

Trümper, J. 1984, Advances in Space Research, 3, 483

Tueller, J., Ajello, M., Barthelmy, S., et al. 2005, ATel, 504, 1

Türler, M., Chernyakova, M., Courvoisier, T. J., et al. 2006, A&A, 451, L1

Ubertini, P., Lebrun, F., Di Cocco, G., et al. 2003, A&A, 411, L131

Udalski, A., Szymanski, M., Kaluzny, J., Kubiak, M., & Mateo, M. 1992, AcA, 42, 253

Ulrich, M. 1973, ApJ, 14, 89

Ulrich, M., Maraschi, L., & Urry, C. M. 1997, ARA&A, 35, 445

Urry, C. M. & Padovani, P. 1995, PASP, 107, 803

Uttley, P. 2006, in , eprint: arXiv:astro-ph/0501157, 101

Uttley, P. & Mchardy, I. M. 2004, Progress of Theoretical Physics Supplement, 155, 170

van Paradijs, J. & McClintock, J. E. 1995, X-ray Binaries, 58

van Paradijs, J. & van der Klis, M. 2002, in The Century of Space Science, Volume I, The Century of Space Science, Volume I, 811

Vedrenne, G., Roques, J. P., Schönfelder, V., et al. 2003, A&A, 411, L63

Veilleux, S., Sanders, D. B., & Kim, D. 1997, ApJ, 484, 92

Veilleux, S., Sanders, D. B., & Kim, D. 1999, ApJ, 522, 139

Véron-Cetty, M. & Véron, P. 2006, A&A, 455, 773

Véron-Cetty, M. & Véron, P. 2010, A&A, 518, A10

Veron-Cetty, M. P. & Veron, P. 1996, VizieR Online Data Catalog (VII/188)

Villata, M., Raiteri, C. M., Kurtanidze, O. M., et al. 2004, A&A, 421, 103

Wagner, S. J. & Witzel, A. 1995, ARA&A, 33, 163

Walker, G., Matthews, J., Kuschnig, R., et al. 2003, PASP, 115, 1023

Walter, R., Rodriguez, J., Foschini, L., et al. 2003, A&A, 411, L427

Watson, C., Henden, A. A., & Price, A. 2012, VizieR Online Data Catalog, 1, 02027

Watson, C. L. 2006, Journal of the American Association of Variable Star Observers (JAAVSO), 35, 318

Webster, B. L. & Murdin, P. 1972, Nature, 235, 37

Weedman, D. W. 1977, ARA&A, 15, 69

Weisskopf, M. C., Brinkman, B., Canizares, C., et al. 2002, PASP, 114, 1

White, N. E., Becker, R. H., Pravdo, S. H., et al. 1980, ApJ, 239, 655

Whitehurst, R. & King, A. 1991, MNRAS, 249, 25

Whitney, A. R., Shapiro, I. I., Rogers, A. E. E., et al. 1971, Science, 173, 225

Willott, C. J., Delorme, P., Reylé, C., et al. 2010, AJ, 139, 906

Wilson, R. E. 1979, ApJ, 234, 1054

Wilson, R. E. & Devinney, E. J. 1971, ApJ, 166, 605

Wilson-Hodge, C. A. 1999, Ph.D. Thesis, 6

Wilson-Hodge, C. A., Finger, M. H., Camero-Arranz, A., & Connaughton, V. 2009, ATel, 2324, 1

Winkler, C., Courvoisier, T. J. L., Di Cocco, G., et al. 2003, A&A, 411, L1

Woźniak, P. R., Vestrand, W. T., Akerlof, C. W., et al. 2004, AJ, 127, 2436

Wright, E. L., Eisenhardt, P. R. M., Mainzer, A. K., et al. 2010, AJ, 140, 1868

Wu, J., Zhou, X., Ma, J., et al. 2007, AJ, 133, 1599

Yamamoto, T., Nakahira, S., Kawai, N., et al. 2009, ATel, 2297, 1

Yan, J., Li, H., & Liu, Q. 2012, ApJ, 744, 37

Yan, L., Donoso, E., Tsai, C., et al. 2013, AJ, 145, 55

Zacharias, N., Finch, C., Girard, T., et al. 2010, AJ, 139, 2184

Zacharias, N., Finch, C. T., Girard, T. M., et al. 2012, VizieR Online Data Catalog, 1322, 0

Zacharias, N., Monet, D. G., Levine, S. E., et al. 2004, in BAAS, Vol. 36, American Astronomical Society Meeting Abstracts, 1418

Zasche, P. 2011, New Astronomy, Volume 16, Issue 3, p. 157-160., 16

Zdziarski, A. A., Poutanen, J., Paciesas, W. S., & Wen, L. 2002, ApJ, 578, 357

Zhang, B. K., Dai, B. Z., Wang, L. P., et al. 2012, MNRAS, 421, 3111

Zhang, Y. X., Zhou, X. L., Zhao, Y. H., & Wu, X. B. 2013, AJ, 145, 42

Zhou, A. Y. 2010, ArXiv e-prints, 1002, 2729

Zwintz, K., Weiss, W. W., Kuschnig, R., et al. 2000, A&AS, 145, 481

Appendix A

Calibration of OMC

One of the tasks I have performed during these years has been the calibration of OMC. Every time the OMC calibration is performed, two calibration files, the flat-field correction and the photometric calibration, are sent to the *INTEGRAL* Science Data Centre (ISDC) to be ingested in the instrument characteristic repository. These calibration files ar used by the scientific analysis pipelines and for the monitorization of the instrument. This calibration is usually carried out with a periodicity of 12 revolutions ($\sim$ 36 days). The detailed process of the calibration are explained in Rísquez (2008) and in Domingo (2011) and a brief summary is given below.

OMC has a Charge-coupled device (CCD), so their images have to been corrected following the usual procedure. This can be summarized in the following steps:

A.1 BIAS

The BIAS or polarization current is the charge the electronics adds during the readout proscess to be sure the analogical-digital conversor works in a lineal-response zone. A BIAS exposure is an image with no illumination and with zero-second time of exposure. During the calibration, a master bias is created from the median of 8 images. Two sets of four shots, modifying the readout ports (fet or right) and the gain (high or low). The BIAS is very sensitive to the temperature and for this reason it is measured for every scientific observation.

A.2 Dark current

It is the electric current that flows through photosensitive devices such as CCDs even when no photons are entering the device and is produced when the electrons jump from the valence band to the conduction band in the detector. This mechanism increases with time and with temperature.

The dark current is expected to increase with time and it is measured every time the calibration is performed, but until now it has been always negligible and the data are not corrected for this value. The evolution of the measured values of the dark current are shown in Fig. A.1.

A.3 Flat-field

This part of the calibration has the aim of correct for the individual pixel's response. Small manufacturing defects, optical-system imperfections make the actual response vary across the CCD. Due to some kind of deposition of material in the CCD, the flat-field calibration evolved in different ways until it was stabilized. The evolution of the flat-fields and the strategies OMC team followed to calibrate it are explained in detail in Rísquez (2008) and in Domingo (2011).

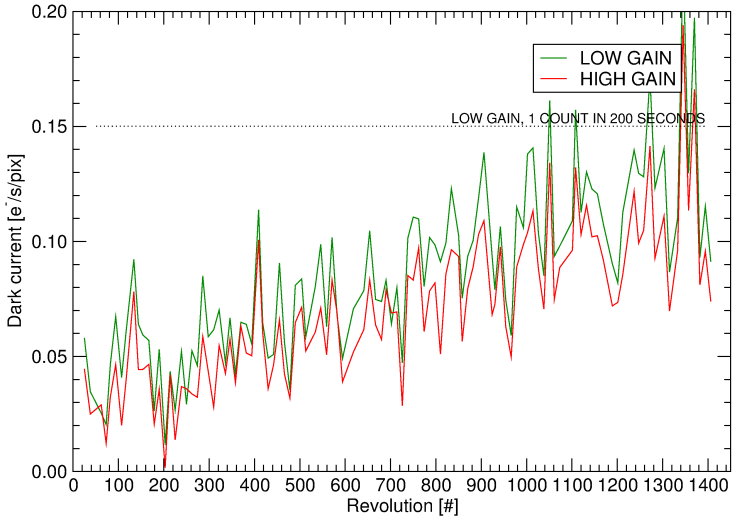

Figure A.1: Historical evolution of the dark current of OMC from the beginning of the mission to revolution 1450, with low gain(in green) and high gain(in red)

Since November 2007 (revolution 0618), when the spots produced by this material reached the 94% of the area of the image, the version 5 of the calibration was implemented and it has been used until now. This method consists in combining all the sky images until the last calibration, but taking just the pixels inside the spotted zone in the moment of each calibration. In this way, a high signal-to-noise is reached inside the spots, but some pixels are still very noisy, so the value of each pixel is replaced by the median of a 5×5 pixels box around itself. In every calibration, three sky images with exposures of 200 s are acquired and combined. The signal-to noise obtained with the sky images is not good enough to quantify the pixel-to-pixel response. A different procedure is carried out to measure this small-scale response using the results of the Earth observation performed by OMC in revolution 0409. Both results are convolved to get the final flat-field correction. To verify the flat-field correction is working in the right way, we measure the stan an observed magnitude. In Fi

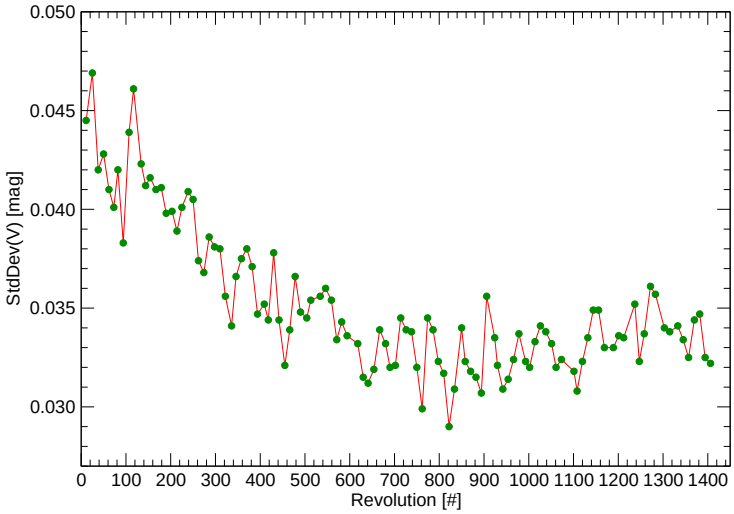

Figure A.2: Standard deviation of the magnitudes of the 50 best photometric stars versus the interval of calibration.

A.4 Photometric Calibration

The objective of the photometric calibration process is toconvert the instrumental fluxes to a standard system, in the case of OMC it is the V-Johnson magnitude system. The Johnson magnitude system is defined such that the star Alpha Lyr (Vega) has V=0.03 and all colors equal to zero. Traditionally, the magnitude of an object can be expressed as:

$$magnitud = calzero - 2.5\log(flux) \tag{A.1}$$

Where *calzero* is the zeropoint of the photometry, it means, the magnitude we would measure from an object whose detected flux were one photon per second. For CCDs, the relation between the magnitudes and the decimal logarithm of the instrumental flux is lineal with a slope of -2.5. To calculate the zeropoint, all the photometric stars observed from 15 days before the calibration to 15 days after the calibration are used. Several thousands of photometric-standard stars are used for each calibration. Photometric-standard stars are stars that have constant and very well-known values of their magnitudes in various passbands of the photometric system of interest, in this case, the Johnson system. Figure A.3 shows an illustration of the calculation of the zeropoint.

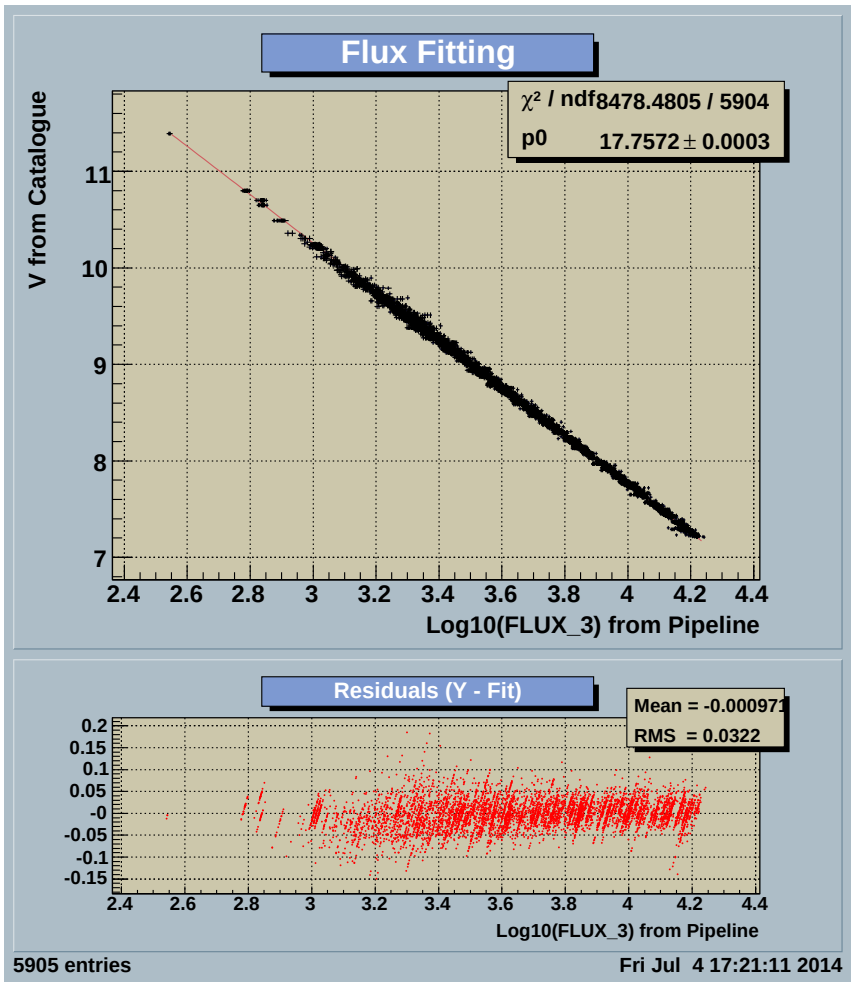

Figure A.3: Flux fitting of the photometric-standard stars used to determine the zeropoint for revolution 1406. In the upper box of the figure, the logarithms of the measured fluxes are plotted versus the catalogued V magnitude. A lineal regression is performed to calculate the zeropoint. The residuals of the fit are shown in the lower box.

The evolution of the zeropoint with time is plotted in Fig. A.4. Because of the effect of the radiation in the lenses, a loss of the sensitivity and then a decrement in the zeropoint would be expected to be observed with time, but the value of the zeropoint remains quite stable. A rapid variation was observed at the begining of the mission, probably due to the deposition of material mention t after that, the CCD has sho

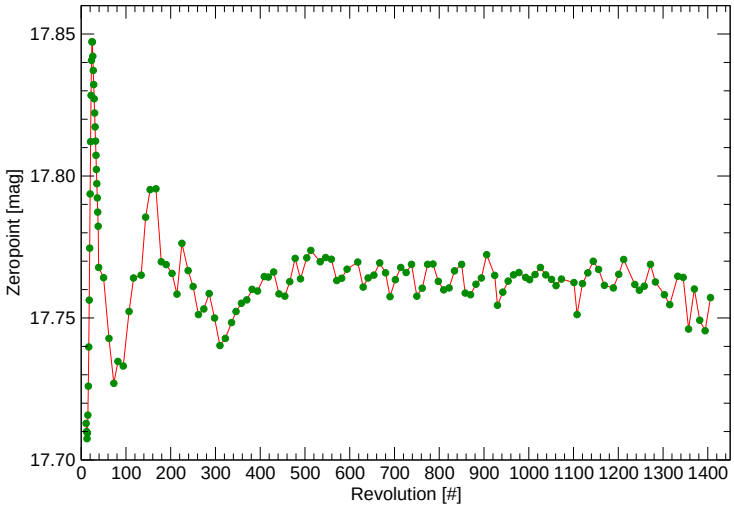

Figure A.4: Evolution of the zeropoint determined in each calibration with time.

Appendix B

INTEGRAL light curves of high-energy sources

This appendix includes the INTEGRAL light curves for the 73 sources from the cross-match of the IBIS catalog with the OMC archive (see Chapter 5), obtained as explained in Chapter 6.

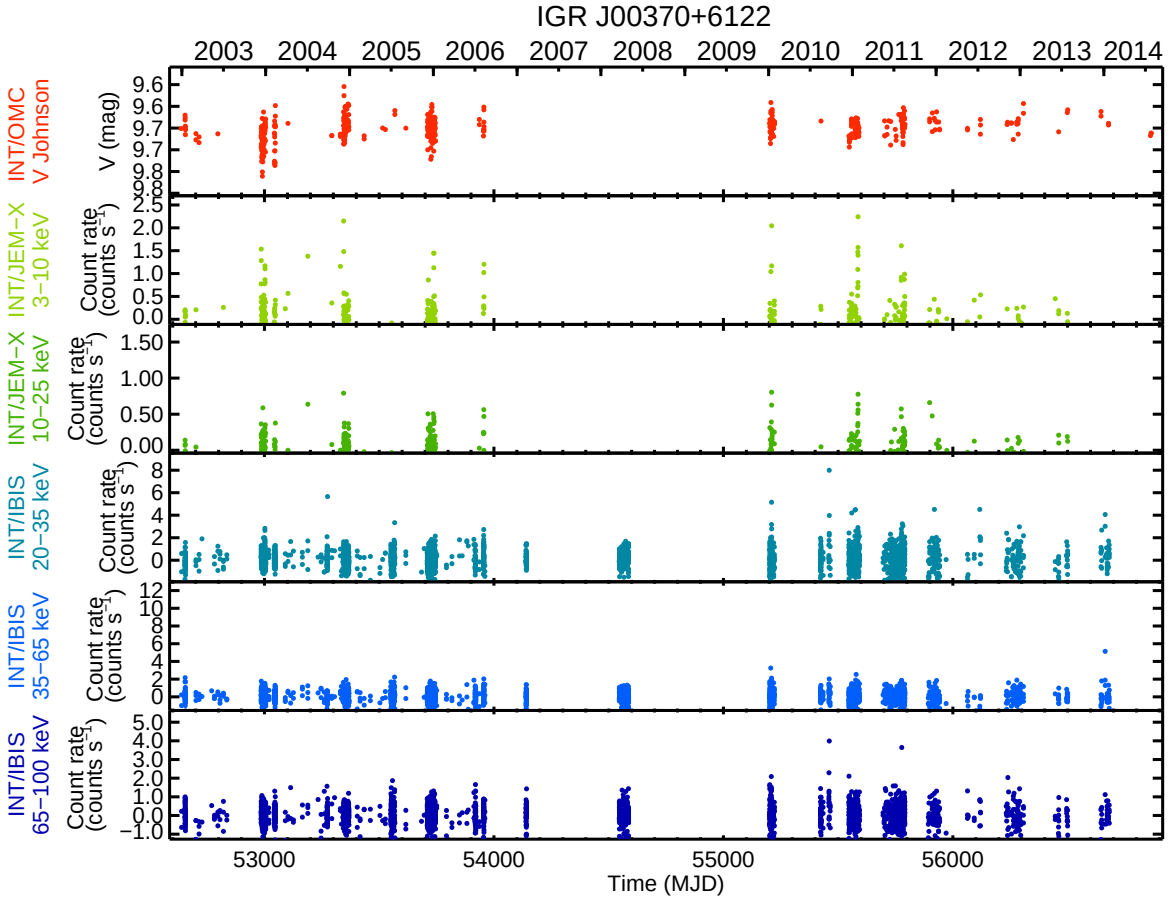
IGR J00370+6122
2003 2004 2005 2006 2007 2008 2009 2010 2011 2012 2013 2014
INT/OMC V Johnson
V (mag)
INT/JEM−X 3−10 keV
INT/JEM−X 10−25 keV
INT/IBIS 20−35 keV
INT/IBIS 35−65 keV
INT/IBIS 65−100 keV
Count rate (counts s⁻¹)
53000 54000 55000 56000
Time (MJD)

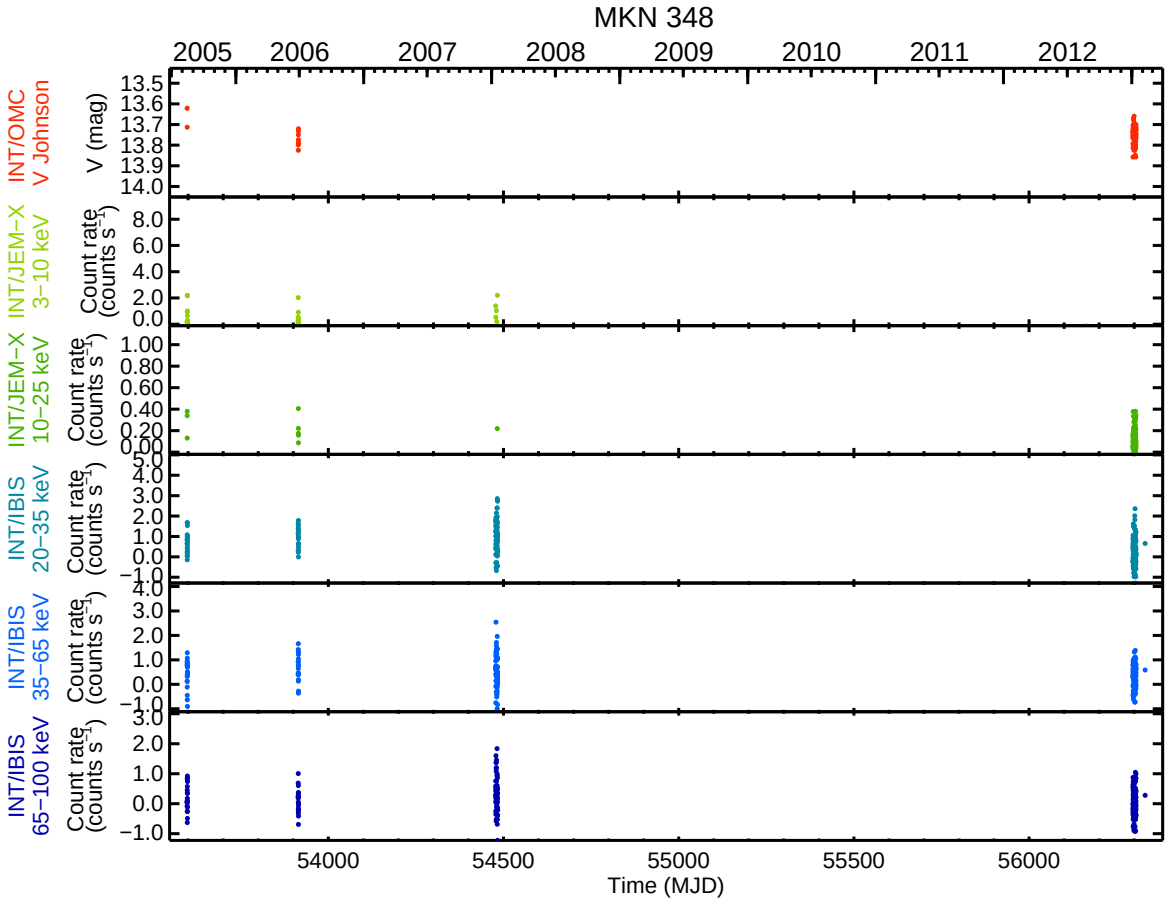
MKN 348
2005 2006 2007 2008 2009 2010 2011 2012
INT/OMC V Johnson
V (mag)
INT/JEM−X 3−10 keV
INT/JEM−X 10−25 keV
INT/IBIS 20−35 keV
INT/IBIS 35−65 keV
INT/IBIS 65−100 keV
Count rate (counts s⁻¹)
54000 54500 55000 55500 56000
Time (MJD)

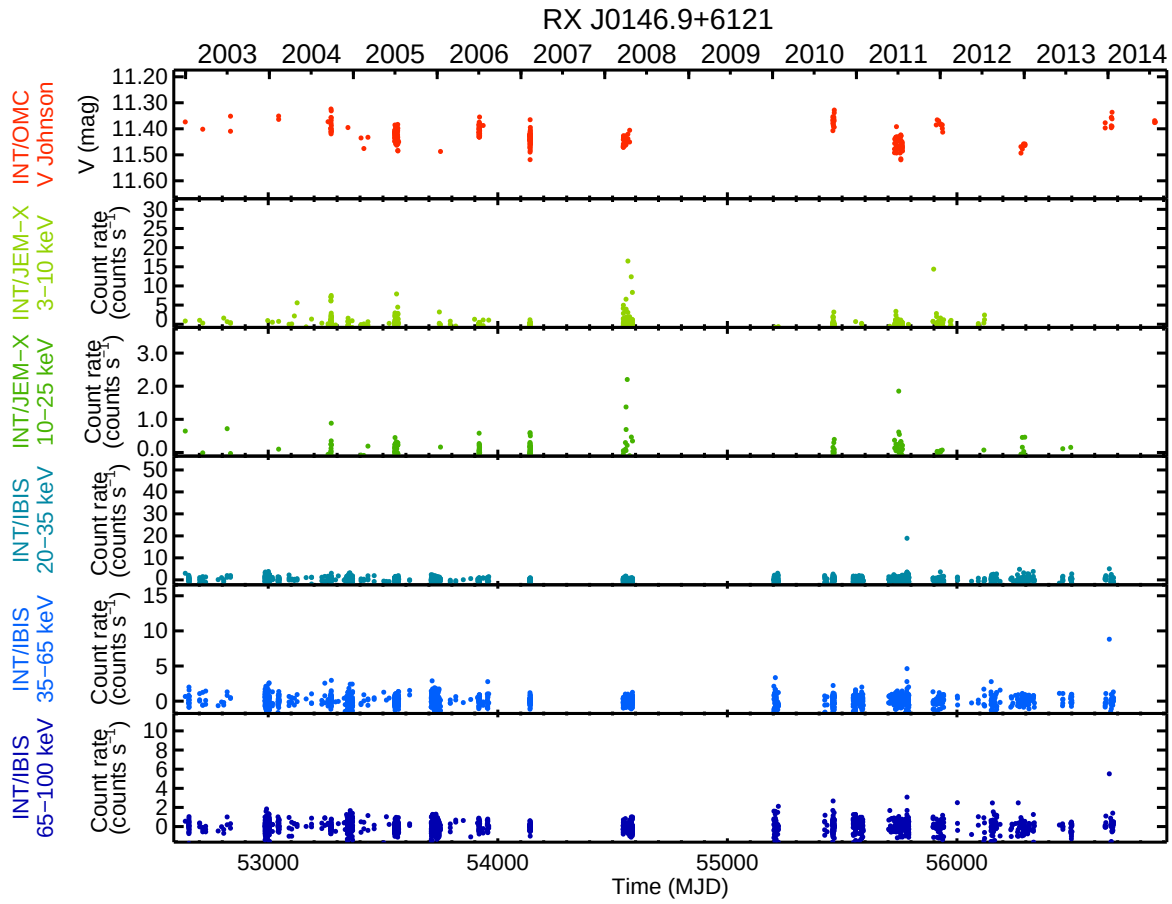
RX J0146.9+6121
2003 2004 2005 2006 2007 2008 2009 2010 2011 2012 2013 2014
INT/OMC V Johnson
V (mag)
INT/JEM−X 3−10 keV
INT/JEM−X 10−25 keV
INT/IBIS 20−35 keV
INT/IBIS 35−65 keV
INT/IBIS 65−100 keV
Count rate (counts s−1)
53000 54000 55000 56000
Time (MJD)

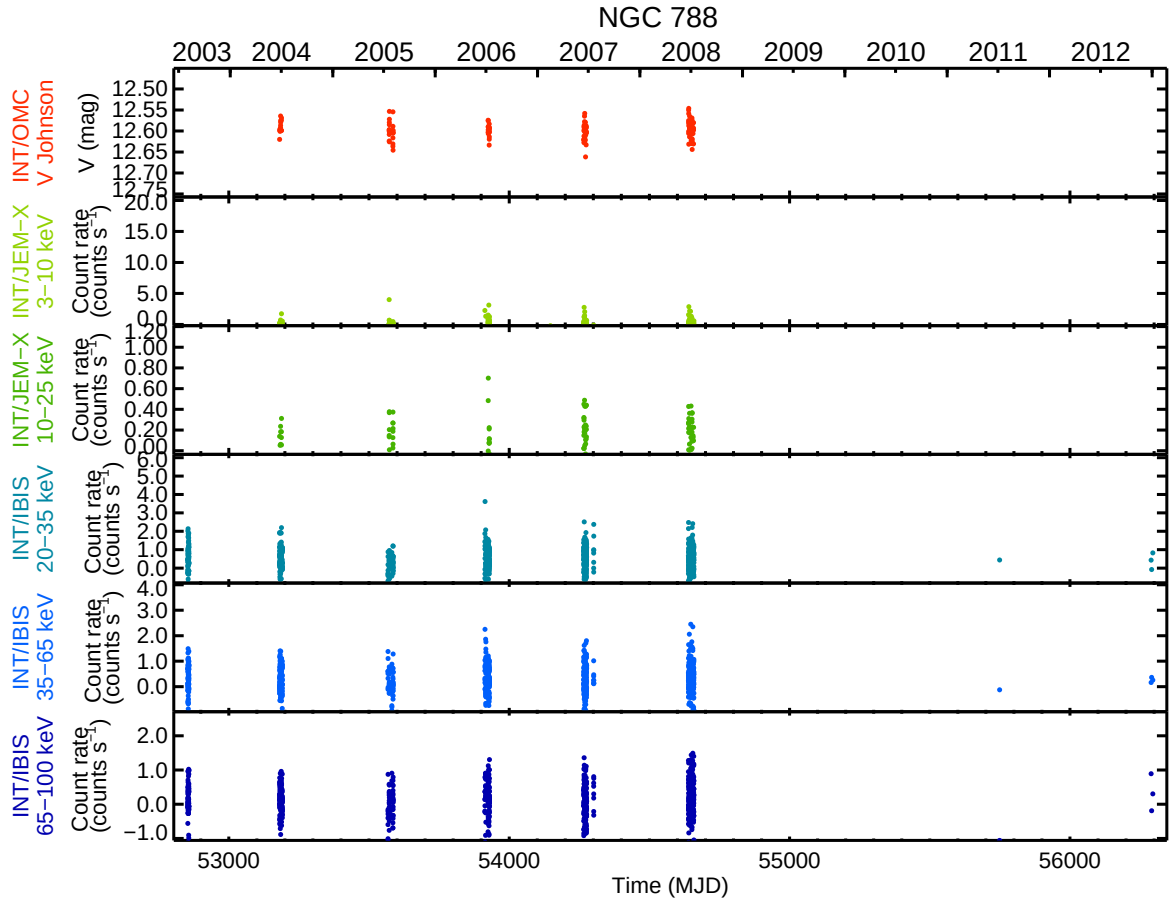
NGC 788
2003 2004 2005 2006 2007 2008 2009 2010 2011 2012
INT/OMC V Johnson
V (mag)
INT/JEM−X 3−10 keV
INT/JEM−X 10−25 keV
INT/IBIS 20−35 keV
INT/IBIS 35−65 keV
INT/IBIS 65−100 keV
Count rate (counts s−1)
53000 54000 55000 56000
Time (MJD)

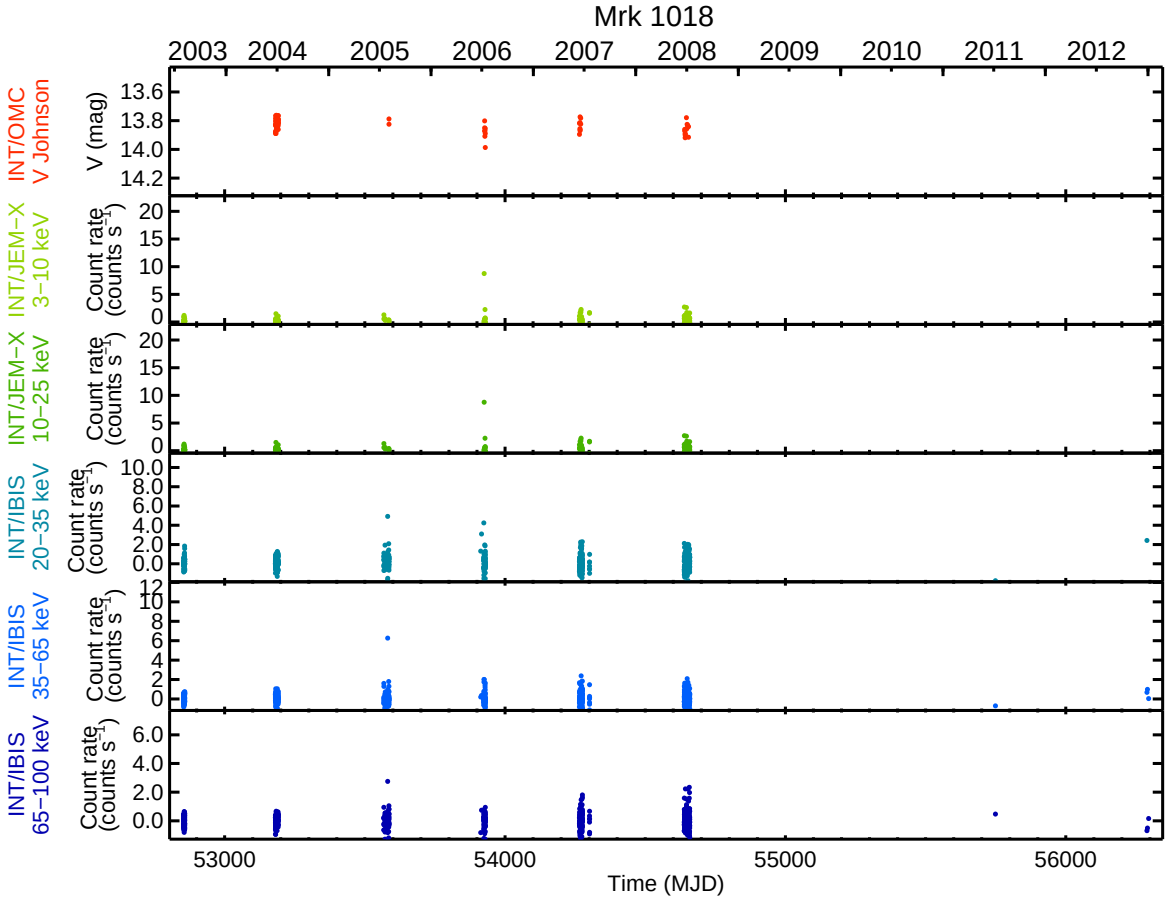
Mrk 1018
2003 2004 2005 2006 2007 2008 2009 2010 2011 2012
INT/OMC V Johnson
V (mag)
INT/JEM−X 3−10 keV
INT/JEM−X 10−25 keV
INT/IBIS 20−35 keV
INT/IBIS 35−65 keV
INT/IBIS 65−100 keV
Count rate (counts s−1)
53000 54000 55000 56000
Time (MJD)

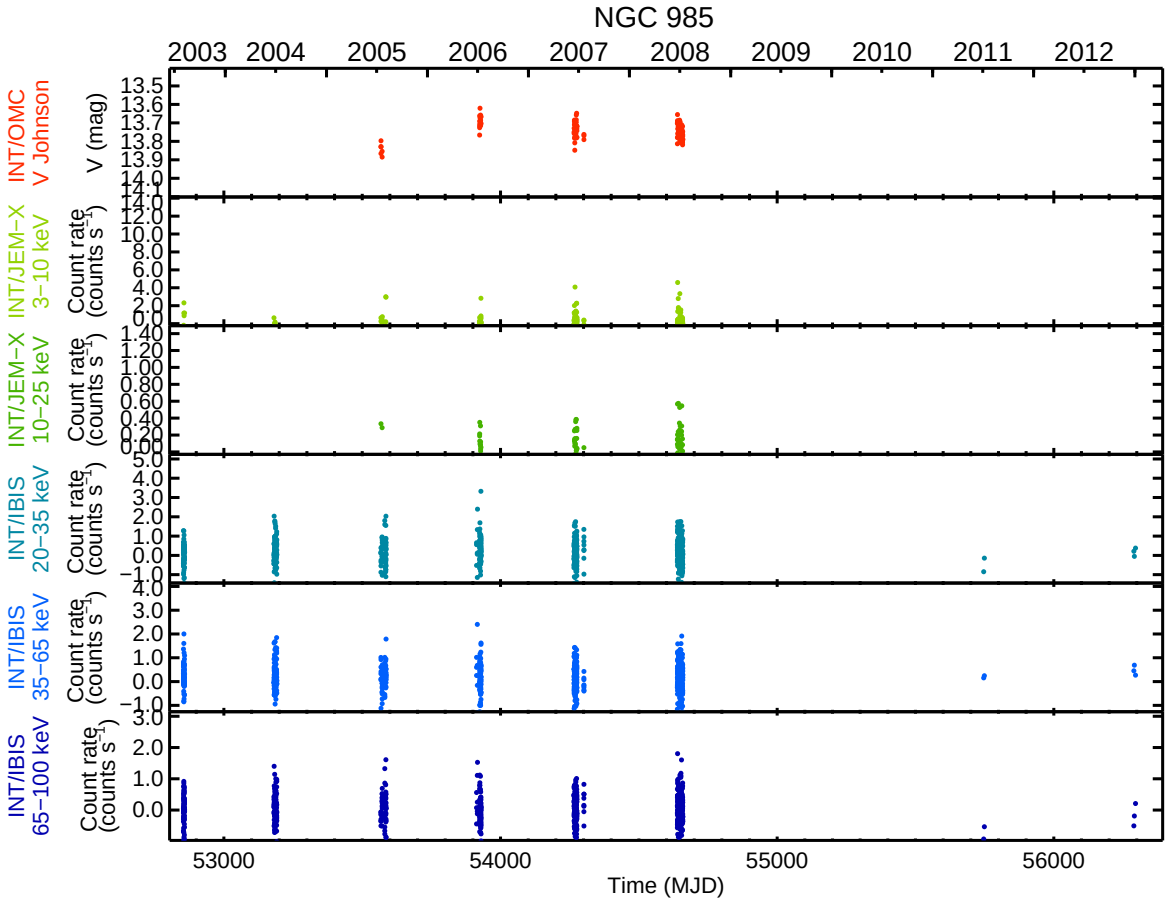
NGC 985
2003 2004 2005 2006 2007 2008 2009 2010 2011 2012
INT/OMC V Johnson
V (mag)
INT/JEM−X 3−10 keV
INT/JEM−X 10−25 keV
INT/IBIS 20−35 keV
INT/IBIS 35−65 keV
INT/IBIS 65−100 keV
Count rate (counts s−1)
53000 54000 55000 56000
Time (MJD)

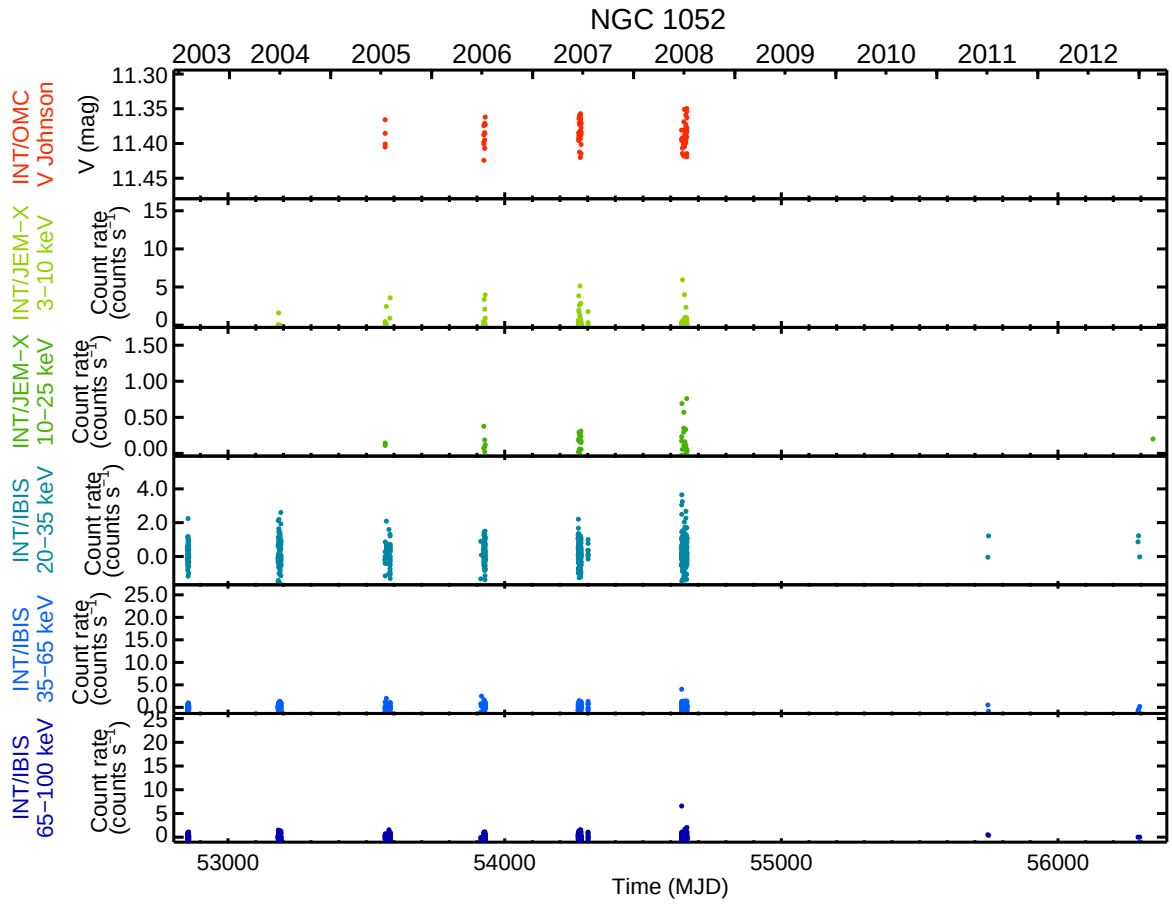
NGC 1052
2003
2004
2005
2006
2007
2008
2009
2010
2011
2012
INT/OMC
V Johnson
V (mag)
INT/JEM−X
3−10 keV
INT/JEM−X
10−25 keV
INT/IBIS
20−35 keV
INT/IBIS
35−65 keV
INT/IBIS
65−100 keV
Count rate (counts s−1)
53000
54000
55000
56000
Time (MJD)

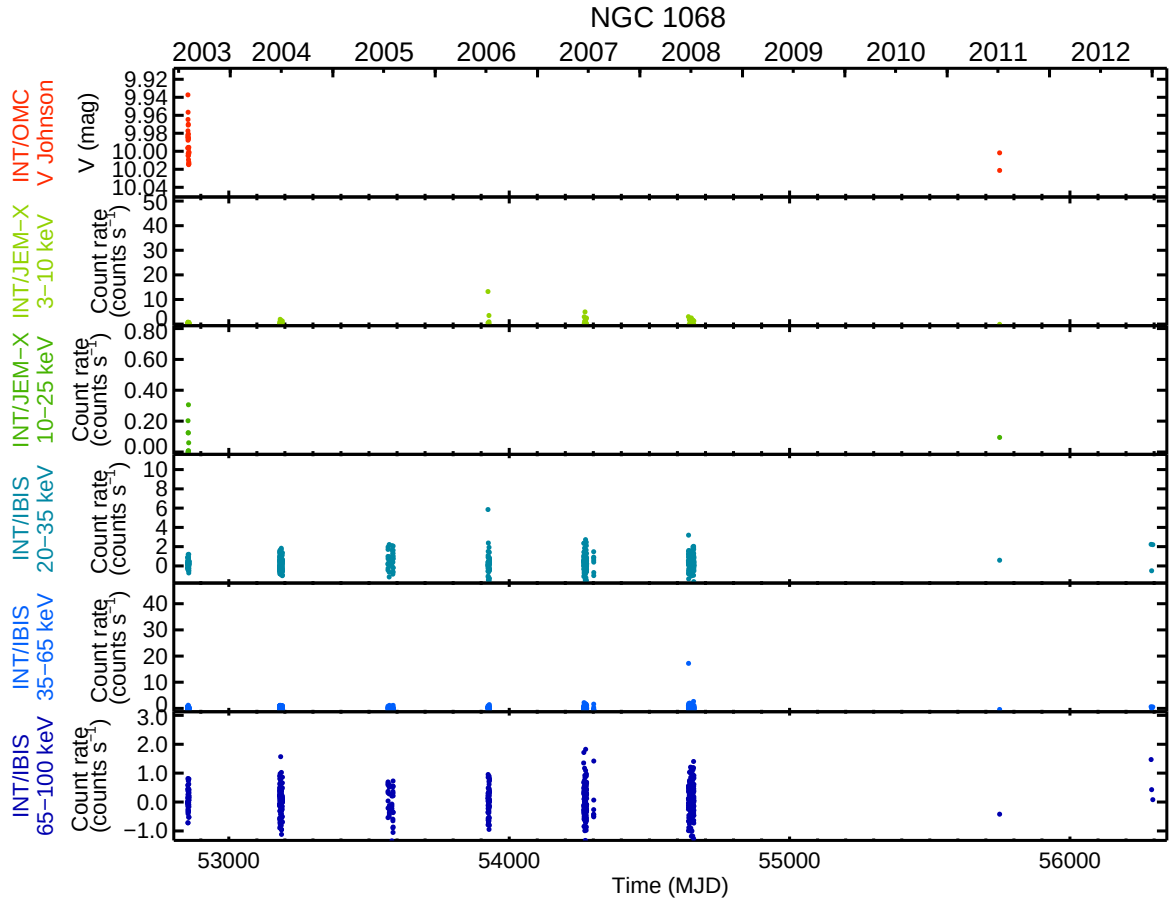
NGC 1068
2003
2004
2005
2006
2007
2008
2009
2010
2011
2012
INT/OMC
V Johnson
V (mag)
INT/JEM−X
3−10 keV
INT/JEM−X
10−25 keV
INT/IBIS
20−35 keV
INT/IBIS
35−65 keV
INT/IBIS
65−100 keV
Count rate (counts s−1)
53000
54000
55000
56000
Time (MJD)

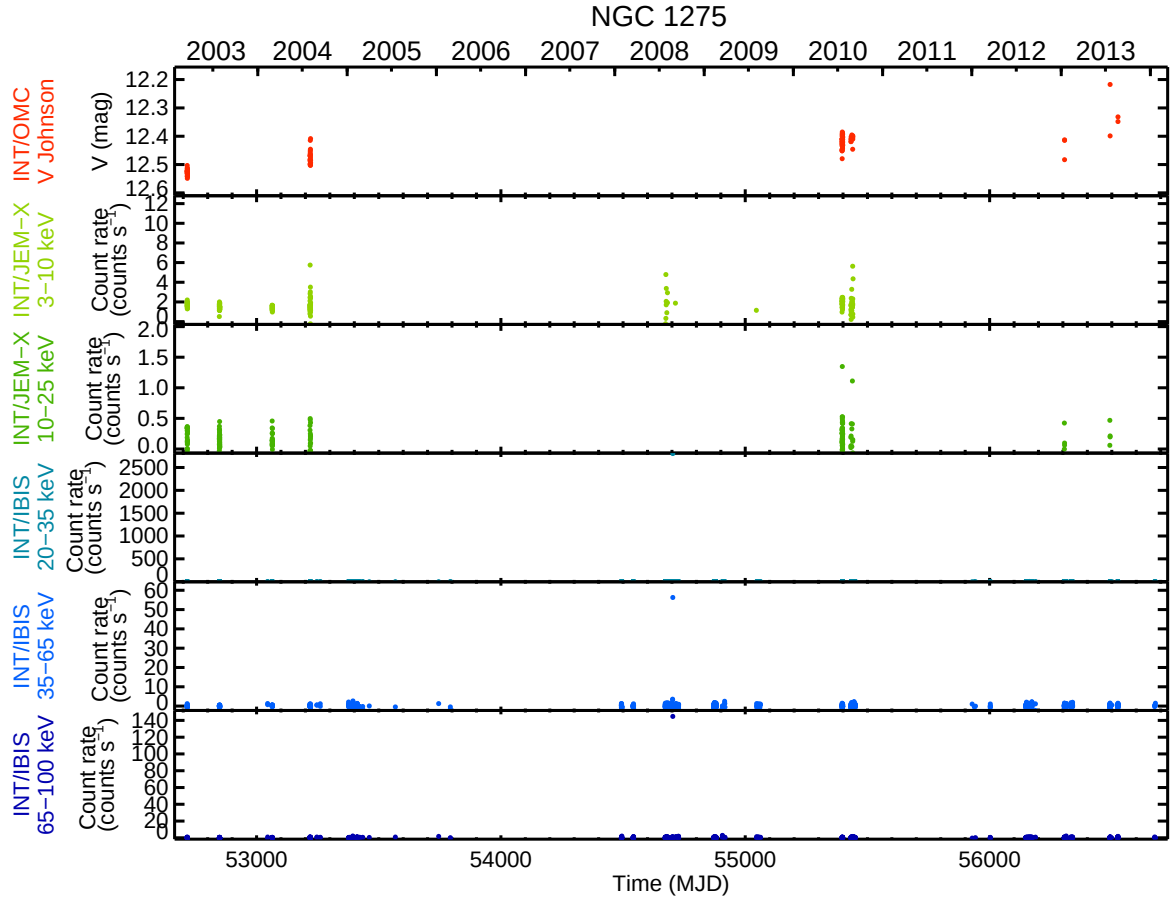
NGC 1275
2003
2004
2005
2006
2007
2008
2009
2010
2011
2012
2013
INT/OMC
V Johnson
V (mag)
INT/JEM−X
3−10 keV
INT/JEM−X
10−25 keV
INT/IBIS
20−35 keV
INT/IBIS
35−65 keV
INT/IBIS
65−100 keV
Count rate (counts s−1)
53000
54000
55000
56000
Time (MJD)

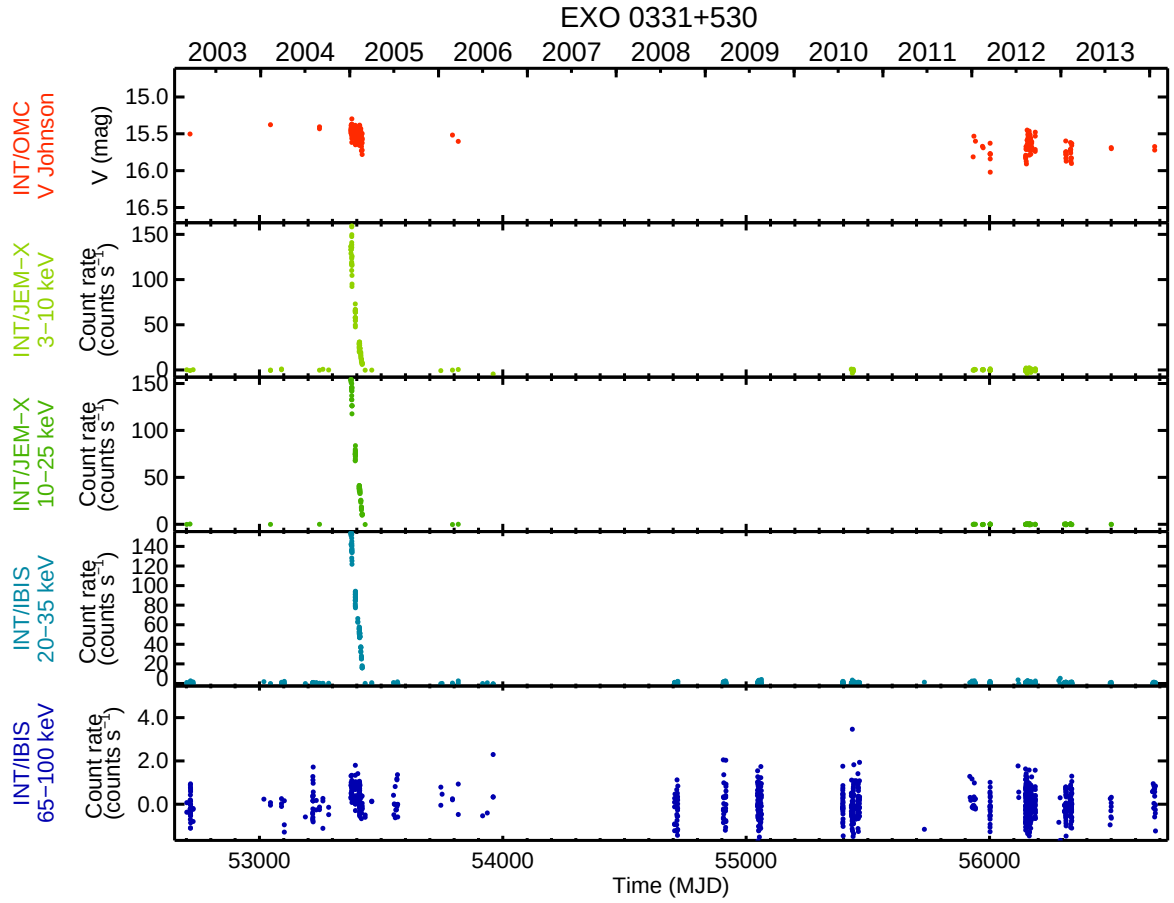
EXO 0331+530
2003
2004
2005
2006
2007
2008
2009
2010
2011
2012
2013
INT/OMC
V Johnson
V (mag)
INT/JEM−X
3−10 keV
INT/JEM−X
10−25 keV
INT/IBIS
20−35 keV
INT/IBIS
65−100 keV
Count rate (counts s−1)
53000
54000
55000
56000
Time (MJD)

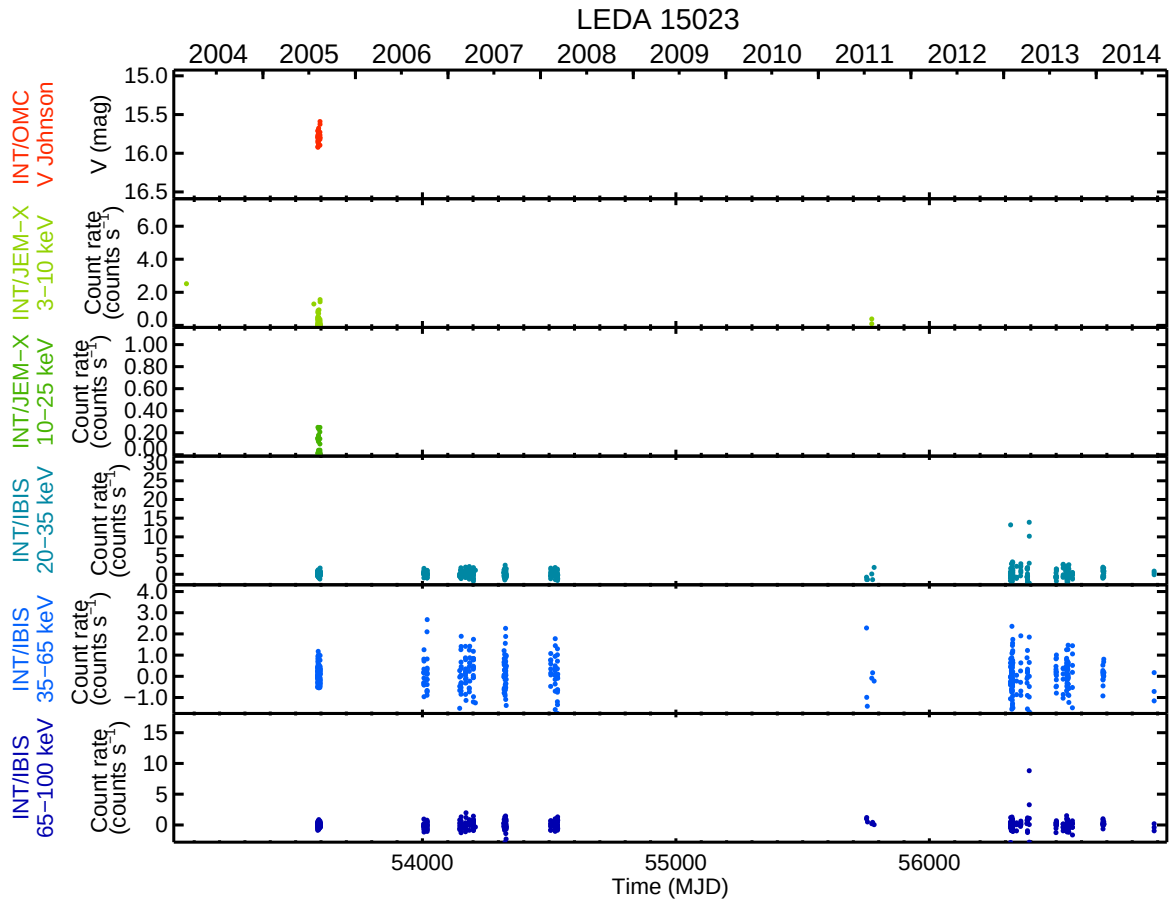
LEDA 15023
2004
2005
2006
2007
2008
2009
2010
2011
2012
2013
2014
INT/OMC
V Johnson
V (mag)
INT/JEM−X
3−10 keV
Count rate (counts s−1)
INT/JEM−X
10−25 keV
INT/IBIS
20−35 keV
INT/IBIS
35−65 keV
INT/IBIS
65−100 keV
54000
55000
56000
Time (MJD)

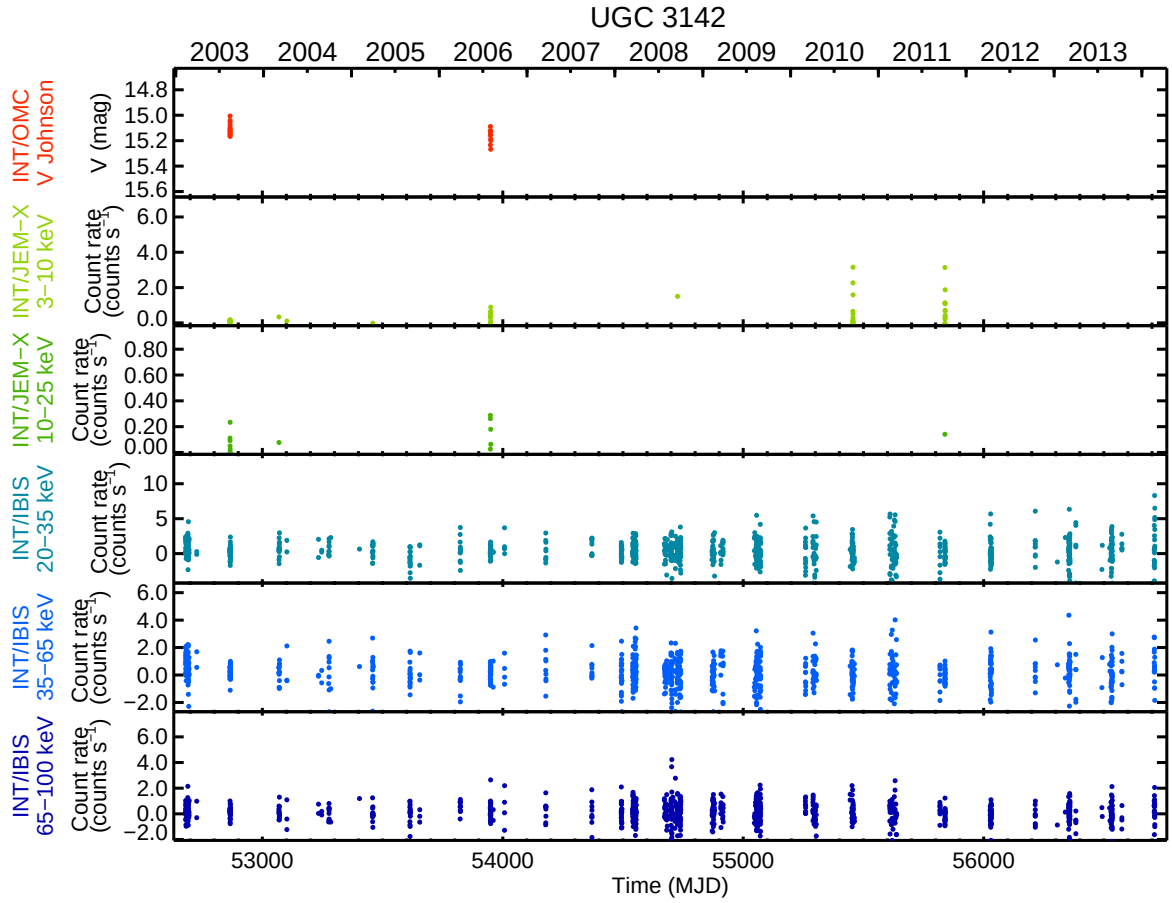
UGC 3142
2003
2004
2005
2006
2007
2008
2009
2010
2011
2012
2013
INT/OMC
V Johnson
V (mag)
INT/JEM−X
3−10 keV
Count rate (counts s−1)
INT/JEM−X
10−25 keV
INT/IBIS
20−35 keV
INT/IBIS
35−65 keV
INT/IBIS
65−100 keV
53000
54000
55000
56000
Time (MJD)

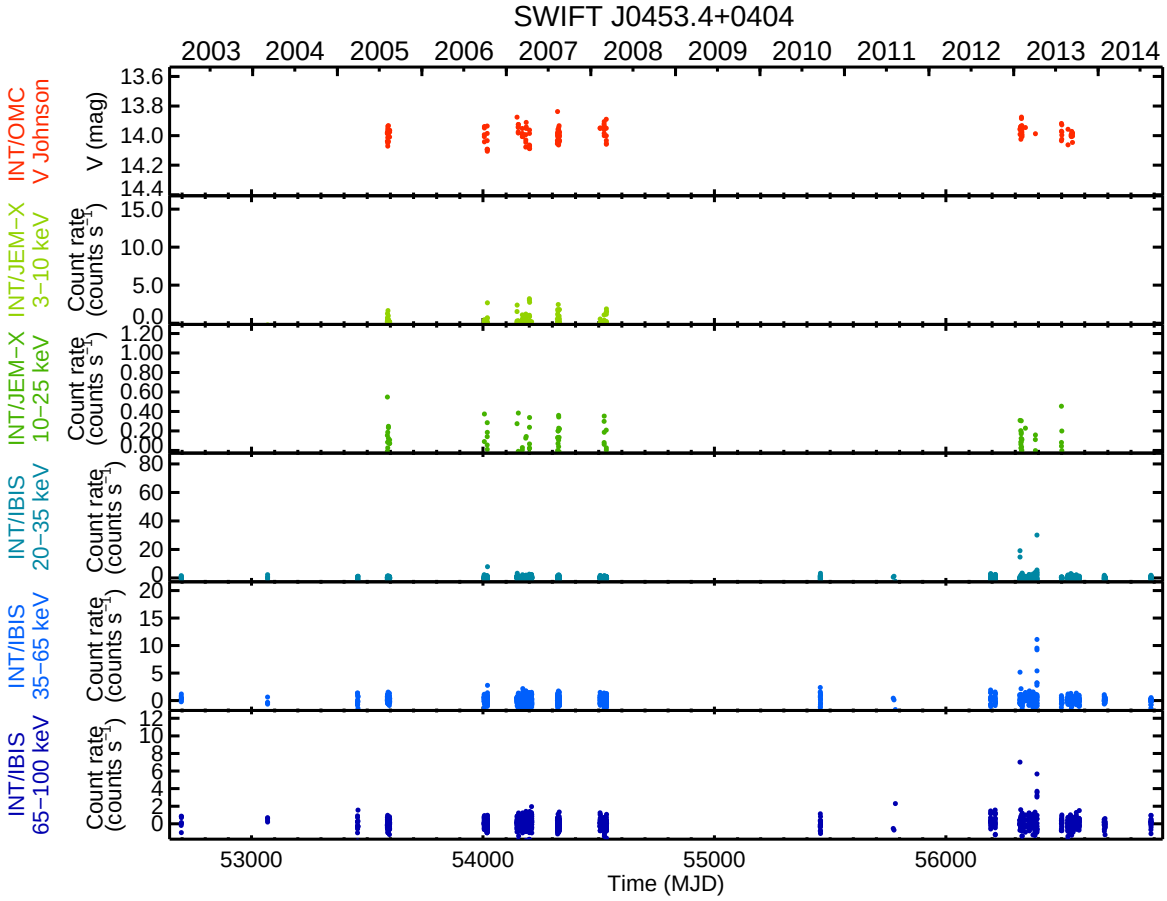
SWIFT J0453.4+0404
2003 2004 2005 2006 2007 2008 2009 2010 2011 2012 2013 2014
INT/OMC V Johnson
V (mag)
INT/JEM−X 3−10 keV
INT/JEM−X 10−25 keV
INT/IBIS 20−35 keV
INT/IBIS 35−65 keV
INT/IBIS 65−100 keV
Count rate (counts s⁻¹)
53000 54000 55000 56000
Time (MJD)

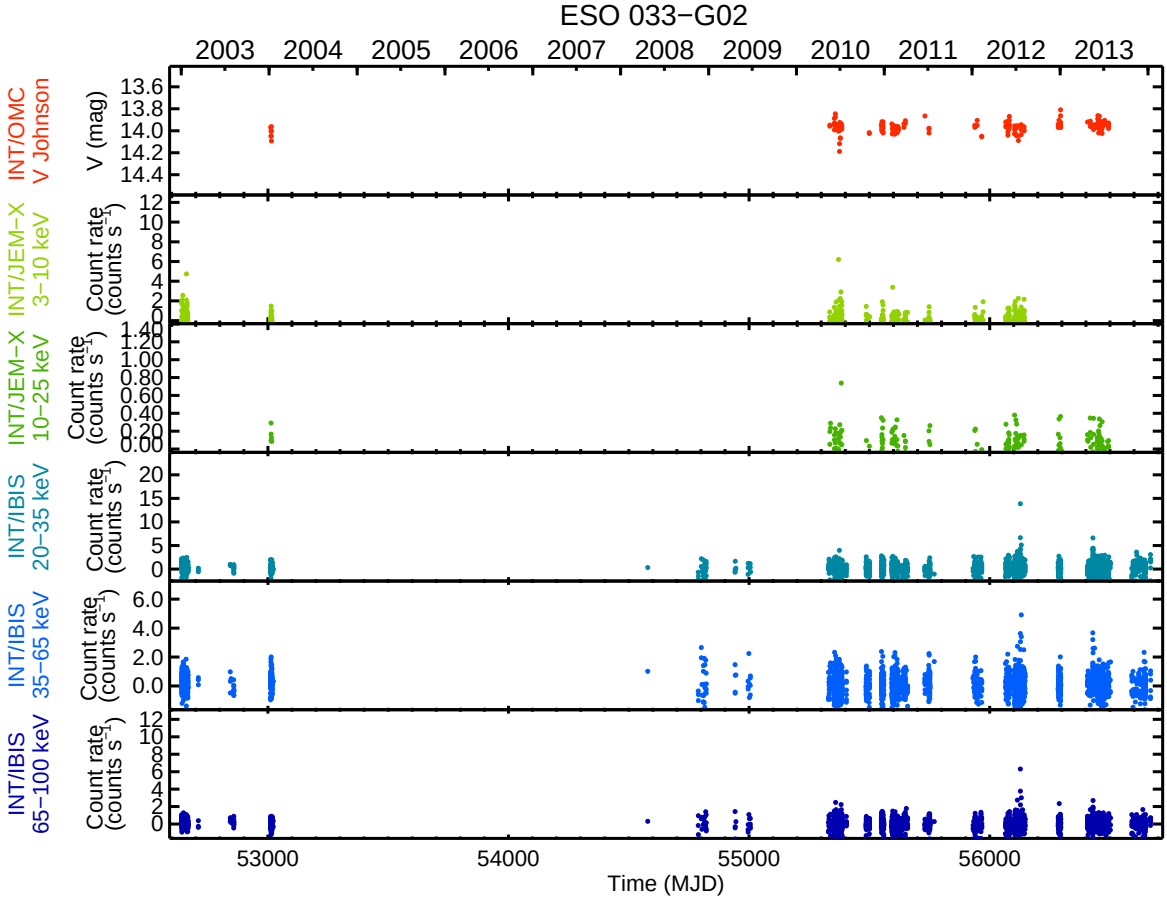
ESO 033−G02
2003 2004 2005 2006 2007 2008 2009 2010 2011 2012 2013
INT/OMC V Johnson
V (mag)
INT/JEM−X 3−10 keV
INT/JEM−X 10−25 keV
INT/IBIS 20−35 keV
INT/IBIS 35−65 keV
INT/IBIS 65−100 keV
Count rate (counts s⁻¹)
53000 54000 55000 56000
Time (MJD)

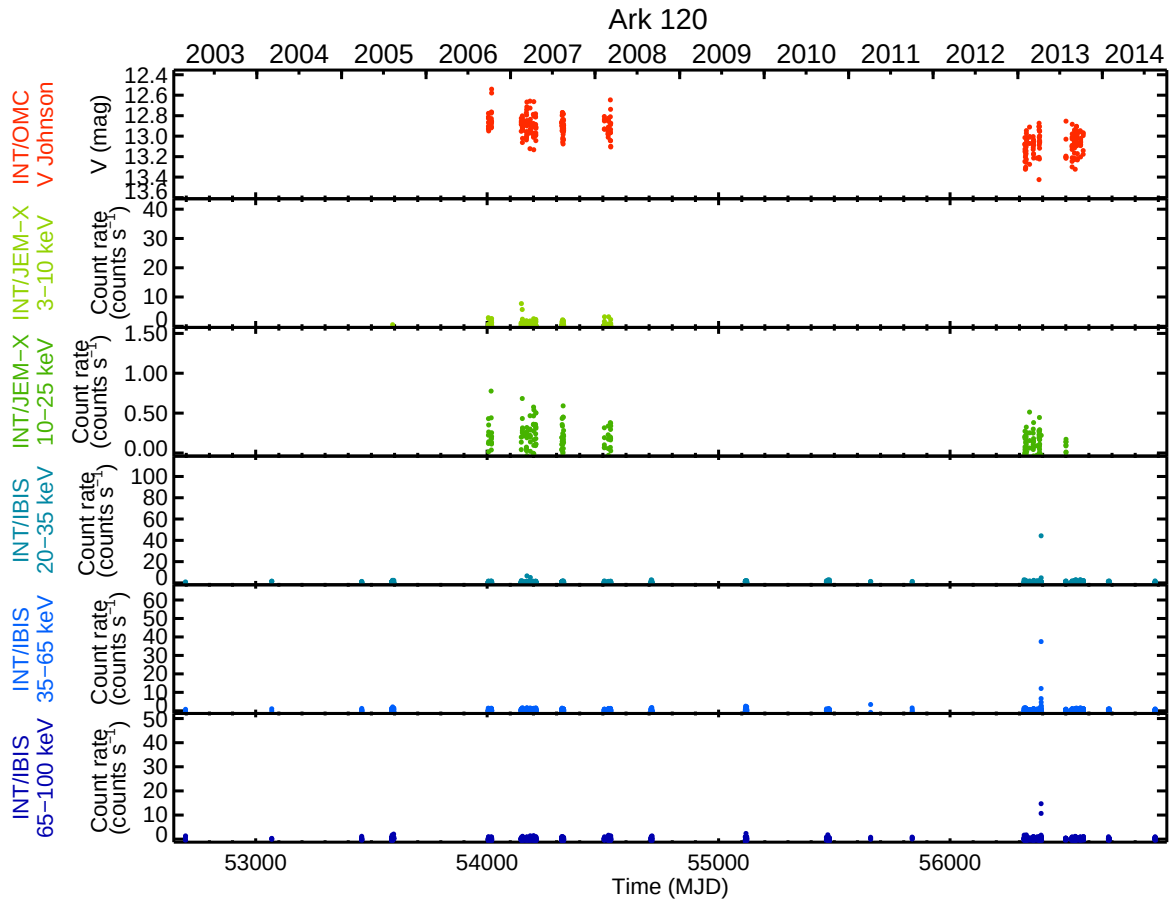
Ark 120
2003
2004
2005
2006
2007
2008
2009
2010
2011
2012
2013
2014
INT/OMC
V Johnson
V (mag)
INT/JEM−X
3−10 keV
INT/JEM−X
10−25 keV
INT/IBIS
20−35 keV
INT/IBIS
35−65 keV
INT/IBIS
65−100 keV
Count rate
(counts s−1)
53000
54000
55000
56000
Time (MJD)

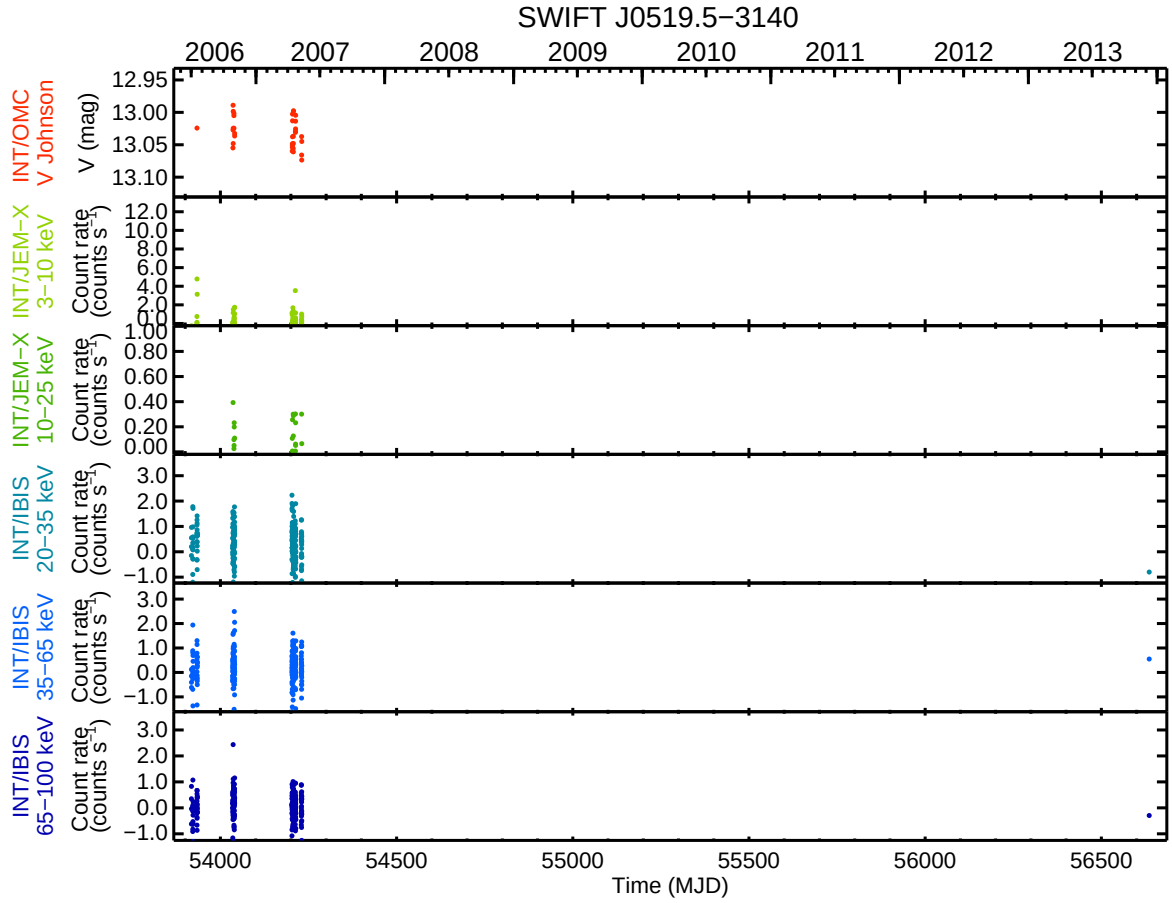
SWIFT J0519.5−3140
2006
2007
2008
2009
2010
2011
2012
2013
INT/OMC
V Johnson
V (mag)
INT/JEM−X
3−10 keV
INT/JEM−X
10−25 keV
INT/IBIS
20−35 keV
INT/IBIS
35−65 keV
INT/IBIS
65−100 keV
Count rate
(counts s−1)
54000
54500
55000
55500
56000
56500
Time (MJD)

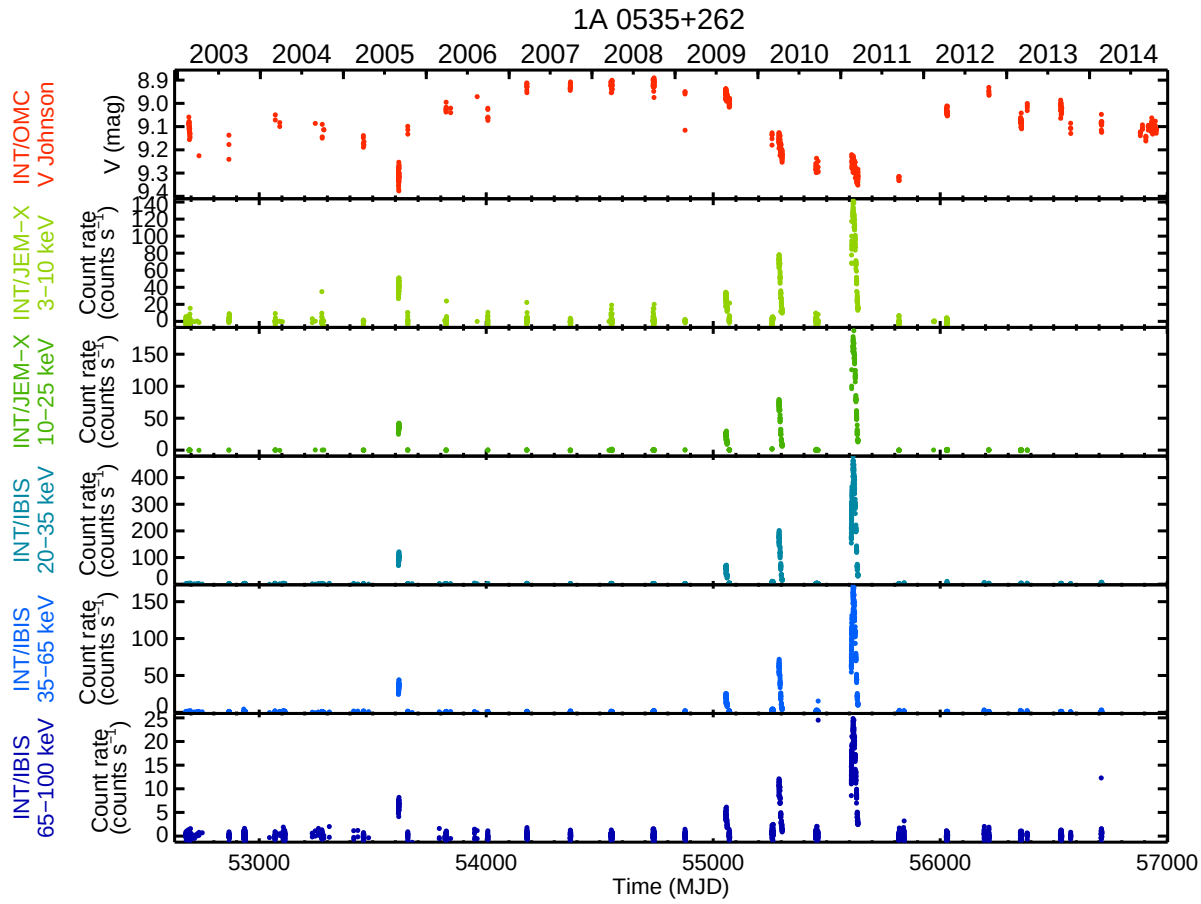
1A 0535+262
2003 2004 2005 2006 2007 2008 2009 2010 2011 2012 2013 2014
INT/OMC V Johnson
V (mag)
INT/JEM−X 3−10 keV
INT/JEM−X 10−25 keV
INT/IBIS 20−35 keV
INT/IBIS 35−65 keV
INT/IBIS 65−100 keV
Count rate (counts s−1)
53000 54000 55000 56000 57000
Time (MJD)

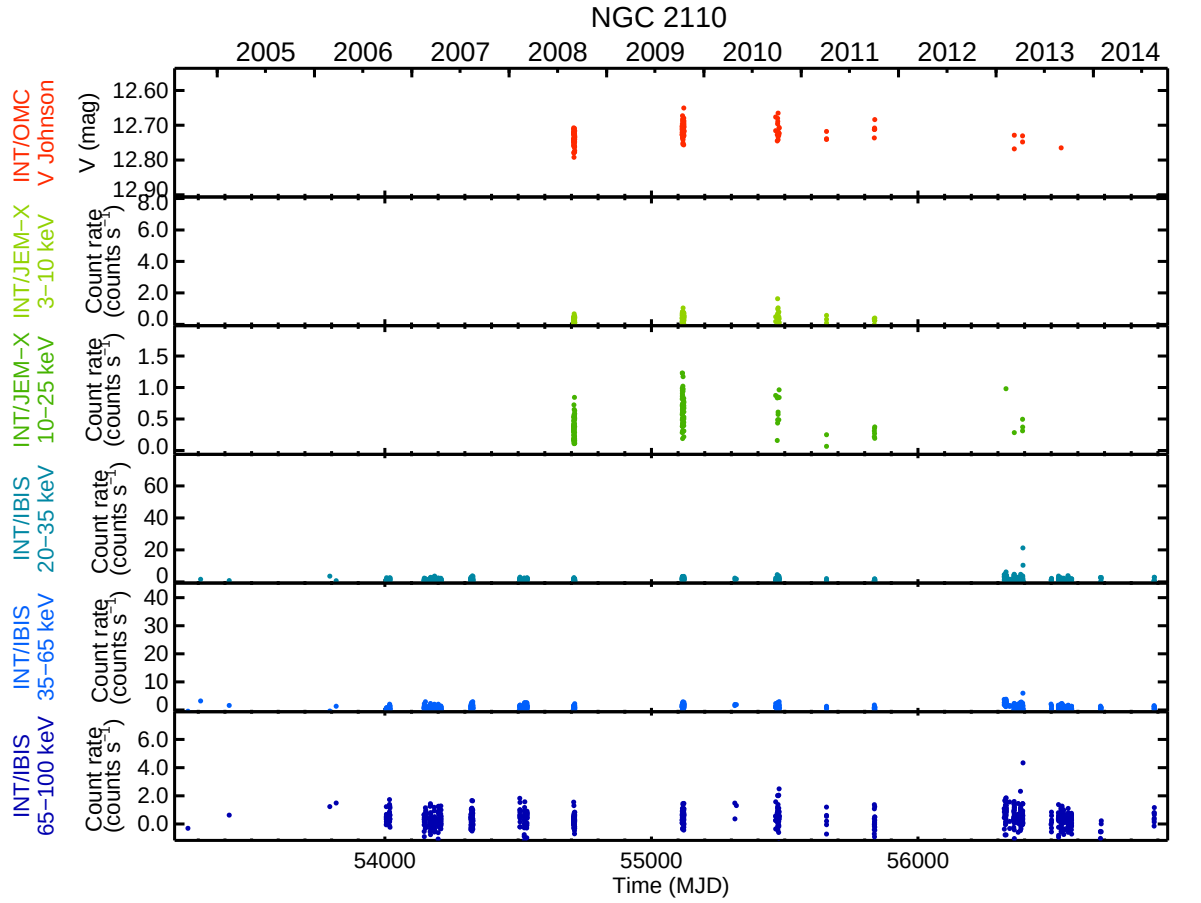
NGC 2110
2005 2006 2007 2008 2009 2010 2011 2012 2013 2014
INT/OMC V Johnson
V (mag)
INT/JEM−X 3−10 keV
INT/JEM−X 10−25 keV
INT/IBIS 20−35 keV
INT/IBIS 35−65 keV
INT/IBIS 65−100 keV
Count rate (counts s−1)
54000 55000 56000
Time (MJD)

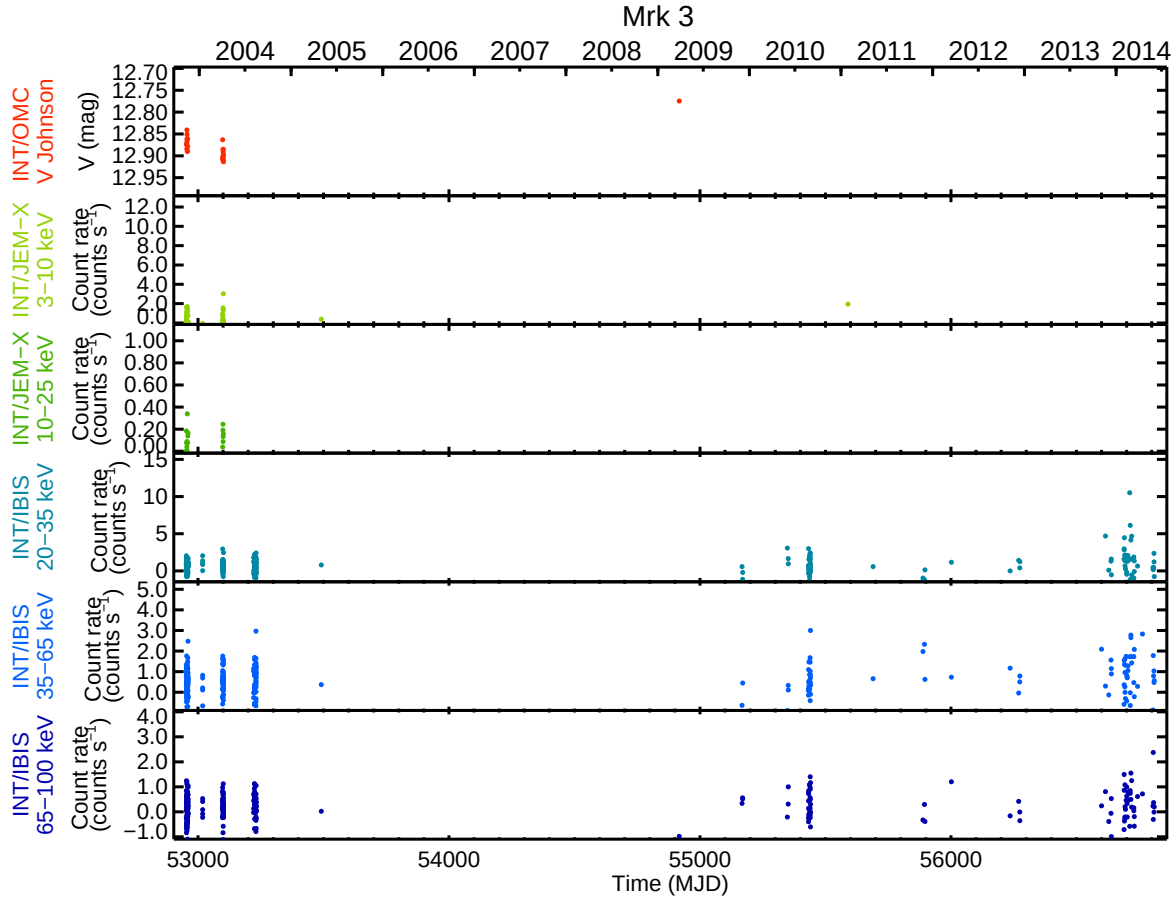
Mrk 3
2004
2005
2006
2007
2008
2009
2010
2011
2012
2013
2014
INT/OMC
V Johnson
V (mag)
INT/JEM−X
3−10 keV
INT/JEM−X
10−25 keV
INT/IBIS
20−35 keV
INT/IBIS
35−65 keV
INT/IBIS
65−100 keV
Count rate (counts s−1)
53000
54000
55000
56000
Time (MJD)

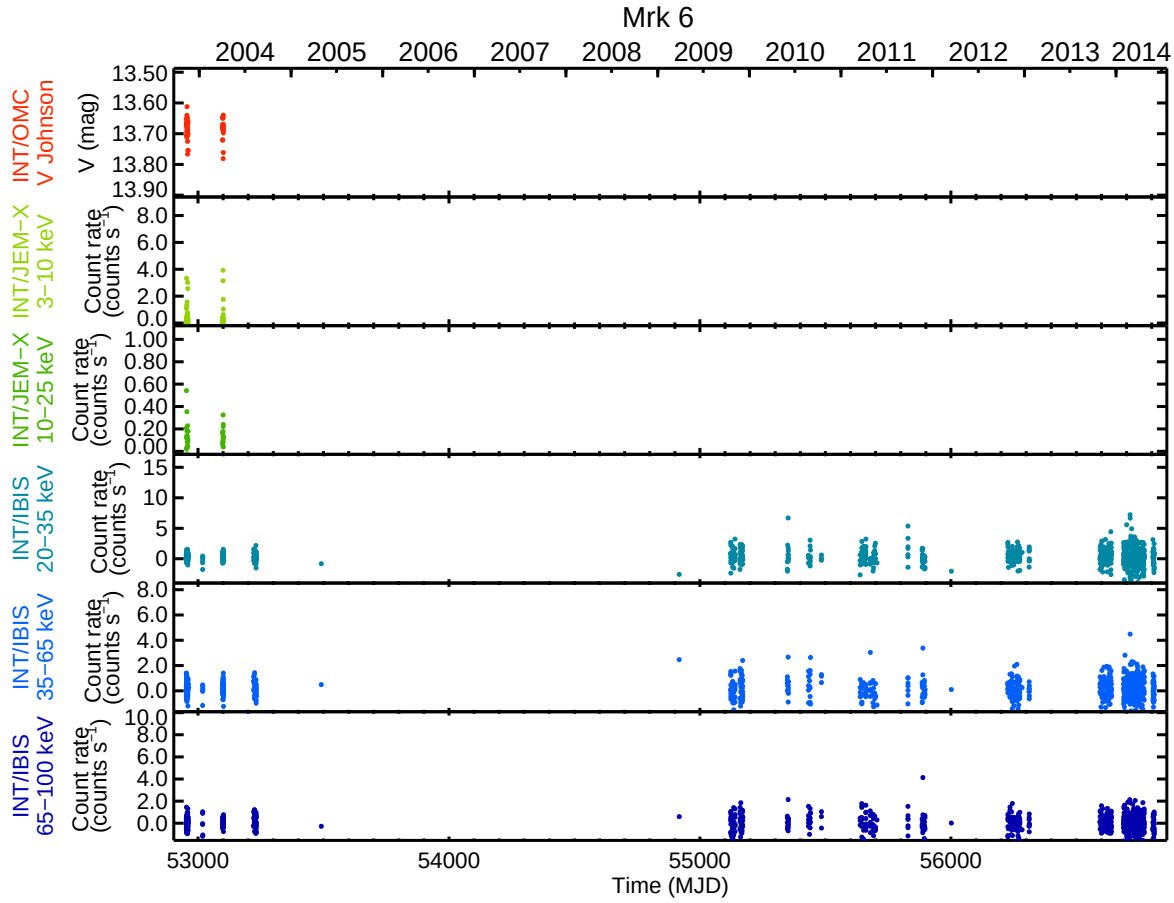
Mrk 6
2004
2005
2006
2007
2008
2009
2010
2011
2012
2013
2014
INT/OMC
V Johnson
V (mag)
INT/JEM−X
3−10 keV
INT/JEM−X
10−25 keV
INT/IBIS
20−35 keV
INT/IBIS
35−65 keV
INT/IBIS
65−100 keV
Count rate (counts s−1)
53000
54000
55000
56000
Time (MJD)

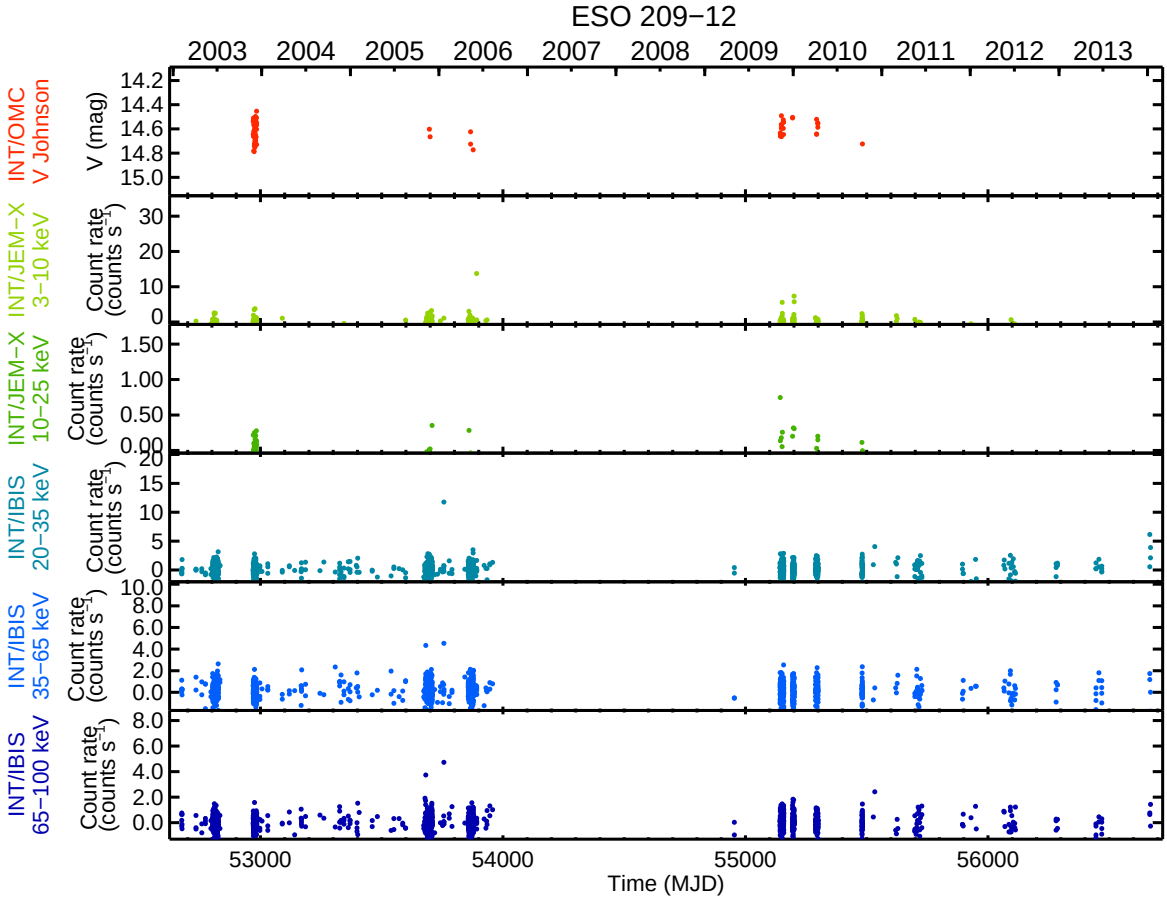
ESO 209−12
2003 2004 2005 2006 2007 2008 2009 2010 2011 2012 2013
INT/OMC V Johnson
V (mag)
INT/JEM−X 3−10 keV
INT/JEM−X 10−25 keV
INT/IBIS 20−35 keV
INT/IBIS 35−65 keV
INT/IBIS 65−100 keV
Count rate (counts s⁻¹)
53000 54000 55000 56000
Time (MJD)

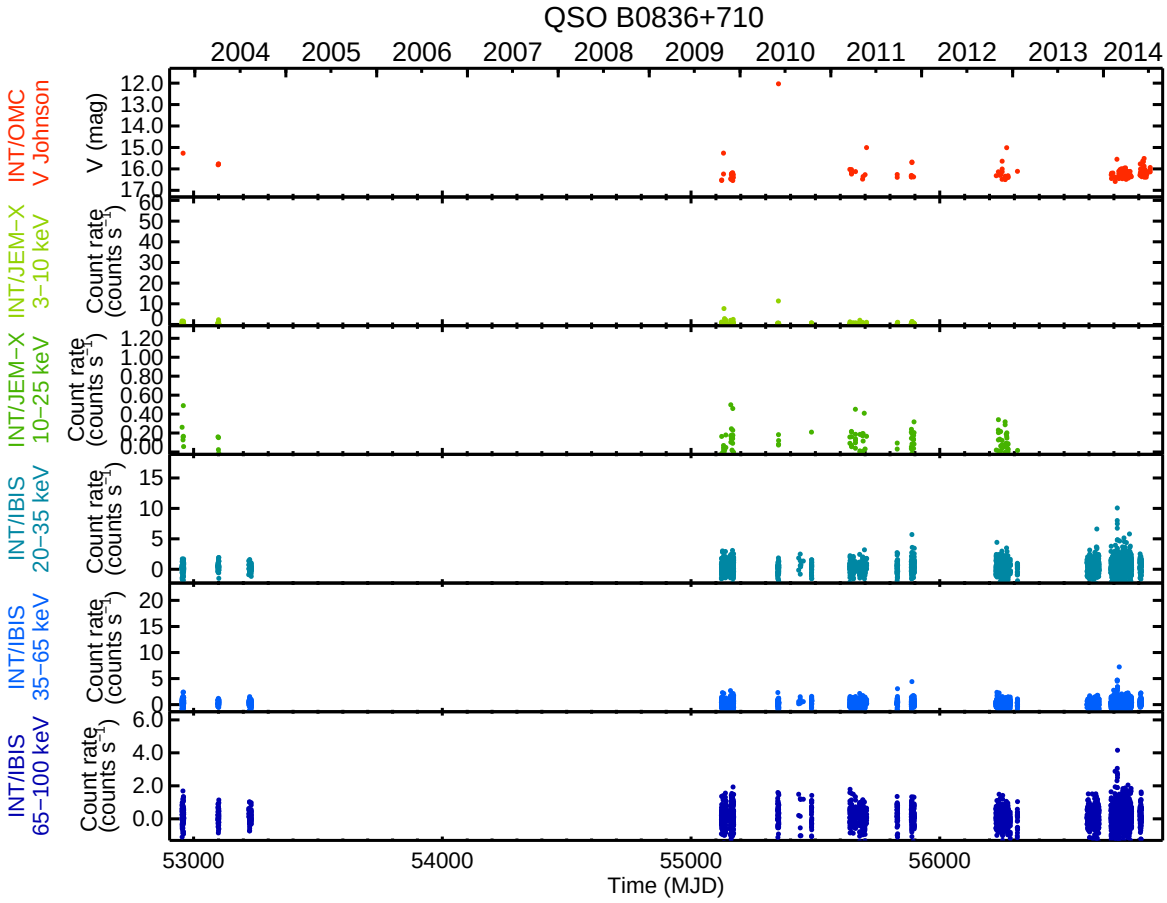
QSO B0836+710
2004 2005 2006 2007 2008 2009 2010 2011 2012 2013 2014
INT/OMC V Johnson
V (mag)
INT/JEM−X 3−10 keV
INT/JEM−X 10−25 keV
INT/IBIS 20−35 keV
INT/IBIS 35−65 keV
INT/IBIS 65−100 keV
Count rate (counts s⁻¹)
53000 54000 55000 56000
Time (MJD)

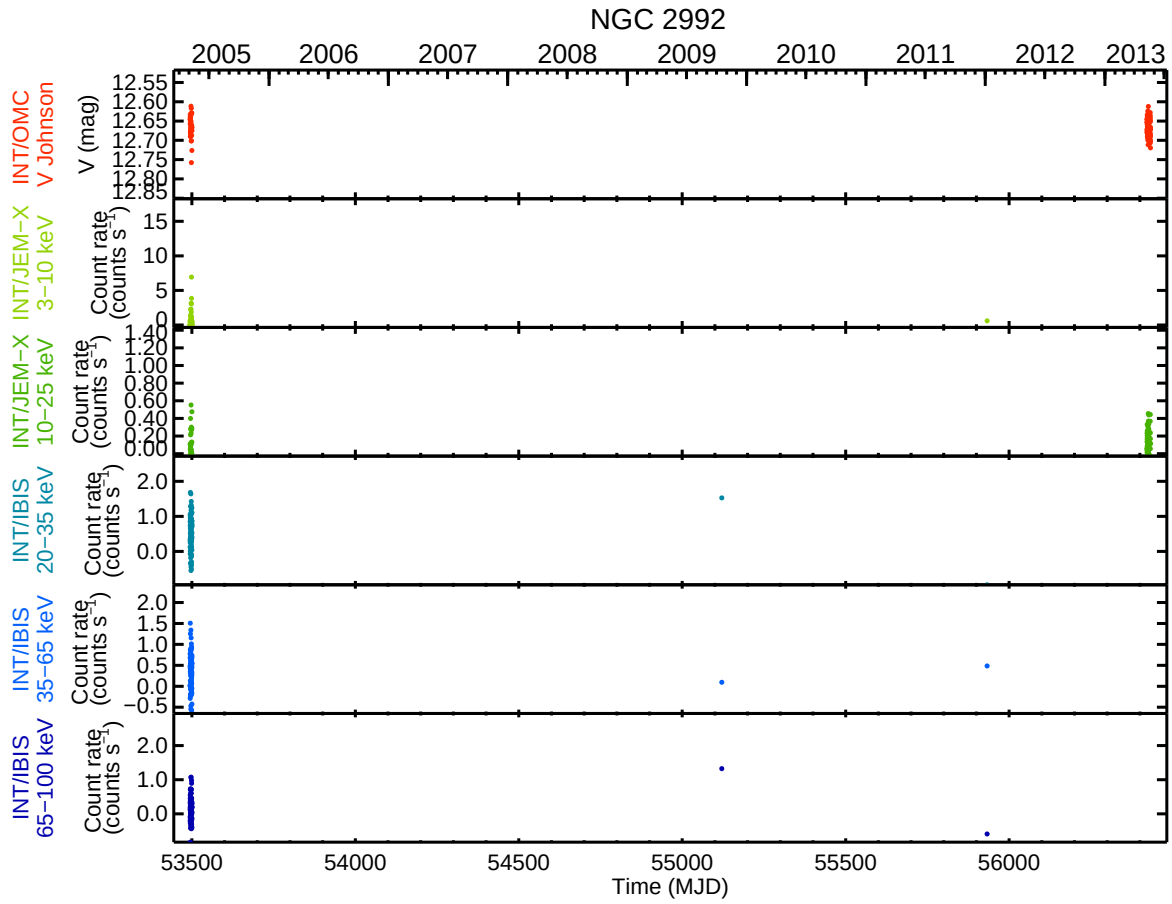
NGC 2992
2005
2006
2007
2008
2009
2010
2011
2012
2013
INT/OMC
V Johnson
V (mag)
INT/JEM−X
3−10 keV
INT/JEM−X
10−25 keV
INT/IBIS
20−35 keV
INT/IBIS
35−65 keV
INT/IBIS
65−100 keV
Count rate (counts s−1)
53500
54000
54500
55000
55500
56000
Time (MJD)

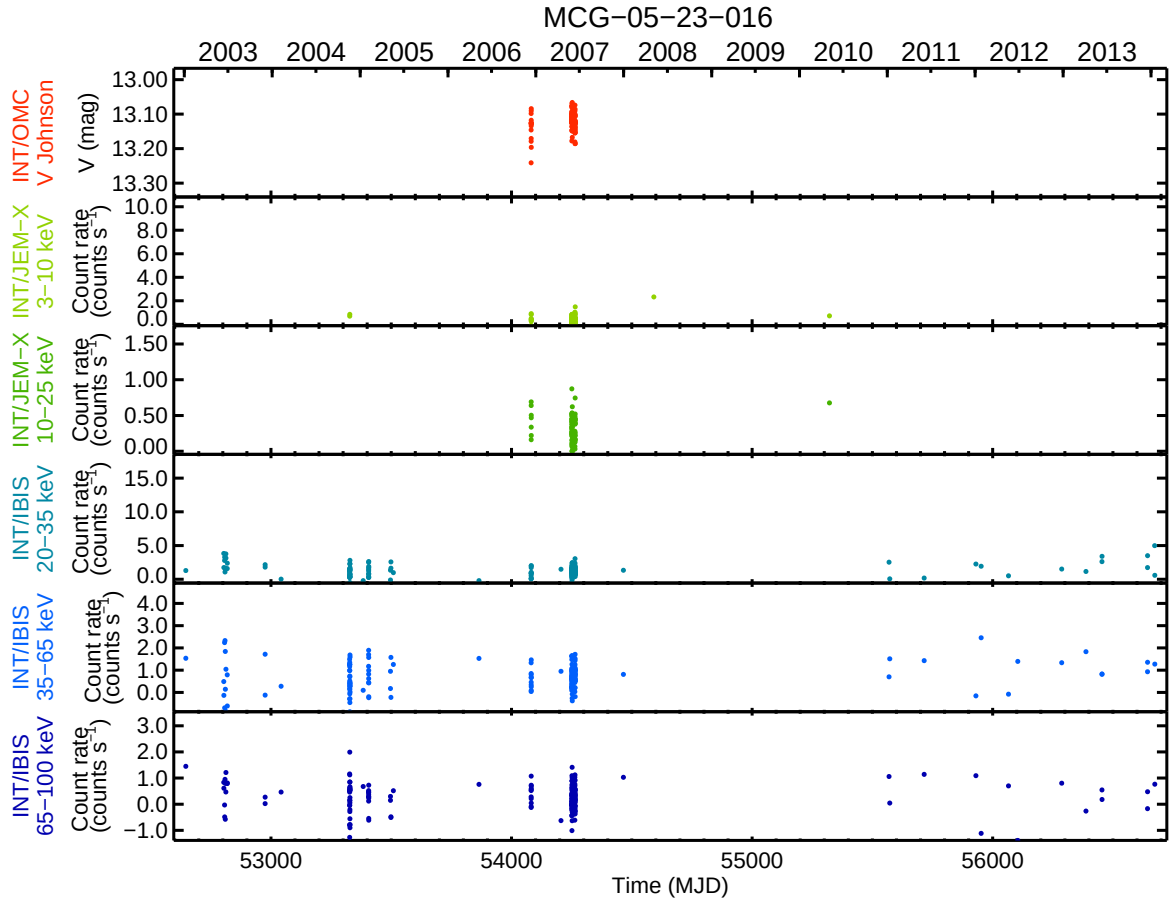
MCG−05−23−016
2003
2004
2005
2006
2007
2008
2009
2010
2011
2012
2013
INT/OMC
V Johnson
V (mag)
INT/JEM−X
3−10 keV
INT/JEM−X
10−25 keV
INT/IBIS
20−35 keV
INT/IBIS
35−65 keV
INT/IBIS
65−100 keV
Count rate (counts s−1)
53000
54000
55000
56000
Time (MJD)

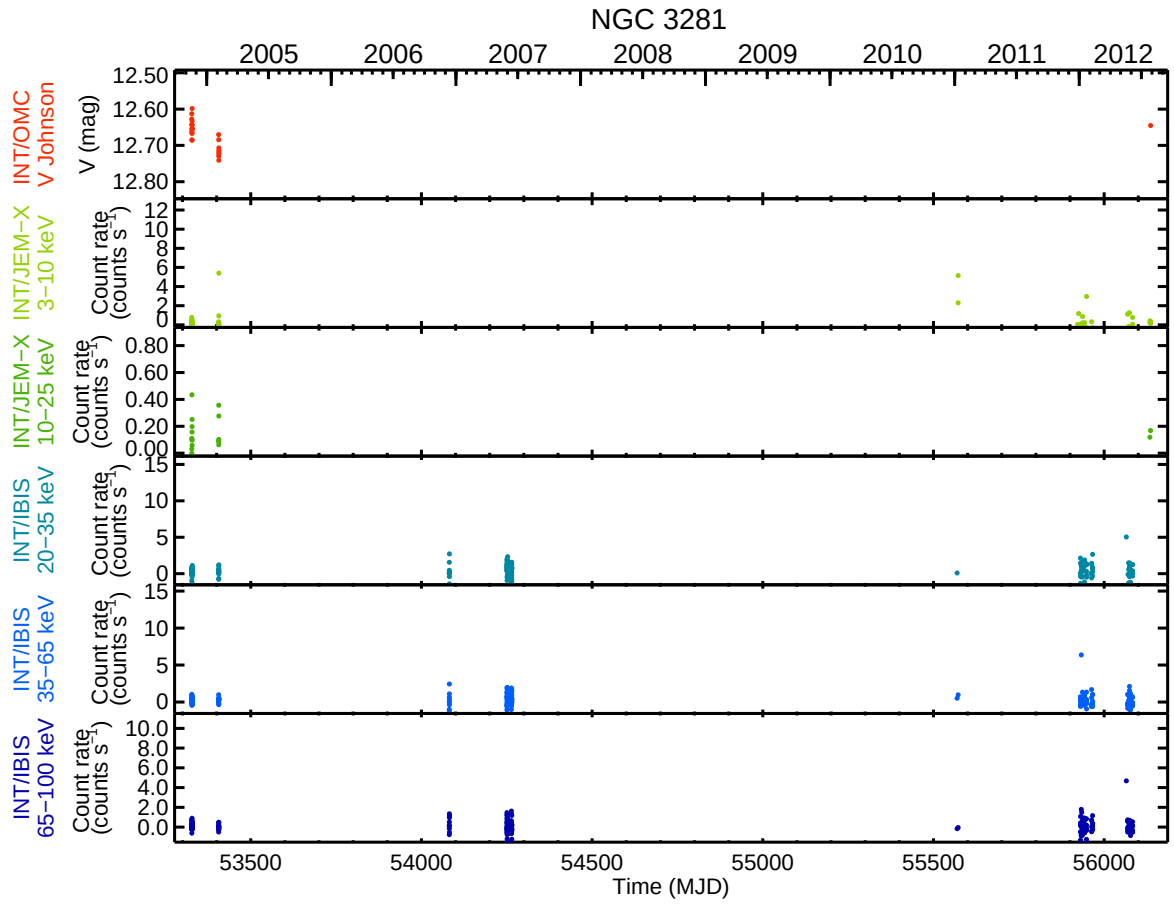
NGC 3281
2005
2006
2007
2008
2009
2010
2011
2012
INT/OMC V Johnson
V (mag)
INT/JEM−X 3−10 keV
INT/JEM−X 10−25 keV
INT/IBIS 20−35 keV
INT/IBIS 35−65 keV
INT/IBIS 65−100 keV
Count rate (counts s−1)
53500
54000
54500
55000
55500
56000
Time (MJD)

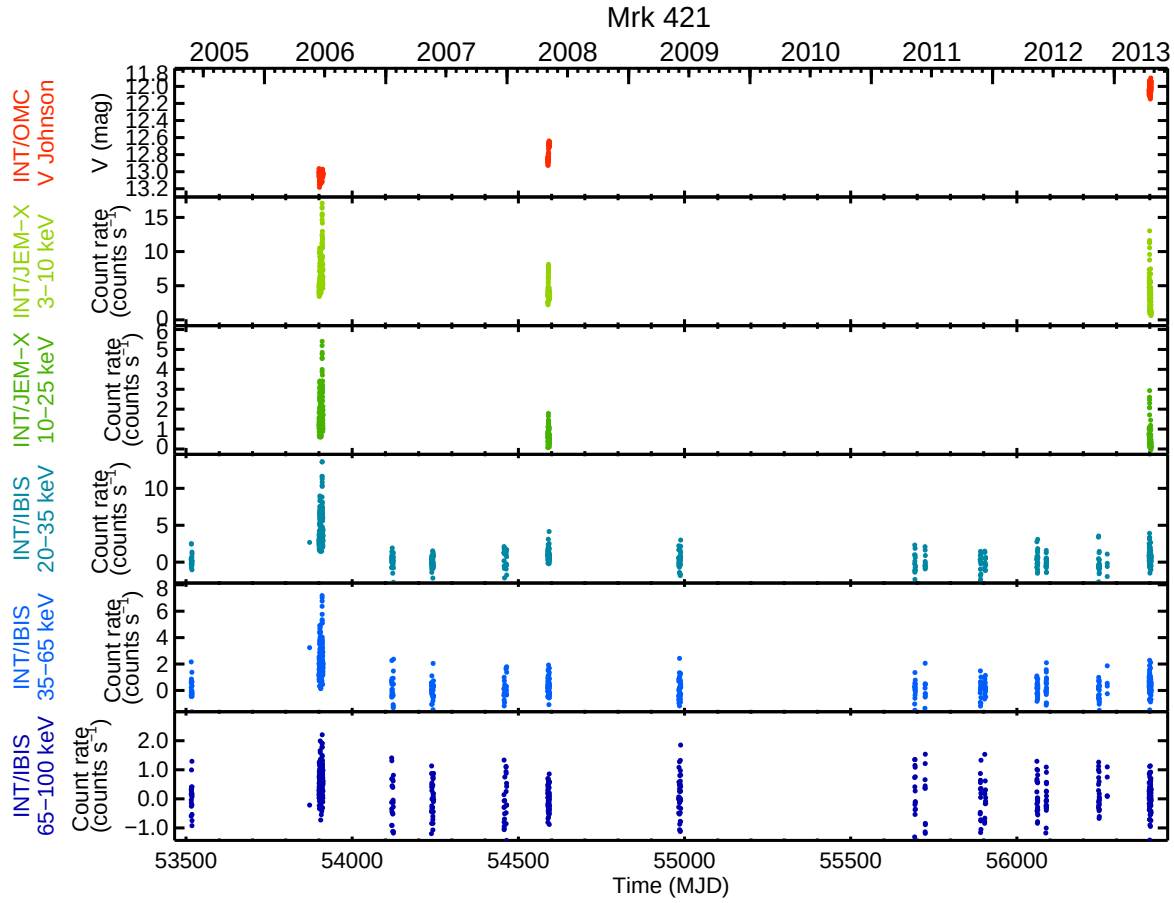
Mrk 421
2005
2006
2007
2008
2009
2010
2011
2012
2013
INT/OMC V Johnson
V (mag)
INT/JEM−X 3−10 keV
INT/JEM−X 10−25 keV
INT/IBIS 20−35 keV
INT/IBIS 35−65 keV
INT/IBIS 65−100 keV
Count rate (counts s−1)
53500
54000
54500
55000
55500
56000
Time (MJD)

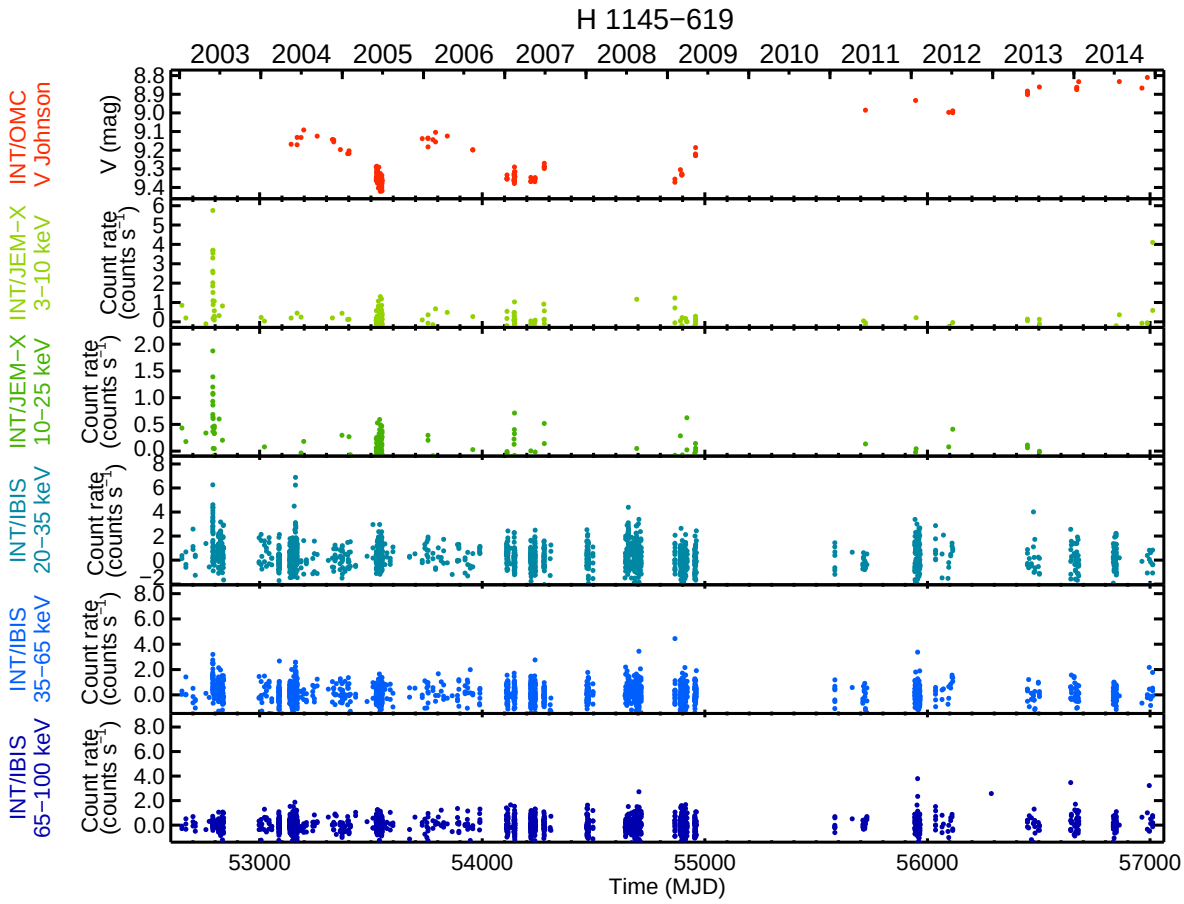
H 1145−619
2003 2004 2005 2006 2007 2008 2009 2010 2011 2012 2013 2014
INT/OMC V Johnson
V (mag)
INT/JEM−X 3−10 keV
INT/JEM−X 10−25 keV
INT/IBIS 20−35 keV
INT/IBIS 35−65 keV
INT/IBIS 65−100 keV
Count rate (counts s−1)
53000 54000 55000 56000 57000
Time (MJD)

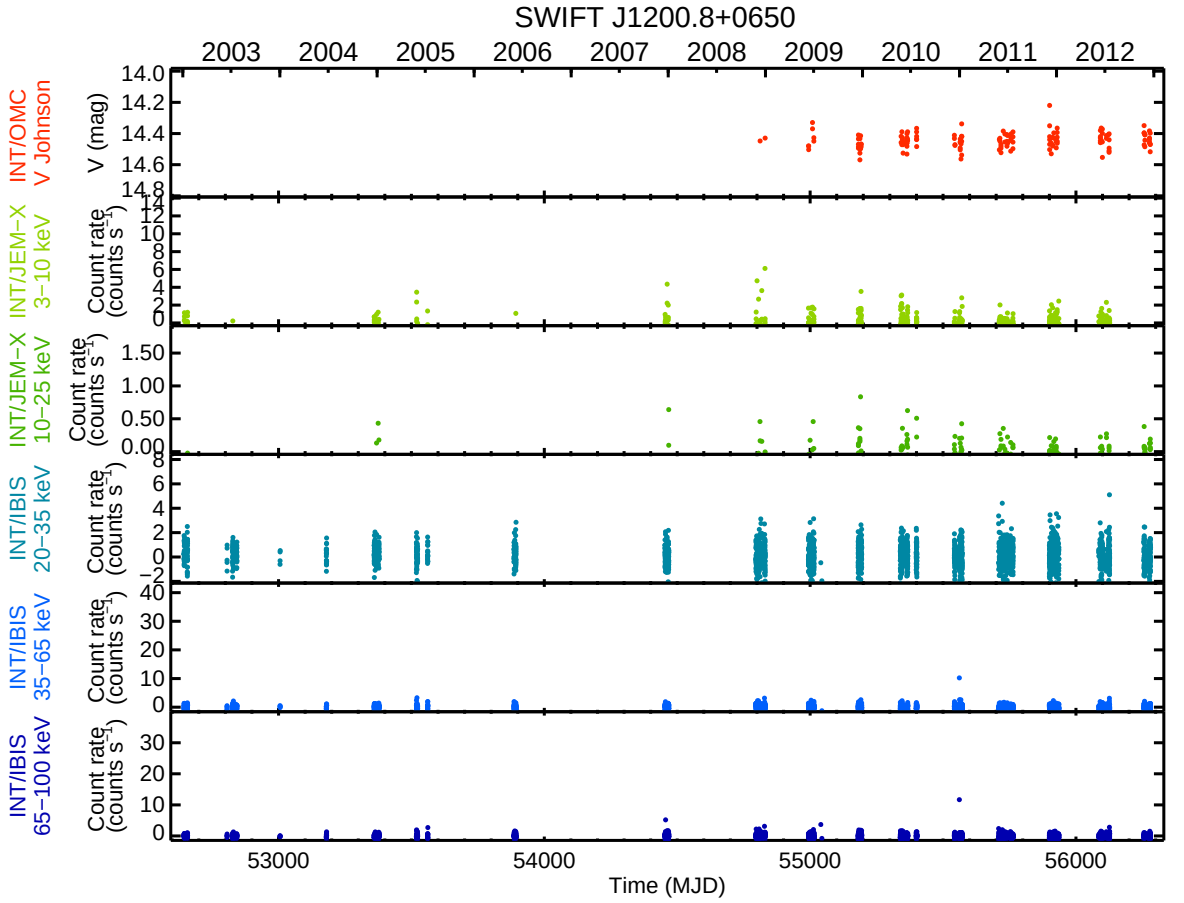
SWIFT J1200.8+0650
2003 2004 2005 2006 2007 2008 2009 2010 2011 2012
INT/OMC V Johnson
V (mag)
INT/JEM−X 3−10 keV
INT/JEM−X 10−25 keV
INT/IBIS 20−35 keV
INT/IBIS 35−65 keV
INT/IBIS 65−100 keV
Count rate (counts s−1)
53000 54000 55000 56000
Time (MJD)

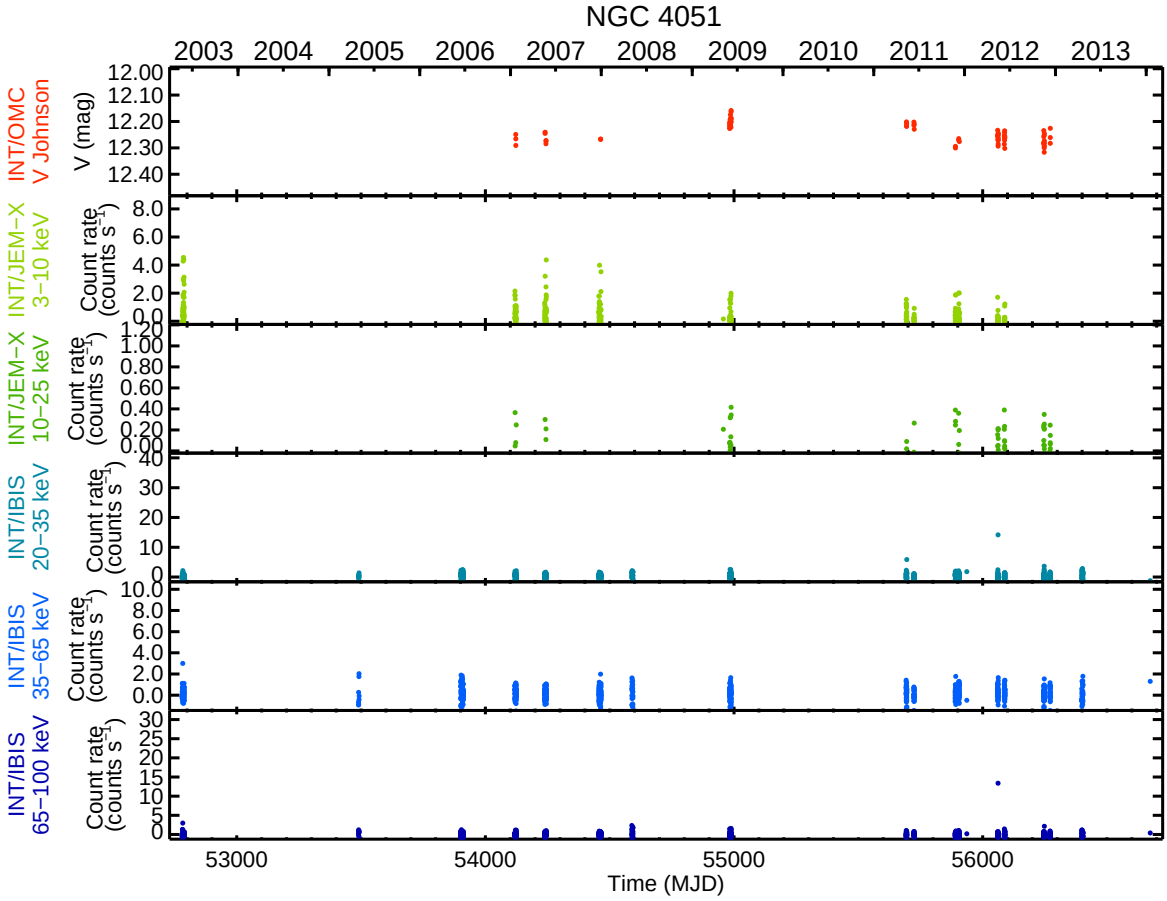
NGC 4051
2003 2004 2005 2006 2007 2008 2009 2010 2011 2012 2013
INT/OMC V Johnson
V (mag)
INT/JEM−X 3−10 keV
INT/JEM−X 10−25 keV
INT/IBIS 20−35 keV
INT/IBIS 35−65 keV
INT/IBIS 65−100 keV
Count rate (counts s−1)
53000 54000 55000 56000
Time (MJD)

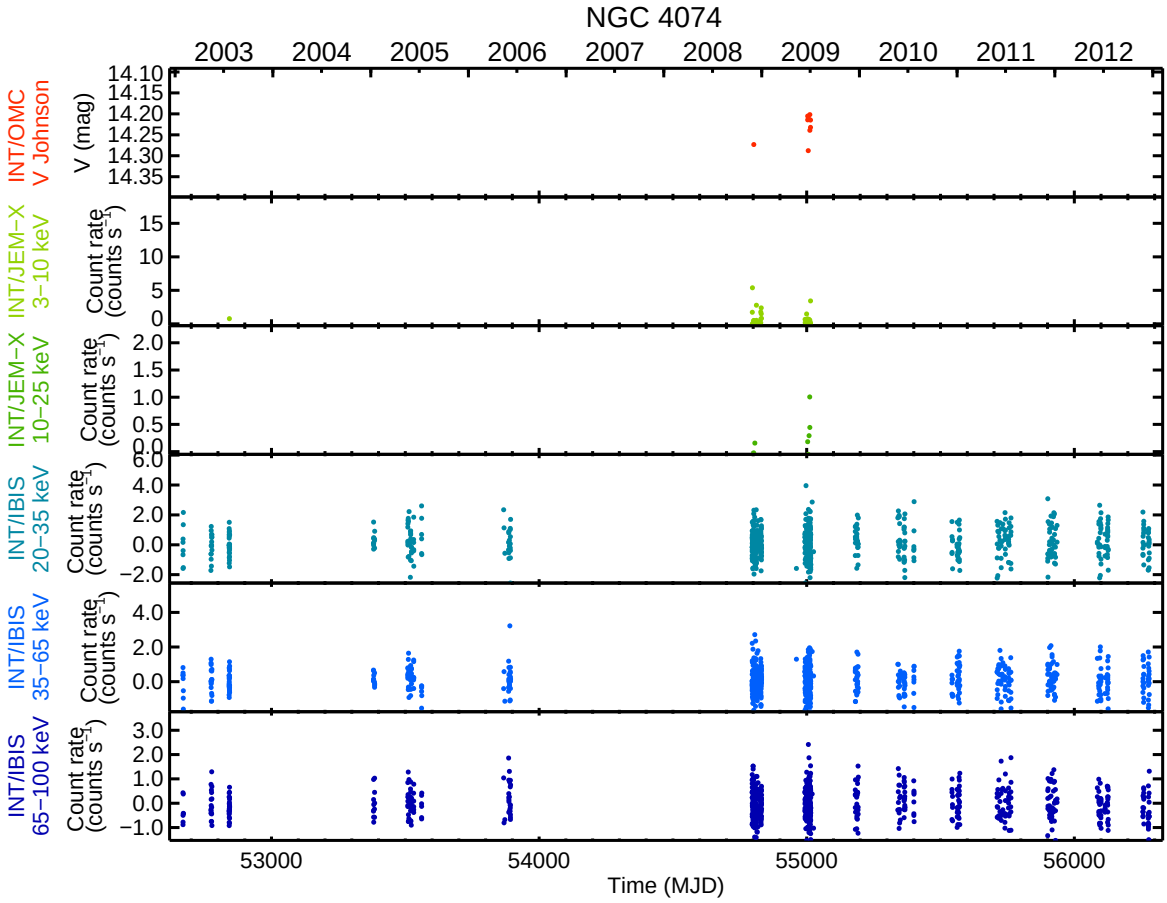
NGC 4074
2003 2004 2005 2006 2007 2008 2009 2010 2011 2012
INT/OMC V Johnson
V (mag)
INT/JEM−X 3−10 keV
INT/JEM−X 10−25 keV
INT/IBIS 20−35 keV
INT/IBIS 35−65 keV
INT/IBIS 65−100 keV
Count rate (counts s−1)
53000 54000 55000 56000
Time (MJD)

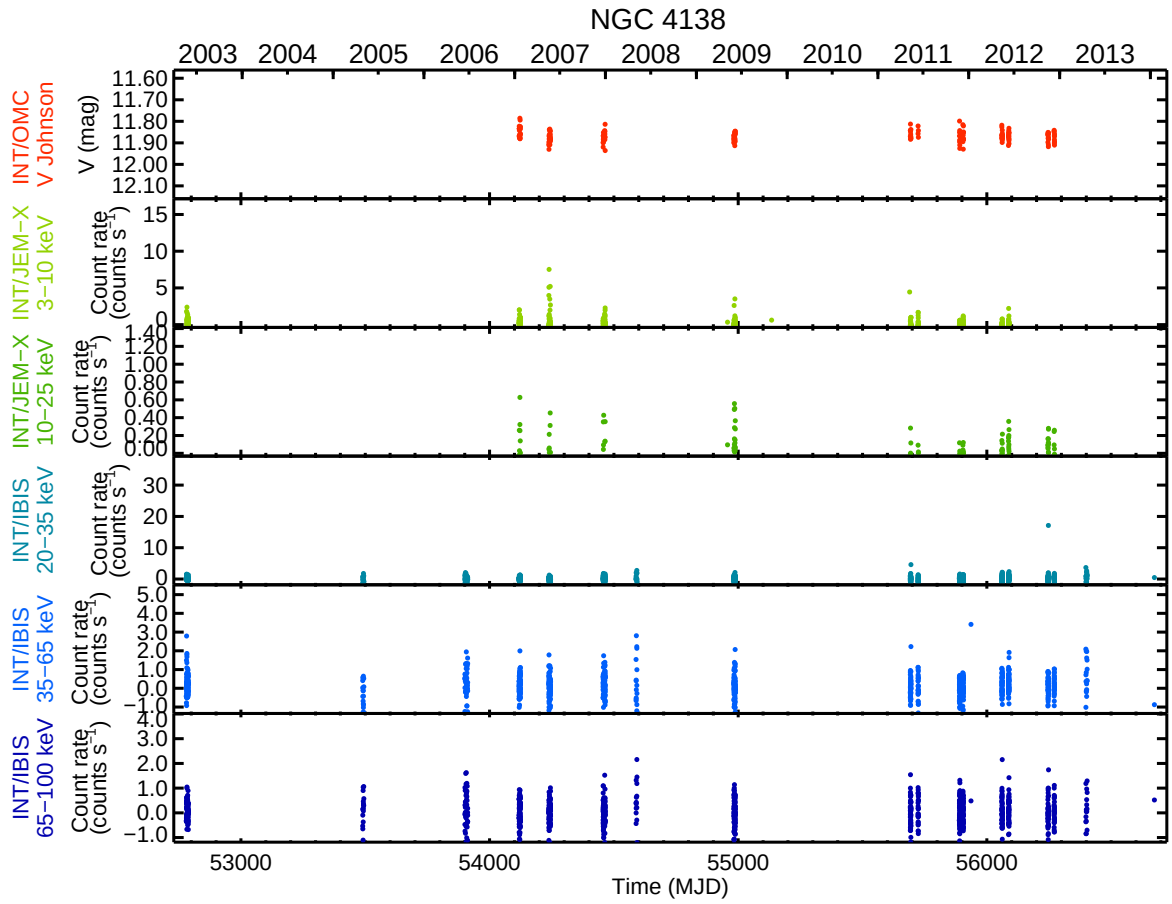
NGC 4138
2003 2004 2005 2006 2007 2008 2009 2010 2011 2012 2013
INT/OMC V Johnson
V (mag)
INT/JEM−X 3−10 keV
INT/JEM−X 10−25 keV
INT/IBIS 20−35 keV
INT/IBIS 35−65 keV
INT/IBIS 65−100 keV
Count rate (counts s−1)
53000 54000 55000 56000
Time (MJD)

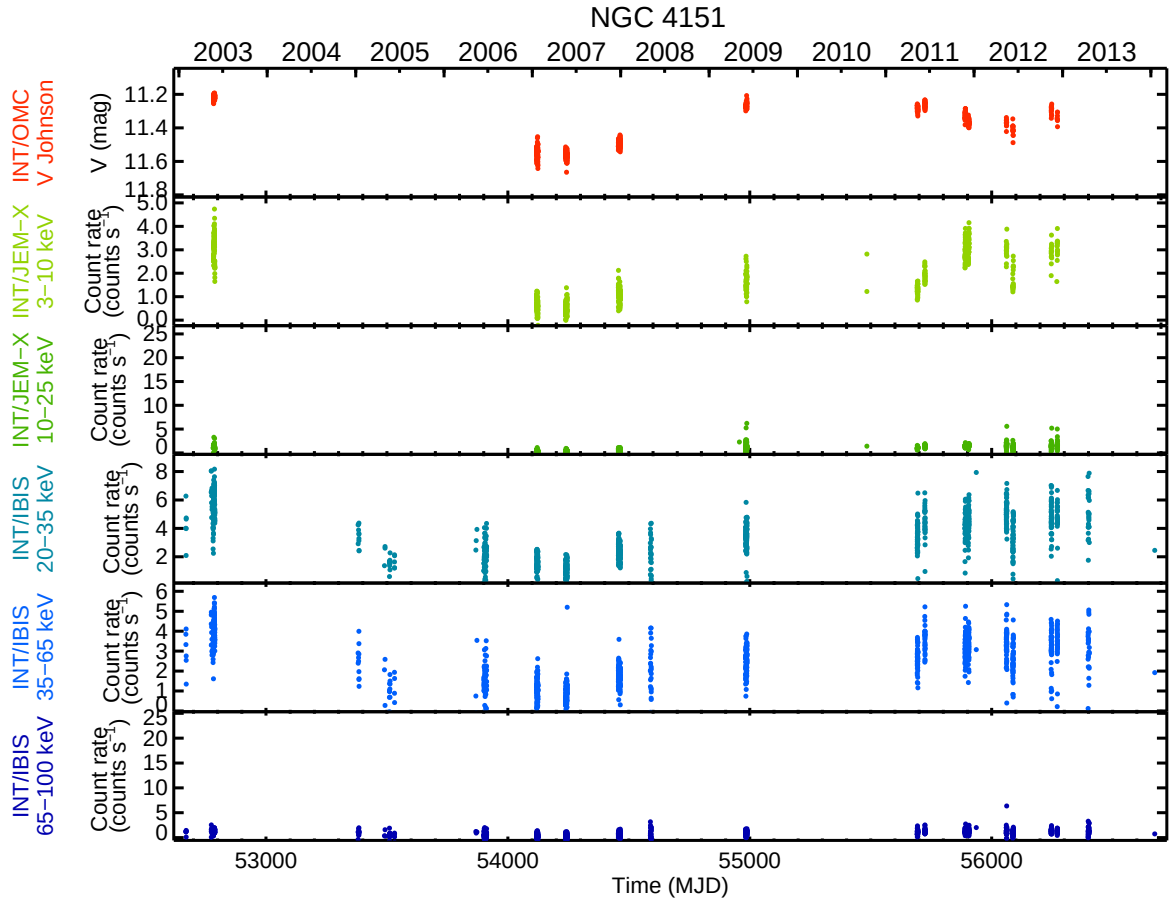
NGC 4151
2003 2004 2005 2006 2007 2008 2009 2010 2011 2012 2013
INT/OMC V Johnson
V (mag)
INT/JEM−X 3−10 keV
INT/JEM−X 10−25 keV
INT/IBIS 20−35 keV
INT/IBIS 35−65 keV
INT/IBIS 65−100 keV
Count rate (counts s−1)
53000 54000 55000 56000
Time (MJD)

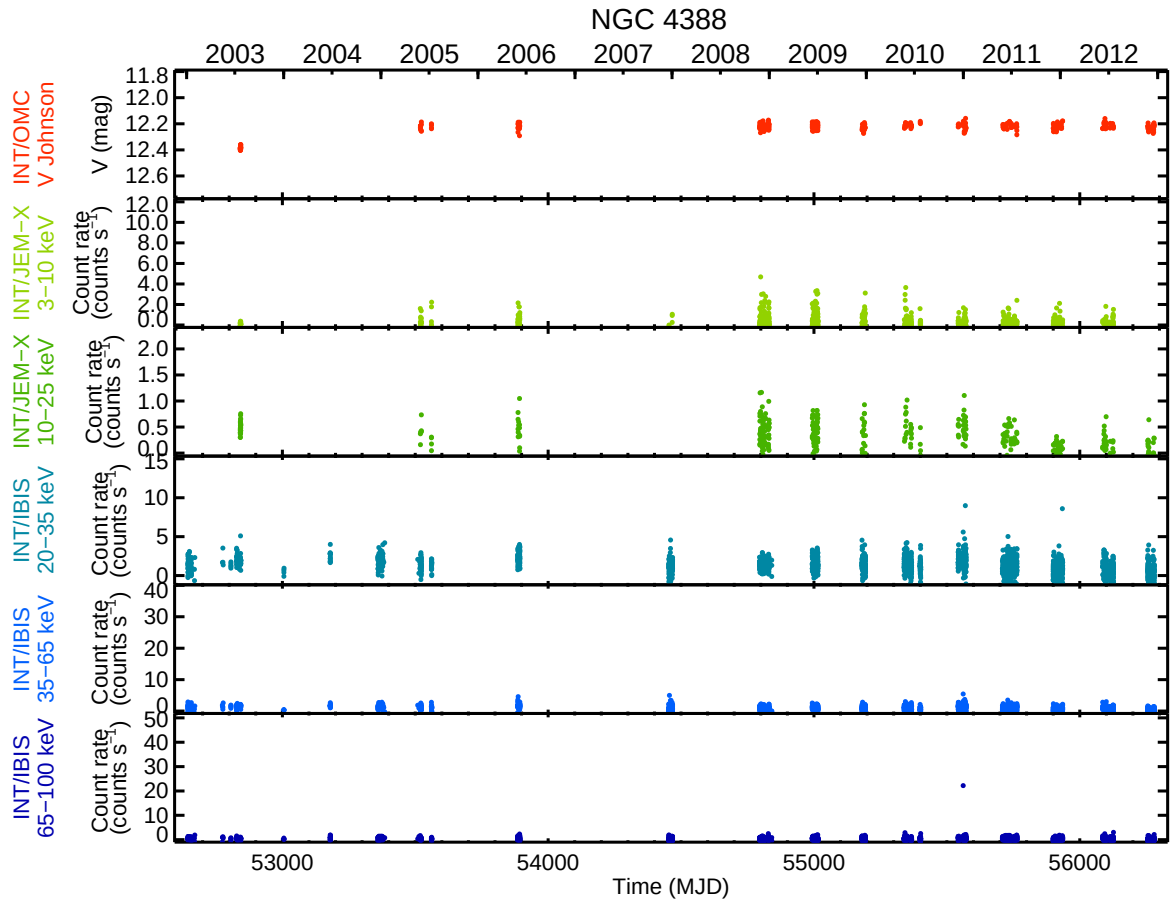
NGC 4388
2003
2004
2005
2006
2007
2008
2009
2010
2011
2012
INT/OMC V Johnson
V (mag)
INT/JEM−X 3−10 keV
INT/JEM−X 10−25 keV
INT/IBIS 20−35 keV
INT/IBIS 35−65 keV
INT/IBIS 65−100 keV
Count rate (counts s⁻¹)
53000
54000
55000
56000
Time (MJD)

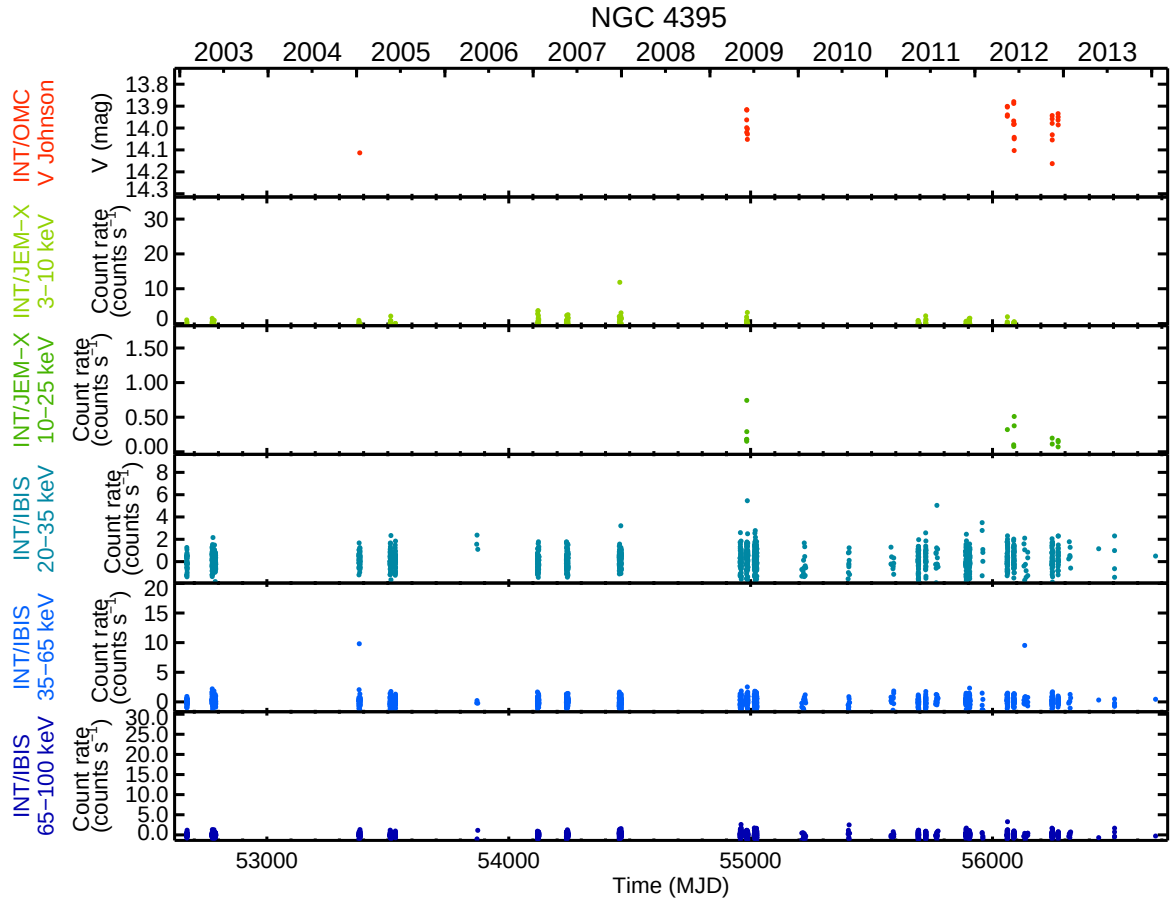
NGC 4395
2003
2004
2005
2006
2007
2008
2009
2010
2011
2012
2013
INT/OMC V Johnson
V (mag)
INT/JEM−X 3−10 keV
INT/JEM−X 10−25 keV
INT/IBIS 20−35 keV
INT/IBIS 35−65 keV
INT/IBIS 65−100 keV
Count rate (counts s⁻¹)
53000
54000
55000
56000
Time (MJD)

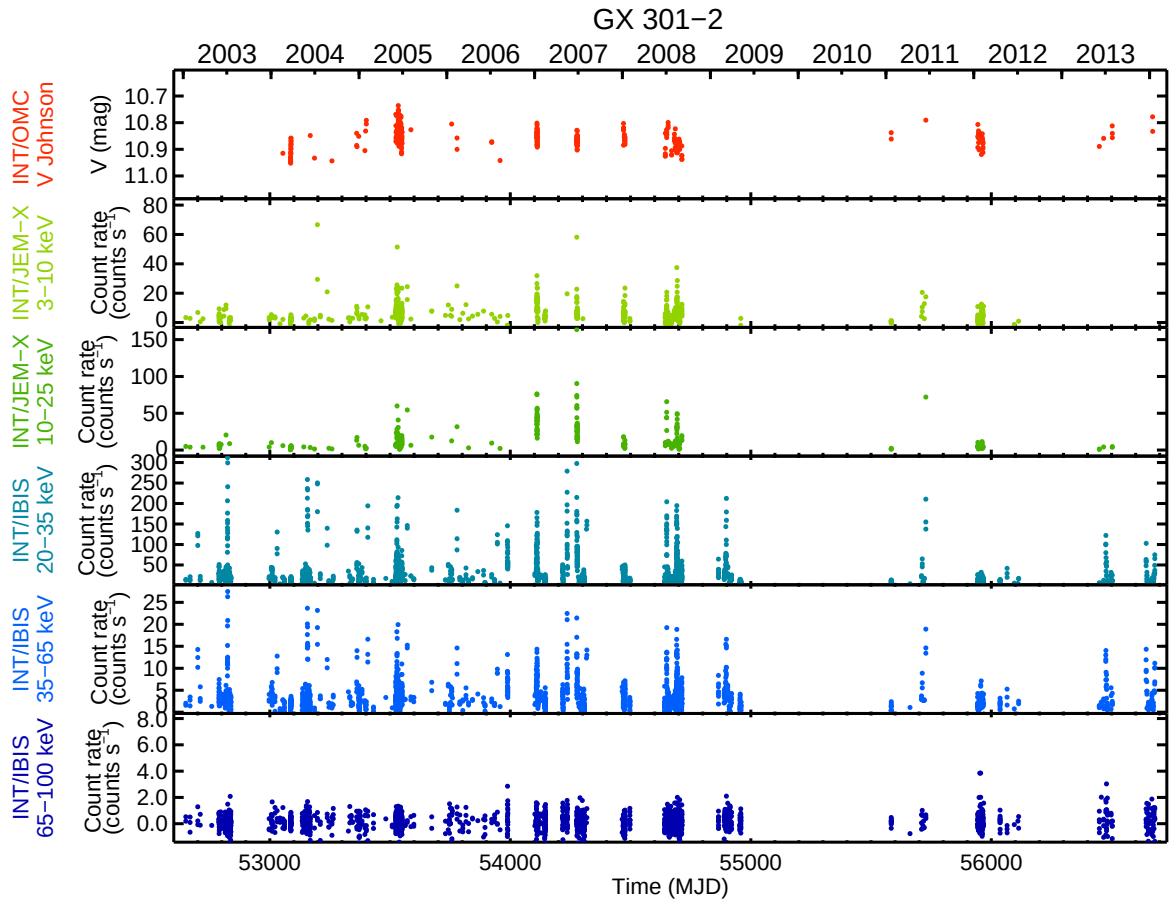
GX 301−2
2003
2004
2005
2006
2007
2008
2009
2010
2011
2012
2013
INT/OMC V Johnson
V (mag)
INT/JEM−X 3−10 keV
INT/JEM−X 10−25 keV
INT/IBIS 20−35 keV
INT/IBIS 35−65 keV
INT/IBIS 65−100 keV
Count rate (counts s−1)
53000
54000
55000
56000
Time (MJD)

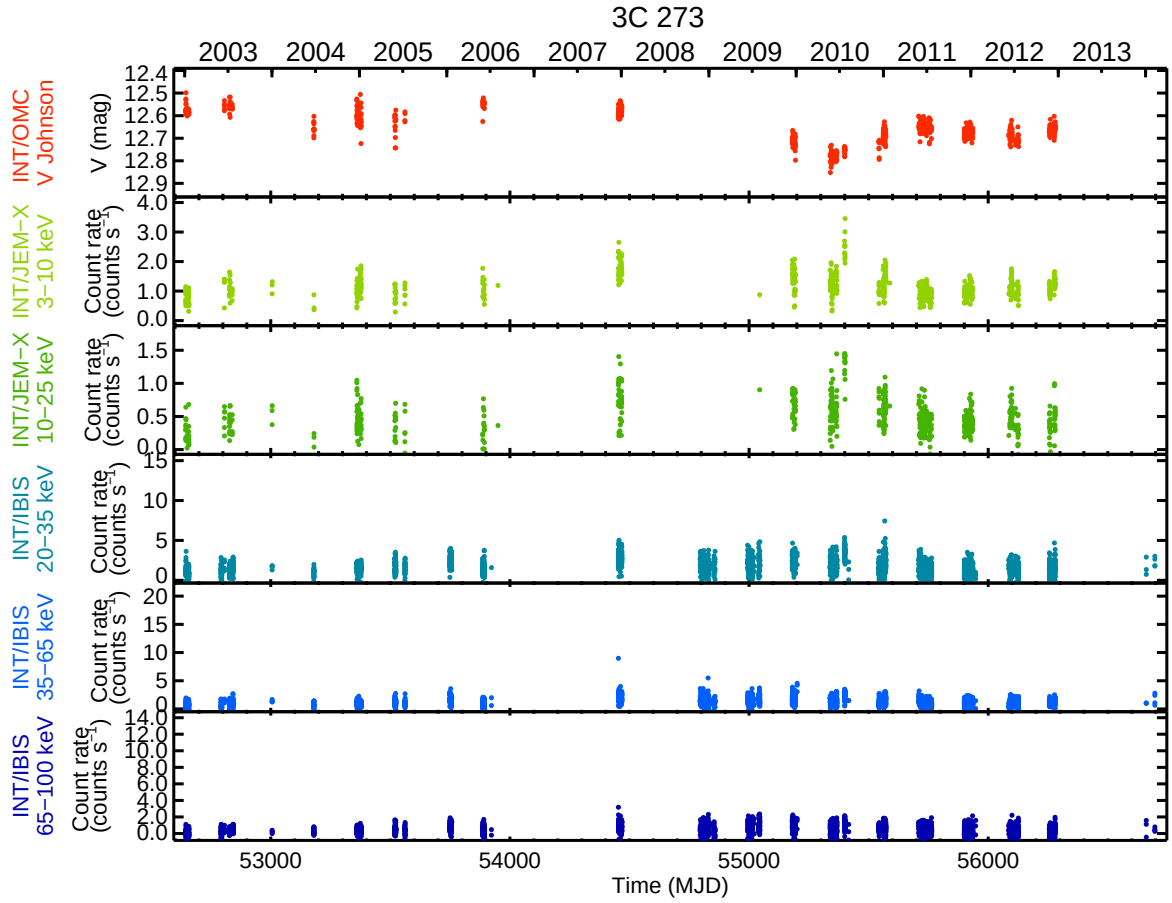
3C 273
2003
2004
2005
2006
2007
2008
2009
2010
2011
2012
2013
INT/OMC V Johnson
V (mag)
INT/JEM−X 3−10 keV
INT/JEM−X 10−25 keV
INT/IBIS 20−35 keV
INT/IBIS 35−65 keV
INT/IBIS 65−100 keV
Count rate (counts s−1)
53000
54000
55000
56000
Time (MJD)

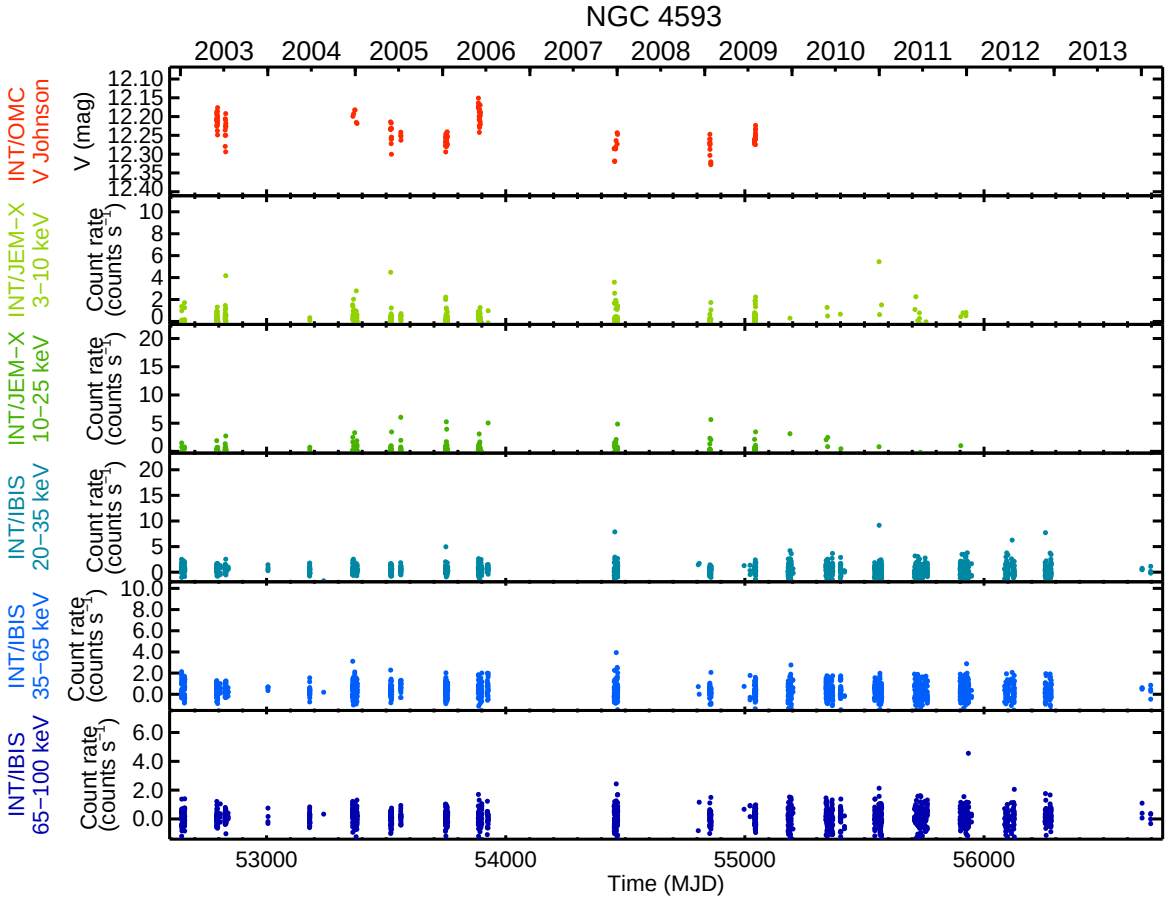
NGC 4593
2003 2004 2005 2006 2007 2008 2009 2010 2011 2012 2013
INT/OMC V Johnson
V (mag)
INT/JEM−X 3−10 keV
INT/JEM−X 10−25 keV
INT/IBIS 20−35 keV
INT/IBIS 35−65 keV
INT/IBIS 65−100 keV
Count rate (counts s⁻¹)
53000 54000 55000 56000
Time (MJD)

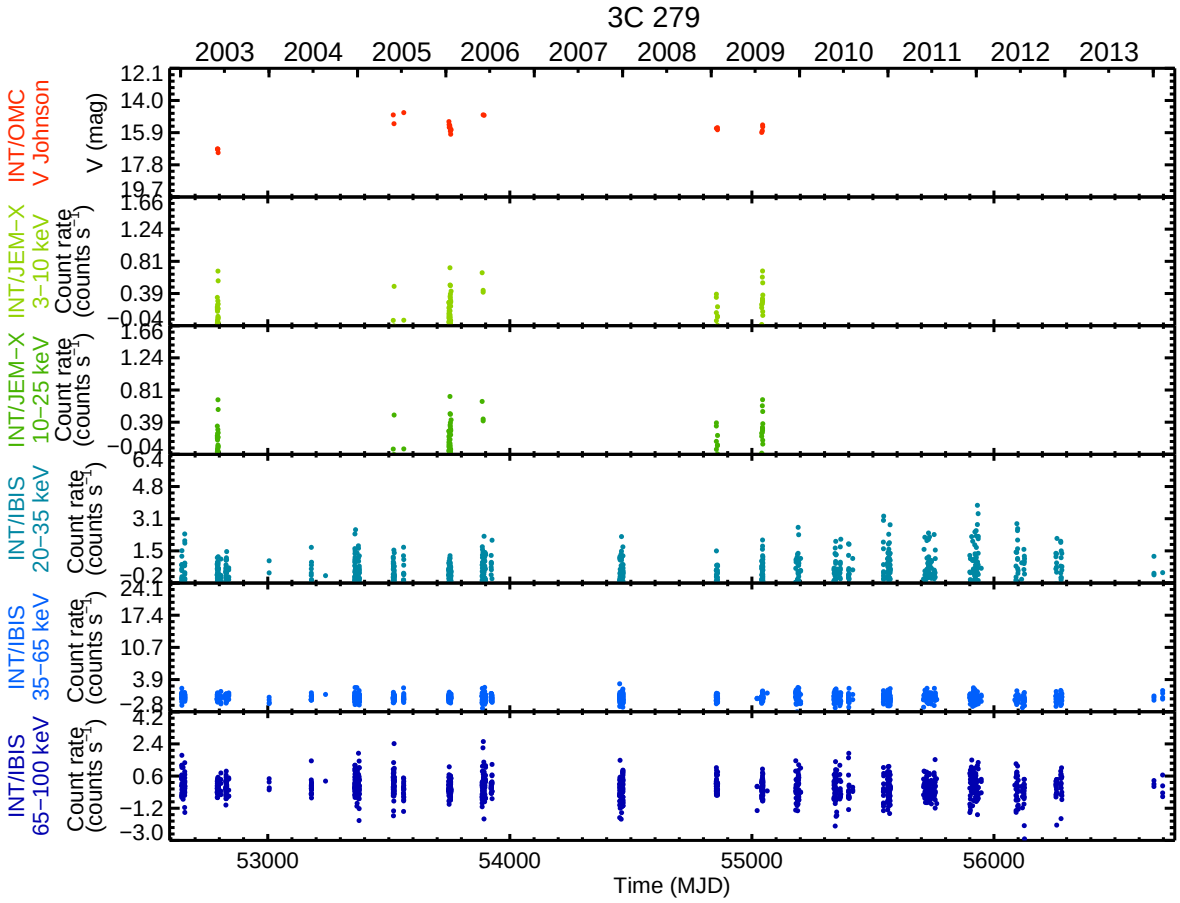
3C 279
2003 2004 2005 2006 2007 2008 2009 2010 2011 2012 2013
INT/OMC V Johnson
V (mag)
INT/JEM−X 3−10 keV
INT/JEM−X 10−25 keV
INT/IBIS 20−35 keV
INT/IBIS 35−65 keV
INT/IBIS 65−100 keV
Count rate (counts s⁻¹)
53000 54000 55000 56000
Time (MJD)

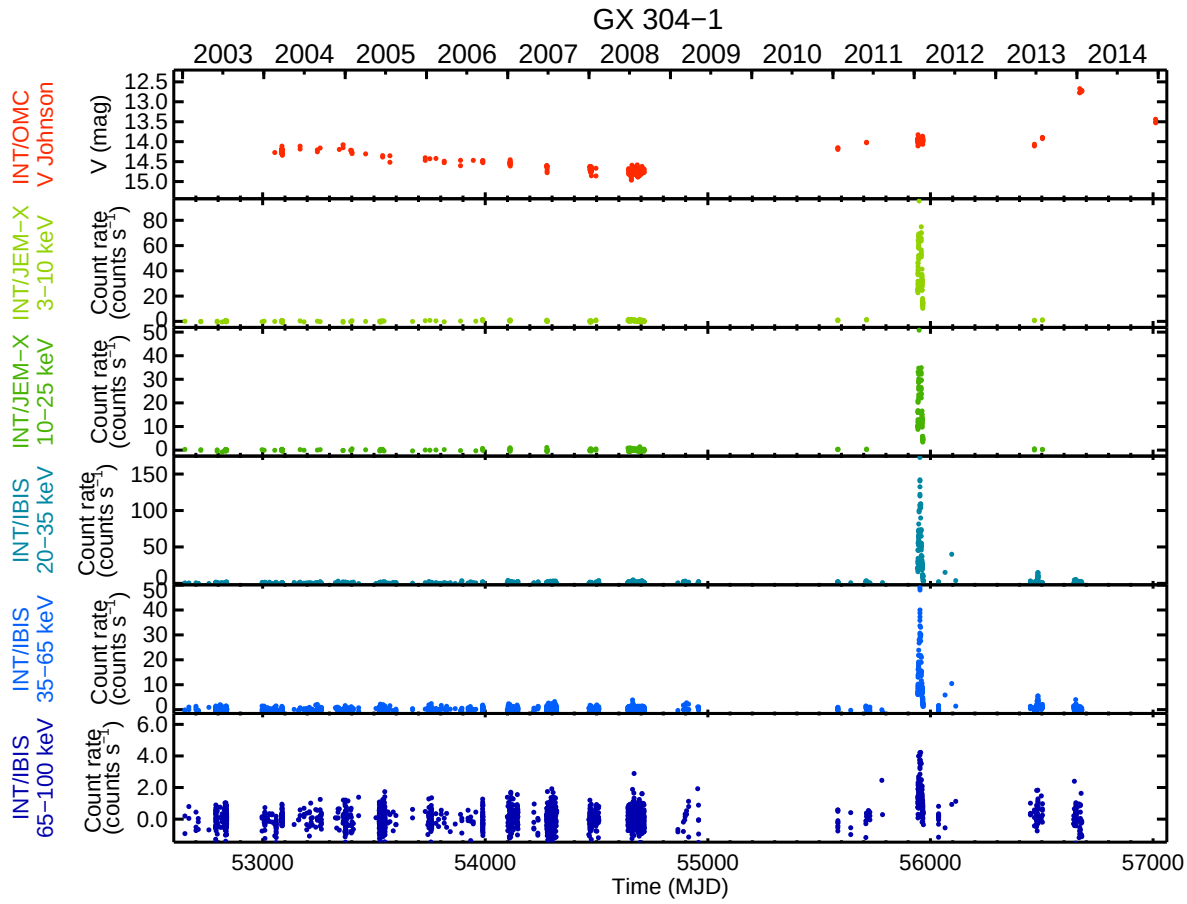
GX 304−1
2003 2004 2005 2006 2007 2008 2009 2010 2011 2012 2013 2014
INT/OMC V Johnson
V (mag)
INT/JEM−X 3−10 keV
INT/JEM−X 10−25 keV
INT/IBIS 20−35 keV
INT/IBIS 35−65 keV
INT/IBIS 65−100 keV
Count rate (counts s−1)
53000 54000 55000 56000 57000
Time (MJD)

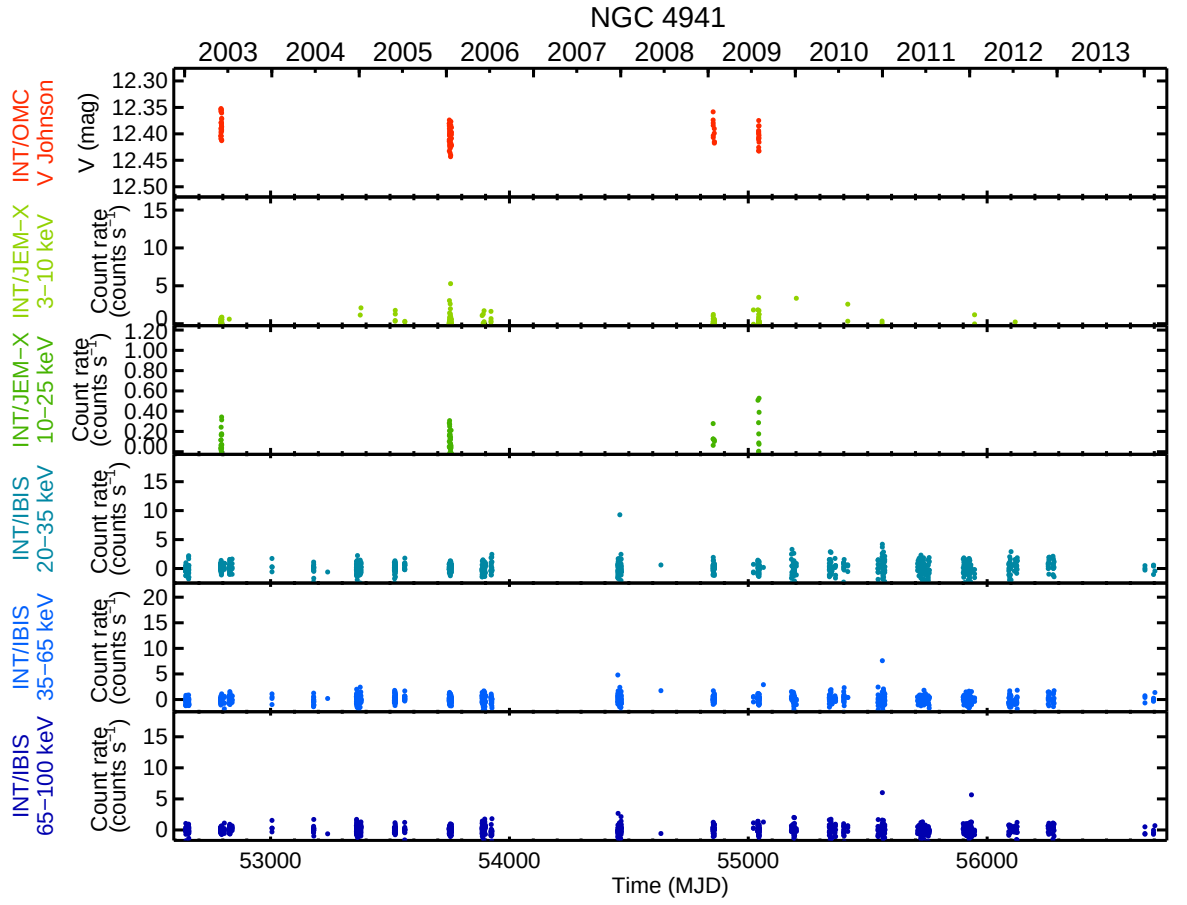
NGC 4941
2003 2004 2005 2006 2007 2008 2009 2010 2011 2012 2013
INT/OMC V Johnson
V (mag)
INT/JEM−X 3−10 keV
INT/JEM−X 10−25 keV
INT/IBIS 20−35 keV
INT/IBIS 35−65 keV
INT/IBIS 65−100 keV
Count rate (counts s−1)
53000 54000 55000 56000
Time (MJD)

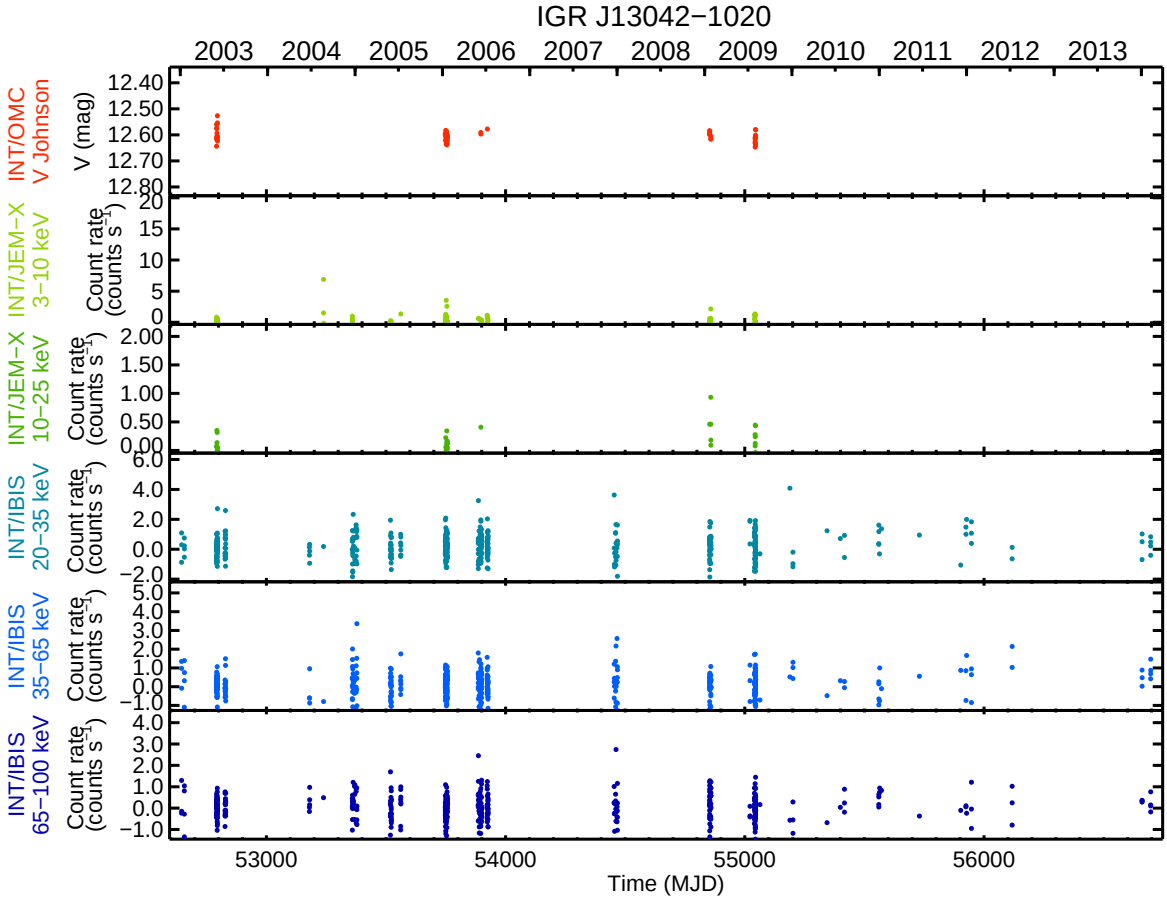
IGR J13042−1020
2003 2004 2005 2006 2007 2008 2009 2010 2011 2012 2013
INT/OMC V Johnson
V (mag)
INT/JEM−X 3−10 keV
INT/JEM−X 10−25 keV
INT/IBIS 20−35 keV
INT/IBIS 35−65 keV
INT/IBIS 65−100 keV
Count rate (counts s⁻¹)
53000 54000 55000 56000
Time (MJD)

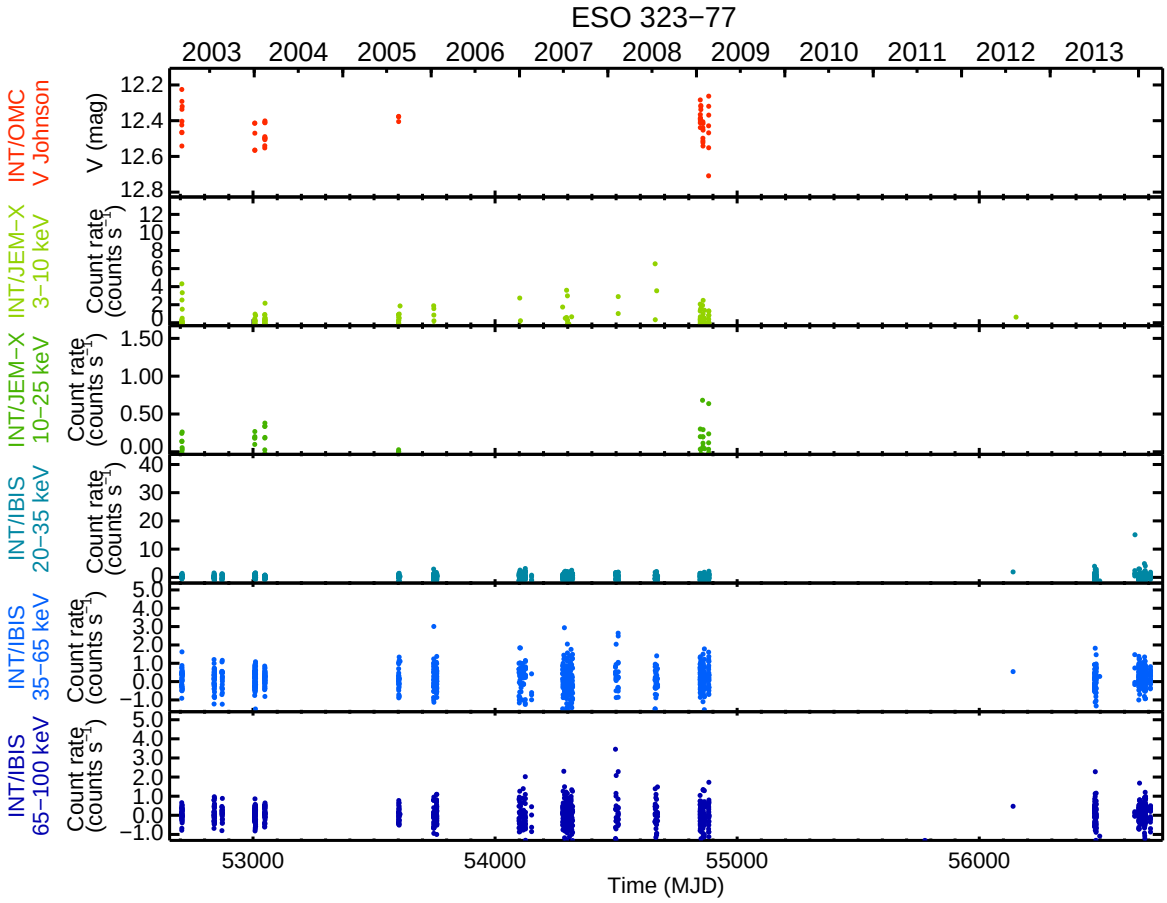
ESO 323−77
2003 2004 2005 2006 2007 2008 2009 2010 2011 2012 2013
INT/OMC V Johnson
V (mag)
INT/JEM−X 3−10 keV
INT/JEM−X 10−25 keV
INT/IBIS 20−35 keV
INT/IBIS 35−65 keV
INT/IBIS 65−100 keV
Count rate (counts s⁻¹)
53000 54000 55000 56000
Time (MJD)

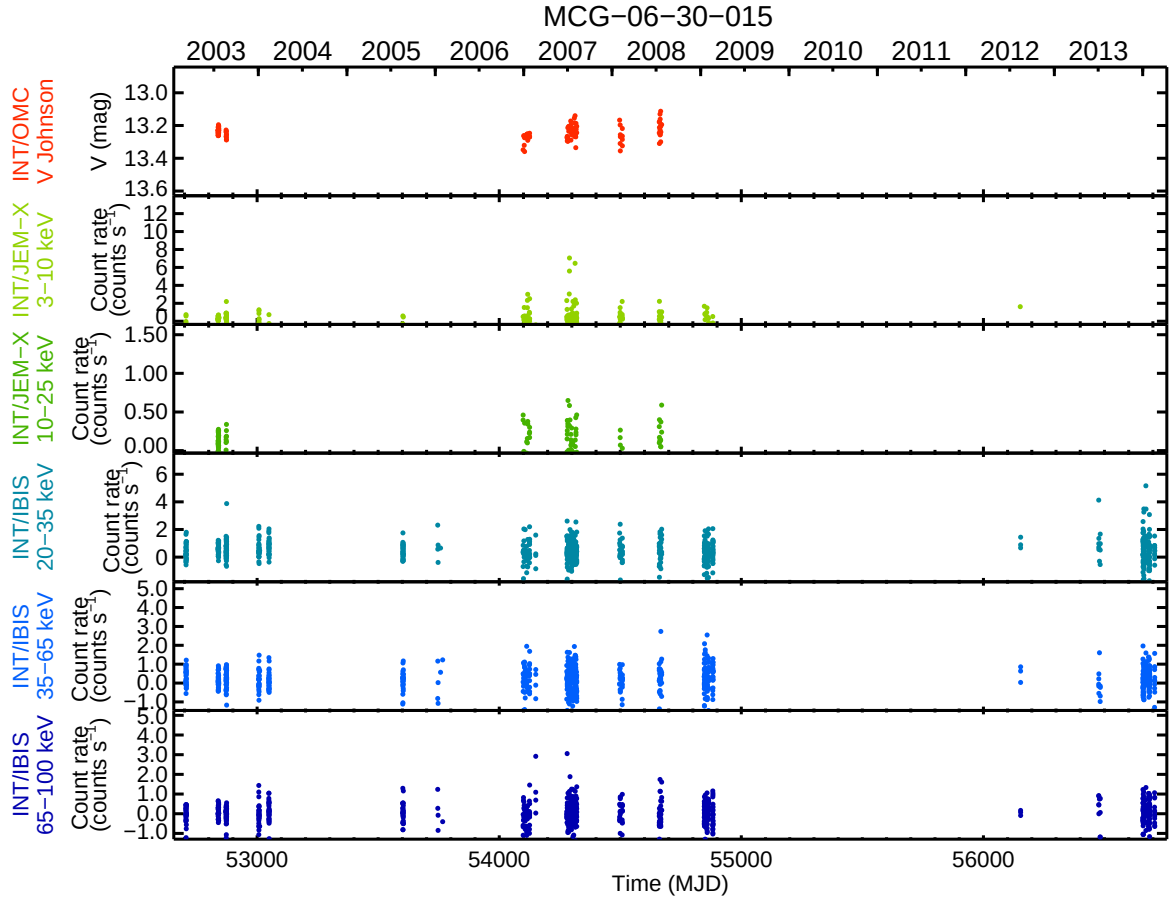
MCG−06−30−015
2003 2004 2005 2006 2007 2008 2009 2010 2011 2012 2013
INT/OMC V Johnson
V (mag)
INT/JEM−X 3−10 keV
INT/JEM−X 10−25 keV
INT/IBIS 20−35 keV
INT/IBIS 35−65 keV
INT/IBIS 65−100 keV
Count rate (counts s−1)
53000 54000 55000 56000
Time (MJD)

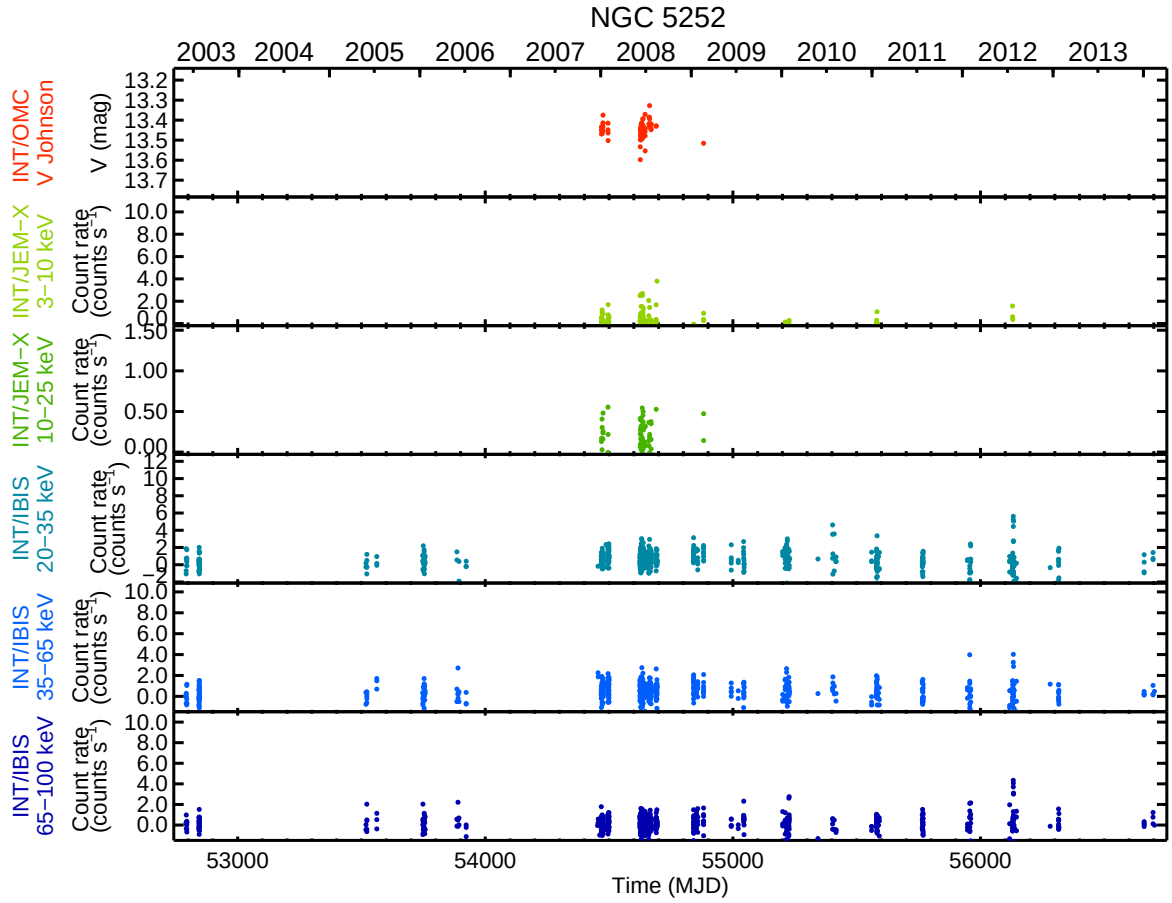
NGC 5252
2003 2004 2005 2006 2007 2008 2009 2010 2011 2012 2013
INT/OMC V Johnson
V (mag)
INT/JEM−X 3−10 keV
INT/JEM−X 10−25 keV
INT/IBIS 20−35 keV
INT/IBIS 35−65 keV
INT/IBIS 65−100 keV
Count rate (counts s−1)
53000 54000 55000 56000
Time (MJD)

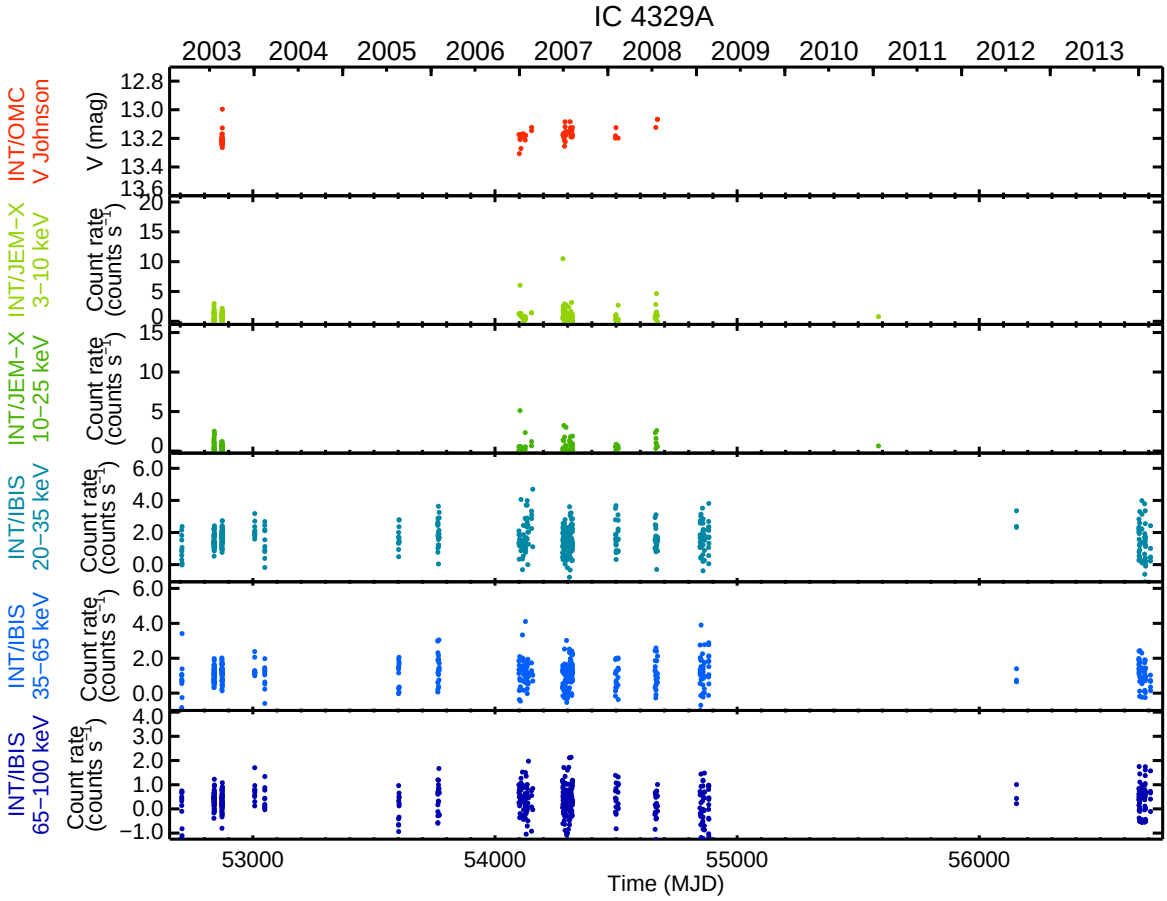
IC 4329A
2003
2004
2005
2006
2007
2008
2009
2010
2011
2012
2013
INT/OMC V Johnson
V (mag)
INT/JEM−X 3−10 keV
INT/JEM−X 10−25 keV
INT/IBIS 20−35 keV
INT/IBIS 35−65 keV
INT/IBIS 65−100 keV
Count rate (counts s−1)
53000
54000
55000
56000
Time (MJD)

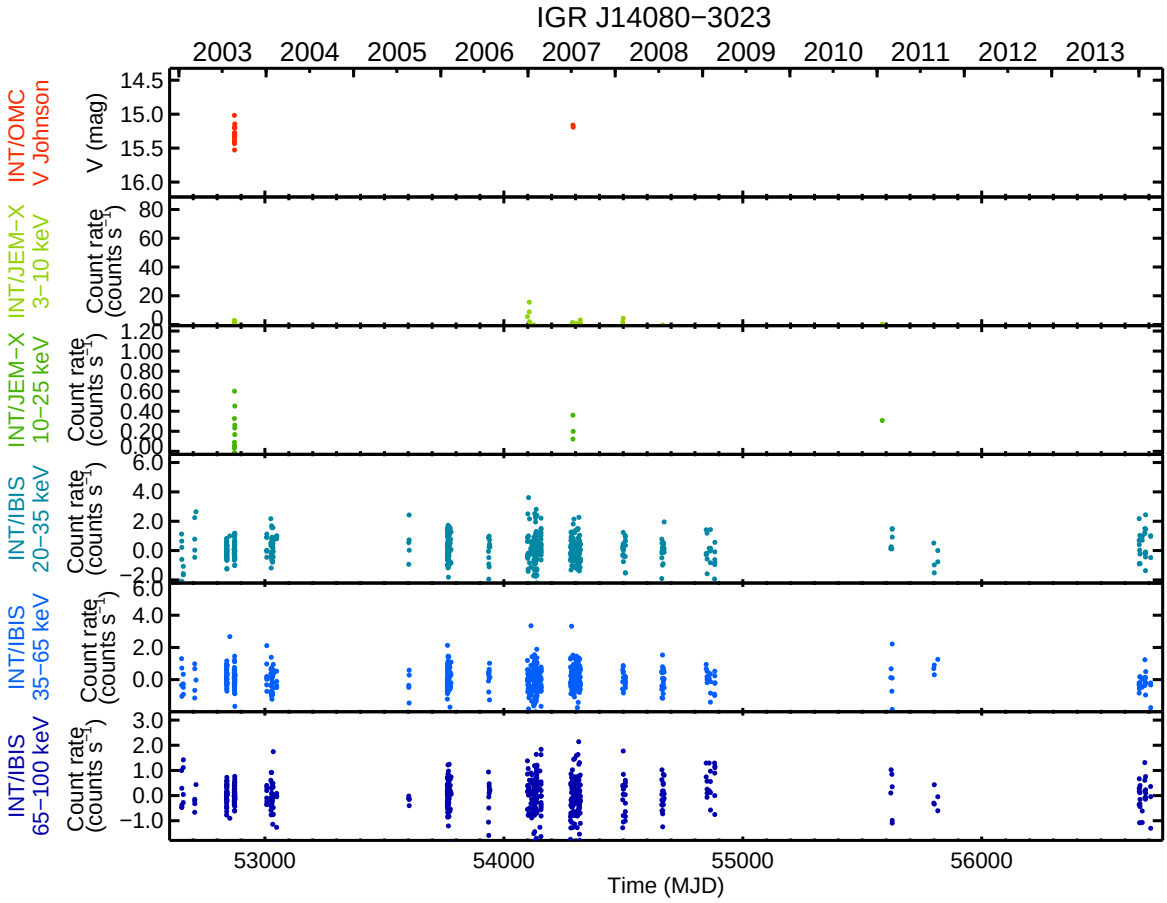
IGR J14080−3023
2003
2004
2005
2006
2007
2008
2009
2010
2011
2012
2013
INT/OMC V Johnson
V (mag)
INT/JEM−X 3−10 keV
INT/JEM−X 10−25 keV
INT/IBIS 20−35 keV
INT/IBIS 35−65 keV
INT/IBIS 65−100 keV
Count rate (counts s−1)
53000
54000
55000
56000
Time (MJD)

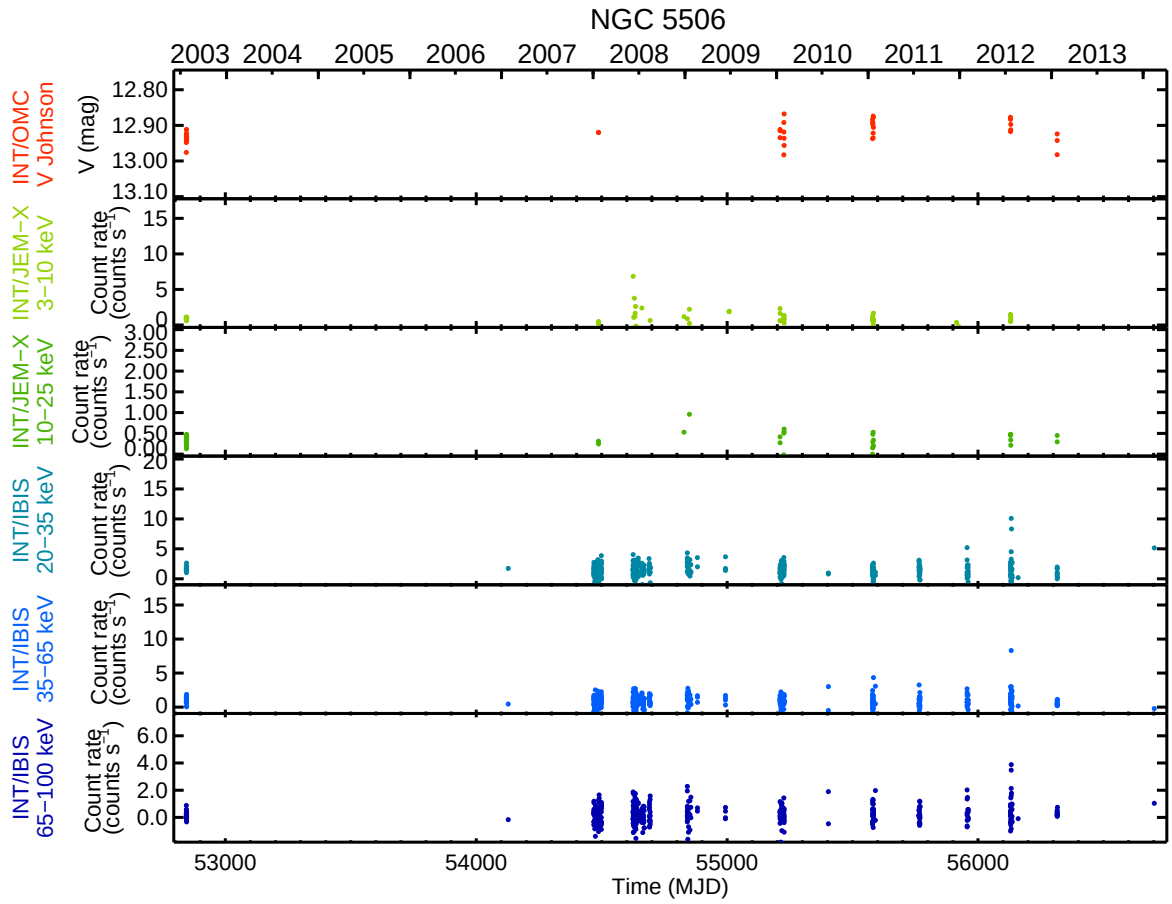
NGC 5506
2003 2004 2005 2006 2007 2008 2009 2010 2011 2012 2013
INT/OMC V Johnson
V (mag)
12.80
12.90
13.00
13.10
INT/JEM−X 3−10 keV
Count rate (counts s−1)
INT/JEM−X 10−25 keV
INT/IBIS 20−35 keV
INT/IBIS 35−65 keV
INT/IBIS 65−100 keV
53000
54000
55000
56000
Time (MJD)

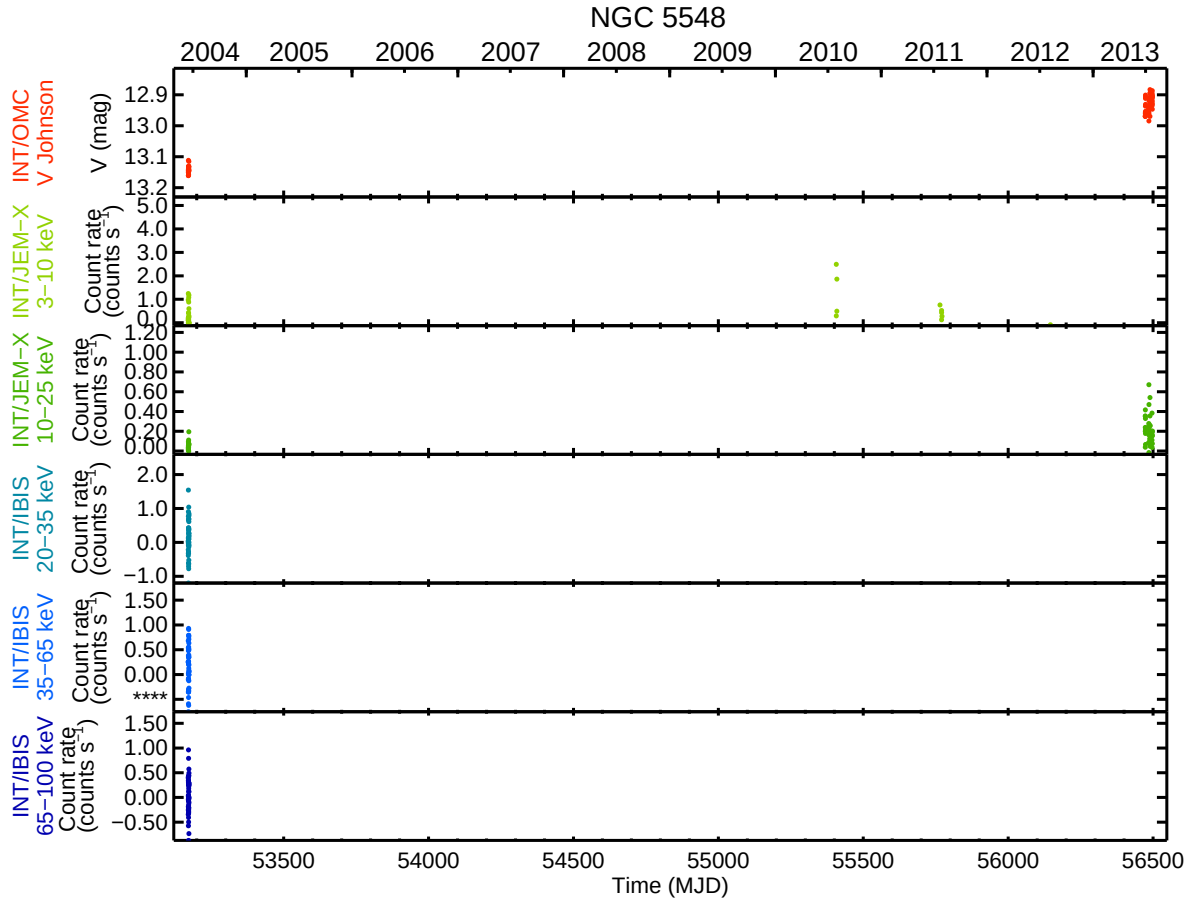
NGC 5548
2004 2005 2006 2007 2008 2009 2010 2011 2012 2013
INT/OMC V Johnson
V (mag)
INT/JEM−X 3−10 keV
Count rate (counts s−1)
INT/JEM−X 10−25 keV
INT/IBIS 20−35 keV
INT/IBIS 35−65 keV
INT/IBIS 65−100 keV
53500
54000
54500
55000
55500
56000
56500
Time (MJD)

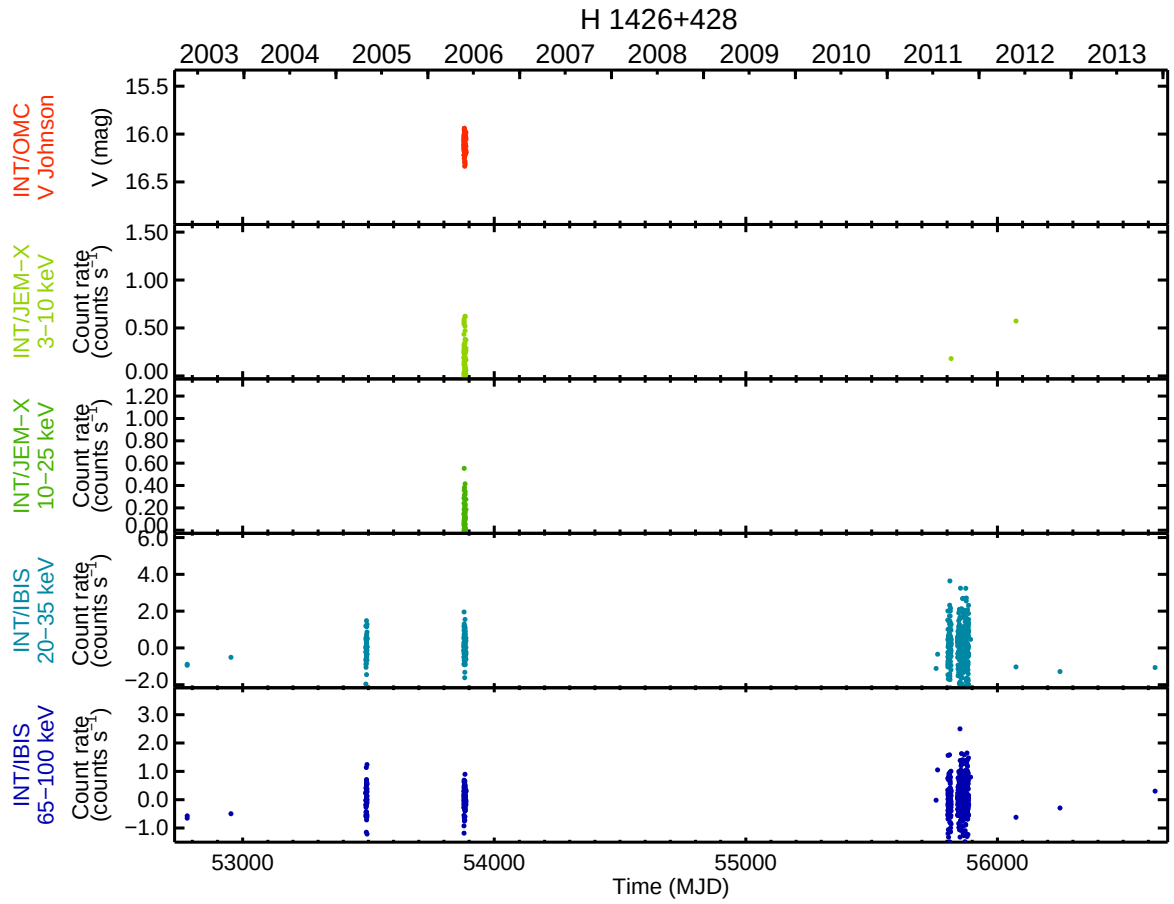
H 1426+428
2003 2004 2005 2006 2007 2008 2009 2010 2011 2012 2013
INT/OMC V Johnson
V (mag)
INT/JEM−X 3−10 keV
INT/JEM−X 10−25 keV
INT/IBIS 20−35 keV
INT/IBIS 65−100 keV
Count rate (counts s−1)
Time (MJD)
53000 54000 55000 56000

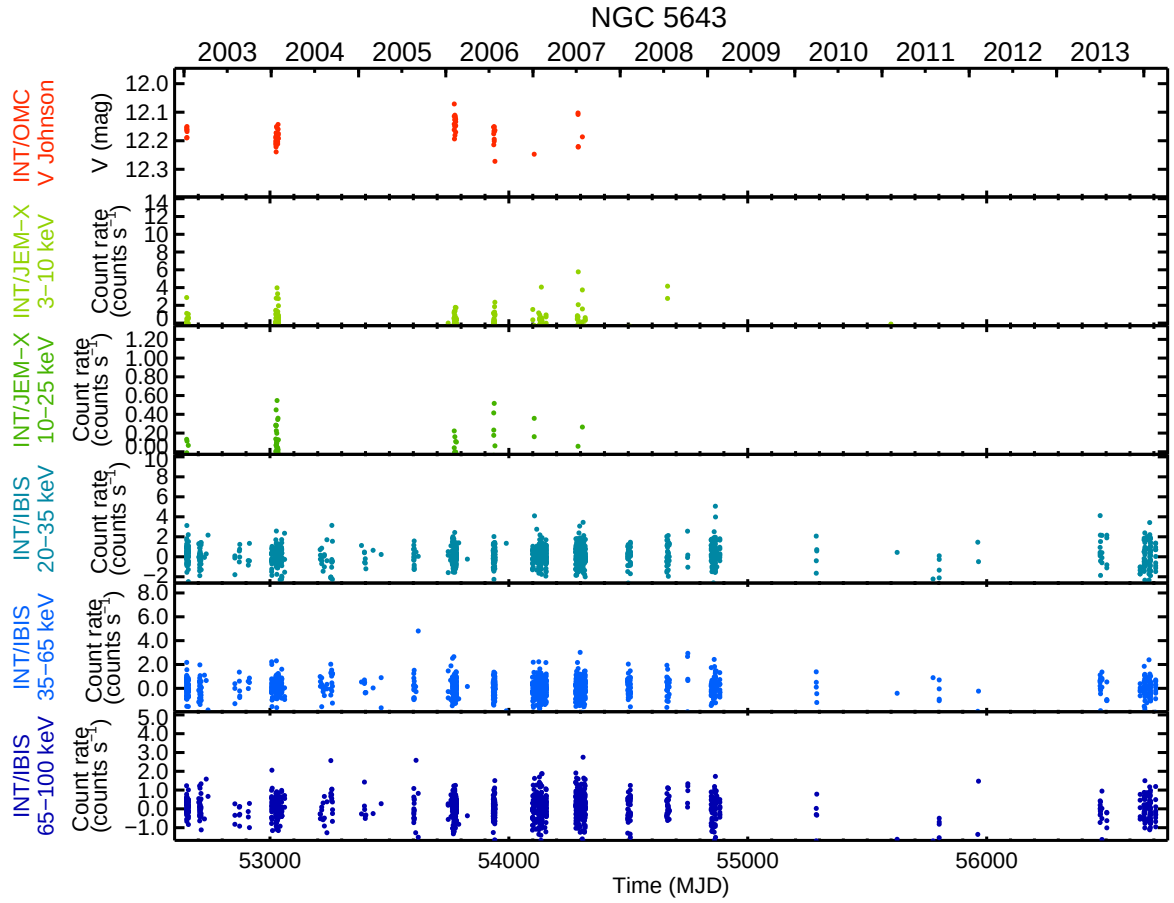
NGC 5643
2003 2004 2005 2006 2007 2008 2009 2010 2011 2012 2013
INT/OMC V Johnson
V (mag)
INT/JEM−X 3−10 keV
INT/JEM−X 10−25 keV
INT/IBIS 20−35 keV
INT/IBIS 35−65 keV
INT/IBIS 65−100 keV
Count rate (counts s−1)
Time (MJD)
53000 54000 55000 56000

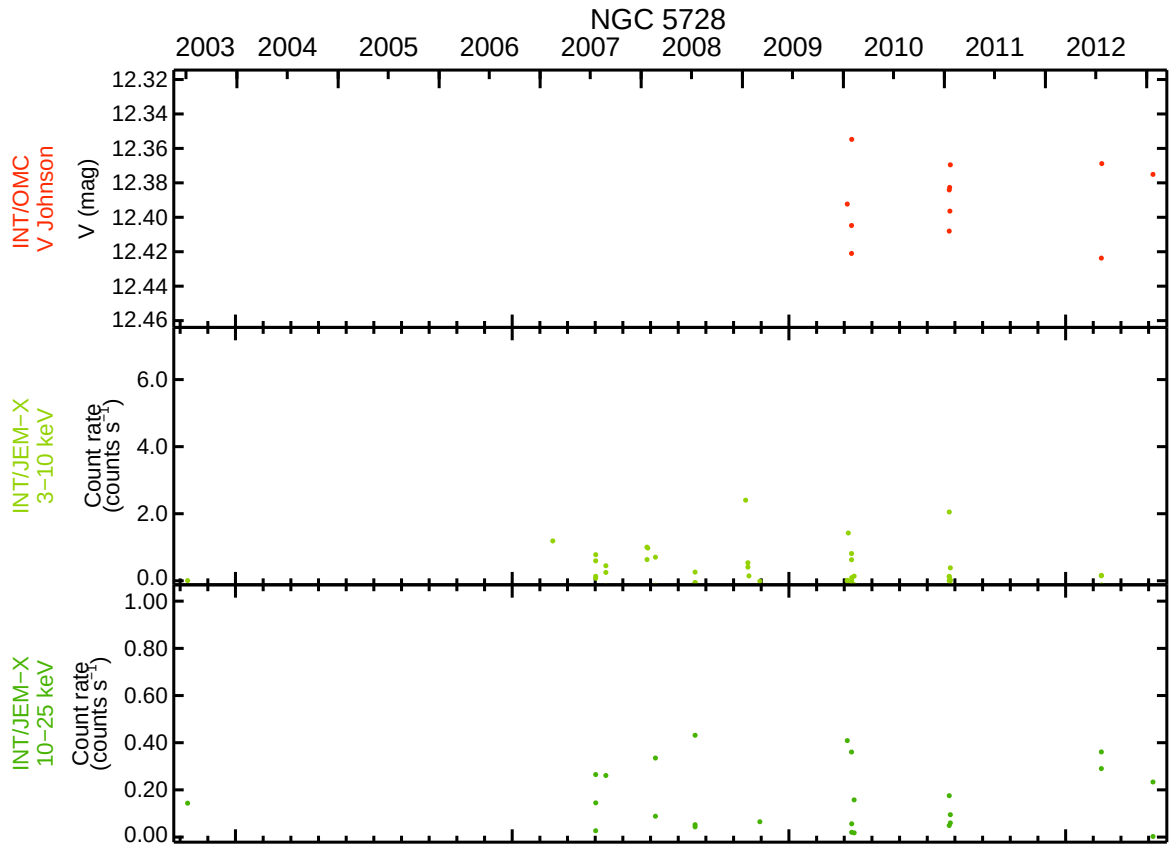
NGC 5728
2003
2004
2005
2006
2007
2008
2009
2010
2011
2012
INT/OMC
V Johnson
V (mag)
12.32
12.34
12.36
12.38
12.40
12.42
12.44
12.46
INT/JEM−X
3−10 keV
Count rate
(counts s−1)
6.0
4.0
2.0
0.0
INT/JEM−X
10−25 keV
Count rate
(counts s−1)
1.00
0.80
0.60
0.40
0.20
0.00

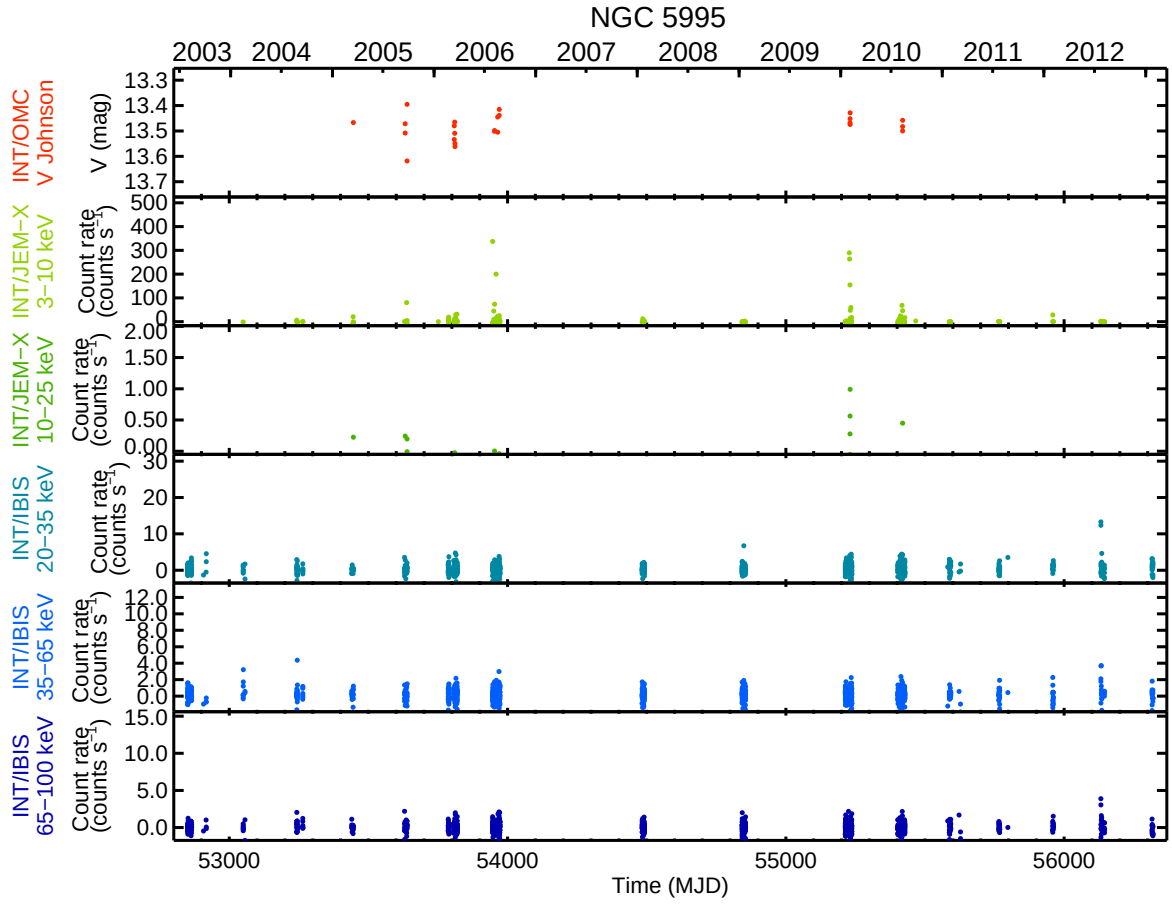
NGC 5995
2003
2004
2005
2006
2007
2008
2009
2010
2011
2012
INT/OMC
V Johnson
V (mag)
13.3
13.4
13.5
13.6
13.7
INT/JEM−X
3−10 keV
Count rate
(counts s−1)
500
400
300
200
100
0
INT/JEM−X
10−25 keV
Count rate
(counts s−1)
2.00
1.50
1.00
0.50
0.00
INT/IBIS
20−35 keV
Count rate
(counts s−1)
30
20
10
0
INT/IBIS
35−65 keV
Count rate
(counts s−1)
12.0
10.0
8.0
6.0
4.0
2.0
0.0
INT/IBIS
65−100 keV
Count rate
(counts s−1)
15.0
10.0
5.0
0.0
53000
54000
55000
56000
Time (MJD)

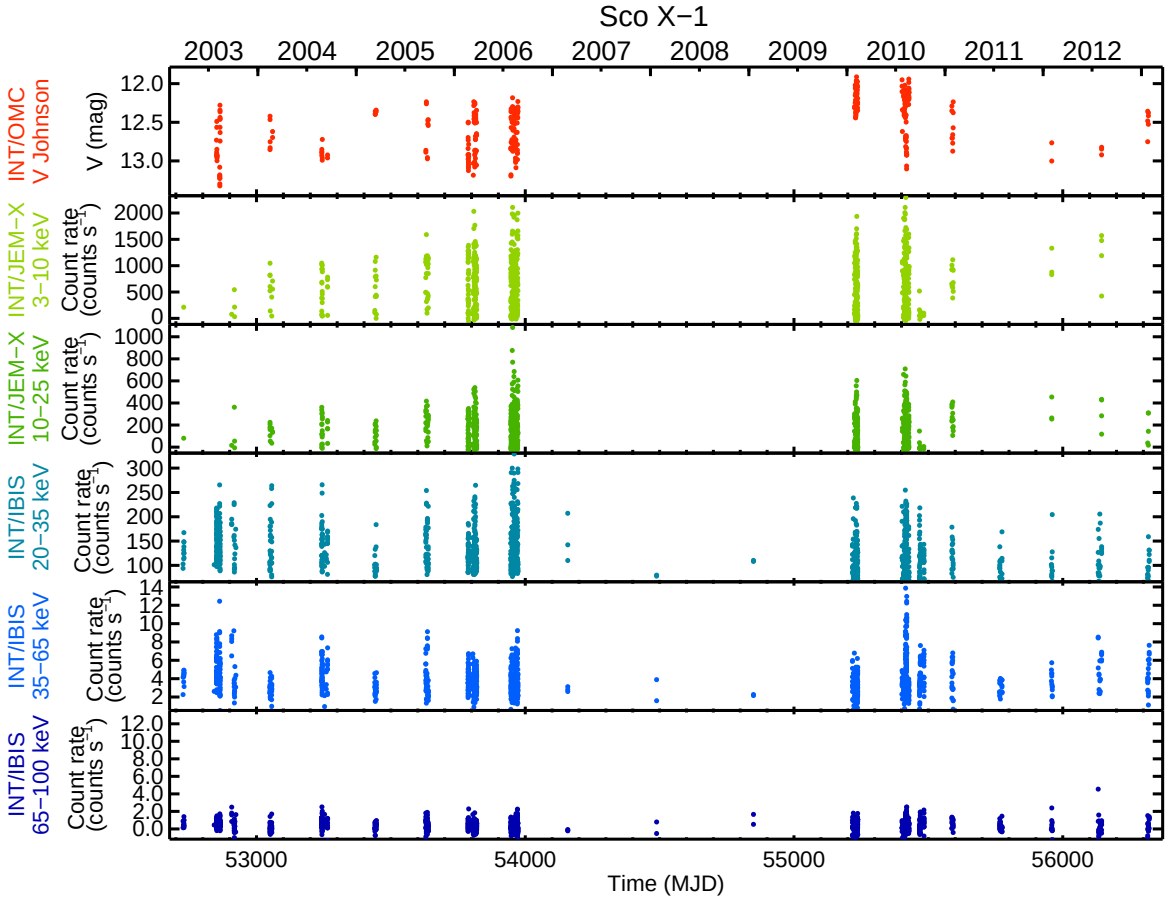
Sco X−1
2003
2004
2005
2006
2007
2008
2009
2010
2011
2012
INT/OMC V Johnson
V (mag)
INT/JEM−X 3−10 keV
INT/JEM−X 10−25 keV
INT/IBIS 20−35 keV
INT/IBIS 35−65 keV
INT/IBIS 65−100 keV
Count rate (counts s−1)
53000
54000
55000
56000
Time (MJD)

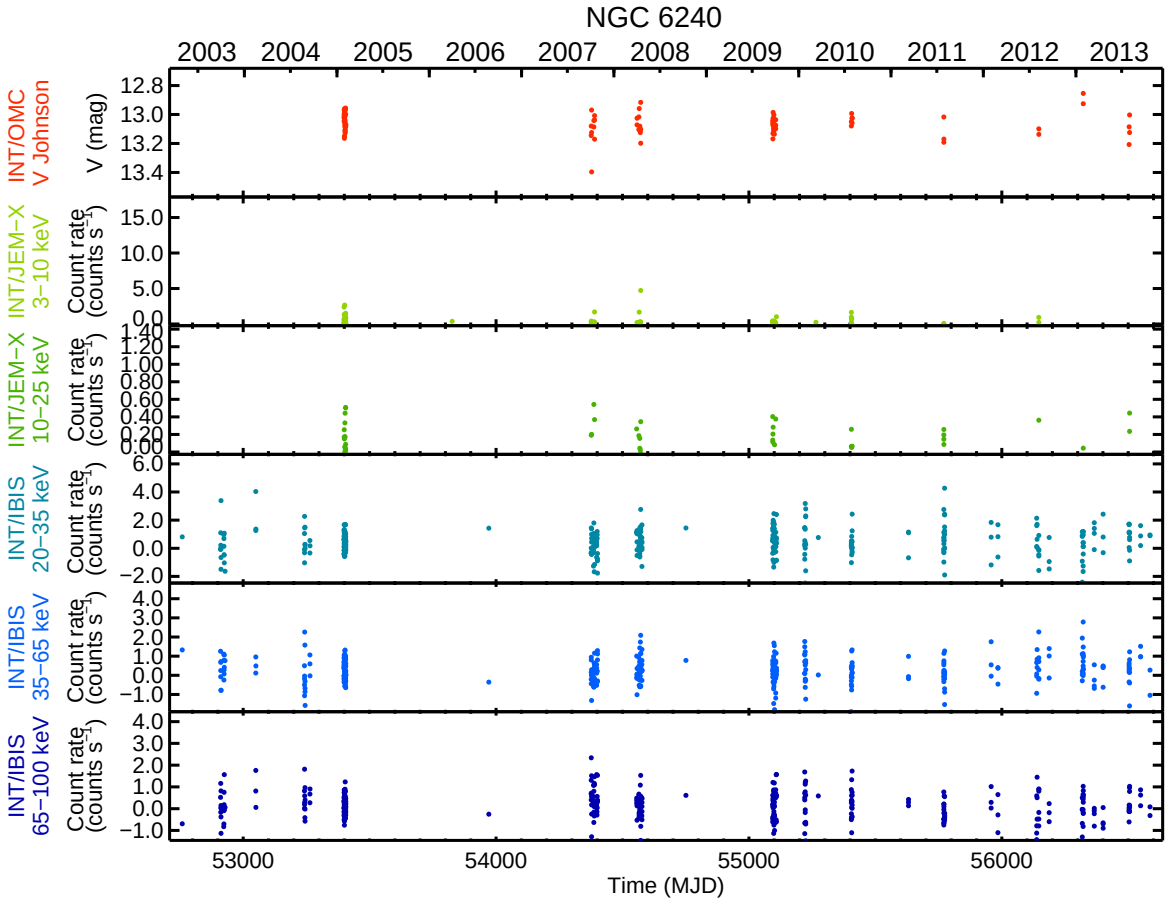
NGC 6240
2003
2004
2005
2006
2007
2008
2009
2010
2011
2012
2013
INT/OMC V Johnson
V (mag)
INT/JEM−X 3−10 keV
INT/JEM−X 10−25 keV
INT/IBIS 20−35 keV
INT/IBIS 35−65 keV
INT/IBIS 65−100 keV
Count rate (counts s−1)
53000
54000
55000
56000
Time (MJD)

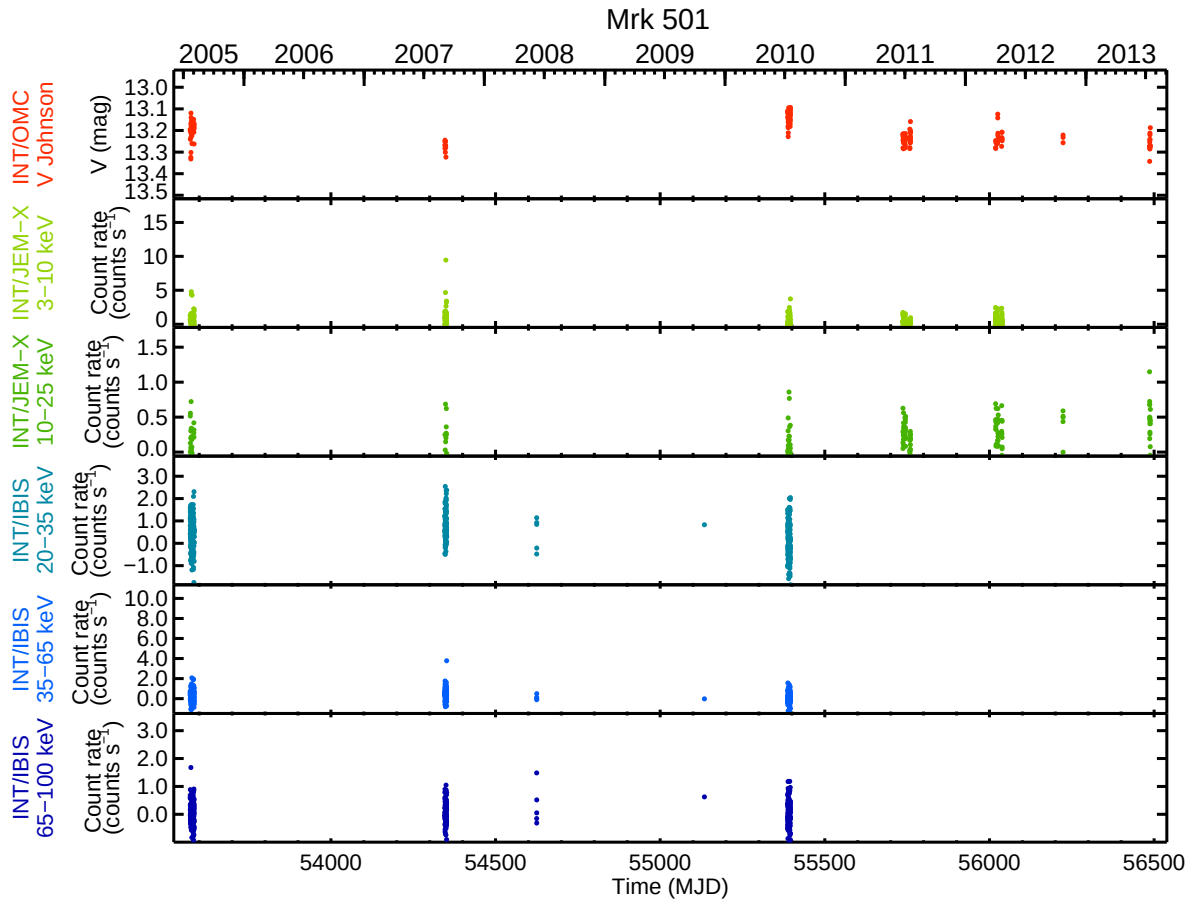
Mrk 501
2005
2006
2007
2008
2009
2010
2011
2012
2013
INT/OMC
V Johnson
V (mag)
INT/JEM−X
3−10 keV
INT/JEM−X
10−25 keV
INT/IBIS
20−35 keV
INT/IBIS
35−65 keV
INT/IBIS
65−100 keV
Count rate (counts s−1)
54000
54500
55000
55500
56000
56500
Time (MJD)

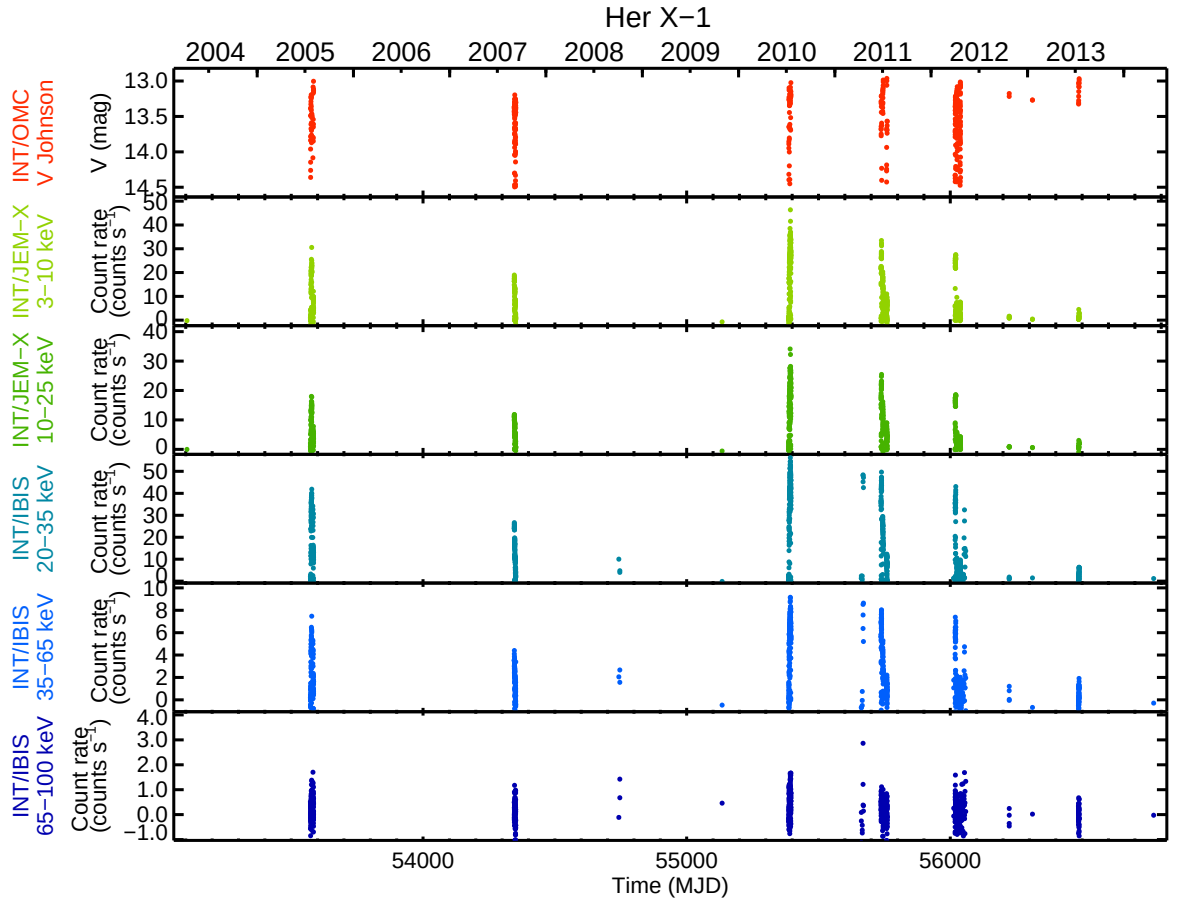
Her X−1
2004
2005
2006
2007
2008
2009
2010
2011
2012
2013
INT/OMC
V Johnson
V (mag)
INT/JEM−X
3−10 keV
INT/JEM−X
10−25 keV
INT/IBIS
20−35 keV
INT/IBIS
35−65 keV
INT/IBIS
65−100 keV
Count rate (counts s−1)
54000
55000
56000
Time (MJD)

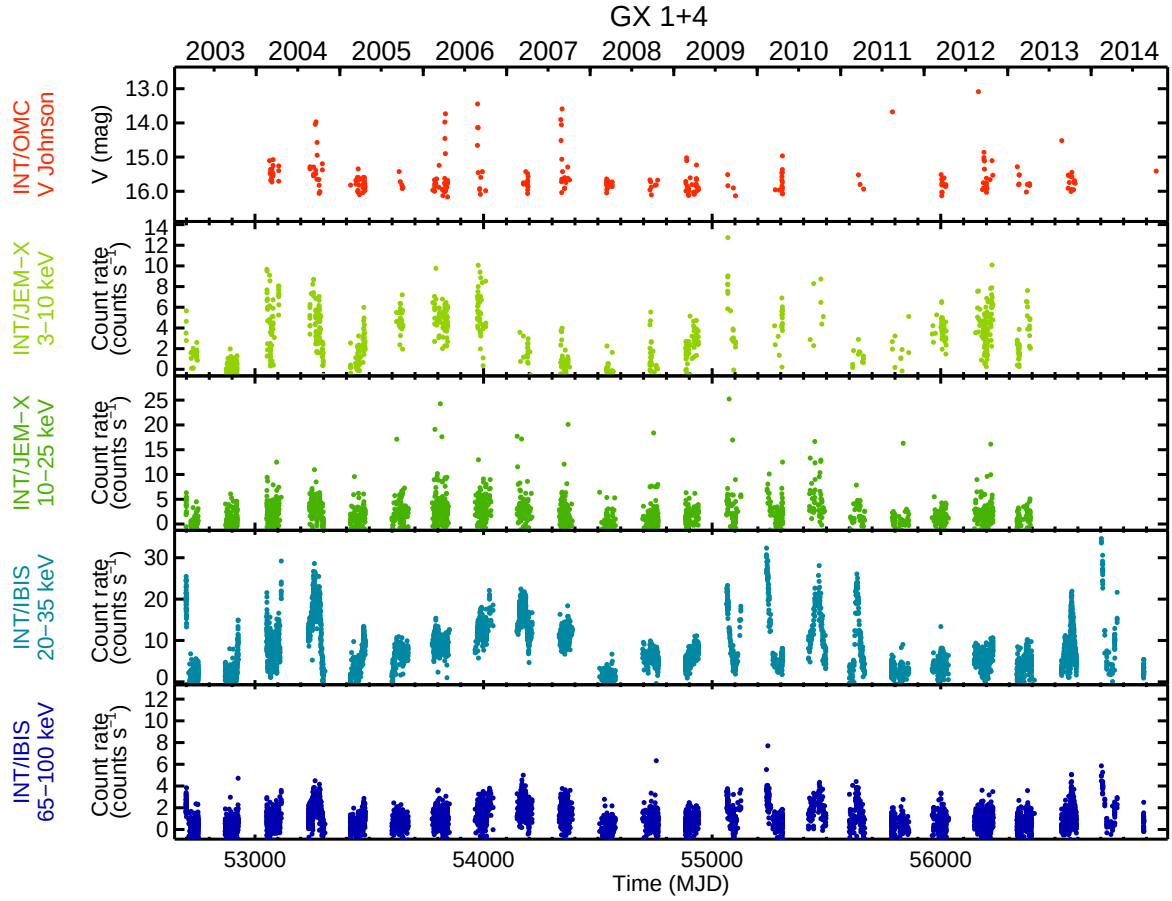
GX 1+4
2003 2004 2005 2006 2007 2008 2009 2010 2011 2012 2013 2014
INT/OMC V Johnson
V (mag)
INT/JEM−X 3−10 keV
INT/JEM−X 10−25 keV
INT/IBIS 20−35 keV
INT/IBIS 65−100 keV
Count rate (counts s−1)
53000 54000 55000 56000
Time (MJD)

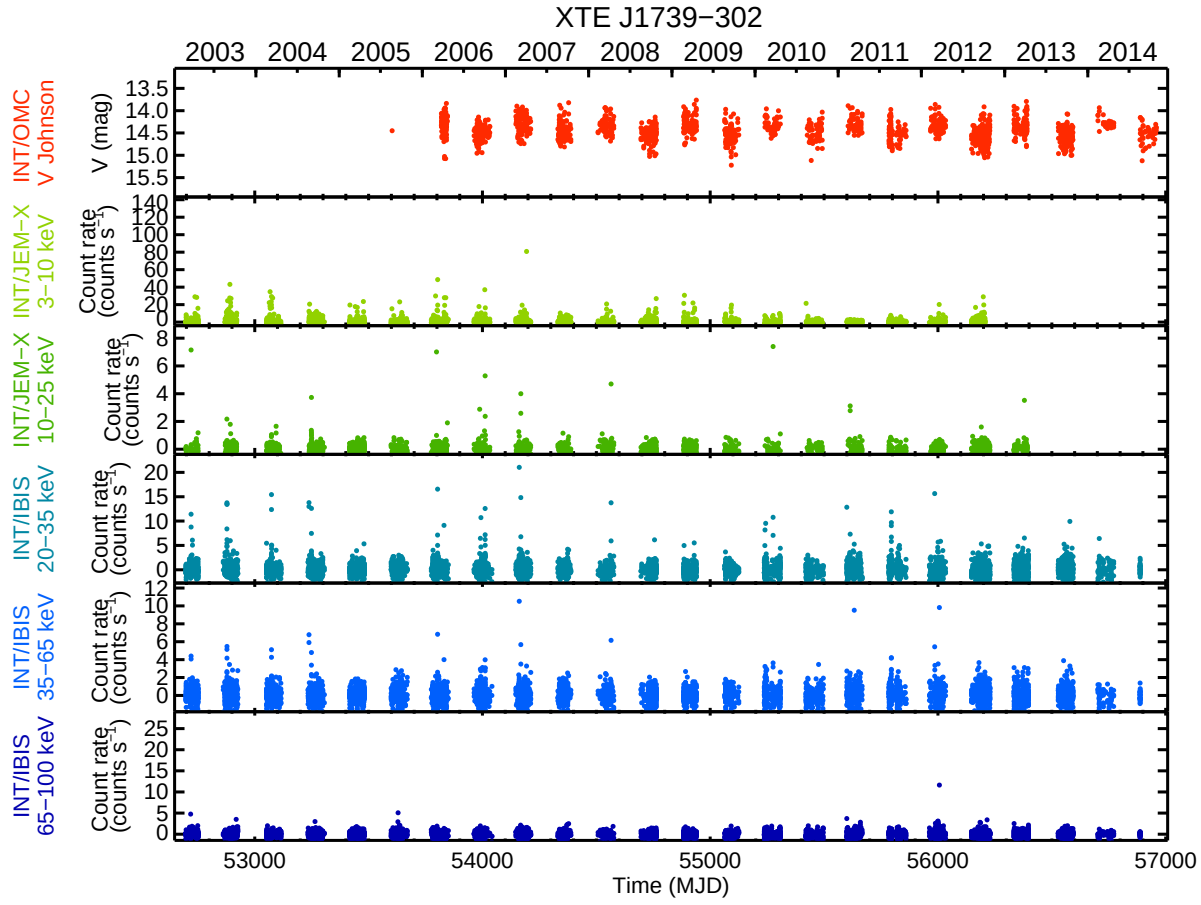
XTE J1739−302
2003 2004 2005 2006 2007 2008 2009 2010 2011 2012 2013 2014
INT/OMC V Johnson
V (mag)
INT/JEM−X 3−10 keV
INT/JEM−X 10−25 keV
INT/IBIS 20−35 keV
INT/IBIS 35−65 keV
INT/IBIS 65−100 keV
Count rate (counts s−1)
53000 54000 55000 56000 57000
Time (MJD)

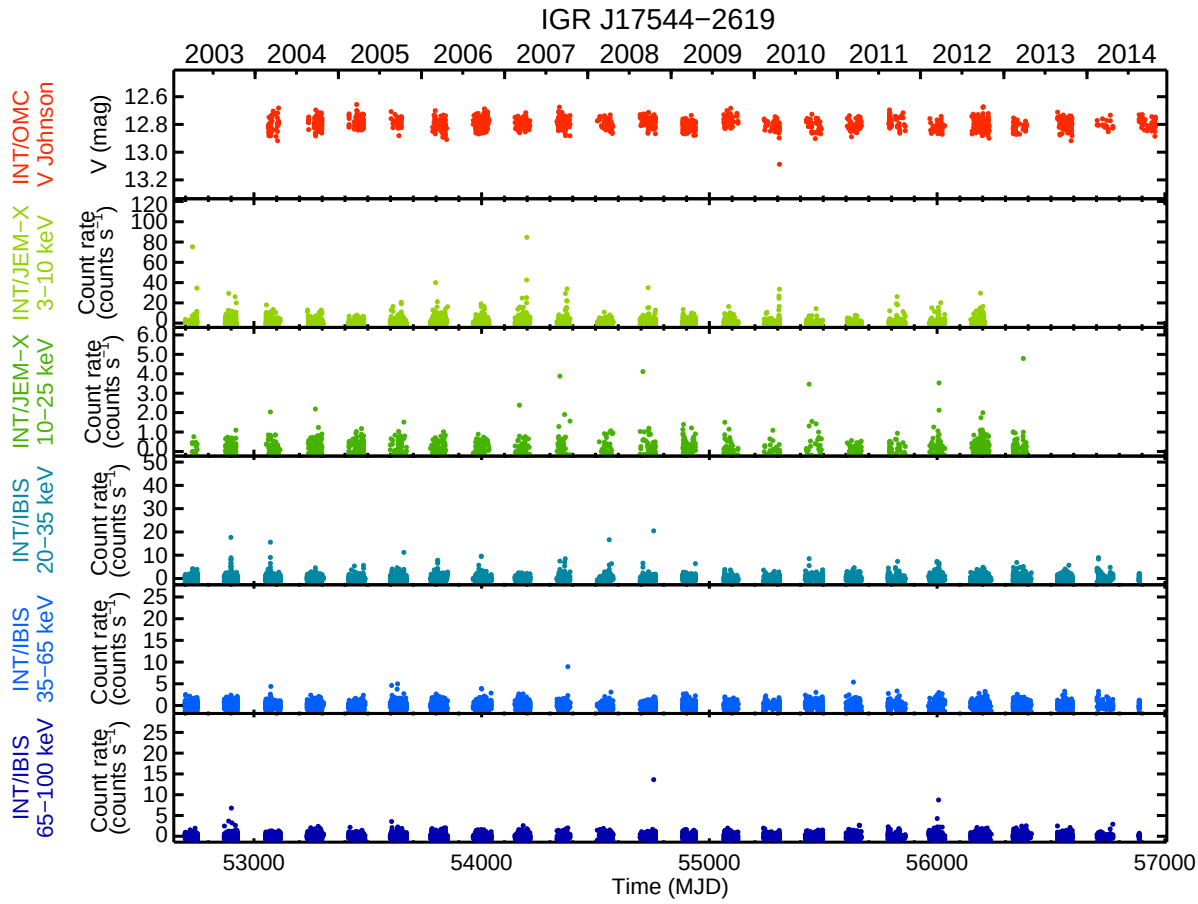
IGR J17544−2619
2003 2004 2005 2006 2007 2008 2009 2010 2011 2012 2013 2014
INT/OMC V Johnson
V (mag)
INT/JEM−X 3−10 keV
INT/JEM−X 10−25 keV
INT/IBIS 20−35 keV
INT/IBIS 35−65 keV
INT/IBIS 65−100 keV
Count rate (counts s−1)
53000 54000 55000 56000 57000
Time (MJD)

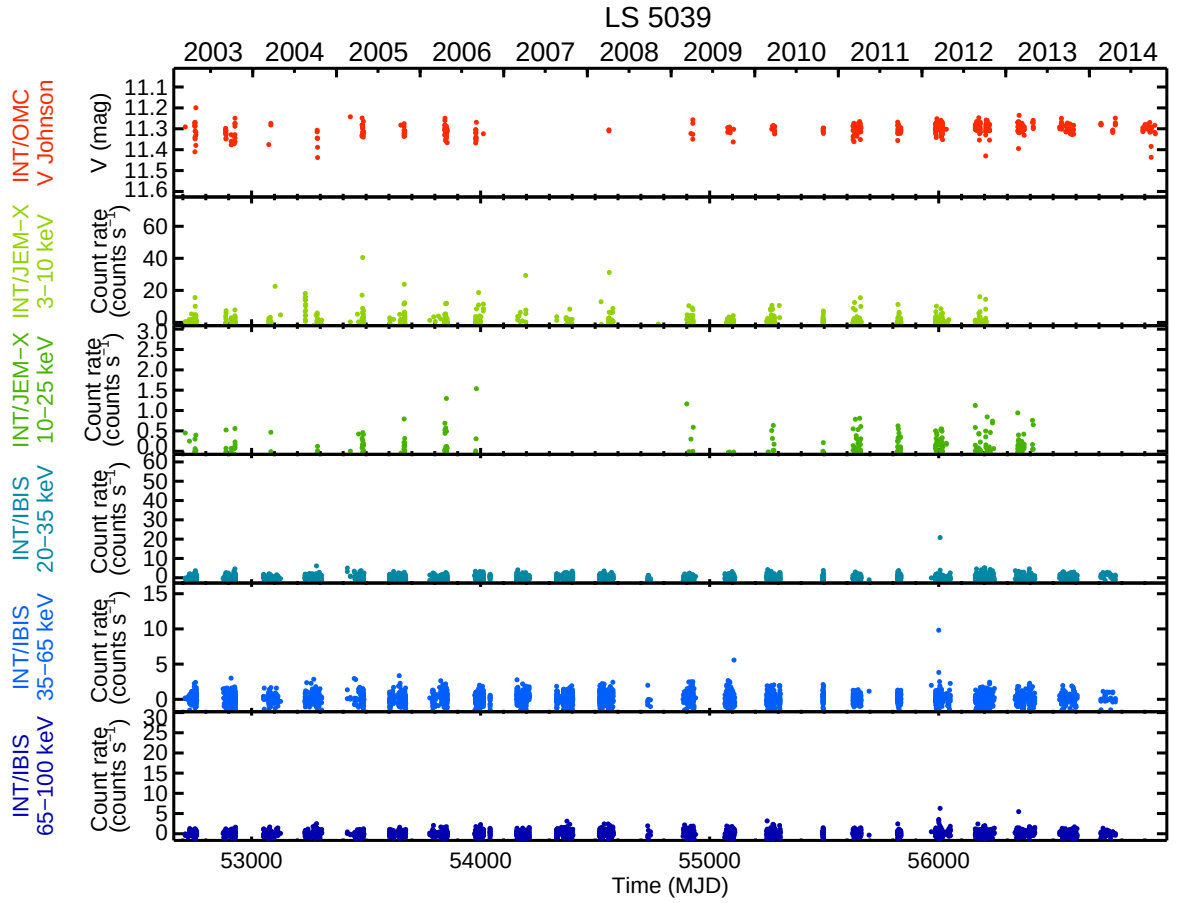
LS 5039
2003 2004 2005 2006 2007 2008 2009 2010 2011 2012 2013 2014
INT/OMC V Johnson
V (mag)
INT/JEM−X 3−10 keV
INT/JEM−X 10−25 keV
INT/IBIS 20−35 keV
INT/IBIS 35−65 keV
INT/IBIS 65−100 keV
Count rate (counts s−1)
53000 54000 55000 56000
Time (MJD)

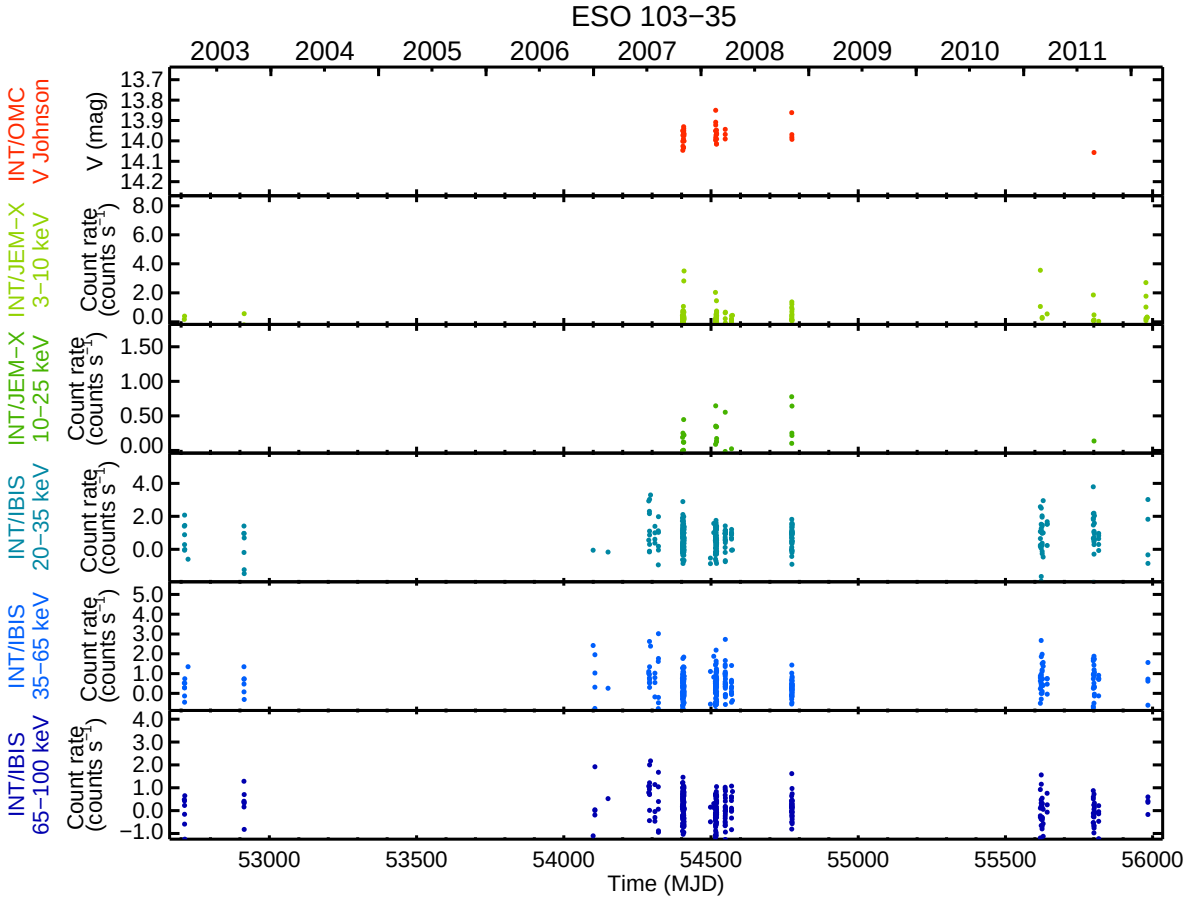
ESO 103−35
2003
2004
2005
2006
2007
2008
2009
2010
2011
INT/OMC V Johnson
V (mag)
INT/JEM−X 3−10 keV
INT/JEM−X 10−25 keV
INT/IBIS 20−35 keV
INT/IBIS 35−65 keV
INT/IBIS 65−100 keV
Count rate (counts s−1)
53000
53500
54000
54500
55000
55500
56000
Time (MJD)

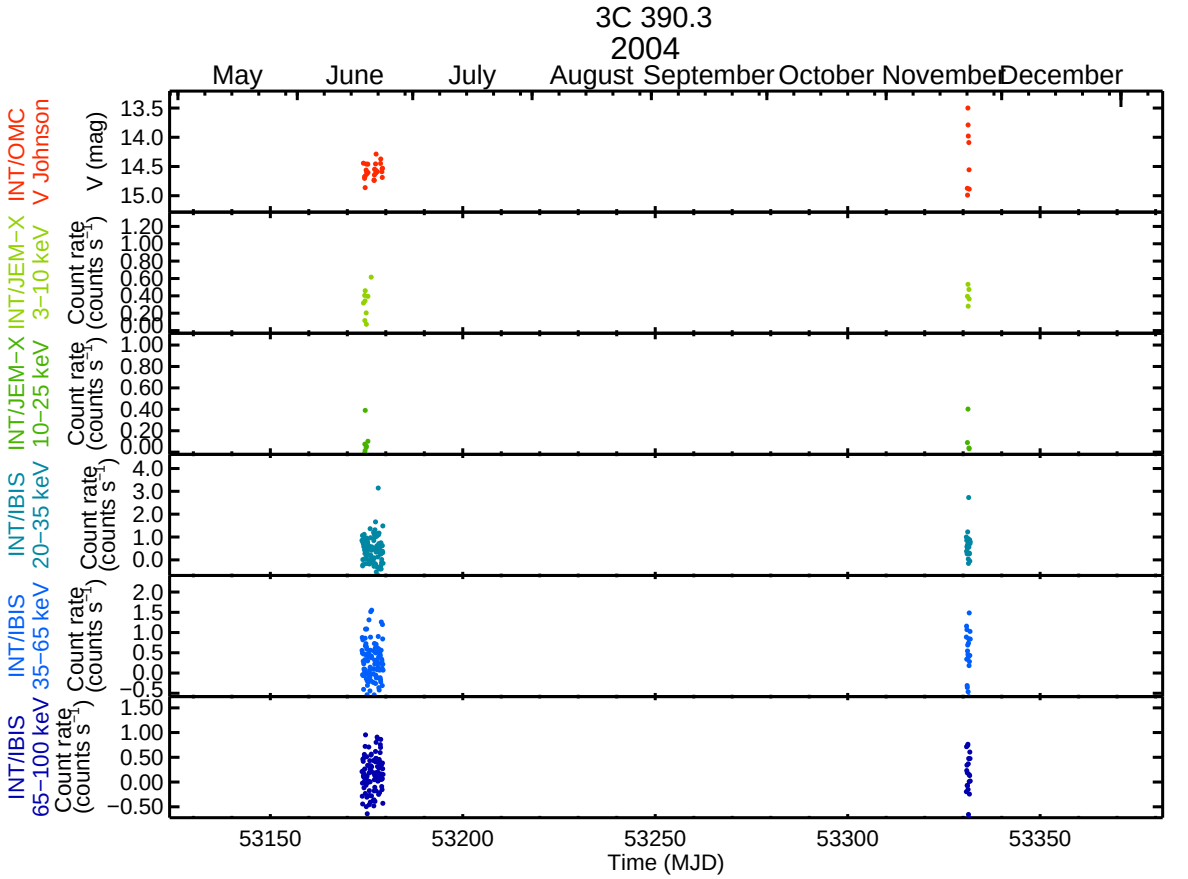
3C 390.3
2004
May
June
July
August
September
October
November
December
INT/OMC V Johnson
V (mag)
INT/JEM−X 3−10 keV
INT/JEM−X 10−25 keV
INT/IBIS 20−35 keV
INT/IBIS 35−65 keV
INT/IBIS 65−100 keV
Count rate (counts s−1)
53150
53200
53250
53300
53350
Time (MJD)

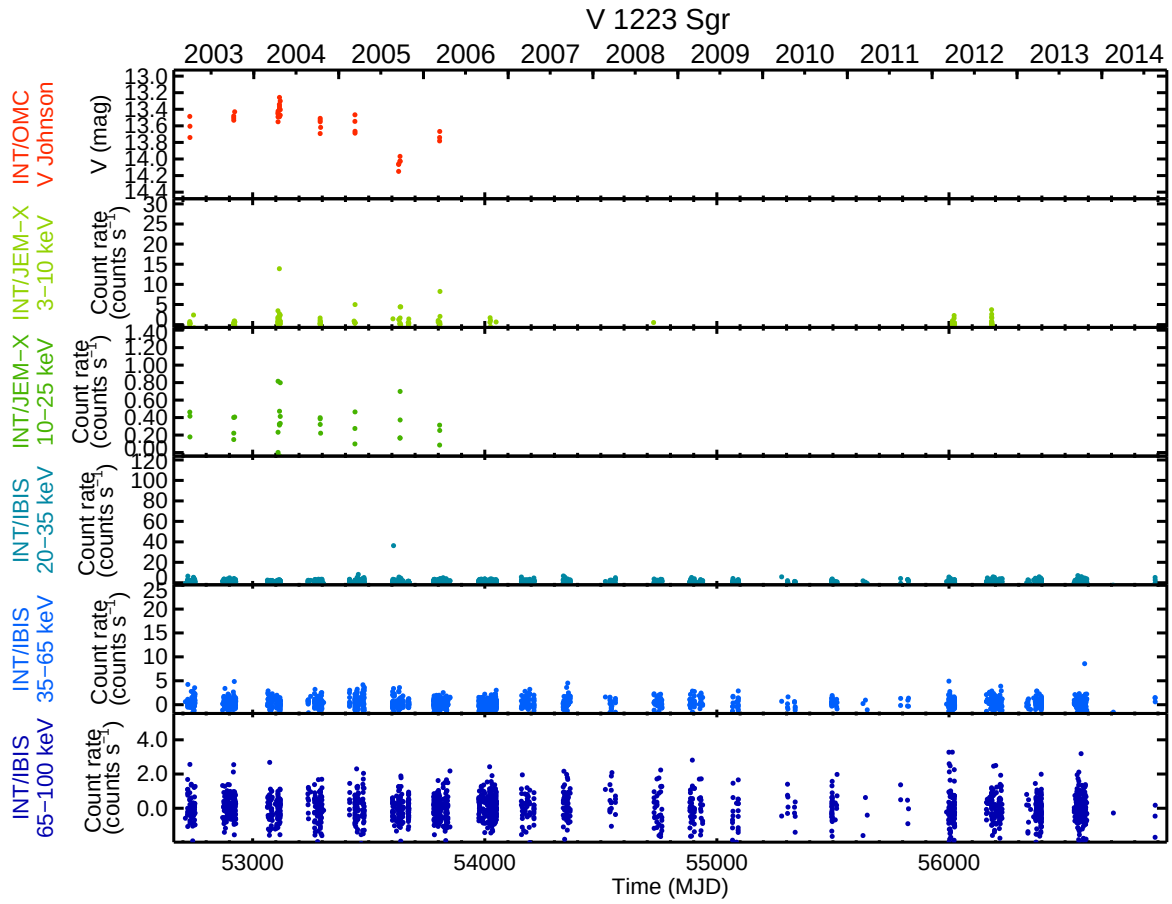
V 1223 Sgr
2003 2004 2005 2006 2007 2008 2009 2010 2011 2012 2013 2014
INT/OMC V Johnson
V (mag)
INT/JEM−X 3−10 keV
INT/JEM−X 10−25 keV
INT/IBIS 20−35 keV
INT/IBIS 35−65 keV
INT/IBIS 65−100 keV
Count rate (counts s−1)
53000 54000 55000 56000
Time (MJD)

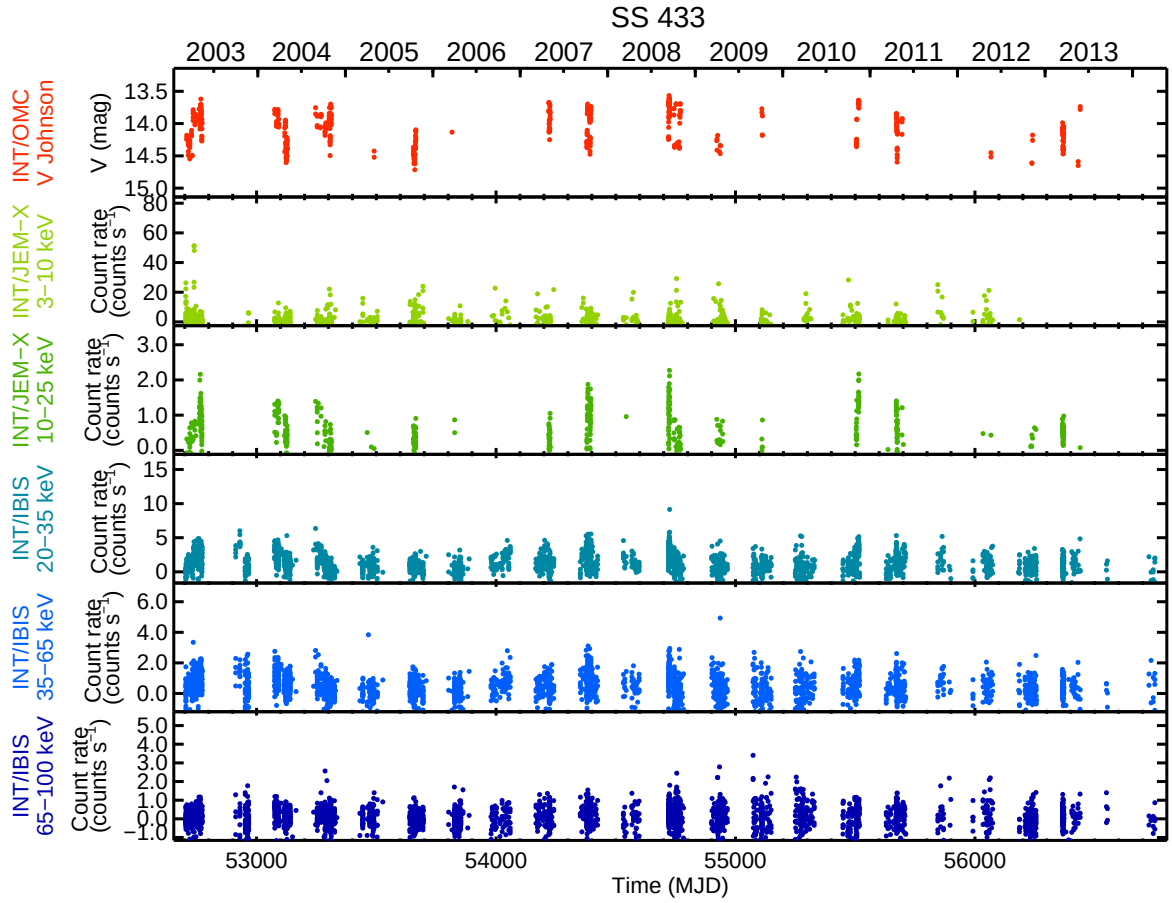
SS 433
2003 2004 2005 2006 2007 2008 2009 2010 2011 2012 2013
INT/OMC V Johnson
V (mag)
INT/JEM−X 3−10 keV
INT/JEM−X 10−25 keV
INT/IBIS 20−35 keV
INT/IBIS 35−65 keV
INT/IBIS 65−100 keV
Count rate (counts s−1)
53000 54000 55000 56000
Time (MJD)

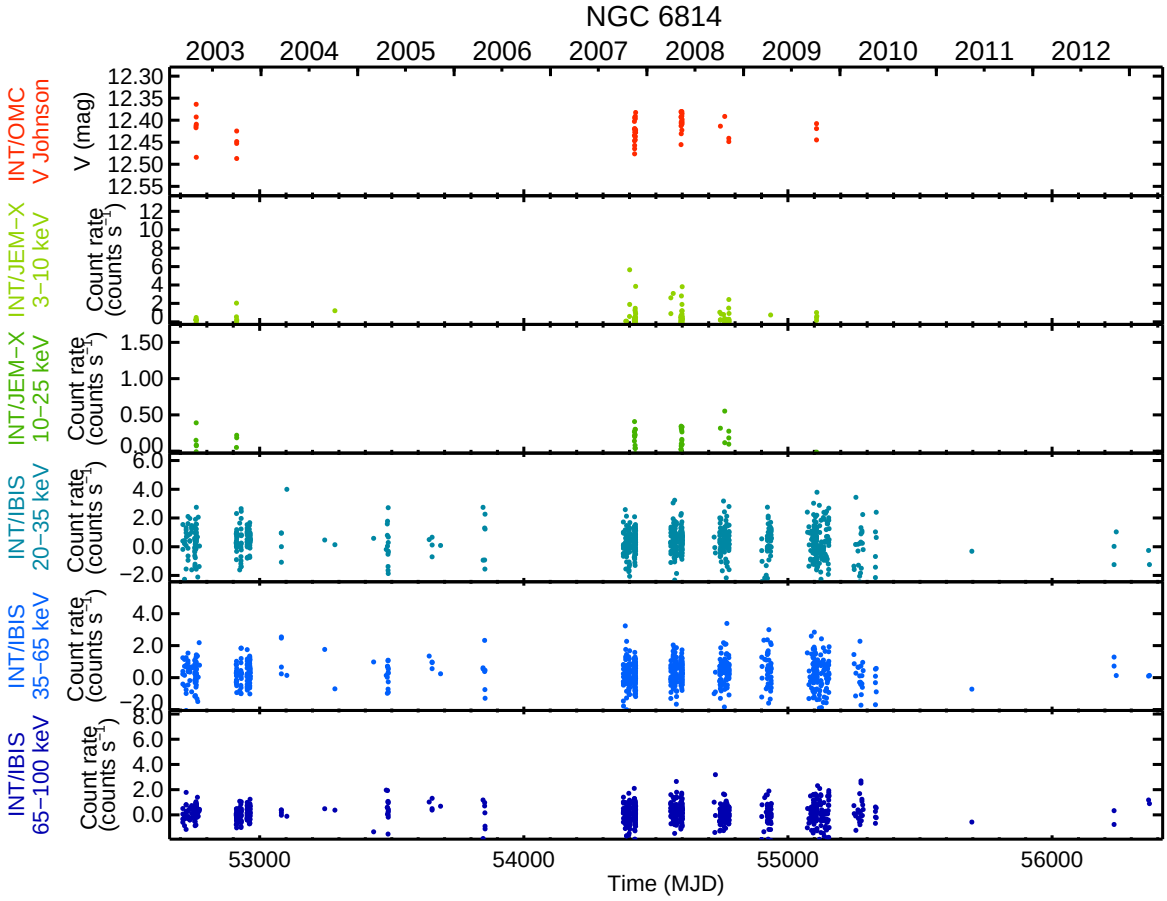
NGC 6814
2003
2004
2005
2006
2007
2008
2009
2010
2011
2012
INT/OMC V Johnson
V (mag)
INT/JEM−X 3−10 keV
INT/JEM−X 10−25 keV
INT/IBIS 20−35 keV
INT/IBIS 35−65 keV
INT/IBIS 65−100 keV
Count rate (counts s−1)
53000
54000
55000
56000
Time (MJD)

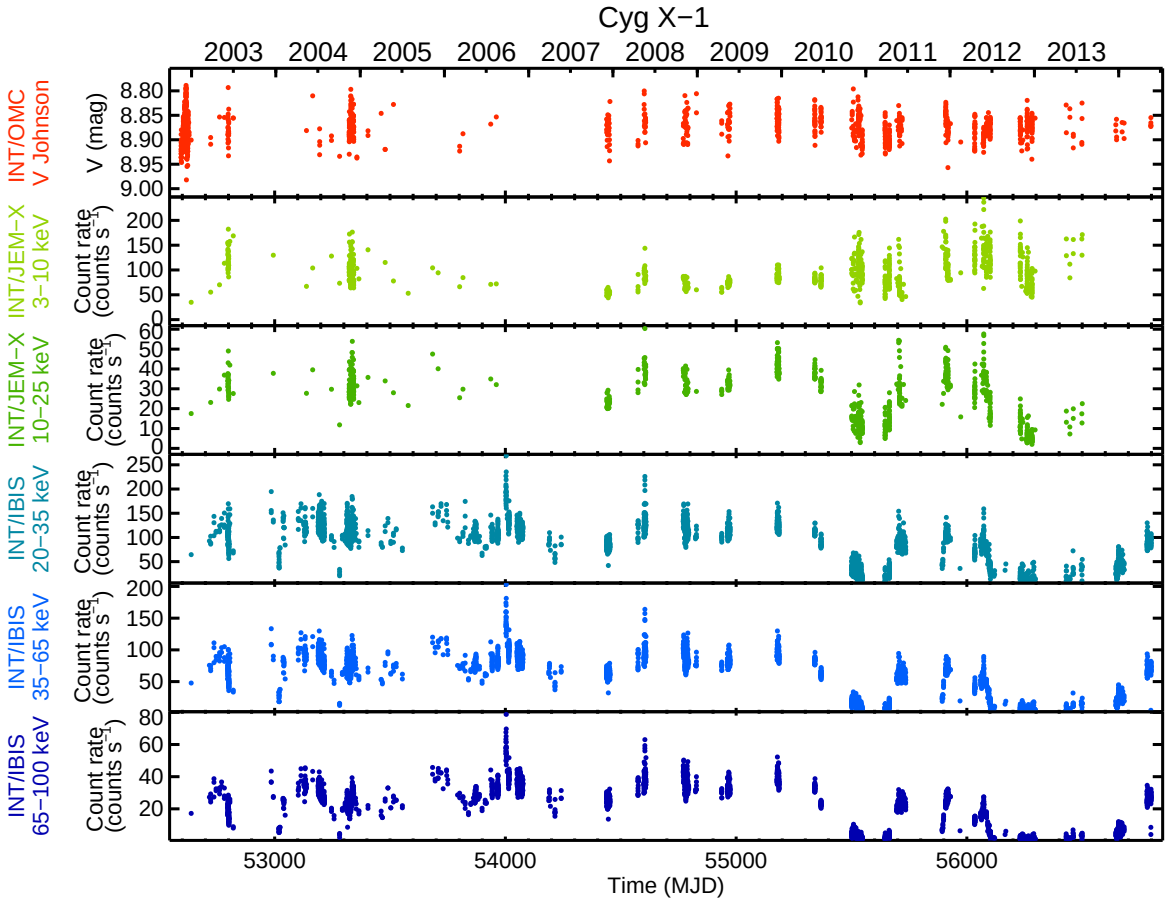
Cyg X−1
2003
2004
2005
2006
2007
2008
2009
2010
2011
2012
2013
INT/OMC V Johnson
V (mag)
INT/JEM−X 3−10 keV
INT/JEM−X 10−25 keV
INT/IBIS 20−35 keV
INT/IBIS 35−65 keV
INT/IBIS 65−100 keV
Count rate (counts s−1)
53000
54000
55000
56000
Time (MJD)

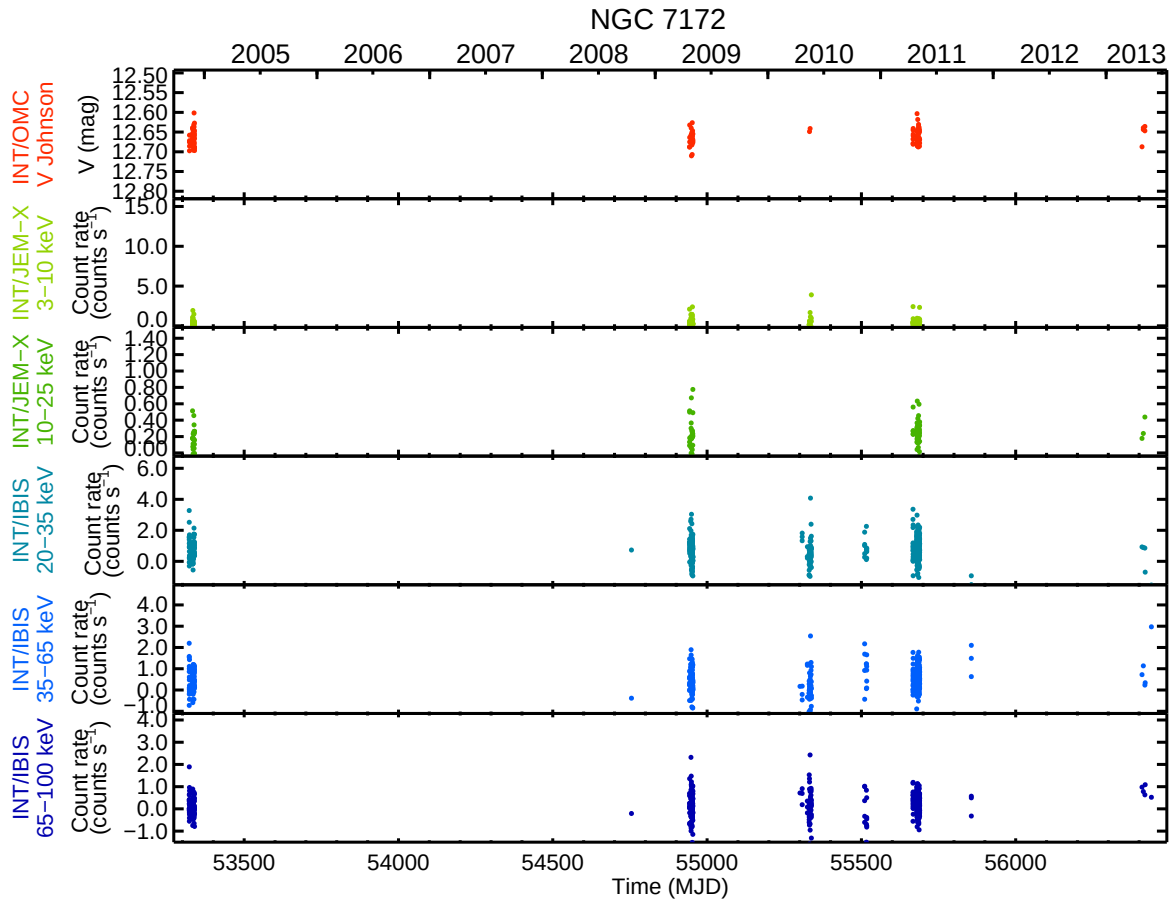
NGC 7172
2005
2006
2007
2008
2009
2010
2011
2012
2013
INT/OMC
V Johnson
V (mag)
INT/JEM−X
3−10 keV
INT/JEM−X
10−25 keV
INT/IBIS
20−35 keV
INT/IBIS
35−65 keV
INT/IBIS
65−100 keV
Count rate (counts s−1)
53500
54000
54500
55000
55500
56000
Time (MJD)

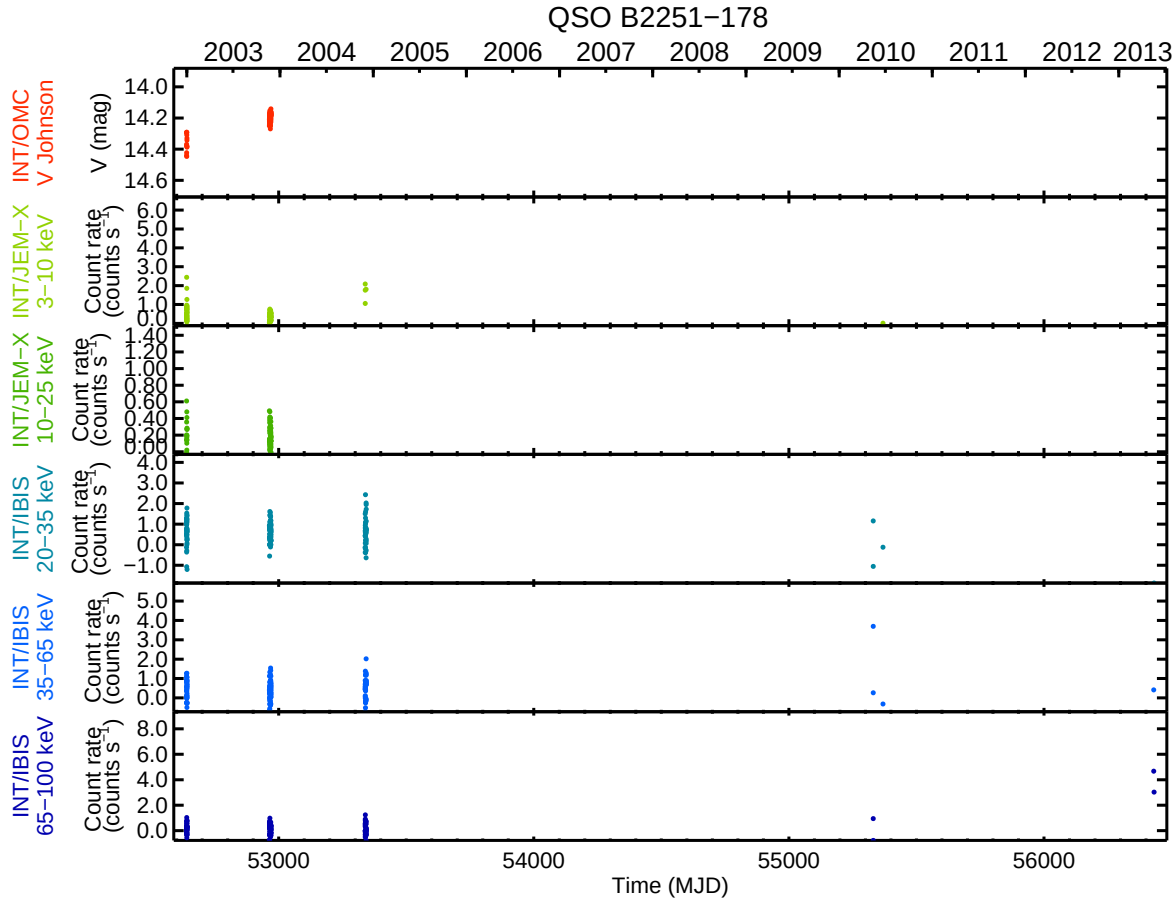
QSO B2251−178
2003
2004
2005
2006
2007
2008
2009
2010
2011
2012
2013
INT/OMC
V Johnson
V (mag)
INT/JEM−X
3−10 keV
INT/JEM−X
10−25 keV
INT/IBIS
20−35 keV
INT/IBIS
35−65 keV
INT/IBIS
65−100 keV
Count rate (counts s−1)
53000
54000
55000
56000
Time (MJD)

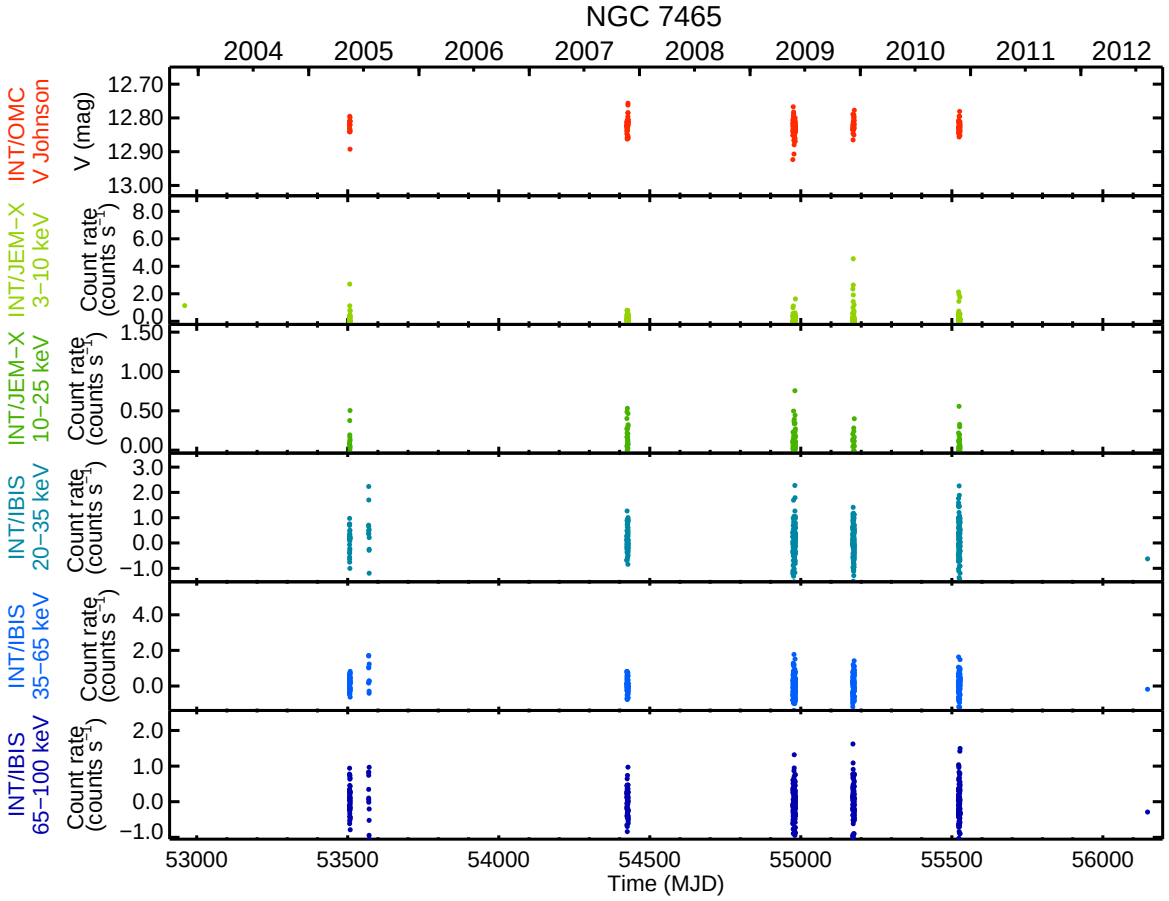
NGC 7465
2004
2005
2006
2007
2008
2009
2010
2011
2012
INT/OMC V Johnson
V (mag)
12.70
12.80
12.90
13.00
INT/JEM−X 3−10 keV
Count rate (counts s⁻¹)
8.0
6.0
4.0
2.0
0.0
INT/JEM−X 10−25 keV
Count rate (counts s⁻¹)
1.50
1.00
0.50
0.00
INT/IBIS 20−35 keV
Count rate (counts s⁻¹)
3.0
2.0
1.0
0.0
−1.0
INT/IBIS 35−65 keV
Count rate (counts s⁻¹)
4.0
2.0
0.0
INT/IBIS 65−100 keV
Count rate (counts s⁻¹)
2.0
1.0
0.0
−1.0
53000
53500
54000
54500
55000
55500
56000
Time (MJD)

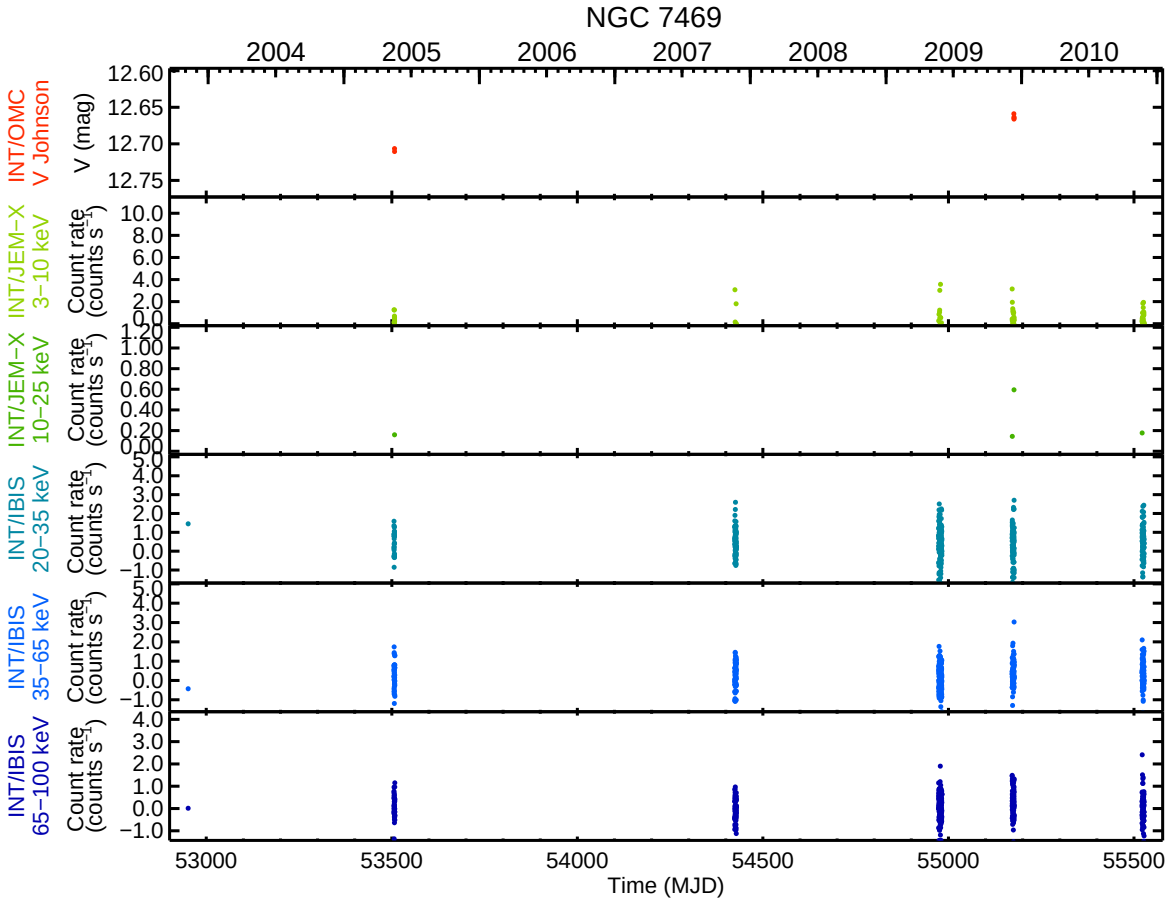
NGC 7469
2004
2005
2006
2007
2008
2009
2010
INT/OMC V Johnson
V (mag)
12.60
12.65
12.70
12.75
INT/JEM−X 3−10 keV
Count rate (counts s⁻¹)
10.0
8.0
6.0
4.0
2.0
0.0
INT/JEM−X 10−25 keV
Count rate (counts s⁻¹)
1.20
1.00
0.80
0.60
0.40
0.20
0.00
INT/IBIS 20−35 keV
Count rate (counts s⁻¹)
5.0
4.0
3.0
2.0
1.0
0.0
−1.0
INT/IBIS 35−65 keV
Count rate (counts s⁻¹)
5.0
4.0
3.0
2.0
1.0
0.0
−1.0
INT/IBIS 65−100 keV
Count rate (counts s⁻¹)
4.0
3.0
2.0
1.0
0.0
−1.0
53000
53500
54000
54500
55000
55500
Time (MJD)

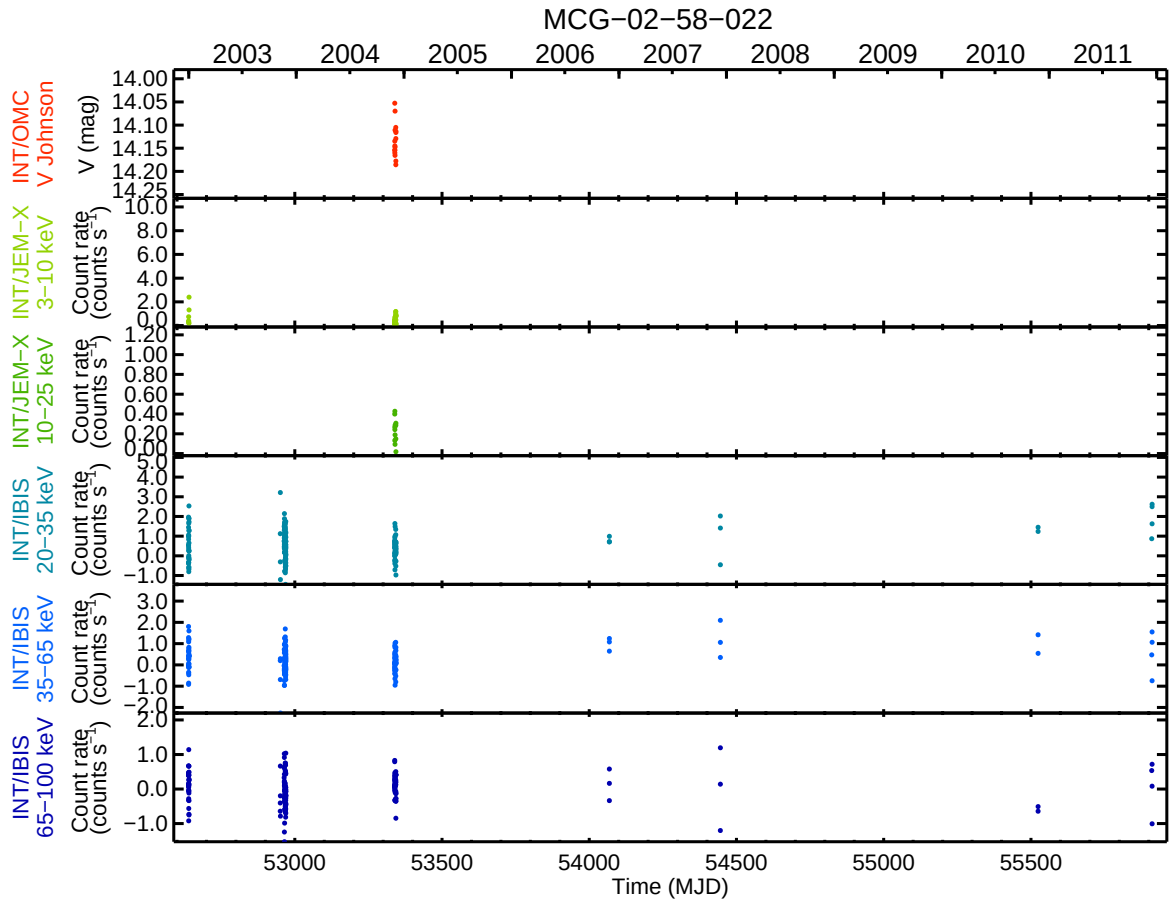
MCG−02−58−022
2003
2004
2005
2006
2007
2008
2009
2010
2011
INT/OMC
V Johnson
V (mag)
14.00
14.05
14.10
14.15
14.20
14.25
INT/JEM−X
3−10 keV
Count rate (counts s−1)
10.0
8.0
6.0
4.0
2.0
0.0
INT/JEM−X
10−25 keV
Count rate (counts s−1)
1.20
1.00
0.80
0.60
0.40
0.20
0.00
INT/IBIS
20−35 keV
Count rate (counts s−1)
5.0
4.0
3.0
2.0
1.0
0.0
−1.0
INT/IBIS
35−65 keV
Count rate (counts s−1)
3.0
2.0
1.0
0.0
−1.0
−2.0
INT/IBIS
65−100 keV
Count rate (counts s−1)
2.0
1.0
0.0
−1.0
53000
53500
54000
54500
55000
55500
Time (MJD)